TECHNICAL PAPERS

(Contents Continued)

ANNOUNCEMENTS

The 1991 IGTI Scholar Lecture

Robert Edward Mayle

Rensselaer Polytechnic Institute,
Troy, NY 12180

The Role of Laminar-Turbulent Transition in Gas Turbine Engines

A critical study of laminar–turbulent transition phenomena and their role in aerodynamics and heat transfer in modern and future gas turbine engines is presented. In order to develop a coherent view of the subject, a current look at transition phenomena from both a theoretical and experimental standpoint are provided and a comprehensive state-of-the-art account of transitional phenomena in the engine's throughflow components given. The impact of transitional flow on engine design is discussed and suggestions for future research and developmental work provided.

Introduction

1928—Whittle publishes theory on the jet engine. 1935— von Ohain begins jet engine development. 1939—First successful flight of a jet plane. In 1989, fifty years later, 15,357[§] gas turbine engines were manufactured.

Since their introduction in 1939, gas turbine engines have dramatically advanced from machines that merely work to one of the most compact conventional power sources presently available. They are fantastic machines, containing up to a quarter of a million parts, rotating at 10,000 rpm while holding tolerances to within 0.25 mm at a radius of half a meter. They operate up to 30 atm at 1680°C, provide power up to 150 MW, and are widely used on land, sea, and in the air. Although considered technically mature by many, gas turbine engine development continues, because increasing the engine's performance by only a few tenths of a percent, or simply maintaining the turbine cooling flow in face of the ever-increasing turbine inlet temperature, still provides large economic benefits.

Gas turbine engines may be grouped into three main categories depending on size: big, medium, and small. In general, these categories correspond respectively to engines used in power generation, large aircraft and medium power units, and small aircraft and land-based vehicles. Except for the small aircraft engines, which use centrifugal compressors, and the smaller vehicular engines, all are axial flow machines. Some dimensions and operating conditions of typical engines in each of these categories are provided in Table 1. The Reynolds

number presented in the last column was calculated using the turbine-inlet conditions, blade height, and throughflow velocity. Although calculated this way, it is quite representative of the airfoil-chord Reynolds number throughout the engine (see Fig. 1) except in the low-pressure turbine, where the chord Reynolds number can be almost a factor of ten lower. For aircraft engines operating at altitude the turbine inlet Reynolds number will be reduced to about one half those shown in the table.

Although the flow in gas turbines is highly turbulent and unsteady, the flow next to the surfaces may be either laminar or turbulent. A widely accepted rule-of-thumb is that this flow "transitions" from laminar to turbulent when the Reynolds number based on the streamwise distance along the surface is roughly[1] 350,000. Presumably then, from Table 1, one may suppose that boundary layer flows in any gas turbine engine are transitional and, in order to calculate the losses and heat transfer on various components in the engine, one must be able to predict boundary-layer development through transition. Although calculating transitional boundary layers is rou-

---

[1]This number varies greatly and is, indeed, one subject of this work.

Table 1

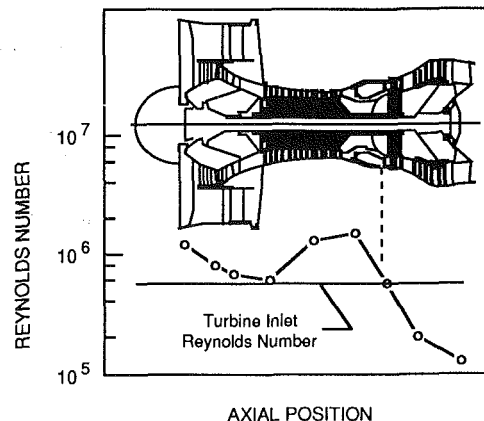|	Mean Turbine Diameter, m	Engine Core Air Flow, kg/s	Turbine Inlet Temperature, °C	Turbine Reynolds Number
Big	2.2	340	1370	820,000
Medium	0.9	120	1480	750,000
Small	0.2	15	1250	450,000

Fig. 1 Reynolds number variation through a medium-sized gas turbine engine (Hourmouziadis, 1989)

tine, it is well recognized that calculating transition accurately is another matter, particularly in gas turbines where the free-stream turbulence level is high and the pressure gradients are so diverse.

For small engines and engine components operating at low Reynolds numbers, the boundary layer has a tendency to remain laminar. This presents a difficult problem for the designer since the flow may (and in many cases does) separate before it becomes turbulent, particularly if the component must operate over a wide range of Reynolds numbers and angles of incidence. Under certain conditions, the flow does not reattach and large losses are incurred. This problem is well known to the designer of a low-pressure turbine, who, upon successfully designing a turbine for sea-level takeoff, discovers it operates 2–5 points below design at altitude. In short, designing low Reynolds number components where separation can occur is still an art that requires a better understanding of the transition process.

Purpose of the Present Study

Within the last few years, data from basic experiments on transition and new full- and large-scale compressor and turbine facilities together with back-to-back cascade tests, new high-frequency measurement systems, and modern computer calculation methods have provided a unique opportunity to understand the role of laminar–turbulent transition in gas turbine engines. However, much of the relevant information and ideas are either scattered or incomplete and await a critical review. In order to develop a coherent view of the subject, particularly in regard to its impact on gas turbine design, the current work was undertaken.

The following account is broken into three main parts. The first concerns a generalized description of transition, its various modes, and a description of each of their roles in gas turbine engines. In the second part, transition is examined from both a theoretical and experimental point of view. First, the concept of transition as a randomly intermittent laminar–turbulent flow is introduced and a brief description of intermittent flow theory is given. Second, both old and new experimental results, including correlations appropriate to gas turbines, are provided. Third, a theoretical development of periodic, unsteady transition is given. In the third and final part, a comprehensive, state-of-the-art account of the important transition phenomena in each of the throughflow components is presented. This is followed by some modern transitional flow design concepts and suggestions for future research work in transitional flows for gas turbines.

Part I—Transition; A General Discussion

In general, there are three important modes of transition. The first, and that most thought of when transition is considered, is called "natural" transition. This mode of transition begins with a weak instability in the laminar boundary layer as described first by Tollmien and Schlichting (see Schlichting, 1979) and proceeds through various stages of amplified instability to fully turbulent flow. The second mode, frequently called "bypass" transition following Morkovin (1969), is caused by large disturbances in the external flow (such as free-stream turbulence) and completely bypasses the Tollmien-Schlichting mode of instability. This is the common mode of transition in gas turbine engines. The third, for the sake of giving it a name, will be called "separated-flow" transition. Here, transition occurs in a separated laminar boundary layer and may or may not involve instability of the Tollmien-Schlichting type. This mode of transition also occurs in gas turbine engines, particularly in the compressors and low-pressure turbines.

In anticipation of a result to be presented later, Fig. 2 shows the topology of the different modes of transition in a Reynolds number–acceleration parameter plane. Here, the momentum thickness Reynolds number is that at the beginning of transition and is defined as $Re_{\theta t} = (U\theta/\nu)_t$. Likewise, the acceleration parameter, representing the effect of free-stream acceleration on the boundary layer, is that at the beginning of transition and is defined as $K_t = (\nu/U_t^2)(dU/dx)_t$. The lines of constant

--- Nomenclature ---

c = airfoil chord
c_p = specific heat, pressure coefficient
c_f = skin friction coefficient
D = leading edge diameter
Gö = Görtler number
h = heat transfer coefficient
I = intermittency function
k = thermal conductivity
k_s = sand grain roughness
K = acceleration parameter $= (\nu/U^2)dU/dx$
L = integral length scale of turbulence
M = mesh size; Mach number
n = turbulent spot production rate
$\hat{n}$ = dimensionless production rate $= n\nu^2/U_t^3$
Nu = Nusselt number
p = pressure
q_{xy} = heat flux
r = radius of surface curvature
Re = Reynolds number
St = Stanton number $= h/\rho c_p U$
t = time
t' = temperature fluctuation
T = temperature
Ta = Taylor's turbulence parameter

Tu = turbulence intensity, percent
u' = velocity fluctuation in x direction
U = velocity in x direction
v' = velocity fluctuation in y direction
V = velocity in y direction
x = surface coordinate in streamwise direction
y = coordinate normal to the surface
z = coordinate perpendicular to the x–y surface
γ = intermittency factor (probability flow is turbulent)
γ_h = thermal intermittency factor
δ = boundary layer thickness
θ = momentum thickness
λ_θ = pressure gradient parameter $= (\theta^2/\nu)dU/dx$
μ = viscosit
ν = kinematic viscosity
ρ = density
σ = turbulent spot propagation parameter
τ = wake-passing period
τ_{xy} = shear stress
ω = wake passing frequency

ω_r = reduced frequency $= \omega c/U$

Subscripts

c = chord
e = exit
i = incident
L = fully laminar
LT = length of transition
n = quantity related to the normal modes of transition (in contrast to the subscript w)
nt = nonturbulent
r = reattachment
s = separation
t = beginning of transition, $\gamma = 0$; turbulent (in contrast to the subscript nt)
T = end of transition, $\gamma = 0.99$; fully turbulent
w = quantity related to wake-induced transition
∞ = free-stream value
0 = surface value

Modifying Marks

$\overline{}$ = ensemble-averaged quantity
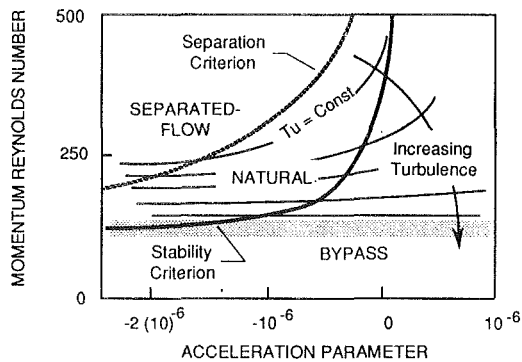$\tilde{}$ = time-averaged quantity

Fig. 2 Topology of the different modes of transition in a Reynolds number–acceleration parameter plane

turbulence level represent the value of the momentum thickness Reynolds number at which transition begins for that value of turbulence and acceleration. The line marked "Stability Criterion" is the line above which a Tollmien–Schlichting type of instability is possible. Above the line marked "Separation Criterion" (defined according to Thwaites, 1949, $Re_\theta^2 K = -0.082$), a laminar boundary layer will separate, which may in turn lead to a separated-flow transition. Presently, nothing is known as to how this criterion depends on turbulence level and therefore it is shown dotted.

In general, one may say that the turbulence level for all the throughflow components in a gas turbine engine, except the fan, is high. Recent ensemble-averaged measurements in compressor and turbine rigs show values of about 5 to 10 percent, except in the wakes, where values as high as 15 to 20 percent are found. The shaded region in Fig. 2 corresponds to the transition Reynolds numbers for turbulence levels between 5 and 10 percent. As a result, transition in gas turbine engines is of the bypass mode, except where the flow is highly decelerated or separated (off to the left in Fig. 2). In these cases, transition may occur in either a natural or bypass mode.

While transition in gas turbines is generally treated (and sometimes perceived) as a two-dimensional, "steady" phenomenon[2] proceeding in the direction from laminar to turbulent, it is actually much more complex. First, it is a stochastic, three-dimensional, unsteady process, which may proceed in either a forward (laminar to turbulent) or "reverse" direction. Second, since the periodic unsteady flows in a gas turbine can cause a "periodic unsteady" transition independent of any other mode, transition may occur by different modes at different locations on the same surface at the same time. In the following, each of the three transition modes, as well as the periodic-unsteady and reverse transition processes, is briefly discussed.

Modes of Transition

Natural Transition. A modern description of the natural transition process may be found from Schlichting (1979). Based on a number of theoretical considerations and experimental observations, it is presently known to involve several important stages. Briefly these are: (1) At a critical value of the momentum thickness Reynolds number the laminar boundary layer becomes susceptible to small disturbances and develops an instability in the form of a two-dimensional Tollmien–Schlichting wave. (2) The instability amplifies within the layer to a point where three-dimensional instabilities grow and develop into loop vortices with large fluctuations. (3) Finally, the highly fluctuating portions of the flow develop into turbulent spots,

which then grow and convect downstream within the laminar layer to coalesce eventually into a fully developed turbulent boundary layer.

While this mode of transition has been extensively studied in relation to the flow over aircraft wings where the incident turbulence level is low, little if any of the results are relevant to the gas turbine designer except those associated with the production and propagation of turbulent spots. In a highly decelerated flow, but at a low free-stream turbulence level, Walker and Gostelow (1990) have detected waves at the Tollmien–Schlichting frequency. It remains to be seen whether or not these instabilities occur in highly decelerated flows at the higher levels found in a gas turbine. To emphasize the effect of turbulence, it should be noted that the above rule-of-thumb for transition, i.e., $Re_{xt} \cong 350{,}000$, is for natural transition with low free-stream turbulence. The momentum thickness Reynolds number transition corresponding to this value is $Re_{\theta t} = 0.664\sqrt{Re_{xt}} = 400$. For transition in gas turbines, however, values of 100 for $Re_{\theta t}$ are not uncommon. This corresponds to $Re_{xt} = 25{,}000$ which is an order of magnitude less than that cited above.

Bypass Transition. For transition at high free-stream turbulence levels, the first and possibly second stages of the natural transition process are completely bypassed such that turbulent spots are directly produced within the boundary layer by the influence of the free-steam disturbances. In this case, linear stability theory is irrelevant and, as shown by Blair (1990) for transition in favorable pressure gradients, no Tollmien–Schlichting waves are found. Since the first stages are bypassed, a theory for this mode need only be concerned with the processes involved in the production, growth, and convection of turbulent spots. This theory was provided by Emmons (1951) and will be considered in more detail later.

Separated-Flow Transition. When a laminar boundary layer separates, transition may occur in the free-shear-layer-like flow near the surface. In this case, the flow may reattach as turbulent forming a laminar-separation/turbulent-reattachment "bubble" on the surface. Transition of this type can occur behind boundary layer trip wires and also as a result of laminar separation in an adverse pressure gradient. In gas turbines, separated-flow transition is common and may occur in an "overspeed" region near an airfoil's leading edge, on either the suction or pressure side, or both, and near the point of minimum pressure on the suction side.

The bubble length depends on the transition process within the free shear layer and, in general, may involve all of the stages listed above for natural transition. For the longer bubbles with low free-stream turbulence levels, much of the flow in the bubble is laminar and Tollmien–Schlichting instabilities have been detected (Gaster, 1969). Whether or not this is the case at higher turbulence levels is not known but, according to Fig. 2, it appears possible.

Since long bubbles produce large losses and large deviations in exit flow angles, they should be avoided. On the other hand, short bubbles are an effective way to force the flow turbulent and may be considered as a means to control performance. The present difficulty is in predicting whether the bubble will be long or short.

Periodic-Unsteady and Reverse Transition

Periodic-Unsteady Transition. Since the flow in a gas turbine is periodically unsteady, so is transition. The largest effect of unsteadiness on transition is caused by the periodic passing of wakes from upstream airfoils or obstructions and is called "wake-induced" transition (Mayle and Dullenkopf, 1989). For transonic airfoils, the periodic passing of a trailing shock wave from an upstream airfoil can also produce a periodic transition

---

[2] For design purposes, of course, only the time-averaged aerodynamic loss and heat load distributions are really needed.

(Johnson et al., 1990). In either case, a transition periodically propagates along the surface independent of any other mode of transition occurring there.

Although much less is presently known about this type of transition compared to the above-mentioned "normal" modes, transition induced by wakes or shocks appears to bypass the first stages of the natural transition process. In fact, it seems that they are so disruptive to the laminar boundary layer that the turbulent spots formed immediately coalesce into a turbulent "strip," which then grows and propagates downstream. Between these turbulent strips, transition by any other process is possible and, indeed, has been detected. Thus, transition in gas turbines can occur in multiple modes (henceforth called "multimoded") and at different locations on the same surface at the same time. In other words, an instantaneous snapshot of the flow over a gas turbine airfoil may show a laminar boundary layer near the leading edge, followed by a wake- or shock-induced transition to turbulent flow and another laminar flow region with a subsequent transition to turbulent flow by any of the other modes listed above. Not only is this process not considered by most designers, it is not yet completely comprehended.

Reverse Transition. Transition from turbulent to laminar flow also exists and is called either "reverse" transition or "relaminarization." This situation, which was first noticed in flows through nozzles with very strong acceleration and later studied by Julien et al. (1969) and Jones and Launder (1972), is of particular importance to the gas turbine designer. This is because the accelerations on the pressure side of most airfoils near the trailing edge, in the exit ducts of combustors, and on the suction side of turbine airfoils near the leading edge are generally higher than that for which reverse transition occurs.

Although little detail of the actual process itself is known, it is not difficult to imagine that the streamwise vortex lines associated with the turbulence in the boundary layer become greatly stretched as a result of the large acceleration and the vorticity dissipated through viscous effects. That is, reverse transition involves a balance between convection, production, and dissipation of turbulent kinetic energy within the boundary layer. Since these processes are well accounted for in most numerical boundary layer computational programs, reverse transition will not be discussed any further, except to note that it can be expected to occur at low turbulence levels if the acceleration parameter, $K = \nu/U^2(dU/dx)$, is greater than $3(10)^{-6}$. For high free-stream turbulence levels, this value is expected to be about the same since without any mechanism for production in the free stream, turbulence there will dissipate before that in the boundary layer.

A corollary of the result for reverse transition is that forward transition cannot occur if K is greater than $3(10)^{-6}$. This was indicated by Schraub and Kline (1965), who observed that streak formations in the sublayers were completely suppressed at this level of acceleration. In this regard, computational programs should not allow transition to occur until K falls below $3(10)^{-6}$.

Part II—Theory and Experiment

Theory—Ideas Old and New. The first real breakthrough in transition was made by Emmons (1951) who pointed out that transition is a stochastic, three-dimensional, unsteady phenomenon, which extends over a region where both laminar and turbulent flow coexist. Previously, transition was thought to be an abrupt yet streamwise fluctuating, more or less two-dimensional breakdown of laminar to turbulent flow. Models that embrace Emmons' thoughts are considered new, while the others may now be considered old. For future gas turbine design systems, there is no question; only the new models will provide the necessary flexibility to predict transition. This was recently demonstrated by Mayle and Dullenkopf (1989, 1991) who extended Emmons' concepts of transition to the unsteady wake-induced, multimoded transition problem for flow on a gas turbine airfoil. In the following, after a brief discussion of the older models, the new ideas and models are presented.

Ideas Old. From a practical standpoint, transition was first treated by simply patching together laminar and turbulent solutions at an appropriate transition location. Both the method of patching and the location were somewhat discretionary, but a common approach was to suppose that transition occurs abruptly at a time-averaged position x_t and match the momentum thicknesses for the two solutions at this location, i.e., $\theta_L(x_t) = \theta_T(x_t)$. While this method is satisfactory for estimating the total loss and heat transfer on a surface when transition is short compared to the length of the surface (such as the transition in short separation bubbles), it produces unrealistic jumps in both the wall shear stress and heat transfer at x_t. Although numerous methods have been suggested to smooth out these jumps, they have become outdated through the use of numerical boundary layer computational methods.

The numerical methods, in general, attack the transition problem from the "turbulent side" by extrapolating turbulent boundary-layer modeling backward into the transition region. This is accomplished by numerically solving the equations of motion together with some form of the turbulent kinetic energy equation and sufficient auxiliary equations. The methods proposed by Launder and Spalding (1972), McDonald and Fish (1973), Cebeci and Smith (1974), Crawford and Kays (1976) and, most recently, by Schmidt and Patankar (1991) are typical. While some of them are quite successful at "postdicting" transitional flows and are presently the mainstay of industry,[3] all of them model transition as a spanwise-averaged, two-dimensional flow. Since the flow actually consists of laminar and turbulent regions, it should be no surprise that they do not always predict transition.

Ideas New. From flow visualization in a simple water channel, Emmons discovered that transition occurs through a random production (in time and position) of "turbulent spots" within the laminar boundary layer, which subsequently grow as they propagate downstream until the flow becomes completely turbulent. These spots protrude beyond the laminar boundary layer, and as shown in Fig. 3(b), are roughly triangular in shape and spread at an angle of about 11 deg as they propagate downstream with an average velocity of about 0.7 the local free-steam value. Although shown smooth in the figure, the boundary of a turbulent spot is quite irregular. Transition to a turbulent boundary layer is completed with an agglomeration of spots.

Based on this observation, Emmons presented a statistical theory for transition and provided an expression for the fraction of time the flow is turbulent at any location within the transition region. His theory, which provides a valid description of the last stage of natural transition and the principal stage of bypass transition (viz., the production and propagation of turbulent spots), is crucial to analyzing transition in gas turbines. Its main features, implications and its natural evolution into a modern treatment of transition follow.

Consider a transitional boundary layer on an x–z surface as shown in Fig. 4 where the free-stream flow is in the x direction. At any time t, the flow above the point $P(x, 0, z)$ on the surface may or may not be turbulent depending on whether or not a turbulent spot covers it. If turbulent spots are produced at a position $P_0(x, z)$ on the surface at the rate of $g(P_0)$ per unit surface area, then the fraction of time the flow at P

---

[3]Much of the turbulent and transition modeling originally proposed in these papers have been extensively modified by industry to suit both their needs and experience. For an example, one may want to see Sharma (1987).
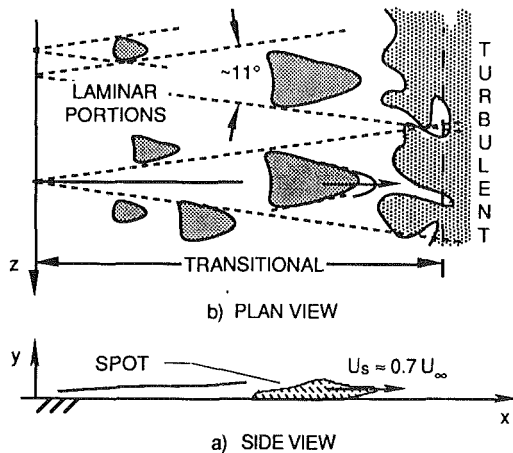
Fig. 3 Turbulent spot geometry and emergence of a turbulent boundary layer through the growth and propagation of turbulent spots
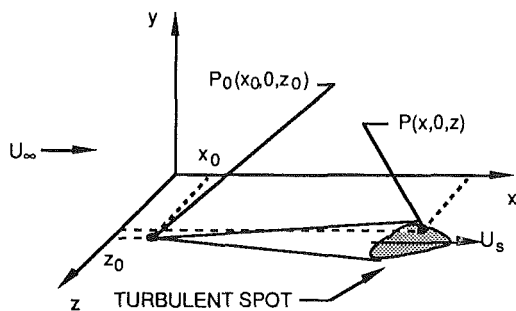

Fig. 5 Distribution of the skin friction coefficient through transition as predicted by Eq. (3) (Dhawan and Narasimha, 1958)

Fig. 4 Coordinate system for a turbulent spot on a surface

(presumably downstream from P_0) is turbulent corresponds to the fraction of time turbulent spots produced at P_0 pass over P. Of course, when P is covered by a turbulent spot, spots produced at all other locations and times that can also cover P cannot be counted. The fraction of time during which the flow over any point P on the surface is turbulent is called the "intermittency," and was shown by Emmons to be given by

$$\gamma(P) = 1 - \exp[-\iiint_R g(P_0)dx_0 dz_0 dt_0] \qquad (1)$$

The integral represents the sum of turbulent spot production, $g(P_0)$, over a volume defined by all point P_0 in an x, z, t space that are sources of turbulent spots that will pass over the point P. Simply stated, $g(P_0)$ accounts for the production of turbulent spots, while their growth and propagation is incorporated in integrating over the surface-time space (x, z, t). In general, $g(P_0)$ depends on both position and time. Its temporal dependence is particularly significant when considering unsteady, periodic transition. For a positive production rate, it is easy to see from Eq. (1) that the intermittency γ varies between zero and one. When $\gamma = 0$, the flow is completely laminar. When $\gamma = 1$, the flow is fully turbulent. For intermediate values, the flow is part of the time laminar and part of the time turbulent, i.e., transitional.

Since the flow in the transition region is part of the time laminar and part of the time turbulent in the relative proportion of $(1-\gamma)/\gamma$, Emmons presumed that the time-averaged flow at any streamwise position may be considered as a superposition of the two according to

$$f = (1 - \gamma)f_L + \gamma f_T, \qquad (2)$$

where f is a boundary-layer flow related quantity, f_L is its local laminar value, and f_L is its local fully turbulent value. For example, the shear stress coefficient through transition may be obtained from

$$c_f = (1 - \gamma)c_{fL} + \gamma c_{fT}. \qquad (3)$$
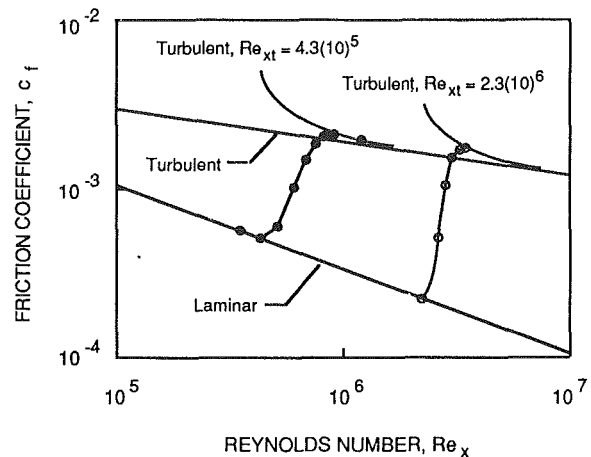
In order to predict the overshoot in c_f that normally follows transition, Dhawan and Narasimha (1958) showed that the turbulent boundary layer should be considered to begin at the beginning of transition. That is, if transition begins at x_t for flow on a flat plate, $c_{fL} = 0.332/\sqrt{Re_x}$ and $c_{fT} = 0.592(Re_x - Re_{xt})^{-0.2}$. This calculation and a comparison with data are shown in Fig. 5.

Dhawan and Narasimha also showed that Eq. (2) is a good approximation for the boundary layer thicknesses and shape factor, although it is only exact for the displacement thickness. An expression similar to Eq. (3) may be written for the Stanton number $St = h/\rho c_p U$ from which the local distribution of surface heat flux may be obtained. However, Sharma (1987) has shown that the thermal boundary layer in flows with pressure gradients develop differently through transition than the momentum boundary layer. To account for this effect, he introduced a thermal intermittency factor γ_h. This will be discussed later.

The next important step was taken by Dhawan and Narasimha who showed, for time-averaged two-dimensional flows, that turbulent spots originate within a narrow (compared to the length of transition) region on the surface at some distance x_t. In particular, after considering a Gaussian distribution with various standard deviations, they determined that $g(P_0)$ is best represented by

$$g(P_0) = n\delta(x_0 - x_t) \qquad (4)$$

where n is the turbulent spot production rate per unit distance in the spanwise, z, direction and $\delta(x)$ is the Dirac delta function. Since then, many measurements (Gostelow, 1989; Blair, 1990; Walker and Gostelow, 1990) indirectly indicate that a Gaussian distribution may be more appropriate, but this refinement is presently considered not necessary. (Since the Dirac delta function is the limiting form of the Gaussian distribution as the standard deviation becomes zero, the average behavior through transition will be described quite well by using Eq. (4) providing the actual region of spot production is small compared to the length of transition.) Substituting Eq. (4) into Eq. (1), one obtains Dhawan and Narasimha's result, viz.,

$$\gamma(x) = 1 - \exp\left[-\frac{n\sigma}{U}(x - x_t)^2\right], \quad (x \geq x_t) \qquad (5)$$

where U is the free-stream velocity and σ is Emmons' dimensionless spot propagation parameter, which depends on the shape and velocity of the spot. Measurements of the spot and its propagation velocity by Schubauer and Klebanoff (1955) indicate that σ is constant and has a value of about 0.27.
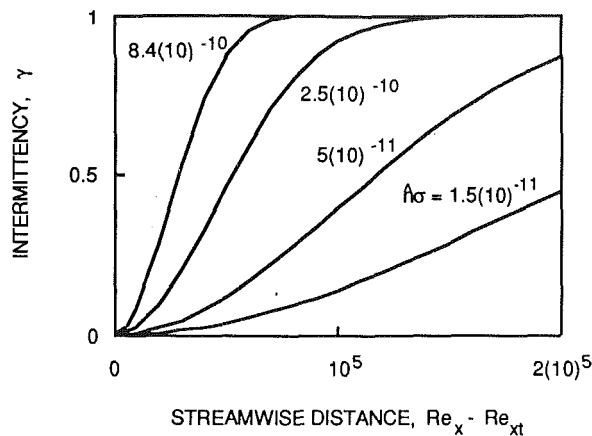
Fig. 6 Intermittency distributions for various spot production rates (the increasing values correspond to turbulence levels of 1, 2, 5, and 10, respectively)

Fig. 7 Intermittency distributions in a boundary layer at various locations through transition

Introducing the local Reynolds number $\mathrm{Re}_x = Ux/\nu$, the above expression may be written as

$$\gamma = 1 - \exp[-\hat{n}\sigma(\mathrm{Re}_x - \mathrm{Re}_{xt})^2], \qquad (6)$$

where $\hat{n} = n\nu^2/U^3$ is a dimensionless spot production parameter. A plot of this function for various $\hat{n}\sigma$ is presented in Fig. 6 where it is seen that an increase in the spot production rate decreases the transition length. From Eq. (6) it is evident that the real problem of transition is to determine the onset of transition, Re_{xt}, and the spot production parameter $\hat{n}$. Indeed, all the results in the next section are presented in this light. That is, what are the effects of various fluid dynamic and thermal parameters on both the onset of transition and spot production rate?

For gas turbines where the free-stream velocity varies significantly over the surfaces, Chen and Thyson (1971) have shown that Eq. (6) may be used providing the velocity U is replaced by the velocity at the onset of transition, U_t, and the propagation parameter σ is replaced by a modified propagation parameter $\bar{\sigma}(U_t/\overline{U})$, which takes into account the growth and propagation of the turbulent spot under the influence of a variable free-stream velocity. In this case, the dimensionless spot production parameter becomes $\hat{n} = n\nu^2/U_t^3$, which only depends on the conditions at x_t. The quantities $\bar{\sigma}$ and $\overline{U}$ are simply the average of σ and U over the distance x_t to x. After reconsidering Narasimha's results (1985, Fig. 25) and using the true onset of transition, the author found that the spot propagation parameter $\bar{\sigma}$ is still nearly constant for accelerating flows.

In reality, the intermittency γ is a function of both the streamwise distance, x, and the distance normal to the surface, y. Figure 7 shows several normalized intermittency distributions across the boundary layer at several streamwise locations for flows with $0 \le K \le 0.75\,(10)^{-6}$. In this format, only the streamwise position within the transition region appears to affect the profile shape. Therefore the data for different values of K are not distinguished. Measurements below $y/\delta \approx 0.2$ are still in dispute. Some researchers have found that the intermittency drops here (Kuan and Wang, 1989; Gostelow and Walker, 1991), while others find it is nearly constant and equal to the value measured on the wall by shear stress gages (Owen, 1970; Acharya, 1985). The differences are apparently due to differences in the turbulent flow discrimination scheme used to determine intermittency. Nevertheless, when streamwise intermittency distributions obtained by hot wires are reported, they generally refer to measurements obtained near $y/\delta = 0.2$ and are called the "near-wall" intermittency results. The results in Fig. 7 have been normalized by this value. The abscissa
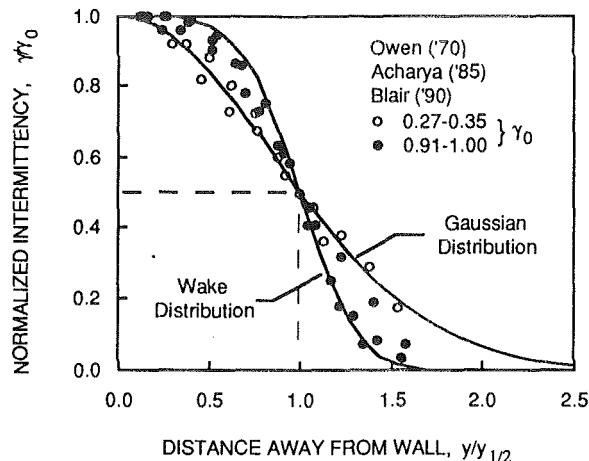
is the distance away from the wall divided by $y_{1/2}$, the distance to where $\gamma/\gamma_0 = 0.5$. The small amount of data presently available indicate that $y_{1/2}$ is about 0.7δ.

In addition, two curves are plotted in this figure. One is a Gaussian distribution with a standard deviation of $0.85y_{1/2}$ given by $\gamma/\gamma_0 = \exp[-0.694(y/y_{1/2})^2]$, while the other is an intermittency distribution for wake flows. The latter, measured by Mayle and Paxson (1991), is given by $\gamma/\gamma_0 = \frac{1}{2}\{1 - \mathrm{erf}[2\sqrt{2}\,(y/y_{1/2} - 1)]\}$ and has a standard deviation of $0.25y_{1/2}$. Comparing the data with the curves, the data near the beginning of transition (open symbols) are close to the Gaussian distribution, whereas the data near the end of transition are closer to the wake-flow distribution. The tendency for the intermittency distribution to become more wakelike as the flow becomes more turbulent agrees with Coles' (1956) observation that the outer region of a fully turbulent boundary layer behaves as a wake. Apparently, this wakelike behavior begins to develop during transition.

Using the New Ideas. Methods to implement the idea of intermittency in calculations of transitional flows have been recently reviewed by Narasimha and Dey (1989). Most of these employ the near-wall intermittency, Eq. (6), with some form of experimental correlation for both the onset and length of transition.[4] Although the list includes both integral and differential methods of solution, all of those employing the differential format calculate transition using turbulent boundary-layer methods with an eddy viscosity somehow modified by the intermittency. Since there is much confusion concerning the intermittency factor in these computational procedures, it is worthwhile to give a brief account of its role in the shear stress and heat flux terms.

Recently, Mayle and Paxson (1991) presented a theory for intermittent flows. Although their analysis and measurements pertained to wake flows, the ideas may easily be carried over to transitional flows. In particular, consider that the flow at any instant may be divided into two physically distinct portions within the boundary layer. One portion contains fluid where the flow is turbulent while the second, everywhere outside this, is nonturbulent. These portions are separated by a distinct but highly contorted interface, as pictured in Fig. 8, which changes with time and position. To characterize these portions, an intermittency function, $I(x, y, z, t)$, may be defined, which has the value of unity when the flow is turbulent, and zero

---

[4]Notice, if $\gamma = 0.99$ is considered to represent the end of transition, Eq. (6) provides a connection between the length of transition Re_{LT} and the spot production rate, viz., $\hat{n}\sigma = 4.61/\mathrm{Re}_{LT}^2$. This expression is, however, only correct for transition with $U = \mathrm{const}$.
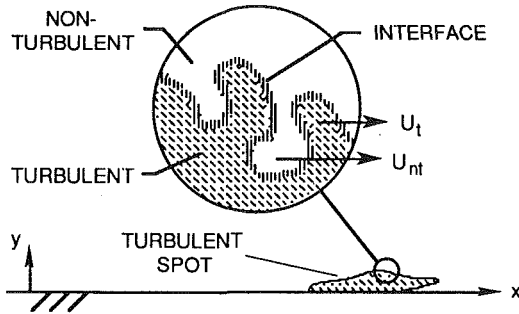
Fig. 8 Supposed interface between the turbulent fluid within and non-turbulent fluid outside a turbulent spot

when it is not. For a given position in space, the ensemble average of the intermittency function yields the intermittency factor,

$$\gamma(x, y, z) = \frac{1}{N} \sum_{1}^{N} I(x, y, z, t).$$

For two-dimensional flows in the x-y plane, γ is independent of z. Since the velocities in the two regimes will in general be different, the streamwise velocity component at any time may be expressed as (for two-dimensional flow)

$$U(x, y, t) = (1 - I)U_{nt}(x, y, t) + IU_t(x, y, t);$$

$$I(x, y, t) = \begin{cases} 1; & \text{turbulent} \\ 0; & \text{nonturbulent} \end{cases}$$

where U_t and U_{nt} are the components in the turbulent and nonturbulent portions, respectively. A subscript t is used here to denote the turbulent portion of the intermittent flow rather than T, which stands for the fully turbulent state. Also, nt is being used rather than L to indicate that the nonturbulent portion of the flow contains both laminar boundary layer and free-stream fluid. These are subtle, but important, differences. Decomposing the velocity in each region into an ensemble-averaged mean velocity, denoted by an overbar, and a fluctuating component denoted by a prime, the instantaneous velocities in the two portions may be written as

$$U_{nt} = \overline{U}_{nt} + u'_{nt} \text{ and } U_t = \overline{U}_t + u'_t.$$

Contrary to the usual averaging process, the ensemble-averaged mean velocities are obtained by averaging only during the time spent in the particular regime. Thus, if N_t is the number of occurrences of turbulent flow in N data samples, the mean velocities in each portion are

$$\overline{U}_{nt}(x, y) = \frac{1}{N - N_t} \sum_{1}^{N} (1 - I)U(x, y, t) \text{ and } \overline{U}_t(x, y)$$

$$= \frac{1}{N_t} \sum_{1}^{N} IU(x, y, t)$$

With these definitions, the mean velocity at any position in the flow is given by

$$\overline{U}(x, y) = \frac{1}{N} \sum_{1}^{N} U(x, y, t) = (1 - \gamma)\overline{U}_{nt}(x, y) + \gamma\overline{U}_t(x, y).$$

Similar expressions may be written for the lateral velocities.

The shear stress and heat flux that appear in the ensemble-averaged equations are now given by

$$\tau_{xy} = \mu \frac{\partial \overline{U}}{\partial y} - (1 - \gamma)\rho\overline{(u'v')}_{nt} - \gamma\rho\overline{(u'v')}_t$$

$$- \gamma(1 - \gamma)\rho(\overline{U}_t - \overline{U}_{nt})(\overline{V}_t - \overline{V}_{nt}) \quad (7)$$

and

$$q_{xy} = k \frac{\partial \overline{T}}{\partial y} - (1 - \gamma)\rho c_p(\overline{v't'})_{nt} - \gamma\rho c_p(\overline{v't'})_t$$

$$- \gamma(1 - \gamma)\rho c_p(\overline{V}_t - \overline{V}_{nt})(\overline{T}_t - \overline{T}_{nt})$$

where k is the thermal conductivity of the fluid, $\overline{V}$ and $\overline{T}$ are the ensemble-averaged values of the lateral velocity and temperature, and v' and t' are their corresponding fluctuations.

The first term in each expression is the molecular stress and heat flux component, while the second and third are the components. by fluctuations in the nonturbulent and turbulent portions of the flow, respectively. The $(\overline{u'v'})_{nt}$ component arises from fluctuations in the nonturbulent portion of the flow, which are transmitted from the turbulent portions mainly by pressure fluctuations. For flows where the nonturbulent portion is irrotational, this stress is zero, while for transitional boundary layer flows where the nonturbulent portion is rotational, Blair (1990) found it to be negligible compared to the turbulent stress. No information is presently available about $(\overline{v't'})_{nt}$.

The $(\overline{u't'})_t$ stress and $(\overline{v't'})_t$ flux components may be considered as the real turbulent shear stress and heat flux. These components are produced by the motion of eddies having various scales, but primarily at scale small compared to δ. They may be called the "small" scale eddy components. As shown by Mayle and Paxson, this shear stress may be modeled using an eddy viscosity model of the form $(\overline{u'v'})_t = \mu_t(\partial \overline{U}_t/\partial y)$. The fourth term in each expression, which is zero for either a completely nonturbulent or turbulent portion of the flow, is only associated with the intermittent behavior, and arises from the mean momentum and thermal exchange between the two regions. Again, these terms are produced by motion of various eddy scales, but the primary scale is that of the intermittent behavior, which is roughly of order δ. These components may be called the "large" scale eddy components and obtain their greatest value when $\gamma \approx 0.5$. In wake flows, Mayle and Paxson found the shear stress component $\gamma(1 - \gamma)(\overline{U}_t - \overline{U}_{nt})(\overline{V}_t - \overline{V}_{nt})$ accounts for 30 percent of the total stress, while Blair's boundary layer measurements indicate that they may be about 15 percent.

Returning to the question of using intermittency in transitional flow models, none of the present computer programs consider the second and fourth terms in the above expressions. As stated above, this could produce a 15–30 percent error in the calculated shear stress τ_{xy}. Secondly, none of the programs model the turbulent component correctly, i.e., most[5] use $\tau_t = \gamma\mu_t(\partial \overline{U}/\partial y)$ rather than $\gamma\mu_t(\partial \overline{U}_t/\partial y)$. Although difficult to assess, Mayle and Paxson have shown that μ_t changes by about 20 percent depending on whether $\overline{U}$ or $\overline{U}_t$ is used.

Experiment—Old and New Results in New Light. Once it is accepted that the primary parameter in transitional flows is intermittency, it is obvious from Eq. (6) and either Eq. (2) or (7) that the real problem of transition becomes one of either predicting or correlating both the onset of transition and the spot production rate, as functions of the various fluid dynamic and thermal parameters that affect them. In general, it may be said that anything that affects the laminar velocity profile affects transition, but it is simpler for the gas turbine designer. Presently, it appears that the onset of transition is completely controlled by free-stream turbulence and unsteadiness. This may seem surprising but is easily understood once the overwhelming effects of unsteadiness, either turbulent or periodic, are realized. On the other hand, it appears that the spot production rate is controlled by the pressure gradient at onset, turbulence, and whether or not the flow separates. Surface roughness, surface curvature, compressibility, and heat transfer do have an effect on the production rate, but it is generally five to ten times less than that of the pressure gradient. If the

---

[5]Sharma (1987) uses $\tau_t = \gamma^2\mu_t(\partial \overline{U}/\partial y)$ and claims (personal communication) better agreement with data than when $\tau_t = \gamma\mu_t(\partial \overline{U}/\partial y)$ is used.
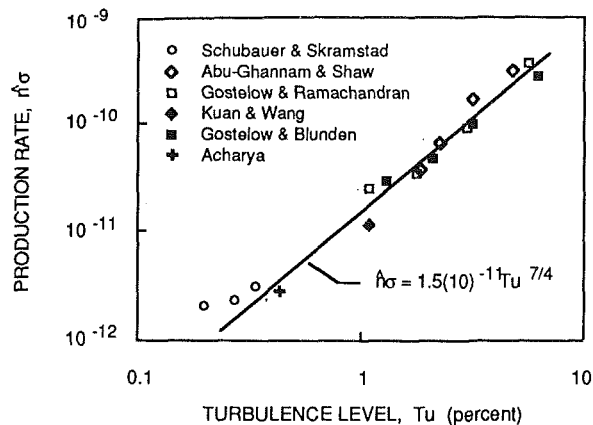
Fig. 9 Spot production rate as a function of the free-stream turbulence level for zero pressure gradient flows

Fig. 10 Momentum thickness Reynolds number at the onset of transition as a function of free-stream turbulence level for zero pressure gradients flows

flow separates, transition is primarily controlled by the momentum thickness Reynolds number at separation and the parameters that affect the length of the laminar shear layer in the bubble. At present these parameters are not known, but there is some evidence that free-stream turbulence is one of them.

A presentation and discussion of each controlling parameter is given below. For each, their effect on the onset of transition and the spot production rate has been correlated using the most reliable data to date. The effects of surface roughness, surface curvature, compressibilty, and heat transfer, which are secondary for transition in gas turbines, are discussed in Appendix A. Although relegated to an appendix, the new ideas presented there should not be overlooked. In the first stages of the high-pressure turbine, film cooling is extensively used and its effect on transition is indeed important, but simple; it causes an "immediate" transition. A discussion of its effect is also relegated to the appendix. Because of its important role in gas turbines, periodic-unsteady transition is treated in a following separate section.

Effect of Free-Stream Turbulence ($dp/dx = 0$). Early work regarding the effect of free-stream turbulence of transition was done at very low levels of turbulence. While useful for the aerodynamic design of aircraft, it is completely inappropriate for gas turbine design purposes except perhaps for fans. Investigations at higher turbulence levels appeared later and were mostly concerned with onset criteria. Only a few measure both the beginning and end of transition and virtually none measured turbulent length scales. Correlating the spot production rate with turbulence level was first presented by Emmons and Bryson (1951) but, for some reason, was not pursued until recently. In the following, similar to the work of Narasimha (1985) and Gostelow and Blunden (1989), the original idea of Emmons and Bryson is not only pursued, but promoted.

The important results are summarized in Figs. 9 and 10. The data presented in these figures are the only data for transition in zero pressure gradient flows that could be reduced in a manner consistent with the ideas expressed above. The method of analysis used to produce these figures was described initially by Narasimha (1957) and is briefly presented in Appendix B. Surprisingly, there are few data available from which the spot production rate can be obtained. Since there is an equivalence between the spot production rate and length of transition for flow with a zero pressure gradient (see footnote 4), some of the older data are usable. Even so, most of the data in these figures suffer from a lack of turbulence information at the onset of transition. As will be shown, both turbulence level and length scale at the beginning of transition are important and must be measured in any future work.
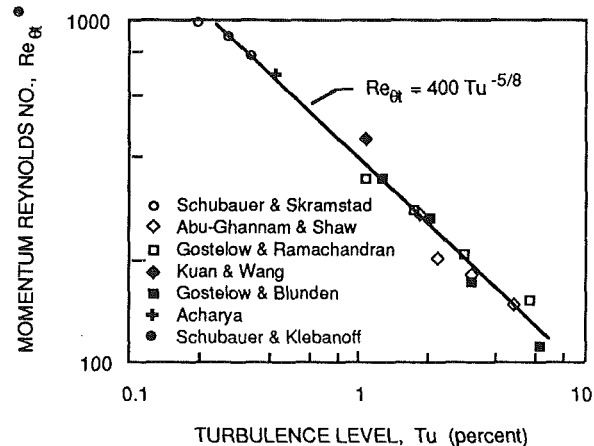
The effect of turbulence level on the spot production rate is shown in Fig. 9. Data shown by the open symbols represent those from transition length measurements, while those shown by the filled symbols are from intermittency measurements. As might be expected, the production of turbulent spots increases as Tu increases. Narasimha (1985) suggested that a modified production rate, viz., $N = \hat{n}\sigma \mathrm{Re}_{\theta t}^3$, is independent of the turbulence level, but Gostelow and Blunden (1989) have shown that this is not quite true. The following correlations indicate that $N \propto Tu^{-1/8}$. In any case, a best fit to the present data provides

$$\hat{n}\sigma = 1.5(10)^{-11} Tu^{7/4}, \qquad (8)$$

where Tu (as in all the following equations and figures) is in percent. If only the data from intermittency measurements are used, the coefficient in this equation becomes $1.25 (10)^{-11}$.

The effect of free-stream turbulence level on the momentum thickness Reynolds number at transition, $\mathrm{Re}_{\theta t}$, is shown in Fig. 10. As is well known, the effect of turbulence is to reduce the Reynolds number at which transition begins. Although many data on the beginning of transition exist, the data shown in this figure are only those that correspond to the data shown in the previous figure. The rest require a correction that is at best an estimate, and will be shown in the next figure. A correlation of the present data provides

$$\mathrm{Re}_{\theta t} = 400 Tu^{-5/8}. \qquad (9)$$

If only the data from intermittency measurements (filled symbols in Fig.10) are used, the coefficient and exponent in this equation become 420 and -0.69, respectively. A result similar to this was previously obtained by Hourmouziadis (1989), viz., $\mathrm{Re}_{\theta t} = 460 Tu^{-0.65}$.

The data and correlation shown in Fig. 10 have been replotted in the more conventional linear format in Fig. 11. The data shown as open circles in the figure were obtained from a variety of measurement methods and after being corrected as described in Appendix B agree reasonably well with the new correlation. For comparison, Abu-Ghannam and Shaw's (1980) correlation is also shown. Since their correlation is frequently used in numerical boundary layer codes, it is worthwhile to point out that they forced it to fit data for $Tu < 0.1$ and to level out at the minimum stability value of $\mathrm{Re}_{\theta t} = 163$. There is really no need to do either. It is now generally accepted that data with $Tu < 0.2$ are affected by acoustic disturbances and not the free-stream turbulence level. (In this regard, Schubauer and Klebanoff's (1955) result for $Tu = 0.03$, which incidentally was evaluated from intermittency measurements, is shown as the filled circle in Fig. 10 just to the upper left of the

Fig. 11 Comparison of present correlation with Abu-Ghannam and Shaw's and other data corrected for differences in the methods of detecting the onset of transition

Fig. 12 The effect of the turbulence grid mesh on the onset of transition

Fig. 13 The correlation between the length of transition and the momentum thickness Reynolds number at the end of transition

ordinate's label.) At the higher turbulence levels, transition occurs in a bypass mode and is completely independent of the Tollmien–Schlichting instability. Therefore, setting a minimum value of $Re_{\theta t}$ based on stability theory is irrelevant.

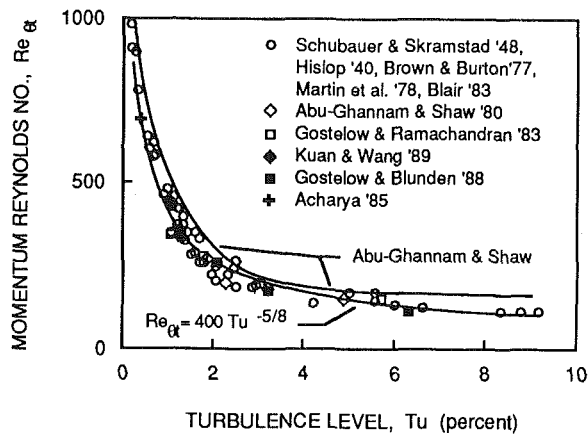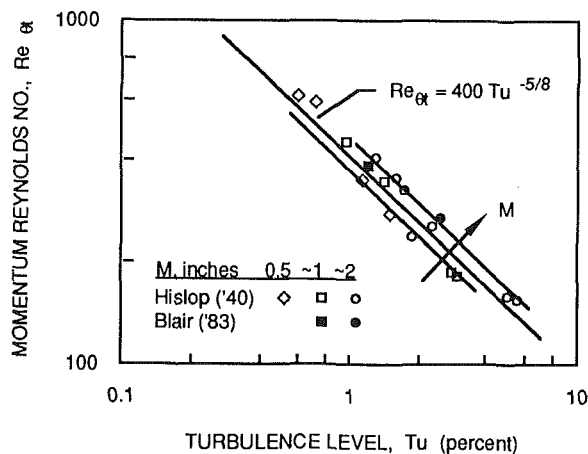In spite of evidence that it is important, the effect of the scale of turbulence on the Reynolds number at transition has not yet been studied. Hall and Gibbings (1972) using Hislop's (1940) data showed that $Re_{\theta t}$ is affected by the mesh size of the screen used to produce the turbulence. This result is shown in Fig. 12 together with the more recent data of Blair (1983). Clearly, the effect is as much as, and probably the principal reason for, the scatter in the previous figure. The maximum difference in $Re_{\theta t}$ between the data and the correlation given by Eq. (9) is roughly ±12 percent, which translates to a significant ±25 percent change in the streamwise location of transition.

The results of Hislop and Blair may be correlated directly using Taylor's turbulence parameter with the momentum thickness as the characteristic length scale of the flow, viz., $Tu\sqrt[5]{\theta/M}$ where M is the mesh size, but a more appropriate parameter would seem to be Ta $= Tu\sqrt[5]{\theta/L}$, where L is the turbulence length scale. Using Blair's data, it was found that the effect of turbulence length scale on $Re_{\theta t}$ could be taken into account by substituting $Tu = 1.93$Ta in Eq. (9). Since this result is based on only two data points, a more trustworthy correlation awaits further measurements.

The Reynolds number based on the length of transition, measured from $\gamma = 0$ to 0.99, is plotted against the momentum thickness Reynolds number at the end of transition in Fig. 13. A reasonable fit to the data provides

$$Re_{LT} = 75\ Re_{\theta t}^{5/4}$$

which, as shown in the figure, is only slightly higher than the simple correlation for the growth of a turbulent boundary layer beginning at the onset of transition. This fact, shown previously in Fig. 5, was used by Sharma (1987) to develop an equation for intermittency based solely on local boundary layer parameters. However, if one subscribes to the belief that the production of turbulent spots depends only on the parameters at the onset of transition x_t and that they simply convect according to Chen and Thyson's model, it is unnecessary to use the local boundary parameters as a measure of the distance from onset of transition.

Effect of Pressure Gradient. Transition measurements in accelerating/decelerating flows are scarce. Most of the work, with some exceptions, is at low turbulence levels and only considers measurements for the onset of transition. A review of these results may be found from Brown and Martin (1979). A more comprehensive set of measurements may be found from Abu-Ghannam and Shaw (1980); however, these were obtained using Preston probe and, according to Narasimha (1985), must be corrected as discussed in Appendix B. Unfortunately, the corrections in flows with pressure gradients are only approximate. The only intermittency measurements from which both the onset of transition and the spot production rate may be determined are those by Blair (1983) for favorable pressure gradients, and Sharma et al. (1982) and Gostelow and co-workers (Gostelow, 1989; Gostelow and Blunden, 1989; Gostelow and Walker, 1991) for adverse pressure gradients.

The onset of transition and its length have normally been presented in terms of the pressure gradient parameter $\lambda_\theta = (\theta^2/\nu)dU/dx$ at transition, i.e., $\lambda_{\theta t}$. If transition is natural, i.e., via amplified disturbances of the Tollmien–Schlichting type, then $\lambda_{\theta t}$ may be expected to play an important role.[6] It is not evident, however, that this is the appropriate parameter for other routes to transition. In fact, Blair's data indicate that the acceleration parameter at transition, i.e., $K_t = (\nu/U_t^2)(dU/dx)_t$, is more appropriate for flows with a favorable pressure gradient where transition is via the bypass mode. Therefore, all of the following results are presented using K_t as the relevant parameter.

The effect of acceleration on the spot production rate, as obtained from the data of Blair, Gostelow, and Sharma, is shown in Fig. 14. In this figure, the ordinate is the spot production rate for $K \neq 0$ divided by its corresponding flat plate value, namely, $(\hat{n}\sigma)_{FP} = 1.5(10)^{-11}Tu^{7/4}$ (see Eq. (8)). In this

---

[6]The critical parameter in stability theory is the curvature of the velocity profile, which near the wall is directly proportional to λ_θ.
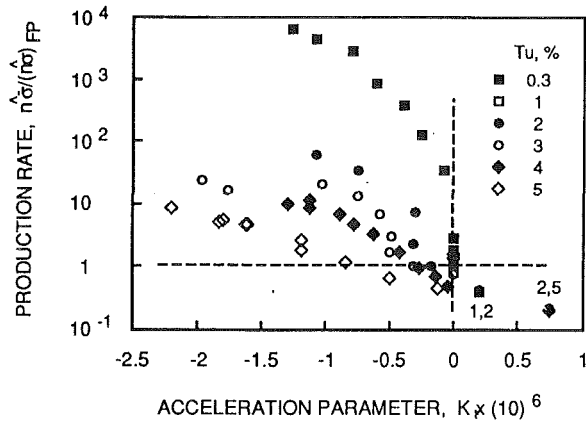
Fig. 14 Turbulent spot production rate as a function of the acceleration parameter at transition for various free-stream turbulence levels
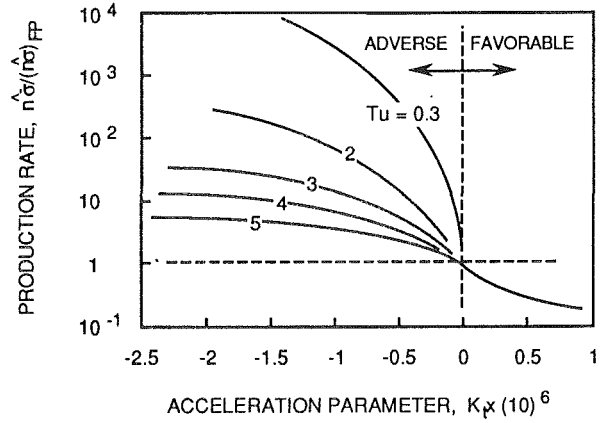
Fig. 15 Suggested correlation of the spot production rate with the acceleration parameter at transition

format, the data for $K_t > 0$, which actually include four data points, $Tu \approx 1$ and 2 at $K_t = 0.2(10)^{-6}$ and $Tu \approx 2$ and 5 at $K_t = 0.75(10)^{-6}$, collapse and appear as only two points at $K_t = 0.2$ and $0.75(10)^{-6}$. It may be worthwhile to note that these data were the only data in this figure obtained from tests conducted with K constant throughout the flow. Hence, for $K_t > 0$, the physics of transition is similar to that on a flat plate and $\hat{n}\bar{\sigma} \propto Tu^{7/4}$. According to the observations of Schraub and Kline (1965), $\hat{n}\bar{\sigma}$ should approach zero as K_t approaches $3(10)^{-6}$.

The results for $K_t < 0$ show a different behavior with turbulence level. (Here it must be remembered that the data in Fig. 14 have been normalized by the flat plate value.) In fact, for the larger negative values of K_t, the effect of turbulence is less and the data can be correlated better using $\hat{n}\bar{\sigma} \propto Tu^{0.15}$. All of this agrees with the ideas presented earlier regarding the various modes of transition. That is, all results for $K_t \geq 0$ fall within the bypass transition regime and should behave similarly with regard to the bypass mechanism, which in this case depends on the free-stream turbulence. The data for large negative values of K_t, however, fall closer to the natural transition regime and depend more on the inherent instabilities of the flow. In other words, the effect of turbulence on transition is much less pronounced for unfavorable than for favorable pressure gradient flows.

A unified correlation of these results was attempted but dismissed until more data for adverse pressure gradients are obtained (as seen, they do not quite match the flat plate results). Until then, the curves shown in Fig. 15 (drawn with some thought) are suggested. Although not shown, correlations based on either Narasimha's parameter N or Walker's (1987) minimum transition length produce errors up to factors of three in the transition length over the complete range of pressure gradients and turbulence levels and are not recommended. The curves in Fig. 15 are expected to provide less than a 50 percent error in $\hat{n}\bar{\sigma}$, which translates to an error of about 25 percent in the length of transition.

The effect of acceleration on the onset of transition is presented in Fig. 16. For reference, the dotted lines in the figure represent the stability criterion (lower line) and the separation criterion as shown in Fig. 2. In general, $Re_{\theta t}$ increases with either an increase in acceleration or a decrease in the free-stream turbulence level. This trend is in agreement with all other data; see, for example, Brown and Martin or Abu-Ghannam and Shaw. For low turbulence levels, the effect of acceleration is significant, while for levels found in gas turbines, it is negligible. That is, at the high levels obtained in gas turbines, the onset of transition is controlled by the free-stream turbulence. This was found for all of the other parameters thought to govern transition (see Appendix A). In this regard,
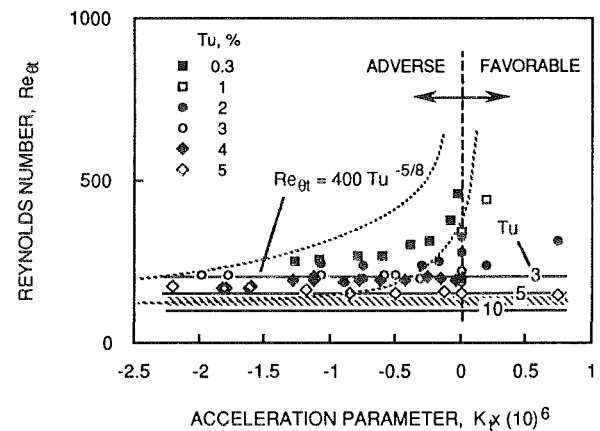
Fig. 16 The Reynolds number of transition as a function of the acceleration parameter at transition for various free-stream turbulence levels

models for the onset of transition such as proposed by Sharma (1987), which use Liepmann's criterion for the onset of transition look promising. This criterion assumes that transition begins when the fluctuating shear stress in the laminar boundary layer equals the friction velocity squared. Sharma et al. (1982) show that this model is easily incorporated in present boundary layer codes. In order to predict transition in generalized flow situations, such as when using Navier–Stokes solvers, this approach appears absolutely necessary since the integrated quantities are not known a priori.

The horizontal lines in Fig. 16 correspond to the correlation given by Eq. (9) and are seen to correlate the data well for $Tu \geq 3$. Hence, for the purpose of gas turbine design, it appears that the onset of transition may simply be predicted by using the flat plate result, viz.,

$$Re_{\theta t} = 400 Tu^{-5/8} \quad \text{(all conditions, } Tu \geq 3\text{)}$$

The shaded band indicates the predicted range of $Re_{\theta t}$ for $5 \leq Tu \leq 10$, viz., $95 < Re_{\theta t} < 146$.

For accelerating flows, Blair (1982) and Sharma (1987) determined that the length of transition is different for the thermal and momentum boundary layers. The effect produces a longer transition for the thermal boundary layer than for the momentum boundary layer in flows developing under favorable pressure gradients, while the reverse is true in flows developing under adverse pressure gradients. It should be noted that this effect is solely pressure gradient dependent and different from that discussed in Appendix A regarding heat transfer effects. Since pressure gradients affect the momentum and thermal development of any flow with a Prandtl number not

equal to one differently, this should not be a surprise. The implications of this result, however, are significant. First, inferring transition information from heat transfer measurements alone in flows with pressure gradients should be considered unreliable. That is, using Eq. (2) with f = St to determine the intermittency distribution is only valid for flows with $dp/dx = 0$. This was clearly pointed out by Sharma (1987), Mayle and Dullenkopf (1989), and Blair (1990). Second, the physics of intermittency from a thermal point of view must be modified.

To account for the difference in thermal and momentum transition lengths, Sharma (1987) introduced a thermal intermittency factor γ_h and correlated the thermal transition length with the Pohlhausen pressure gradient parameter λ_θ. As discussed above, this approach is questionable. Nevertheless, to use his correction, the intermittecy γ in the expression for heat flux in Eq. (7) should be replaced by γ_h where

$$\gamma_h = 1 - \exp[-(\hat{n}\sigma)_h(\text{Re}_x - \text{Re}_{xt})^2]$$

and

$$(\hat{n}\sigma)_h = \hat{n}\sigma[1 + (21 \text{ or } 7.25)\lambda_\theta]^{-2.68}.$$

The first value in parentheses of the above expression is to be used for transition in favorable pressure gradients while the second is for adverse.

Separated-Flow Transition. Of all the transition modes, there is none more crucial to compressor and low-pressure turbine design and none more neglected that this mode. The benefits are, for the most part, to be found in the efficiency of small engines and the low-pressure turbine and compressor of medium-sized engines. As pointed out by Hourmouziadis (1989), understanding and utilizing separated-flow transition through separation bubbles can easily increase low turbine efficiency by several points. Similar gains may be expected in small-engine turbine efficiencies. Furthermore, since compressor airfoils normally operate separated somewhere and since their off-design operating characteristics depend mainly on the nature of the separated flow, it is expected that a design utilizing controlled transition through separation bubbles will have as great an impact on compressor performance. In light of this, it is quite surprising that more work of a fundamental nature has not been done in this area.

Separation bubbles come in two types, short and long, with the distinction between the two being their effect on the overall pressure distribution. Short bubbles have only a local displacement effect, so that, before and after them, the pressure distribution is close to that predicted for the flow over the surface without separation. Long bubbles interact with the exterior flow to such an extent that the pressure distribution over the whole surface is appreciably different from that predicted without them. Since small changes in either Reynolds number or angle of attack of an airfoil can cause a bubble to change catastrophically (called "bursting") from short to long, leading to a dramatic loss in lift and possible stall, it is of utmost importance to understand the process before successful designs with separation bubbles can be realized.

For calculating flows with separation, the important steps have already been taken. One essential ingredient of successfully predicting these flows is the ability to predict the bubble's displacement effect on the mainstream flow. This can be done by most modern boundary-layer type, viscous–inviscid interaction computational programs or Navier–Stokes' solvers. A second essential ingredient is a good transition model. Present models are usually based on the work of Horton (1969) and Roberts (1980), and assume instantaneous transition at an empirically determined transition location within the bubble. For short bubbles, this may not be too bad, but it precludes using modern numerical codes from correctly predicting separated flow with transition.
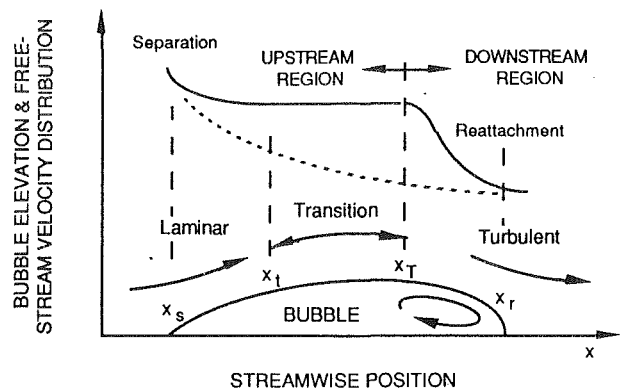
Fig. 17 Flow around a separation bubble and corresponding free-stream velocity distribution
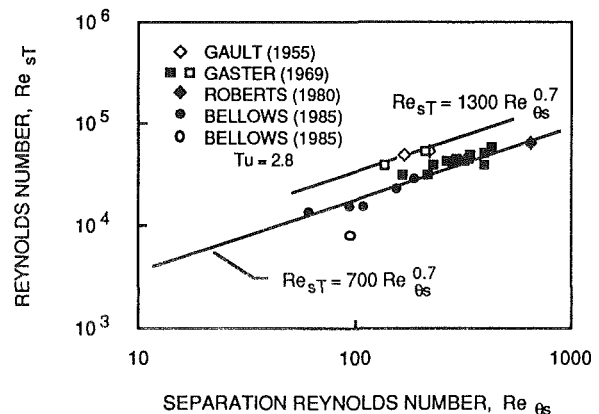
Fig. 18 Reynolds number based on the constant pressure portion of the bubble as a function of the momentum thickness Reynolds number at separation

The essential features[7] of a laminar separation bubble with transition before reattachment are illustrated in Fig. 17. The actual flow is highly three dimensional and unsteady, so this figure is only a pictorial representation of the time-averaged situation. At separation (marked x_s in the figure), the pressure gradient according to Thwaites (1949) is given by $\lambda_{\theta s} \cong -0.082$ where the subscript s refers to conditions at separation. After separation, the flow may be divided into two main regions, which are in general characterized by their corresponding pressure distribution. They are: (1) an upstream region of nearly constant pressure, and (2) a downstream region with a large pressure recovery. In Fig. 17, these are shown respectively as regions of constant free-stream velocity and deceleration. In the past, the first region was always called the laminar region and the end of the second region was always associated with reattachment (marked x_r). However, after re-examining Gaster's (1969) data (Figs. 10–21), the first region is really composed of an unstable laminar shear flow ending with the formation of turbulent spots at some position, say x_t, and a transition region between x_t and x_T. These results seem to have been overlooked and, as will be seen, form an important link between transition in separated and unseparated flows.

A plot of the Reynolds number based on the conditions at separation and the distance $(x_T - x_s)$ versus the momentum thickness Reynolds number $\text{Re}_{\theta s}$ is shown in Fig. 18. The data are taken directly from measurements of Gault (1955), Gaster (1969), Roberts (1980), and Bellows (1985). Only data for which $\text{Re}_{\theta s}$ were measured (not calculated) are presented. Even though all of the data except one are for low free-stream

---
[7]This figure is based on re-examining old data in light of the present work and differs from that generally accepted today.
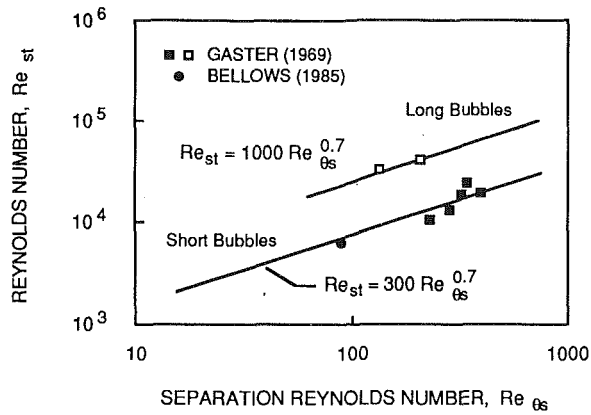
Fig. 19 Distance between separation and transition as a function of the separation Reynolds number

Fig. 20 The actual length of transition in separation bubbles as a function of the separation Reynolds number

turbulence levels ($Tu = 0.2$–0.5) and are inappropriate for gas turbines, the ideas are presented to provide a much needed framework for future investigations at the higher levels.

In general, most of the data fall along one line given by

$$(\text{Re}_x)_{sT} = \text{Re}_{xT} - \text{Re}_{xs} = 700 \ \text{Re}_{\theta s}^{0.7} \qquad (10)$$

This result is significantly different from that proposed by Walker (1989) based on stability considerations and a minimum turbulent spot merging distance.

All of the data that lie close to the line given by Eq. (10) are for short bubbles. The data for $Tu = 2.8$, also a short bubble, fall below the rest, which is consistent with the trend found by Roberts (1980). The four data points lying above the rest are, however, for long bubbles and can be correlated by simply replacing the coefficient in Eq. (10) with 1300. While these may provide better correlations for predicting flows with separation bubbles, they certainly provide no further insight than before with regard to the transition and "bursting" processes.

From the analysis and results presented by Mayle and Paxson (1991), it can be shown that the turbulence level in intermittent flows with low free-stream turbulence is approximately given by $Tu \approx \gamma(Tu)_T$ where the subscript T refers to the turbulence level in the turbulent portion of the flow. Using this and assuming $(Tu)_T$ is constant and equal to the value at the end of transition, the turbulence measurements taken by Gaster (7 data points) and Bellows (1 point) were used to determine $\gamma(x)$ and, hence, the onset of transition in the shear layer x_t similar to the method described in Appendix B for transition in unseparated flows. The Reynolds number based on the difference between this distance and separation, $(\text{Re}_x)_{st} = \text{Re}_{xt} - \text{Re}_{xs}$, is plotted in Fig. 19. The two highest data are from Gaster's measurements in long bubbles, while the lower data are from those in short bubbles. Both may be correlated by using the same Reynolds number variation given in Eq. (10) to provide

$$(\text{Re}_x)_{st} = 300 \ \text{Re}_{\theta s}^{0.7} \quad \text{(short bubbles)}$$

$$(\text{Re}_x)_{st} = 1000 \ \text{Re}_{\theta s}^{0.7} \quad \text{(long bubbles)} \qquad (11)$$

Subtracting these lengths from the total laminar-transition length provides the actual transition length in separated flows. This was done using all the data presented in Fig. 18 and the results are plotted in Fig. 20. Here the ordinate is now Re_{LT}, the Reynolds number based on the transition length, i.e., $\text{Re}_{LT} = U_s(x_T - x_t)/\nu$. Although a considerable scatter exists, it is apparent that the transition-length Reynolds number is independent of whether the bubble is short or long. A correlation of the data in this figure is given by

$$\text{Re}_{LT} = 400 \ \text{Re}_{\theta s}^{0.7}. \qquad (12)$$

The results imply that the difference between long and short bubbles is not the length of transition, but the length of the unstable laminar shear layer. Apparently, once transition begins it depends only on the separation Reynolds number and perhaps the free-stream turbulence. One would also expect the length of the laminar shear layer to depend on turbulence, but as found for attached transitional flows in adverse pressure gradients, its effect may be overshadowed by the inherent instabilities of the velocity profile. This raises some interesting questions. First, are there two modes of instability for separated boundary layer flows? If one considers Rayleigh's inviscid-instability analysis, the answer is yes. Secondly, do these two modes give rise to the two different lengths of the laminar shear layer in a separation bubble?
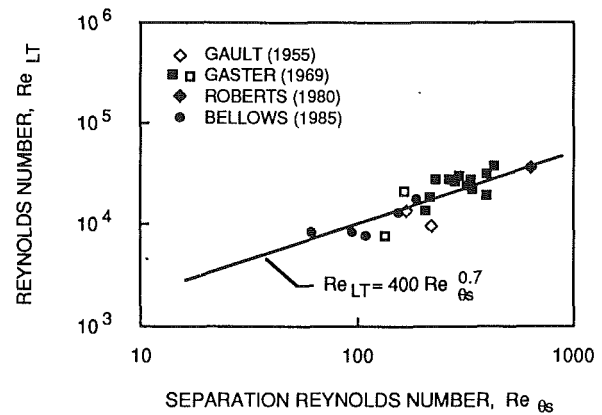
Since transition, for the most part, takes place in the constant pressure region of the bubble, the production rate of turbulent spots in separation bubbles may be obtained using Eq. (12) together with that developed for transition in attached flows with zero pressure gradient, viz., $\hat{n}\sigma = 4.61/\text{Re}_{LT}^2$. This provides

$$\hat{n}\sigma = 2.28(10)^{-5}/Re_{\theta s}^{1.4} \qquad (13)$$

and allows one to use all the techniques developed for attached transitional flows to determine separated transitional flows. Presently, it is suggested that Eq. (11) be used to determine the onset of transition in separated flows.

All of this is somewhat tentative, and requires further experimental investigation, particularly with regard to the effect of turbulence level. Nevertheless, in an effort to present a collective picture of transition for attached and separated flows, it is interesting to present all the results in one figure. One such presentation is shown in Fig. 21 where the transition length Reynolds number is plotted against the momentum thickness Reynolds number at transition. Since the momentum thickness Reynolds number changes little between separation and the onset of transition, one has $\text{Re}_{\theta t} \approx \text{Re}_{\theta s}$ for transition in separation bubbles. For clarity, only lines representing the data are shown.

The upper straight line is for attached flat-plate transition at all turbulence levels. Eliminating Tu between Eqs. (8) and (9) and substituting for $\hat{n}\sigma$ in terms in Re_{LT} results in the expression $\text{Re}_{LT} = 126 \ \text{Re}_{\theta t}^{1.4}$. Transition in favorable pressure gradients occurs above this line, while transition in adverse pressure gradients occurs below. The dotted lines represent transition lengths at a constant turbulence level for different pressure gradients. Transition in separation bubbles with low free-stream turbulence occurs along the lower straight line and is given by Eq. (12). In addition, a curved line has been drawn that represents the transition length for attached flows at various turbulence levels but with $\lambda_{\theta t} \approx -0.082$. This line has been obtained by using only the data to the far left in Fig. 14. The line is different from that for transition in separation bubbles

Transactions of the ASME

Fig. 21 Topolgy of transition in a Reynolds number transition length and momentum thickness plane for various pressure gradients and free-stream turbulence levels

Fig. 23 Multiple modes of transition on a surface as the result of an unsteady, periodic passing of a wake

Fig. 22 Unsteady wake propagation through a rotor blade row

and indicates that transition in separation bubbles is shorter than for attached flow, even though the pressure gradient parameters $\lambda_{\theta t}$ and $\lambda_{\theta s}$ are the same. What is interesti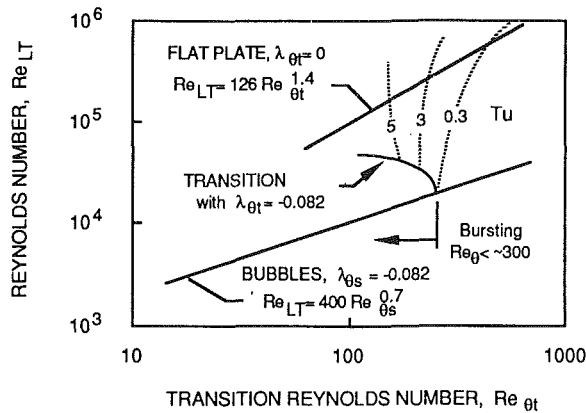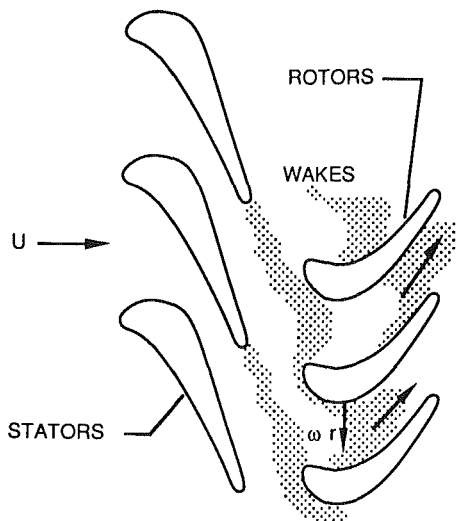ng is that the two merge somewhere around $\mathrm{Re}_{\theta t} = 300$, which roughly coincides with the maximum value for "bursting," as reported by Gaster, below which one may have either short or long bubbles.

Periodic-Unsteady Transition. Unsteady flows in gas turbines caused by wakes from upstream airfoils or obstructions, such as shown in Fig. 22, have recently received much attention. One reason is that only recently have data from new full- and large-scale (rotating) compressor and turbine facilities been compared back-to-back to (nonrotating) cascade tests. Results of these comparisons have shown large time-averaged discrepancies in predicted losses and surface heat loads. On the suction surface, modern measurement techniques and data acquisition systems (see Hodson, 1984; Ashworth et al., 1985; Doorly and Oldfield, 1985a, 1985b; Doorly et al., 1985; Doorly, 1988; Dring et al., 1986; Dunn, 1986; Dunn et al., 1986; LaGraff et al., 1989; Wittig et al., 1988; Dong and Cumpsty, 1990a, 1990b) have allowed one to determine the discrepancy caused by an improper account of laminar–turbulent transition. In particular, it has been shown that the transition, as a result of the unsteady passing of wakes from the upstream airfoils, is unsteady and cannot be predicted using steady-flow boundary layer analysis.

Recent measurements by Johnson et al. (1990) have shown that a passing shock wave from an upstream airfoil can also induce transition. In their case, the shock wave caused a small, concentrated vortex on the pressure side of the airfoil near its leading edge and induced transition as it moved along the surface. Since a theory is not yet available for this unsteady shock-induced mode of transition, it is presently proposed that it be treated identically to that for wake-induced transition.

Models for unsteady wake-induced transition have been proposed by several investigators; namely, Doorly (1988), Sharma et al. (1988), Addison and Hodson (1990a, 1990b), Mayle and Dullenkopf (1989, 1991), and Hodson (1990). While Sharma, Addison and Hodson, and Hodson were mainly concerned with the effect of transition on the aerodynamic loss and showed that the time-averaged loss depended on the reduced frequency, Doorly and Mayle and Dullenkopf were mostly concerned with its effect on the time-averaged heat load distribution. Much earlier, however, Walker (1974) described a model for unsteady transition on compressor blades, which depended on the unsteady formation and collapse of separation bubbles, and Pfeil and Herbst (1979), after conducting an innovative set of experiments, qualitatively described the model for wake-induced transition, which is now generally accepted as correct.

In particular, Pfeil and Herbst and later Pfeil et al. (1983) showed that the wakes caused the boundary layer to become turbulent during their "impingement" on the plate. This, they pointed out, formed wake-induced transition zones, which propagated down the plate at a velocity less than the wake passing velocity. Although not formally stated, they implied that the time-averaged condition of the boundary layer may be obtained from

$$\tilde{f} = (1 - \tilde{\gamma})f_L + \tilde{\gamma}f_T \qquad (14)$$

which is similar to Eq. (2) except that $\tilde{\gamma}$ is now the time-averaged intermittency. In addition, Pfeil and Herbst also discovered regions of natural transition occurring between those induced by the wake. This is significant in that it implies that multiple modes of transition can occur independently of one another on the same surface at the same instant. The situation is shown in Fig. 23 where the intermittency distribution along such a surface is plotted. While instantaneous distributions of intermittency are shown for the wake-induced transition regions, the time-averaged distribution for the normal-mode transition region is shown. An instant later, the intermittency distributions associated with the wakes will have moved downstream (to the right) and broadened. The normal-mode transition is now considered to originate at x_{tn}, while the wake-induced transition is considered to originate at x_{tw}. At the instant depicted, the boundary layer, which is first laminar (to the left of x_{tw}), becomes turbulent (at x_{tw}), then laminar (between x_{tw} and x_{tn}) and turbulent again.

Doorly used the intermittency concept and assumed that the high turbulence content of the wake produces a turbulent patch

Fig. 24 Coalescence of turbulent spots into turbulent strips as a result of a passing highly turbulent wake

Fig. 25 Time-averaged intermittency distribution as a function of the reduced streamwise distance

Fig. 26 The distribution of a wake-induced transitional heat transfer coefficient as predicted by the Mayle–Dullenkopf model

in an otherwise laminar boundary layer during each passing. To obtain the time-averaged flow, he used Eq. (14) and an intermittency determined by computing the temporal position of the wake and its width along the surface. That is, he assumed transition propagated at the same rate as the wake. Measurements by Pfeil et al., Addison and Hodson, LaGraff et al., and Liu and Rodi (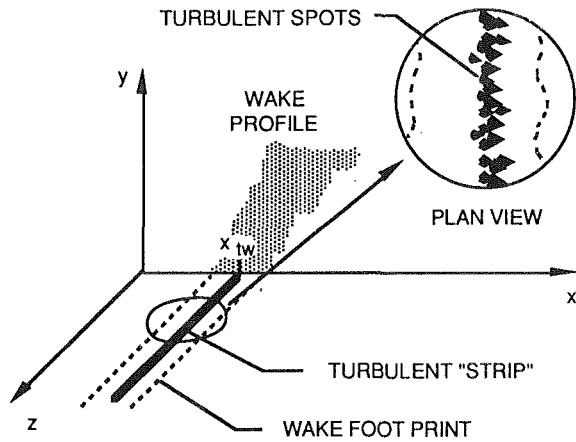1989) indicate that this is not the case. Comparison with time-averaged heat-flux measurements showed only a qualitative agreement.

Mayle and Dullenkopf based their model on Emmons' turbulent spot theory. Their extension of Emmons' theory consists of two main points. First they considered that transition can occur in multiple modes such that two or more modes of transition can be occurring simultaneously as shown in Fig. 23. Second, they considered the production function for turbulent spots, $g(P_0)$ in Eq. (1), to be a function of time and space. In addition, they assumed that the production of turbulent spots caused by the passing wake was so intense that the spots immediately coalesced into turbulent "strips," such as shown in Fig. 24, which then propagated and grew along the surface within the laminar boundary layer. Contrary to Doorly, however, once the turbulent strip was formed it was allowed to propagate and grow independently of the wake. As a result, their theory predicts a wake-induced intermittency distribution with no need to calculate the wake position.

Assuming that the turbulent spots, which are produced normally (through a normal "steady" mode) and by the periodic passing of wakes imbedded in the free stream (wake-induced transition), are independent, Mayle and Dullenkopf found that the time-averaged intermittency $\tilde{\gamma}$ is given by

$$\tilde{\gamma}(x) = 1 - [1 - \gamma_n(x)][1 - \tilde{\gamma}_w(x)] \qquad (15)$$

where γ_n and $\tilde{\gamma}_w$ are the intermittency distributions for normal and wake-induced transition. The tilde refers to a time-averaged quantity over the wake passing period. The intermittency γ_n is given by Eq. (6) where the onset of transition and the spot production rate are given by the expressions for the appropriate normal mode of transition (e.g., Eqs. (8) and (9) for natural transition with $dp/dx = 0$).

Assuming a square wave distribution for the turbulent-strip production function and evaluating the production rate from experiments, Mayle and Dullenkopf found a relatively simple expression for the time-averaged, wake-induced intermittency $\tilde{\gamma}_w$, namely

$$\tilde{\gamma}_w(x) = 1 - \exp\left[-1.9\left(\frac{x - x_{tw}}{U\tau} \right) \right]. \qquad (16)$$

In this expression, U is the airfoil's incident velocity and τ is the wake-passing period.
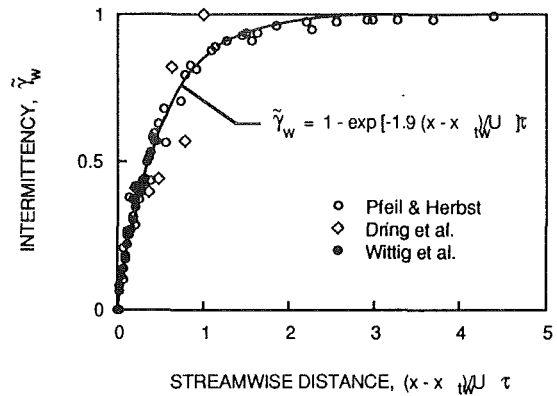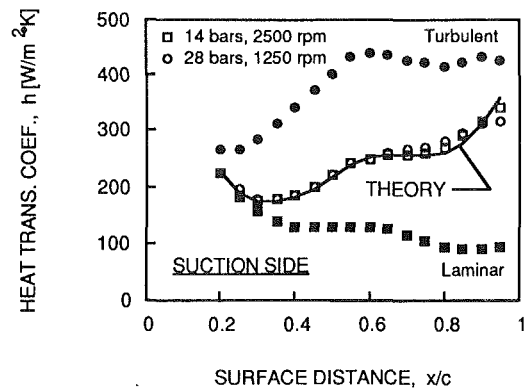
Figure 25 presents a comparison of this result with data from experiments conducted in a wind tunnel, a cascade facility, and a large-scale rotating turbine facility. The agreement is seen to be excellent. Expressing τ in terms of the wake-passing frequency ω and introducing a chord length c, an equation incorporating the reduced frequency ω_r is obtained, i.e.,

$$\tilde{\gamma}_w(x) = 1 - \exp\left[-0.302\omega_r\left(\frac{x - x_{tw}}{c} \right) \right]$$

where $\omega_r = \omega c/U$. From this it can be deduced that the time-averaged loss for wake-induced transitional flow on a surface will depend only on the reduced frequency ω_r, as found by Sharma et al. and Hodson, and the beginning of transition x_{tw}/c.

From Eq. (14) with $f = $ St, Eqs. (6), (16), calculated values of $\mathrm{St}_L(x)$ and $\mathrm{St}_T(x)$, and knowing the spot production rate and onset of transition (both x_{tn} and x_{tw}), the time-averaged surface heat flux distribution caused by wake-induced and any normal mode of transitional flow on the surface may be determined. Similarly, equating f to the energy thickness, the time-averaged loss may be obtained. The result of one such calculation is shown in Fig. 26 where the heat transfer coefficient on a first-stage turbine blade with wakes passing at two different frequencies is presented. The calculation, which includes the time-averaged multimode effects of a wake-induced transition that begins near $x/c = 0.25$ and a normal transition that begins near $x/c = 0.8$, is seen to be in excellent agreement with the data. In order to make this comparison, however, the beginning of transition x_{tw} had to be experimentally obtained.

Presently, there is very little information about x_{tw}. Correlation of Pfeil and Herbst's (1979) flat-plate results provides a transition Reynolds number based on the momentum thickness at transition of 145, i.e., $\mathrm{Re}_{\theta tw} = 145$. This lies above the value predicted using Fig. 10 and seems to exclude a simple

connection between $\mathrm{Re}_{\theta tw}$ and the maximum intensity of turbulence in the wake. In fact, a value of $\mathrm{Re}_{\theta t} = 145$ corresponds to $Tu \approx 4$ percent, which is about four times lower than the maximum value in the wake as reported by Pfeil et al. Recently, Addison and Hodson (1991) presented a theory that assumes that x_{tw} varies with time according to the convected turbulence level in the wake and its effect on $\mathrm{Re}_{\theta tw}$. While this is undoubtedly true for wakes with very low turbulence levels, the result just mentioned seems to contradict their assumption for wakes normally found in gas turbines. However, the possibility does exist that the effect of turbulence beyond a certain "saturation" level is of little consequence in producing a turbulent strip. From the above comparison, this level might be about 4 percent. The discussion so far has not mentioned the turbulence length scale effect in the wake. As shown for other modes of transition, this effect cannot be neglected. This should also be expected for wake-induced transition. Along a somewhat different line of thought, it may be expected that the "jet-" or "sink-like" behavior of a wake as it passes over the surface (see Kerrebrock and Mikolajczak, 1970) could also trigger transition. Dong and Cumpsty (1990b), however, found no evidence that this actually happens. Hence, while the mechanism for wake-induced turbulent spots in Pfeil and Herbst's experiment seems to reside in the intensity and scale of turbulence within the wake, the connection is not yet known.

In regard to transition on airfoils, a correlation of the data from Dring et al. (1986) provides $\mathrm{Re}_{\theta tw} \approx 45$, which is lower than any value to be expected from considering a bypass mechanism based on wake turbulence. It appears that transition is provoked in this case by a periodic formation and collapse of a suction side leading edge bubble caused by the variation in incidence angle form the passing wake. On the other hand, this does not appear to be the case in any of the other unsteady airfoil experiments, viz., Addison and Hodson (1990a), Dong and Cumpsty (1990b), Mayle and Dullenkopf (1989, 1991), Dullenkopf et al. (1991), and Liu and Rodi (1990). In fact, for most of those just mentioned, the onset of wake-induced transition appears to occur on the suction surface at the point of minimum pressure. Obviously, more work is required before a complete understanding of the production mechanism for wake-induced turbulent strips is obtained.

Part III—Transition in Throughflow Components

Transition Phenomena in Compressors. Even though the flow in a compressor is complex and involves large regions of three-dimensional endwall and clearance-leakage flows, the skin friction losses associated with the airfoils usually account for half of the loss in stage efficiency at design. Off design, however, this loss rises dramatically as a result of massive airfoil separation. For compressors, as low-pressure turbines, the separation process is closely tied to transition such that the interplay between the two must be understood. Therefore, the basic role of transition in compressors is not only in reducing on-design losses, but in improving the off-design behavior and, as a result, increasing the off-design margin. Success, however, crucially depends on understanding transition in adverse pressure gradients, transition in separated flows, and wake-induced transition. In fact, nowhere else, except perhaps in the low-pressure turbine, is it more crucial in the engine to understand such a variety of transition modes and their interaction than in the compressor.

Modern compressor airfoils are generally designed with a prescribed velocity distribution. While this design method allows for greater flexibility and, possibly, larger stage efficiencies, than the design methods of the past, it requires a good understanding and an ability to predict the boundary layer development along the airfoil. Since a compressor operates over a wide range of flow conditions, from low to high inlet Reynolds and Mach numbers as well as at high positive and
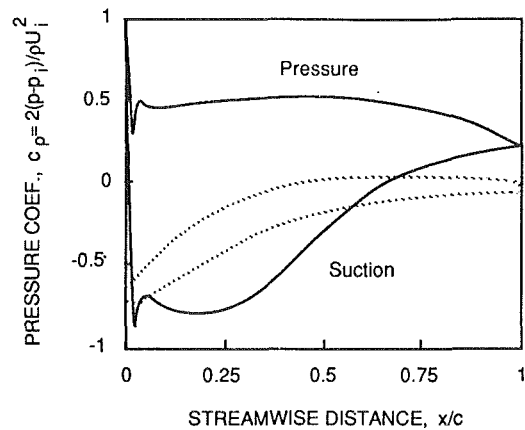
Fig. 27 Pressure distributions at design for a typical controlled-diffusion compressor airfoil
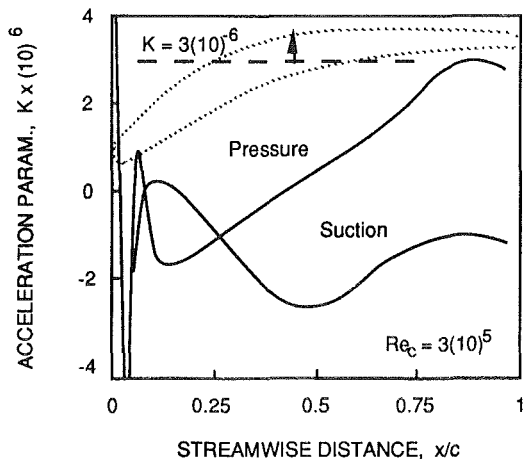
Fig. 28 Acceleration parameters for the airfoil pressure distributions shown in Fig. 27 with $\mathrm{Re}_c = 3(10)^5$

negative incidence angles, designing compressors, as designing low-pressure turbines, is sometimes considered more of an art than a science.

General Flow Considerations. A modern compressor-airfoil pressure distribution is shown in Fig. 27. Here, the pressure coefficients based on inlet conditions for both the pressure and suction sides are plotted as functions of the distance along the airfoil. After an inital leading edge variation caused by a change in surface curvature, the pressure rises slightly over the first half of the pressure surface and then decreases over the last half. On the suction side, after the leading edge effect, the pressure decreases to a minimum and then rises such that the pressure gradient is first strongly adverse and then only mildly so. The concept of this design is to obtain the highest possible turning (increase of pressure across the row) with the lowest loss by promoting a laminar boundary layer over the forward portion of the suction side with transition near the point of minimum pressure. The largest adverse pressure gradient is then imposed on the flow immediately after transition when the turbulent boundary layer is the thinnest, and therefore least likely to separate. Further aft, as the boundary layer grows, the pressure gradient is relaxed to prevent separation. In cascade tests (e.g., Hobbs and Weingold, 1984), designs of this sort normally provide a low loss up to off-design angles of about ±7 deg and then a catastrophically increasing loss when the boundary layers separate without reattaching. Since these tests are usually conducted with a low free-stream turbulence level, this behavior may not be typical for the engine. Nevertheless, the problem is to predict transition correctly on
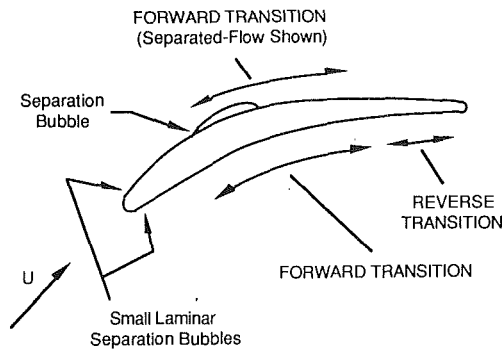
Fig. 29 Transition on a typical compressor airfoil at design conditions

TURBULENCE LEVEL, Tu [percent]

Fig. 30 The critical acceleration parameter for transition and separation

the suction side since the whole design concept depends on the boundary layer being turbulent as the flow diffuses.

The distributions of the acceleration parameter corresponding to the airfoil pressure distributions shown in Fig. 27 are presented in Fig. 28 for a chord Reynolds number of $Re_c = 3(10)^5$. The large variations in the distributions near the leading edge, resulting from the curvature changes, usually cause small, leading-edge laminar separation bubbles to form. Generally, these bubbles have no effect on airfoil performance and little effect on subsequent boundary layer growth unless the airfoil operates at large off-design incidence angles (see later). Since K is inversely proportional to the chord Reynolds number, the acceleration parameter for other values of the chord Reynolds number can easily be obtained. The value above which reverse transition occurs is also shown.

The transitional flows that usually exist on a compressor airfoil at design are sketched in Fig. 29. On the pressure surface, transition usually begins before the point of maximum pressure. Near the trailing edge on the pressure surface, acceleration parameters approaching those necessary to reverse the transition process are not uncommon. Hence, as recently shown by Dong and Cumpsty (1990a), it is possible to have a flow on the pressure surface that is always in a transitional state. Although this situation may be calculated with reasonable accuracy using modern computational procedures and the methods described in Part II, it is generally of little consequence since the loss incurred on the pressure side of the airfoil at design is always small compared to that on the suction side.

Not only is the boundary layer development on the suction side more complicated than that on the pressure side, it is more important to predict. On this side, transition usually begins near the point of minimum pressure and occurs via either the bypass or separated-flow mode depending on Reynolds number. For a successful design, transition must be completed before the boundary layer experiences the strong adverse pressure gradient. After transition, the turbulent boundary layer is generally maintained in a state of "controlled diffusion" (Stratford, 1959) by designing $K \approx \text{const}/Re_\theta$. This condition provides boundary layer growth at a constant shape factor and skin friction coefficient (see Jones and Launder, 1972). In older designs, the adverse pressure gradient on the suction surface was stronger aft. This produced a longer transition and usually a turbulent boundary layer separation near the trailing edge. Contrary to the off-design behavior of controlled-diffusion airfoils, these designs lead to a more gradual loss in performance with increasing angle of attack until separation moves ahead of transition. As shown by Wisler (1985), they may also provide a larger compressor flow range.

Since either a bypass or separated-flow transition can occur on the suction side, it is worthwhile here to reconsider the criteria for transition and separation in light of the results presented in Part II. Since laminar separation occurs when $\lambda_{\theta s} = Re_{\theta s}^2 K_s \approx -0.082$, transition will always begin before separation when $K > K_{\text{crit}} = -0.082/Re_{\theta t}^2$. Using Eq. (9), this
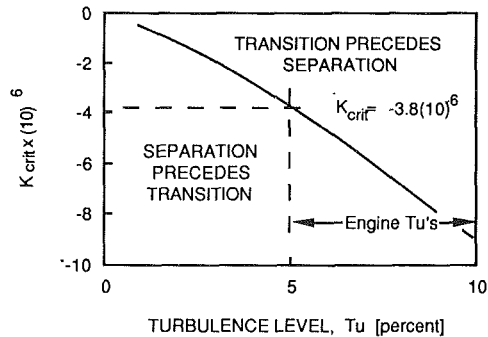
criterion can be expressed in terms of the free-stream turbulence level, namely, $K_{\text{crit}} = -5.13(10)^{-7} Tu^{5/4}$. This result is plotted in Fig. 30. Above the line transition will occur before the laminar boundary layer separates, while below the line separation precedes transition.

With engine turbulence levels greater than 5 percent, K_{crit} will always be less than $-3.8(10)^{-6}$. Therefore, as an example, for the airfoil shown in Fig. 28, transition on the suction side will precede separation in the engine since K is everywhere greater than K_{crit} except at the leading edge where, as previously discussed, laminar separation bubbles can occur. If tests were conducted at low free-stream turbulence level, however, say $Tu = 1$, the same calculation provides $K_{\text{crit}} = -5.1(10)^{-7}$ indicating that the boundary layer will separate before it transitions. Therefore, cascade tests operated at reduced turbulence level (e.g., Roberts, 1975; Cyrus, 1988; Schulz and Gallus, 1988) may be completely misleading. This situation was recently shown by Dong and Cumpsty (1990a) who found that a separation bubble that existed on the suction surface at low turbulence levels disappeared at a higher level. In their case, however, the losses were hardly affected, since transition on the airfoil began in a strong, adverse pressure gradient region. As a result, the production of turbulent spots was large and the transition length was short compared to the length for which the flow was turbulent.

The effect of Reynolds number can be ascertained from Figs. 28 and 30. As the chord Reynolds number decreases, the acceleration parameter increases according to $K \propto 1/Re_c$. Therefore, a point on the airfoil in an adverse pressure gradient for which K was originally greater than K_{crit} can have $K < K_{\text{crit}}$ at a lower Reynolds number. That is, as the Reynolds number decreases, the flow there can separate before transition. While this behavior is discussed in more detail in the section on low-pressure turbines, it is interesting to stop and consider this progression from a "transition first" to "separation first" flow.

Since transition is a temporal and spatial stochastic process, laminar separation can occur in a transitioning flow between the turbulent spots as shown in Fig. 31. For this flow, separation and reattachment is an unsteady process where laminar separation bubbles form and collapse between the turbulent spots. When separation occurs within the transition zone, i.e., $x_t < x_s$, the bubble is probably "short." As the Reynolds number is reduced, however, separation moves forward until it reaches the position x_t, at which point $Re_{\theta s} = Re_{\theta t}$. With a further reduction of Reynolds number, separation moves upstream of transition, i.e., $x_s < x_t$, and a region of completely laminar separated flow develops between separation at x_s and transition at x_t. Apparently, this is when long bubbles become possible.

In Fig. 29, the effect of periodic unsteady flow was not considered. The major effect is caused by wakes from previous airfoils or obstructions. The unsteady convection of wakes through airfoil rows was first described by Smith (1966) and

Fig. 31 Instantaneous plan view of transition with separation

Fig. 33 Effect of wake-induced transition on separation bubbles

Fig. 32 Pattern of airfoil–wake interactions

Fig. 34 Transition on a compressor airfoil at off-design incidence

subsequently analyzed by Kerrebrock and Mikolajczak (1970). The process is shown in Fig. 32 where one must imagine the various wake segments as being convected with the flow. These wakes not only produce fluctuations in velocity (total pressure), but in incidence, turbulence, and total temperature as well.
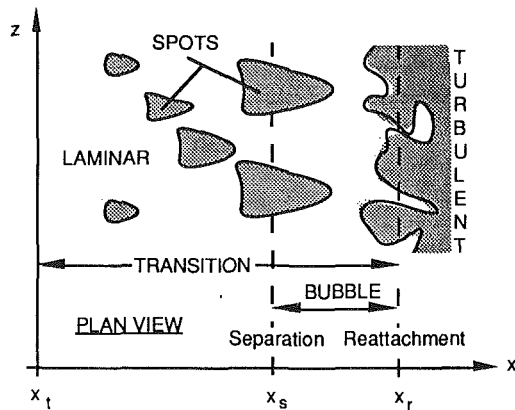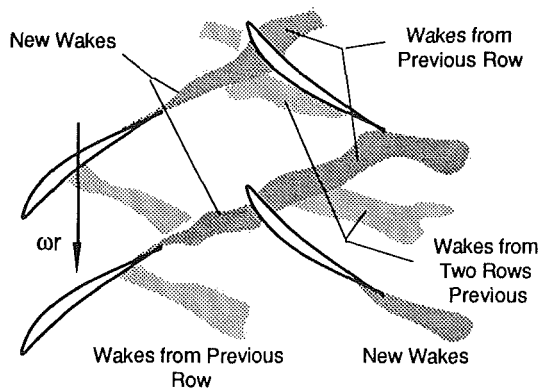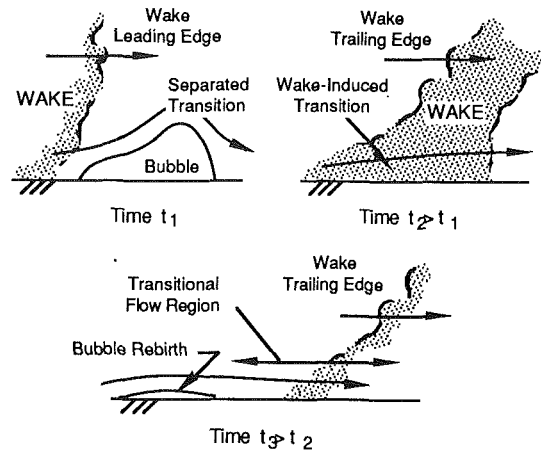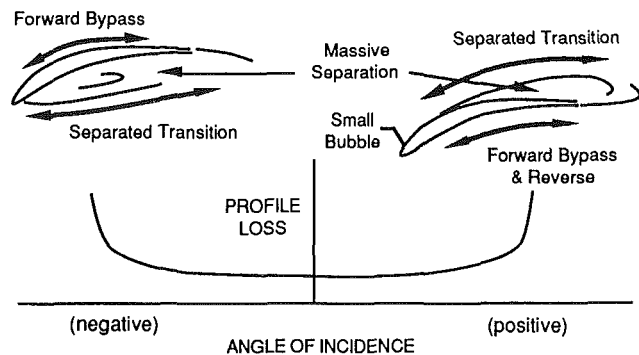
The effect of velocity and incidence fluctuations is most acute where the pressure gradients on an airfoil are the greatest. In general, this is near the airfoil's leading edge. Here, the fluctuations can produce oscillating separation bubbles. As far as transition is concerned, however, the variation in turbulence level is most important (except at off-design conditions and low Reynolds numbers where the incidence fluctuations can drastically alter the leading edge separation bubble). Since wake-induced transition begins earlier than any normal-mode transition, the time-averaged losses with the periodic passing of wakes will be larger. The same may be said for shock-induced transition as described by Johnson et al. (1990), although their work was done on turbines.

The unsteady transition caused by wakes (or shock waves) produces a multimoded transition situation such as described in Part II. An interesting effect arises, however, from their interaction. For example, consider the interaction between transition induced by a wake and that from a separation bubble as shown in Fig. 33. Before interaction and when the wake is upstream of the separation bubble, time t_1, two distinct regions of transition are found. As the wake-induced transition convects downstream and passes over the separation point, time t_2, the bubble "disappears" because the flow at the original point of separation is turbulent and able to withstand the adverse pressure gradient. Once transition induced by the wake passes, however, time t_3, the bubble reforms and transition downstream is a combination arising from both. Evidence of this interaction has only recently been found by Dong and Cumpsty (1990b) and Schröder (1989). No information exists

on the interaction between wake-induced transition and the massively separated flow that occurs at off-design conditions, but it is not difficult to imagine large oscillations of separated and attached flow occurring as a result of the process just described.

Between design and off-design conditions, the transition and separated regions become progressively larger. (Considering separation occurs at transition, $Re_{\theta s} = Re_{\theta t}$ and assuming $Tu = 5$ percent, the separation bubble will have a length of $Re_{LT} = 42,500$ if it is long; 1000 if it is short.) The progression may not be always regular in that a separation bubble may suddenly burst as previously discussed. Nevertheless, at large off-design incidences, large regions of flow separation are normal. This is shown in Fig. 34. Flows of this sort are also found on airfoils operating at chord Reynolds numbers near 100,000 (Roberts, 1975; Cyrus, 1988; Mueller et al., 1983; Citavy and Jilek, 1990); however, much of the work was conducted at low free-stream turbulence levels with the exception being that presented by Citavy and Norbury (1977). In any case, at either large off-design incidences or low Reynolds numbers, acceleration parameters less than the critical value (Fig. 30) are obtained and separation occurs before transition, i.e., $Re_{\theta s} < Re_{\theta t} \approx 100$ to 150. The present problem, however, is that there is not enough information at the higher turbulence levels to predict accurately the laminar and transitional lengths associated with these separated flow regions.

At large positive angles of incidence (Fig. 34 right), a small laminar separation bubble is found on the suction surface near the leading edge, where a sharp negative spike in K usually exists. At large negative angles (Fig. 34 left), this bubble disappears. Farther downstream on the suction surface, the flow separates completely with separation occurring much earlier for positive angles than negative, if separation at the negative angles occurs at all. Although only the extreme situations where
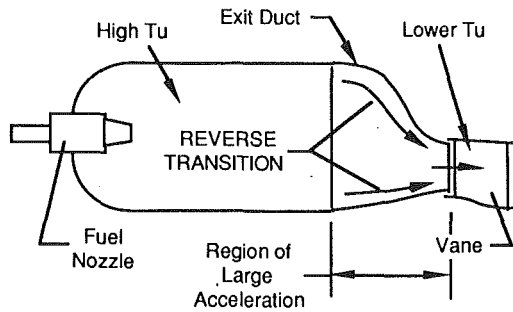
Fig. 35 Transition in an exit duct of a straight-through burner

Fig. 36 Transition in a reverse-curved exit duct

complete separation occurs are shown, it is possible at intermediate angles that the flow reatttaches turbulently after an extended transitional-separated flow. In fact, by considering the pressure distributions and the ideas of transition and separation presented above, it is not difficult to visualize the progression from the on- to extreme off-design situations as presented in Figs. 29 and 35, respectively. The difficulty, of course, is in predicting it. On the pressure surface, an extended region of transitional flow is again found at large positive angles of incidence (Fig. 34) but, because of higher accelerations, it begins later than that at design and may never be completed. While a leading edge bubble will not occur at these angles, at large negative incidence angles it develops into a massive separation, which may or may not reattach. Whether it does or not depends on the length of the laminar and transitional shear layer in the bubble and the interaction with the whole flow field.

Some Specific Design Considerations

(a) To model transition and separation correctly, all tests for compressor design purposes must be operated at high inlet turbulence levels with appropriate turbulent length scales.

(b) To calculate transitional flows on compressor airfoils correctly, one must allow for transition in both the forward and reverse directions with periodic wake-induced transition.

(c) To calculate separated-flow transition and the massive separation at low Reynolds numbers and off-design angles of incidence correctly, one must consider modeling the laminar, transitional, and turbulent shear layer flows, which may be large in extent and may or may not be near a surface.

(d) Designers should consider the change of K relative to K_{crit} for variations of Reynolds number and angle of incidence.

(e) Designers should consider forcing a short, separated-flow transition by a local change in surface curvature (and therefore a local change in K) as a method of controlling transition and increasing design margin.

Suggested Transition Research for Compressors

(a) Experiments should be conducted to investigate separated-flow transition at high turbulence levels and appropriate turbulent length scales.

(b) Experiments should be conducted to investigate the unsteady interaction between large separated regions and the periodic passing of wakes.

Transition Phenomena in Combustors. Transition is generally not thought of as occurring in combustors. However, as shown recently by Paxson and Mayle (1991), laminar boundary layers can and do exist in flows with extreme turbulence as long as the pressure gradient is favorable. Consequently, in the exit ducts of combustors where large favorable pressure gradients are obtained, laminar and transitional flows occur with transition being in either direction. Usually, there is no effect on the aerodynamic performance of the combustor unless, as possible in reverse-curved exit ducts, the duct is so poorly designed that it separates. Therefore, the main role of transition in combustors is its effect on heat transfer. Since convective heat transfer to the liner walls is significant only in the exit duct, it is only here that one may expect a benefit from understanding the role of transition.
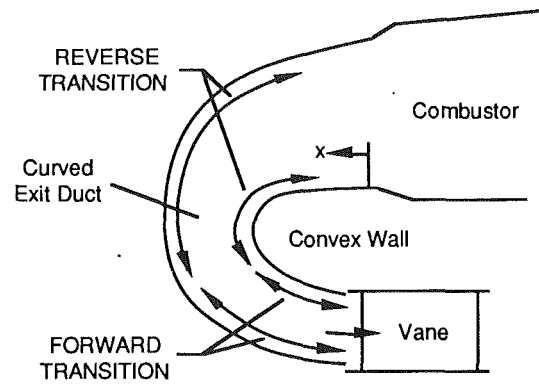
General Flow Considerations. For the most part, a combustor may be considered as a highly turbulent, constant pressure, low-velocity device. In the exit ducts, however, acceleration is significant and the accelaration parameter reaches some of the highest values in the engine. This has a twofold effect. First, the acceleration causes a reduction in the mainstream turbulence intensity and shifts the frequency range of turbulence toward the lower frequencies. In this sense, the exit duct acts as low-pass filter. However, the resulting turbulence is still large and stubbornly persists, particularly the low-frequency components, through most of the turbine. Second, the high acceleration causes the boundary layers on the walls, whether film cooled or not, to transition from turbulent to laminar flow. This latter effect may be alternatively viewed as an initiation of a new boundary layer, which, because of its low Reynolds number, is laminar. Depending on the acceleration, turbulence levels, and duct length, the flow may then again transition, but in a forward direction.

This situation is shown in Fig. 35 for flow through an exit duct in a typical medium-sized engine where forward transition may not occur, and in Fig. 36 for flow through a reverse-curved exit duct where forward transition usually follows the reverse transition process on both walls. In the latter case, forward transition is initiated in a highly accelerated region and the production of turbulent spots is relatively small (Fig. 15). This produces an extended transition, which may or may not be complete before the end of the duct. In either case, however, the convective heat load will increase through the duct in contrast to that predicted if turbulent flow were assumed to exist throughout. That is, because of transition, the heat loads will be highest in the aft portion of the duct even though the acceleration there is minimal.

In a reverse-curved exit duct, if transition does not begin before the minimum pressure location on the convex wall, the laminar boundary layer there may separate. This situation is easily avoided, as usually done, by designing the duct such that the pressure gradient parameter λ_θ is always greater than -0.082 on the convex wall. On the concave wall, the scenario is much the same as that on the convex wall but, since the boundary layers are thicker, the heat loads are roughly half those found on the convex wall. Therefore, transition on the concave wall is not as critical from a cooling standpoint as that on the convex wall.

The acceleration parameter for the convex wall of a typical reverse-curved exit duct is shown in Fig. 37. At its entrance, K is higher than $20(10)^{-6}$ and over half of its surface is higher than that for reverse transition, viz., $K = 3(10)^{-6}$. Hence, the flow over the forward portion of the surface will be laminar (albeit highly disturbed).
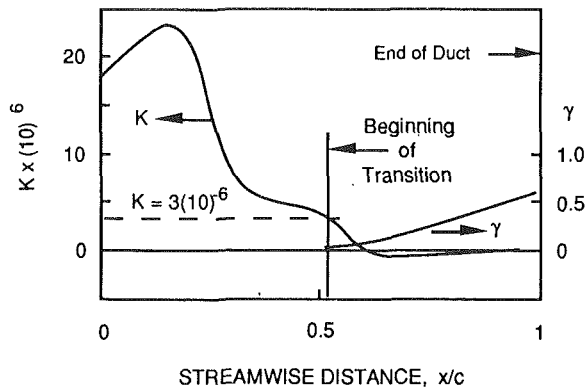
Fig. 37 Acceleration parameter and intermittency distributions on the convex wall for a reverse-curved exit duct

Fig. 38 Stanton number and heat transfer coefficient distributions on the convex wall for a reverse-curved exit duct

To the author's knowledge, no information is available in the published literature on flows or heat transfer in combustor exit ducts. In order to illustrate the ideas presented above, therefore, a simple calculation was performed for the convex wall of a reverse-curved exit duct using the acceleration parameter distribution in shown in Fig. 37. The momentum thickness Reynolds number was calculated for the flow and the onset of transition determined using Eq. (9) with $Tu = 7$ percent. Admittedly this value for Tu is low, but it must be remembered that the very large fluctuations are usually associated with the large-scale turbulence, which simply appear as an unsteady free stream to the boundary layer. Furthermore, no data on Tu are available for these flows. In any case, since transition was predicted to begin within the region where K is greater than that required for reverse transition, transition was assumed to begin where $K = 3(10)^{-6}$ according to the implications of reverse transition on forward transition as discussed in Part I. Here, the need for conducting transition experiments at high turbulence levels in large favorable pressure gradients becomes obvious.

The intermittency distribution was calculated using Eq. (6) (modified according to Chen and Thyson) and Figs. 9 and 15. The result is also shown in Fig. 37 and indicates that transition is only half completed by the end of the duct. For a designer counting on turbulent flow before the minimum pressure location to prevent separation, this could be disastrous.

The corresponding Stanton number distribution is shown in Fig. 38, where both the fully laminar and turbulent distributions are shown for comparison. The Stanton number for transition was calculated using Eq. (2) with x_t as the beginning of the turbulent boundary layer. The Stanton number along the wall is seen to increase continually through transition as does the heat transfer coefficient (plotted in arbitrary units). This is directly opposite the trend that would be predicted if the flow was assumed to be turbulent throughout and suggests that heat loads on combustor exit ducts should be predicted by using boundary layer codes that allow both forward and reverse transition.

Some Specific Design Considerations

(a) To calculate heat loads on combustor exit ducts correctly, boundary layer codes that allow both forward and reverse transition should be used.

(b) Designers should consider that the boundary layer on the convex wall of a reverse-curved exit duct may not be turbulent before the point of minimum pressure.

Suggested Transition Research for Combustors

(a) Experiments should be conducted to examine reverse transition at high free-stream turbulence levels.

(b) Experiments should be conducted to examine forward transition with large accelerations at high free-stream turbulence levels.
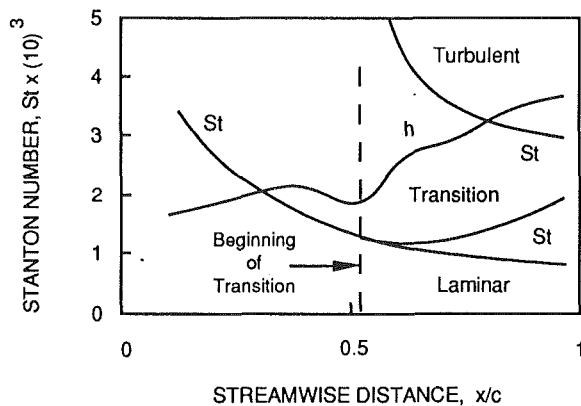
Transition Phenomena in Turbines. Predicting flows in the turbine is presently ahead of the ability to predict the flow in any other component of the engine and is now so sophisticated that many unsteady and three-dimensional effects can more or less be routinely handled (see Sharma et al., 1990). This situation is mainly a consequence of efforts begun in the late 1960s to predict airfoil heat loads accurately in face of the ever-increasing turbine inlet temperatures. Since turbine airfoils fail locally, the need for predicting the local airfoil heat load is crucial to providing adequate cooling and acceptable durability. "Adequate" in this sense implies cooling schemes that are "tailored" to the heat load distribution in order not to incur large losses in engine efficiency due to excessive cooling flow. Two other reasons for the advanced state of turbine flow prediction are: (1) Flows in the compressor and combustor involve large separated regions and are therefore much more difficult to predict, and (2) the numerical error of earlier codes overshadowed the aerodynamic losses that are the designer's primary concern in a compressor. In addition, measurements of boundary layer parameters and heat transfer distributions in large-scale test facilities, such as those conducted by Langston et al. (1977), Graziani et al. (1980), Dring et al. (1982), and Hodson (1984), were used to "verify" many of the modern computational programs.

Since the flow on a turbine airfoil is transitional and since turbulent heat transfer is generally three to five times larger than laminar, transition has always played a significant role in turbines. In the high turbine, the primary role of transition is in affecting heat load distributions. For modern, extensively film-cooled turbines, however, transition in the first stages is becoming less important. As shown by Blair et al. (1989a, 1989b), the trend toward low aspect ratios with large regions of vortical flow also decreases the role transition plays in the overall heat load and aerodynamics. Since aerodynamic losses are mostly attributed to the turbulent flow after transition, the effect of transition on losses is generally small in the high-pressure turbine. In the low-pressure turbine, the flow is primarily two-dimensional and has a low Reynolds number. Here, as described by Hourmouziadis (1989), understanding the role of transition is crucial to an aerodynamically efficient design. The one to two point increase in efficiency for the latest low-pressure turbine designs demonstrates this point well. For small gas turbines, which operate at Reynolds numbers similar to those found in the low-pressure turbine of a medium-sized engine, transition is important to both the aerodynamic and thermal design. In this case, however, because of the low aspect ratios and eventually because of a greater reliance on film cooling, its effect may not be as dramatic.

As the turbine operation changes from sea level takeoff to cruise, the most critical changes occur in the low-pressure turbine. This is because the operating Reynolds numbers are low there to begin with and a further decrease can cause separation

Fig. 39 Pressure distributions for a typical high-pressure turbine airfoil

Fig. 40 Distributions of the acceleration parameter for airfoil pressure distributions in Fig. 39 at $Re_c = 6(10)^5$

to occur before transition. In this respect, the role of transition in low-pressure turbines is more similar to that in compressors undergoing large variations in mass flow than to that in a high turbine. As a result, much of that discussed above with regard to the various mechanisms of transition in compressors is directly applicable to low-pressure turbines. In the following, the general description of transitional flow is subdivided into two parts. The first concerns transition in the high-pressure turbine, while the second concerns that in the low-pressure turbine.
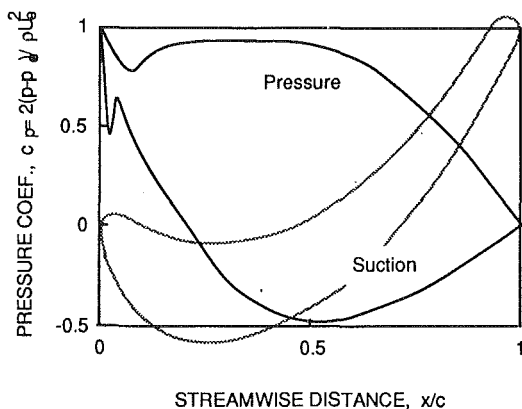
General Flow Considerations—High-Pressure Turbines. A midspan pressure distribution for a typical high-pressure turbine airfoil is shown in Fig. 39. The airfoil overlaid on the figure corresponds to a second-stage stator. After an initial variation, the pressure on the pressure surface is nearly constant until midchord and then decreases. On the suction surface, the pressure gradient is favorable over much of the forward portion of the airfoil and mildly adverse over the remaining half. The ratio between the distances of favorable and adverse pressure gradients (forward or aft loaded) has always been a question of design philosophy, which really depends on one's understanding of transition. This was shown by Sharma et al. (1982) who investigated the boundary layer development on a surface for both forward and aft-loaded type pressure distributions.

The variation in pressure near the leading edge, a consequence of the change in surface curvature there, is always found on turbine airfoils and occurs on either the pressure or suction surface or both. It is particularly noticeable on high-pressure turbine airfoils, where large leading edges are designed in order to reduce the heat load and provide space for internal cooling schemes. As in compressors, and on airfoils without film cooling, small laminar separation bubbles may occur here, which generally have little consequence unless, as discussed before, they are the source of an unsteady, wake-induced transition (Dring et al., 1986). In some situations, however, a short bubble with turbulent reattachment is found (Bellows and Mayle, 1986). For airfoils with a film-cooled leading edge, Mick and Mayle (1988) have shown that these bubbles do not occur.

Distributions of the acceleration parameter for the suction and pressure sides of the airfoil shown in Fig. 39 are presented in Fig. 40. These are shown for a Reynolds number, based on the axial chord, of $Re_c = 6(10)^5$. For other Reynolds numbers, the values shown here should be multiplied by the inverse of the Reynolds number ratio. For other angles of incidence, both the shape of the distributions and magnitudes change. For the conditions presently being considered, the acceleration parameter exceeds that for reverse transition near the leading edge on the suction surface and over more than half of the latter portion on the pressure surface. In addition, the acceleration parameter is less than the critical value of $-3.8(10^{-6})$, cor-

responding to a free-stream turbulence level greater than 5 percent, near the leading edge on the pressure surface. These trends are typical of all high-pressure turbine airfoils. If the flow separates near the leading edge on the pressure side and reattaches turbulent, it will always transition back to laminar. This was also shown to happen on the suction surface by Hodson (1984).
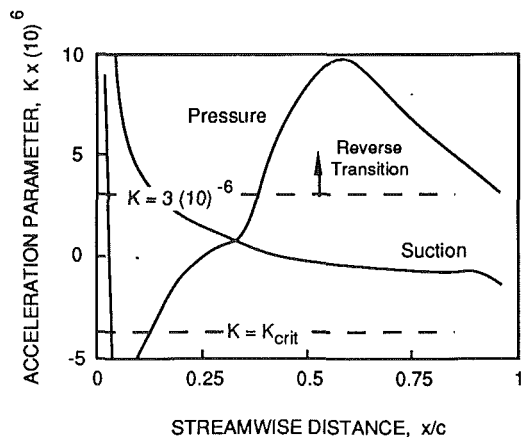
Although Taylor–Görtler vortices may develop on the concave portion on the pressure surface within the boundary layer (either naturally, see Appendix A, or downstream of a separation bubble), the strong favorable pressure gradient will quickly lead to their dissipation. On the suction surface, the adverse pressure gradient following the minimum pressure location is mild and, because $K > K_{crit}$, transition will occur before separation (at engine turbulence levels) unless the chord Reynolds number is roughly three times smaller. The length of transition, of course, depends on where it begins, i.e., where $Re_\theta(x) = Re_{\theta t} \approx 150$ ($Tu = 5$). If the onset of transition is before the minimum pressure location, transition will be more extended than if its onset is aft of this location. Until recently, its extent was considered to depend mainly on $Re_{\theta t}$, which is wrong (see Fig. 15). It depends on the turbulence and acceleration parameter at the beginning of transition. One of the major complaints regarding past transition models is that they predicted a transition length that was too short. If transition begins within a region having a favorable pressure gradient, the length can be quite long as shown above for the exit duct of a combustor.

Two typical situations for boundary layer development on high-pressure turbine airfoils at design conditions are presented in Fig. 41. One is for a leading edge separation/turbulent-reattachment bubble on the suction side, while the other is for a bubble on the pressure side. Although a first-stage stator is shown as one of the airfoils, the flow described for it can occur on an airfoil in any other row. For a film-cooled airfoil, the boundary layer transitions immediately at injection (see Appendix A). Downstream, however, in the extremely favorable pressure gradients, the flow could become laminar-like as shown by Warren and Metzger (1972). The author remembers well the markings on the forward portion of a film-cooled suction surface, which indicated little mixing of the coolant until the gage point, at which location everything became uniform across the span. If this is any indication of laminar and turbulent/relaminarizing flows co-existing beside one another in the spanwise direction followed by transition to a completely turbulent flow, the whole idea of transition on film-cooled surfaces should be reviewed.

For an airfoil without film cooling, the flow on the suction surface with a leading edge bubble first transitions in the reverse direction and remains laminar to a position where K falls below
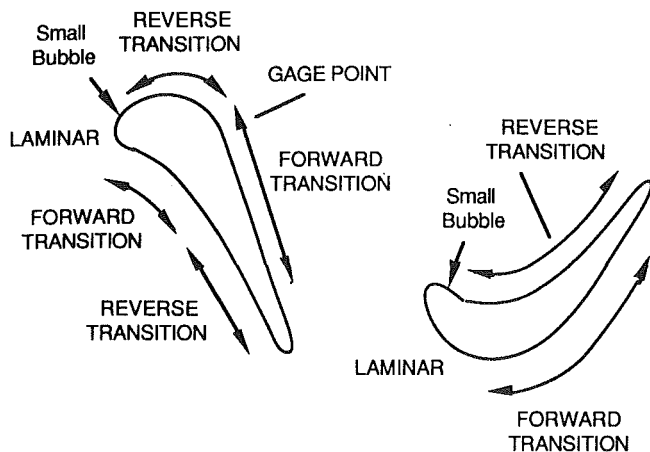
Fig. 41 Transition on a high-pressure turbine airfoil

Fig. 42 Stanton number distributions for a high-pressure turbine rotor (Dring et al., 1986)

Fig. 43 Typical low-pressure turbine acceleration parameters

Fig. 44 Transition on a low-pressure turbine airfoil at various Reynolds numbers

$3(10)^{-6}$. If the momentum thickness Reynolds number at this location is greater than that given by Eq. (9), the flow begins transition immediately; otherwise transition is delayed to the position where Re_θ equals the value given by Eq. (9). Without a leading edge bubble, the flow remains laminar until $Re_\theta = Re_{\theta t}$. In these cases, transition can be extended over a significant portion of the surface if it begins before the position of minimum pressure.

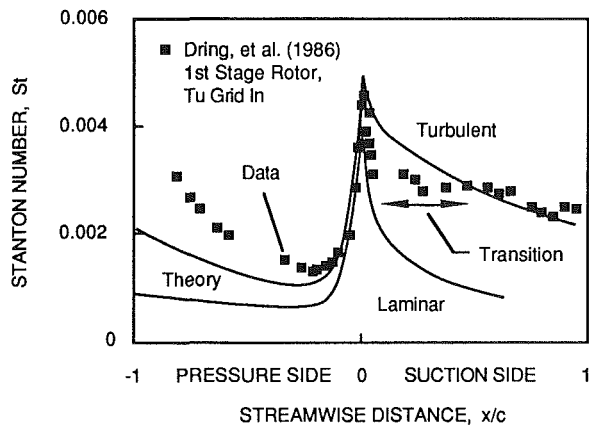On the pressure surface without a leading edge bubble, the flow first transitions in the forward direction and then once K rises above $3(10)^{-6}$ begins to transition in the reverse direction. With a leading edge separation/turbulent-reattachment bubble, however, the flow remains turbulent until K rises above $3(10)^{-6}$ and then begins a reverse transition process. Apparently, as shown in Fig. 42 where the predicted and measured Stanton numbers on a first stage rotor are compared, this flow is not yet straightforward to calculate. Although the comparison is shown for a rotor blade, the discrepancy on the pressure side is typical. The problem appears to be associated with the balance between the production of turbulent spots and the dissipation of turbulence in strong favorable pressure gradients.

For airfoils with a significant laminar portion, the effect of the wake is important in both predicting loss and the heat load distribution. The combined effect of bypass transition and periodic-unsteady wake-induced transition was experimentally shown by Wittig et al. (1988) and theoretically described first by Mayle and Dullenkopf (1989). Details of the phenomenon have already been presented in Part II. Here, however, it might be worthwhile to note that if transition by any normal mode begins downstream of a wake-induced transition, it will even-

tually overwhelm the latter. This is simply a consequence of the fact that the streamwise development of transition via any normal mode depends on the square of the distance from onset, while that for wake-induced transition depends linearly on the distance. The effect of wakes on the reverse transition process is completely unknown, but Dullenkopf et al. (1991) have found that the wakes affect the whole pressure surface more or less uniformly in proportion to the residence time of the wakes.
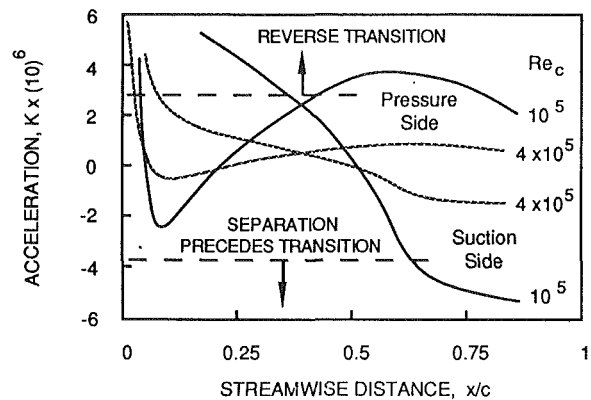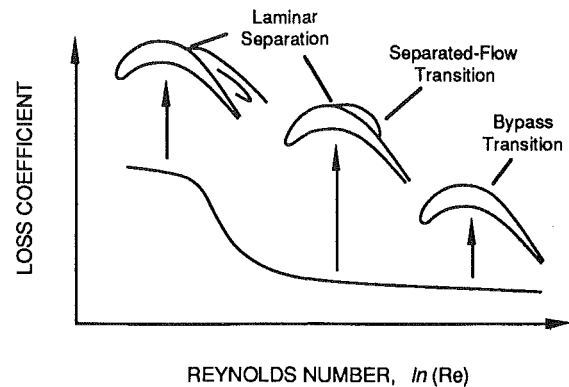
General Flow Considerations—Low Pressure Turbines. Distributions of the acceleration parameter for the suction and pressure surfaces of a typical low-pressure turbine airfoil are shown in Fig. 43. These distributions are shown for two different operating Reynolds numbers, $Re_c = 10^5$ and $4(10)^5$. Since $K \propto 1/Re_c$, one curve is easily obtainable from the other. Similar distributions and values will be found for turbines in a small engine. Note the difference between the magnitudes in this figure and those in Fig. 40. Also compare them with the distributions shown in Fig. 28 for the compressor.

Since it is possible to draw curves of constant Re_c in this figure, the position where $K = K_{crit}$ for different operating Reynolds numbers, i.e., the location where separation may occur before transition, can be ascertained. If $K < K_{crit}$ and $\lambda_\theta = Re_\theta^2 K = -0.082$ before this location, separation will precede transition. As the chord Reynolds number is reduced, it is obvious from Fig. 43 that the position where $K = K_{crit}$ moves upstream.

The flow on a low-pressure turbine airfoil within a typical operating range of Reynolds numbers is shown[8] in Fig. 44. At

---

[8]An excellent review on low-pressure turbine technology and design methodology has been presented by Hourmouziadis (1989), which is recommended reading for all designers of gas turbine airfoils. Much of the following description is unashamedly borrowed from this work but modified according to the new ideas presented herein.

high Reynolds numbers, transition occurs far enough upstream that the flow is turbulent over most of the airfoil. Near the trailing edge, depending on design, turbulent separation is possible. With decreasing Reynolds number, any turbulent separation disappears and transition (via the bypass mode) moves downstream. This is the situation pictured to the right in the figure, i.e., fully attached flow with transition. The loss corresponding to this flow is lowest. With a further decrease in Reynolds number, however, the location where $K = K_{\text{crit}}$ moves forward and laminar separtion ahead of transition becomes possible. If separation does occur, the bubble is short and the flow reattaches as turbulent. In this case (shown in the center of the figure), the loss is only slightly higher than the previous case. For lower Reynolds numbers, the laminar shear layer and transition lengths increase until, as discussed in the section on compressors, reattachment before the trailing edge is no longer possible and the airfoil completely separates. This flow with its associated large loss is pictured to the left in the figure.

The objective of the designer, of course, is to design an airfoil that provides the lowest loss through its operating range. This requires one to predict the Reynolds number at which the separation bubble "bursts" and the losses change dramatically. That is, one must be able to predict separated-flow transition. Presently, as pointed out in Part II, this is the mode of transition of which the least is known.

Since the flow is laminar over a substantial portion of a low-pressure turbine airfoil, wake-induced transition plays an important role in the turbine's performance. Recently, Schröder (1990) has detected strong interactions between wakes and separation bubbles much like that found by Dong and Cumpsty (1990b) in a large-scale compressor facility and as shown in Fig. 33. Using hot-film surface gages, Schröder deduced that a wake-induced transition periodically eliminated a short separated-flow transition bubble, which normally occured slightly downstream of the minimum pressure location. With wake-induced transition occurring earlier than normal transition, via either the bypass or separated-flow mode, the time-averaged losses will increase. For typical turbine airfoils, these losses may be about 25–100 percent of their "steady" flow component (Sharma et al., 1988). For low Reynolds number situations where airfoils have an extended region of separated flow, however, Binder et al. (1989) have found that wake-induced transition actually reduced the loss. Apparently, this is a result of the periodic reduction in a massive separation bubble.

Some Specific Design Considerations

(a) To model transition and separation correctly, all tests for turbine design purposes must be operated at high inlet turbulence levels and appropriate turbulent length scales. This is particularly true for low-pressure turbine tests.

(b) To calculate transitional flows on turbine airfoils correctly, one must allow for transition in both the forward and reverse direction with periodic wake-induced transition.

(c) To calculate separated-flow transition and the massive separation at low Reynolds numbers in low-pressure turbines correctly, one must consider modeling the laminar, transitional, and turbulent shear layer flows, which may or may not be near the airfoil's surface.

(d) Designers should consider the change of K relative to K_{crit} for variations of Reynolds number in low-pressure turbines.

(e) Designers should consider forcing a short, separated-flow transition by a local change in surface curvature (and therefore a local change in K) as a method of controlling transition in low-pressure turbines.

Suggested Transition Research for Turbines

(a) Experiments should be conducted to investigate for-ward transition at high free-stream turbulence levels with appropriate turbulent length scales and large accelerations.

(b) Experiments should be conducted to determine a design criterion for the onset of wake-induced transition.

(c) Experiments should be conducted to investigate low-Reynolds-number separated-flow transition at high turbulence levels.

(d) Experiments should be conducted to investigate the effect of large acceleration for a film-cooled surface.

Conclusions

Some New Concepts. The following concepts concern both transition in general and transition in gas turbines. They are mostly new and a result of the present work.

(a) Transition information obtained at low free-stream turbulence levels is virtually useless for the gas turbine designer.

(b) Transition in gas turbines is controlled mainly by the free-stream turbulence, pressure gradient, and the periodic, unsteady passing of wakes.

(c) The onset of transition in gas turbines depends only on the free-stream turbulence (level and scale), the periodic unsteady effect of wakes and shock waves, and whether the acceleration is greater or less than that for reverse transition.

(d) The length of transition in gas turbines depends only on the free-stream turbulence and pressure gradient.

(e) The effects of surface roughness, surface curvature, compressibility, and heat transfer on transition in gas turbines are secondary to those of free-stream turbulence.

(f) Transition in gas turbines in an accelerating flow region is always of the bypass type. This can certainly be said for transition in most gas turbine flows except that near separation.

(g) Transition on gas turbine airfoils can be a multimoded type, which implies that transition can occur at two different locations on the same surface at the same time.

(h) Transition and separation can occur within the same general region on a surface as a mosaic of alternating and fluctuating turbulent spots and laminar separation bubbles, and the whole process can be completely interrupted by the periodic passing of a wake-induced transition.

Although the concept of improving aerodynamic performance by forcing transition through short separation bubbles is not new, the author has not seen an airfoil design with an abrupt midchord change in curvature (and hence pressure) in order to force a controlled separated-flow transition. Whether this would increase off-design performance without an increase in on-design loss is not known. The problem is, of course, to design the airfoil such that the forced separation bubble is always short.

Suggestions for Future Work. While many suggestions were already given, those provided in this section are more general in nature and include suggestions for both fundamental and developmental work. The list, given in my order of priority, is not meant to be exhaustive and it is expected that the reader may be able to supply many suggestions of her or his own.

(a) Measurements of turbulence intensity and spectral characteristics in an engine cannot be overemphasized.

(b) Experiments should be conducted to investigate separated-flow transition at high turbulence levels and appropriate length scales.

(c) Experiments should be conducted to investigate forward transition at high free-stream turbulence levels with appropriate turbulent length scales and large accelerations.

(d) Experiments should be conducted to determine a design criterion for the onset of wake-induced transition

(e) Attempts should be made to relate the onset of transition to local conditions within a laminar boundary layer or free-shear layer, such as maximum turbulence intensity, so that models such as those proposed herein can be included in computational fluid dynamic codes.

(f) Investigators of transition should report values of $\hat{n}$ and $Re_{\theta t}$ from which all other information on the near-wall intermittency can be obtained.

(g) Investigators of transition should report the free-stream turbulence level, turbulent length scale, and the acceleration parameter at the onset of transition.

Acknowledgments

References

Abu-Ghannam, B. J., and Shaw, R., 1980, "Natural Transition of Boundary Layers—The Effects of Turbulence, Pressure Gradient and Flow History," *J. Mech. Eng. Sci.*, Vol. 22, pp. 213–228.

Acharya, M., 1985, "Pressure-Gradient and Free-Stream Turbulence Effects on Boundary-Layer Transition," Brown Boveri Forschungszentrum, Baden, Switzerland, Forschungsbericht KLR 85-127 C (see also Feiereisen, W. J., and Acharya, M., 1986, "Modeling of Transition and Surface Roughness Effects in Boundary-Layer Flows," *AIAA Journal*, Vol. 24, pp. 1642–1649).

Addison, J. S., and Hodson, H. P., 1990a, "Unsteady Transition in an Axial Flow Turbine, Part 1—Measurements on the Turbine Rotor," ASME JOURNAL OF TURBOMACHINERY, Vol. 112, pp. 206–214.

Addison, J. S., and Hodson, H. P., 1990b, "Unsteady Transition in an Axial Flow Turbine, Part 2—Cascade Measurements and Modeling," ASME JOURNAL OF TURBOMACHINERY, Vol. 112, pp. 215–221.

Addison J. S., and Hodson. H. P., 1991, to be presented at the 1991 ASME Turbo Expo Congress.

Ashworth, D. A., LaGraff, J. E., Schultz, D. L., and Grindrod, K. J., 1985, "Unsteady Aerodynamic and Heat Transfer Processes in a Transonic Turbine Stage," ASME *Journal of Engineering for Gas Turbines and Power*, Vol. 107, pp. 1022–1030.

Bellows, W. J., 1985, "An Experimental Study in Leading Edge Separating-Reattaching Boundary Layer Flows," Ph.D. Thesis, Rensselaer Polytechnic Institute, Troy, NY.

Bellows, W. J., and Mayle, R. E., 1986, "Heat Transfer Downstream of a Leading Edge Separation Bubble," ASME JOURNAL OF TURBOMACHINERY, Vol. 108, pp. 131–136.

Binder, A., Schröder, T., and Hourmouziadis, J., 1989, "Turbulence Measurements in a Multistage Low-Pressure Turbine," ASME JOURNAL OF TURBOMACHINERY, Vol. 111, pp. 153–161.

Blair, M. F., 1982, "Influence of Free-Stream Turbulence on Boundary Layer Transition in Favorable Pressure Gradients," ASME *Journal of Engineering for Power*, Vol. 104, pp. 743–750.

Blair, M. F., 1983, "Influence of Free-Stream Turbulence on Turbulent Boundary Layer Heat Transfer and Mean Profile Development, Part I—Experimental Data," ASME *Journal of Heat Transfer*, Vol. 105, pp. 33–40.

Blair, M. F., 1990, "Boundary Layer Transition in Accelerating Flows With Intense Freestream Turbulence," submitted for publication in the *J. Fluid Mech.*

Blair, M. F., Dring, R. P., and Joslyn, H. D., 1989a, "The Effect of Turbulence and Stator/Rotor Interactions on Turbine Heat Transfer: Part I—Design Operating Conditions," ASME JOURNAL OF TURBOMACHINERY, Vol. 111, pp. 87–96.

Blair, M. F., Dring, R. P., and Joslyn, H. D., 1989b, "The Effects of Turbulence and Stator/Rotor Interactions on Turbine Heat Transfer: Part II—Effects of Reynolds Number and Incidence," ASME JOURNAL OF TURBOMACHINERY, Vol. 111, pp. 97–103

Brown, A., and Martin, B. W., 1979, "Heat Transfer to Turbine Blades, With Special Reference to the Effects of Mainstream Turbulence," ASME Paper No. 79-GT-26.

Brown, B., and Burton, R. C., 1977, "The Effects of Free-Stream Turbulence Intensity and Velocity Distribution on Heat Transfer to Curved Surfaces," ASME Paper No. 77-GT-48.

Cebeci, T., and Smith, A. M. O., 1974, *Analysis of Turbulent Boundary Layers*, Academic Press, New York.

Chen, K. K., and Thyson, N. A., 1971, "Extension of Emmons' Spot Theory to Flows on Blunt Bodies," *AIAA Journal*, Vol. 9, pp. 821–825.

Citavy, J., and Norbury, J. F., 1977, "The Effect of Reynolds Number and Turbulence Intensity on the Performance of Compressor Cascade With Prescribed Velocity Distribution," *J. Mech. Engng. Sci.*, Vol. 19, pp. 93–100.

Citavy, J., and Jilek, J., 1990, "The Effect of Low Reynolds Number on Straight Compressor Cascades," ASME Paper No. 90-GT-221.

Coles, D., 1956, "The Law of the Wake in the Turbulent Boundary Layer," *J. Fluid Mech.*, Vol. 1, pp. 191–226.

Crawford, M. E., and Kays, W. M., 1976, "STAN-5—A Program for Numerical Computation of Two-Dimensional Internal and External Boundary Layer Flows," NASA CR-2742.

Cyrus, V., 1988, "The Effect of the Reynolds Number on the Three-Dimensional Flow in a Straight Compressor Cascade," ASME Paper No. 88-GT-269.

Dhawan, S., and Narasimha, R., 1958, "Some Properties of Boundary Layer Flow During Transition From Laminar to Turbulent Motion," *J. Fluid Mech.*, Vol. 3, pp. 418–436.

Dong, Y., and Cumpsty, N. A., 1990a, "Compressor Blade Boundary Layers: Part 1—Test Facility and Measurements With No Incident Wakes," ASME JOURNAL OF TURBOMACHINERY, Vol. 112, pp. 222–230.

Dong, Y., and Cumpsty, N. A., 1990b, "Compressor Blade Boundary Layers: Part 2—Measurements With Incident Wakes," ASME JOURNAL OF TURBOMACHINERY, Vol. 112, pp. 231–240.

Doorly, D. J., and Oldfield, M. L. G., 1985a, "Simulation of the Effects of Shock Wave Passing on a Turbine Rotor Blade," ASME *Journal of Engineering for Gas Turbines and Power*, Vol. 107, pp. 998–1006.

Doorly, D. J., and Oldfield, M. L. G., 1985b, "Simulation of Wake Passing in a Stationary Turbine Rotor Cascade," *J. Propulsion and Power*, Vol. 1, pp. 316–318.

Doorly, D. J., Oldfield, M. L. G., and Scrivener, C. T. J., 1985, "Wake-Passing in a Turbine Rotor Cascade," *Heat Transfer and Cooling in Gas Turbines*, AGARD-CP-390, pp. 7-1 to 7-18.

Doorly, D. J., 1988, "Modeling the Unsteady Flow in a Turbine Rotor Passage," ASME JOURNAL OF TURBOMACHINERY, Vol. 110, pp. 27–37.

Dring, R. P., Joslyn, H. D., Hardin, L. W., and Wagner, J. H., 1982, "Turbine Rotor–Stator Interaction," ASME *Journal of Engineering for Power*, Vol. 104, pp. 729–742.

Dring, R. P., Blair, M. F., Joslyn, H. D., Power, G. D., and Verdon, J. M., 1986, "The Effects of Inlet Turbulence and Rotor/Stator Interactions on the Aerodynamics and Heat Transfer of a Large-Scale Rotating Turbine Model," NASA CR 4079.

Dullenkopf, K., Schulz, A., and Wittig, S., 1991, "The Effect of Incident Wake Conditions on the Mean Heat Transfer of an Airfoil," ASME JOURNAL OF TURBOMACHINERY, Vol. 113, pp. 412–418.

Dunn, M. G., 1986, "Heat-flux Measurements for the Rotor of a Full-Stage Turbine: Part I—Time-Averaged Results," ASME JOURNAL OF TURBOMACHINERY, Vol. 108, 1, pp. 90–97.

Dunn, M. G., George, W. K., Rae, W. J., Woodward, S. H., Moller, J. C., and Seymour, P. J., 1986, "Heat-Flux Measurements for the Rotor of a Full-Stage Turbine: Part II—Description of Analysis Technique and Typical Time-Resolved Measurements," ASME JOURNAL OF TURBOMACHINERY, Vol. 108, 1, pp. 98–107.

Emmons, H W., 1951, "The Laminar-Turbulent Transition in Boundary Layer—Part I," *J. Aero. Sci.*, Vol. 18, pp. 490–498.

Emmons, H. W., and Bryson, A. E., 1951, "The Laminar–Turbulent Transition in a Boundary Layer, Part II," *Proc. 1st U.S. Nat. Congress of Theoretical and Applied Mechanics*, pp. 859–868.

Feindt, E. G., 1956, "Untersuchungen über die Abhängigkeit des Umschlages laminar-turbulent von Oberflächenrauhigkeit und der Druckverteilung," *Schiffbautechn. Gesellschaft*, Vol. 50, pp. 180–203.

Gaster, M., 1969, "The Structure and Behavior of Laminar Separation Bubbles," ARC R&M 3595.

Gault, D. E., 1955, "An Experimental Investigation of Regions of Separated Laminar Flow," NACA TN 3505.

Görtler, H., 1940, "Über eine dreidimensionale Instabiltät laminar Grenzschichten an konkaven Wänden," *Nachr. Wiss. Ges. Göttingen, Math. Phys. Klasse*, Neue Folge 2, No. 1; see also ZAMM, Vol. 21, 1941, pp. 250–252.

Gostelow, J. P., and Ramachandran, R. M., 1983, "Some Effects of Free Stream Turbulence on Boundary Layer Transition," *Proc. 8th Australasian Fluid Mech. Conf.*

Gostelow, J. P., 1989, "Adverse Pressure Gradient Effects on Boundary Layer Transition in a Turbulent Free Steam," *9th Int. Symp. on Air Breathing Engines*, Vol. 2, pp. 1299–1306.

Gostelow, J. P., and Blunden, A. R., 1989, "Investigations of Boundary Layer Transition in an Adverse Pressure Gradient," ASME JOURNAL OF TURBOMACHINERY, Vol. 111, pp. 366–375.

Gostelow, J. P., and Walker, G. J., 1991, "Similarity Behavoir in Transitional Boundary Layers Over a Range of Adverse Pressure Gradients and Turbulence Levels," ASME JOURNAL OF TURBOMACHINERY, Vol. 113, this issue.

Graziani, R. A., Blair, M. F., Taylor, J. R., and Mayle, R. E., 1980, "An Experimental Study of Endwall and Airfoil Surface Heat Transfer in a Large Scale Turbine Blade Cascade," ASME *Journal of Engineering for Power*, Vol. 102, pp. 257–267.

Hall, D. J., and Gibbings, J. G., 1972, "Influence of Stream Turbulence and Pressure Gradient Upon Boundary Layer Transition," *J. Mech. Engng. Sci*, Vol. 14, pp. 134–146.

Hislop, G. S., 1940, "The Transition of a Laminar Boundary Layer in a Wind Tunnel," Ph.D. Thesis, Cambridge University, United Kingdom.

Hobbs, D. E., and Weingold, H. D., 1984, "Development of Controlled Diffusion Airfoils for Multistage Compressor Application," ASME *Journal of Engineering for Gas Turbines and Power*, Vol. 106, pp. 271–278.

Hodson, H. P., 1984, "Boundary Layer and Loss Measurements on the Rotor of an Axial-Flow Turbine," ASME *Journal of Engineering for Gas Turbines and Power*, Vol. 106, pp. 391–399.

Hodson, H. P., 1990, "Modelling Unsteady Transition and Its Effects on Profile Loss," AGARD-CP-468, Paper 18.

Horton, H. P., 1969, "Semi-emperical Theory for the Growth and Bursting of Laminar Separation Bubbles," ARC CP1073.

Hourmouziadis, J., 1989, "Aerodynamic Design of Low Pressure Turbines," AGARD Lecture Series, No. 167.

Johnson, A. B., Oldfield, M. L. G., Rigby, M. J., and Giles, M. B., 1990, "Nozzle Guide Vane Shock Wave Propagation and Bifuraction in a Transonic Turbine Rotor," ASME Paper No. 90-GT-310.

Jones, W. P., and Launder, B. E., 1972, "The Prediction of Laminarization With a Two-Equation Model of Turbulence," *Int. J. Heat Mass Transfer*, Vol. 15, pp. 301–314.

Julien, H. L., Kays, W. M., and Moffat, R. J., 1969, "The Turbulent Boundary Layer on a Porous Plate: Experimental Study of the Effects of a Favorable Pressure Gradient," Stanford University, Thermo. Sci. Div. Rep. HMT-4.

Kerrebrock, J. L., and Mikolajczak, A. A., 1970, "Intra-Stator Transport of Rotor Wakes and Its Effect on Compressor Performance, "ASME *Journal of Engineering for Power*, Vol. 92, pp. 359–369.

Kuan, C., and Wang, T., 1989, "Some Intermittent Behavior of Transitional Boundary Layer," AIAA Paper No. 89-1890.

LaGraff, J. E., Ashworth, D. A., and Schultz, D. L., 1989, "Meaurement and Modeling of the Gas Turbine Blade Transition Process as Disturbed by Wakes," ASME JOURNAL OF TURBOMACHINERY, Vol. 111, pp. 315–322.

Langston, L. S., Nice, M. L., and Hooper, R. M., 1977, "Three-Dimensional Flow Within a Turbine Cascade Passage," ASME *Journal of Engineering for Power*, Vol. 99, pp. 21–28.

Launder, B. E., and Spalding, D. B., 1972, *Mathematical Models of Turbulence*, Academic Press, New York.

Liepmann, H. W., 1943, "Investigations on Laminar Boundary-Layer Stability and Transition on Curved Boundaries," NACA ACR 3H30 (NACA-WR-W-107).

Liepmann, H. W., and Fila, G. H., 1947, "Investigations of Effects of Surface Temperature and Single Roughness Elements on Boundary-Layer Transition," NACA TN 1196.

Liu, X., and Rodi, W., 1989, "Measurements of Unsteady Flow Over and Heat Transfer From a Flat Plate," ASME Paper No. 89-GT-2.

Liu, X., and Rodi, W., 1990, private communication.

Martin, B. W., Brown, A., and Garrett, S. E., 1978, "Heat Transfer to a PVD Rotor Blade at High-Subsonic Passage Throat Mach Number," *Proc. Inst. Mech. Engrs.*, Vol, 192, pp. 225–235.

Mayle, R. E., and Dullenkopf, K., 1989, "A Theory for Wake-Induced Transition," ASME JOURNAL OF TURBOMACHINERY, Vol. 112, pp. 188–195.

Mayle, R. E., and Dullenkopf, K., 1991, "More on the Turbulent-Strip Theory for Wake-Induced Transition," ASME JOURNAL OF TURBOMACHINERY, Vol. 113, pp. 428–432.

Mayle, R. E., and Paxson, D. E., 1991, "A New Look at Wake Flows," submitted for publication to the *J. Fluid Mech.* (see also Paxson, D. E., 1989, Ph.D. Thesis, Rensselaer Polytechnic Institute).

McDonald, H., and Fish, R. W., 1973, "Practical Calculations of Transitional Boundary Layers," *Int. J. Heat Mass Transfer.*, Vol. 16, No. 9.

Mehendale, A. B., Han, J. C., and Ou, S., 1990, "Influence of High Mainstream Turbulence on Leading Edge Heat Transfer," *AIAA/ASME Thermophysics and Heat Transfer Symposium*, ASME HTD-Vol. 138, pp. 27–35.

Mick, W. J., 1987, "Transition and Heat Transfer in Highly Accelerated Rough-Wall Boundary Layers," Ph.D. Thesis, Rensselaer Polytechnic Institute, Troy, NY.

Mick, W. J., and Mayle, R. E., 1988, "Stagnation Film Cooling and Heat Transfer, Including Its Effect Within the Hole Pattern," ASME JOURNAL OF TURBOMACHINERY, Vol. 110, pp. 66–72.

Morkovin, M. V., 1969, "On the Many Faces of Transition," *Viscous Drag Reduction*, C. S. Wells, ed., Plenum Press, New York, pp. 1–31.

Mueller, T. J., Pohlen, L. J., Conigliaro, P. E., and Jansen, B. J., Jr., 1983, "The Influence of Free-Stream Disturbances on Low Reynolds Number Airfoil Experiments," *Experiments in Fluids*, Vol. 1, pp. 3–14.

Narasimha, R., 1957, "On the Distribution of Intermittency in the Transition Region of a Boundary Layer," *J. Aero. Sci.*, Vol. 24, pp. 711–712.

Narasimha, R., Devasia, K. J., Gururani, G., and Badri Narayanan, M. A., 1984, "Transitional Intermittency in Boundary Layers Subjected to Pressure Gradient," *Experiments in Fluids*, Vol. 2, pp. 171–176.

Narasimha, R., 1985, "The Laminar–Turbulent Transition Zone in the Boundary Layer," *Prog. Aerospace Sci.*, Vol. 22, pp. 29–80.

Narasimha, R., and Dey, J., 1989, "Transition-Zone Models for 2-Dimensional Boundary Layers: A Review," *Sãdhanã*, Vol. 14, pp. 93–120.

Owen, F. K., 1970, "Transition Experiments on a Flat Plate at Subsonic and Supersonic Speeds," *AIAA Journal*, Vol. 8, pp. 518–523.

Paxson, D. E., and Mayle, R. E., 1991, "Laminar Boundary Layer Interaction With an Unsteady Passing Wake," ASME JOURNAL OF TURBOMACHINERY, Vol. 113, pp. 419–427.

Pfeil, H., and Herbst, R., 1979, "Transition Procedure of Instationary Boundary Layers," ASME Paper No. 79-GT-128.

Pfeil, H., Herbst, R., and Schröder, T., 1983, "Investigation of the Laminar-Turbulent Transition of Boundary Layers Disturbed by Wakes," ASME *Journal of Engineering for Power*, Vol. 105, pp. 130–137.

Riley, S., Johnson, M. W., and Gibbings, J. C., 1989, "Boundary Layer Transition of Strongly Concave Surfaces," ASME Paper No. 89-GT-321.

Roberts, W. B., 1975, "The Effect of Reynolds Number and Laminar Separation on Axial Cascade Performance," ASME *Journal of Engineering for Power*, Vol. 97, pp. 261–274.

Roberts, W. B., 1980, "Calculation of Laminar Separation Bubbles and Their Effect on Airfoil Performance," *AIAA J.*, Vol. 18, pp. 25–31.

Rüd, K., and Wittig, S., 1986, "Laminar and Transitional Boundary Layer Structures in Accelerating Flow With Heat Transfer," ASME JOURNAL OF TURBOMACHINERY, Vol. 108, pp. 116–123.

Schlichting, H., 1979, *Boundary-Layer Theory*, McGraw-Hill, New York.

Schmidt, R. C., and Patankar, S. V., 1991, "Simulating Boundary Layer Transition With Low-Reynolds-Number $k - \epsilon$ Turbulence Models: Part I—An Evaluation of Prediction Characteristics; Part II—An Approach to Improving the Predictions," ASME JOURNAL OF TURBOMACHINERY, Vol. 113, pp. 10–26.

Schraub, F. A., and Kline, S. J., 1965, Stanford University, Mech. Engng. Dept. Rept. MD-12.

Schröder, T., 1989, "Measurements With Hot-Film Probes and Surface-Mounted Hot-Film Gauges in a Multistage Low-Pressure Turbine," *1989 European Propulsion Forum*, Bath, United Kingdom, Vol. 15, pp. 1–27.

Schröder, T., 1990, oral presentation, 1990 Turbo Expo Congress, Brussels.

Schubauer, G. B., and Skramstad, H. K., 1948, "Laminar Boundary-Layer Oscillations and Transition on a Flat Plate," NACA Rept. 909.

Schubauer, G. B., and Klebanoff, P. S., 1955, "Contribution to the Mechanism of Boundary-Layer Transition," NACA TN 3489.

Schulz, H. D., and Gallus H. E., 1988, "Experimental Investigation of the Three-Dimensional Flow in an Annular Compressor Cascade," ASME JOURNAL OF TURBOMACHINERY, Vol. 110, pp. 467–478.

Sharma, O. P., Schlinker, R. H., Wells, R. A., and Bailey, D. A., 1982, "Boundary Layer Development on Turbine Airfoil Suction Surfaces," ASME *Journal of Engineering for Power*, Vol. 104, pp. 698–706.

Sharma, O. P., Renaud, E., Butler, T. L., Milsaps, K., Jr., Dring, R. P., and Joslyn, H. D., 1988, "Rotor–Stator Interaction in Axial-Flow Turbines," AIAA Paper No. 88-3013.

Sharma, O. P., 1987, "Momentum and Thermal Boundary Layer Development on Turbine Airfoil Suction Surfaces," AIAA Paper No. 87-1918.

Sharma, O. P. Renaud, E., Butler, T. L., Milsaps, K., Jr., Dring, R. P., and Joslyn, H. D., 1988, "Rotor–Stator Interaction in Axial-Flow Turbines," AIAA Paper No. 88-3013.

Smith, L. H., Jr., 1966, "Wake Dispersion in Turbomachines," ASME *Journal of Basic Engineering*, Vol. 88, pp. 688–690.

Stratford, B. S., 1959, "An Experimental Flow With Zero Skin Friction Throughout Its Region of Pressure Rise," ASME *J. Fluid Mech.*, Vol. 5, pp. 17–35.

Taylor, R. P., 1990, "Surface Roughness Measurements on Gas Turbine Blades," ASME JOURNAL OF TURBOMACHINERY, Vol. 112, pp. 175–180.

Thwaites, B., 1949, "Approximate Calculation of the Laminar Boundary Layer," *Aeronautical Quar.*, Vol. 7, pp. 245–280.

Walker, G. J., 1974, "The Unsteady Nature of Boundary Layer Transition on an Axial Compressor Blade," ASME Paper No. 74-GT-135.

Walker, G. J., 1987, "Transitional Flow on Turbomachine Blading," AIAA Paper No. 87-0010.

Walker, G. J., 1989, "Modeling of Transitional Flow in Laminar Separation Bubbles," *9th Int. Symp. Air Breathing Engines*, pp. 539–548.

Walker, G. J., and Gostelow, J. P., 1990, "Effects of Adverse Pressure Gradients on the Nature and Length of Boundary Layer Transition," ASME JOURNAL OF TURBOMACHINERY, Vol. 112, pp. 196–205.

Wang, T., and Simon, T. W., 1985, "Heat Transfer and Fluid Mechanics Measurements in Transitional Boundary Layers on Convex-Curved Surfaces," ASME Paper No. 85-HT-60.

Warren, J. M., and Metzger, D. E., 1972, "Heat Transfer With Film Cooling in the Presence of a Laminarizing Mainstream," ASME Paper No. 72-HT-11.

Wisler, D. C., 1985, "Loss Reduction in Axial-Flow Compressors Through Low-Speed Model Testing," ASME *Journal of Engineering for Gas Turbines and Power*, Vol. 107, pp. 354–363.

Wittig, S., Schulz, A., Dullenkopf, K., and Fairbank, J., 1988, "Effects of Free-Stream Turbulence and Wake Characteristics on the Heat Transfer Along a Cooled Gas Turbine Blade," ASME Paper No. 88-GT-179.

APPENDIX A

Secondary Effects

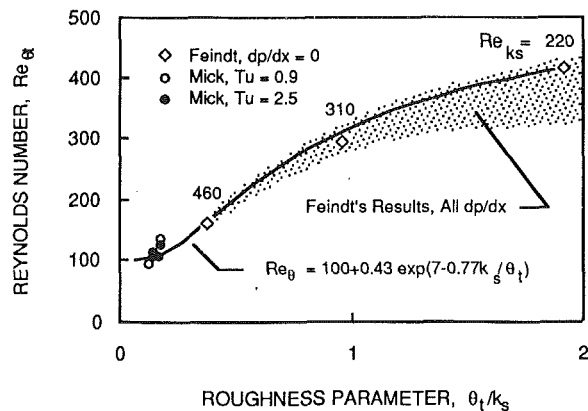**Effect of Surface Roughness.** Although much work has

Fig. A1 The momentum thickness Reynolds number at the onset of transition as a function of the roughness parameter

Fig. A2 A comparison between the effects of roughness and free-stream turbulence for various sized engines

been done on the effects of roughness on laminar and turbulent flows, little has been done on its effect on boundary layer transition except for single roughness elements. The only relevant works concerning the effect of distributed roughness on transition were done by Feindt (1956) and, more recently, by Mick (1987). Both Feindt and Mick obtained information on the onset of transition while Mick, who deduced his results from heat transfer measurements, also obtained information on the end of transition.

A graph of Feindt's results is given in Fig. A1 where the transition Reynolds number is plotted against the ratio of momentum thickness to sand grain roughness height. In this format, transition occurs when the Reynolds number lies above the data. An approximate conversion between the equivalent sand grain roughness and a centerline average roughness is to multiply the latter by 6. Feindt obtained his data for pressure gradients varying from strongly adverse to moderately favorable. These data are indicated by the shaded pattern in the figure. Several points for $dp/dx = 0$ have been shown together with their corresponding values of roughness Reynolds numbers. Note that these values of Re_{ks} are 3 to 6 times greater than the minimum value of 70 required for fully rough turbulent flow. Mick's data are also shown and although most were obtained for an acceleration above the value for reverse transition, two correspond to flow with zero pressure gradient. A slightly modified form of an equation Mick found that correlated both his and Feindt's zero pressure gradient data is also shown in the figure.

The main features of this figure are replotted in Fig. A2. For gas turbines, the expected range of transition Reynolds numbers is roughly that shown by the incline-lined pattern. This corresponds to turbulence levels between 5 and 10 percent. In addition, The minimum values of θ_t/k_s for the different groups of engines listed in Table 1 are shown. The values of k_s used to calculate these minimums were obtained from the recent work by Taylor (1990) who measured roughness on several in-service first-stage turbine rotor blades from medium-sized engines. He found roughness size varied over the surface from about 2–10 μm with the roughest just aft of the leading edge on the suction side and about midchord on the pressure side. These, by the way, correspond to the positions where slower moving particles in the combustion gases impinge on the first stage rotor blades. Mick's tests were actually carried out to obtain information on roughness effects under the most adverse conditions. For compressors, the minimum values of θ_t/k_s are expected to be greater. In any case, the result from this figure is interesting. Since turbulence causes an earlier onset of transition than roughness for all engines, except perhaps the small engines and the low-pressure turbine under the worse conditions, the effect of roughness on the onset can generally be neglected.
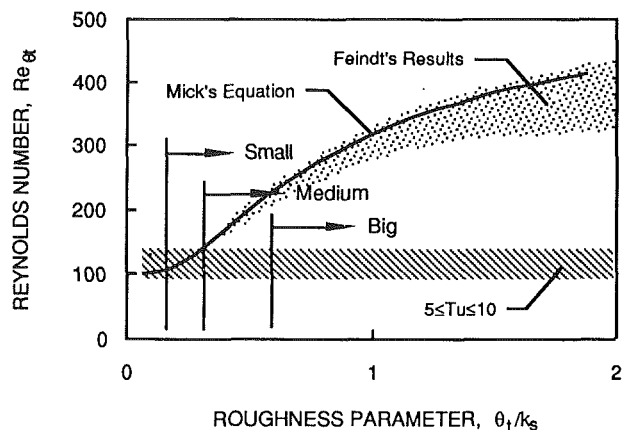
There are virtually no data except Mick's from which one can obtain information regarding spot production rates. Since his results are mainly for flows with strong pressure gradients and are inferred from heat transfer measurements, interpretation is questionable (see discussion in text relative to pressure gradient effects). Nevertheless, if these questions are presently set aside and an approximate correction using Sharma's correlation for pressure gradient effects (see text) is made, Mick's data indicate that the ratio of spot production rate on a rough surface to that on a smooth surface is roughly 30 for $Tu = 0.9$ and 10 for $Tu = 2.5$ ($\theta_t/k_s \approx 0.16$). A crude extrapolation for higher turbulence levels provides a factor somewhere between one and six, which translates to a reduction in the transition length of about 60 percent. For a smaller roughness, a smaller effect will be found.

Effect of Curvature Curvature effects on transition were examined rather early by Görtler (1940), who considered the theoretical aspects of stability, and Liepmann (1943), who conducted experiments. Görtler determined that a laminar boundary layer on a concave surface becomes unstable as a result of centrifugal forces to three-dimensional disturbances and formed streamwise vortices within the layer. Liepmann showed that transition on a convex surface is only slightly delayed, as did the recent measurements of Wang and Simon (1985), but that it may occur substantially earlier on a concave surface. Although all of this work was done at relatively low turbulence levels, it follows that the onset of transition on a convex surface at higher free-stream turbulence levels will be virtually identical to that for a flat surface.

For $Tu = 0.03$, Liepmann found that transition occurred on a concave surface when $G\ddot{o} = Re_{\theta t} \sqrt{\theta/r} \geq 7$ where $G\ddot{o}$ is the Görtler number and r is the radius of curvature. Recently, experiments on concave surfaces at higher turbulence levels were reported by Riley et al. (1989). Their results together with Liepmann's are shown in Fig. A3 where the transition Reynolds number is plotted against the square root the surface radius to momentum thickness ratio at transition. In this format, all straight lines passing through the origin correspond to a constant Görtler number and transition for any turbulence level occurs when the Reynolds number lies above that data for that turbulence level. Liepmann's data lie close to the $G\ddot{o} = 7$ line. The rise in transition Reynolds number above this line found by Riley et al. is caused by the Görtler vortices increasing the velocity gradients near the wall thereby delaying transition. For highly curved surfaces, this effect dominates that of turbulence. Since curvature effects diminish toward the right in this figure, horizontal lines corresponding to the flat plate transition results, Eq. (9) in text, have been drawn there. Lines suggested by the data (admittedly debatable) have also been drawn through the results of Riley et al. to blend with these.

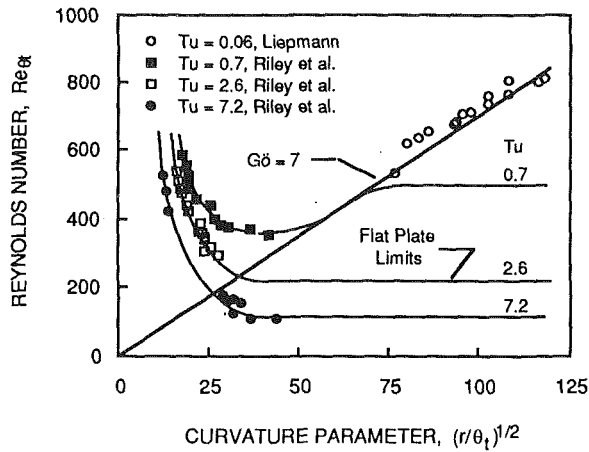**Fig. A3 Reynolds number at the onset of transition on a concave surface as a function of the curvature parameter**
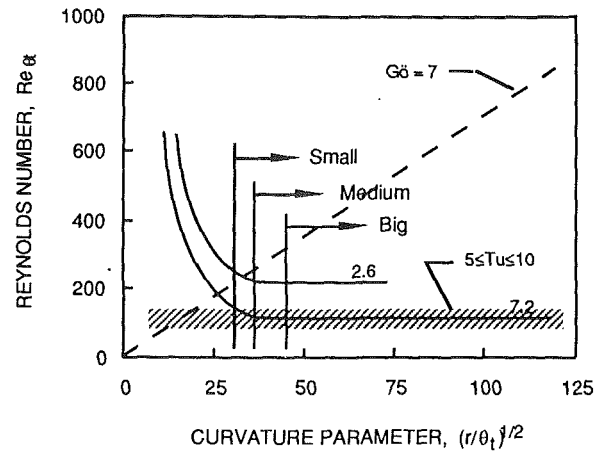

Fig. A4 A comparison between the effects of curvature and free-stream turbulence for various sized engines

From this, it is seen that concave curvature can either decrease, as found by Liepmann, or increase the transition Reynolds number depending on the strength of curvature and turbulence level.

The main features of Fig. A3 are reproduced in Fig. A4 together with the expected range of transition Reynolds numbers for gas turbines. For the most part, the curve of $Tu = 7.2$ falls within this band except for $\sqrt{r/\theta} \leq 30$ where the vortices delay transition. Typical minimum values of radius-to-momentum thickness ratios for the various sized engines are also shown. From this it may be concluded that curvature has a negligible effect on the onset of transition in all cases except perhaps in small engines and low turbines of medium-sized engines where it could cause a slight delay. Since the minimum values of $\sqrt{r/\theta}$ were based on turbine blade curvatures and flow conditions, and since these values are substantially greater for compressors, the effect of surface curvature in compressors may be neglected.

There are virtually no reliable data from which one may determine the spot production rate $\hat{n}\sigma$ for transition on a concave surface. For flow on a convex surface, the heat transfer data Wang and Simon (1985) were examined. Here, it was found that $\hat{n}\sigma$ is relatively unaffected up to a Görtler number of four and then decreases to about 80 percent of its flat plate value at Gö = 7. The latter situation corresponds to an increase of roughly ten percent in the transition length. Since this is based on only three data points, its validity remains to be confirmed.

Effect of Compressibility. Nearly all measurements in compressible transitional flows are thirty years old and, although not mentioned, most data were obtained at low turbulence levels. In general, efforts concentrated on obtaining an onset Reynolds number and transition length by measuring either the distribution of surface shear stess or heat transfer, but more recently through surface intermittency detection methods. In 1985, Narasimha analyzed all previous data and concluded that much work is still required before the effects of compressibility on transition are understood. For the most part, this conclusion still stands. In gas turbine flows, however, two distinct effects must be recognized. The first is simply the effect of Mach number on the onset and production rate, while the second is the effect of a shock wave in forcing transition through laminar boundary layer separation. The latter was considered in the text under the section titled Periodic-Unsteady Transition.

The first effect was considered by Chen and Thyson, who correlated the spot production rate as a function of the Mach number using the data of others for low free-stream turbulence flows. Their analysis indicates that $\hat{n}\sigma \propto (1 + 0.078M^{1.92})^{-2}$
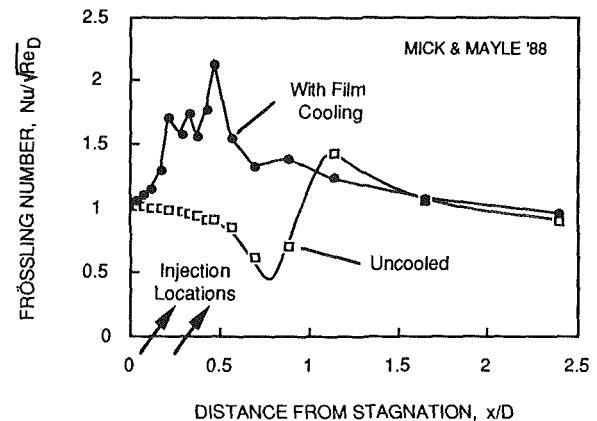
Fig. A5 Effect of film cooling on transition

$(2.5 < M < 5)$. Narasimha (1985, pp. 66–67), after analyzing more recent data, concluded that the effect of Mach number on the onset is roughly given by $Re_{\theta t} \propto \sqrt{1 + 0.38M^{0.6}}$ $(0.2 < M < 2.4$ and $0.1 < Tu < 3)$. Although this suggests that $\hat{n}\sigma \propto (1 + 0.38M^{0.6})^{-2}$, Narasimha concluded the exponent should be -1.5. In any case, it appears that the onset of transition is delayed and the spot production rate is decreased as the Mach number increases. Without any further information, however, the magnitude of the effect is questionable. At M = 1, Chen and Thyson's factor on $\hat{n}\sigma$ is 1.17 while Narasimha's is 1.6–2.2. This represents a possible 8–30 percent increase in the length of transition. Presently, most transitional boundary layer codes use Chen and Thyson's correlation, but it should be noted that this does not account for the effect of Mach number on the onset of transition. Perhaps Narasimha's result, which indicates a 17 percent increase in $Re_{\theta t}$ at M = 1, should be used, but only with caution.

Effect of Heat Transfer. It is well known that heating or cooling the flow affects transition at low levels of free-stream turbulence. For air flowing along a heated wall, Liepmann and Fila (1947) found that $Re_{\theta t}/(Re_{\theta t})_{isothermal}$ varies roughly as $1 - 2\Delta T/T_0$, where ΔT is the wall-to-freestream temperature difference and T_0 is the wall temperature. Since transition occurred via the natural transition mode, this result is of little use for gas turbine design purposes. The only published results for transition on a cooled surface appropriate to the gas turbine situation are those presented by Rüd and Wittig (1986) who show for $Tu > 2$ that the effect of T_w/T_∞ on either the onset or length of transition is negligible. This effect on $Re_{\theta t}$ is not difficult to understand considering the negligible effect at high

turbulence levels for flows with pressure gradients. The negligible effect on the length of transition implies that the spot production rate is unaffected by heat transfer at high freestream turbulence levels.

Effect of Film Cooling. A great concern for a designer of a cooled turbine airfoil is the effect of film cooling on the state of the boundary layer. Since film holes are typically much larger than the boundary layer thickness at injection, in general, it may be said that injection of coolant into the flow through a series of holes completely disrupts the flow near the surface and provides a source of high turbulence within the downstream developing boundary layer. This seems to be true even if care is taken to inject the coolant at shallow angles to the surface in the mainstream flow direction. Hence, one should expect film cooling to "trip" a laminar boundary layer turbulent.

This is shown in Fig. A5 where heat transfer results both with and without film cooling have been plotted for film cooling on the leading edge of an airfoil. In this figure, the Frössling number, $Nu/\sqrt{Re_D}$, where Nu is the Nusselt number and Re_D is the Reynolds number based on the leading edge diameter, D, and upstream velocity, is plotted against the distance measured from stagnation. For no injection, holes covered, a separated-flow transition occurs near $x/D \approx \pi/4$. With blowing, however, and in spite of the high acceleration, it appears that neither a laminar boundary layer exists nor a forced transition occurs except that caused by the injection itself. Recent measurements by Mehendale et al. (1990) at engine levels of turbulence substantiate these findings.

For situations where the acceleration downstream of injection is sufficient to cause reverse transition, i.e., $K > 3(10)^{-6}$, Warren and Metzger (1972) have shown that the heat transfer approaches that for laminar flow. This implies that even though injection can cause transition, a subsequent strong acceleration can cause the flow to become laminar again. Such a situation is common for film-cooled airfoils in the first stages of the turbine.

APPENDIX B

Data Reduction

When measurements of $\gamma(x)$ were available, the function $\sqrt{-\ln(1-\gamma)}$ was plotted against x according to Narasimha (1957), and a straight line fitted to the data in the range where $0.25 < \gamma < 0.75$. From Eq. (5) in the text, it is easy to see that the slope of the line is equal to $\sqrt{n\sigma/U}\ (=\sqrt{\hat{n}\sigma\ U/\nu})$ and the x intercept is x_t. This is shown in Fig. B1. The measured value of Re_θ at x_t was then taken to be $Re_{\theta t}$. Even though this process was described back in the 1950s, surprisingly few intermittency data are available. The pioneering example is that of Schubauer and Klebanoff (1955).

For flows with $dp/dx = 0$, the spot production rate could be determined using various transition length measurements and Dhawan and Narasimha's (1958) correlation for γ, i.e.,

$$\gamma = 1 - \exp\left[-0.412\frac{(x-x_t)^2}{(x_{75}-x_{25})^2}\right], \tag{B1}$$

where x_{25} and x_{75} correspond to the distances where $\gamma = 0.25$ and 0.75. This expression has been found to correlate near-wall intermittency measurements even in flows with pressure gradients. From this and Eq. (6) in the text, one obtains $\hat{n}\sigma = 4.61/Re_{LT}^2$ where Re_{LT} is the transition length Reynolds number measured from onset to where $\gamma = 0.99$. It should be noted that this latter expression is valid only for flows with zero pressure gradient. If the measurements of transition were obtained using Preston tubes, then a correction according to
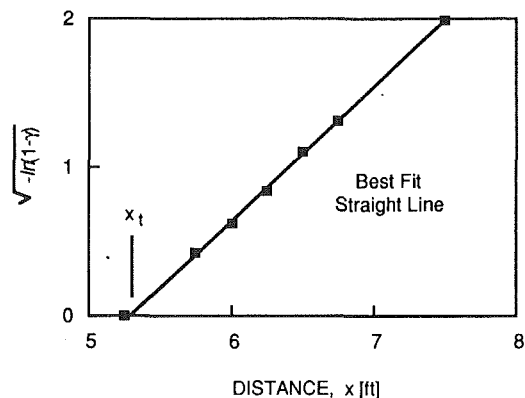
Fig. B1 Plot of Schubauer and Kelbanoff's data in $\sqrt{-\ln(1-\gamma)}$ and x coordinates
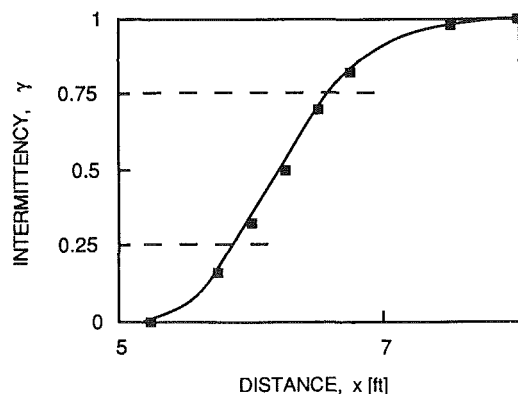
Fig. B2 Resulting intermittency curve fit for Schubauer and Klebanoff's data
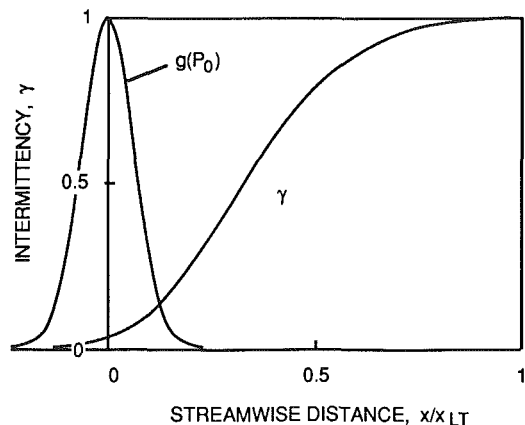
Fig. B3 Intermittency distribution for a Gaussian spot production function

Narasimha (1985) was applied to the data to obtain Re_{LT}. For the present definition of x_{LT}, this becomes $Re_{LT} = 1.27(U/\nu)(x_{max} - x_{min})$ where x_{max} and x_{min} are the locations of the maximum and minimum Preston tube readings.

Data for $dp/dx \neq 0$ were reduced as explained above except that $\sqrt{-\ln(1-\gamma)}$ was plotted against $x/\sqrt{\overline{U}}$ where $\overline{U}$ is the average velocity through transition. In this case, the slope of the best straight line fit through the data becomes $\sqrt{\hat{n}\ \bar{\sigma}}$. This is particularly important for flows with a favorable pressure gradient where U can change significantly through the extended transition. For adverse pressure gradients, transition is short and the difference between U and $\overline{U}$ is small.

Some data, notably those obtained in favorable pressure gradients (Narasimha et al., 1984; Blair, 1990), can be fit by two straight lines when plotted in the format of Fig. B1. The

Fig. B4 Plot of $\sqrt{-\ln(1-\gamma)}$ for the Gaussian spot production function shown in Fig. B4

line that fits the data in the early stage of transition always has a smaller slope than the one that fits the data in the latter stage and indicates that the spot production rate is smaller in the earlier stage than in the latter. In addition, the intercept x_t determined by the line in the latter stage is always about midway through the first stage and indicates that the production of turbulent spots as determined from the data in the latter stage is a result of something happening midway through the first. Narasimha et al. refer to this early stage of transition as "sub-transition." Here, however, it is proposed that the "first stage" of transition in favorable pressure gradients is simply an extended region over which turbulent spots are produced. That is, for favorable pressure gradients, Eq. (4) in the text is not a good approximation for the spot production function $g(P_0)$ and should be replaced by a function that reflects a production of spots over an extended region. If $g(P_0)$ is replaced by a Gaussian distribution, which has a standard deviation equal to two percent of the transition length, the curves shown in Figs. B3 and B4 result. In Fig. B3 the normalized Gaussian production function and resulting intermittency distribution are shown. In Fig. B4, a curve that can be approximated by two straight lines is quite evident. Therefore, it is suggested that turbulent spots are really produced over an extended region in the flow, unlike Dhawan and Narasimha's (1958) conclusion, and that this region is significant for transition in flows with a favorable pressure gradient. For transition in flows with an adverse pressure gradient, turbulent spots appear to be produced within a region that is narrow compared to the length of transition. All the results shown in the text for favorable pressure gradients were reduced using the data in the latter stage of transition.

Fig. B4 Plot of $\sqrt{-\ln(1-\gamma)}$ for the Gaussian spot production function shown in Fig. B4

line that fits the data in the early stage of transition always has a smaller slope than the one that fits the data in the latter stage and indicates that the spot production rate is smaller in the earlier stage than in the latter. In addition, the intercept x_t determined by the line in the latter stage is always about midway through the first stage and indicates that the production of turbulent spots as determined from the data in the latter stage is a result of something happening midway through the first. Naras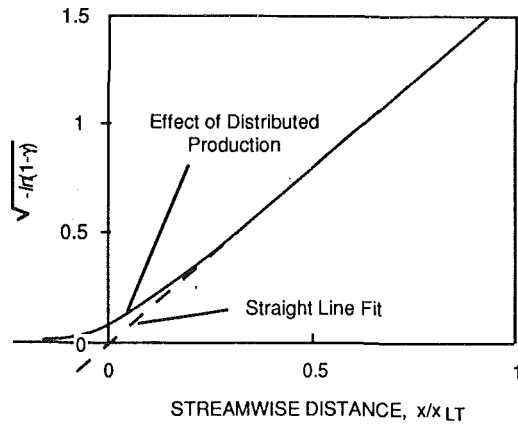imha et al. refer to this early stage of transition as "sub-transition." Here, however, it is proposed that the "first stage" of transition in favorable pressure gradients is simply an extended region over which turbulent spots are produced. That is, for favorable pressure gradients, Eq. (4) in the text is not a good approximation for the spot production function $g(P_0)$ and should be replaced by a function that reflects a production of spots over an extended region. If $g(P_0)$ is replaced by a Gaussian distribution, which has a standard deviation equal to two percent of the transition length, the curves shown in Figs. B3 and B4 result. In Fig. B3 the normalized Gaussian production function and resulting intermittency distribution are shown. In Fig. B4, a curve that can be approximated by two straight lines is quite evident. Therefore, it is suggested that turbulent spots are really produced over an extended region in the flow, unlike Dhawan and Narasimha's (1958) conclusion, and that this region is significant for transition in flows with a favorable pressure gradient. For transition in flows with an adverse pressure gradient, turbulent spots appear to be produced within a region that is narrow compared to the length of transition. All the results shown in the text for favorable pressure gradients were reduced using the data in the latter stage of transition.
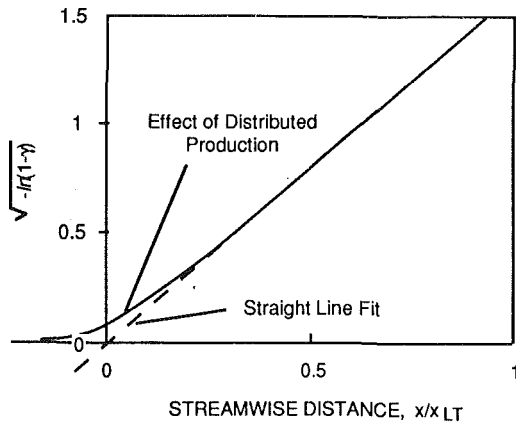
——— DISCUSSION ———

W. B. Roberts[9]

I would like to comment on Professor Mayle's discussion of Separated-Flow Transition. Professor Mayle states that "If the flow separates, transition is primarily controlled by the momentum thickness Reynolds number at separation and the *parameters* (my italics) that affect the length of the laminar shear layer in the bubble. At present these parameters are not known, but there is some evidence that free-stream turbulence is one of them."

I partially agree with the first part of this statement—before laminar separation the development of the boundary layer, as characterized by the momentum thickness, determines how

---

[9] Flow Application Research, 1543 Vernal Ave., Fremont, CA 94539.
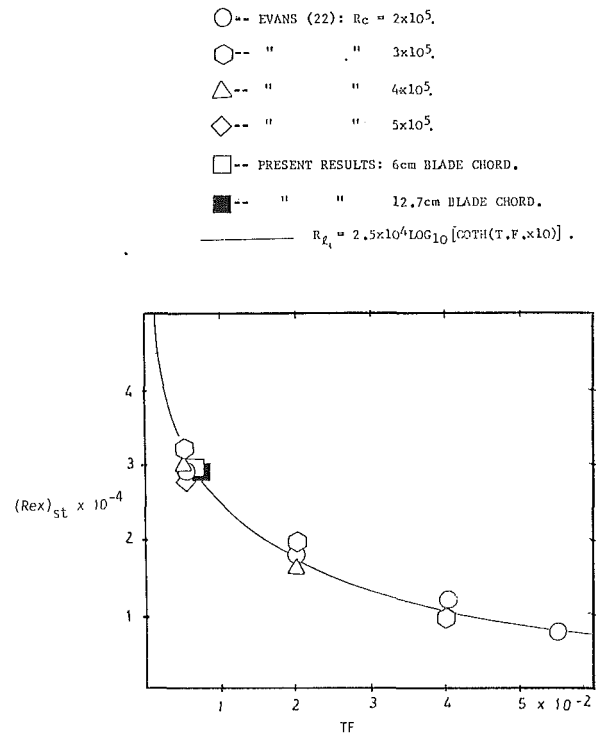
Fig. A Variation of Reynolds number based on transition length, $(Re_x)_{st}$, with turbulence factor, TF

near the separated shear layer is to transition. However, after separation the *only* factor that has a first-order effect on the transition process is the free-stream turbulence. If the flow is separated, roughness or curvature cannot affect the free shear layer and heat transfer effects are, at the most, of second order. The only mechanism remaining to enhance the growth of turbulent spots in a free shear layer is free stream turbulence. This is shown by Fig. A, which is taken from Roberts (1973, 1980). Note that Fig. A shows that after separation, laminar free shear layer length is independent of Reynolds number (see Evans, 1971) and depends only on free-stream turbulence level. Further strong evidence of this effect is shown in Fig. B, which is taken from Roberts' Doctoral Dissertation (1973). Note the strong negative effect of increasing turbulence level on the laminar free shear layer length Reynolds number between 0 and 2 percent. Above 2 percent, the length Reynolds number continues to decrease at a lower rate. Figure B can be supplemented with this author's observations during industrial cascade testing at low blade chord Reynolds number and very high turbulence levels (Roberts, 1980): At $Re < 10^5$ laminar separation bubbles were observed for turbulence intensities of as high as 10 percent, and for the same low Reynolds numbers the bubble lengths were shorter for the higher turbulence levels, i.e., the trend shown in Fig. B continues for turbulence intensities as high as 10 percent. These data relate well to gas turbine engines since turbulence intensities in multistage turbomachines range from atmospheric turbulence levels at the inlet (i.e., very low) to as high as 10 percent + in blade wakes.

The facts quoted above lead this author to the conclusion that Professor Mayle's correlations for bubble transition length, Eqs. (11) and (12), are incomplete in that no provision is made for the effect of turbulence. The correlation given by Roberts (1973, 1980):

$$(Re_x)_{st} = 2.5 \times 10^4 \log_{10}(\coth[TF \times 10]) \qquad (1)$$

where $TF = T_u(c/L)^{1/5}$, is reasonably good for approximate engineering estimates in that it takes into account turbulence level for short and long bubbles. Note that the above relation

Fig. B Variation of Reynolds number based on transition length, $(Re_x)_{st}$, with turbulence intensity, T_u

is in the nomenclature of the present paper and takes into account the integral length scale of the turbulence as well as the turbulence intensity.

Although Eq. (1) above is better than nothing, what is needed to predict transition length properly in laminar separation bubbles is a series of systematic tests for which bubble separation Reynolds number and turbulence level are varied over the entire pertinent spectrum that exists for internal and external flows. Indeed, it is surprising that such a fundamental fluid dynamic study has not already been done.

References

Evans, B. J., 1971, "Effects of the Free-Stream Turbulence Level on Blade Performance in a Compressor Cascade," Cambridge University, Engineering Dept. Rept. No. Turbo/TR26, Cambridge, United Kingdom.

Roberts, W. B., 1973, "A Study of the Effect on Reynolds Number and Laminar Separation Bubbles on the Flow Through Axial Compressor Cascades," Doctoral Dissertation, Université Libre de Bruxelles, Belgium, May.

Roberts, W. B., 1980, "Blade Optimization for Low Reynolds Number Automotive Fans," Final Report for General Motors Laboratory Contract No. PO RS 857902, Oct.

Author's Closure

Yes, free-stream turbulence is important in the separated-flow transition process and although stated so in the paper, I must confess, it is very weakly said. However, I do have difficulty saying at this time that it is "the *only* factor." There just aren't enough data.

First, let me explain that the data in Dr. Roberts' figures (see his 1973 reference) correspond to Reynolds numbers based on the length of the flat region in the free-stream velocity distribution as shown in Fig. 17 of the present paper. Second, let me emphasize that Gaster's results show that the constant pressure shear layer is both laminar and transitional. In the present notation then, Dr. Roberts' ordinates are Re_{sT} and not Re_{st} as stated. Recognizing this, the data in Fig. 18 of the present paper and Dr. Roberts' Figs. A and B are comparable and seem to say that both $Re_{\theta t}$ and Tu are important. Although not presented in the original paper, I found that both effects could be accounted for by the correlation $Re_{sT} = 700 \exp(-0.3Tu)\, Re_{\theta s}^{0.7}$, which is the expression given in Eq. (10) of the paper multiplied by a turbulence factor $e^{-0.3Tu}$. I was sufficiently uncertain at that time, and remain so even now, to recommend this correlation unconditionally. There just aren't enough data. In addition, whether or not this factor may be applied separately to each of the laminar and transitional portions of the shear layer is completely uncertain and remains to be investigated.

In closing, I wish to thank Dr. Roberts for again emphasizing the need in this area for more work of a fundamental nature.
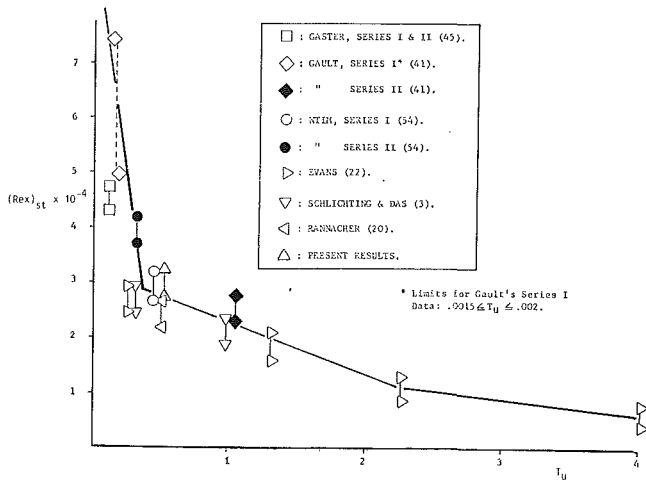
Fig. B Variation of Reynolds number based on transition length, $(Re_x)_{st}$, with turbulence intensity, T_u

is in the nomenclature of the present paper and takes into account the integral length scale of the turbulence as well as the turbulence intensity.

Although Eq. (1) above is better than nothing, what is needed to predict transition length properly in laminar separation bubbles is a series of systematic tests for which bubble separation Reynolds number and turbulence level are varied over the entire pertinent spectrum that exists for internal and external flows. Indeed, it is surprising that such a fundamental fluid dynamic study has not already been done.

References

Evans, B. J., 1971, "Effects of the Free-Stream Turbulence Level on Blade Performance in a Compressor Cascade," Cambridge University, Engineering Dept. Rept. No. Turbo/TR26, Cambridge, United Kingdom.

Roberts, W. B., 1973, "A Study of the Effect on Reynolds Number and Laminar Separation Bubbles on the Flow Through Axial Compressor Cascades," Doctoral Dissertation, Université Libre de Bruxelles, Belgium, May.

Roberts, W. B., 1980, "Blade Optimization for Low Reynolds Number Automotive Fans," Final Report for General Motors Laboratory Contract No. PO RS 857902, Oct.

Author's Closure

Yes, free-stream turbulence is important in the separated-flow transition process and although stated so in the paper, I must confess, it is very weakly said. However, I do have difficulty saying at this time that it is "the *only* factor." There just aren't enough data.

First, let me explain that the data in Dr. Roberts' figures (see his 1973 reference) correspond to Reynolds numbers based on the length of the flat region in the free-stream velocity distribution as shown in Fig. 17 of the present paper. Second, let me emphasize that Gaster's results show that the constant pressure shear layer is both laminar and transitional. In the present notation then, Dr. Roberts' ordinates are Re_{sT} and not Re_{st} as stated. Recognizing this, the data in Fig. 18 of the present paper and Dr. Roberts' Figs. A and B are comparable and seem to say that both $Re_{\theta t}$ and Tu are important. Although not presented in the original paper, I found that both effects could be accounted for by the correlation $Re_{sT} = 700 \exp(-0.3Tu) \, Re_{\theta s}^{0.7}$, which is the expression given in Eq. (10) of the paper multiplied by a turbulence factor $e^{-0.3Tu}$. I was sufficiently uncertain at that time, and remain so even now, to recommend this correlation unconditionally. There just aren't enough data. In addition, whether or not this factor may be applied separately to each of the laminar and transitional portions of the shear layer is completely uncertain and remains to be investigated.

In closing, I wish to thank Dr. Roberts for again emphasizing the need in this area for more work of a fundamental nature.
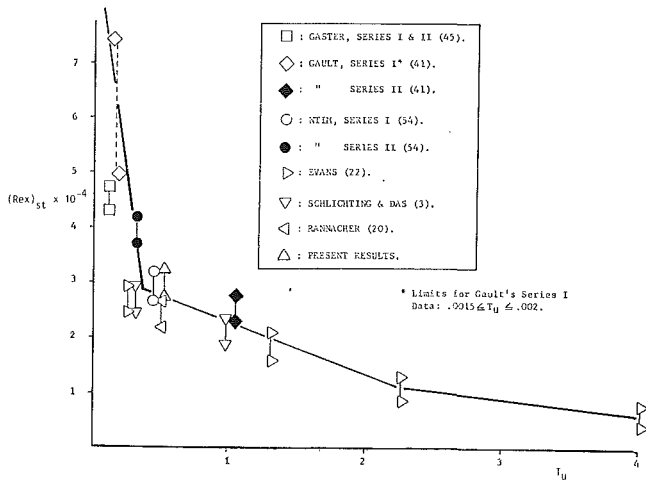
M. Barnett
Theoretical and
Computational Fluid Dynamics,
United Technologies Research Center,
East Hartford, CT

D. E. Hobbs
Fan and Compressor Technology,
Pratt and Whitney,
East Hartford, CT

D. E. Edwards
Applied Computational Fluid Dynamics,
United Technologies Research Center,
East Hartford, CT

Inviscid-Viscous Interaction Analysis of Compressor Cascade Performance

An inviscid-viscous interaction technique for the analysis of quasi-three-dimensional turbomachinery cascades has been developed. The inviscid flow is calculated using a time-marching, multiple-grid Euler analysis. An inverse, finite-difference viscous-layer analysis, which includes the wake, is employed so that boundary layer separation can be modeled. This analysis has been used to predict the performance of a transonic compressor cascade over the entire incidence range. The results of the numerical investigation in the form of cascade total pressure loss, exit gas angle, and blade pressure distributions are compared with existing experimental data and Navier-Stokes solutions for this cascade, and show that this inviscid-viscous interaction procedure is able to predict cascade loss and airfoil pressure distributions accurately. Several other aspects of the present interaction analysis are examined, including transition and wake modeling, through comparisons with data.

Introduction

A viscous analysis for compressor and turbine cascades, which is capable of properly representing strong inviscid-viscous interaction effects such as boundary-layer separation and shock/boundary-layer interaction, is needed to predict off-design aerodynamic performance. Near the design point, where inviscid-viscous interactions are usually weak, an inviscid potential-flow analysis coupled to simple direct boundary-layer and wake-mixing analyses generally provides good predictions of cascade performance. However, such an analysis is usually inaccurate away from the design point where strong-interaction effects become important, and alternate approaches, capable of modeling these effects, are necessary.

Two approaches that are capable of analyzing strong inviscid-viscous interactions in internal flows have become increasingly popular over the last decade or so. An overview of the two techniques and some typical results of each are provided by Stow (1985). One approach relies on solution of the Navier-Stokes equations, and the other relies on use of the Inviscid-Viscous Interaction (IVI) approach. Examples of recently developed two-dimensional and quasi-three-dimensional Navier-Stokes techniques include those of Norton et al. (1984), Shamroth et al. (1984), Dawes (1986), Schäfer et al. (1986), Chima (1987), and Davis et al. (1987). Navier-Stokes analyses provide useful prediction techniques for off-design behavior but, because of their relatively high computational costs, their use within blade design systems is currently limited. A number of inviscid-viscous interaction techniques for internal flows have been developed, among them the analyses of Hansen et al.

(1979), Janssens and Hirsch (1983), Calvert and Ginder (1985), Olling and Dulikravich (1987), and Barnett and Verdon (1989). Some of these analyses (Hansen et al., 1979; Janssens and Hirsch, 1983) use only the "direct" mode (i.e., boundary-layer edge velocity or pressure specified) for the attached boundary-layer and use approximate modeling for the separated-flow regions while the other analyses use the "inverse" mode (i.e., displacement thickness or skin friction specified) to allow detailed calculations of the separated boundary layer. Not all of the inviscid-viscous interaction analyses mentioned above incorporate the viscous wake, which can be an important effect in some cases.

The principal use of any cascade aerodynamic design analysis is to provide accurate predictions of the performance of cascades. The usual parameters that characterize cascade performance are the flow turning and the entropy rise (or total pressure loss) through the cascade passages. The ultimate goal of the designer is to achieve an optimal cascade design, which requires predictions of the performance over the entire operating range of the cascade. Thus far, a limited amount of effort has been devoted to predicting the performance of cascades using either the Navier-Stokes or the inviscid-viscous interaction approaches. Although efforts have been made to apply Navier-Stokes analyses to predict performance, the accuracy of the predictions have, for the most part, been inadequate. A notable exception to this is the analysis of Davis et al. (1987), who recently presented the results of an investigation of the performance of two compressor cascades and demonstrated generally excellent agreement with experimental performance data (Davis et al., 1988). Some efforts to use the inviscid-viscous interaction approach to predict performance have been reported (e.g., Hansen et al., 1979, Calvert and Ginder, 1985, and Janssens and Hirsch, 1983). Although some

of the results are encouraging, there is still a significant amount of work needed to improve the ability of the IVI approach to predict performance accurately—this provides the principal motivation for the present investigation.

The development of an inviscid–viscous interaction analysis that is capable of providing predictions with accuracy comparable to that possible with Navier–Stokes analyses, but at an appreciable reduction in computational cost, would provide a viable tool for use within current design systems. If, in addition, such an analysis can be extended to provide meaningful results for cases where the flow is massively separated, then the analysis will be applicable across the entire operating range of cascades and would be significantly more valuable, since compressors operate over a wide range of flow conditions from low to high inlet Mach and Reynolds numbers as well as at high positive and negative incidence angles. Thus, the analysis described here is the result of the initial phase of an effort ultimately to satisfy all of these criteria: accuracy, wide range of applicability, and computational efficiency.

The present inviscid–viscous interaction analysis, known as IVICAS (for Inviscid–Viscous Interaction CAScade analysis) has been developed by coupling a steady, compressible, direct/inverse, finite-difference viscous-layer solution procedure with an explicit, time-marching, multiple-grid Euler solver. The Euler analysis permits the accurate prediction of flows with strong shocks, such as those associated with the tip sections of fans. Quasi-three-dimensional effects due to radius-change, blade rotation and varying streamtube height are included; the first two effects should be incorporated in both the viscous and the inviscid solutions but are, at the present time, only accounted for within the inviscid analysis.

The results of the initial effort to validate the IVICAS analysis will be presented in this paper, as well as a description of the newly developed elements of this procedure. A significant result of the present investigation is the observation that good agreement with both experimental data and Navier–Stokes solutions for the cascade total pressure loss is obtained across

almost the entire incidence range, and the incidence at which the rapid increase in loss occurs at either end of the range is accurately predicted. These results indicate that the IVI approach can be used by designers over the full operating range of cascades to develop optimal designs, and to determine the operating limits of cascades.

The principal objective during the initial phase of the investigation described here has been the development of an approach that properly represents the physics of compressor cascade flows and accurately predicts cascade aerodynamic performance across a wide range of operating conditions. The issue of computational efficiency has not yet been directly addressed.

General Concepts

For flows of practical interest in either external or internal aerodynamics, the Reynolds number is usually sufficiently high so that the flow past an airfoil or blade can be divided into two regions: an "inner" dissipative region consisting of boundary layers and wakes, and an "outer" inviscid region. The principal interaction between the flows in the viscous and inviscid regions arises from the displacement thickness effect, which leads to thickened semi-infinite equivalent bodies with corresponding changes in surface pressures. If the interaction is "weak" then the complete flow problem can be solved sequentially. This traditional approach for calculating the interaction between the inviscid and viscous parts of the flow is based on a direct hierarchy between the inviscid and viscous regions, which is applicable as long as the disturbances to the inviscid flow due to the viscous displacement effect remain weak everywhere.

However, flows over airfoils involve both a weak overall interaction arising from standard displacement thickness effects and also from wake curvature effects, and local strong-displacement interactions caused, for example, by boundary-layer separations, shock/boundary-layer interactions, and trailing-edge/near-wake interactions. These features can lead

——————— **Nomenclature** ———————

B_x = blade length measured along machine axis
c = blade chord length
C_p = $(P-P_1)/(P_{t_1}-P_1)$ = pressure coefficient
f = transformed stream function
F = u/u_e = local-to-edge tangential velocity ratio
g = H/H_e = local-to-edge total enthalpy ratio
h = static temperature integral
H = total enthalpy, or streamtube spanwise height
$\bar{m}$ = $\rho_e\mu_e\delta^*$ = displacement thickness parameter
M = Mach number
N = scaled distance normal to reference curve
P, P_t = static and total pressures, respectively
Pr, Pr_t = molecular and turbulent Prandtl numbers, respectively
Re = $\rho_1 V_1 c/\mu_1$ = Reynolds number
s, n = arc length, surface normal coordinates, respectively
T = static temperature

Tu = free-stream turbulence level, percent
u_1, u_2 = velocity components in (x, y) directions, respectively
u, v = velocity components in direction of local tangent, normal to surface or wake streamline, respectively
V = $(u_1^2 + v_1^2)^{1/2}$ = magnitude of total velocity
x, y = Cartesian coordinates, x aligned with machine axis, y normal to axis
β_1 = inlet flow angle, measured from lower tangential (clockwise)
β_2 = exit flow angle, measured from upper tangential (clockwise)
γ = ratio of specific heats
δ^* = displacement thickness
$\bar{\epsilon}$ = ratio of turbulent to molecular viscosity coefficients
θ = momentum thickness
$\hat{\theta}$ = T/T_e = local-to-edge static temperature ratio
Θ = angle of tangent to body

or displacement surface relative to x axis
κ = wake streamline curvature
μ = molecular viscosity coefficient
ξ, η = Levy–Lees independent boundary-layer coordinates
ρ = density
τ = cascade pitch
ψ = stream function
ω = relaxation factor
$\bar{\omega}$ = $(P_{t_1}-P_{t_2})/(P_{t_1}-P_1)$ = loss coefficient

Subscripts

e = viscous-layer outer edge
S = blade surface
W = wake streamline
1 = inlet
2 = exit

Superscripts

n = time step counter
$+, -$ = upper and lower edges of wake streamline, respectively

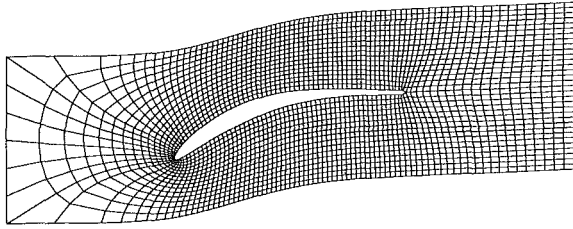Fig. 1 Typical C-grid for transonic compressor cascade

Fig. 2 Sketch of surface cell and notation

to singularities in a classical boundary-layer solution and a subsequent breakdown of a weak-interaction solution procedure. In addition, viscous displacements in the strong-interaction region cause substantial changes in the local inviscid pressure field and can, in some cases (e.g., massive separation), cause substantial changes in the global pressure field as well. The concept of an inner viscous region and an outer inviscid region still holds, but the classical hierarchical structure of the flow no longer applies. Thus, in a local strong-interaction region, the hierarchy changes from direct (i.e., pressure determined by the inviscid flow) to interactive (i.e., pressure by a mutual interaction between the inviscid and the viscous-layer flows), and this change must be accommodated within a comprehensive inviscid–viscous interaction analysis.

The approach taken here employs an inviscid–viscous interaction model to calculate high Reynolds number (Re) flows through quasi-three-dimensional cascades. The flow in the outer inviscid region is governed by the Euler equations and that in the inner viscous region is governed by Prandtl's viscous-layer equations, and the procedure for coupling the two solutions accounts for the nonhierarchical nature of strong interactions.

Numerical Procedure

The general procedure employed in the IVICAS analysis uses two main elements: an inviscid solver, which consists of a time-marching Euler analysis, and a compressible, finite-difference viscous-layer solver. The wake viscous-layer solver, which has to be able to treat asymmetric wakes and the possibility of reversed-flow regions extending into the wake, was developed during this investigation, and will be described in detail below. The inviscid and viscous equations are coupled through the appropriate boundary conditions, which are applied at the common surfaces shared by the two flows, i.e., at blade surfaces and along the streamline that originates at the blade trailing edge (i.e., the "wake streamline"). Finally, the solution for the complete flow is obtained by "globally" iterating between the viscous and inviscid solutions, varying the displacement thickness parameter $\bar{m}$, which appears in the boundary conditions for both solutions, until the viscous-layer edge velocity distribution matches the corresponding inviscid velocity distribution. One global iteration consists of a single solution of the viscous-layer equations and a specified number of time steps of the Euler solver, both carried out for the same distribution of $\bar{m}$. The "semi-inverse" approach developed by Carter (1979) is used to determine a new distribution of $\bar{m}$, which is based on the difference between the calculated viscous and inviscid velocity distributions at the common boundaries.

Inviscid Analysis. The flow in the outer inviscid region is represented by the solution of the unsteady, quasi-three-dimensional, compressible Euler equations, which is advanced in time until a steady-state solution is obtained. The analysis employed here uses the algorithm developed by Ni (1982) and employs an explicit, finite-area formulation in conjunction with a multiple-grid approach and local time stepping to improve the rate of convergence to a steady-state solution. The inviscid region of the flows considered herein is assumed to
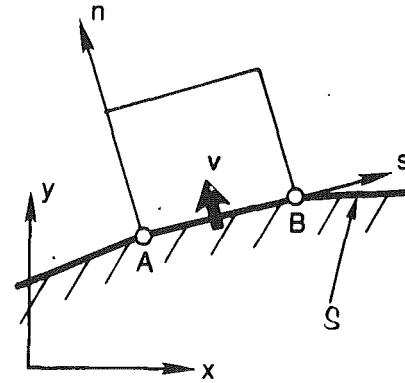
be isoenergetic, so that the total enthalpy is constant (except for the effects of radius change), obviating the need to solve the inviscid energy equation.

The Euler equations are discretized on a periodic C-grid, which is generated using an elliptic Poisson equation solution procedure similar to those of Thompson et al. (1974) and Sorenson (1981). An example of this periodic C-grid is shown in Fig. 1 for a transonic compressor cascade to be discussed in the Results section. It should be noted that the use of the C-grid results in a cut line in the mesh, which runs from the blade trailing edge to the downstream boundary, so that the cut line corresponds to two overlapping lines of grid points. This feature will be important in the later discussion of the wake boundary conditions.

The effect of the viscous displacement thickness on the inviscid flow is represented by mass transpiration through the surfaces of the blades, and by a jump in the normal velocity component along the wake streamlines. The distributions of the transpiration velocity along the wake streamlines are specified so that the inviscid streamlines are displaced to conform to the effective displacement body, which consists of the airfoil geometry plus the displacement thickness. There are also jumps in the static and total pressures across the wake streamline; the former is proportional to the streamline curvature, and the latter is associated with shocks, generally of different strengths, which may be present in the suction and pressure surfaces of the blades. Both of these pressure-related effects have been neglected in the present analysis, for reasons discussed later.

The distribution of the transpiration velocity along blade surfaces is given by the relation

$$\rho v|_s = \frac{d}{ds}\left(\rho_e u_e \delta^*\right) \tag{1}$$

where δ^* is the displacement thickness, v is the surface-normal velocity component, positive in the direction of the outward-facing normal to the blade surface, and the arc length s is assumed to be increasing with increasing distance from the leading-edge stagnation point on both the suction and pressure surfaces of the blade. Assuming that fluid is injected through the cell faces that are in contact with the blade surface, e.g., face AB in Fig. 2, the mass flux through the face, positive when fluid is injected into the cell, is given by

$$\rho v|_s ds = \rho_e u_e \delta^*|_B - \rho_e u_e \delta^*|_A \tag{2}$$

where u_e is positive directed in the positive s direction; this is the discrete form of equation (1). While equation (2) provides for the proper mass flux through the face, another boundary condition is required to enforce tangency of the flow to the *displacement* surface. This is accomplished by setting the appropriate value of u as follows. The displacement thickness distribution is known so that the slope of the displacement body surface, denoted by tan Θ, can be calculated. Once $\rho v|_s$ has been determined from equation (2), the blade surface tangential velocity component u is determined from

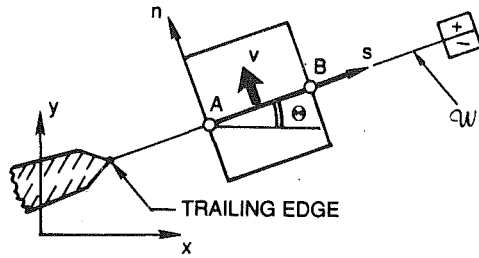**Fig. 3   Sketch of wake cells and notation**

$$\left.\frac{v}{u}\right|_S = \tan(\Theta - \phi) \tag{3}$$

where $\tan \phi$ is the slope of the tangent to the blade surface. Special care must be taken when $\Theta - \phi \to \pm \pi/2$ and when $v \to 0$.

The physical boundary conditions that are applied along the wake streamline to account for viscous effects are

$$[\![\rho v]\!]_{\text{W}} = \frac{d}{ds}(\rho_e u_e \delta^*)_{\text{W}} \tag{4}$$

and

$$[\![P]\!]_{\text{W}} = \kappa \rho_e u_e^2 (\delta^* + \theta)_{\text{W}} \tag{5}$$

where v is the velocity component in the direction normal to the wake streamline, positive when directed upward (see Fig. 3), P is the static pressure, δ^*_{W} and θ_{W} are the displacement and momentum thickness, respectively, of the entire wake at a given location along the wake streamline, and κ is the wake streamline curvature, which is taken as positive when the wake streamline is concave upward. The symbol $[\![f]\!]$ represents the jump in the quantity f, taken as the upper minus the lower value, i.e., $f^+ - f^-$.

The boundary condition given by equation (4) is applied in a manner similar to that used for the surface boundary conditions, i.e., conditions on the jumps of the flux and the normal velocity across the cell faces are imposed along the wake streamline. The procedure used to impose the correct flux and normal velocity jump conditions at each time step during the solution of the Euler equations is described next.

It is assumed here that the coincident C-grid mesh lines, which run from the trailing edge to the downstream boundary, follow the wake streamline. This assumption will be discussed further below. Referring to Fig. 3 and denoting the values on the upper and lower "surfaces" of the wake streamline by the superscripts $^+$ and $^-$, respectively, the upper and lower surface values of v are given by

$$v^{\pm} = \bar{v} \pm \frac{1}{2}[\![v]\!] \tag{6}$$

where $\bar{v}$ denotes the average, or "periodic," component of the normal velocity along the wake streamline. Note that there is no jump in the wake streamline tangential velocity component, consistent with the assumption of zero jumps in the static and total pressures.

The inviscid solution for the unknowns ρ, ρu_1, and ρu_2 is obtained by advancing the Euler equations in time, so that the latest time-step value of a variable, ρu_1, for example, is equal to the previous time-step value plus the change in the variable, i.e.,

$$\rho u^{n+1} = \rho u_1^n + \delta \rho u_1 \tag{7}$$

where δ denotes the change in the quantity between the two time steps and the superscript n denotes its value at the previous time step. Thus, before the boundary conditions are applied, the changes in all of the flow quantities throughout the entire solution domain, including the boundary points, are computed from the appropriate flux balances. The values along boundaries are then corrected to enforce the appropriate

boundary conditions. To impose the jump condition along the wake streamline, the changes in all of the quantities computed there during the explicit flux balance are first made periodic, e.g.,

$$\delta \overline{\rho u}_1 = \frac{1}{2}(\delta \rho u_1^+ + \delta \rho u_1^-), \tag{8}$$

where the overbar denotes the periodic value. The updated periodic values of the quantities are then determined, e.g.,

$$\overline{\rho u}_1^{n+1} = \frac{1}{2}[(\rho u_1^+)^n + (\rho u_1^-)^n] + \delta \overline{\rho u}_1 \tag{9}$$

Note that the first right-hand-side term is the periodic component of ρu_1 (i.e., $\overline{\rho u}_1$) at time step n. Finally, the upper and lower surface values of the quantities are determined using the *known* jump in ρv, obtained from equation (4), and the relations

$$[\![\rho u_2]\!] = [\![\rho v]\!]\cos \Theta \tag{10}$$

and

$$[\![\rho u_1]\!] = -[\![\rho v]\!]\sin \Theta \tag{11}$$

which follow from the assumption that, consistent with the assumed zero jumps in the static and total pressures, $[\![\rho u]\!] = 0$, where u is the velocity component in the direction of the tangent to the wake streamline, positive directed downstream. Here Θ represents the angle that the tangent to the wake streamline makes relative to the x axis, positive measured counterclockwise (see Fig. 3). The necessary final relation is given by

$$(\rho u_1^{\pm})^{n+1} = \overline{\rho u}_1^{n+1} \pm \frac{1}{2}[\![\rho u_1]\!] \tag{12}$$

The relations for ρu_2 are exactly analogous. The density is assumed to be constant across the wake streamline, i.e., $[\![\rho]\!] = 0$.

In the present implementation of the inviscid boundary conditions, the wake jump condition is applied at the blade trailing-edge point, instead of applying a solid surface tangency condition there. The appropriate tangency condition is ambiguous, since there are two tangents to the displacement body surface at the trailing edge, one from the pressure surface and one from the suction surface. A number of different trailing-edge boundary conditions were considered and it was determined, through numerical experimentation, that the most physically plausible solutions were generally obtained using the aforementioned wake jump condition. Further examination of this issue in the future is warranted, however, since unsatisfactory solutions sometimes result in the vicinity of the trailing edge, as will be shown in the Results section.

For convenience in the numerical solution procedure, the wake streamline boundary conditions are applied along the two coincident mesh lines originating at the blade trailing edge. Therefore, for proper application of the boundary conditions, these mesh lines must be (nearly) coincident with the actual wake streamline when the complete solution has converged. In the present analysis, this is accomplished by periodically adjusting the grid in the region aft of the blade trailing edge to force the coincident grid lines to align with the calculated inviscid wake streamline. The corresponding interior nodes along each blade-to-blade grid line are then translated by the amount needed to maintain the same general mesh topology. The Poisson solver used to generate the initial C-grid is *not* reapplied during the grid updates since the modified grid remains smooth. For the calculations presented in the Results section, the grid is adjusted after every 25 global iterations.

Referring to Fig. 1, the flow variables are assumed to be periodic along the grid line that corresponds to the top and bottom boundaries of the C-grid, which are periodic with the pitch length τ. The boundary conditions along the upstream and downstream boundaries of the solution domain are the

nonreflective boundary conditions described by Ni (1982). In the present analysis, the static pressure is specified at the downstream boundary and, for the subsonic inlet conditions considered here, the inlet flow angle β_1 is specified, and both are assumed to be uniform in the tangential (blade-to-blade) direction.

Viscous Analysis. The blade surface boundary layers are calculated using the finite-difference, compressible stream-function approach developed by Carter (1978), which allows for both a direct mode (i.e., edge velocity specified) and an inverse mode (i.e., mass flow parameter, $\bar{m} = \rho_e u_e \delta^*$, specified) calculation. The inverse mode is required to predict boundary-layer separation, which cannot be done in direct mode due to the well-known Goldstein singularity, which arises at the separation point when the latter approach is used.

A detailed description of the direct/inverse boundary-layer solution procedure used on blade suction and pressure surfaces was given by Carter (1978) and will not be repeated here. The boundary-layer equations are solved in finite-difference form on both surfaces by marching downstream from the leading-edge stagnation point, which is determined by finding the point along the blade surface at which the inviscid surface tangent velocity component changes sign. The viscous-layer solution stations are taken to be at the locations of the inviscid grid points lying on the blade surfaces and wake mesh cut line. At the stagnation point, the appropriate laminar boundary-layer similarity solution is obtained numerically, and this is used as the initial plane of data from which the boundary-layer equations are marched downstream. The boundary-layer equations are solved in direct mode in the vicinity of the leading-edge stagnation point, and the inverse mode is used downstream of the first point on each surface at which an adverse pressure gradient has been detected, and for the remainder of the surface and wake viscous-layer calculations. The viscous wake analysis used here was developed for the present application, and will be described in greater detail below.

The inverse mode used in the present wake viscous-layer analysis assumes that the displacement thickness parameter distribution in the wake, $\bar{m}_w = (\rho_e u_e \delta^*)_w$, is specified, where ρ_e and u_e are the density and wake streamline tangential velocity component, respectively, at the edges of the viscous layer and δ^*_w is the displacement thickness of the complete wake. The classical Prandtl viscous-layer equations for conservation of mass, tangential momentum, and energy, with the latter expressed in terms of the total enthalpy here, are solved in the wake. The equations are not given, since they can be found in any standard text on viscous flow (e.g., Schlichting, 1979). They are transformed into standard Levy–Lees variables, where $\xi = \int_0^s \rho_e u_e \mu_e ds$ and $\eta = \rho_e u_e (2\xi)^{-1/2} \int_0^N (\rho/\rho_e) dN$ are the independent variables and $F = u/u_e$, $f = (2\xi)^{-1/2} \psi$ and $g = H/H_e$ are the dependent variables. This transformation allows recovery of the similarity solution at the leading-edge stagnation point and reduces the truncation error of the viscous solution over that associated with use of the primitive independent (s, N) variables. The quantity ψ is the standard compressible stream function defined in terms of the wake streamline tangential and viscous-layer scaled normal velocity components u and $\tilde{v} = \mathrm{Re}^{1/2} v$, respectively, from the relations

$$\rho u = \frac{\partial \psi}{\partial N} \text{ and } \rho \tilde{v} = -\frac{\partial \psi}{\partial s} \tag{13}$$

where N is the boundary-layer scaled coordinate, $N = \mathrm{Re}^{1/2} n$, and n is the distance away from the wake streamline measured in the normal direction, positive above the streamline (see Fig. 3).

The governing equations are transformed into the following form:

$$F = \frac{\partial f}{\partial \eta}, \tag{14}$$

$$\frac{\partial}{\partial \eta} \left(l \bar{\epsilon} \frac{\partial F}{\partial \eta} \right) - 2\xi F \frac{\partial F}{\partial \xi} + \left(f + 2\xi \frac{\partial f}{\partial \xi} \right) \frac{\partial F}{\partial \eta}$$
$$+ 2\xi (\hat{\theta} - F^2)\beta = 0 \tag{15}$$

and

$$\frac{1}{\mathrm{Pr}} \frac{\partial}{\partial \eta} \left[l \left(1 + \frac{\bar{\epsilon} \mathrm{Pr}}{\mu \mathrm{Pr}_t} \right) \frac{\partial g}{\partial \eta} \right] + \frac{(\gamma - 1)\mathrm{M}_e^2}{1 + \frac{\gamma - 1}{2}\mathrm{M}_e^2} \frac{\partial}{\partial \eta} \left[l \left(1 - \frac{1}{\mathrm{Pr}} \right) F \frac{\partial F}{\partial \eta} \right]$$
$$- 2\xi F \frac{\partial g}{\partial \xi} + \left(\sqrt{2\xi} f + 2\xi \frac{\partial f}{\partial \xi} \right) \frac{\partial g}{\partial \eta} = 0 \tag{16}$$

representing the continuity, s momentum, and energy equations, respectively. Here the quantity $\hat{\theta}$ is equal to T/T_e, the local-to-edge static temperature ratio, which is related to g and F through the relation

$$\hat{\theta} = g + \frac{\gamma - 1}{2} \mathrm{M}_e^2 (g - F^2) \tag{17}$$

$l = \rho\mu/\rho_e\mu_e$, $\bar{\epsilon}$ is the ratio of the turbulent to molecular viscosity coefficients, and β is the pressure gradient parameter, defined by

$$\beta = \frac{1}{u_e} \frac{du_e}{d\xi} \tag{18}$$

The molecular viscosity coefficient μ is determined using the Sutherland viscosity law.

These equations are solved in finite-difference form after using a first-order accurate discretization for the ξ derivatives and a second-order accurate discretization for the η derivatives. The following boundary conditions are applied in the wake: $\eta = 0$ is assumed to lie along a streamline (i.e., stream function = const), so that, without loss of generality,

$$f = 0 \text{ at } \eta = 0 \tag{19}$$

The remaining boundary conditions are applied at the two edges of the viscous layer and are given by

$$F(\eta_e^+) = F(\eta_e^-) = g(\eta_e^+) = g(\eta_e^-) \equiv 1 \tag{20}$$

where η_e^+ and η_e^- are the upper and lower viscous-layer edge values of the η coordinate, respectively. The boundary conditions given by equation (20) enforce the approach of the variables to their correct edge values and are consistent with the assumption that the static and total pressure jumps across the viscous wake are zero.

The viscous equations in the wake are solved implicitly by starting at the trailing edge where the velocity, stream function, and total enthalpy profiles are known from the just completed suction and pressure surface boundary-layer solutions, providing the necessary initial conditions for marching the viscous-layer equations downstream in parabolic fashion. As mentioned above, the equations are solved in inverse mode, with the jump in the stream function between the viscous-layer upper and lower edges specified from the following relation obtained by integrating equation (14) across the entire wake (from η_e^- to $_e^+$) and using the standard definition of the displacement thickness δ^*:

$$f(\eta_e^+) - f(\eta_e^-) = \left(h + \eta_e^+ - \eta_e^- - \frac{\bar{m}_w}{\sqrt{2\xi}} \right), \tag{21}$$

where

$$h = \int_{\eta_e^-}^{\eta_e^+} (\hat{\theta} - 1) d\eta \tag{22}$$

and $\bar{m}_w = (\rho_e u_e \delta^*)_w$ is specified, along with h; the latter is obtained from the previous global iteration. In inverse mode,

the quantities β and u_e are unknown and thus a supplemental equation relating these two variables is needed; it is provided by using the discretized form of equation (18).

The finite-difference form of the nonlinear system of governing equations (14)–(22) is linearized and solved at each marching station, using Newton iteration to converge the equations locally. Since the coupling between the energy equation and the other two governing equations is generally weak, the former equation is solved uncoupled from the other two, after each local iteration on the continuity and momentum equations is completed, to obtain the profile of g. The continuity and momentum equations are solved implicitly using a tridiagonal inversion algorithm, which is modified to account for the application of one boundary condition (equation (19)) at $\eta = 0$ and the others (equation (20)) at the upper and lower edges of the viscous layer, as well as to account for the application of a jump condition on f (equation (21)) between the upper and lower edges. Finally, the so-called FLARE approximation is applied to turn off the axial convection terms($F\partial F/\partial\xi$) and $F\partial g/\partial\xi$) locally wherever $F < 0$ to prevent instabilities in the viscous-layer solution along blade surfaces and in the wake.

Turbulence and transition modeling are important elements of the present cascade analysis. The effects of turbulence in blade surface boundary layers are represented by the algebraic model of Cebeci and Smith (1974), modified to account for separated flow as described by Carter and Wornom (1975), and in the wake are represented by the model of Chang et al. (1986). Transition effects are determined using the empirical models of Dunham (1972) for natural transition, and Roberts (1979) for predicting the location of transition within transitional separation bubbles. The original model of Dunham adjusted the transition parameter for both favorable and adverse pressure gradient effects, but in the present implementation, adjustments are only made for the latter. In the case of natural transition, the streamwise intermittency distribution is determined from the universal function developed by Narasimha (1957). In the case of bubble transition, transition is assumed to occur instantaneously, at the location predicted by Roberts' correlation. It should be noted that, although the bubble transition model was developed from suction-surface correlations, in the present study it has been applied on both surfaces of the blades. Both transition models have been used extensively by many others, and hence they will not be described here. However, the way in which the transition models are implemented within the present analysis will be discussed below, because it has been found that the implementation can significantly influence the convergence characteristics of the inviscid–viscous interaction calculation.

Empirical transition models such as those used here are generally applied by interrogating the last available complete viscous solution to determine the type of transition (natural or bubble), the location of the transition points, transition length, and streamwise intermittency distribution. Once this is done, the solution is then advanced to the next global iteration (or time step, for time-marching Navier–Stokes techniques). In effect, the transition parameters are lagged by one or more iterations, depending on how often the parameters are updated. Lagging the transition parameters can lead to problems with convergence of the solution, because the location of transition, and sometimes even the type of transition, may develop nonconvergent behavior, often in the form of a limit cycle. In the initial implementation of the aforementioned transition models into the present analysis, the behavior was observed in a majority of the calculations. Thus, an approach was developed to alleviate this problem, and is described below.

Because we believe that the convergence difficulties described above are often associated with lagging the transition parameters, an attempt was made to solve this problem by reducing the number of lagged quantities as much as possible. Thus, the transition locations on both blade surfaces are de-

termined while marching the viscous-flow equations downstream, rather than after obtaining the complete viscous solution on the surfaces. This is accomplished in the present analysis by interrogating the viscous solution at each marching station to determine whether either the natural or the bubble transition model predicts transition. If either of them does, then transition is assumed to occur and the turbulence model is used with the appropriate streamwise intermittency distribution, for the remainder of the downstream viscous-layer calculation. The transition length and streamwise intermittency distribution, needed in the case of natural transition, are calculated using the previous global iteration values for the region downstream of the transition point, but this partial lagging of the transition parameters does not noticeably degrade the performance of the natural transition model. The present implementation of the transition models was tested for several cases discussed in the Results section.

Inviscid–Viscous Coupling. The iteration procedure used to couple the viscous and inviscid equations in the present analysis is based on the semi-inverse technique introduced by Carter (1979). In this method, the distribution of the displacement thickness parameter $\bar{m}$ is simultaneously prescribed for solving both the viscous equations in inverse mode and the inviscid equations. In general, the resulting viscous-layer edge and inviscid surface and wake streamline tangential velocity distributions, u_{e_V} and u_{e_I}, respectively, will not agree. The $\bar{m}$ distribution is then updated in an attempt to force the viscous and inviscid velocity distributions to agree, to within a specified tolerance, at all of the solution points on the blade surface and along the wake streamline, at which point the solution is considered to be converged. The semi-inverse iteration technique uses the local ratio of the inviscid and viscous velocities to determine an updated value of $\bar{m}$ at each point from the relation

$$\bar{m}^{new} = \bar{m}^{old}\left[1 + \omega \left(\frac{u_{e_V}}{u_{e_I}} - 1 \right) \right] \qquad (23)$$

where ω is relaxation factor and u_{e_V} and u_{e_I} are the local viscous edge and inviscid surface and wake tangential velocity components, respectively. The superscript *old* refers to the values of $\bar{m}$ used to obtain the most current values of u_{e_V} and u_{e_I}, and *new* refers to the updated value of $\bar{m}$ to be used during the next global iteration of IVICAS.

The number of updates to the $\bar{m}$ distribution needed to converge the solution varies, generally increasing as the strength of the inviscid–viscous interaction increases. A specified maximum number of time steps is taken with the Euler solver for every update of $\bar{m}$; fewer than the maximum are taken if the inviscid solution converges to within the specified tolerance during the current global iteration. For the present investigation, 30 time steps have been specified for each update, unless otherwise noted. The viscous-layer equations are solved once for each update of $\bar{m}$.

Results

The present inviscid–viscous interaction cascade analysis is being developed to provide a tool that will accurately model many of the phenomena that are important in cascades. The results presented below have been obtained as part of an effort to validate the IVICAS analysis, and to guide future efforts to improve the present approach. Thus, results have been obtained for several different cascades, operating over a wide range of conditions for which experimental data exist, in order to evaluate different aspects of this numerical procedure. The particular aspects that have been investigated and are reported on here are, first, the overall ability of the analysis to predict

the performance of a transonic compressor cascade over its full operating range; second, the effect of varying the Reynolds number on the predicted character of transition and on the performance parameters, as well as the effect of the present implementation of the transition models on the robustness of the numerical algorithm; and finally, the accuracy of the present viscous wake analysis.

All of the cascades considered here have circular-arc blunt trailing edges. Inherent in boundary-layer theory is the assumption that there exists a predominant flow direction, and that viscous diffusion in that direction is negligible compared with diffusion in the direction normal to it. Unfortunately, this assumption renders the IVI approach invalid in the vicinity of blunt trailing edges. Therefore, the original blunt trailing-edge geometries considered here have been modified for the present calculations by replacing the circular-arc trailing edges with wedge-shaped trailing edges with a total included wedge angle of approximately 45–60 deg. The present inviscid grid generation scheme restricts the degree of streamwise clustering of grid points at a wedge-shaped trailing edge; therefore the meshes used for this investigation are relatively coarse there, with significantly less resolution than is needed to resolve the details of the flow in the trailing-edge/near-wake region accurately. It should be noted that a technique that relieves some of the restrictions of the IVI approach, permitting consideration of blunt trailing edges, was introduced by Werle and Verdon (1980) and recently demonstrated for cascades by Barnett and Verdon (1989), and will be incorporated into the present analysis in the near future.

The IVI solutions shown in this paper were considered to be converged when the relative difference between the viscous-layer edge velocity and the inviscid velocity at all points on the blade surface and wake streamline is less than 0.001. For all the solutions presented below, it has been assumed that upstream of the cascade leading edge and downstream of the trailing edge, the streamtube height is constant and varies linearly between those two locations. In addition, because the streamline curvature is generally only significant in the near wake very close to the trailing edge, and the present meshes do not resolve the near wake, the curvature effect has been neglected in the present calculations, i.e., the static pressure jump along the wake streamline, given by equation (5), is assumed to be equal to zero. Unless otherwise noted, in the present calculations the inviscid C-grid was constructed using 161 streamwise points, 40 along the wake streamline (20 on each side of the cut line) and 17 tangential points (e.g., see Fig. 1). For the viscous-layer calculations, 61 grid points were distributed across the surface boundary layer and 121 points across the wake viscous layer. The viscous-layer solution stations on the blade surface and along the wake streamline coincide with the locations of the inviscid grid points along those boundaries.

All the IVI calculations shown here have been performed on an Apollo DN 10000 super-workstation. The CPU time required for the calculations performed on the grid described above is approximately 35 seconds per global iteration, using 30 inviscid time steps during each iteration. The ratio of inviscid to viscous CPU time is approximately 4:1, but can be higher, depending on the particular case. Because the IVICAS code is still under development, it was compiled and run without optimization. Thus, a significant reduction in the CPU time needed to execute the code is expected when it is optimized to take advantage of the vectorization and/or parallelization capabilities of current computers.

A number of predictions of the cascade loss are presented below. The loss is ideally made up to two components, viscous loss and shock-induced loss. The viscous loss is determined here by using a compressible flow-mixing calculation (Stewart, 1955) and the inviscid loss is determined using a technique that evaluates shock loss directly by locating shocks and integrating

Table 1 Aerodynamic conditions for transonic compressor cascade

Inc.	M_1	β_1	M_2	β_2	H_2/H_1	$\bar{\omega}$	Re
-10.0	.7312	57.0	.5920	89.28	.9584	-.0782	1.028×10^6
-4.8	.7257	51.8	.5821	91.21	.8900	.0250	1.044×10^6
-2.8	.7313	49.8	.5861	90.20	.8635	.0227	1.034×10^6
0.0	.7654	47.0	.5604	90.84	.8657	.0199	8.710×10^5
3.2	.7346	43.8	.5574	89.87	.8094	.0236	1.058×10^6
5.0	.7355	42.0	.5395	90.26	.8036	.0384	1.108×10^6
7.0	.7376	40.0	.4902	90.85	.8542	.1441	9.002×10^5

the total pressure loss along them to determine the total shock loss. The latter procedure avoids uncertainties associated with the unavoidable presence of numerical losses arising when solving the discretized inviscid equations. The mixing calculation is performed just upstream of the trailing edge, where a spurious increment to the predicted viscous component of the loss is produced. In the results presented below for the transonic compressor cascade, both the total (viscous plus shock) loss and the viscous loss alone are shown, plotted with separate symbols. This gives an indication of the magnitude of the shock-induced loss for these cases. Only the viscous component of the loss is presented for the subsonic and low-speed cascades, since the flows are shock-free. The values of the downstream flow angle β_2 presented here were also determined using the mixing analysis of Stewart (1955).

The base pressure loss has been neglected in the present analysis; however, empirical methods have been used to estimate the base pressure effects. For the transonic compressor cascade discussed below, the magnitude of the base pressure loss, $\bar{\omega}_b$, is estimated to be $\bar{\omega}_b \leq 0.0016$, which is approximately 10 percent of the minimum loss predicted for this cascade. For the other cascades considered here, the base pressure loss is estimated to be of comparable magnitude relative to the total loss.

The values of the constants γ and Pr_t are 1.4 and 0.95, respectively, for all the results presented below.

Transonic Compressor Cascade—Performance With Varying Incidence. The transonic, linear compressor cascade reported by Stephens and Hobbs (1979) is considered first. The experiments were conducted at DFVLR in a closed-loop wind tunnel. The IVICAS inviscid–viscous interaction procedure was used to predict several test conditions spanning the operating range of inlet gas angles of the cascade for a common inlet Mach number of approximately 0.73. The aerodynamic conditions used for these computations are the experimental conditions given in Table 1, which have been corrected as suggested in the original report of the experimental data (Stephens and Hobbs, 1979); in particular, the values of the inlet Mach number that are given in the table have been increased from the measured values by 0.03 and the exit-to-inlet streamtube height ratio was adjusted accordingly to preserve continuity. The corrected conditions are the same as those used for the Navier–Stokes calculations reported by Davis et al. (1988). The first column gives the incidence, in degrees, of the inlet flow relative to its design-point value of 47 deg. Note that the values of $\bar{\omega}$ and Re given in Table 1 have also been adjusted for consistency. Finally, it should be noted that the inlet Mach number is not specified as a boundary condition, and the predicted values of M_1 can therefore differ from those given in the table, as will be discussed later.

The turbulence model used in the Navier–Stokes analysis of Davis et al. (1988), with which the present results are compared, was developed by Baldwin and Lomax (1978), and is similar to that previously developed by Cebeci and Smith (1974) and used in the IVICAS analysis. The principal difference is that the former model does not use the boundary-layer thickness
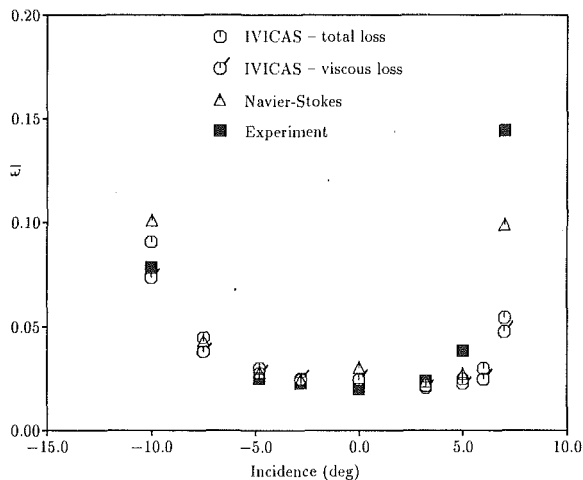
Fig. 4 Predicted loss versus incidence for transonic compressor cascade

Fig. 5 Exit gas angle versus incidence for transonic compressor cascade

to determine the length scale for the outer region, as is done in the latter, because the edge of the boundary layer is sometimes difficult to identify in a Navier–Stokes analysis. Instead, the turbulent length scale is related to the normal distance from the surface to the location of maximum vorticity at each station. However, because of the similarities between the two models, the differences between the IVI and Navier–Stokes results due to turbulence modeling should be minimal. The Navier–Stokes calculations were carried out assuming fully turbulent flow, with instantaneous transition just aft of the leading-edge stagnation point (Davis et al., 1988); thus the same assumption was made for the present calculations.

It should be noted that the Navier–Stokes calculations were performed using the actual circular-arc trailing-edge geometry, while the trailing-edge geometry has been modified, as discussed earlier, for the IVI calculations. This allows an evaluation of the effect of the present trailing-edge treatment, as will be discussed below.

Convergence of the transonic compressor cascade calculations was attained in anywhere from about 100 global iterations for the design-point case to approximately 300 iterations for the two most severe cases, at the extremes of the operating range. For these two cases, 60 time steps were taken during each global iteration, instead of the usual 30.

The measured mass-averaged total pressure loss parameter, $\bar{\omega} = (P_{t_1} - P_{t_2})/(P_{t_1} - P_1)$, is presented as a function of incidence in Fig. 4, along with the loss predicted by the IVICAS analysis and the Navier–Stokes analysis of Davis et al. (1988). Additional points corresponding to incidences not tested experimentally were obtained using the two analyses to verify the predictions of the trends at either end of the incidence range, and are included in Fig. 4. The values of $\bar{\omega}$ predicted by IVI and Navier–Stokes analyses are referenced in each case to the corresponding *calculated* inlet Mach number to account for differences between the measured and calculated inlet Mach number from case to case, as well as for differences between the resulting values of M_1 obtained from the two analyses for each case. The values of the total loss predicted by the IVICAS analysis and presented here consist of the sum of the viscous and the inviscid (shock-induced) contributions to the loss, represented by the open circular symbols, and the viscous loss alone, represented by the flagged open circles. The predictions for the loss obtained using the IVICAS analysis are in good agreement with both the measurements and the Navier–Stokes predictions of the total loss, except at the largest positive incidence case measured, 7 deg, where the total loss is significantly underpredicted. This may be due in part to uncertainty in the measured value of the incidence, since the loss is very
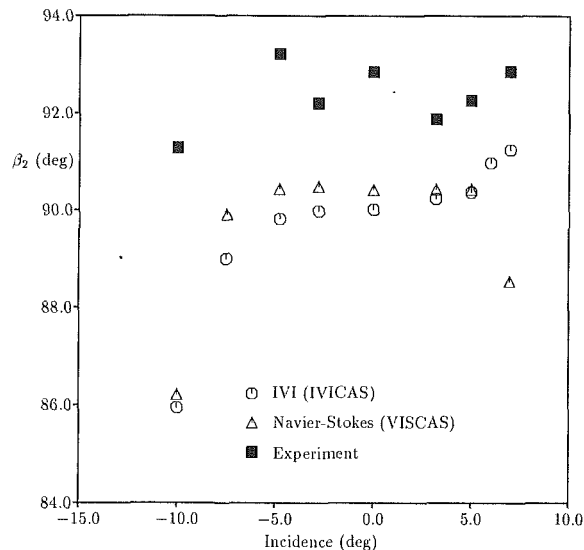
sensitive to changes in the incidence in this range, or it may be due to underprediction of the shock strength associated with smearing of the inviscid solution caused by numerical dissipation. Overall, the inviscid–viscous interaction procedure accurately predicts both the absolute level of the loss in the vicinity of the design point and the positive and negative incidences at which the loss increases very rapidly as the magnitude of the incidence is increased. Although the agreement with the absolute level of the loss at the farthest off-design conditions is not as good as that observed nearer the design point, the limits of the incidence range for this cascade have been correctly determined.

Figure 5 shows the comparison between the predicted and measured exit flow angle as a function of incidence. The predictions of the IVI and Navier–Stokes analyses are in excellent agreement with each other, with the exception of the most extreme positive incidence. Both predictions differ from the experimentally measured exit flow angle by approximately 2 deg over most of the incidence range. The latter discrepancy is probably due in large part to the difference between the specified and true streamtube height variations between the calculations and the experiment. Numerical investigations have shown that the predicted exit flow angle is sensitive to the streamtube height distribution within the cascade (Davis et al., 1988). In addition, the angle is difficult to measure accurately; thus there is a significant degree of uncertainty in the measured values. In an attempt to determine the cause for the discrepancy between the values of β_2 predicted by the IVI and Navier–Stokes analyses at 7 deg incidence, an additional data point has been obtained at 6.0 deg incidence using the IVICAS analysis. As shown in Fig. 5, the interaction analysis predicts a rapid and consistent increase in β_2 for incidence angles exceeding 5 deg. This behavior is contrary to what is usually observed, wherein β_2 decreases relative to the design-point value as the incidence angle is increased well into the positive incidence range (although this trend is not evident in the measured β_2 distribution for this cascade). The anomalous behavior of the predicted performance at high positive incidence angles, as well as the overall underprediction of β_2 across the incidence range, will be further examined as this effort continues.

The airfoil surface static pressure distribution predicted by the IVICAS analysis for the design condition (0 deg incidence) is compared with the experimental data and with the Navier–Stokes and inviscid (Euler) solutions, the latter indicating the relative effect of inviscid–viscous interaction on the solution, in Fig. 6. The ideal value of P/P_t at the sonic condition is
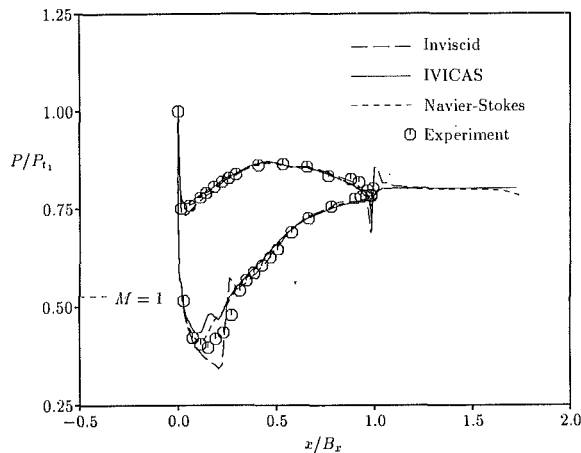
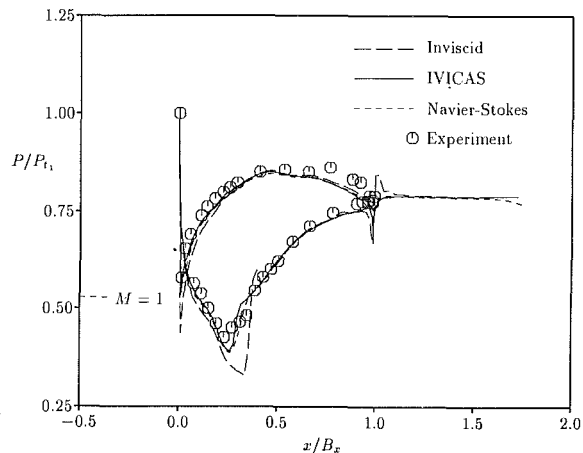**Fig. 6   Pressure distribution, 0.0 deg incidence**

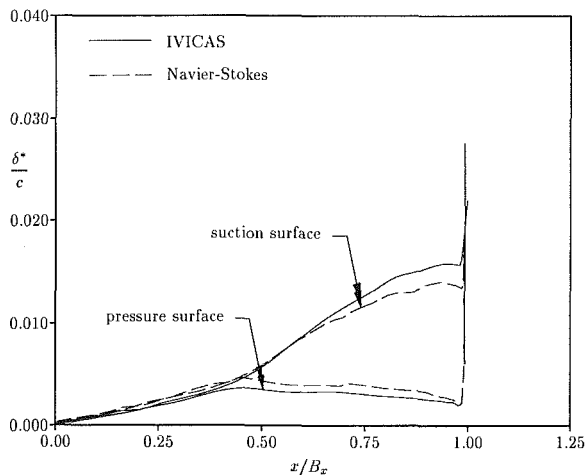**Fig. 8   Pressure distribution, −4.8 deg incidence**

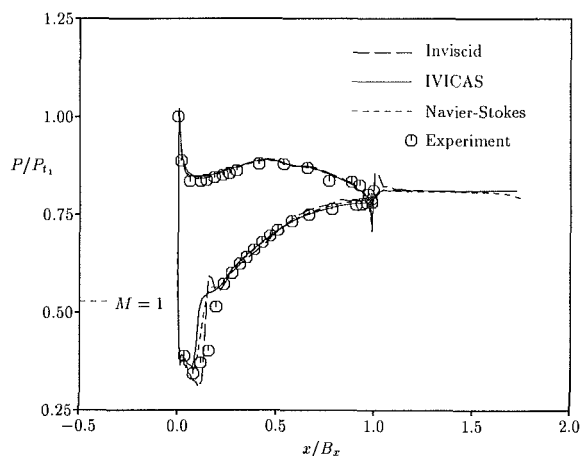**Fig. 7   Predicted displacement thickness distribution, 0 deg incidence**

Fig. 9   Pressure distribution, 5.0 deg incidence

indicated on this figure and on the other plots of the blade surface pressure distribution for this cascade. The IVI solution is in good agreement with both the experimental data and the Navier–Stokes solution except in the immediate vicinity of the minimum pressure point, where both analyses slightly over-predict the pressure. The effects of inviscid–viscous interaction are shown to be quite significant in the transonic region of the suction surface, with the inviscid analysis predicting a well-defined shock, whereas the predictions of the two viscous analyses show a relatively gradual compression to subsonic conditions. Figure 7 shows that the predictions of the IVI and Navier–Stokes analyses for the displacement thickness distributions on both blade surfaces are in good agreement, with the IVICAS analysis predicting slightly thicker suction and thinner pressure-surface displacement thickness distributions than are predicted by the Navier–Stokes analysis. Since viscous effects produce a smooth displacement body (airfoil plus displacement thickness), there is a rapid increase in the displacement thickness at the trailing edge to counteract the rapid decrease in the airfoil thickness there.

The predictions of the IVICAS analysis for the −2.8 deg and 3.2 deg incidence cases show similar agreement with both the experimental data and the Navier–Stokes solutions as is shown in Figs. 6 and 7 for the 0 deg incidence case.

The airfoil surface pressure distributions for the more difficult off-design cases of −4.8 deg and 5.0 deg are presented in Figs. 8 and 9, respectively. The IVI predictions again show very good agreement with both the experimental data and the results of the Navier–Stokes analysis, although for the case of

−4.8 deg incidence both numerical solutions show somewhat lower pressures upstream of the trailing edge on both blade surfaces (Fig. 8). The displacement thickness distributions obtained from the IVI and Navier–Stokes analyses are compared in Figs. 10 and 11 for the −4.8 deg and 5.0 deg incidence cases, respectively. As in the design-point case, the agreement between the predicted displacement thickness distributions is good. Both analyses predict that the flow is fully attached except in the immediate vicinity of the trailing edge, where both predict a small separated region on the suction surface, and in the 5.0 deg incidence case a small separation bubble at the foot of the suction-surface shock ($x/B_x \approx 0.10$) is predicted by the two analyses.

The most difficult cases for cascade viscous analyses to predict are at conditions near the stall and choking incidences, where massive separation may occur. Time-marching approaches, which most Navier–Stokes algorithms employ to obtain an asymptotic steady-state solution, become increasingly difficult to drive to steady conditions (i.e., convergence) as the extent of separation grows. On the other hand, the conventional wisdom with respect to the inviscid–viscous interaction approach considers massive separation to be beyond the range of applicability of IVI analyses (e.g., see Janssens and Hirsch, 1983, and Hassan, 1988). However, it should be noted that there is recent evidence that IVI approaches can be used for isolated airfoils beyond the point of stall; for example, see Le Balleur (1989) and Barnett (1988). As shown below, the
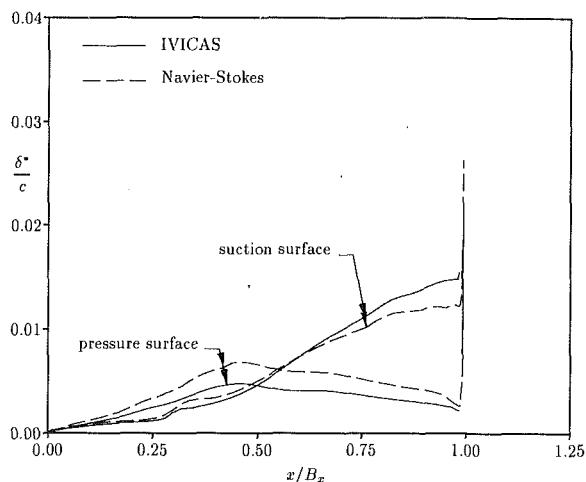
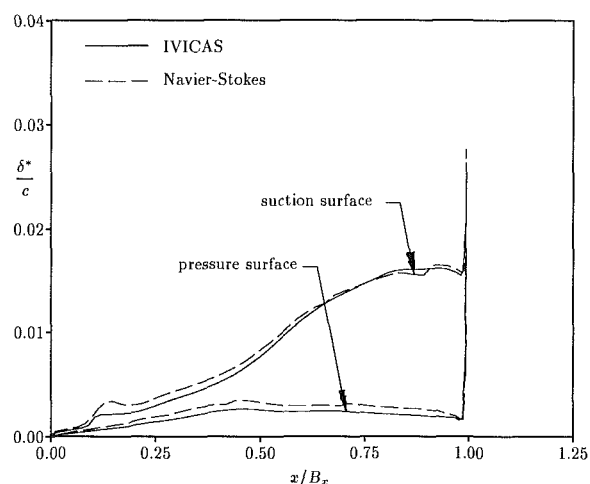**Fig. 10 Predicted displacement thickness distribution, −4.8 deg incidence**

Fig. 11 Predicted displacement thickness distribution, 5.0 deg incidence

Fig. 12 Pressure distribution, −10.0 deg incidence

Fig. 13 Predicted displacement thickness distribution, −10.0 deg incidence

Fig. 14 Pressure distribution, 7.0 deg incidence

present IVI analysis has been successfully applied to cases with massive separation.

Figure 12 shows the pressure distribution obtained from the IVICAS analysis along with the experimental data and the Navier–Stokes result for the case of −10 deg incidence, for which the cascade where the massively separated. The IVI result is in good agreement with both the data and the Navier–Stokes result, except in the aft portion of the cascade where the massive-separation region is located. However, the agreement between the two *numerical* results remains good even there, although the pressure distributions differ in the wake. The measured flow field associated with the massively separated case probably had extensive three dimensionality, which would account for much of the discrepancy between the data and the numerical results. Further, the turbulence models used in the two analyses are known to be inadequate for separated flows, with a tendency to cause an underprediction of the extent of separation. The displacement thickness distributions obtained for this case from the IVICAS and Navier–Stokes analyses are presented in Fig. 13. The qualitative agreement is very good, although the Navier–Stokes analysis consistently predicts a larger displacement thickness on both blade surfaces. Both analyses predict that the flow separates on the suction surface at $x/B_x \approx 0.40$, and remains separated over the remainder of the suction surface. It should be noted that the IVICAS analysis does *not* predict that the flow is choked for this case.

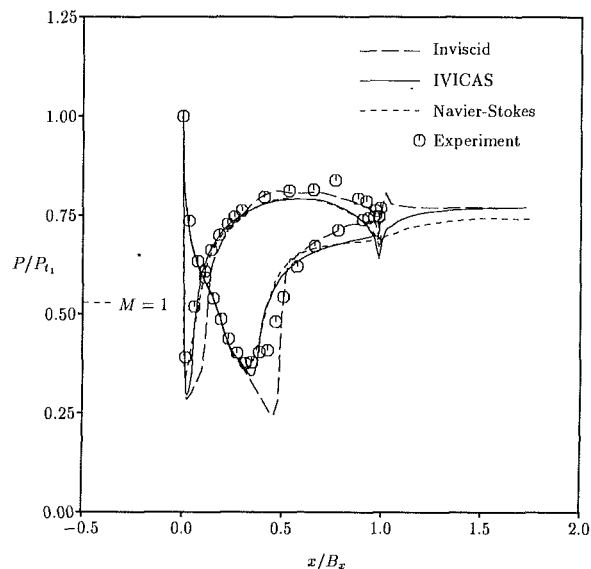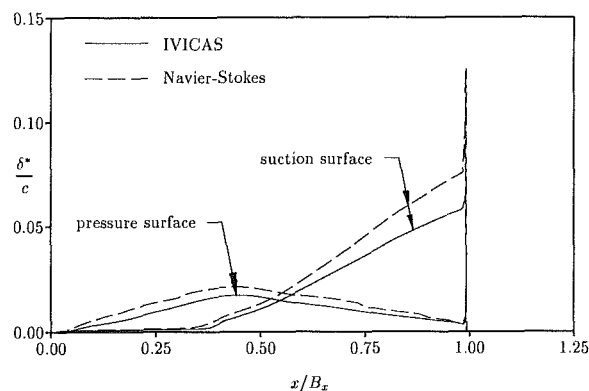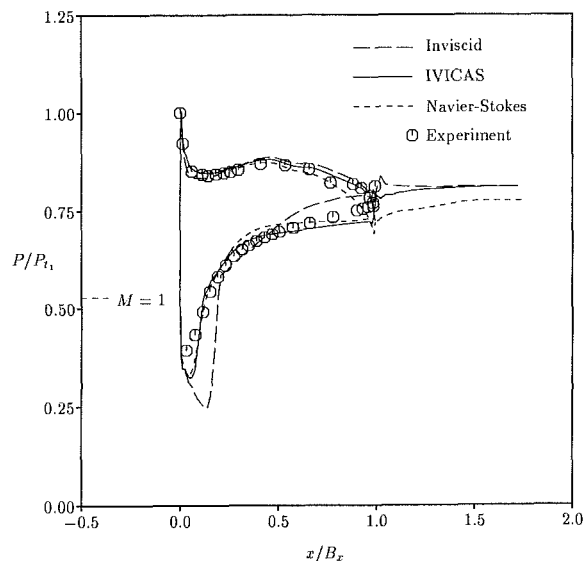The other massively separated case corresponds to 7 deg incidence. The pressure distribution obtained using the IVICAS analysis is compared with the experimental data and the Navier–Stokes solution in Fig. 14. The agreement of the interaction result with both the data and the Navier–Stokes so-
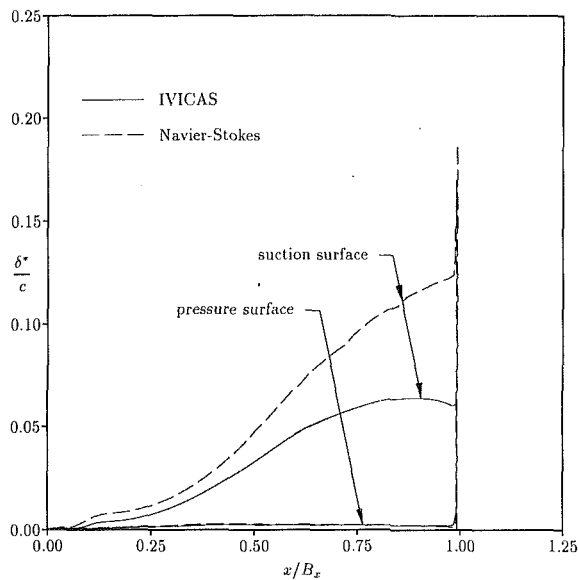
Fig. 15 Predicted displacement thickness distribution, 7.0 deg incidence

Fig. 16 Pressure distribution, 0.0 deg incidence

Table 2 Summary of exit pressure variation results for 0 deg incidence case

Case	M_1	P_2/P_{t_1}	$\bar{\omega}$	β_2
I	0.7396	0.8029	0.0242	88.14°
II	0.7654	0.7901	0.0257	88.14°

lution is reasonbly good in the forward portion of the cascade but worsens in the aft portion. Unlike all the previous cases, here the IVI result does not agree well with the Navier–Stokes result in the aft region of the cascade. The interaction analysis encountered difficulties in the immediate vicinity of the trailing edge, as evidenced by the oscillations in the pressure distribution and the excessively abrupt matching of the pressure and suction-surface pressures at the trailing edge. The treatment of the trailing edge is the likely source of the difficulty: Use of a coarse grid there, wedging of the blunt trailing edge, and use of the wake boundary condition at the trailing edge point, combined with the severity of this case, may have contributed in varying degrees to the observed behavior. Further study will be needed to resolve this issue. The displacement thickness distributions predicted by the two analyses are presented in Fig. 15, which shows that the Navier–Stokes analysis predicts a considerably thicker displacement body on the blade suction surface than is predicted by the IVI analysis. The IVI and Navier–Stokes analyses predict that the suction-surface boundary layer separates at $x/B_x \approx 0.10$ and 0.075, respectively, and remains detached over the remainder of the suction surface.

The solutions for all the cases discussed in the Results section were obtained assuming a value for the exit pressure corresponding to the value that satisfies continuity through the cascade based on the experimentally measured values of the inlet Mach number and streamtube contraction ratio. Numerical losses and viscous blockage effects generally cause the inlet Mach number obtained when the solution has converged to be different from the experimental value. This effect was evaluated for the design-point case discussed above. The case was recalculated with the exit pressure varied until the calculated inlet Mach number closely matched the adjusted measured value. Figure 16 shows the pressure distributions obtained from the two calculations along with the experimental data. Case I refers to the mismatched inlet Mach number calculation and Case II corresponds to the case where the calculated value of M_1 was matched to the measured value. The agreement with the experimental data in the vicinity of the minimum pressure is significantly improved when M_1 is matched, while the underprediction of the pressure in the vicinity of the trailing edge is increased from the slight underprediction in the result obtained without matching the inlet Mach number. A summary of the results is shown in Table 2, where the loss coefficient
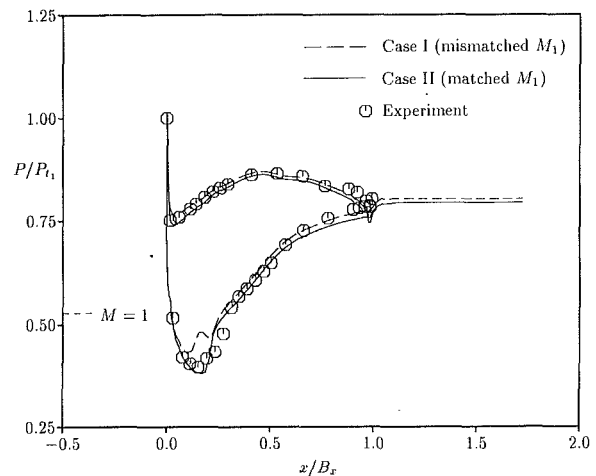
has been adjusted to be consistent with the calculated inlet Mach number for each case.

The comparisons with the Navier–Stokes results presented above allow an evaluation of the effects of both the present trailing-edge treatment and the neglect of streamtube contraction effects in the viscous layer, for these cases. For most of the cases presented, the present predictions of the displacement thickness and surface pressure (as well as other quantities not presented here) agree quite well, even in the vicinity of the trailing edge, with those obtained from the Navier–Stokes analysis, which includes both streamtube contraction effects in both the inviscid and viscous regions of the flow and a complete representation of the blunt trailing edge. Thus, it is concluded that neither the present trailing-edge treatment nor the neglect of streamtube contraction effects in the viscous layer have seriously affected the results of the IVI analysis for this cascade, except for the isolated case of 7 deg incidence, where difficulties were encountered at the trailing edge, as discussed above.

Subsonic Compressor Cascade—Performance With Varying Reynolds Number. Engine performance at high altitude often degenerates because of the low Reynolds numbers occurring within the compressor, leading to increased loss and reduced operating incidence range. Thus, it is important that the compressor design system be able accurately and reliably to predict the onset of transition as the Reynolds number is varied. Although the *accuracy* of transition predictions is principally dependent on the empirical models used, it can also be affected by the way in which the transition models are implemented. On the other hand, the *robustness*, and hence reliability, of the viscous analysis can be very strongly affected by the particular implementation of the transition models. Therefore, the present strategy for implementing the existing natural and bubble transition models discussed in the Numerical Procedure section was developed with the intention of improving the robustness of the IVICAS analysis when used in the "variable" transition mode, i.e., when the type and location of transition is not specified, but is computed as part of the overall inviscid-viscous interaction calculation.

In order to validate the transition model implementation, several calculations were carried out for a linear compressor cascade, which was tested at subsonic conditions for a range

Fig. 17 Subsonic compressor cascade geometry (modified trailing edge)
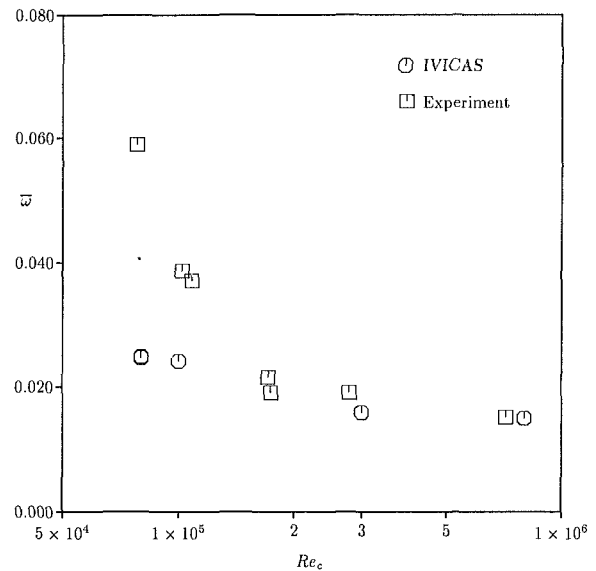

Fig. 18(a) Loss coefficient versus Reynolds number for subsonic compressor cascade

Fig. 18(b) Exit flow angle versus Reynolds number for subsonic compressor cascade

of Reynolds numbers with a fixed inlet Mach number. Varying the Reynolds number can affect the location and type of transition significantly, and will therefore exercise the transition models over a range of conditions. The experiments were conducted at DFVLR in the same closed-loop wind tunnel used for the transonic cascade experiment discussed above, and are reported by Starken et al. (1986). The cascade gap-to-chord ratio is 0.863. A single cascade passage, with the trailing edge shown as modified for the calculations, is illustrated in Fig. 17. In the experiment, a high level of free-stream turbulence was introduced ($Tu \approx 3.5$ percent) to simulate the high levels of turbulence found in turbomachinery. The inlet Mach number $M_1 = 0.538$, the inlet flow angle $\beta_1 = 52.7$ deg, and four representative values of the Reynolds number, spanning the range examined in the experiment, were chosen for the present calculations, namely Re $= 8 \times 10^4$, 1×10^5, 3×10^5, and 8×10^5. Rather than using the actual measured values of H_2/H_1, a single representative value for the streamtube contraction ratio is used for all of the calculations, namely $H_2/H_1 = 0.986$, which is the value measured at the cascade design condition. This is done for two reasons. First, the principal intent here is to determine how well the present analysis can predict the basic effects of Reynolds number variation, isolated from other effects, such as variations in H_2/H_1. Second, the original experimental data were obtained with large variations in H_2/H_1, yet the measured losses are only very mildly affected by these variations. In particular, for the experimental measurements at Re $\approx 1.7 \times 10^5$, H_2/H_1 varied by more than 10 percent, yet despite this, the two measured values of $\bar{\omega}$ shown in Fig. 18(a) are seen to be quite close to one another.

The number of inviscid–viscous iterations needed to converge the cases corresponding to Re $= 1 \times 10^5$ and 3×10^5 were 143 and 92, respectively, with a relaxation factor $\omega = 0.25$. The cases corresponding to the two extremes, namely Re $= 8 \times 10^4$ and 8×10^5, proved to be more difficult to converge than the two intermediate Re cases. In fact, in the lower Re case, convergence was never attained due to a limit cycle, associated with the transition models, which developed during the inviscid–viscous iterations and could not be eliminated through modification of the relaxation factor or transition modeling parameters. In the higher Re case, a similar limit cycle developed. However, in this case the limit cycle was eliminated by increasing the multiplicative constant in the bubble transition model from the given value of 2.5×10^4 to
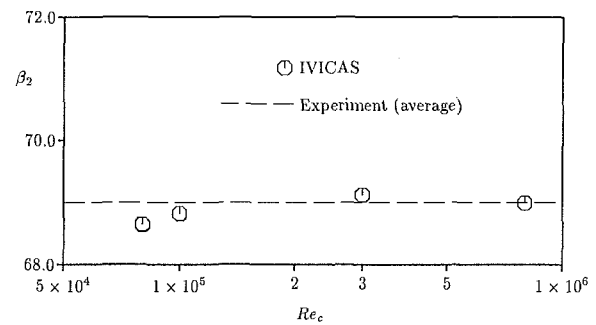
7.5×10^4 (see equation (1) in Roberts, 1979). The solution converged in 269 iterations with this ad hoc modification.

The calculated values of the loss coefficient $\bar{\omega}$ are presented in Fig. 18(a) as a function of the Reynolds number, along with the experimentally measured values. The latter are typical in magnitude and show the expected trend with varying Re (e.g., see Johnson and Bullock, 1965). In these cases, the flow is subsonic and thus the shock-induced loss is zero. Two calculated values for $\bar{\omega}$ are given for the case of Re $= 8 \times 10^4$, corresponding to the values at the farthest forward and aft positions of the separation bubble during the limit cycles. The values are virtually identical, showing that $\bar{\omega}$ is quite insensitive to the location of the transition point for this case. The calculations predict the experimental trend of decreasing loss with increasing Re, although the results show a smaller sensitivity to Reynolds number than is indicated by the data, particularly at the lower values of Re. The very large values of the experimentally measured loss observed at the lower Reynolds numbers is probably due to lack of closure of a leading-edge separation bubble on the suction surface, resulting in massive separation. The present analysis has not predicted massive separation in association with leading-edge separation bubbles for the cases considered, and thus does not reproduce the large levels of loss measured at the lower Reynolds numbers.

Figure 18(b) shows the downstream flow angle β_2 as a function of the Reynolds number. Since the streamtube contraction ratio was not fixed from case to case in the experiments (but is fixed in the calculations), the measured exit flow angle, which is very sensitive to this quantity, shows a great deal of scatter. Starken et al. (1986) discussed this problem and presented a
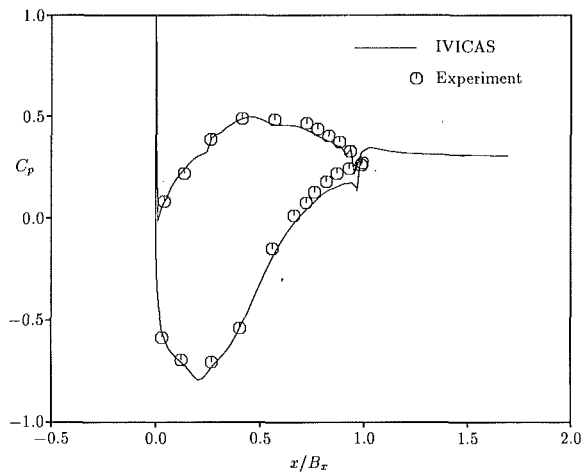
Fig. 19 Pressure distribution, low-speed compressor cascade

plot of the "average" value of β_2 as a function of β_1. For the inlet flow angle corresponding to these cases, they reported $\beta_2 \approx 69$ deg, as represented by the dashed line in Fig. 18(b). The IVICAS analysis predicts the expected trend of β_2 decreasing as Re is decreased for the three lowest values of Re, although the highest Reynolds number result does not follow this trend, the reason for which is not understood at present. The predicted values for β_2 vary about the average experimental value.

The present implementation of the existing transition models yields a greater degree of robustness when the IVICAS analysis is run in the variable transition mode than the previous, more traditional implementation, but still encounters problems for some isolated cases. It is not clear whether this is due to a flaw in the implementation of the models, or the models themselves. However, the present success in converging the solution for the highest Re case by modifying the modeling constant in the bubble transition correlation indicates that the latter is the principal contributor to this behavior in some cases.

Low-Speed Compressor Cascade—Prediction of Viscous Wake Properties. The ability to model viscous wakes accurately in cascades is important for a number of reasons. First, wakes must be accurately represented to determine the blockage due to viscous effects correctly. In addition, the ability to model large-scale trailing-edge separations accurately depends on the wake modeling because, in such cases, the separated region often extends into the wake. Finally, information about the wakes of upstream blade rows is needed to determine the correct forcing functions for aeroelastic and/or aeroacoustic analyses of cascades.

An experiment designed to generate extensive data within the near and far wakes of compressor cascades was reported by Hobbs et al. (1982). The linear cascade was tested in the United Technologies Research Center Large-Scale Cascade, and the experimental facility, measurement techniques, and blade geometry are described in that paper. The experiment was carried out at large scale in order to achieve acceptable measurement accuracy near the cascade trailing edge. Two blade geometries were investigated in the experiment and one of them is considered here, namely the controlled diffusion fore-loaded cascade geometry designated "Build I" by Hobbs et al. (1982); it is the same as that described by Stephens and Hobbs (1979), for which results are presented above, but scaled up so that, in conjunction with the low speed of the experimental configuration, the airfoil chord Reynolds number is maintained within the correct range.

The conditions for this case are the following: $M_1 = 0.1132$, $M_2 = 0.0912$, $\beta_1 = 52.0$ deg, and Re $= 4.78 \times 10^5$. The corresponding inviscid grid employs 161 streamwise points with 60 along the wake streamline (30 on each side of the mesh cut

line) and 17 tangential points. The calculation has been performed using the transition models described above, assuming that the free-stream turbulence level Tu is 1 percent, which is representative of the levels found in the experimental facility. The solution converged in 165 iterations with a relaxation factor $\omega = 0.25$.

The resulting solution predicts bubble transition on the pressure surface and natural transition on the suction surface, at $x/B_x \approx 0.24$ and 0.32, respectively. The surface static pressure distribution obtained from the IVICAS analysis is compared with the experimental data in Fig. 19. The agreement is good except in the immediate vicinity of the trailing edge, where the predicted pressure distribution is slightly higher than the data on the suction surface, and somewhat anomalous behavior is exhibited on both surfaces just upstream of the trailing edge, probably associated with the treatment of the trailing-edge geometry and the lack of axial mesh resolution there.

In order to evaluate the viscous wake analysis developed for the IVICAS procedure, comparisons between the present predictions and the measurements (Hobbs et al., 1982) of various quantities in the wake have been made, and are shown in Figs. 20–22. The results shown in Figs. 20 and 21 are presented as a function of the axial distance downstream of the trailing edge nondimensionalized by the axial component of the chord length, B_x (i.e., $x/B_x = 0.0$ at the trailing edge). Figure 20 shows the distribution of the minimum velocity across the wake profiles. With the exception of the near-wake region, the minimum velocity agrees reasonably with the experimental data. Figures 21(a) and 21(b) show the predicted and measured displacement and momentum thickness distributions, nondimensionalized by the cascade pitch τ. The predicted value of δ^* at the trailing edge agrees with the measured value, but decays more slowly in the near wake than the measured distribution does. The predicted rate of decay agrees better with the data in the far wake. The predicted θ distribution agrees qualitatively with the data, with the magnitude overpredicted by about 35 percent in the far wake. It should be noted that the ratio of the viscous loss predicted by applying the mixing calculation *at the trailing-edge point* to the experimentally measured loss is very close to the ratio of the calculated to measured trailing-edge momentum thickness, as it should be. In Figs. 20 and 21, the lack of resolution in the near-wake region is evidenced by the poor prediction of the local gradients there, a problem that would be largely resolved by increasing the axial clustering of the grid points locally. In addition, the effect of the wake turbulence model on the accuracy of the near-wake solution should be assessed.

The predicted and measured axial velocity profiles are compared at four axial stations in Fig. 22. The experimental data and the numerical results are compared at the nearest stations; the values are given in Fig. 22, where $x/B_x \mid_{exp}$ and $x/B_x \mid_{num}$ correspond to the experimental and numerical locations of the axial stations, respectively. The y coordinates of the profiles have been shifted to place the minimum velocity at $y = 0$ for comparison purposes and each successive curve and the associated data have been offset to the right by 0.20 for clarity. The general agreement between the measured and calculated profiles is good, with the greatest discrepancy occurring in the vicinity of the knee of the velocity profiles on the side of the wake originating on the blade pressure surface.

For the case considered here, the IVICAS analysis predicts the wake quantities reasonably well, although more work is needed to improve this capability. In particular, the effect of increasing the streamwise concentration of grid points near the trailing edge to resolve the very large gradients in the near wake should be examined. Earlier studies have shown that insufficient resolution of the near-wake region degrades the accuracy of the solution in *both* the near and far wake (e.g., see Barnett and Verdon, 1987). In addition, the blunt trailing edge of the actual geometry must be represented more accu-
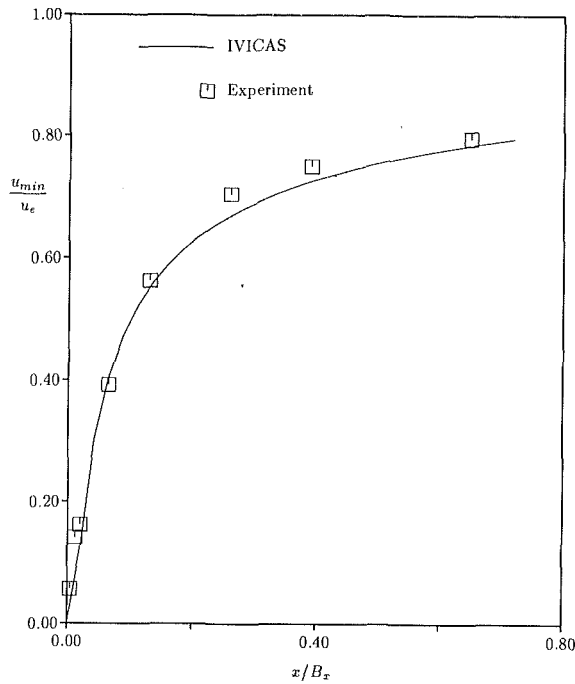
Fig. 20 Minimum wake velocity distribution, low-speed compressor cascade

Fig. 21(a) Wake displacement thickness distribution, low-speed compressor cascade

Fig. 21(b) Wake momentum thickness distribution, low-speed compressor cascade

rately, as discussed earlier, and the spurious numerical loss produced at the trailing edge must be reduced. The wake boundary conditions should be modified to account for the possibility of total pressure jumps induced by shocks on blade surfaces, although this was not a factor in the low-speed cascade examined here. Finally, the wake turbulence model needs to be improved or alternative models must be considered to represent the mixing process more realistically in the near and far turbulent wake.

Concluding Remarks

An inviscid–viscous interaction technique known as IVICAS has been developed to analyze quasi-three-dimensional turbomachinery cascades. The analysis has been applied to a number of cases representing a wide range of operating conditions.

Several conclusions have resulted from this investigation. The IVICAS analysis has been shown to predict the performance characteristics of a transonic compressor cascade accurately near the design point, as well as the incidence angles at which the large increase in loss occurs at either end of the operating range of the cascade. The present analysis has demonstrated the ability to predict the flow at conditions where massive separation occurs, although more work is needed to improve the capability of the IVICAS code in this regime. In addition, the analysis has been tested over a range of Reynolds numbers to examine the impact of representative natural and bubble transition models on the predictions. The transition models have been implemented in a manner that maintains the robustness of the interaction analysis by exploiting the marching nature of the boundary-layer solution procedure to minimize the lagging of any of the quantities needed to update the predicted location and type of transition. The transition models themselves need to be improved to permit better predictions of the effects of Reynolds number variation on the flow. Finally, a viscous wake analysis has been developed and reasonable accuracy demonstrated through comparisons with experimental data.
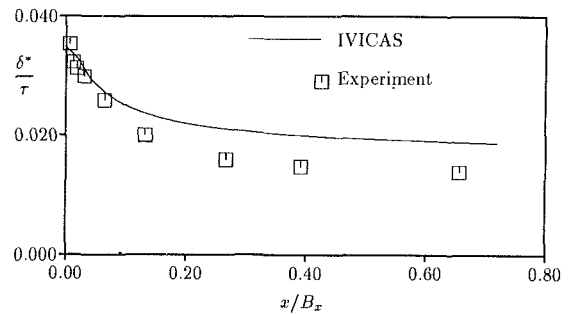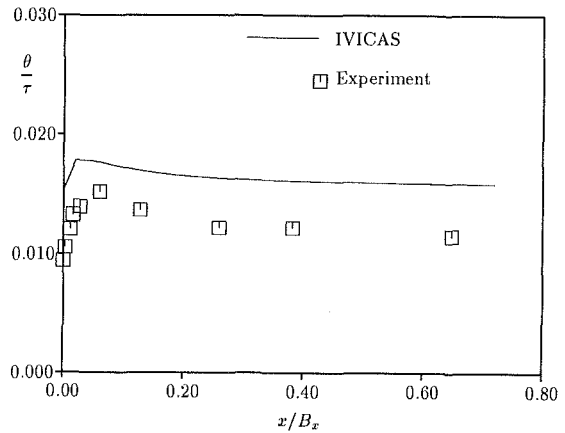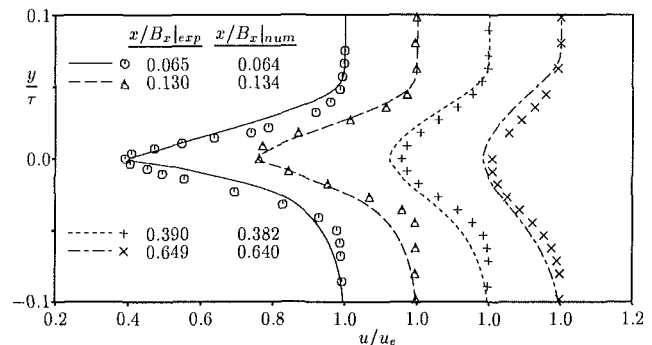
Fig. 22 Wake velocity profiles, low-speed compressor cascade (symbols—experimental data, curves—numerical results)

The results of this study indicate the aspects of the IVICAS analysis that need to be improved. In particular, since accurate predictions of cascade loss and flow turning are very important, primary consideration will be given to the quantification and reduction of the numerically induced loss and further validation and improvement of the ability of the IVICAS analysis to predict flow turning.

The long-term objective of the work described here is the development of an accurate, computationally efficient analysis that is applicable over a wide range of operating conditions. The present study represents the initial phase of this effort, which thus far has only been concerned with the issues of accuracy and range of applicability. The issue of computational efficiency will be considered as this effort continues. The results presented herein demonstrate the potential that the present IVI approach has to provide accurate results over the complete operating range of compressor cascades, accounting for the effects of incidence, Mach number, and Reynolds number variations.

Acknowledgments

References

Baldwin, B. S., and Lomax, H., 1978, "Thin-Layer Approximation and Algebraic Model for Separated Turbulent Flows," AIAA Paper No. 78-257.

Barnett, M., 1988, "Analysis of Crossover Between Local and Massive Separation on Airfoils," AIAA J., Vol. 26, No. 5, pp. 513–521.

Barnett, M., and Verdon, J. M., 1987, "Viscid/Inviscid Interaction Analysis of Subsonic Turbulent Trailing-Edge Flows," AIAA Journal, Vol. 25, No. 9, pp. 1184–1193.

Barnett, M., and Verdon, J. M., 1989, "Theoretical Prediction of High Reynolds Number Viscid/Inviscid Interaction Phenomena in Cascades," Proceedings of the Fourth Symposium on Numerical and Physical Aspects of Aerodynamic Flows, Long Beach, CA.

Calvert, W. J., and Ginder, R. B., 1985, "A Quasi-Three Dimensional Calculation System for the Flow Within Transonic Compressor Blade Rows," ASME Paper No. 85-GT-22.

Carter, J. E., 1978, "Inverse Boundary-Layer Theory and Comparison With Experiment," NASA TP-1208.

Carter, J. E., 1979, "A New Boundary Layer Inviscid Iteration Technique for Separated Flow," AIAA Paper 79-1450.

Carter, J. E., and Wornom, S. F., 1975, "Solutions for Incompressible Separated Boundary Layers Including Viscous-Inviscid Interaction," NASA Sp-347.

Cebeci, T., and Smith, A. M. O., 1974, Analysis of Turbulent Boundary Layers, 1st ed., Academic Press, New York, Chap. 6, pp. 211–257.

Chang, K. C., Bui, M. N., Cebeci, T., and Whitelaw, J. H., 1986, "The Calculation of Turbulent Wakes," AIAA J., Vol. 24, No. 2, pp. 200–201.

Chima, R. V., 1987, "Analysis of Inviscid and Viscous Flows in Cascades With an Explicit Multiple-Grid Algorithm," AIAA J. Propulsion, Vol. 3, No. 5, pp. 397–405.

Davis, R. L., Hobbs, D. E., and Weingold, H. D., 1988, "Prediction of Compressor Cascade Performance Using a Navier–Stokes Technique," ASME JOURNAL OF TURBOMACHINERY, Vol. 110, pp. 520–531.

Davis, R. L., Ni, R. H., and Carter, J. E., 1987, "Cascade Viscous Flow Analysis Using the Navier–Stokes Equations," AIAA J. Propulsion, Vol. 3, No. 5, 406–414.

Dawes, W. N., 1986, "Computation of Off-Design Flows in a Transonic Compressor Rotor," ASME Journal of Engineering for Gas Turbines and Power, Vol. 108, pp. 144–150.

Dunham, J., 1972, "Predictions of Boundary Layer Transition on Turbomachinery Blades," AGARD AG-164.

Hansen, E. C., Serovy, G. K., and Sockol, P. M., 1979, "Axial-Flow Compressor Turning Angle and Loss by Inviscid–Viscous Interaction Blade-to-Blade Computation," ASME Paper No. 79-GT-5.

Hassan, A. A., 1988, "The Design of Shock-Free Compressor Cascades Including Viscous Boundary-Layer Effects," ASME JOURNAL OF TURBOMACHINERY, Vol. 110, pp. 354–362.

Hobbs, D. E., Wagner, J. H., Dannenhoffer, J. F., and Dring, R. P., 1982, "Experimental Investigation of Compressor Cascade Wakes," ASME Paper No. 82-GT-299.

Janssens, P., and Hirsch, Ch., 1983, "A Viscid Inviscid Interaction Procedure for Two-Dimensional Cascades," AGARD CP 351, pp. 3–1–18.

Johnson, I. A., and Bullock, R. O., eds., 1965, "Aerodynamic Design of Axial-Flow Compressors" (revised ed.), NASA SP-36, pp. 205–207.

Le Balleur, J. C., 1989, "New Possibilities of Viscous–Inviscid Numerical Techniques for Solving Viscous Flow Equations With Massive Separation," Proceedings of the Fourth Symposium on Numerical and Physical Aspects of Aerodynamic Flows, Long Beach, CA.

Narasimha, R., 1957, "On the Distribution of Intermittency in the Transition Region of a Boundary Layer," J. Aero. Sci., Vol. 24, pp. 711–712.

Ni, R. H., 1982, "A Multiple Grid Scheme for Solving the Euler Equations," AIAA J., Vol. 20, No. 11, pp. 1565–1571.

Norton, R. J., Thompkins, W. T., Jr., and Haimes, R., 1984, "Implicit Finite Difference Schemes With Non-simply Connected Grids—A Novel Approach," AIAA Paper No. 84-0003.

Olling, C. R., and Dulikravich, G. S., 1987, "Viscous–Inviscid Computations of Transonic Separated Flows Over Solid and Porous Cascades," ASME JOURNAL OF TURBOMACHINERY, Vol. 109, pp. 220–228.

Roberts, W. B., 1979, "Calculation of Laminar Separation Bubbles and Their Effect on Airfoil Performance," AIAA Paper No. 79-0285.

Schäfer, O., Fruhauf, H. H., Bauer, B., and Guggolz, M., 1986, "Application of a Navier–Stokes Analysis to Flows Through Plane Cascades," ASME Journal of Engineering for Gas Turbines and Power, Vol. 108, pp. 103–111.

Schlichting, H., 1979, Boundary-Layer Theory, 7th ed., McGraw-Hill, New York, Chap. XIII, pp. 330–331.

Shamroth, S. J., McDonald, H., and Briley, W. R., 1984, "Prediction of Cascade Flowfields Using the Average Navier–Stokes Equations," ASME Journal of Engineering for Gas Turbines and Power, Vol. 106, pp. 383–390.

Sorenson, R. L., 1981, "A Computer Program to Generate Two-Dimensional Grids About Airfoils and Other Shapes by the Use of Poisson's Equation," NASA TM-81198.

Starken, H., Steinert, W., and Fuchs, R., 1986, "Experimental Investigation of the Compressor Cascade MTU-SKG 4.1. Part 1: Test Procedure and Cascade Performance," DFVLR Report IB-325-08-86.

Stephens, H. E., and Hobbs, D. E., 1979, "Design and Performance Evaluation of Supercritical Airfoils for Axial Flow Compressors," NAVAIR Report FR11455.

Stewart, W. L., 1955, "Analysis of Two-Dimensional Compressible Flow Loss Characteristics Downstream of Turbomachine Blade Rows in Terms of Basic Boundary-Layer Characteristics," NACA TN 3515.

Stow, P., 1985, "Incorporation of Viscous–Inviscid Interactions in Turbomachinery Design," in: Thermodynamics and Fluid Mechanics of Turbomachinery, Vol. II, NATO ASI Series E: Applied Sciences, No. 97B, A. S. Ücer, P. Stow, and Ch. Hirsch, eds., pp. 887–921.

Thompson, J. F., Thames, F. C., and Mastin, C. W., 1974, "Automatic Numerical Generation of Body-Fitted Curvilinear Coordinate System for Field Containing Any Number of Arbitrary Two-Dimensional Bodies," J. Computational Physics, Vol. 15, No. 3, pp. 299–319.

Werle, M. J., and Verdon, J. M., 1980, "Viscid/Inviscid Interaction for Symmetric Trailing Edges," United Technologies Research Center Report R79-914493-5.

C. J. Hwang

J. L. Liu

Institute of Aeronautics and Astronautics,
National Cheng Kung University,
Tainan, Taiwan

Inviscid and Viscous Solutions for Airfoil/Cascade Flows Using a Locally Implicit Algorithm on Adaptive Meshes

A numerical solution procedure, which includes a locally implicit finite volume scheme and an adaptive mesh generation technique, has been developed to study airfoil and cascade flows. The Euler/Navier–Stokes, continuity, and energy equations, in conjunction with Baldwin–Lomax model for turbulent flow, are solved in the Cartesian coordinate system. To simulate physical phenomena efficiently and correctly, a mixed type of mesh, with unstructured triangular cells for the inviscid region and structured quadrilateral cells for the viscous, boundary layer, and wake regions, is introduced in this work. The inviscid flow passing through a channel with circular arc bump and the laminar flows over a flat plate with/without shock interaction are investigated to confirm the accuracy, convergence, and solution-adaptibility of the numerical approach. To prove the reliability and capability of the present solution procedure further, the inviscid/viscous results for flows over the NACA 0012 airfoil, NACA 65-(12)10 compressor, and one advanced transonic turbine cascade are compared to the numerical and experimental data given in related papers and reports.

Introduction

In recent years, considerable progress has been made in the numerical analyses of airfoil and cascade flows. The available approaches can be categorized as: (*a*) inviscid analyses (Jameson et al., 1981; Denton, 1985); (*b*) coupled analyses between inviscid and viscous flowfields (Hwang et al., 1988; Nakahashi et al., 1989); (*c*) full viscous flowfield analyses (Maksymiuk and Pulliam, 1987; Davis et al., 1988). Even though the inviscid method can provide efficient and accurate predictions in some flow cases, several problems were mentioned by Denton (1985) and some limitations were described by Shamroth et al. (1984). To study the shear-induced and heat transfer phenomena, two major approaches, (*b*) and (*c*), have been developed. Making a distinction between the viscous shear layer and inviscid core flow, approach (*b*) includes the viscous/inviscid technique (Hwang et al., 1988) and viscous/inviscid zonal method (Nakahashi et al., 1989). Although the problems that cover the representation of massive separated regions and arbitrary division of the flowfield into viscous and inviscid parts should be seriously considered, approach (*b*) takes less computing time than approach (*c*). For this reason, an Euler/Navier–Stokes zonal method is employed in this study.

In the current design work of aircraft and turbomachinery, flows around isolated airfoil and airfoil cascade are inves-

tigated by using the conventional flow solvers, which are based on the fixed, quadrilateral, and structured meshes (H-mesh, O-mesh, C-mesh, etc.). To resolve the flow features with appropriate distribution of grid points, the solution-adaptive unstructured mesh has been described recently in several works (Siden et al., 1990; Davis and Dannenhoffer, 1989; Mavriplis, 1988). In those papers, only one type of element (triangular or quadrilateral) was used to mesh the entire domain. To simulate two-dimensional cascade flowfields efficiently and correctly, Nakahashi et al. (1989) adopted the structured, quadrilateral elements for viscous layers, and unstructured triangular meshes were used in the inviscid flow regions. Similar to the grid structure given by Nakahashi et al. (1989), the mixed type of elements and the solution-adaptive technique are used to study the viscous, transonic airfoil and turbine cascade flows in this work.

Numerical methods for compressible inviscid and viscous flows fall into three major classes: finite difference, finite volume, and finite element methods. To achieve solutions for airfoil and cascade flows, many explicit/implicit algorithms have been presented to solve the compressible Euler or Navier–Stokes equations. For inviscid turbomachinery calculations, Denton (1985) divided the explicit schemes into four groups and discussed the advantages and disadvantages of each classification. Without using the solution-adaptive technique, Nakahashi et al. (1989) introduced the zonal approach to study the two-dimensional cascade flow. For the viscous flow region

around the cascade blade, the Reynolds-averaged Navier–Stokes equations with the thin-layer approximation were solved by an implicit approximate factorization scheme. In the inviscid region, the two-step Taylor–Galerkin finite element method was employed to solve the Euler equations. By using a solution-adaptive unstructured mesh, Siden et al. (1990) introduced the two-step explicit Taylor–Galerkin finite element method to simulate two-dimensional viscous compressible cascade flows. As described by Siden et al. (1990), the generation of correctly aligned stretched elements, the development of more sophisticated smoothing, and the addition of some implicitness into the algorithm are important issues of future work. Even though implicit factorization schemes are not bounded by stability conditions, they involve solutions of large systems of algebraic equations and are heavily restricted by the grid structure. Free of those requirements, a locally implicit scheme with quadrilateral mesh has been developed by Reddy and Jacocks (1987) to study inviscid airfoil flows, and the scheme was extended by Nayani (1988) for solving the thin layer Navier–Stokes equations. The scheme is locally implicit, but globally explicit and is unconditionally stable under local linearized analysis. In this paper, the locally implicit scheme is further developed to couple with finite volume spatial discretization based on the unstructured triangular/structured quadrilateral meshes in the Cartesian coordinate system.

From the above discussions, it is apparent that some problems still exist even though several methods have been developed. The purpose of this work is to demonstrate a numerical solution procedure for the airfoil and cascade flows. The procedure includes: (a) locally implicit time integration, (b) cell-centered finite volume spatial discretization, (c) artificial dissipation, and (d) adaptive mesh generation. The Euler/Navier–Stokes, continuity, and energy equations are solved in conjunction with the Baldwin–Lomax model (Baldwin and Lomax, 1978) for turbulent flow. Unstructured triangular cells for the inviscid region and structured quadrilateral cells for the viscous, boundary layer, and wake regions are employed. To evaluate the present solution procedure, several basic flow problems, such as inviscid flow passing through a channel with circular arc bump, and laminar flows over flat plate with/without shock interaction, are studied. Finally, the Euler/Navier–Stokes solutions of flows over the NACA 0012 airfoil, NACA 65-(12)10 compressor, and an advanced transonic turbine cascade are compared to the data given in related papers and reports.

Governing Equations

By choosing the chord length c and flow properties at inlet/free-stream condition as reference variables, the two-dimensional unsteady continuity, Navier–Stokes, and energy equations are written in nondimensional form for the Cartesian coordinate system as follows:

$$\frac{\partial U}{\partial t} + \frac{\partial F}{\partial x} + \frac{\partial G}{\partial y} = \frac{1}{R_e}\left[\frac{\partial R}{\partial x} + \frac{\partial S}{\partial y}\right] \tag{1}$$

where

$$U = \begin{bmatrix} \rho \\ \rho u \\ \rho v \\ e \end{bmatrix}, \quad F = \begin{bmatrix} \rho u \\ \rho u^2 + P \\ \rho uv \\ (e+P)u \end{bmatrix}, \quad G = \begin{bmatrix} \rho v \\ \rho uv \\ \rho v^2 + P \\ (e+P)v \end{bmatrix}$$

$$R = \begin{bmatrix} 0 \\ \tau_{xx} \\ \tau_{xy} \\ r_4 \end{bmatrix}, \quad S = \begin{bmatrix} 0 \\ \tau_{xy} \\ \tau_{yy} \\ s_4 \end{bmatrix}$$

$$\begin{aligned} \tau_{xx} &= 2\mu u_x + \lambda(u_x + v_y) \\ \tau_{yy} &= 2\mu v_y + \lambda(u_x + v_y) \\ \tau_{xy} &= \mu(u_y + v_x) \\ r_4 &= u\tau_{xx} + v\tau_{xy} + \frac{\mu}{\mathrm{Pr}}\frac{1}{(\gamma-1)}(a^2)_x \\ s_4 &= u\tau_{xy} + v\tau_{yy} + \frac{\mu}{\mathrm{Pr}}\frac{1}{(\gamma-1)}(a^2)_y \end{aligned}$$

The unknown variables ρ, u, v, and e represent the gas density, velocity components in x, y directions, and total energy per unit volume. The parameters μ and λ are referred to as the coefficients of viscosity, and λ is taken to be $-2/3\mu$ (Stokes hypothesis). Sutherland's law is employed to determine μ. The Reynolds number and Prandtl number are denoted as Re and Pr. In this paper, the working fluid is air, and it is assumed to be perfect. That is, the pressure P is given by the equation of state, and γ is the ratio of specific heats.

$$P = (\gamma - 1)\left[e - \frac{\rho}{2}(u^2 + v^2)\right] \tag{2}$$

The two-layer algebraic model of Baldwin and Lomax (1978) is included to determine the eddy viscosity, and the Reynolds heat flux terms are approximated using the constant Prandtl number assumption. Thus,

$$\mu = \mu_l + \mu_t \tag{3}$$

$$k = \frac{1}{\gamma - 1}\left(\frac{\mu_l}{\mathrm{Pr}_l} + \frac{\mu_t}{\mathrm{Pr}_t}\right) \tag{4}$$

where the subscripts l and t refer to laminar and turbulent flows, respectively. The two-layer turbulent model is mathematically simple and the most widely used. The inner layer is governed by the Prandtl–van Driest formulation, and the outer layer follows the modified Clauser approximation. Even though the model has some drawbacks (Colantuoni et al., 1989), it is very useful in attached flows and in weakly separated flows, for which it gives reasonable agreement with experiment.

Solution Algorithm

The governing equations in equation (1) can be rewritten as

$$\frac{\partial U}{\partial t} + \nabla \cdot (\mathbf{F}_c - \mathbf{F}_v) = 0 \tag{5}$$

where $\mathbf{F}_c$ and $\mathbf{F}_v$ represent the convective and viscous flux vectors. In this section, term $\mathbf{F}_v$ is ignored for convenience to describe the numerical formulation. By integrating equation (5) over space and using Gauss's theorem, the following expression is obtained:

$$\frac{\partial}{\partial t}\int\int_\Omega U dA + \int_{\partial\Omega}\mathbf{F}_c \cdot d\mathbf{l} = 0 \tag{6}$$

where

$$d\mathbf{l} = \mathbf{n}dl$$

and $\mathbf{n}$ is the unit normal vector in the outward direction. Ω is the domain of interest and $\partial\Omega$ is the boundary of domain. A fully implicit finite volume discretization scheme is applied to equation (6) over the entire flowfield. Flow variables at cell faces are obtained from the averages of the flow variables at the cell centers. Those values and artificial dissipation terms are introduced for line integrals and numerical stability. Then, for each triangular mesh i (Fig. 1(a)), equation (6) becomes

$$A_i\left(\frac{U^{n+1} - U^n}{\Delta t}\right)_i + Q_i(U^{n+1}) - D_i(U^{n+1}) = 0 \tag{7}$$

where

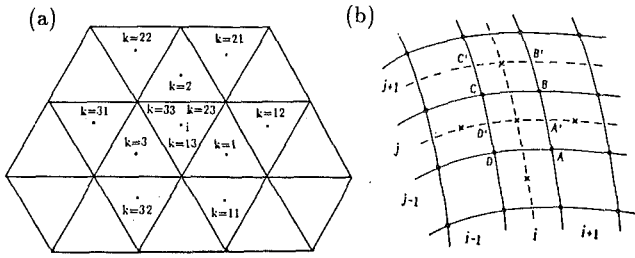$$Q_i(U) = \sum_{k=1}^{3}(\mathbf{F}_c \cdot d\mathbf{l})_{ik}$$

Fig. 1 Definitions of unstructured triangular and structured quadrilateral meshes for the cell-centered scheme

In equation (7), A_i is a cell area and D_i is the artificial dissipation operator. Through numerical experiments, Jameson et al. (1981) used a quadrilateral grid and established an effective form for D_i. The isotropic value for scaling the dissipation has been extended to unstructured triangular meshes by Mavriplis (1987, 1988). In the present work, a directionally scaled dissipation model is developed. The use of directional scaling provides anisotropic dissipation to each direction. The mathematical form is described as follows:

$$D_i(U) = \sum_{k=1}^{3} d_{ik} \qquad (8)$$

where

$$d_{ik} = \epsilon_{ik}^{(2)}(U_k - U_i) - \epsilon_{ik}^{(4)}(\nabla^2 U_k - \nabla^2 U_i)$$

$$\epsilon_{ik}^{(2)} = K^{(2)} \psi_{ik} \bar{\nu}_{ik}$$

$$\epsilon_{ik}^{(4)} = K^{(4)} \psi_{ik} \max[0, (1 - 32\bar{\nu}_{ik})]$$

$$\psi_{ik} = [|\mathbf{V}\cdot d\mathbf{l}| + a|d\mathbf{l}|]_{ik}$$

$$\nu_i = \frac{|\nabla^2 P_i|}{\sum\limits_{k=1}^{3}(P_i + P_k)}$$

$$\bar{\nu}_{ik} = \max(\nu_i, \nu_k, \nu_{k1}, \nu_{k2}, \nu_{k3})$$

$$\nabla^2 U_i = \sum_{k=1}^{3} U_k - 3U_i$$

The subscripts $k1$, $k2$, and $k3$ represent the indices of three triangular cells, which surround the cell k (Fig. 1(a)). $\nabla^2 U_i$ is expressed as an undivided Laplacian operator. ψ_{ik} is the spectral radius of Jacobian matrix $(\partial \mathbf{F}_c/\partial U \cdot d\mathbf{l})$ on the cell face between cell i and cell k. The coefficients $K^{(2)}$ and $K^{(4)}$ are user input, and the values are taken as $1.0 \sim 1.25$ and $1/32$, respectively.

To improve the convergence speed, a local time stepping technique is employed. As a rule, one wishes to adjust Δt at each point so that it is proportional to the grid spacing and the characteristic speed of the flow. $(A/\Delta t)_i$ shown in equation (7) is chosen as

$$\left(\frac{A}{\Delta t}\right)_i = \frac{\sum\limits_{k=1}^{3} \psi_{ik}}{\text{CFL}} \qquad (9)$$

where CFL is the Courant–Friedrichs–Lewy number. By using a Taylor series expansion for temporal differences, equation (7) is linearized and can be constructed in the delta form as follows:

$$L_i(\Delta U) = \text{Res}_i^n = -Q_i(U^n) + D_i(U^n) \qquad (10)$$

where

$$L_i(\Delta U) = CI\Delta U_i + CK_1\Delta U_1 + CK_{11}\Delta U_{11}$$
$$+ CK_{12}\Delta U_{12} + CK_{13}\Delta U_{13} + CK_2\Delta U_2$$
$$+ CK_{21}\Delta U_{21} + CK_{22}\Delta U_{22} + CK_{23}\Delta U_{23}$$
$$+ CK_3\Delta U_3 + CK_{31}\Delta U_{31} + CK_{32}\Delta U_{32}$$
$$+ CK_{33}\Delta U_{33}$$

and

$$CI = \frac{1}{2}\left(\sum_{k=1}^{3} \mathbf{M}_{ik}\right) + \left(\frac{\sum\limits_{k=1}^{3}\psi_{ik}}{\text{CFL}} + \sum_{k=1}^{3}\epsilon_{ik}^{(2)} + 3\sum_{k=1}^{3}\epsilon_{ik}^{(4)}\right) I$$

$$CK_L = \frac{1}{2}\mathbf{M}_{iL} - \left(\epsilon_{iL}^{(2)} + 3\epsilon_{iL}^{(4)} + \sum_{k=1}^{3}\epsilon_{ik}^{(4)}\right)I, \quad L = 1, 2, 3$$

$$CK_{L1} = CK_{L2} = CK_{L3} = \epsilon_{iL}^{(4)}I, \quad L = 1, 2, 3$$

$$I = \text{Diag}[1, 1, 1, 1]$$

$$\mathbf{M} = \frac{\partial \mathbf{F}_c}{\partial U} \cdot d\mathbf{l}$$

To solve equation (10), a locally implicit scheme (Reddy and Jacocks, 1987) is employed. This algorithm is based on a relaxation procedure for solving time-dependent partial differential equations to obtain steady-state solutions. The scheme is locally implicit, but globally explicit and is unconditionally stable under local linearized analysis (Nayani, 1988). It does not require the assembly of any global matrices and does not need any matrix system solvers. In this work, the technique is extended to unstructured triangular meshes. For each cell i, the equation for iterative corrections is written as

$$CdU_i = \text{Res}_i^n - L_i(\Delta U) \qquad (11)$$

$$\Delta U_i^{(m+1)} = \Delta U_i^{(m)} + w_{in}dU_i, \quad m = 1, 2 \qquad (12)$$

where C is a diagonal matrix defined as a modification to the coefficient matrix CI.

$$C = \left[\frac{\sum\limits_{k=1}^{3}\psi_{ik}}{\text{CFL}}\left(1.0 + \frac{\text{CFL}}{2}\right) + 0.5\left(\sum_{k=1}^{3}\epsilon_{ik}^{(2)} + 3\sum_{k=1}^{3}\epsilon_{ik}^{(4)}\right)\right]I$$
$$(13)$$

ΔU shown on the right-hand side of equation (11) takes the latest available values from equation (12). The inner iteration for $\Delta U^{(m+1)}$ can be computed rapidly since the dU corrections are explicit scalar equations. Starting at the first element and sweeping to the latest element, two symmetric inner iterations are performed for each time step. At the end of a time step, the outer relaxation is introduced.

$$U_i^{n+1} = U_i^n + w_{out}\Delta U_i \qquad (14)$$

By incorporating a smoothing process to ΔU implicitly, the iterative process can be made more robust and convergence to the steady state solution is speeded up. The smoothing operator $\bar{L}_i(\Delta U)$, that is added to $L_i(\Delta U)$ in equation (10), is given as

$$\bar{L}_i(\Delta U) = -w_{\text{imp}}\left(\psi_{i1}\Delta U_1 + \psi_{i2}\Delta U_2 + \psi_{i3}\Delta U_3 - \sum_{k=1}^{3}\psi_{ik}\Delta U_i\right)$$
$$(15)$$

and a diagonal matrix $\bar{C}$ is added to C in equation (13),

$$\bar{C} = \left(0.5 w_{\text{imp}}\sum_{k=1}^{3}\psi_{ik}\right)I \qquad (16)$$

The coefficients w_{in} and w_{out} in equations (12) and (14) are inner and outer relaxation parameters of order 1.2 (overrelaxation), while w_{imp} in equation (16) is an implicit smoothing

parameter of order 0.1. It may be noted that the implicit smoothing term does not affect the solution in the steady state since the residual terms are not altered.

For the viscous flow region, the Navier–Stokes equations are solved and the structured grid is used. To compute the shear stress and heat conduction terms, Green's theorem is employed. For example, the contributions u_x and u_y to the viscous flux across cell face BC (Fig. 1(b)) are

$$\int \int_{\Omega'} u_x d\Omega' = \int_{\partial\Omega'} u\, dy \qquad (17)$$

$$\int \int_{\Omega'} u_y d\Omega' = -\int_{\partial\Omega'} u\, dx \qquad (18)$$

where Ω' is the auxiliary cell $A'B'C'D'$, and $\partial\Omega'$ is the boundary of Ω'. The detailed treatments of viscous stresses and heat conduction terms for thin-layer Navier–Stokes equations are described by Swanson (1985). In this paper, the streamwise-like differences associated with the viscous flux quantities are also included. Thus, the full Navier–Stokes solutions are solved by using the locally implicit time integration and finite volume space discretization in a Cartesian coordinate system. Because the structured quadrilateral cells are used in this topic, the numerical formulation of inviscid parts is same as that presented by Reddy and Jacocks (1987). To simplify the numerical treatment, the viscous terms are expressed in explicit form. The finite volume equation is written as follows:

$$L_{i,j}(\Delta U) = \mathrm{Res}^n_{i,j} = -Q_{i,j}(U^n) + D_{i,j}(U^n) \qquad (19)$$

where

$$Q_{i,j}(U) = \int_{\partial\Omega} (\mathbf{F}_c - \mathbf{F}_v)\cdot d\mathbf{l}$$

Boundary Conditions

At the body surface, no-penetration and no-slip conditions are imposed for the inviscid and viscous flows, respectively. The pressure value is obtained by the following equation:

$$\rho(y_\eta u - x_\eta v)(y_\xi u_\xi - x_\xi v_\xi) = (x_\xi^2 + y_\xi^2)P_\eta - (x_\xi x_\eta + y_\xi y_\eta)P_\xi \qquad (20)$$

where ξ and η represent the body-fitted coordinate lines. In this work, the adiabatic wall condition is assumed. For the supersonic flows passing through the channel or over the flat plate, the free-stream conditions are specified at the inlet and space extrapolation is applied on the exit plane. About the subsonic flow over a flat plate, one-dimensional characteristics are used to treat the boundary condition. In the calculations of airfoil flows, the flow angle at upstream is imposed. The entropy, tangential velocity component, and Riemann invariants are extrapolated from the free-stream or interior points. For the cascade flow around the NACA 65-(12)10 compressor blade, the total pressure, total density, and flow angle are specified at the inlet; the magnitude of velocity is obtained from the values of interior points. On the exit plane, the static pressure is prescribed; the density and velocity components are extrapolated. Except that the one-dimensional Riemann invariants are applied at inlet, the boundary treatment of exit condition for the turbine cascade flow is same as that of compressor case. In addition, the periodicity condition for cascade flows is easily satisfied by considering points outside the calculation domain to have the same flow properties as points one pitch distant within the domain and then equating all properties at corresponding points on the periodic boundaries.

Mesh Generation and Adaptive Criterion

The flow solver is coupled with a mesh generation procedure, which is capable of generating structured quadrilateral and unstructured triangular cells. The quadrilateral meshes for the boundary layer/wake regions are formed by a conventional differential equation technique (Sorenson, 1980), and the triangular meshes are generated based on the front concept (Lo, 1985; Hwang et al., 1989). For initial grid generation, quadrilateral meshes were generated first and then the empty parts of the flow field were filled with unstructured elements. The grid generation processes for triangular meshes include mainly: (a) two-step strategy of distribution of nodes, and (b) triangulation according to the already distributed interior and boundary nodes. In this work, two steps are employed to decide the distribution of nodes. In the first step, the idea of front is used to obtain the positions of nodes. After the rough distribution of nodes has been set up, the second step is introduced. In this step, six candidate nodes surrounding the given node i are generated by equal distribution on the perimeter of circle with radius δ_i, where the node spacing δ_i is provided by the flow solutions on the background mesh. The indicator for mesh regeneration is decided by the density gradient. Based on the indicator on the background grid, the triangular meshes are reconstructed. Detailed descriptions of the above procedure are given by Hwang et al. (1989). The boundary nodes of the triangular element region are chosen as the boundary conditions for the quadrilateral mesh generation program. According to the above procedure, an adaptive mesh system is created and the flow features, such as shock, boundary layer, and wake, are simulated efficiently and correctly.

Results and Discussion

The approach described above is applied to compute inviscid and viscous flows through different regimes (subsonic, transonic, and supersonic flows). Comparing with the related data, the present solution procedure is proved to be accurate and reliable for studying the airfoil and turbomachinery flows.

Code Validation. The validation of a code is extremely important and is a key investment in CFD. Here, we present the Euler solution for supersonic channel flow and Navier–Stokes/Euler results for flows over a flat plate with/without shock boundary layer interaction. To understand the solution-adaptability of this work, the sequence of meshes, Mach number distributions, and convergence history (average absolute residuals of normalized x momentum ρu) for a supersonic flow passing a channel with 4 percent thick circular arc bump are presented in Figs. 2–4. Comparing with the mesh (Struijs et al., 1989), which was obtained by the grid enrichment technique based on the pressure or streamwise entropy gradients, a similar grid pattern (Fig. 2) is generated. In this case, the third adaptive mesh (Fig. 2(d)) is obtained by reducing the searching radius in the second step of the mesh generation procedure. This results in the increase of elements on the circular arc region, and the residual jump, which happens at the start of the third adaption (Fig. 4).

In order to evaluate the solution procedure of the Navier–Stokes equations, the quadrilateral cells (Fig. 5) for an oblique shock impinging on a laminar boundary layer, which is developed on a flat plate (Hakkinen et al., 1959), were employed. The numerical data shown in Fig. 6 show the pressure plateau and the negative skin friction coefficients in the separation zone. From those results, it is apparent that the present solutions are acceptable. By using a grid structure given in Fig. 7(a), the skin friction coefficient for laminar flow over a flat plate is calculated and compared with the Blasius solution. From this result shown in Fig. 7(b), the accuracy of the zonal method, which is used to solve the Euler and Navier–Stokes equations, is confirmed.

Inviscid Solutions of Airfoil and Cascade Flows. From the basic code validation, the accuracy, convergence, and reliability of the numerical approach presented in this paper are confirmed. Because the major purpose of this work is to study airfoil/cascade flow problems, Euler solutions of flows over

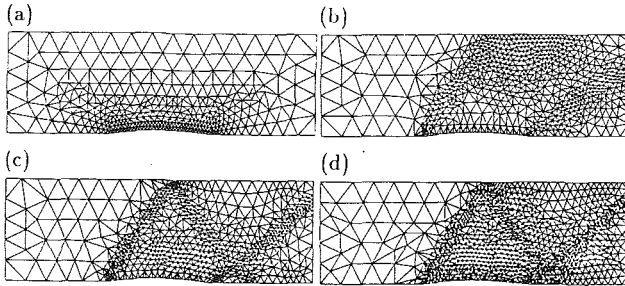INITIAL : 647 ELEMENTS , FINAL : 2548 ELEMENTS

Fig. 2 The sequence of meshes for flow passing through a channel with 4 percent thick circular arc bump ($M_\infty = 1.4$)
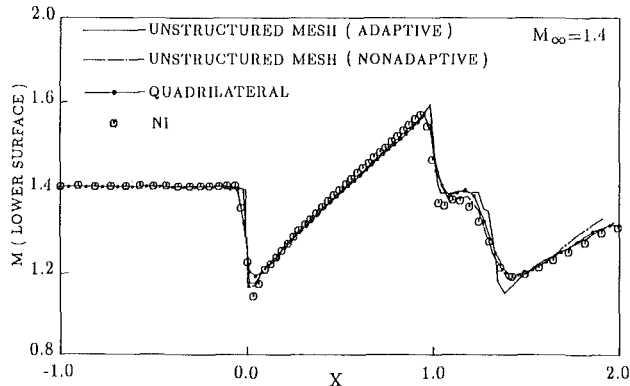

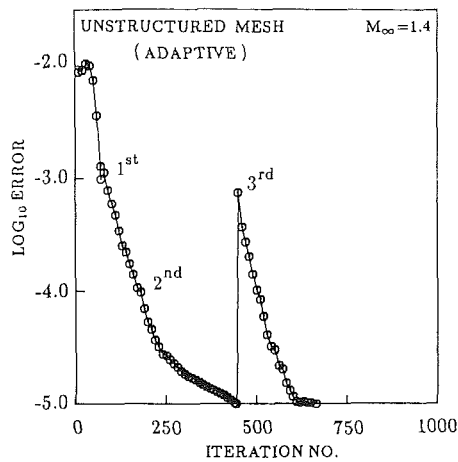Fig. 3 Mach number distributions of inviscid flow passing through a channel with 4 percent thick circular arc bump

Fig. 4 Convergence history for inviscid flow passing through a channel with 4 percent thick circular arc bump

(65 * 74 GRID POINTS)

Fig. 5 Flow structure and grid distribution for laminar shock boundary layer interaction flow ($M_\infty = 2.0$, $Re_L = 2.96 \times 10^5$)
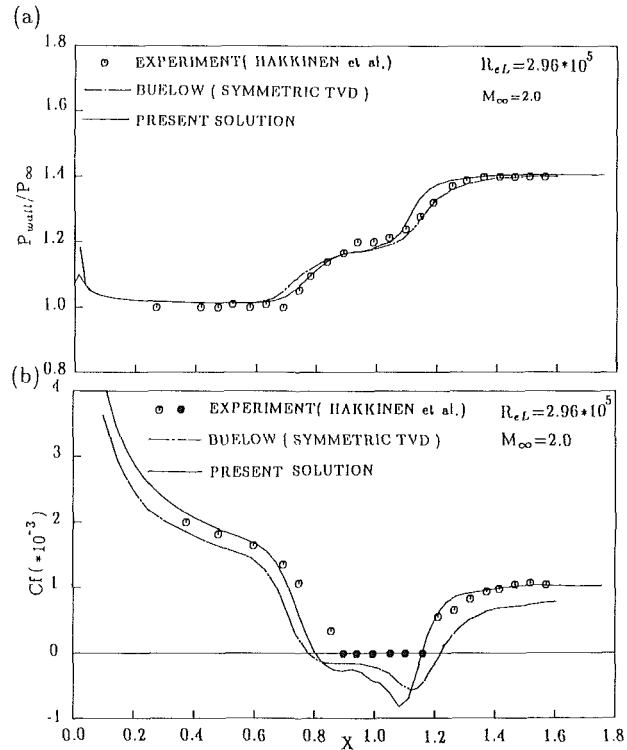
Fig. 6 Distributions of wall pressure and skin friction coefficient for laminar shock boundary layer interaction flow
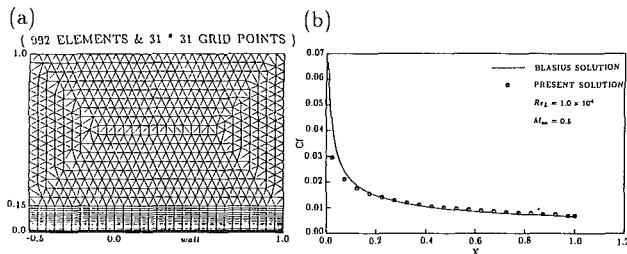
Fig. 7 Distributions of grid and skin friction coefficient for laminar flow over a flat plate

the NACA 0012 airfoil and NACA 65-(12)10 compressor cascade have been conducted. The triangular mesh shown in Fig. 8 is used to predict the inviscid flow over a NACA 0012 airfoil at 1.25° incidence with free-stream Mach number of 0.8. From the pressure distributions plotted in Fig. 9(a), the present result exhibits fairly good agreement with numerical data given by Jameson and Mavriplis (1986), and fewer grids are required to capture the shock discontinuity. The normalized supersonic points and residual of density, which are presented in Fig. 9(b), demonstrate the convergence of the present approach.

For NACA 65-(12)10 compressor cascade inviscid flow, two grid systems, triangular mesh and mixed mesh (Fig. 10), are employed. The inlet Mach number (M_{inlet}), angle of attack (α), inlet angle (β_{inlet}), and solidity are chosen as 0.76, 16.5 deg, 45 deg, and 1.0. By solving the Euler equations, pressure dis-

tributions are given in Fig. 11. The flow solver with unstructured triangular cell has a tendency to produce small wiggles in the blade surface pressures. This is probably due to failure for numerical smoothing to damp out small wiggles propagating from the high gradient leading edge region (Siden et al., 1990). It is interesting to mention that for mixed-type mesh system, the finer quadrilateral cells are located near blade surface, and the small wiggles disappear. In this calculation, the back pressure rise ratio is 1.25, and shows a good comparison with the experimental datum (1.218) of Briggs (1952).

(a)
NACA 0012 AIRFOIL MESH (4686 ELEMENTS)
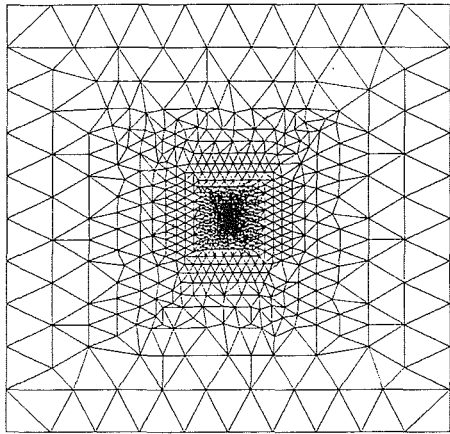
(b)
NEAR AIRFOIL MESH

Fig. 8   Grid distribution for NACA 0012 airfoil

(a)

NACA 0012 AIRFOIL   • JAMESON & MAVRIPLIS
MACH 0.8   · · PRESENT SOLUTION
ALPHA 1.25
CL=0.3473 CD=0.0728 CM=-0.0134

(b)
NACA 0012 AIRFOIL

NSUP

Fig. 9   Surface pressure distribution and convergence history for inviscid flow over a NACA 0012 airfoil

(a)
NACA 65-(12)10 CASCADE MESH (2296 ELEMENTS)

(b)
(867 ELEMENTS & 145 * 31 GRID POINTS)
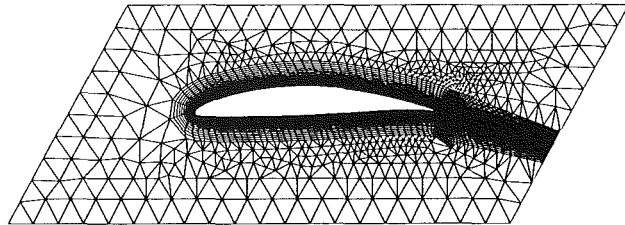
Fig. 10   Unstructured triangular mesh and mixed type of mesh for inviscid flow passing through the NACA 65-(12)10 compressor cascade

□ EXPERIMENT (BRIGGS)
PRESENT SOLUTIONS :
× (MIXED TYPE OF MESH)
◆ (TRIANGULAR MESH)
NACA 65-(12)10 CASCADE
MACH   0.76   ALPHA   16.5
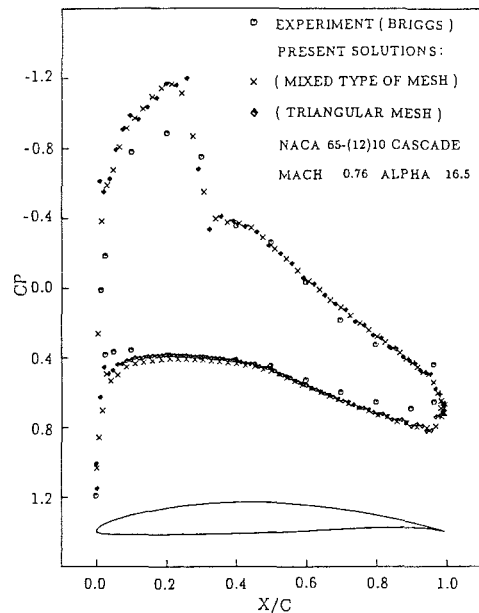
Fig. 11   Pressure distributions for inviscid flow passing through the NACA 65-(12)10 compressor cascade

Solutions of Airfoil and Cascade Flows by the Viscous/ Inviscid Zonal Approach.   To understand further the capability of the zonal method for viscous flows, the Navier–Stokes and Euler equations are solved on the structured quadrilateral and unstructured triangular meshes, respectively. The transonic turbulent flows over a NACA 0012 airfoil and through one advanced turbine casc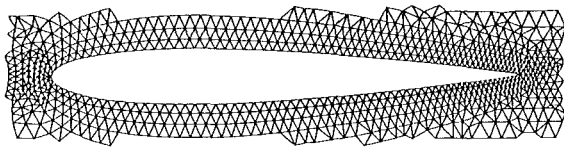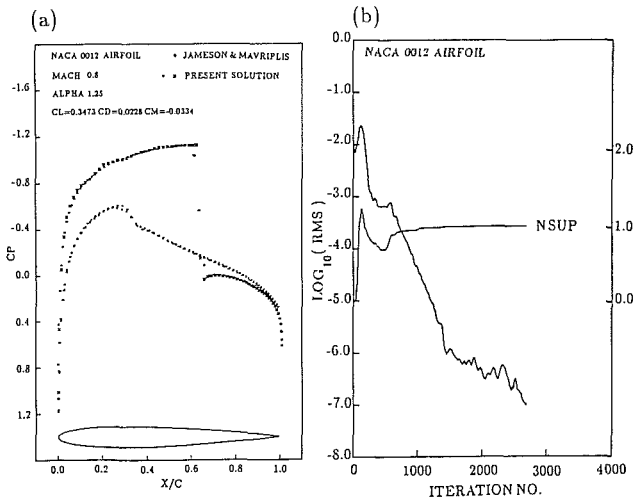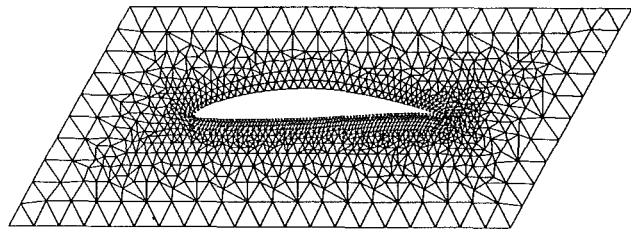ade are investigated. The adaptive grids for the airfoil flow calculation are displayed in Fig. 12. The minimum cell distance between the first cell and the surface of airfoil is 2.04×10^{-4} chord. The far-field boundaries of the computational domain are located at 10 chords. For transonic turbulent flow ($M_\infty = 0.756$, $Re_\infty = 4.01 \times 10^6$) with zero angle of attack, the pressure distributions are presented in Fig. 13. Those results show good agreement with the experimental data (Thibert et al., 1979).

An advanced transonic turbine flow (depicted in Fig. 14 for mesh distribution) has been extensively tested in four European wind tunnel (Kiock et al., 1986) for different exit flow conditions. The computational domain is the same as the test section of the wind tunnel, which was located at Oxford University, United Kingdom. The flow with a designed Reynolds number of 8×10^5, which is based on the true chord and the flow variables on the exit boundary, is investigated. Inflow conditions are applied corresponding to a flow angle of 30 deg incidence on the upstream boundary and a design Mach number of 0.988 on the exit boundary. The calculation is carried out with the assumption of fully turbulent flow. The adaptive mesh is shown in Fig. 14(b), and the better grid distributions on the suction side and trailing edge regions are observed. The Schlieren picture from GO (Kiock et al., 1986) showed the compression shocks at two locations ($x/c \simeq 0.65$ and 0.98), and this is also demonstrated at the present solution-adaptive mesh pattern. The isentropic Mach number distributions on the blade surface for nonadaptive and adaptive meshes are in fairly good agreement with the experimental data (Fig. 15). The computed exit angle (β_{exit}) and loss coefficient $\left(1 - \dfrac{|\mathbf{v}_{exit}|^2}{|\mathbf{v}_{exit,is}|^2} \right)$ are 66.73

Fig. 12   Grid distributions for turbulent flow over a NACA 0012 airfoil

Fig. 13   Pressure distributions for turbulent flow over a NACA 0012 airfoil

Fig. 14   Grid distributions for turbulent flow passing through the transonic turbine cascade

Fig. 15   Isentropic Mach number distributions for turbulent flow passing through the transonic turbine cascade

of the method were investigated for some basic flows. A fairly good agreement by comparisons with related experimental/numerical data is observed. From the numerical results of flows over NACA 0012, NACA 65-(12)10 compressor, and advanced transonic turbine cascades, the present solution procedure is an efficient and accurate approach for studying the airfoil and cascade flows.

deg and 0.057. Those values show a good comparison with the experimental data 67.76 deg and 0.040. In this calculation, the present method requires approximately 0.48 s/point/iteration on the computer, VAX 8600.

Conclusions

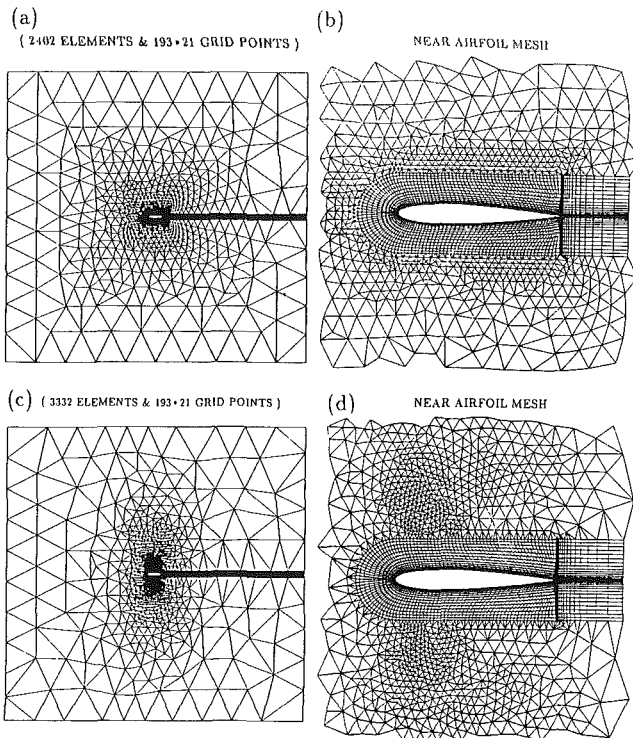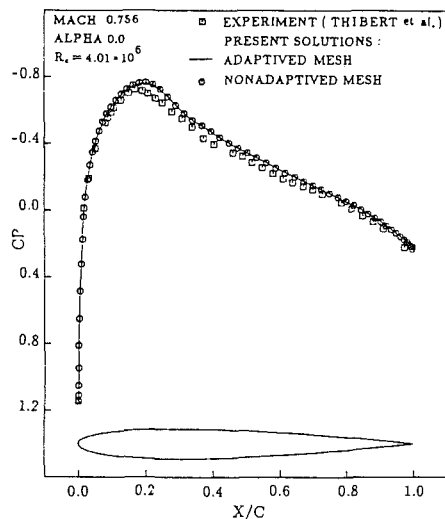A locally implicit finite volume cell-centered scheme for numerical integration of the Euler/Navier–Stokes, continuity, and energy equations in conjunction with Baldwin–Lomax model for turbulent flow has been developed in the Cartesian coordinate system. In this work, a zonal approach and adaptive mesh generation technique are coupled with structured quadrilateral meshes and unstructured triangular elements to study the viscous and inviscid flows. The accuracy and convergence

References

Baldwin, B. S., and Lomax, H., 1978, "Thin Layer Approximation and Algebraic Model for Separated Turbulent Flows," AIAA Paper No. 78-257.

Briggs, W. B., 1952, "Effect of Mach Number on the Flow and Application of Compressibility Corrections in a Two-Dimensional Subsonic-Transonic Compressor Cascade Having Varied Porous-Wall Suction at the Blade Tips," NACA TN 2649.

Buelow, P. E., 1989, "Comparison of TVD Schemes Applied to the Navier-Stokes Equations," AIAA Paper No. 89-0847.

Colantuoni, S., Terlizzi, A., and Grasso, F., 1989, "A Validation of a Navier-Stokes 2D Solver for Transonic Turbine Cascade Flows," AIAA Paper No. 89-2451.

Davis, R. L., Hobbs, D. E., and Weingold, H. D., 1988, "Prediction of Compressor Cascade Performance Using a Navier–Stokes Technique," ASME JOURNAL OF TURBOMACHINERY, Vol. 110, pp. 520-531.

Davis, R. L., and Dannenhoffer, J. F., 1989, "Adaptive Grid Embedding Navier-Stokes Technique for Cascade Flows," AIAA Paper No. 89-0204.

Denton, J. D., 1985, "Solution of the Euler Equations for Turbomachinery Flows; Part I. Basic Principles and Two Dimensional Applications," in: Thermodynamics and Fluid Mechanics of Turbomachinery, Vol. 1, Martinus Nijhoff, Dordrecht/Boston/Lancaster, pp. 283-311.

Hakkinen, R. J., Greber, I., Trilling, L., and Abarbanel, S. S., 1959, "The Interaction of an Oblique Shock Wave With a Laminar Boundary Layer," NASA Memo 2-18-59W.

Hwang, C. J., Jiang, F. L., Hsieh, J. M., and Chang, S. B., 1988, "Numerical Analysis of Airfoil and Cascade Flows by the Viscous/Inviscid Interactive Technique," ASME JOURNAL OF TURBOMACHINERY, Vol. 110, pp. 532–539.

Hwang, C. J., Wu, S. J., and Sun, Z. Y., 1989, "Application of Adaptive Finite Element Methods to the Euler Equations," *Proceedings of the Seventh International Conference on Finite Element Methods in Flow Problems*, pp. 99–104.

Jameson, A., Schmidt, W., and Turkel, E., 1981, "Numerical Solutions of the Euler Equations by Finite Volume Methods Using Runge–Kutta Time-Stepping Schemes," AIAA Paper No. 81-1259.

Jameson, A., and Mavriplis, P., 1986, "Finite Volume Solution of the Two-Dimensional Euler Equations on a Regular Triangular Mesh," *AIAA Journal*, Vol. 24, No. 4, pp. 611–618.

Kiock, R., Lehthaus, F., Baines, N. C., and Sieverding, C. H., 1986, "The Transonic Flow Through a Plane Turbine Cascade as Measured in Four European Wind Tunnels," ASME *Journal of Engineering for Gas Turbines and Power*, Vol. 108, pp. 277–284.

Lo, S. H., 1985, "A New Mesh Generation Scheme for Arbitrary Planar Domains," *International Journal for Numerical Methods in Engineering*, Vol. 21, pp. 1403–1426.

Maksymiuk, C. M., and Pulliam, T. H., 1987, "Viscous Transonic Airfoil Workshop Results Using ARC2D," AIAA Paper No. 87-0415.

Mavriplis, D. J., 1987, "Solutions of the Two-Dimensional Euler Equations on Unstructured Triangular Meshes," Ph.D. Thesis, Princeton University, Princeton, NJ.

Mavriplis, D. J., 1988, "Accurate Multigrid Solution of the Euler Equations on Unstructured and Adaptive Meshes," AIAA Paper No. 88-3706-CP.

Nakahashi, K., Nozaki, O., Kikuchi, K., and Tamura, A., 1989, "Navier–Stokes Computations of Two- and Three-Dimensional Cascade Flowfields," *Journal of Propulsion and Power*, Vol. 5, No. 3, pp. 320–326.

Nayani, S. N., 1988, "A Locally Implicit Scheme for Navier–Stokes Equations," Ph.D. Thesis, The University of Tennessee, Knoxville, TN.

Ni, R. H., 1982, "A Multiple-Grid Scheme for Solving the Euler Equations," *AIAA Journal*, Vol. 20, No. 11, pp. 1565–1571.

Reddy, K. C., and Jacocks, J. L., 1987, "A Locally Implicit Scheme for the Euler Equations," AIAA Paper No. 87-1144.

Shamroth, S. J., McDonald, H., and Briley, W. R., 1984, "Prediction of Cascade Flow Fields Using the Averaged Navier–Stokes Equations," ASME *Journal of Engineering for Gas Turbines and Power*, Vol. 106, pp. 383–390.

Siden, G. L. D., Dawes, W. N., and Albraten, P. J., 1990, "Numerical Simulation of the Two-Dimensional Viscous Compressible Flow in Blade Cascades Using a Solution-Adaptive Unstructured Mesh," ASME JOURNAL OF TURBOMACHINERY, Vol. 112, pp. 311–319.

Sorenson, R. L., 1980, "A Computer Program to Generate Two-Dimensional Grids About Airfoils and Other Shapes by the Use of Poisson's Equations," NASA TM 81198.

Struijs, R., Vankeirsbilck, P., and Deconinck, H., 1989, "An Adaptive Grid Polygonal Finite Volume Method for the Compressible Flow Equations," AIAA Paper No. 89-1959-CP.

Swanson, R. C., 1985, "A Multistage Time-Stepping Scheme for the Navier–Stokes Equations," AIAA Paper 85-0035.

Thibert, J. J., Granjacques, M., and Ohman, L. H., 1979, "NACA 0012 Airfoil, AGARD Advisory Report No. 138, Experimental Data Base for Computer Program Assessment," pp. A1–9.

Prediction of Cascade Performance Using an Incompressible Navier-Stokes Technique

G. V. Hobson

B. Lakshminarayana

Department of Aerospace Engineering,
Pennsylvania State University,
University Park, PA 16801

A fully elliptic, control volume solution of the two-dimensional incompressible Navier–Stokes equations for the prediction of cascade performance over a wide range is presented in this paper. The numerical technique is based on a new pressure substitution method. A Poisson equation is derived from the pressure-weighted substitution of the full momentum equations into the continuity equation. The analysis of a double circular arc compressor cascade is presented, and the results are compared with the available experimental data at various incidence angles. Good agreement is obtained for the blade pressure distribution, boundary layer and wake profiles, skin friction coefficient, losses and outlet angles. Turbulence effects are simulated by the low-Reynolds-number version of the k–ε turbulence model.

Introduction

A fully elliptic calculation of internal flows is essential in order that regions of pressure ellipticity and streamwise diffusion can be accurately resolved. The resolution of these elliptic regions is essential for the numerical simulation of flow past airfoils and cascades that are operating at, or close to, their optimum condition, which could entail some regions of flow separation.

In flows where there is such strong viscid–inviscid interaction, it is essential that the full Navier–Stokes equations be solved. When compared with the parabolic marching technique as proposed by Pouagare and Lakshminarayana (1985), the method described below is not computationally efficient. The pressure-based method has recently been shown by Abdallah (1989) to be computationally more efficient than the artificial compressibility method. With the current increase in computer speeds, this type of computation can be justified. The most important justification for elliptic techniques is that physical phenomena, including viscid–inviscid flow interactions, separated flow regions, and pressure distributions, are accurately resolved.

The computational procedure developed in this paper is based on the original Navier–Stokes solution method developed by Caretto et al. (1972). The original SIMPLE or pressure correction method (PCM) algorithm suffered severely from geometric limitations because the equations were written in Cartesian coordinates and the staggered grid arrangement utilized did not enable easy transformation of the equations into generalized coordinates. The pressure correction method requires the solution of a Poisson pressure correction equation and a subsequent explicit correction of the velocity and pressure

field. Rhie and Chow (1983), who proposed the pressure weighted method (PWM), were the first to compute on a regular, or nonstaggered, grid. This was achieved by substituting the full momentum equations into the integral form of the continuity equation. Their solution procedure, however, still relied on the basic SIMPLE or pressure correction algorithm. Hah (1984) and Davis et al. (1988) provided cascade viscous flow solutions using, respectively, relaxation and time-marching techniques. Both formulations were for compressible flow; however, Hah computed incompressible flow.

The new pressure substitution method (PSM), developed and utilized in this paper, permits the solution of the static pressure and allows for a direct coupling of the momentum and pressure equations to be solved in block form. Three different formulations with nonstaggered grids have been suggested by Shih and Ren (1984). Some of these employ the Poisson equation for pressure in place of the continuity equation. Their formulation was derived in nonconservative, finite difference form in contrast to the derivation of the equations in conservative form in the present study. Thus, the code developed in this paper uses pressure weighting to allow the solution of the discretized equations on a regular grid, and the equations are coupled by the substitution of the pressure-weighted form of the momentum equations into the integral form of the continuity equation.

A refined turbulence model has been incorporated into this procedure, which is an extension of the widely used k–ϵ model as proposed by Launder and Spalding (1974). The effects of turbulence are simulated by the low-Reynolds-number version of the k–ϵ turbulence model as proposed by Lam and Bremhorst (1981). Rodi and Scheuerer (1985) used a similar extended version of the k–ϵ equations, but with a boundary layer procedure, which was valid for flows without separation. The extensions entail the simulation of viscous and near-wall effects, and laminar to turbulent flow transition, and in particular its dependence on the free-stream turbulence intensity.

The original contribution of this paper is the development of a new pressure substitution method that is more efficient than the pressure correction method. The fully validated code, proposed by Hobson and Lakshminarayana (1989), is used in a simulation mode to carry out a parametric study of cascade flows. The objective of the paper is to demonstrate the capability of a Navier–Stokes code to capture the entire flowfield, including losses, wake and boundary layer profiles, and the extent of flow separation. Most importantly, the code is utilized to understand the effect of free-stream turbulence and incidence angle on cascade performance.

Theoretical Formulation

Mathematical Model. The equations governing two-dimensional incompressible flow are the continuity equation

$$\frac{\partial}{\partial x}(\rho u) + \frac{\partial}{\partial y}(\rho v) = 0 \tag{1}$$

and the general form of the conservation equation for momentum

$$\frac{\partial}{\partial x}(\rho u \phi) + \frac{\partial}{\partial y}(\rho v \phi) = \frac{\partial}{\partial x}\left[\Gamma^\phi \frac{\partial \phi}{\partial x}\right] + \frac{\partial}{\partial y}\left[\Gamma^\phi \frac{\partial \phi}{\partial y}\right] + S^\phi \tag{2}$$

In the above two equations, ρ is the fluid density and u and v are the velocities in the x and y directions, respectively, as shown in Fig. 1.

For the dependent variables, ϕ, to be solved, the diffusion constants and source terms are as follows.

Conservation Equation	ϕ	Γ^ϕ	S^ϕ
x momentum	u	$\mu + \mu_t$	$-\dfrac{\partial p}{\partial x}$
y momentum	v	$\mu + \mu_t$	$-\dfrac{\partial p}{\partial y}$
Turbulent kinetic energy	k	$\mu + \dfrac{\mu_t}{\sigma_k}$	$P - \rho\epsilon$
Turbulent dissipation	ϵ	$\mu + \dfrac{\mu_t}{\sigma_\epsilon}$	$\dfrac{\epsilon}{k}[C_{\epsilon 1}f_1 P - C_{\epsilon 2}f_2 \rho \epsilon]$

$$\tag{3}$$

In the above table, μ is the dynamic viscosity, p is the static pressure, k the turbulent kinetic energy, and ϵ the rate of dissipation of turbulent kinetic energy.

The eddy viscosity, μ_t, is related to the turbulent kinetic energy k and the rate of dissipation ϵ by

$$\mu_t = \rho C_\mu f_\mu \frac{k^2}{\epsilon} \tag{4}$$

where C_μ is an empirical constant and f_μ a function that expresses viscous and near-wall effects on the eddy viscosity. The function f_μ, given by Lam and Bremhorst (1981), reads

$$f_\mu = [1 - \exp(-0.0165\mathrm{Re}_y)]^2\left[1 + \frac{20.5}{\mathrm{Re}_t}\right] \tag{5}$$

Nomenclature

A = discretization coefficient

B = pressure gradient coefficient

C = pressure gradient coefficient

C_f = skin friction coefficient $= \tau_w / \frac{1}{2}(\rho w_i^2)$

C_L = lift coefficient

C_p = pressure coefficient $= (p_i - p_l) / \frac{1}{2}(\rho w_i^2)$

$C_\mu, C_{\epsilon 1}, C_{\epsilon 2}$ = empirical constants in the turbulence model

f_μ, f_1, f_2 = empirical functions in turbulence model

G_1, G_2 = contravariant velocity components

J = Jacobian of the transformation

k = turbulent kinetic energy

L_i = inlet turbulence length scale

L_2 = norm, sum of moduli of errors

n = distance normal to blade surface

p = static pressure

p_T = total pressure

P = production of turbulent kinetic energy

$\mathrm{Re}_y, \mathrm{Re}_t$ = turbulent Reynolds numbers

S = source term

Tu = turbulence intensity $= \left[\overline{(u')^2}\right]^{1/2}/u_\infty$

u = axial velocity

v = tangential velocity

w = total velocity component

x = axial direction, physical domain

y = tangential direction, physical domain

α = transformation coefficient, angle of incidence

β = transformation coefficient

γ = transformation coefficient

Γ = diffusion coefficient

δ_o = outlet flow deviation angle

ϵ = dissipation rate

η = cross-stream direction, computational domain

μ = molecular viscosity

μ_t = turbulent (eddy) viscosity

ξ = streamwise coordinate, computational domain

ρ = density

$\sigma_k, \sigma_\epsilon$ = empirical constants in turbulence model

τ_w = wall shear stress $= \mu(\partial u/\partial y)_{\mathrm{wall}}$

ϕ = dependent variable

Φ = dissipation function

ω = total pressure loss coefficient $= (p_{T_i} - p_{T_o})/(\rho w_i^2/2)$

Superscripts

ϕ = dependent variable

m = iteration counter

u = axial momentum equation coefficient

v = tangential momentum equation coefficient

Subscripts

i = inlet station

l = local values

n, e, s, w = control volume faces

N, E, S, W = grid points, at compass locations

o = outlet station

O = central grid point

P = pressure

U = cross derivative terms

T = stagnation quantity
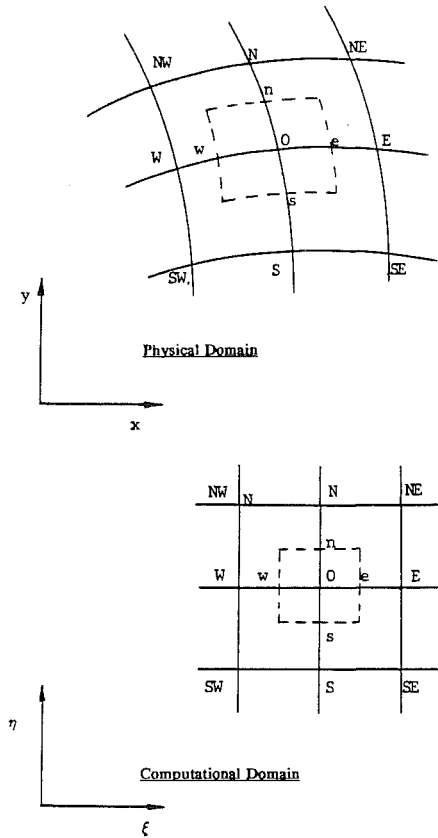
∞ = boundary layer edge

Fig. 1 Schematic representation of a control volume in physical and computational space

where the turbulent Reynolds numbers Re_y and Re_t are defined as

$$Re_y = \frac{\sqrt{k}y\rho}{\mu} \; ; \qquad Re_t = \frac{k^2\rho}{\epsilon\mu} \qquad (6)$$

The term Φ is defined as

$$\Phi = 2\left\{\left[\frac{\partial u}{\partial x}\right]^2 + \left[\frac{\partial v}{\partial y}\right]^2 + \left[\frac{\partial v}{\partial x} \cdot \frac{\partial u}{\partial y}\right]\right\} + \left[\frac{\partial u}{\partial y}\right]^2 + \left[\frac{\partial v}{\partial x}\right]^2 \qquad (7)$$

and the production, P, of turbulent kinetic energy k, is

$$P = \mu_t \Phi \qquad (8)$$

The empirical low-Reynolds-number functions f_1 and f_2 appearing in the ϵ equation are

$$f_1 = 1 + \left[\frac{0.06}{f_\mu}\right]^3 \; ; \qquad f_2 = 1 - \exp(-Re_t^2) \qquad (9)$$

For the remaining empirical constants, the standard values cited by Rodi and Scheuerer (1985) have been used: $C_\mu = 0.09$, $C_{\epsilon1} = 1.44$, $C_{\epsilon2} = 1.92$, $\sigma_k = 1.0$, and $\sigma_\epsilon = 1.3$.

Transformation of the Basic Equation. Equations (1) and (2) are transformed into generalized coordinates ξ, η by the general transformation $\xi = \xi(x, y)$ and $\eta = \eta(x, y)$. The transformed equations are

$$\frac{\partial}{\partial \xi}(\rho G_1) + \frac{\partial}{\partial \eta}(\rho G_2) = 0 \qquad (10)$$

and

$$\frac{\partial}{\partial \xi}(\rho G_1 \phi) + \frac{\partial}{\partial \eta}(\rho G_2 \phi) =$$

$$\frac{\partial}{\partial \xi}\left\{\frac{\Gamma^\phi}{J}\left[\alpha\frac{\partial\phi}{\partial\xi} - \beta\frac{\partial\phi}{\partial\eta}\right]\right\} + \frac{\partial}{\partial \eta}\left\{\frac{\Gamma^\phi}{J}\left[\gamma\frac{\partial\phi}{\partial\eta} - \beta\frac{\partial\phi}{\partial\xi}\right]\right\} + S^\phi J \qquad (11)$$

where

$$G_1 = u\frac{\partial y}{\partial \eta} - v\frac{\partial x}{\partial \eta} \; ; \qquad G_2 = v\frac{\partial x}{\partial \xi} - u\frac{\partial y}{\partial \xi} \qquad (12)$$

and

$$\alpha = \left[\frac{\partial x}{\partial \eta}\right]^2 + \left[\frac{\partial y}{\partial \eta}\right]^2 \; ; \qquad \beta = \frac{\partial x}{\partial \xi}\frac{\partial x}{\partial \eta} + \frac{\partial y}{\partial \xi}\frac{\partial y}{\partial \eta}$$

$$\gamma = \left[\frac{\partial x}{\partial \xi}\right]^2 + \left[\frac{\partial y}{\partial \xi}\right]^2 \; ; \qquad J = \frac{\partial x}{\partial \xi}\frac{\partial y}{\partial \eta} - \frac{\partial x}{\partial \eta}\frac{\partial y}{\partial \xi} \qquad (13)$$

G_1 and G_2 are directly related to the contravariant velocity components and J is the Jacobian of the transformation.

Discretization of the Transport Equations. Equations (10) and (11) are integrated over the control volume as shown in Fig. 1.

$$[\rho G_1]_w^e + [\rho G_2]_s^n = 0 \qquad (14)$$

$$\left\{(\rho G_1\phi) - \frac{\Gamma^\phi}{J}\left[\alpha\frac{\partial\phi}{\partial\xi}\right]\right\}_w^e + \left\{(\rho G_2\phi) - \frac{\Gamma^\phi}{J}\left[\gamma\frac{\partial\phi}{\partial\eta}\right]\right\}_s^n =$$

$$-\left\{\frac{\Gamma^\phi}{J}\left[\beta\frac{\partial\phi}{\partial\eta}\right]_w^e + \frac{\Gamma^\phi}{J}\left[\beta\frac{\partial\phi}{\partial\xi}\right]_s^n\right\} + S^\phi J \qquad (15)$$

where n, s, e, and w are the locations of the intersection between the control volume faces and the grid lines.

The discretized form of the continuity equation (14) will be dealt with in the next section. Equation (15) will now be fully discretized.

In the present scheme, all properties are defined at the nodes $0, N, S, E$, and W. Thus the following general approximations are made for the above finite difference expressions on the left-hand side of equation (15):

$$[\rho G_1\phi]_e \approx [\rho G_1]_e \frac{1}{2}[\phi_O + \phi_E]$$

$$\left\{\frac{\Gamma^\phi}{J}\left[\alpha\frac{\partial\phi}{\partial\xi}\right]\right\}_e \approx \left[\frac{\Gamma^\phi}{J}\alpha\right]_e (\phi_O - \phi_E)/\Delta\xi \qquad (16)$$

Quantities such as $[\rho G_1]_e$ and $[\Gamma^\phi\alpha/J]_e$ are obtained by linear interpolation in the physical plane. Similar forms of equation (16) are substituted into (15). This results in a relationship between ϕ_o and the neighboring values:

$$A_O^\phi \phi_O = A_N^\phi \phi_N + A_S^\phi \phi_S + A_E^\phi \phi_E + A_W^\phi \phi_W + S_U^\phi + S_P^\phi J \qquad (17)$$

or

$$A_O^\phi \phi_O = \Sigma A_i^\phi \phi_i + S_U^\phi + S_P^\phi J \qquad (18)$$

where S_U^ϕ, which contains the cross derivative terms, is the first term on the right-hand side of (15). The A_i^ϕ contain the convection and diffusion terms as given by the coefficients on the right-hand side of equation (16).

S_P^ϕ contains the pressure gradient terms:

$$\phi = u; \quad S_P^u = -B^u\frac{\partial p}{\partial \xi} - C^u\frac{\partial p}{\partial \eta}$$

$$\phi = v; \quad S_P^v = -B^v\frac{\partial p}{\partial \xi} - C^v\frac{\partial p}{\partial \eta} \qquad (19)$$

where

$$B^u = \frac{\dfrac{\partial y}{\partial \eta}}{A_O^u} \; ; \qquad C^u = -\frac{\dfrac{\partial y}{\partial \xi}}{A_O^u}$$

$$B^v = -\frac{\dfrac{\partial x}{\partial \eta}}{A_O^v} \; ; \qquad C^v = \frac{\dfrac{\partial x}{\partial \xi}}{A_O^v} \qquad (20)$$

A_O is the sum of all the A_i at the N, S, E, and W points. These

coefficients are modified according to the hybrid differencing scheme proposed by Spalding (1972). The transformation is such that $\Delta\xi = \Delta\eta = 1$ and as such all multiples of these terms have been neglected.

Pressure Substitution Method. The method will be explained by neglecting such scalar quantities as temperature and the turbulence quantities. For simplicity the explanation of the method will be restricted to rectangular Cartesian coordinates.

The implicit, discretized u and v momentum equations at node 0 in Cartesian coordinates is derived from equations (18) and (19)

$$u_O^{m+1} = \Sigma A_i^u u_i^{m+1} - B^u \frac{\partial p^m}{\partial x}$$

$$v_O^{m+1} = \Sigma A_i^v v_i^{m+1} - C^v \frac{\partial p^m}{\partial y} \qquad (21)$$

where all the coefficients on the right-hand side have been divided by A_O^ϕ.

A Poisson pressure equation is to be derived from the combined continuity and momentum equations. Consider the integral form of equation (1) and not equation (14)

$$[\rho u]_w^e + [\rho v]_s^n = 0 \qquad (22)$$

It is assumed that a new set of velocities u^{m+1} and v^{m+1} are obtained from equation (21), where the superscript m denotes the initial guess and the superscript $m+1$ denotes the new implicit solution of the relevant variable. In general, u^{m+1} and v^{m+1} will not satisfy the continuity equation; instead, a net mass source is produced. This derivation of the net source is now presented.

When considering equation (22), it is noted that u is to be evaluated at station e, but this must be determined from values at stations E and O as shown in Fig. 1. These values are determined from the following relationships:

$$u_E^{m+1} = \Sigma A_i^u u_i^{m+1} \Big|_E - B_E^u \frac{\partial p^m}{\partial x} \Big|_E \qquad (23)$$

$$u_O^{m+1} = \Sigma A_i^u u_i^{m+1} \Big|_O - B_0^u \frac{\partial p^m}{\partial x} \Big|_O \qquad (24)$$

$$u_e^{m+1} = \Sigma A_i^u u_i^{m+1} \Big|_e - B_e^u \frac{\partial p^m}{\partial x} \Big|_e \qquad (25)$$

The following two assumptions are now made with regard to the first term on the right-hand side of equation (25) and the coefficient of the last term of the same equation, i.e., we assume:

$$\Sigma A_i^u u_i^{m+1} \Big|_e = \frac{1}{2}\left[\Sigma A_i^u u_i^{m+1}|_O + \Sigma A_i^u u_i^{m+1} \Big|_E \right]$$

$$B_e^u = \frac{1}{2} [B_O^u + B_E^u] \qquad (26)$$

Upon substitution of the rearranged forms of equations (23) and (24) and equation (26) into equation (25), the following equation results:

$$u_e^{m+1} = \frac{1}{2} \left\{ \left[u_E^{m+1} + u_O^{m+1} \right] + \left[B_O^u \frac{\partial p^m}{\partial x} \Big|_0 + B_E^u \frac{\partial p^m}{\partial x} \Big|_E \right] \right. $$
$$\left. - (B_O^u + B_E^u) \frac{\partial p^m}{\partial x} \Big|_e \right\} \qquad (27)$$

or

$$u_e^{m+1} = \bar{u}_e^{m+1} + \frac{1}{2}\left[B_O^u \frac{\partial p^m}{\partial x} \Big|_O + B_E^u \frac{\partial p^m}{\partial x} \Big|_E \right] - B_e^u \frac{\partial p^m}{\partial x} \Big|_e \qquad (28)$$

$$\bar{u}_e^{m+1} = \frac{1}{2} [u_E^{m+1} + u_O^{m+1}] \qquad (29)$$

Similar equations can be derived for u_w^{m+1}, u_n^{m+1}, and u_s^{m+1}. Equation (28) and its derivation are referred to as the pressure-weighted method (PWM). This was first introduced by Rhie and Chow (1983), who found a similar form to be effective in coupling the momentum and continuity equations. Let u_e^* be equal to the first three terms on the right-hand side of equation (28), i.e.,

$$u_e^* = \bar{u}_e^{m+1} + \frac{1}{2}\left[B_O^u \frac{\partial p^m}{\partial x} \Big|_O + B_E^u \frac{\partial p^m}{\partial x} \Big|_E \right] \qquad (30)$$

The assumption is made that the following form of the continuity equation is satisfied:

$$[\rho u^{m+1}]_w^e + [\rho v^{m+1}]_s^n = 0 \qquad (31)$$

This is the ultimate converged solution that is sought. Most researchers, such as Caretto et al. (1972), Rhie and Chow (1983), and Hah (1984), now invoke the pressure correction method (PCM) and solve a pressure correction (p') equation. Then, the intermediate velocity field and the previous pressure field are updated by the gradient of the pressure correction and the actual pressure correction, respectively. This explicit correction step is neglected in the present work, with no detrimental effect. In most test cases, this procedure showed better convergence behavior than the original PCM procedure.

Upon substitution of equation (27), and similar forms of it for u_w^{m+1}, u_n^{m+1}, and u_s^{m+1}, into equation (30), the following pressure equation results:

$$-\rho B_e^u \frac{\partial p}{\partial x} \Big|_e + \rho B_w^u \frac{\partial p}{\partial x} \Big|_w - \rho C_n^v \frac{\partial p}{\partial y} \Big|_n \; \rho C_s^v \frac{\partial p}{\partial y} \Big|_s = S_P^m \qquad (32)$$

In discretized form, the implicit pressure equation is

$$A_O^p p_O^{m+1} = A_N^p p_N^{m+1} + A_S^p p_S^{m+1} + A_E^p p_E^{m+1} + A_W^p p_W^{m+1} + S_p^m \qquad (33)$$

The source term of equation (32) is

$$S_P^m = [\rho u^*]_w^e + [\rho v^*]_s^n \qquad (34)$$

where u^* and v^* are of the form of equation (29).

The major difference between this derivative and that of Rhie and Chow (1983) is evident when one considers equation (29). The present method does not include a pressure gradient term at the control volume face for the solution of the pressure equation (32). The Shih and Ren (1984) formulation, which was non-conservative, did not include the pressure-weighted method. In comparison with the pressure weighted method, which includes dissipation dependent on the pressure gradient, their pressure equation only has velocity gradients in the source term.

The extension of this algorithm to generalized coordinates is similar to the formulation presented by Rhie and Chow (1983).

Boundary Conditions. The inlet flow conditions are specified, and at the exit plane (which is at least two chord lengths down stream of the cascade) the streamwise derivative of all the solution variables is set equal to zero. No-slip boundary conditions are used for the velocities at a solid wall. A periodic solver by Napolitano (1985) was used to relax the discretized equations upstream and downstream of the blade profiles.

The boundary condition required to solve the pressure equation is that the normal derivative of the pressure vanishes at the solid boundary in the computational plane. The actual pressure value at the blade profile is determined by extrapolating from the interior nodes to the wall with the condition of zero normal derivative of the pressure.

On the blade surfaces, both the turbulent kinetic energy (k) and the normal derivative of the dissipation rate (ϵ) were set equal to zero, as recommended by Patel et al. (1985).

Results and Discussion
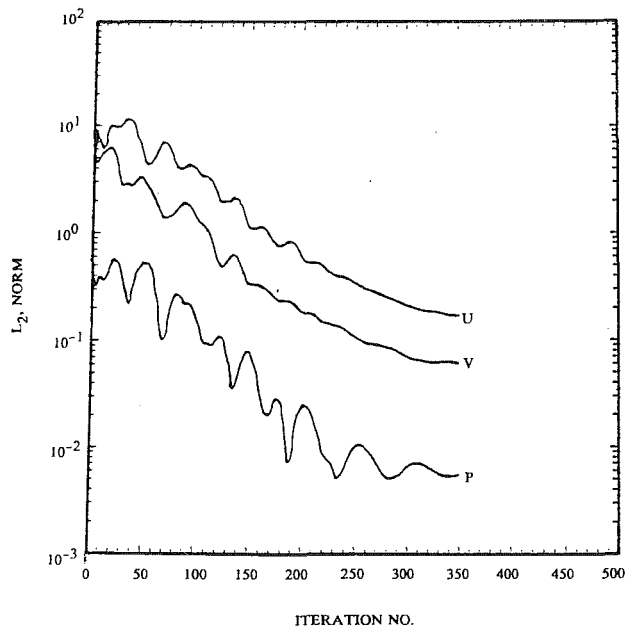
A detailed numerical investigation has been conducted for

Fig. 2   Convergence history for turbulent flow in a double circular arc cascade

Fig. 3   Predicted and measured blade surface pressure coefficient

a cascade geometry, in which results calculated by the above PSM have been compared with the available experimental data. The PSM has been validated and compared to the PCM for various complex flows by Hobson and Lakshminarayana (1989).

Double Circular Arc Cascade: -1.5 deg Incidence. For the test case of turbulent flow through a cascade, the predictions made by the present method were compared with the experimental data obtained by Deutsch and Zierke (1986a, 1986b) and Zierke and Deutsch (1990). The blade section is a double circular arc with a camber of 65 deg and a chord of 228.6 mm, with a leading and trailing edge radius of 9.14 μm. The solidity of the cascade was 2.14, the stagger angle was 20.5 deg, and the aspect ratio was 1.61. The measurements were made at a chord Reynolds number based on the inlet absolute flow velocity of 5.0×10^5 (with air as the test medium) and at three different incidence angles, $+5.0$ deg, -1.5 deg, and -8.0 deg. The computed test case was for the near-design case of -1.5 deg incidence.

The modified version of the GRAPE code, written by Sorenson (1981), was used to generate the H-grid, which extended half a chord upstream and one and a half chords downstream of the blade. The inlet angle of the grid was aligned with the incoming flow at 51.5 deg and the outlet grid angle was set equal to the measured outlet flow angle of 2.1 deg. The grid lines were normal to the blade surface and this orthogonality was relaxed away from the blades. Typical Navier–Stokes calculations using a 130 streamwise by 100 tangential computational grid took 300 outer iterations to decrease the residuals by two orders of magnitude. A typical convergence history (Fig. 2) shows the sum of the L_2 norm of the errors for the complete flowfield at each iteration. The top, middle, and bottom curves are the norms for the u-momentum, v-momentum, and pressure equations, respectively. For the loss versus incidence prediction, it is felt that two orders of magnitude reduction of the errors is adequate for engineering accuracy. However, for the -1.5 deg incidence case, the residuals were reduced by four orders of magnitude in roughly 2000 iterations. This corresponded to 20 minutes on the ETA-10 supercomputer, using only the optimization capabilities of the compiler, which vectorizes inner DO-loops. The slopes of the conver-
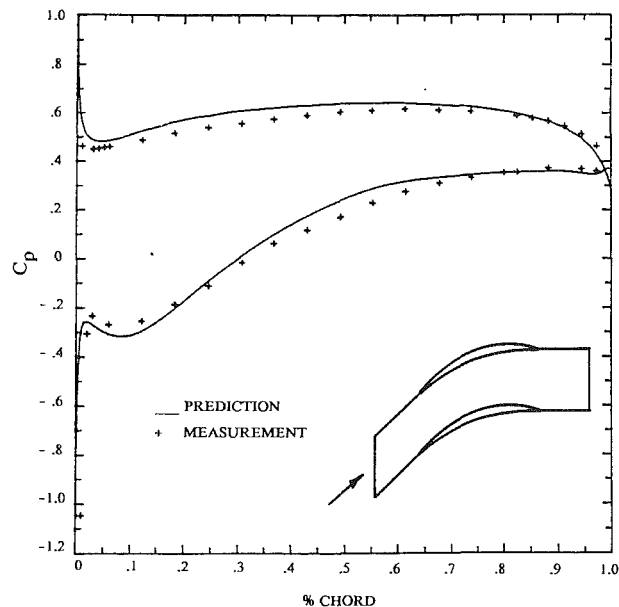
gence plots were not monotonic and flattened out after 300 iterations.

Although an inlet free-stream turbulence intensity (Tu) of 0.18 percent was quoted in the original paper by Deutsch and Zierke (1986a), this was measured in the wind tunnel without the cascade in place. A value of free-stream turbulence intensity of 2 percent was used, after consultation with Zierke (1989), with an associated length scale, L_i, of 1 mm (L_i/CHORD $= 0.004$). The value of 2 percent inlet free-stream turbulence intensity enabled the turbulence model to account for the transition of the blade surface boundary layer (lower values did not result in any transition on the pressure surface). This gives the inlet turbulent kinetic energy, k_i, as

$$k_i = 1.5(U_i Tu)^2 \qquad (35)$$

where U_i is the inlet free-stream velocity. The high inlet free-stream turbulence intensity is due to the flow distortion caused by the cascade resulting in a production of turbulence. Following Rodi and Scheuerer (1985), the inlet turbulent dissipation rate ϵ_i is calculated from the following:

$$\epsilon_i = \frac{k_i^{3/2}}{L_i} \qquad (36)$$

Figure 3 shows a comparison of the calculated and measured static pressure distribution. The pressure surface has a large favorable pressure gradient near the leading edge. The distribution is flat over most of the rest of the blade, and becomes favorable once again at the trailing edge. The suction surface has a large adverse pressure gradient near the leading edge, followed by a mild favorable gradient between 4 and 10 percent chord. The code was not able to capture the pressure spike exactly at the leading edge, but was able to follow the distribution after the leading edge closely. Zierke and Deutsch (1990) note that the very large adverse pressure gradient at the leading edge of the suction surface implies a leading edge separation bubble. No evidence of leading edge separation was predicted by the code. The adverse pressure gradient over the rest of the suction surface is computed and the final vanishing adverse pressure gradient near 80 percent chord is also predicted with the code. The experimental measurements indicated a separation region near the trailing edge. Surface flow visualization tests using the chemical sublimation method showed, with a 95 percent confidence level, a region of low shear stress at 45.1 $\pm$ 2.3 percent chord.

Fig. 4 Comparison of the computed and measured velocity distribution on the suction surface
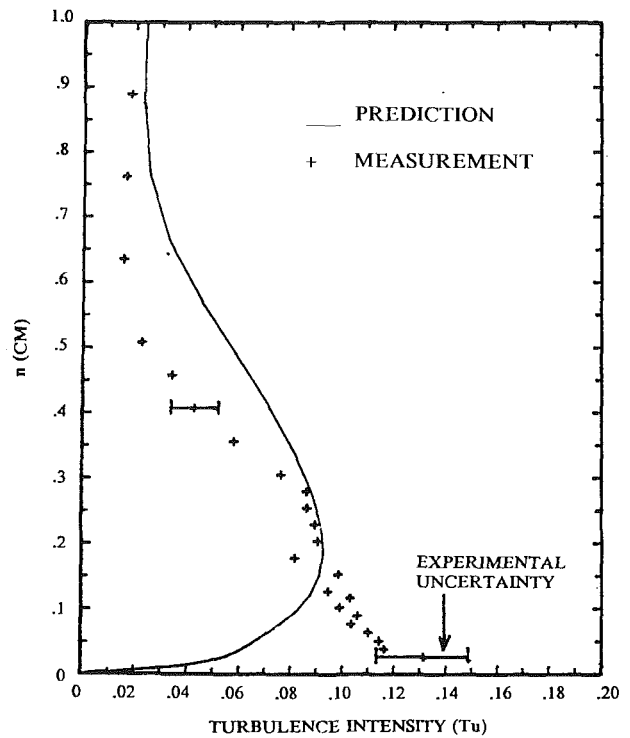
Fig. 5(b) Comparison of the computed and measured turbulence intensity on the suction surface: 49.9 percent chord
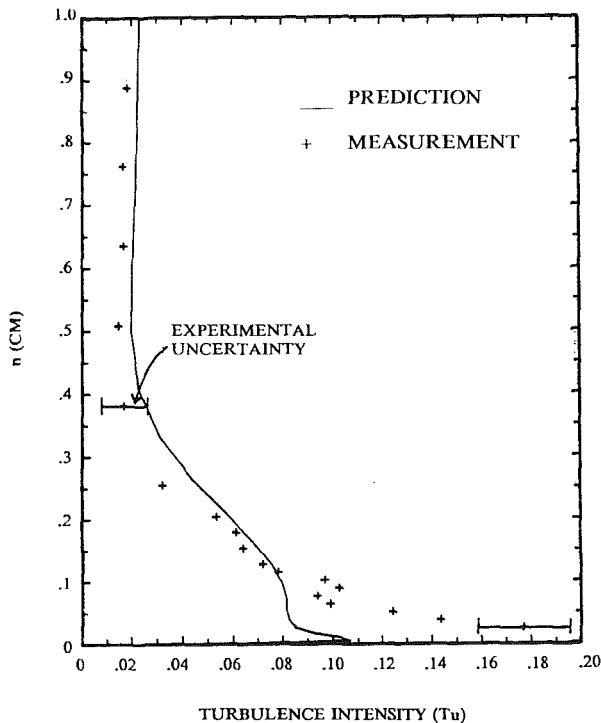
Fig. 5(a) Comparison of the computed and measured turbulence intensity on the suction surface: 19.7 percent chord
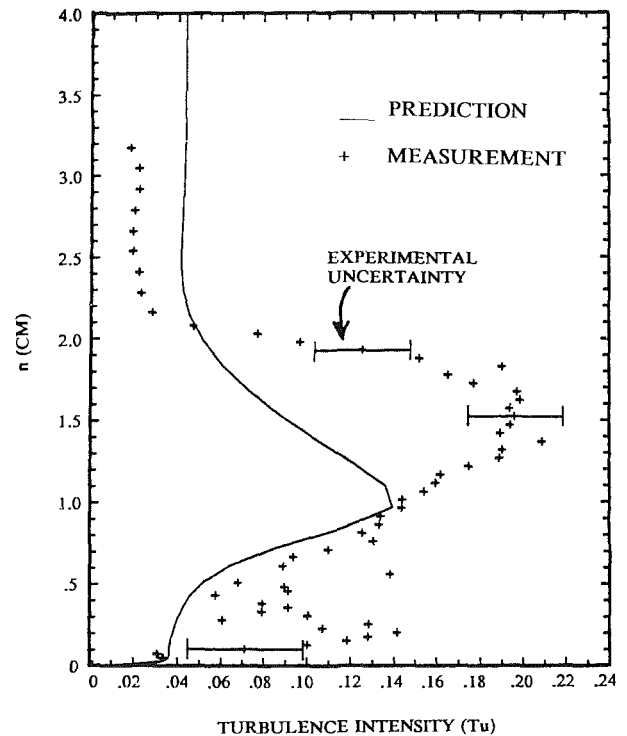
Fig. 5(c) Comparison of the computed and measured turbulence intensity on the suction surface: 90.3 percent chord

Suction Surface Boundary Layers. Suction surface boundary layer profiles were measured by Zierke and Deutsch (1990) with a single component TSI laser-Doppler velocimeter (LDV) at 11 chordwise locations. Figure 4 shows the comparison of the predicted and experimental data for three of the chord locations. The three locations are at 19.7, 48.9, and 90.2 percent chord. Good agreement is achieved over most of the blade profile where the boundary layer remains attached. Both the

free-stream velocities and the boundary layer profiles are predicted accurately.

The velocity profile is not accurately predicted in the separated region. Liu et al. (1988) computed the same cascade test case, but at 5.0 deg incidence. They used the Baldwin–Lomax (1978) turbulence model, which did not predict any flow separation, and the two-equation (k-ϵ) model introduced
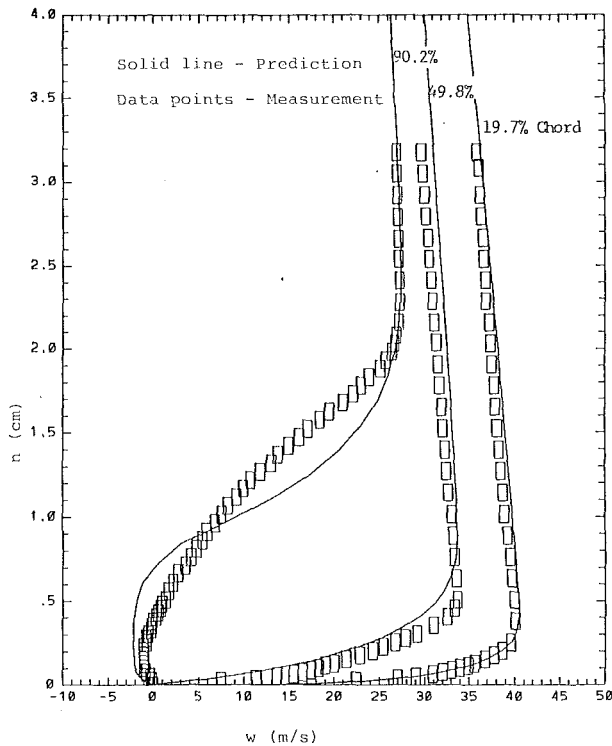
Fig. 6 Comparison of the computed and measured velocity distribution on the pressure surface

Fig. 7 Comparison of the computed and measured skin friction coefficient on the blade surface

by Launder and Spalding (1974), which predicted flow separation at 90 percent chord. The present computations show too large a reverse flow, and there is subsequently not enough diffusion, thus resulting in the overall growth of the boundary layer being suppressed. The reason postulated for the failure of the turbulence model to predict separated flow is that the values of k, ϵ, and thus μ_t are excessively damped in the recirculating region, as the turbulent Reynolds numbers, Re_y and Re_t, are too small in the reverse flow region. The eddy viscosity model based on k and ϵ cannot account for the anisotropy of the turbulence due to streamline curvature in the separated region.

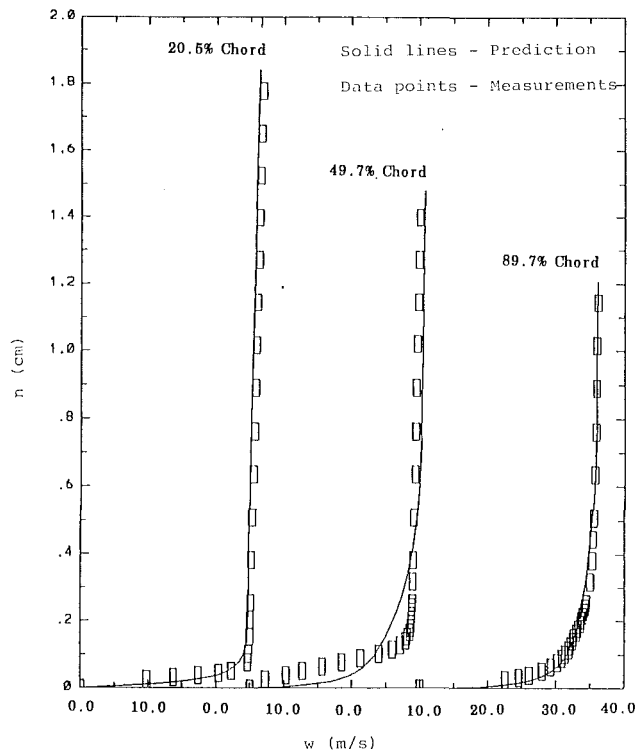The prediction of separation of the flow from the suction surface is in good agreement with the flow visualization measurements. The code computed the onset of separation to be at 50 percent chord, which agrees well with the 45.1 percent measured.

The behavior of the turbulence quantities, such as the turbulent kinetic energy and dissipation on the suction surface, is of interest. The distribution of turbulent kinetic energy through the suction surface boundary layer at the three chordwise locations considered earlier is presented in Fig. 5. At 19.7 percent chord the maximum turbulence is close to the wall. The boundary conditions at the solid wall are that k goes to zero. Along the blade surface the first grid point was always within $y^+ < 1.0$ away from the wall. The maximum value for turbulent kinetic energy moves away from the wall as the boundary layer develops over the suction surface. Over the attached flow portion of the blade, the position of this maximum coincides with the measured maximum turbulence intensity. In the separated flow region, the position of the maximum value of k is 30 percent closer to the wall than the measured maximum turbulence intensity. This is a possible explanation for the boundary layer growth in the separation bubble being underpredicted. The turbulence model is able to predict the increase of turbulent kinetic energy due to streamwise diffusion effects that take place as the boundary layer separates between 49.8 and 90.2 percent chord and the free-
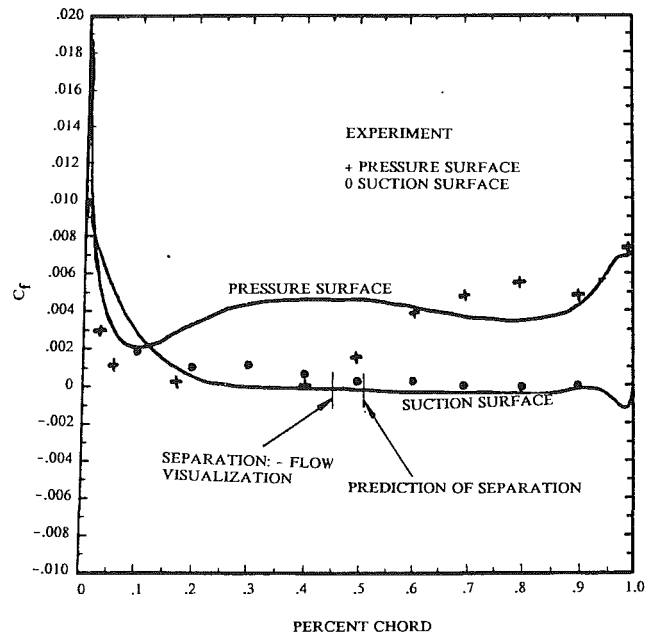
stream accelerates due to increased blockage. The free-stream turbulence intensity at the edge of the boundary layer is predicted well for both the 19.7 and 49.8 percent chords, and overpredicted in the separation region.

Pressure Surface Boundary Layers. Pressure surface boundary layer profiles were measured at 12 locations. Figure 6 shows the comparison of the predicted and experimental data for the three chord locations on the pressure surface. The locations are at 20.5, 49.7, and 89.7 percent chord. Excellent agreement is achieved over the front portion of the blade. The analysis of the experimental data by Zierke and Deutsch (1990) showed that the boundary layer experiences transition from 55.1 percent chord to 70.3 percent chord. The agreement at midchord is acceptable; however, the turbulence model seems to overpredict the transitional boundary layer. Close to the trailing edge where the boundary layer is fully turbulent, a good agreement is once again achieved.

Prediction of Skin Friction. The comparison of the blade surface skin friction distribution is presented in Fig. 7. Transition of the pressure surface boundary layer from laminar to turbulent flow is predicted by this technique. The onset of transition is predicted to be at 10 percent chord, which is early in comparison to the experimentally determined transition process. Transition seems to be complete by 30 percent chord; thus, the length of the transitional region is in agreement with that which is determined experimentally. The experimental points were determined by fitting a spline through the measured boundary layer profiles. The level of skin friction coefficient in the fully turbulent region is accurately predicted, as well as the final increase at the trailing edge. Good agreement is achieved between the predicted and experimental skin friction coefficient on the suction surface of the blade. Shown on this figure is the separation point as determined by the flow visualization technique, and the separation point as predicted by the code with good agreement. The levels of skin friction are very close to zero over most of the rear part of the blade.

Leading and Trailing Edge Flows. A complete flowfield with velocity vector plot is presented in Fig. 8(a), and details
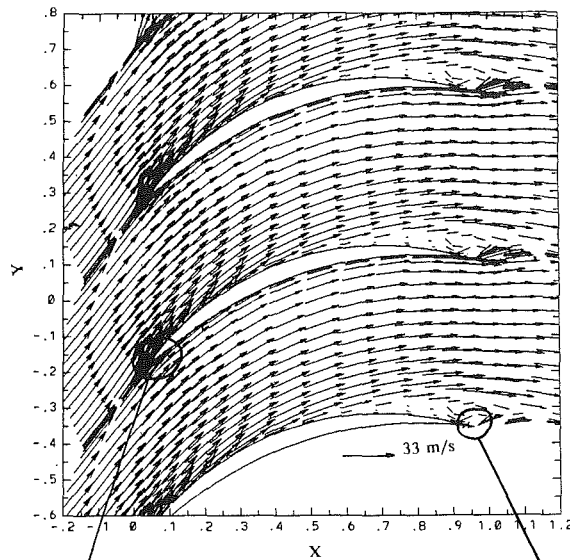
Fig. 8(a)   Velocity vector distribution through the double circular arc cascade – 1.5 deg incidence
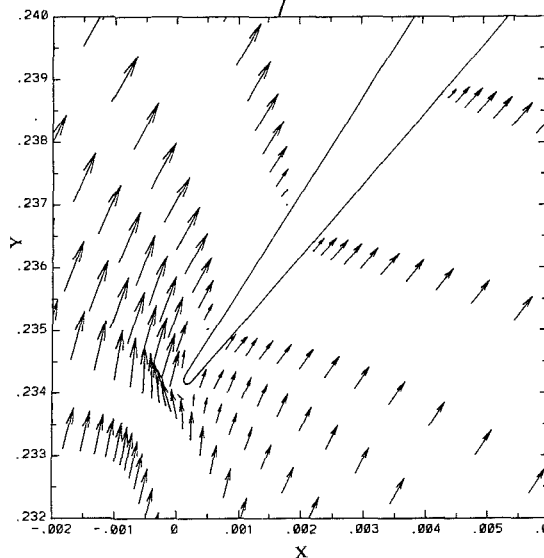

Fig. 8(b)   Detail of leading edge flow
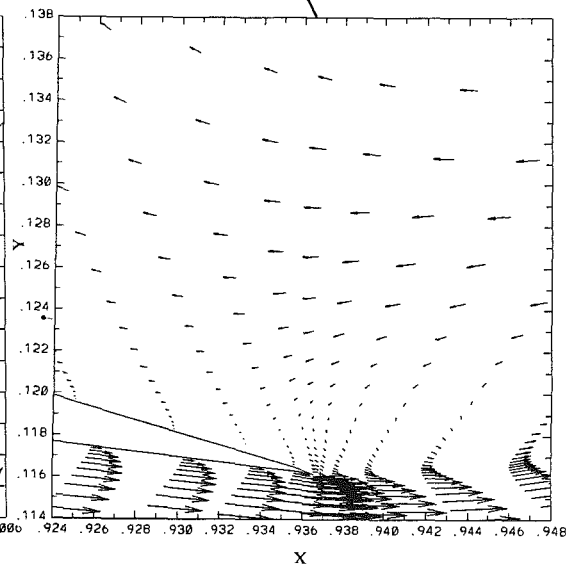
Fig. 8(c)   Detail of trailing edge flow

are shown for the leading edge (Fig. 8b) and trailing edge flows (Fig. 8c) . The separated flow region is clearly visible over the rear part of the suction surface.

Even though the incidence angle was set at −1.5 deg at a distance of half a chord upstream of the cascade, the angle of attack at the leading edge is positive. This angle was locally determined to be equal to 5.5 deg, which is rather high. The code is able to capture the upstream influence of the cascade on the flow and in particular the effect on the stagnation streamline. Flow reversal is predicted around the rounded leading edge from the stagnation point over to the suction surface. On the suction surface, the onset of a leading edge separation bubble is evident; however, as stated earlier, the code did not predict any flow reversal.

The trailing edge flow region is most interesting from a microscopic viewpoint. Firstly, as is shown, the separated flow reattaches to the suction surface right at the trailing edge at 99 percent chord. Thus, the flow leaves the trailing edge in the same direction from both surfaces. No unsteady trailing edge

vortices are shed, as would be the case if the separation bubble were not to reattach. This leads to a steady solution computationally. However, the code still needs to deal with the unsteady separated region, which has now moved into the freestream. Secondly, the trailing edge wake is immediately "washed out" by the flow in that region, and the only wake evident is that due to the detached separation region. The high shear generated by the flow differential from pressure to suction side at the trailing edge is the cause of sudden decay of the trailing edge wake. This is analogous to a jet-wake flow, with the pressure side flow being the jet flow, and the suction side separation the wake flow.

Wake Profiles.   It should be remarked here that the terminology "wake" here refers to the separated region that reattaches downstream. The conventional wake has been "washed" out by the reverse flow in that region as mentioned earlier. LDV measurements of the near wakes were made at 6 and 9.7 percent chord downstream of the trailing edge, while

106.0% CHORD

109.7% CHORD

PREDICTED

MEASURED

131.7% CHORD
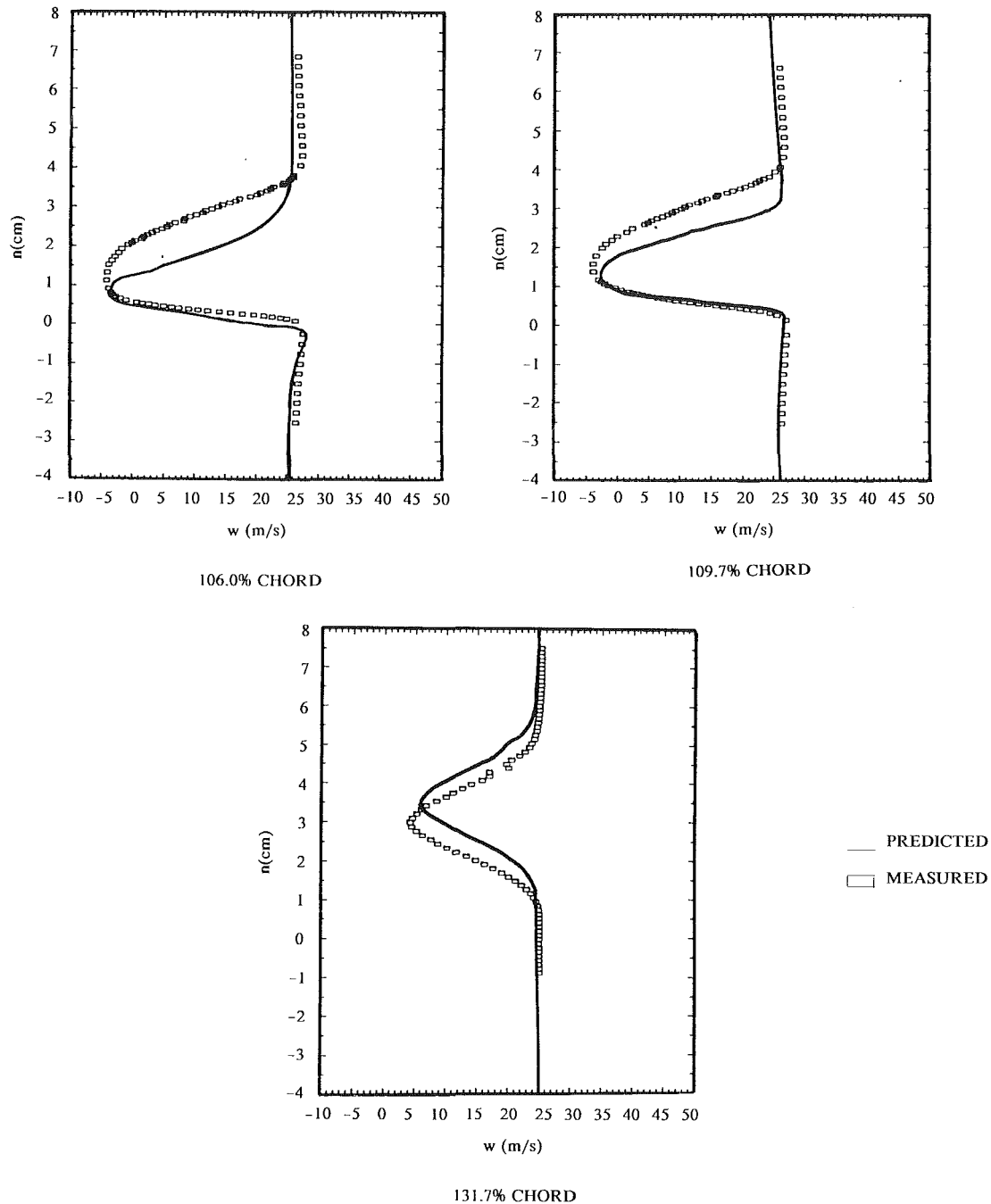
Fig. 9 Comparison of computed and measured axial velocity distribution in the wake

five-hole probe measurements of the far wake were made at 31.7 percent chord downstream of the trailing edge. Figure 9 shows the comparison between the prediction and experimentally measured data for the wake profile at the three measurement locations. Although the overall wake profile is not well predicted, some features are well simulated in this complex flow region where the separated flow and the wake interact. The amount of reverse flow at the wake center is captured, as well as the pressure side profile. The greatest discrepancy, on the suction side near the trailing edge, is due to the inability of the code and the turbulence model in particular to capture the growth of the separated boundary layer.

More accurate predictions of the far wake are computed. The symmetry of the far wake as well as the trajectory of the wake centerline is captured, and the overall defect is predicted within engineering accuracy.

The predicted loss coefficient, 0.084, for this profile compares within 10 percent of 0.094, which was determined from the experimental data. The tangential location of the wake is

Table 1

α (deg)	C_L		Percent error
	Experiment	Computed	
−1.5	0.821	0.846	3.05
5.0	0.952	1.009	5.99

Table 2

α (deg)	$\bar{\omega}$		Percent error
	Experiment	Computed	
−1.5	0.094	0.084	10.64
5.0	0.151	0.139	7.95

Table 3

α (deg)	δ_o (deg)		Percent error
	Experiment	Computed	
−1.5	14.1	13.5	5.25
5.0	16.0	14.4	10.13

reasonably predicted. The wake centerline trajectory is captured well, considering the complexity of the flow with intense mixing between the separated flow on the suction side and the pressure side boundary layer. The far wake location is off by only 5 mm from the measured value.

Double Circular Arc Cascade: Variable Incidence Study. Turning now to the overall prediction of cascade performance with the Navier–Stokes technique, the computation of the above test case was performed at various incidence angles. Zierke and Deutsch (1990) have tested the DCA cascade at −8.5, −1.5, and 5.0 deg angles of incidence. From $\alpha = -1.5$ to $\alpha = 5.0$ deg, the C_L versus α curve displays the classical behavior of an airfoil at increasing angles of attack. The lift coefficient for the high negative incidence case is surprisingly higher than the positive incidence case, which seems to suggest that the flowfield is significantly affected by the laminar separation bubble that forms on the pressure surface at the leading edge.

The code was used to predict the global flow parameters for -1.5 and 5.0 deg incidence. Table 1 shows the comparison between the lift coefficient determined from the experimentally measured blade surface pressure distribution and the computed pressure distribution. Over the incidence range considered, the accuracy of the prediction is within 6 percent of the measured values. However, the gradient of lift versus incidence is over-predicted by 20 percent, which is due to small lift increase over the considered incidence range.

Similarly, the loss predictions are acceptable for the two incidences. The gradient of loss versus incidence is better predicted than the lift. The consistent underprediction of the loss coefficient is due to the inability of the turbulence model to capture the growth of the separation bubble accurately on the rear part of the suction surface.

The errors in the prediction of the outlet deviation angle, as shown in Table 3, are comparable to the errors for the lift prediction. These errors are slightly higher, but the error on the amount of flow turning through the cascade is consistent with those for the lift prediction.

Variation of Inlet-Free-Stream Turbulence Intensity. Having achieved confidence in the code, an attempt was made to understand the effect of inlet free-stream turbulence intensity on the cascade performance. A parametric study was carried out by varying the turbulence intensity level; the turbulence length scale was kept constant. At the high incidence angle case ($\alpha = 5.0$ deg) the inlet free-stream turbulence intensity was increased to 4 and 8 percent, respectively. The effect of this increase on the blade loading was computationally studied. Figure 10 shows the pressure distribution for varying turbulence intensity. Although the overall lift coefficient did not vary by more than 2 percent, an interesting result is evident in the increase of exit static pressure. This results in a decrease in the total pressure loss coefficient through the cascade of 14 percent ($\omega = 0.119$) for the 4 percent turbulence case and 18 percent ($\omega = 0.114$) for the 8 percent turbulence case. The decrease in total pressure loss coefficient that is computed has also been experimentally measured by Evans (1972).

Figure 11 shows the effect of increasing turbulence intensity on the blade surface skin friction. Although the value of blade surface skin friction coefficient is increased for increasing turbulence levels, this merely indicates that the boundary layers are decreasing in thickness. The increase in turbulence from 2
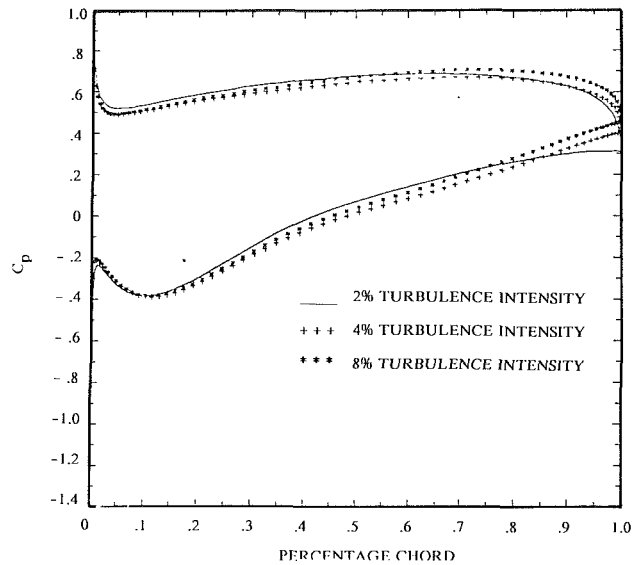
Fig. 10 Effect of increasing turbulence intensity on the distribution of static pressure coefficient
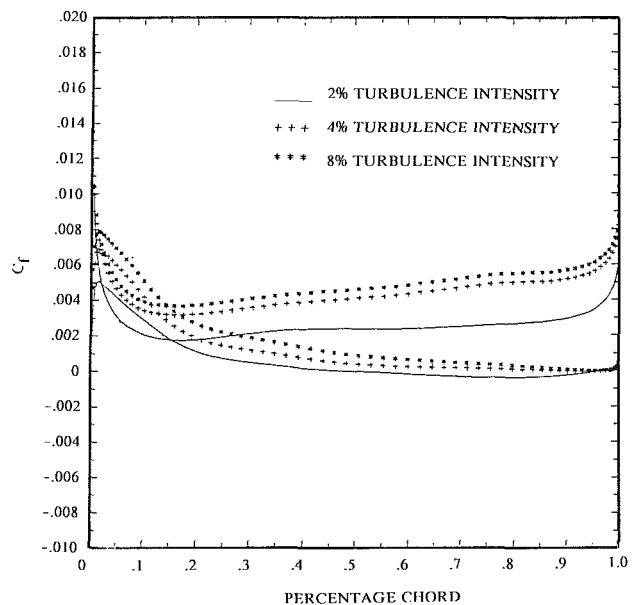
Fig. 11 Effect of increasing turbulence intensity on the distribution of blade skin friction coefficient

to 4 percent caused the suction surface layer to remain attached over the complete length of the blade. The 5.0 deg incidence case at 2 percent inlet turbulence intensity showed suction surface boundary layer separation at 55 percent chord, and this was experimentally determined by Deutsch and Zierke (1986b) to occur at 60 percent chord. This result is consistent with that reported by Schlichting and Das (1963). They showed that the influence of the increase in turbulence level decreased the loss coefficient substantially over the Reynolds number range of $0.5-5.0 \times 10^5$, with the major contribution to the decrease in loss coefficient being the elimination of the separation of the suction surface boundary layer.

On the pressure surface, the effect on the skin friction distribution was most effective when the turbulence levels were increased from 2 to 4 percent. The increase in turbulence level from 4 to 8 percent decreased the boundary layers on both surfaces, and thus only a small decrease in the loss coefficient was computed.

Conclusion

A new technique for computing viscous–incompressible flowfields is presented and validated for cascades. The present method permits computation on a regular grid instead of on a staggered grid and allows for the solution of the pressure and not the pressure correction. In most test cases, this procedure showed better convergence behavior than the original pressure correction method. The method closely couples the velocity and pressure field, and thus does not suffer from pressure oscillations.

For complex flow situations such as a separated compressor cascade, the code exhibits satisfactory convergence behavior.

The global parameters such as pressure distribution, lift coefficient, and losses are well predicted within engineering accuracy.

The agreement between the computed and measured boundary layer profiles for attached flows on both blade surfaces is very good.

Separated flow predictions need to be further investigated, most probably with higher order models that take into account the streamline curvature and anisotropy of the turbulence in the separated region.

Details of the leading edge flow and particularly the reattachment of the separated trailing edge flow on the suction surface have been resolved, which shed more light on these complex flow regions.

The code has predicted the cascade performance over a moderate incidence range; however, the minimum loss or high negative incidence test case still needs to be computed.

The effect of increasing the free-stream turbulence intensity has been investigated. At high positive incidence the flow separation was inhibited when the turbulence intensity was increased resulting in a decrease in the total pressure loss coefficient.

For flow over complex geometries with pressure gradients or separation, the minimum turbulence model that must be used is the low-Reynolds-number k-ϵ model. Its ability to predict transition dependent on free-stream turbulence intensity is well known, and it was used in the present study to predict separated flow.

Acknowledgments

References

Abdallah, S., 1989, Private Communication.

Baldwin, B. S., and Lomax, H., 1978, "Thin Layer Approximation and Algebraic Model for Separated Turbulent Flows," AIAA Paper No. 78-257.

Caretto, L. S., Gossman, A. D., Patankar, S. V., and Spalding, D. B., 1972, "Two Calculation Procedures for Steady Three Dimensional Flows With Recirculation," Proc. Third International Conference on Numerical Methods in Fluid Dynamics, Springer-Verlag, New York, pp. 60–68.

Davis, R. L., Hobbs, D. E., and Weingold, H. D., 1988, "Prediction of Cascade Performance Using a Navier–Stokes Technique," ASME JOURNAL OF TURBOMACHINERY, Vol. 110, pp. 520–531.

Deutsch, S., and Zierke, W. C., 1986a, "The Measurement of Boundary Layers on a Compressor Blade in a Cascade at High Positive Incidence Angle. Part I. Experimental Techniques and Results," NASA CR 179491.

Deutsch, S., and Zierke, W. C., 1986b, "The Measurement of Boundary Layers on a Compressor Blade in a Cascade at High Positive Incidence Angle. Part II. Data Report," NASA CR 179492.

Evans, R. L., 1972, "The Effect of Freestream Turbulence on the Profile Boundary Layer and Losses in a Compressor Cascade," Aeronautical Research Council (United Kingdom), Report No. 1282.

Hah, C., 1984, "A Navier–Stokes Analysis of Three-Dimensional Turbulent Flows Inside Turbine Blade Rows at Design and Off-Design Conditions," ASME Journal of Engineering for Gas Turbines and Power, Vol. 106, pp. 421–429.

Hobson, G. V., and Lakshminarayana, B., 1989, "Fully Elliptic Incompressible Flow Calculations on Regular Grid by a New Pressure Substitution Method," AIAA Paper No. 90-0239.

Lam, C. K. G., and Bremhorst, K., 1981, "A Modified Form of the k-ϵ Model for Predicting Wall Turbulence," ASME Journal of Fluids Engineering, Vol. 103, pp. 456–460.

Launder, B. E., and Spalding, D. B., 1974, "The Numerical Computation of Turbulent Flows," Computer Methods in Applied Mechanics and Engineering, pp. 269–289.

Liu, J., Sockol, P. M., and Prahl, J. M., 1988, "Navier–Stokes Cascade Analysis With a Stiff k-ϵ Turbulence Solver," AIAA Paper No. 88-0594.

Napolitano, M., 1985, "A Fortran Subroutine for the Solution of Periodic Block-Tridiagonal Systems," Communications in Applied Numerical Methods, Vol. 1, pp. 11–15.

Patel, V. C., Rodi, W., and Scheuerer, G., 1985, "A Review and Evaluation of Turbulence Models for Near Wall and Low Reynolds Number Flows," AIAA Journal, Vol. 23, pp. 1308–1319.

Pouagare, M., and Lakshminarayana, B., 1985, "A Space-Marching Method for Viscous Incompressible Internal Flows," AIAA Paper No. 85-0170.

Rhie, C. M., and Chow, W. L., 1983, "Numerical Study of the Turbulent Flow Past an Airfoil With Trailing Edge Separation," AIAA Journal, Vol. 21, pp. 1525–1532.

Rodi, W., and Scheuerer, G., 1985, "Calculation of Heat Transfer to Convection-Cooled Gas Turbine Blades," ASME Journal of Engineering for Gas Turbines and Power, Vol. 107, pp. 620–627.

Schlichting, H., and Das, A., 1963, "Recent Research on Cascade Flow Problems," DFL-Bericht No. 202, Braunschweig.

Shih, T. M., and Ren, A. L., 1984, "Primitive Variable Formulations Using Nonstaggered Grids," Numerical Heat Transfer, Vol. 7. pp. 413–428.

Sorenson, R. L., 1981, "A Computer Program to Generate Two-Dimensional Grids About Airfoils and Other Shapes by the Use of Poisson's Equation," NASA TM 81198.

Spalding, D. B., 1972, "A Novel Finite Difference Formulation for Differential Expressions Involving Both First and Second Derivatives," Int. Journal for Numerical Methods in Engineering, Vol. 4, pp. 551–559.

Zierke, W. C., 1989, Private Communication.

Zierke, W. C., and Deutsch, S., 1990, "The Measurement of Boundary Layers on a Compressor Blade in Cascade: Part 4—Flow Fields for Incidence Angles of -1.5 and -8.5 Degrees," ASME JOURNAL OF TURBOMACHINERY, Vol. 112, pp. 241–255.

Conclusion

A new technique for computing viscous–incompressible flowfields is presented and validated for cascades. The present method permits computation on a regular grid instead of on a staggered grid and allows for the solution of the pressure and not the pressure correction. In most test cases, this procedure showed better convergence behavior than the original pressure correction method. The method closely couples the velocity and pressure field, and thus does not suffer from pressure oscillations.

For complex flow situations such as a separated compressor cascade, the code exhibits satisfactory convergence behavior.

The global parameters such as pressure distribution, lift coefficient, and losses are well predicted within engineering accuracy.

The agreement between the computed and measured boundary layer profiles for attached flows on both blade surfaces is very good.

Separated flow predictions need to be further investigated, most probably with higher order models that take into account the streamline curvature and anisotropy of the turbulence in the separated region.

Details of the leading edge flow and particularly the reattachment of the separated trailing edge flow on the suction surface have been resolved, which shed more light on these complex flow regions.

The code has predicted the cascade performance over a moderate incidence range; however, the minimum loss or high negative incidence test case still needs to be computed.

The effect of increasing the free-stream turbulence intensity has been investigated. At high positive incidence the flow separation was inhibited when the turbulence intensity was increased resulting in a decrease in the total pressure loss coefficient.

For flow over complex geometries with pressure gradients or separation, the minimum turbulence model that must be used is the low-Reynolds-number $k-\epsilon$ model. Its ability to predict transition dependent on free-stream turbulence intensity is well known, and it was used in the present study to predict separated flow.

Acknowledgments

References

Abdallah, S., 1989, Private Communication.

Baldwin, B. S., and Lomax, H., 1978, "Thin Layer Approximation and Algebraic Model for Separated Turbulent Flows," AIAA Paper No. 78-257.

Caretto, L. S., Gossman, A. D., Patankar, S. V., and Spalding, D. B., 1972, "Two Calculation Procedures for Steady Three Dimensional Flows With Recirculation," *Proc. Third International Conference on Numerical Methods in Fluid Dynamics*, Springer-Verlag, New York, pp. 60–68.

Davis, R. L., Hobbs, D. E., and Weingold, H. D., 1988, "Prediction of Cascade Performance Using a Navier–Stokes Technique," ASME JOURNAL OF TURBOMACHINERY, Vol. 110, pp. 520–531.

Deutsch, S., and Zierke, W. C., 1986a, "The Measurement of Boundary Layers on a Compressor Blade in a Cascade at High Positive Incidence Angle. Part I. Experimental Techniques and Results," NASA CR 179491.

Deutsch, S., and Zierke, W. C., 1986b, "The Measurement of Boundary Layers on a Compressor Blade in a Cascade at High Positive Incidence Angle. Part II. Data Report," NASA CR 179492.

Evans, R. L., 1972, "The Effect of Freestream Turbulence on the Profile Boundary Layer and Losses in a Compressor Cascade," Aeronautical Research Council (United Kingdom), Report No. 1282.

Hah, C., 1984, "A Navier–Stokes Analysis of Three-Dimensional Turbulent Flows Inside Turbine Blade Rows at Design and Off-Design Conditions," ASME *Journal of Engineering for Gas Turbines and Power*, Vol. 106, pp. 421–429.

Hobson, G. V., and Lakshminarayana, B., 1989, "Fully Elliptic Incompressible Flow Calculations on Regular Grid by a New Pressure Substitution Method," AIAA Paper No. 90-0239.

Lam, C. K. G., and Bremhorst, K., 1981, "A Modified Form of the $k-\epsilon$ Model for Predicting Wall Turbulence," ASME *Journal of Fluids Engineering*, Vol. 103, pp. 456–460.

Launder, B. E., and Spalding, D. B., 1974, "The Numerical Computation of Turbulent Flows," *Computer Methods in Applied Mechanics and Engineering*, pp. 269–289.

Liu, J., Sockol, P. M., and Prahl, J. M., 1988, "Navier–Stokes Cascade Analysis With a Stiff $k-\epsilon$ Turbulence Solver," AIAA Paper No. 88-0594.

Napolitano, M., 1985, "A Fortran Subroutine for the Solution of Periodic Block-Tridiagonal Systems," *Communications in Applied Numerical Methods*, Vol. 1, pp. 11–15.

Patel, V. C., Rodi, W., and Scheuerer, G., 1985, "A Review and Evaluation of Turbulence Models for Near Wall and Low Reynolds Number Flows," *AIAA Journal*, Vol. 23, pp. 1308–1319.

Pouagare, M., and Lakshminarayana, B., 1985, "A Space-Marching Method for Viscous Incompressible Internal Flows," AIAA Paper No. 85-0170.

Rhie, C. M., and Chow, W. L., 1983, "Numerical Study of the Turbulent Flow Past an Airfoil With Trailing Edge Separation," *AIAA Journal*, Vol. 21, pp. 1525–1532.

Rodi, W., and Scheuerer, G., 1985, "Calculation of Heat Transfer to Convection-Cooled Gas Turbine Blades," ASME *Journal of Engineering for Gas Turbines and Power*, Vol. 107, pp. 620–627.

Schlichting, H., and Das, A., 1963, "Recent Research on Cascade Flow Problems," DFL-Bericht No. 202, Braunschweig.

Shih, T. M., and Ren, A. L., 1984, "Primitive Variable Formulations Using Nonstaggered Grids," *Numerical Heat Transfer*, Vol. 7. pp. 413–428.

Sorenson, R. L., 1981, "A Computer Program to Generate Two-Dimensional Grids About Airfoils and Other Shapes by the Use of Poisson's Equation," NASA TM 81198.

Spalding, D. B., 1972, "A Novel Finite Difference Formulation for Differential Expressions Involving Both First and Second Derivatives," *Int. Journal for Numerical Methods in Engineering*, Vol. 4, pp. 551–559.

Zierke, W. C., 1989, Private Communication.

Zierke, W. C., and Deutsch, S., 1990, "The Measurement of Boundary Layers on a Compressor Blade in Cascade: Part 4—Flow Fields for Incidence Angles of -1.5 and -8.5 Degrees," ASME JOURNAL OF TURBOMACHINERY, Vol. 112, pp. 241–255.

--------- **DISCUSSION** ---------

W. C. Zierke[1] and S. Deutsch[1]

The paper by Hobson and Lakshminarayana introduces a new technique for handling the computational difficulties associated with the assumption of incompressibility for the Navier–Stokes equations. From the point of view of the experimenter whose cascade data the authors attempt to match, however, the paper represents, first and foremost, an honest try at the calculation of this interesting and complex flowfield.

Although for the most part the flowfield is adequately captured, there are regions in which the computation could be improved. Transition is obviously one such region. We note here that the authors do not spend a great deal of space discussing their transition model, and we believe that this is symptomatic of the simplicity and empiricism of current transition models. Certainly, such models are not nearly so sophisticated as current turbulence models. The sensitivity of the transition model to the free-stream turbulence intensity is particularly distressing. From the point of view of an experimentalist, there is every reason to measure the turbulence intensity at an inlet plane a chord or so upstream of the blade row (which we measured as 0.18 percent) to provide an upstream boundary condition. There is no compelling reason to make the same measurement immediately upstream of the blade row. The authors used an inlet free-stream turbulence intensity of 2.0 percent, which seems to be based on the value of 1.5 percent that we measured with a hot wire just outside a leading-edge

[1]Applied Research Laboratory, Pennsylvania State University, State College, PA 16804.

boundary layer. Evidently, their computations, especially their transition model, were quite sensitive to this value. Transition on the pressure surface is still not adequately predicted. From our experiment, we concluded that a very small separation "bubble" existed on this surface that causes at least a partial transition to turbulence. Clearly, research into the transition process and the subsequent development of transition models is very much needed.

A second region in which the calculation could be improved is in the region of separated flow on the suction surface. In particular, it is not all apparent to us why the flow would choose to reattach at 99 percent chord. It seems to us that this reattachment is the reason that the predicted near-wake profiles deviate so much from the measured profiles on the suction side. Perhaps the authors would care to comment on this.

The usefulness of the calculations is apparent both in the incidence angle parametric study and, most particularly, in the detail with which the incidence flow is captured. This improved resolution, above the experiment, makes it possible to determine the actual incidence angle and in this way helps to explain the measured pressure profile. We look forward to increasingly sophisticated attempts, by the authors and others, to calculate these flow fields.

Authors' Closure

The authors would like to thank Drs. Zierke and Deutsch for their interesting comments. The low-Reynolds-number form of the two-equation turbulence model used accounts for the effect of free-stream turbulence intensity on transition. This model has been shown by Rodi and Scheuerer (1985) and Schmidt and Patankar (1988) to be sensitive to the level of inlet free-stream turbulence intensity. For boundary layer calculations they found that good predictions of transition could be made by correctly specifying inlet turbulence levels. However, the dissipation levels had to be related to turbulent kinetic energy levels by a constant of proportionality, which in turn was dependent on the level of turbulence. The authors did not attempt to use this specification of the inlet turbulence, but rather used the turbulence model as given by Lam and Bremhorst (1981). For inlet free-stream turbulence intensities of 2 percent, transition, although not accurately, was predicted.

The reattachment of the suction side boundary layer at 99 percent chord was also a surprise to the authors. A possible explanation is that this is a steady-state solution of what is obviously an unsteady flow process. It would be interesting if this steady-state solution were now to be continued in an unsteady mode so that the stability of the flow at the trailing edge could be determined. The authors suspect that vortices are being shed from the trailing edge of the blade, which the present computations are not able to predict. The separation zone "washes out" anywhere from 10 to 30 percent chord length downstream of the trailing edge. The computation and measurements are consistent here. In a recent paper Schulz et al. (1990) observed, "The flow perceives the corner stall as a solid obstruction, which ends abruptly downstream of the blade trailing edge. Here the flows from both sides of the separated zone merge again." The authors believe that the same mechanisms are applicable in this two-dimensional cascade flow.

References

Schmidt, R. C., and Patankar, S. V., 1988, "Two Equations Low-Reynolds-Number Turbulence Modelling of Transitional Boundary Layer Flows Characteristic of Gas Turbine Blades," NASA CR 4145.

Schulz, H. D., Gallus, H. E., and Lakshminarayana, B., 1990, "Three-Dimensional Separated Flowfield in the Endwall Region of an Annular Compressor Cascade in the Presence of Rotor-Stator Interaction, Parts 1 and 2," ASME JOURNAL OF TURBOMACHINERY, Vol. 112, pp. 669–690.

boundary layer. Evidently, their computations, especially their transition model, were quite sensitive to this value. Transition on the pressure surface is still not adequately predicted. From our experiment, we concluded that a very small separation "bubble" existed on this surface that causes at least a partial transition to turbulence. Clearly, research into the transition process and the subsequent development of transition models is very much needed.

A second region in which the calculation could be improved is in the region of separated flow on the suction surface. In particular, it is not all apparent to us why the flow would choose to reattach at 99 percent chord. It seems to us that this reattachment is the reason that the predicted near-wake profiles deviate so much from the measured profiles on the suction side. Perhaps the authors would care to comment on this.

The usefulness of the calculations is apparent both in the incidence angle parametric study and, most particularly, in the detail with which the incidence flow is captured. This improved resolution, above the experiment, makes it possible to determine the actual incidence angle and in this way helps to explain the measured pressure profile. We look forward to increasingly sophisticated attempts, by the authors and others, to calculate these flow fields.

Authors' Closure

The authors would like to thank Drs. Zierke and Deutsch for their interesting comments. The low-Reynolds-number form of the two-equation turbulence model used accounts for the effect of free-stream turbulence intensity on transition. This model has been shown by Rodi and Scheuerer (1985) and Schmidt and Patankar (1988) to be sensitive to the level of inlet free-stream turbulence intensity. For boundary layer calculations they found that good predictions of transition could be made by correctly specifying inlet turbulence levels. However, the dissipation levels had to be related to turbulent kinetic energy levels by a constant of proportionality, which in turn was dependent on the level of turbulence. The authors did not attempt to use this specification of the inlet turbulence, but rather used the turbulence model as given by Lam and Bremhorst (1981). For inlet free-stream turbulence intensities of 2 percent, transition, although not accurately, was predicted.

The reattachment of the suction side boundary layer at 99 percent chord was also a surprise to the authors. A possible explanation is that this is a steady-state solution of what is obviously an unsteady flow process. It would be interesting if this steady-state solution were now to be continued in an unsteady mode so that the stability of the flow at the trailing edge could be determined. The authors suspect that vortices are being shed from the trailing edge of the blade, which the present computations are not able to predict. The separation zone "washes out" anywhere from 10 to 30 percent chord length downstream of the trailing edge. The computation and measurements are consistent here. In a recent paper Schulz et al. (1990) observed, "The flow perceives the corner stall as a solid obstruction, which ends abruptly downstream of the blade trailing edge. Here the flows from both sides of the separated zone merge again." The authors believe that the same mechanisms are applicable in this two-dimensional cascade flow.

References

Schmidt, R. C., and Patankar, S. V., 1988, "Two Equations Low-Reynolds-Number Turbulence Modelling of Transitional Boundary Layer Flows Characteristic of Gas Turbine Blades," NASA CR 4145.

Schulz, H. D., Gallus, H. E., and Lakshminarayana, B., 1990, "Three-Dimensional Separated Flowfield in the Endwall Region of an Annular Compressor Cascade in the Presence of Rotor-Stator Interaction, Parts 1 and 2," ASME JOURNAL OF TURBOMACHINERY, Vol. 112, pp. 669–690.

A Zonal Approach for Navier-Stokes Computations of Compressible Cascade Flow Fields Using a TVD Finite Volume Method

M. Furukawa

M. Yamasaki

M. Inoue

Department of Mechanical Engineering
for Power,
Kyushu University,
Fukuoka, Japan

A new zonal approach for computation of compressible viscous flows in cascades has been developed. The two-dimensional, Reynolds-averaged Navier-Stokes equations are discretized spatially by a cell-centered finite volume formulation. In order to make the present approach robust, the inviscid fluxes at cell interfaces are evaluated using a highly accurate TVD scheme based on the MUSCL-type approach with the Roe's approximate Riemann solver. The viscous fluxes are determined in a central differencing manner. To simplify the grid generation, a composite zonal grid system is adopted, in which the computational domain is divided into nonoverlapping zones, and structured grids are generated independently in each zone. The zonal boundary between two zones is uniquely defined by cell interfaces of one zone, which ensures the uniqueness of the zonal boundary. Communication from one zone to the other is accomplished by numerical fluxes across the zonal boundary. It should be noted that the complete conservation of the numerical fluxes across the zonal boundary can be satisfied by directly evaluating the numerical fluxes using the finite volume method and by ensuring the uniqueness of the zonal boundary. In order to demonstrate the versatility of the present zonal approach, numerical examples are presented for viscous flows through a transonic turbine cascade.

Introduction

In recent years, many numerical schemes for the Navier-Stokes simulation of compressible flows in cascades have been developed. In most of these schemes (for example, Chima, 1985, 1987; Dawes, 1987; Davis et al., 1987; Kwon, 1988; Nakahashi et al., 1987; Norton et al., 1984; Schafer et al., 1986; Weinberg et al., 1986), the inviscid terms, namely the convective and pressure terms, are discretized in central differencing manners where conventional numerical dissipation terms are explicitly added for stability. These schemes require fine tuning of numerical dissipation coefficients to achieve desirable resolution of boundary layers and shock waves. It is generally difficult to optimize the numerical dissipation coefficients, which impairs the accuracy and reliability of the schemes in predicting cascade performance.

Highly accurate Total Variation Diminishing (TVD) schemes based on Riemann solvers have been developed for the Euler equations (see for example Chakravarthy and Osher, 1985; Harten, 1983; Yee and Harten, 1987). The TVD schemes have nonoscillatory but sharp shock-capturing properties without any tuning of the numerical dissipation terms. Because of this robust nature of the TVD schemes, they have been used for a very wide class of external flow problems. In addition, the TVD schemes can also be extended for the evaluation of the inviscid terms of the Navier-Stokes equations (Chakravarthy et al., 1985). According to the studies on the application of the TVD schemes to the Navier-Stokes equations by van Leer et al. (1987), and Vatsa et al. (1987), it was found that built-in numerical dissipation terms introduced by the highly accurate TVD schemes based on Riemann solvers automatically become small in boundary layers so as not to dominate the natural diffusion. For the cascade flow problems, Rai (1987) and Yamamoto et al. (1988) introduced the TVD formulations.

In applications of numerical schemes to practical engineering problems, the use of a single-grid system causes difficulty in grid generation because of complex geometries. For example, in the case of turbine cascades with high stagger, it is difficult to generate a periodic C-type grid without skewness of the grid, because grid lines must be continuous at periodic boundaries. To avoid this difficulty, zonal approaches with the composite or overlaid grid system have been developed by several researchers. In the zonal approaches, a computational domain

is divided into zones, and grids are generated independently in each zone. The division of the computational domain introduces interfaces between the zones, which are referred to as the zonal boundaries. The most important point in the zonal approaches is on the treatment of the zonal boundaries. The following treatments have been proposed: the chimera scheme for interpolations on overlaid grids (Benek et al., 1985), Rai's scheme for a TVD finite difference formulation (Rai, 1984), a scheme based on characteristic boundary conditions (Bush, 1985), and the FDM-FEM hybrid scheme (Nakahashi and Obayashi, 1987). Rai (1987) and Nakahashi et al. (1987) applied their zonal approaches to the Navier–Stokes computation of cascade flow fields. Only in Rai's scheme is the conservation of numerical fluxes across the zonal boundaries taken into account. However, the fluxes are evaluated by the finite difference method in Rai's scheme, and so the flux conservation across the zonal boundaries is not exactly satisfied.

In this paper, we propose a new zonal approach for the computation of compressible viscous flows in cascades, in which a highly accurate TVD, finite volume formulation with the composite zonal grid system is implemented in order to produce a Navier–Stokes solver with robustness and high accuracy for the prediction of cascade performance. The emphasis in this paper is on the treatment of the zonal boundary. In the present zonal approach, the zonal boundary is constructed of interfaces of computational cells, and communication from one zone to the other is accomplished by numerical fluxes across the zonal boundary. The complete conservation of the fluxes at the zonal boundary can be satisfied by directly evaluating the fluxes using the finite volume formulation and by ensuring the uniqueness of the zonal boundary between two zones.

Finite Volume Formulation

The two-dimensional, Reynolds-averaged Navier–Stokes equations are integrated over a computational cell. The integrated equations can be written in nondimensional form as

$$\frac{\partial}{\partial t} \int_\Omega Q d\Omega + \int_{\partial\Omega} H dS = \frac{1}{\text{Re}} \int_{\partial\Omega} R dS \qquad (1)$$

where the cell region is denoted by Ω, the cell boundary by $\partial\Omega$, and the distance along the boundary by S. In the above, Re denotes the Reynolds number, and Q, H, and R are the vectors of conserved variables, inviscid fluxes, and viscous fluxes, respectively, which are given by

$$Q = \begin{bmatrix} \rho \\ \rho u \\ \rho v \\ e \end{bmatrix}, \qquad H = \begin{bmatrix} \rho U \\ \rho u U + p n_x \\ \rho v U + p n_y \\ (e+p)U \end{bmatrix}$$

$$R = \begin{bmatrix} 0 \\ \tau_{xx} n_x + \tau_{xy} n_y \\ \tau_{xy} n_x + \tau_{yy} n_y \\ f_x n_x + f_y n_y \end{bmatrix} . \qquad (2)$$

with

$$U = u n_x + v n_y$$

$$\tau_{xx} = \mu(4u_x - 2v_y)/3$$

$$\tau_{xy} = \mu(u_y + v_x) \qquad (3)$$

$$\tau_{yy} = \mu(4v_y - 2u_x)/3$$

$$f_x = u\tau_{xx} + v\tau_{xy} + (\mu/\text{Pr})(\gamma-1)^{-1}(a^2)_x$$

$$f_y = u\tau_{xy} + v\tau_{yy} + (\mu/\text{Pr})(\gamma-1)^{-1}(a^2)_y$$

Here, ρ is the density, u and v are the velocity components in the x and y directions, respectively, e is the total energy per unit volume, p is the pressure, n_x and n_y are the x and y components of the unit vector outward normal to the cell boundary, γ is the ratio of specific heats, and a is the sound speed. Using the molecular viscosity given by Sutherland's law, μ_l, the eddy viscosity, μ_t, the laminar Prandtl number, Pr_l, and the turbulent Prandtl number, Pr_t, μ and μ/Pr are expressed as

$$\mu = \mu_l + \mu_t \qquad (4)$$

$$\mu/\text{Pr} = \mu_l/\text{Pr}_l + \mu_t/\text{Pr}_t \qquad (5)$$

The algebraic turbulence model of Baldwin and Lomax (1978) is adopted to estimate the eddy viscosity, and the boundary layer transition is determined in accordance with the criterion of transition based on the Baldwin and Lomax model. In the present scheme, Pr_l and Pr_t are assumed to be constant. Only the perfect gas case will be considered, in which case the pressure and sound speed can be given by

$$p = (\gamma-1)[e - \rho(u^2+v^2)/2] \qquad (6)$$

$$a^2 = \gamma(\gamma-1)[e/\rho - (u^2+v^2)/2] \qquad (7)$$

Using the cell-centered finite volume formulation with a quadrilateral structured cell system shown in Fig. 1, equation (1) is spatially discretized as

$$\frac{\partial}{\partial t}(A_{i,j} Q_{i,j})$$

$$= (SF)_{i,j-1/2} + (SF)_{i+1/2,j} + (SF)_{i,j+1/2} + (SF)_{i-1/2,j} \qquad (8)$$

where $F = -H + R/\text{Re}$, $A_{i,j}$ is the cell area, $Q_{i,j}$ is the vector of conserved variables averaged over the cell, subscript i

---

Nomenclature

a = sound speed
A = computational cell area
e = total energy per unit volume
F = flux vector consisting of inviscid and viscous fluxes
H = inviscid flux vector
M = Mach number
n = unit vector outward normal to cell interface
p = pressure
Pr_l = laminar Prandtl number
Pr_t = turbulent Prandtl number
Q = vector of conserved variables
R = viscous flux vector
Re = Reynolds number
s = flux limiter

S = length of cell interface
u = velocity component in x direction
v = velocity component in y direction
W = interpolation coefficient, equation (23)
x, y = coordinates
β = flow angle relative to axial direction
γ = ratio of specific heats
Δt = time step
κ = parameter in equation (9)
μ_l = molecular viscosity
μ_t = eddy viscosity
ρ = density

Subscripts

1 = inlet
2 = exit
$i, 1$ = computational cell in zone 2
i, j = computational cell in any zone
k, L = computational cell in zone 1

Superscripts

(1) = zone 1
(2) = zone 2
n = time level
+ = right state at cell interface
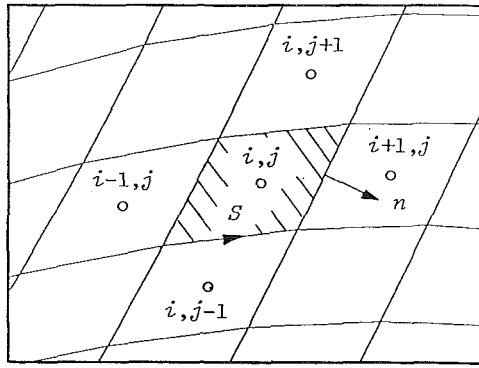− = left state at cell interface
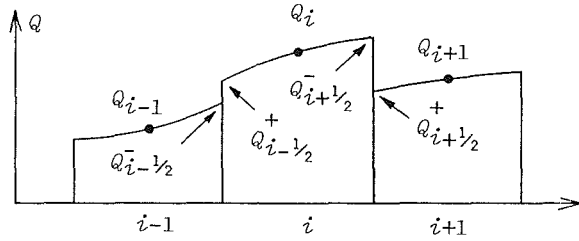
Fig. 1 Computational cells

Fig. 2 Projection stage

+ 1/2, j denotes the cell interface between the cells (i, j) and $(i+1, j)$, and S is the length of the cell interface.

Evaluation of Inviscid Fluxes by TVD Scheme

The inviscid flux vector H at each cell interface is computed by the following, highly accurate TVD scheme. The TVD scheme used is based on the MUSCL-type approach of an upwind scheme, which consists of a projection stage and an evolution stage (van Leer, 1985).

Projection Stage. To raise the order of accuracy of the scheme, the cell-centered values of the conserved variables are extrapolated toward the cell interfaces according to piecewise distributions of conserved variables in each cell, as shown in Fig. 2. The projection with a differentiable limiter (Anderson et al., 1985) is used in the present scheme. For the projection in the i direction on the cell (i, j), the extrapolated conserved variables, $Q^-_{i+1/2, j}$ and $Q^+_{i-1/2, j}$, are given by

$$Q^-_{i+1/2, j} = Q_{i, j} + \left\{\frac{s}{4} [(1-\kappa s)\Delta_- + (1+\kappa s)\Delta_+]\right\}_{i, j}$$

$$Q^+_{i-1/2, j} = Q_{i, j} - \left\{\frac{s}{4} [(1-\kappa s)\Delta_+ + (1+\kappa s)\Delta_-]\right\}_{i, j} \quad (9)$$

where

$$(\Delta_+)_{i, j} = Q_{i+1, j} - Q_{i,j} , \quad (\Delta_-)_{i, j} = Q_{i, j} - Q_{i-1, j} \quad (10)$$

$$s = (2\Delta_+\Delta_- + \epsilon)/[(\Delta_+)^2 + (\Delta_-)^2 + \epsilon] \quad (11)$$

with $\epsilon = 10^{-6}$ to prevent division by zero in regions of null gradients. In the above, s is the limiter, which is introduced to preserve the nonoscillatory nature of the scheme, that is, to avoid oscillations at discontinuities, such as shock waves. The parameter κ determines the spatial accuracy: $\kappa = -1$ corresponds to the second-order fully upwind scheme, and $\kappa = 1/3$ to the third-order upwind-biased scheme. For the numerical results presented in this paper, the third-order upwind-biased scheme is used. The formulas similar to equation (9) hold for the projection in the j direction, and so it is found that the cell-centered, conserved variables at the cells adjacent to the cell considered are required for the projection.
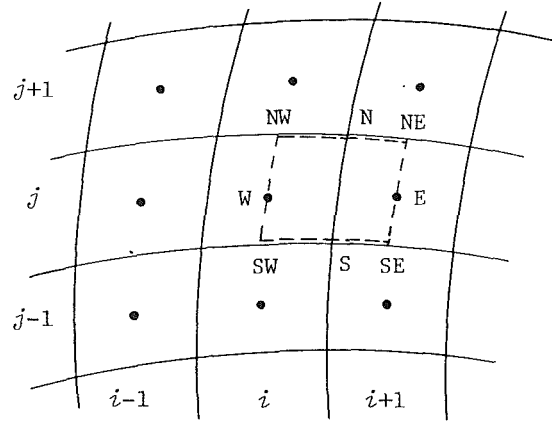

Fig. 3 Evaluation of first-order derivatives

Evolution Stage. The numerical inviscid flux vector $H_{i+1/2, j}$ can be evaluated by solving the Riemann problem with the left and right states, $Q^-_{i+1/2, j}$ and $Q^+_{i+1/2, j}$, at the cell interface. In the present approach, the upwind scheme based on the approximate Riemann solver of Roe (1981) is adopted, in which the inviscid flux is constructed as

$$H_{i+1/2, j}$$

$$= \frac{1}{2} [H(Q^+_{i+1/2, j}, \mathbf{n}_{i+1/2, j}) + H(Q^-_{i+1/2, j}, \mathbf{n}_{i+1/2, j})$$

$$- |A(\tilde{Q}_{i+1/2, j}, \mathbf{n}_{i+1/2, j})| \cdot (Q^+_{i+1/2, j}, Q^-_{i+1/2, j})] \quad (12)$$

where

$$A = \frac{\partial H}{\partial Q} = R\Lambda R^{-1}, \quad |A| = R|\Lambda|R^{-1} \quad (13)$$

Here, $\mathbf{n}$ is the unit vector normal to the cell interface, A is the Jacobian matrix of H, and $\tilde{Q}$ denotes the averaged variables computed by Roe's averaging. In addition, Λ is the diagonal matrix containing the eigenvalues of A, and R and R^{-1} are the matrix of right eigenvectors and the matrix of left eigenvectors, respectively. The matrices Λ, R, and R^{-1} have been given by Chakravarthy (1986).

Evaluation of Viscous Fluxes

In order to construct the numerical viscous flux vector $R_{i+1/2, j}$ at the cell interfaces, it is necessary to evaluate first-order derivatives of the velocity components and the sound speed. At the cell interface $(i+1/2, j)$ shown as the side SN in Fig. 3, using Green's theorem, the first-order derivatives can be evaluated in the following central differencing manner:

$$\left(\frac{\partial u}{\partial x}\right)_{i+1/2, j} = (u_E\Delta y_E + u_N\Delta y_N + u_W\Delta y_W + u_S\Delta y_S)/A'$$

$$\left(\frac{\partial u}{\partial y}\right)_{i+1/2, j} = -(u_E\Delta x_E + u_N\Delta x_N + u_W\Delta x_W + u_S\Delta x_S)/A' \quad (14)$$

where

$$u_E = u_{i+1, j}, \quad u_W = u_{i, j}$$

$$u_N = (u_{i+1, j+1} + u_{i, j+1} + u_{i, j} + u_{i+1, j})/4$$

$$u_S = (u_{i+1, j} + u_{i, j} + u_{i, j-1} + u_{i+1, j-1})/4$$

$$\Delta x_E = x_{NE} - x_{SE}, \quad \Delta y_E = y_{NE} - y_{SE} \quad (15)$$

$$\Delta x_N = x_{NW} - x_{NE}, \quad \Delta y_N = y_{NW} - y_{NE}$$

$$\Delta x_W = x_{SW} - x_{NW}, \quad \Delta y_W = y_{SW} - y_{NW}$$

$$\Delta x_S = x_{SE} - x_{SW}, \quad \Delta y_S = y_{SE} - y_{SW}$$

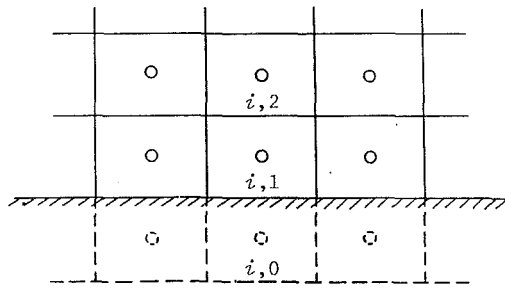In Fig. 3, the region denoted by NE, NW, SW, SE is an

Fig. 4 Fictitious cells

Fig. 5 Zonal boundary treatment

auxiliary cell surrounding the cell interface $(i+1/2, j)$, and A' in equation (14) denotes the area of the auxiliary cell. Using the first-order derivatives of the velocity components and the sound speed evaluated by the above formulas, the viscous fluxes are given by equations (2) and (3).

Time Integration

For simplicity, equation (8) can be written in the form

$$\frac{dQ}{dt} = W(Q) \tag{16}$$

where W represents the numerical flux vector consisting of the inviscid and viscous fluxes. A three-stage Runge–Kutta scheme (Jameson and Venkatakrishnan, 1985) is applied to integrate the above set of coupled ordinary differential equations in time. In this time-stepping scheme, the solution is advanced from time level n to $n+1$ as

$$Q^{(0)} = Q^n$$
$$Q^{(1)} = Q^{(0)} + \alpha_1 \cdot \Delta t \cdot W(Q^{(0)})$$
$$Q^{(2)} = Q^{(0)} + \alpha_2 \cdot \Delta t \cdot W(Q^{(1)}) \tag{17}$$
$$Q^{(3)} = Q^{(0)} + \alpha_3 \cdot \Delta t \cdot W(Q^{(2)})$$
$$Q^{n+1} = Q^{(3)}$$

with

$$\alpha_1 = 0.21 , \quad \alpha_2 = 0.5 , \quad \alpha_3 = 1.0$$

This scheme is second-order accurate in time for linear equations. In the time stepping, the second terms on the right-hand side of equation (9) and the viscous fluxes are evaluated only at the first stage. In order to accelerate the convergence to steady-state solution, the variable time step determined by the bound on the Courant number is used.

Boundary Conditions

In the present approach, boundaries of a computational domain are constructed of cell interfaces, since the cell-centered finite volume formulation is used. Hence, the boundary conditions must be imposed by the fluxes through the boundaries. In order to evaluate the fluxes through the boundaries in the same way as the fluxes through the interior cell interfaces, fictitious cells are introduced just outside the boundaries, and the values of conserved variables corresponding to the boundary conditions are allocated to the fictitious cells. In addition, the shape of the fictitious cell is assumed to be the same as that of the adjacent interior cell.

Solid Wall Boundary. For the inviscid fluxes, the momentum fluxes due to the pressure remain, but all the other inviscid fluxes vanish. The pressure at the solid wall is set equal to the cell-centered value of pressure at the interior cell adjacent to the wall. Using the fictitious cells shown by dashed lines in Fig. 4, the viscous fluxes at the wall are evaluated by applying
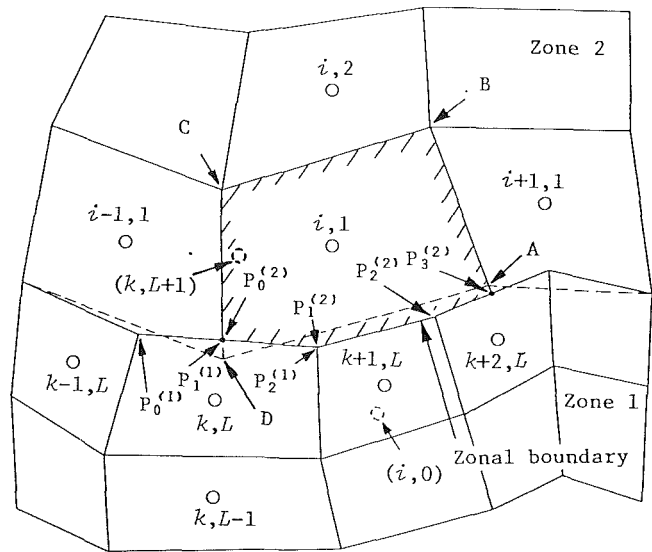
the same scheme as that applied to the interior cell interfaces. To satisfy the no-slip and adiabatic conditions, the cell-centered values at the fictitious cells $(i, 0)$ are specified as follows:

$$u_{i,0} = -u_{i,1} , \quad v_{i,0} = -v_{i,1}$$
$$\rho_{i,0} = \rho_{i,1} , \quad e_{i,0} = e_{i,1} \tag{18}$$

Inflow and Outflow Boundaries. The inviscid and viscous fluxes across the inflow and outflow boundaries are determined by the same scheme as that applied to the interior cell interfaces, using the fictitious cells. This boundary treatment prevents nonphysical reflections at the boundaries, because the inviscid fluxes are evaluated according to the approximate Riemann solver in which the signal propagation properties of the Euler equations are simulated.

At the fictitious cells adjacent to the inflow boundary, the cell-centered, conserved variables are specified as

$$\rho/\rho_1 = 1$$
$$u/a_1 = M_1 \cos \beta_1$$
$$v/a_1 = M_1 \sin \beta_1 \tag{19}$$
$$e/(\rho_1 a_1^2) = \gamma^{-1}(\gamma - 1)^{-1} + M_1^2/2$$

where M is the Mach number, β is the flow angle relative to the axial direction, and the subscript 1 indicates inlet conditions.

At the fictitious cells adjacent to the outflow boundary, the pressure is prescribed, and the density and velocity components are set equal to the cell-centered values of those at the adjacent interior cells.

Zonal Boundary Treatment

In the present zonal approach, a computational domain is divided into nonoverlapping zones, and structured grids are independently generated in each zone. The division of computational domain introduces new boundaries referred to as "zonal boundaries." The emphasis in this paper is on the treatment of the zonal boundaries.

Uniqueness of Zonal Boundary. Consider the composite zonal grid system shown in Fig. 5. If the zonal boundary is not straight, the independent generation of zonal grids causes overlap and clearance between two zones, which means that the two zonal boundaries defined in each zone do not coincide
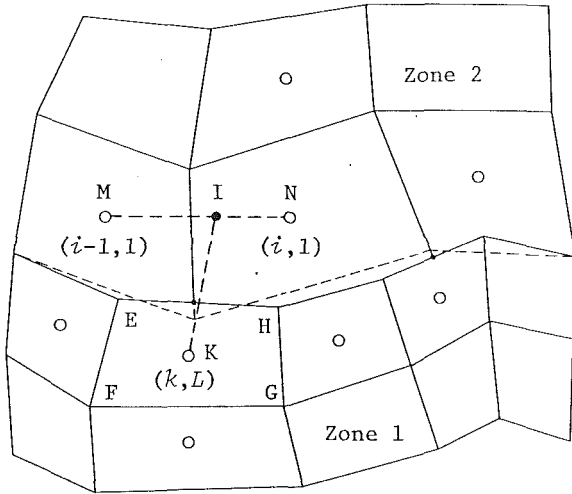
Fig. 6 Interpolation for fictitious cells at zonal boundary

Fig. 7 Flux conservation at zonal boundary

spatially with each other. In order to avoid the fact, the common zonal boundary between the two zones is defined by the boundary of one zone, zone 1 in Fig. 5. Consequently, for the cell $(i, 1)$ of zone 2 in Fig. 5, the cell area must be evaluated by the polygon $P_0^{(2)} P_1^{(2)} P_2^{(2)} P_3^{(2)} BC$ rather than by the quadrilateral $ABCD$, and the length of the cell side $(i-1/2, 1)$ must be evaluated by the line segment $CP_0^{(2)}$ rather than by the line segment CD. It should be noted that this uniqueness of the zonal boundary is important to the flux conservation across the zonal boundary.

The cells adjacent to the zonal boundary, such as the cell (k, L) of zone 1 and the cell $(i,1)$ of zone 2 in Fig. 5, will be referred to as "zonal cells" in the following. To treat the zonal cells in the same way as the interior cells, the fictitious cells are introduced just outside the zonal boundary.

Inviscid Fluxes at Zonal Boundary.   In order to apply the projection defined by equation (9) to the zonal cells, it is necessary to find the cell-centered values of conserved variables at the fictitious cells adjacent to the zonal cells. At the fictitious cell $(k, L+1)$ adjacent to the zonal cell (k, L) of zone 1 in Fig.5, the cell-centered value $Q_{k, L+1}^{(1)}$ is estimated by interpolating the value at point I shown in Fig. 6 as follows:

$$Q_{k, L+1}^{(1)} = (l_N Q_{i-1, 1}^{(2)} + l_M Q_{i, 1}^{(2)})/(l_M + l_N) \qquad (20)$$

where $l_M = \overline{IM}$ and $l_N = \overline{IN}$. As shown in Fig. 6, the point I is defined as the intersection of the line segment MN and the extension from the cell center (k, L) toward the following direction:

$$\mathbf{KI}/|\mathbf{KI}| = (\mathbf{FE} + \mathbf{GH})/|\mathbf{FE} + \mathbf{GH}| \qquad (21)$$

In the above, the superscripts (1) and (2) represent the values at zone 1 and zone 2, respectively. The cell-centered values at the fictitious cells adjacent to the zonal cells of zone 2, such as at the fictitious cell $(i, 0)$, are interpolated in the same manner.

In the case of Fig. 5, the inviscid fluxes across the zonal boundary are evaluated by applying the evolution defined by equation (12) to the zonal cell interfaces of zone 1, because the zonal boundary is defined by the boundary of zone 1. For the evolution at an interface $(k, L+1/2)$ of a zonal cell (k, L), the left state at the interface, $Q_{k, L+1/2}^{-(1)}$, is given by the projection in zone 1, but the right state, $Q_{k, L+1/2}^{+(1)}$, is not known. The right states at the zonal cell interfaces of zone 2 adjacent to the cell (k, L), $Q_{i-1, 1/2}^{+(2)}$ and $Q_{i, 1/2}^{+(2)}$, are given by the projections in zone 2, however. Therefore, using $Q_{i-1, 1/2}^{+(2)}$ and $Q_{i, 1/2}^{+(2)}$, $Q_{k, L+1/2}^{+(1)}$ can be estimated as
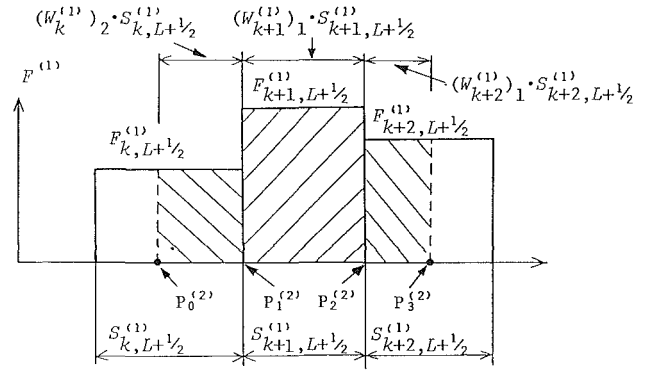
$$Q_{k, L+1/2}^{+(1)} = \sum_{m=1}^{M_k^{(1)}} (W_k^{(1)})_m \cdot Q_{i_0(k)+m-1, 1/2}^{+(2)} \qquad (22)$$

where $(W_k^{(1)})_m$ denotes the interpolation coefficient defined by

$$(W_k^{(1)})_m = \overline{P_m^{(1)} P_{m-1}^{(1)}}/S_{k, L+1/2}^{(1)} \qquad (23)$$

$$S_{k, L+1/2}^{(1)} = \sum_{m=1}^{M_k^{(1)}} \overline{P_m^{(1)} P_{m-1}^{(1)}} \qquad (24)$$

In the above, $i_0(k)$ denotes the index number of the zonal cell of zone 2 adjacent to the vertex $P_0^{(1)}$ of the zonal cell (k, L), i.e., $i_0(k) = i-1$ in Fig. 5, m is the local number of the line segment $P_m^{(1)} P_{m-1}^{(1)}$ in the cell (k, L), and $M_k^{(1)}$ is the total of number of line segments, i.e., $M_k^{(1)} = 2$ for the cell (k, L) in Fig. 5. Consequently the application of the evolution to the left state $Q_{k, L+1/2}^{-(1)}$ given by the projection in zone 1 and the right state $Q_{k, L+1/2}^{+(1)}$ estimated by equation (22) yields the inviscid fluxes $H_{k, L+1/2}^{(1)}$ across the zonal boundary.

Viscous Fluxes at Zonal Boundary.   The viscous fluxes across the zonal boundary, too, are evaluated at the zonal cell interfaces $(k, L+1/2)$ of zone 1 in Fig. 5. The cell-centered values at the adjacent fictitious cells $(k, L+1)$ are given by equation (20), and so the viscous fluxes $R_{k, L+1/2}^{(1)}$ can be determined by the same scheme as that applied to the interior cell interfaces. It should be noted that the introduction of the fictitious cells simplifies the evaluation of the inviscid and viscous fluxes at the zonal boundary.

Flux Conservation Across Zonal Boundary.   In Fig. 5, the numerical fluxes at the zonal cell interfaces $(k, L+1/2)$ of zone 1, $F_{k, L+1/2}^{(1)}$, which consist of the inviscid and viscous fluxes, are given according to the procedures described above. Hence, equation (8) can be applied to the zonal cells (k, L) of zone 1. On the other hand, to apply equation (8) to the zonal cells $(i, 1)$ of zone 2, the fluxes across the zonal cell interfaces $(i, 1/2)$, $F_{i, 1/2}^{(2)}$, must be found. It should be noted that the conservation of the fluxes has to be satisfied across the zonal boundary. In the present approach, the flux conservation across the zonal boundary is satisfied by interpolating $F_{i, 1/2}^{(2)}$ in the following manner: As shown in Fig. 7, assuming that the fluxes known at the zonal cell interfaces $(k, L+1/2)$ of zone 1, $F_{k, L+1/2}^{(1)}$, are constant along each interface, the value of $(SF)_{i, 1/2}^{(2)}$ is set equal to the shaded area shown in Fig. 7, that is, $(SF)_{i, 1/2}^{(2)}$ is evaluated as

DO $k = 1, K$; DO $m = 1, M_k^{(1)}$

$i = $ Table $^{(1)}(k, m)$

$$(SF)_{i, 1/2}^{(2)} = (SF)_{i, 1/2}^{(2)} - (W_k^{(1)})_m \cdot (SF)_{k, L+1/2}^{(1)} \qquad (25)$$

DO END

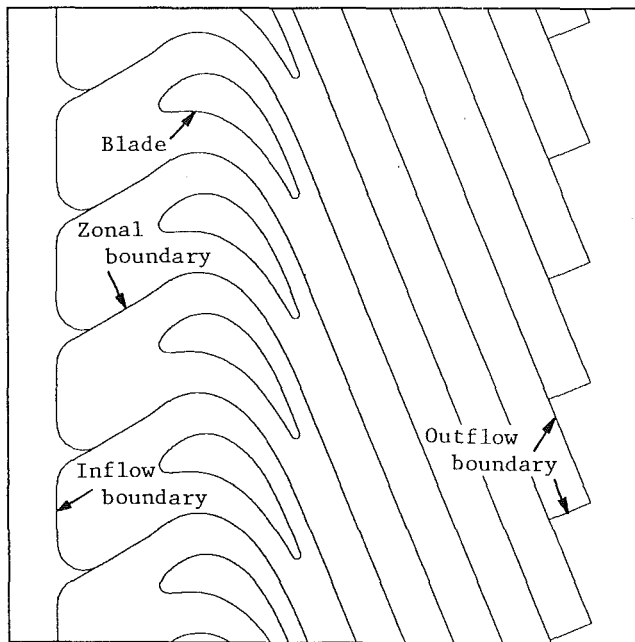where Table$^{(1)}(k, m)$ gives the index number i of the zonal cell
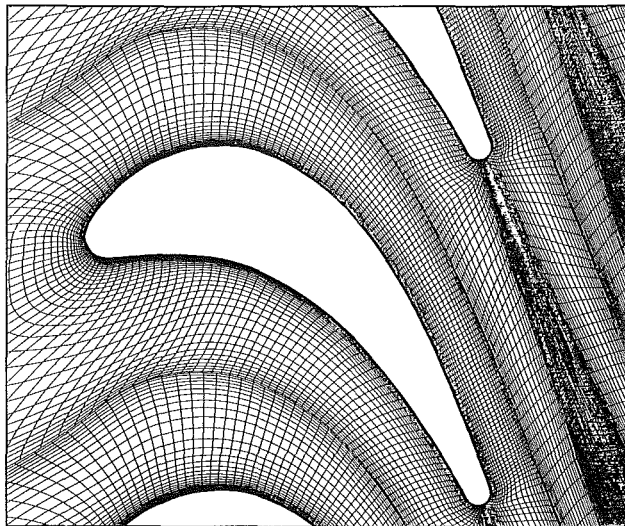
Fig. 8 Computational domain

Fig. 9 Composite zonal grid

Table 1 Computational conditions

	Case 1	Case 2	Case 3
Reynolds number Re_2	7.8×10^5	9.0×10^5	8.0×10^5
Inlet flow angle β_1	$30°$	$30°$	$30°$
Inlet Mach numbe $.M_1$	0.268	0.270	0.282
Isentropic exit Mach number $M_2$is	0.985	1.11	1.34

(a) Density contours
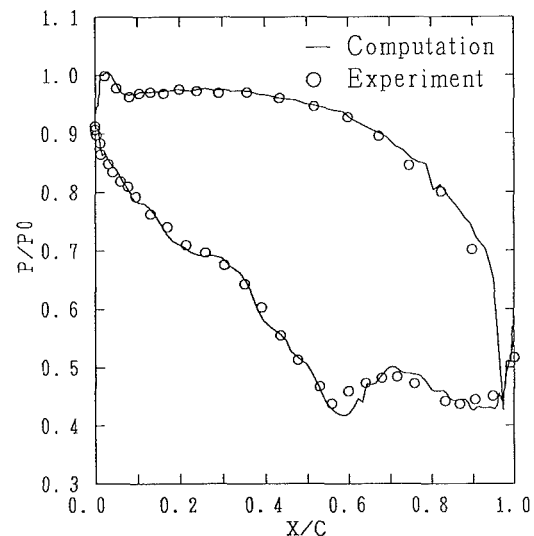
(b) Blade surface pressure distribution

Fig. 10 Computational results for Case 1 with the zonal grid

of zone 2 adjacent to the line segment $P_m^{(1)}P_{m-1}^{(1)}$ in the zonal cell (k, L) of zone 1.
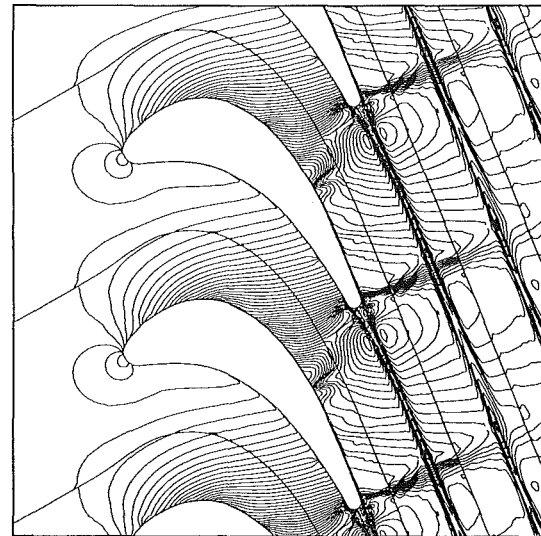
Numerical Examples

Numerical results are presented for two-dimensional flows through a transonic turbine cascade tested experimentally in four European wind tunnels (Sieverding, 1973; Lehthaus, 1978; Kiock et al., 1986). The computational domain and grid are shown in Figs. 8 and 9, respectively. A composite zonal grid system with a C-type grid is generated, in which the periodic boundaries are treated as the zonal boundaries, that is, in which the grid lines are discontinuous at the periodic boundaries. The total number of computational cells is $446*50$, and the numbers of cells on the pressure and suction surfaces are 70 and 120, respectively. The minimum grid spacing at the wall is $1*10^{-5}$ chord length. Computational conditions are summarized in Table 1, where the Reynolds number, Re_2, is based on the chord length and the exit conditions.

Density contours and blade surface pressure distributions computed by the present zonal approach are shown in Figs. 10, 11, and 12 for Cases 1, 2, and 3, respectively, where the surface pressure distributions normalized by the inlet stagnation pressure are compared with experimental results (Sieverding, 1973; Lehthaus, 1978; Kiock et al., 1986). It is found that the fully conservative nature of the present approach permits the smooth transition of shock waves across the zonal boundaries. The appearance of the shock waves at the zonal

(a) Density contours
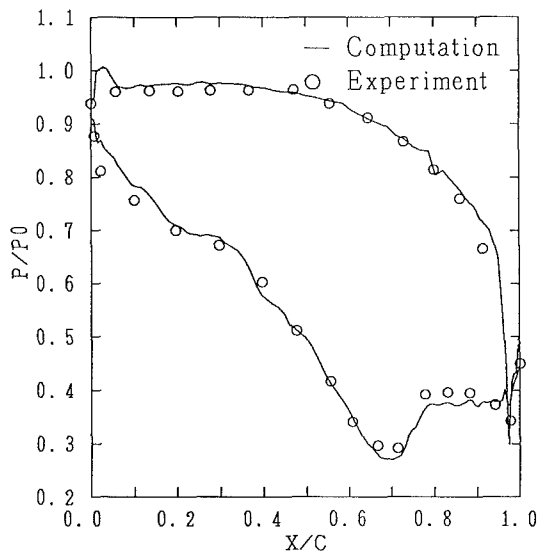
(a) Density contours

(b) Blade surface pressure distribution

Fig. 11 Computational results for Case 2 with the zonal grid

(b) Blade surface pressure distribution

Fig. 12 Computational results for Case 3 with the zonal grid

boundaries caused no numerical instability in the present calculations, which results from the use of the TVD formulation and the satisfaction of the complete flux conservation across the zonal boundaries.The computed surface pressure distributions are in excellent agreement with the experimental results except for a separation region on the suction surface near the trailing edge for Case 3. Hence, the present zonal approach is found to be a highly accurate formulation. The discrepancy between the computational and experimental results in the separation region for Case 3 may be due to the application for the Baldwin–Lomax turbulence model to the separation region and due to the unsteadiness caused by the separation.

Figure 13 is a Schlieren picture for Case 1 (Kiock et al., 1986), which shows shock waves at around 60 percent chord and the trailing edge on the suction surface. These two shocks are well captured in the computation using the present zonal approach as shown in Fig. 10. The Navier–Stokes solver with the highly accurate TVD, finite volume formulation has been applied to the nonzonal grid shown in Fig. 14, which is a conventional C-type grid with the periodic continuity of grid lines. In this periodic C-type grid, the total number of com-

Fig. 13 Schlieren picture for Case 1 (Kiock et al., 1986)

Fig. 14 Periodic C-type grid

Fig. 16 Velocity vectors in separation region for Case 3 with the zonal grid

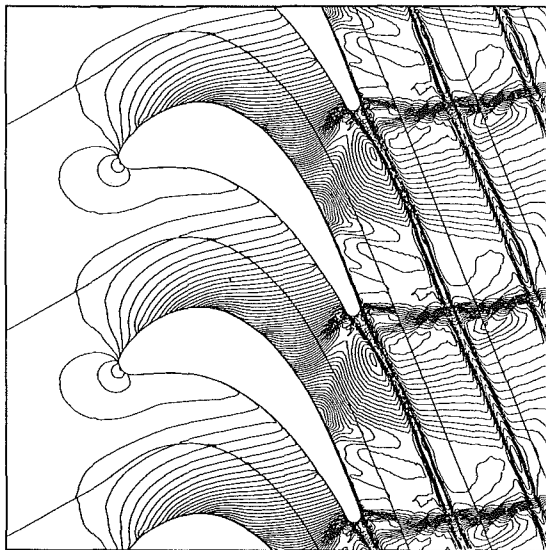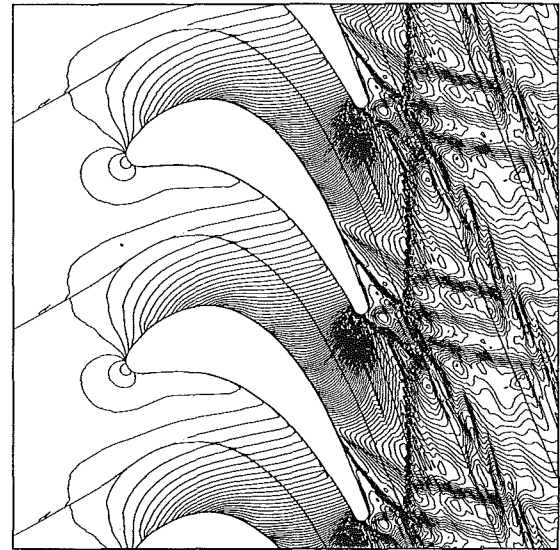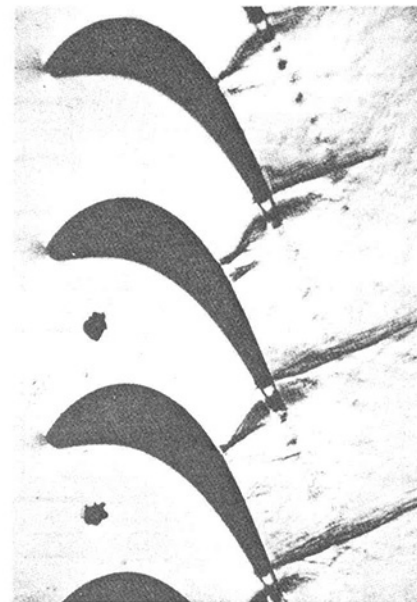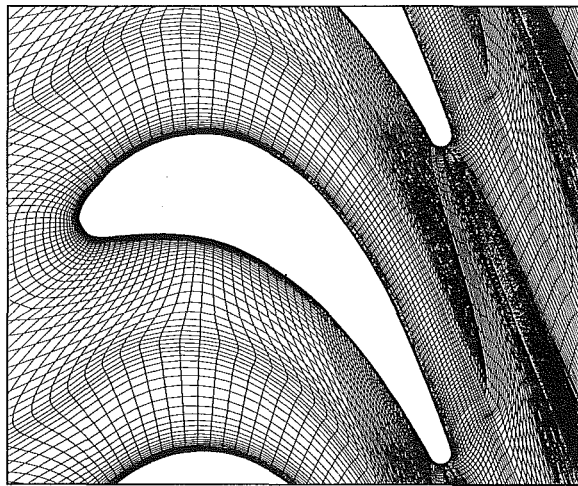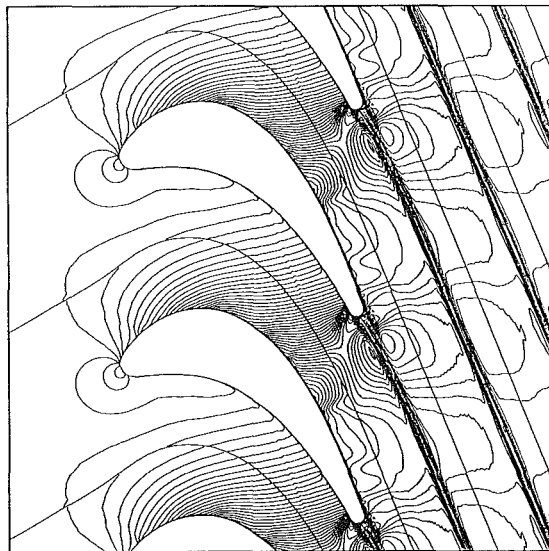(a) Density contours
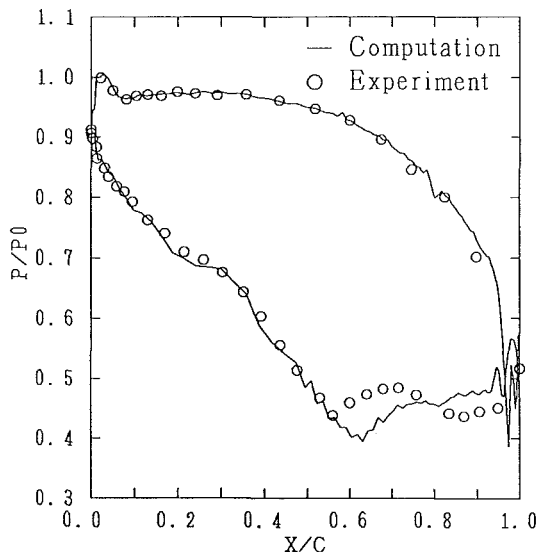
(b) Blade surface pressure distribution

Fig. 15 Computational results for Case 1 with the periodic C-type grid

putational cells, the number of cells on the blade surface, and the minimum grid spacing at the wall are equal to those of the zonal grid shown in Fig. 9. Computational results for Case 1 with the periodic C-type grid are shown in Fig. 15. In contrast to the results for the zonal grid, Fig. 10, the two shock waves on the suction surface are not captured, and a large discrepancy between the computational and experimental results exists in the suction surface pressure distribution. These are caused by skewness of the periodic C-type grid.

The separation region for Case 3 is clearly shown by velocity vectors in Fig. 16. The transition of the separation region across the zonal boundary is found to be smooth. Figures 17(a) and 17(b) show velocity vectors near a zonal boundary, which are computed with and without the uniqueness of the zonal boundary. Distortions of the solution exist near the zonal boundary without the uniqueness. It should be noted that the distortions of the solution are inhibited by ensuring the uniqueness of the zonal boundary.

The computed and measured cascade performance is compared as a function of exit Mach number in Fig. 18. The computed performance is evaluated by transferring an inhomogeneous flow solution at the outflow boundary to a hypothetical state of homogeneous flow using the laws of conservation. Reasonable agreement exists between the computed and measured cascade performance.

Concluding Remarks

A new zonal approach for the computation of compressible viscous flows in cascades has been developed. In the present approach, a highly accurate TVD, finite volume formulation with a composite zonal grid system is implemented in order to produce a Navier–Stokes solver with robustness and high accuracy for the prediction of cascade performance. The inviscid fluxes at interfaces of computational cells are evaluated using the highly accurate TVD scheme based on the MUSCL-type approach with Roe's approximate Riemann solver, which makes the present approach robust.

To simplify the generation of grids without skewness, a composite zonal grid system is adopted, where the zonal boundaries are constructed of cell interfaces, and communication from one zone to the other is accomplished by numerical fluxes across the zonal boundaries. The complete conservation of the numerical fluxes at the zonal boundary can be satisfied by directly evaluating the fluxes using the finite volume for-
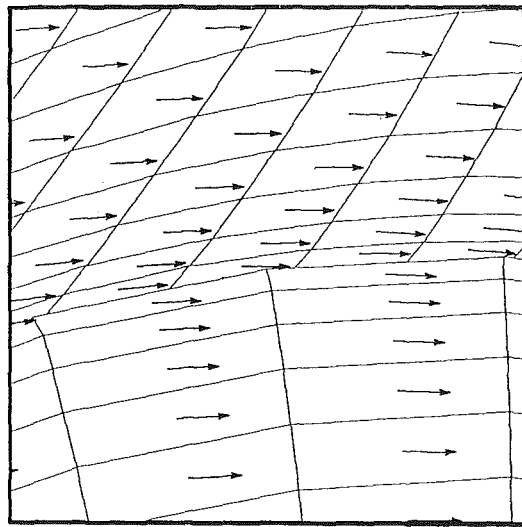
(a) With uniqueness of zonal boundary
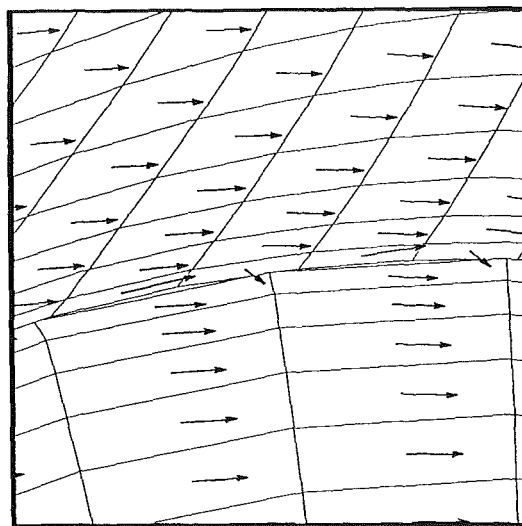
(b) Without uniqueness of zonal boundary

Fig. 17 Velocity vectors near zonal boundary for Case 1

(a) Loss coefficient

(b) Exit flow angle

Fig. 18 Computed and measured cascade performance

mulation and by ensuring the uniqueness of the zonal boundary. This complete conservation results in the highly accurate nature of the present zonal approach. In addition, it is easy to implement the present treatment of the zonal boundary owing to the introduction of the fictitious cells just outside the zonal boundary.

Numerical examples have been presented for viscous flows through a transonic turbine cascade. In the present examples, a composite zonal grid system with a C-type grid is used, where the periodic boundaries are treated as the zonal boundaries. Further investigation is needed on optimization of zoning.

References

Anderson, W. K., Thomas, J. L., and van Leer, B., 1985, "A Comparison of Finite Volume Flux Vector Splittings for the Euler Equations," AIAA Paper No. 85-0122.

Baldwin, B. S., and Lomax, H., 1978, "Thin Layer Approximation and Algebraic Model for Separated Turbulent Flow," AIAA Paper No. 78-257.

Benek, J. A., Buning, P. G., and Steger, J. L., 1985, "A 3-D Chimera Grid Embedding Technique," AIAA Paper No. 85-1523.

Bush, R. H., 1985, "External Compression Inlet Predictions Using an Implicit Upwind, Multiple Zone Approach," AIAA Paper No. 85-1521.

Chakravarthy, S. R., and Osher, S., 1985, "A New Class of High Accuracy TVD Schemes for Hyperbolic Conservation Laws," AIAA Paper No. 85-0363.

Chakravarthy, S. R., Szema, K.-Y., Goldberg, U. C., Gorski, J. J., and

Osher, S., 1985, "Application of a New Class of High Accuracy TVD Schemes to the Navier–Stokes Equations," AIAA Paper No. 85-0165.

Chakravarthy, S. R., 1986, "The Versatility and Reliability of Euler Solvers Based on High-Accuracy TVD Formulations," AIAA Paper No. 86-0243.

Chima, R. V., 1985, "Inviscid and Viscous Flows in Cascades With an Explicit Multiple-Grid Algorithm," *AIAA Journal*, Vol. 23, No. 10, pp. 1556–1563.

Chima, R. V., 1987, "Explicit Multigrid Algorithm for Quasi-Three-Dimensional Viscous Flows in Turbomachinery," *Journal of Propulsion and Power*, Vol. 3, No. 5, pp. 397–405.

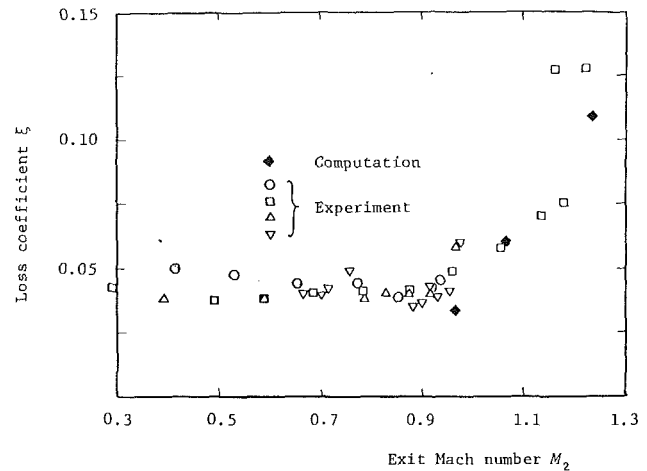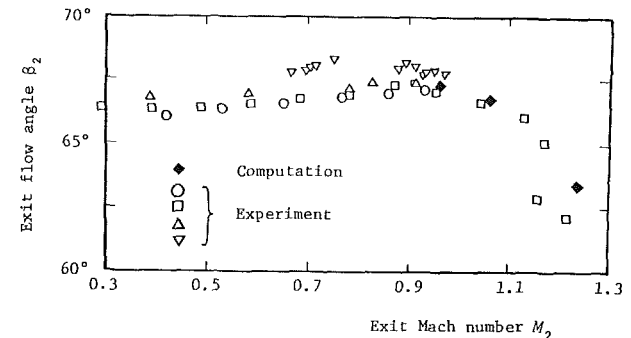Dawes, W. N., 1987, "A Numerical Analysis of the Three-Dimensional Viscous Flow in a Transonic Compressor Rotor and Comparison With Experiment," ASME JOURNAL OF TURBOMACHINERY, Vol. 109, No. 1, pp. 83–90.

Davis, R. L., Ni, R. H., and Carter, J. E., 1987, "Cascade Viscous Flow Analysis Using the Navier–Stokes Equations," *Journal of Propulsion and Power*, Vol. 3, No. 5, pp. 406–414.

Harten, A., 1983, "High Resolution Schemes for Hyperbolic Conservation Laws," *Journal of Computational Physics*, Vol. 49, pp. 357–393.

Jameson, A., and Venkatakrishnan, V., 1985, "Transonic Flows About Oscillating Airfoils Using the Euler Equations," AIAA Paper No. 85-1514.

Kiock, R., Lehthaus, F., Baines, N. C., and Sieverding, C. H., 1986, "The Transonic Flow Through a Plane Turbine Cascade as Measured in Four European Wind Tunnels," ASME *Journal of Engineering for Gas Turbines and Power*, Vol. 108, No. 2, pp. 277–284.

Kwon, O. K., 1988, "Navier–Stokes Solution for Steady Two-Dimensional Transonic Cascade Flows," ASME JOURNAL OF TURBOMACHINERY, Vol. 110, No. 3, pp. 339–346.

Lehthaus, F., 1978, "Berechnung der transsonischen Stromung durch ebene Turbinengitter nach dem Zeit-Schritt-Verfahren," *VDI-Forschungsheft 586*, pp. 5–24.

Nakahashi, K., Nozaki, O., Kikuchi, K., and Tamura, A., 1987, "Navier–Stokes Computations of Two- and Three-Dimensional Cascade Flow Fields," AIAA Paper No. 87-1315.

Nakahashi, K., and Obayashi, K., 1987, "FDM-FEM Zonal Approach for Viscous Flow Computations Over Multiple-Bodies," AIAA Paper No. 87-0604.

Norton, R. J. G., Thompkins, W. T., and Haimes, R., 1984, "Implicit Finite Difference Schemes With Non-simply Connected Grids—A Novel Approach," AIAA Paper No. 84-0003.

Rai, M. M., 1984, "A Conservative Treatment of Zonal Boundaries for Euler Equation Calculations," AIAA Paper No. 84-0164.

Rai, M. M., 1987, "Unsteady Three-Dimensional Navier–Stokes Simulations of Turbine Rotor–Stator Interaction," AIAA Paper No. 87-2058.

Roe, P. L., 1981, "Approximate Riemann Solvers, Parameter Vectors, and Difference Schemes," *Journal of Computational Physics*, Vol. 43, pp. 357–372.

Schafer, O., Fruhauf, H.-H., Bauer, B., and Guggolz, M., 1986, "Application of a Navier–Stokes Analysis to Flows Through Plane Cascades," ASME *Journal of Engineering for Gas Turbines and Power*, Vol. 108, No. 1, pp. 103–111.

Sieverding, C. H., 1973, "Experimental Data on Two Transonic Turbine Blade Sections and Comparison With Various Theoretical Methods," in: *Transonic Flows in Turbomachinery*, VKI LS 59.

Van Leer, B., 1985, "Upwind-Difference Methods for Aerodynamic Problems Governed by the Euler Equations," *Lectures in Applied Mathematics*, Vol. 22, Part 2, pp. 327–336.

Van Leer, B., Thomas, J. L., Roe, P. L., and Newsome, R. W., 1987, "A Comparison of Numerical Flux Formulas for the Euler and Navier–Stokes Equations," AIAA Paper No. 87-1104.

Vatsa, V. N., Thomas, J. L., and Wedan, B. W., 1987, "Navier–Stokes Computations of Prolate Spheroids at Angle of Attack," AIAA Paper No. 87-2627.

Weinberg, B. C., Yang, R. J., McDonald, H., and Shamroth, S. J., 1986, "Calculation of Two and Three-Dimensional Transonic Cascade Flow Fields Using the Navier–Stokes Equation," ASME *Journal of Engineering for Gas Turbines and Power*, Vol. 108, No. 1, pp. 93–102.

Yamamoto, S., Daiguji, H., and Ishigaki, H., 1988, "An Implict Time-Marching Scheme for Solving the Compressible Navier–Stokes Equations," in: *Computational Fluid Dynamics*, G. D. V. Davis and C. Fletcher, eds., Elsevier Science Publishers B.V., North-Holland.

Yee, H. C., and Harten, A., 1987, "Implicit TVD Schemes for Hyperbolic Conservation Laws in Curvilinear Coordinates," *AIAA Journal*, Vol. 25, No. 2, pp. 266–274.

W. Steinert

Institut für Antriebstechnik,
5000 Köln 90, Federal Republic of Germany

B. Eisenberg

MAN Gutehoffnungshütte AG, Oberhausen,
4200 Oberhausen, Federal Republic of
Germany

H. Starken

Institut für Antriebstechnik,
5000 Köln 90, Federal Republic of Germany

Design and Testing of a Controlled Diffusion Airfoil Cascade for Industrial Axial Flow Compressor Application

Similar to jet engine development, modern design methods are used today to improve the performance of industrial compressors. In order to verify the loading limits, a cascade profile representative for the first rotor hub section of an industrial compressor has been designed by optimizing the suction surface velocity distribution using a direct boundary layer calculation method. The blade shape was computed with an inverse full potential code and the resulting cascade was tested in a cascade wind tunnel. The experimental results confirmed the design intent and resulted in a low loss coefficient of 1.8 percent at design condition and an incidence range of nearly 12 deg (4 percent loss level) at an inlet Mach number of 0.62.

I Introduction

Modern axial-flow compressors for industrial applications are characterized by the fact that they are always adapted to the specific requirements of the downstream process. While gas turbine compressors as a rule are operated along a performance curve, which follows the pattern of a throttle curve in the performance map, industrial compressors generally must permit large mass flow variations. Therefore, it is often found that industrial compressors have to operate at design points with variations between 65 and 110 percent of the design mass flow, at constant pressure ratio. At the same time, a compromise must be found between the highest possible efficiency and an economic pressure ratio per stage.

The development of industrial axial-flow compressors from MAN GHH [1] therefore centers around the following main aspects:

- large variations in pressure ratio and flow volume for adaption to the process conditions
- high efficiency for reducing energy costs
- minimum size and maximized operational reliability

To satisfy these requirements, the various blade rows of the compressor stages must be so designed as to provide the largest possible working range between choking and separation at highest possible inlet Mach number. While the low loss range decreases with rising Mach number, a lower Mach number means larger compressor units. Therefore, an acceptable compromise has to be found between size and operating range. This leads to blading designs in a Mach number range where the influence of incidence on profile losses is comparatively low.

Axial-flow compressors of this type therefore are still using profile configurations with a subsonic inlet flow over the full blade length, because any transonic inlet flow would cause additional losses in efficiency by shock waves and would narrow the working range.

Although a transonic design would reduce the unit size, it would still mean a lower efficiency, which cannot be tolerated in the present energy situation.

On account of these conditions and in contrast to the design of gas turbine compressors, the stage pressure ratio to be selected is still comparatively low. Furthermore, low tip speeds are limiting the maximum volume that can pass through the compressor inlet. To achieve the greatest possible volumetric throughflow, a fixed size of the casing has to be chosen for reasons of cost. Therefore, industrial axial flow compressors are nowadays being built with a small hub/tip ratio around 0.45.

This, however, limits the maximum number of blades that can be arranged on the rotor hub. As a result, the pitch/chord ratios in the outer sections are relatively high so that an optimal flow through the blade rows is very difficult to achieve. For this reason the outer sections are designed with comparatively small deflections. If the stage is additionally designed for constant energy transfer over the blade length, the low tip speed and long blades will produce high aerodynamic blade loads on the hub.

Since industrial axial-flow compressors must be able to cope with a wide working range, every effort is made to locate operating points very near to the surge line. Special controls have been developed for this, which allow the compressor to run along an operating line parallel to the surge line with a margin of approximately 8–10 percent. The blade strength must be sufficient to provide adequate safety against an occasional crossing of the surge line. On account of the three aspects

---

referred to above, i.e., large pitch/chord ratio, large profile thickness for reasons of strength, and high deflection, the profiles of the hub sections in industrial axial-flow compressors are subjected to the highest loads with respect to the diffusion factor.

As part of ongoing optimization efforts of axial-flow compressors, a front stage has been developed with the aid of advanced design methods. Requirements to be satisfied by the blading were as follows:

- higher stage pressure ratio in the front stage
- improved off-design performance
- higher efficiency

To meet these requirements, the blade sections were to be designed by methods that permit controlled diffusion along the blade surfaces. These methods allow an optimization of suction and pressure side velocities in such a way that a boundary layer separation is avoided.

II Cascade Design

Transferred to the cascade design, the above requirements for the blading led to the following aspects:

- high loading
- large incidence range
- separation-free profile boundary layers

To meet these demands, modern design methods have to be used for the profile development to permit the velocity distribution inside the blade passage to be prescribed.

Besides the mode of solving the flow field equations (potential theory, Navier–Stokes), these methods can be subdivided into direct and inverse calculation methods. In the direct approach, the flow field is fully described by the specified cascade geometry and the flow conditions upstream and downstream of the cascade.

The inverse design method is based on the velocity distribution on the profile surfaces. These given data, the required pitch/chord ratio, and the inlet/exit flow conditions permit the associated flow channel to be defined (Fig. 1). The inverse design method requires multiple variations of the velocity distribution until an acceptable profile geometry is obtained.

The answer to the question as to which of the two methods—direct approach by specifying the geometry with subsequent variation, or inverse approach based on a given velocity distribution—would be more suitable depends on the respective application. Where a completely new cascade design is to be developed, the inverse method is well suited if no experience is available with the cascade configuration. Unlike in the direct design practice, this permits a velocity distribution to be used in all iterations, which offers optimum properties as far as its boundary layer behavior is concerned. If, however, the profile geometry must be modified for reasons of strength, the direct method is the superior one. A typical example would be the leading edge radius, which is generally prescribed by a certain size. The direct methods are also required for determining the off-design performance.

The design project under consideration used a combination of both methods. Within a research project of "Forschungsvereinigung Verbrennungskraftmaschinen e.V." (FVV) [2–5], an inverse and a direct calculation method for high inlet flow Mach numbers in the subsonic range were provided.

Fig. 1 Calculated iso-Mach lines of MAN GHH 1-S1 cascade

The inverse method was developed by E. Schmidt at Stuttgart University [6, 7]. It is used for calculating the steady compressible potential flow of a channel of unknown configuration. The velocity field is determined by solving the potential equation with finite differences, making full allowance for the change in type of differential equation (elliptical–hyperbolic). This approach permits the design of profiles with high subsonic inlet flow Mach numbers where local supersonic areas are formed on the profile surfaces. By prescribing an appropriate velocity distribution, compression shocks can be reduced in their effect or even be fully avoided. Allowance for the variation of the axial velocity density ratio is made by the introduction of a variable thickness stream layer. A distinction is made in this regard between the blockage effect of the side walls and the downstream wake region. The final metal contour is determined by subtracting the displacement thickness from the channel contour determined by the potential method. For this purpose, the integral boundary layer method of McNally [8] is applied. The same method is used to optimize the prescribed velocity distribution required as input into the inverse method. The design under consideration was performed on a cylindrical stream surface. Meanwhile the method has been extended also to include axisymmetric stream surfaces with variable radii for both rotors and stators [9].

The direct calculation program is based on a flux-finite-element method originally developed in 1978 by Lucchi and Schmidt [10]. This method was adapted to industrial use by "Deutsche Forschungsanstalt für Luft und Raumfahrt e.V." (DLR) [2–5, 11]. It predicts the cascade flow using potential flow theory together with the artificial density concept in supersonic flow areas. It was extended by adding the abovementioned boundary layer and a mixing calculation in an iterative mode. The effect of the boundary layer on the flow field is determined by adding the calculated displacement thicknesses to the metal profile. The present version allows local supersonic

---

Nomenclature

c = chord length
H_{12} = boundary layer shape factor
M = Mach number
p = static pressure
p_t = total pressure
t/c = pitch-to-chord ratio
x = coordinate in chordwise direction

β = flow angle with reference to circumferential direction
β_s = stagger angle with reference to circumferential direction
η = coordinate in circumferencial direction

ω = total pressure loss coefficient $= (p_{t1} - p_{t2}) / (p_{t1} - p_1)$
Ω = axial velocity density ratio (AVDR)
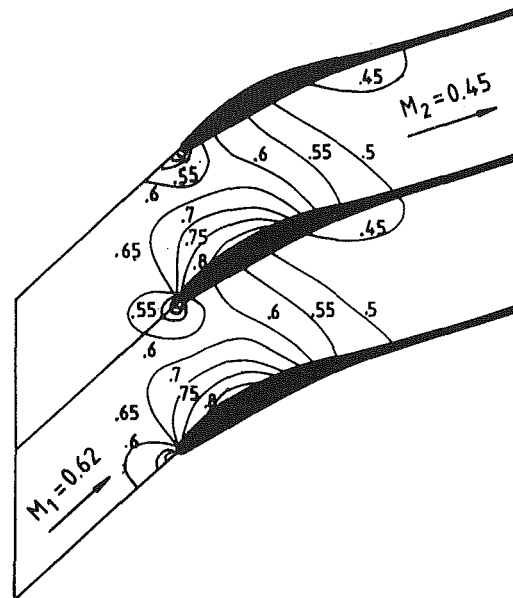
Subscripts

1 = inlet plane
2 = outlet plane

Fig. 2 Definition of cascade inlet and exit flow conditions

Fig. 4 Shape factor development on suction side

Fig. 3 Mach number distribution of design and direct calculation

Fig. 5 Cross-sectional view of transonic cascade wind tunnel

areas up to maximum. Mach numbers around $M = 1.3$ as well as weak compression shocks resulting from this. The AVDR influence is included in the calculation. The exit flow angle is determined iteratively by varying β_2 until suction and pressure surface velocity distributions meet at the trailing edge. A calculated result of the design point of this cascade with the iso-Mach lines is shown in Fig. 1.

Design calculations of the first stage of the related test compressor have shown that the hub section was subject to the highest aerodynamic loading. The requirements for this section were as follows:

M_1 = 0.62	M_2 = 0.45	β_s = 120.0 deg
β_1 = 137 deg	β_2 = 110.6 deg	
t/c = .68	Ω = 1.1	

The definitions of the above data are presented in Fig. 2.

Preliminary strength assessments of the required maximum profile thickness resulted in a value of 11 percent of the chord length. The initial velocity distribution was selected in such a way that the boundary layer was kept laminar as long as possible in order to reduce the minimum loss level. Behind the transition point at about 40 percent of chord a decreasing velocity gradient ensured a separation free turbulent diffusion up to the trailing edge. Having adjusted the velocity distribution to the required circulation and profile thickness, the Mach number distribution of Fig. 3 was obtained.

A precise determination of the profile contour may be problematic in certain cases, due to the fact that the velocities of the profile surfaces are specified in advance and that the profile is to be determined from the geometric difference between two

calculated periodic stream lines. The pronounced velocity gradients at the profile leading edge require a good adaption of the flow field in this area. Therefore in a recent program version the leading edge region is calculated by multiple grid refinement. Due to limited calculation time and storage capacity, the present design was performed using a simplified grid at the leading edge. The final geometry of the front section was then determined with the aid of the direct calculation program providing a leading edge radius for manufacturing.

In the design process the optimization of the loading was performed by increasing the suction surface diffusion until the boundary layer calculation approached separation, which was checked by the shape factor H_{12}. Therefore the loading limits were not determined by conventional parameters (diffusion factor, de Haller number) rather than by the boundary layer behavior. Regarding the shape factor development, it is important to notice that the boundary layer calculation using the inverse design velocity distribution was free from separation with a criterion selected as $H_{12} > 2.5$. The direct-calculation, however, indicated a rise in the shape factor near the trailing edge (Fig. 4) to a value of 2.8, which is beyond the separation criterion. Even though both methods are using the same boundary layer code, the results are different. The reason for this is the different approach used in the calculation methods. In the design process starting with the inverse velocity distribution, the boundary layer displacement thickness is subtracted from the potential profile. The resulting profile, called the "metal profile," is used as input into the direct calculation. Due to the reduced rear thickness, the diffusion of this profile is higher, resulting in thicker boundary layers and higher shape factors.
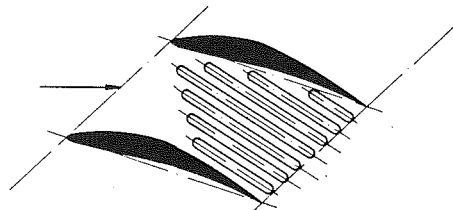
Fig. 6 Side wall suction slots
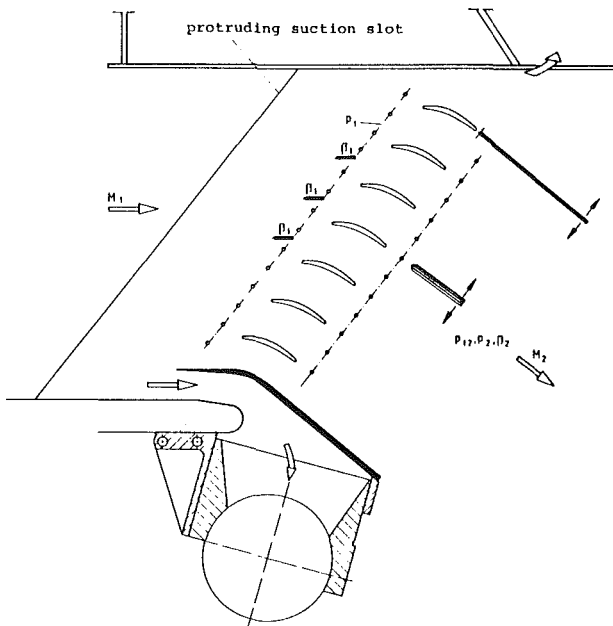
Fig. 7 Test section arrangement
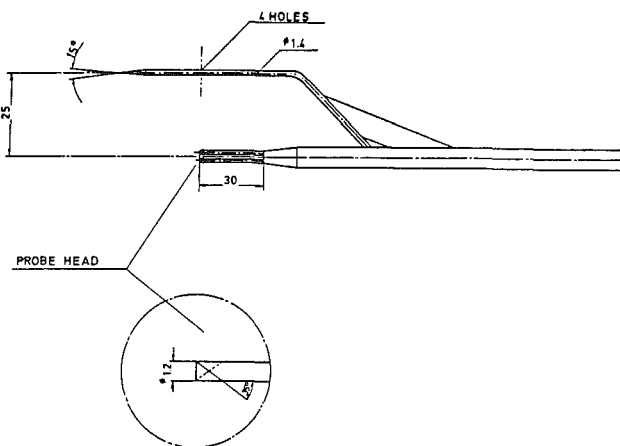
Fig. 8 Combined downstream probe

Fig. 9 Loss development with Mach number at positive incidences
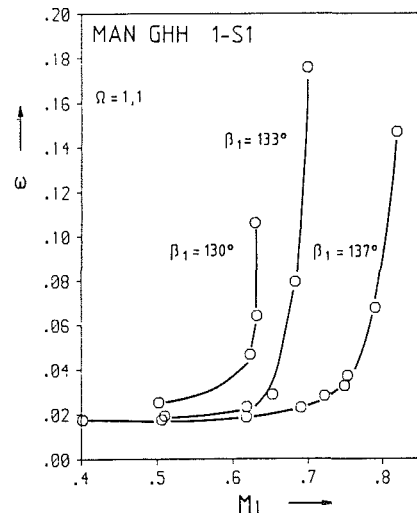
Fig. 10 Loss development at design and negative incidences

In the present case the direct calculation therefore predicts suction surface separation near the trailing edge.

After finishing the design process, it was not clear whether or not the profile was free from separation at the design point. For this reason, an experimental verification was carried out, which also provided the actual operating range of the cascade.

III Facility and Measurement Technique

The cascade wind tunnel is a continuously running facility operating in a closed loop driven by two radial flow compressors with a flow capacity of 10 m^3/s each. One of these compressors is connected to the suction system, which is used to reduce the upstream side wall boundary layer through protruding slots, to adjust the periodicity by controlling the outer passage pressure recovery, and to vary the axial velocity density ratio through slotted side walls.

The pressure ratio of 4 renders a possible Mach number range from 0.2 to 1.4 and a variation of the axial velocity density ratio even at supersonic inlet velocities. The cascade span is 168 mm and the cascade height can be varied between 150 mm and 450 mm. Figure 5 shows a cross section of the tunnel. The blades are mounted between Plexiglas windows in the rotatable side walls of 2-m diameter. The upper floor is fixed and carries a variable half nozzle. At the rear there is a slotted transonic floor connected to the suction system, which was closed in the present tests. The bottom floor can be moved horizontally and vertically to adjust the geometry of the bottom bypass passage.

A probe traversing system is mounted in the downstream tunnel area and provides a rotation of the probes around the upstream probe head. The traversing is generally carried out at cascade midspan.

For the test series seven blades of 70-mm chord length were installed in the wind tunnel. The fourth blade was equipped with 10 pressure taps on the suction side and the fifth with 10 pressure taps on the pressure side in such a way that the flow in one blade passage could be recorded. The local surface Mach number was calculated using the upstream total pressure. In
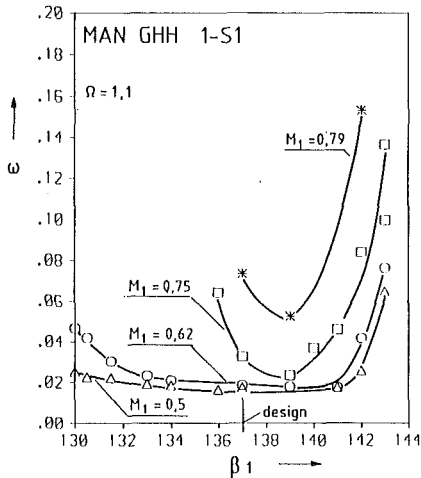
Fig. 11 Loss coefficient versus inlet flow angle
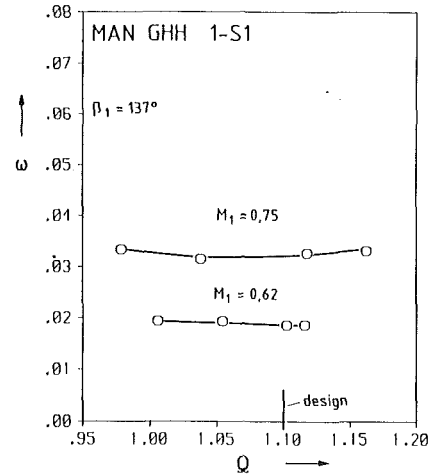
Fig. 14 Loss coefficient versus axial velocity density ratio
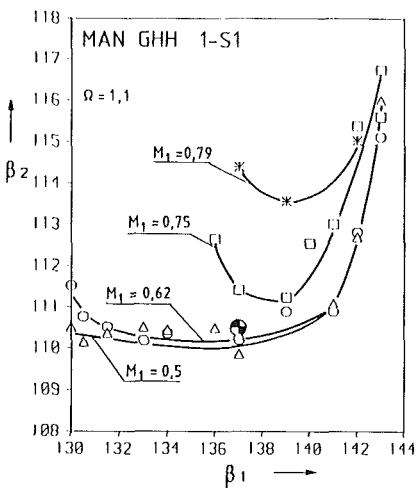
Fig. 12 Exit flow angle versus inlet flow angle
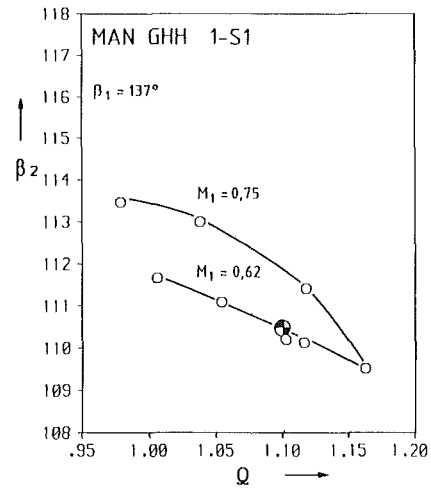
Fig. 15 Exit flow angle versus axial velocity density ratio
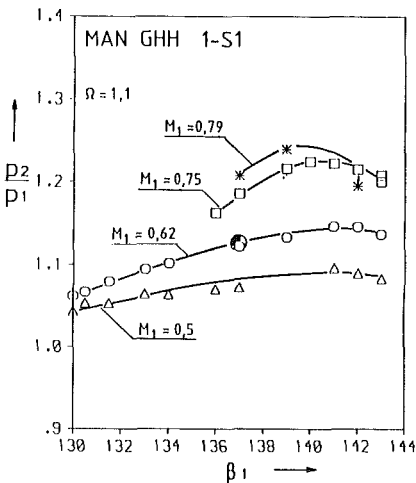
Fig. 13 Static pressure ratio versus inlet flow angle
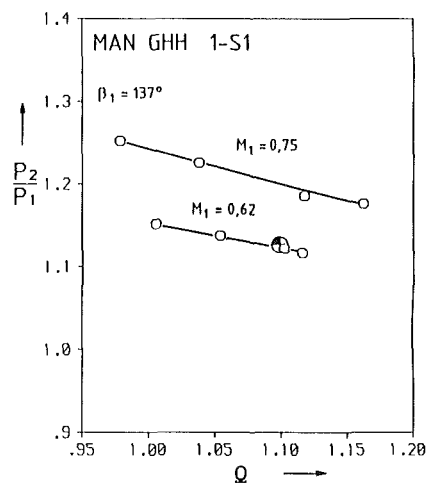
Fig. 16 Static pressure ratio versus axial velocity density ratio

order to vary the axial velocity density ratio, side wall slots were provided in the cascade passage as shown in Fig. 6.

Inlet total pressure and temperature were measured in the settling chamber. In a plane half a gap axially upstream of the leading edges, the inlet static pressure was measured ahead of the center blades at one side wall. In the same plane the inlet flow angle was checked by three flow angle probes (Fig. 7).

In a plane half a gap axially downstream of the trailing edges, the total pressure, static pressure, and flow angle distribution were measured by moving a combined probe (Fig. 8) stepwise over slightly more than one blade pitch at cascade midspan.

The final data evaluation was carried out off-line on the central computer using the two-dimensional momentum
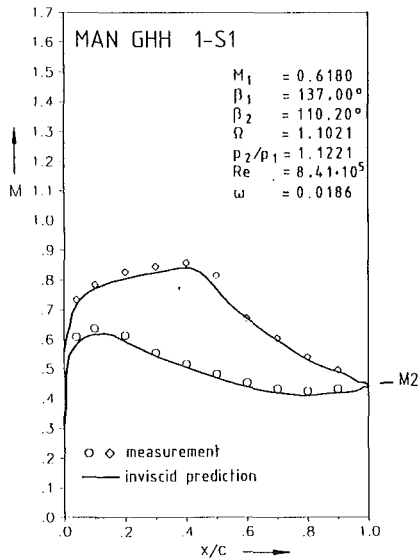
Fig. 17 Predicted and measured surface Mach numbers at design condition
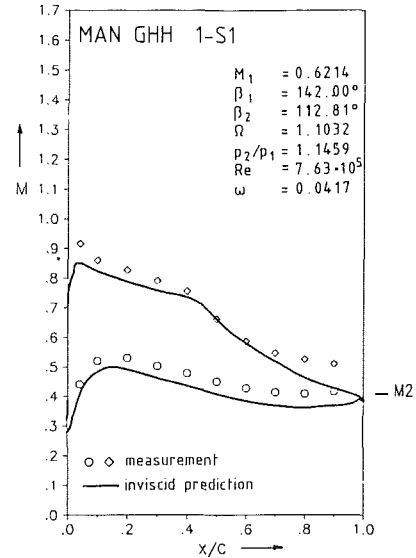
Fig. 19 Predicted and measured surface Mach numbers at +5 deg of incidence
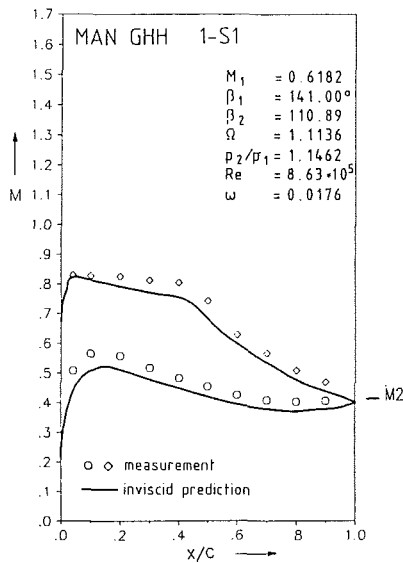
Fig. 18 Predicted and measured surface Mach numbers at +4 deg of incidence
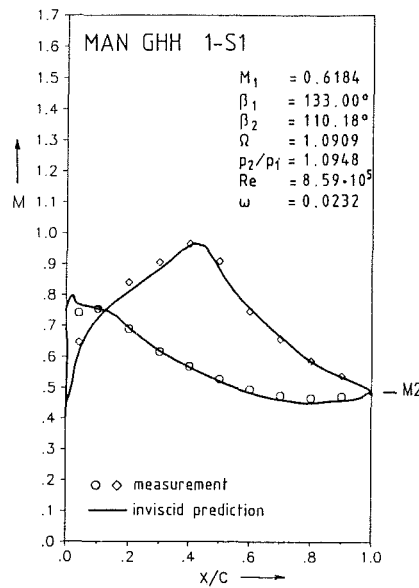
Fig. 20 Predicted and measured surface Mach numbers at −4 deg of incidence

method as described by Schimming and Starken [12]. In this method the downstream measured flow distributions are transferred to uniform conditions by application of the continuity, energy, and two momentum equations. The final test data, therefore, include a mixing process downstream of the cascade resulting in small corrections of total pressure loss, static pressure rise, and exit flow angle. In this calculation no variation of the axial velocity density ratio between the measuring and the far downstream plane is considered.

IV Test Results

The test series were performed by varying the inlet Mach number at fixed inlet flow angles, keeping the AVDR as close as possible to the design value of $\Omega = 1.10$. Some of the resulting loss curves are shown in Figs. 9 and 10. Figure 9 presents the curves at positive and Fig. 10 the corresponding curves at design and negative incidences.

These curves show the typical loss behavior with inlet Mach number of a compressor cascade. At positive incidences this is characterized by an overall loss rise at higher inlet flow

angles, whereby the final steep loss rise is only slightly affected by β_1. Contrary to this, at negative incidences the final loss rise moves to lower inlet Mach numbers with decreasing inlet flow angle due to choking of the cascade. The highest Mach number range is achieved at $\beta_1 = 139$ deg or 2 deg of incidence.

More interesting, however, than these curves are the loss data plotted as a function of the inlet flow angle as presented in Fig. 11 with the inlet Mach number as independent parameter and for the design AVDR of $\Omega = 1.1$. The resulting curves show a large operating range of the cascade at the design inlet Mach number of $M_1 = 0.62$. If a 4 percent loss level is taken as limiting value, the range extends from $i = +5.0$ deg to $i = -6.5$ deg. With increasing inlet Mach number, this operating range is, of course, considerably reduced mainly due to choking of the cascade, and the range is thereby shifted to higher incidences with a minimum loss level at $\beta_1 = 139$ deg. The corresponding dependencies of the exit flow angle and the static pressure ratio of the cascade are shown in Figs. 12 and 13. Taking into account the measurement accuracy of the exit flow angle with ± 0.3 deg the agreement with the design values is excellent. For a complete valuation of these data the axial velocity density
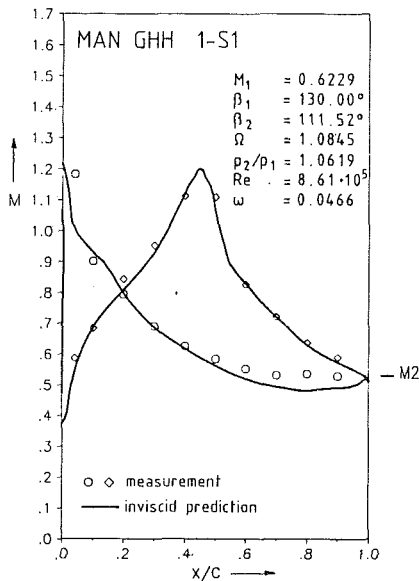
Fig. 21 Predicted and measured surface Mach numbers at − 7 deg of incidence

MAN GHH 1-S1

M_1 = 0.6229
β_1 = 130.00°
β_2 = 111.52°
Ω = 1.0845
p_2/p_1 = 1.0619
Re = 8.61·10^5
ω = 0.0466

○ ◇ measurement
——— inviscid prediction
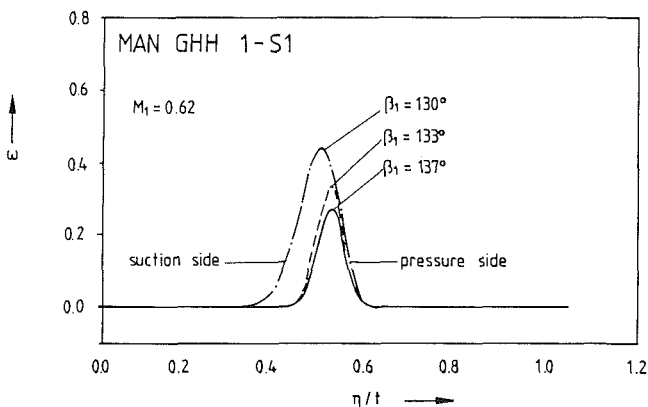
Fig. 22 Total pressure loss distribution measured behind the cascade

MAN GHH 1-S1

M_1 = 0.62

β_1 = 130°
β_1 = 133°
β_1 = 137°

suction side ——— ——— pressure side

ratio (AVDR) influence also has to be considered. The corresponding dependencies are shown in Figs. 14–16 for the design inlet flow condition. In the measured range no influence on the losses but, of course, on the exit flow angle and on the pressure ratio was observed. However, in the loss rise regions the losses depend also on Ω.

The favorable results of the low loss level at the design point is due to the extended laminar boundary layer on the suction surface combined with a separation-free turbulent recompression. A comparison of the measured surface Mach numbers with the inviscid direct calculation (Fig. 17) shows very good agreement and confirms the design intent. Flow visualization by releasing ink through surface pressure taps showed a laminar separation bubble around 50 percent of chord and an unseparated turbulent recompression on the suction side.

This favorable behavior continues at positive incidences up to the point where the transition point on the suction surface moves upstream to the leading edge, which is, of course, related to the position of the maximum velocity point. This condition is reached around $\beta_1 = 141$ deg. The experimental and theoretical velocity distribution at this point, as presented in Fig. 18, are slightly different, but the suction surface distribution is very similar to that suggested by Walker [13] as an optimum distribution. Walker proposed a certain low-diffusion "unstable laminar" region to generate natural transition followed by a high turbulent diffusion. The present data confirm this idea of an optimum velocity distribution with a maximum on

loading at minimum losses. However, the drawback of this distribution is also quite obvious from Fig. 11. With an incidence increase of only one degree the loss coefficient rises by a factor of 2.5. Due to the suction peak at this inlet flow angle (Fig. 19), the transition point moves to the leading edge, causing turbulent separation near 60 percent of chord. The "Walker distribution" like that of Fig. 18 is therefore only useful if a profile is to be designed at maximum incidence condition and not, as usual, at the design operating point of the turbomachine.

With increasing negative incidences the suction surface peak velocity around 45 percent of chord is rising considerably, leading to higher turbulent diffusion, thicker boundary layers, and, consequently, higher losses. Around − 4 deg of incidence sonic velocity is reached (Fig. 20) and at − 7 deg the cascade is very near to choking, which was measured at $M_1 = 0.63$. In the latter case (Fig. 21) shock waves lead to boundary thickening and separation on the suction surface and therefore to a further loss rise. In Fig. 22 the measured wake traverses are shown at 0, − 4, and − 7 deg of incidence and design inlet Mach number. The loss rise is clearly caused by separation on the suction side because the wake is extending to this side. The negative incidence range is therefore limited by suction surface separation just prior to choking of the cascade. This is identical to the loss behavior of supercritical cascades but different from subsonic ones, which are generally limited by pressure surface leading edge separation. There is a surprisingly good agreement between the measurement and the inviscid prediction in Fig. 21, although the suction surface boundary layer is completely separated behind 50 percent of chord. This confirms the observations in other cascade tests, especially high-speed ones, that profile separations are not necessarily connected with near constant pressures along the surfaces. The pressure rise within the separated area leads to considerable back flow from the trailing edge to the separation point, as has been visualized in other tests. The structure of the flow within the separated area is probably responsible for the different pressure distributions generated along the surfaces.

V Conclusion

By combining a boundary layer calculation with an inverse and a direct flow calculation method, a successful optimization of a compressor cascade blade section with regard to low losses and acceptable incidence range was achieved. The velocity distribution developed in this design resulted in a minimum loss coefficient of 1.8 percent, a positive incidence range of 5 deg, and a negative incidence range of 6.5 deg (4 percent loss level) at an inlet Mach number of 0.62.

The inviscid prediction of the surface Mach number distribution agrees very well with the experimental results at negative incidences even under separated conditions. At positive incidences some differences were observed.

The experiments revealed a separation-free operation of the cascade at the design point and confirmed, therefore, the inverse design velocity distribution, rather than the prediction that used the metal profile to calculate the boundary layer behavior and resulted in a rear separation.

References

1 Turanskyj, L., and Voss, H., "Recent Developments to Increase Operating Efficiences and Performance of Industrial Axial-Flow Compressors," *Trans. IMechE*, 1987.

2 Schmidt, E., and Klimetzek, F., "Verlustarme, superkritische Schaufelgitter," *FVV-Forschungsberichte*, Vol. 344-1, 1984.

3 Weber, A., Rechter, H., and Starken, H., "Verlustarme, superkritische Verdichterprofile," *FVV-Forschungsberichte*, Vol. 344-2, 1984.

4 Schmidt, E., and Klimetzek, F., "Verlustarme, superkritische Schaufelgitter," *FVV-Forschungsberichte*, Vol. 392-1, 1987.

5 Weber, A., et al., "Verlustarme, superkritische Schaufelgitter," *FVV-Forschungsberichte*, Vol. 392-2, 1987.

6 Schmidt, E., "Numerische Berechnung und experimentelle Untersuchung des transsonischen Strömungsfeldes in stark umlenkenden Schaufelgittern," Dissertation Universität Stuttgart, Germany, 1976.

7 Schmidt, E., "Computation of Supercritical Compressor and Turbine Cascades With a Design Method for Transonic Flows," ASME *Journal of Engineering for Power*, Vol. 102, Jan. 1980, pp. 68–74.

8 McNally, W. D., "FORTRAN Program for Calculating Compressible and Turbulent Boundary Layers in Arbitrary Pressure Gradients," NASA TN D-5681, Washington, May 1970.

9 Schmidt, E., and Grein, H.-D., "Verdichterbeschaufelungsentwurf," *FVV-Forschungsberichte*, Vol. 433, 1989.

10 Lucci, C. W., and Schmidt, W., "Nachrechnung transsonischer Gitter," Dornier-Bericht No. 79/25B.

11 Weber, A., et al., "Theoretical and Experimental Analysis of a Compressor Cascade at Supercritical Flow Conditions," ASME-Paper 87-GT-256, 1987.

12 Schimming, P., and Starken, H., "Data Reduction of Two-Dimensional Cascade Measurements," AGARD-AG-207, 1975.

13 Walker, G. J., "A Family of Surface Velocity Distributions for Axial Compressor Blading and Their Theoretical Performance," ASME Paper No. 75-GT-34, 1975.

APPENDIX

Table 1 Profile coordinates of MAN GHH 1-S1

Suction side		Pressure side	
x	y	x	y
0.00417	0.00157	0.00455	-0.00155
0.00490	0.00459	0.00555	-0.00369
0.00572	0.00605	0.00685	-0.00526
0.00787	0.00857	0.01065	-0.00740
0.01938	0.01838	0.01935	-0.00875
0.02919	0.02479	0.02915	-0.00917
0.03929	0.03051	0.03924	-0.00949
0.04910	0.03558	0.04904	-0.00969
0.06161	0.04158	0.06154	-0.00975
0.07421	0.04723	0.07414	-0.00961
0.08672	0.05255	0.08665	-0.00931
0.09913	0.05757	0.09905	-0.00889
0.11163	0.06237	0.11155	-0.00834
0.14295	0.07346	0.14285	-0.00677
0.17426	0.08335	0.17415	-0.00440
0.23678	0.09986	0.23666	0.00140
0.29919	0.11229	0.29907	0.00728
0.36170	0.12045	0.36157	0.01240
0.42431	0.12372	0.42418	0.01691
0.48680	0.12075	0.48668	0.02062
0.54929	0.11249	0.54918	0.02329
0.61168	0.10105	0.61159	0.02444
0.67426	0.08663	0.67419	0.02379
0.73674	0.07003	0.73668	0.02099
0.79922	0.05164	0.79918	0.01607
0.86160	0.03288	0.86157	0.00844
0.92287	0.01438	0.92286	-0.00040
1.00044	-0.00924	1.00022	-0.01424

R. P. Shreeve

Y. Elazar

J. W. Dreon

A. Baydar

Turbopropulsion Laboratory,
Naval Postgraduate School,
Monterey, CA 93943

Wake Measurements and Loss Evaluation in a Controlled Diffusion Compressor Cascade

The results of two component laser-Doppler velocimeter (LDV) surveys made in the near wake (to one fifth chord) of a controlled diffusion (CD) compressor blade in a large-scale cascade wind tunnel are reported. The measurements were made at three positive incidence angles from near design to angles thought to approach stall. Comparisons were made with calibrated pressure probe and hot-wire wake measurements and good agreement was found. The flow was found to be fully attached at the trailing edge at all incidence angles and the wake profiles were found to be highly skewed. Despite the precision obtained in the wake velocity profiles, the blade loss could not be evaluated accurately without measurements of the pressure field. The blade trailing edge surface pressures and velocity profiles were found to be consistent with downstream pressure probe measurements of loss, allowing conclusions to be drawn concerning the design of the trailing edge.

Introduction

Controlled diffusion (CD) blading shapes were introduced into the design systems for axial compressors only a few years ago (Hobbs and Weingold, 1984). The CD blade contour, for a given inlet air angle, turning angle, solidity, and streamline contraction, is usually the result of an inviscid design process operated sequentially or interactively with surface boundary layer predictions. The resulting blade shape is one on which the suction-side boundary layer is predicted not to separate at design conditions (Sanger, 1983). The inviscid-plus-boundary layer design procedure results in shapes that can have significant (but controllable) trailing edge thicknesses where a Kutta condition has been imposed (Hobbs and Weingold, 1984; Sanz, 1988). The closing of the trailing edge shape, with a radius for example, is a matter of some judgment since a generalized model of a compressor blade base flow suitable for design purposes has not been established. The need for such modeling has previously stimulated both cascade (Hobbs et al., 1982) and large-scale trailing edge simulation studies (Patersen and Weingold, 1985; McCormick et al., 1988). However, the understanding that can be obtained from single experiments on specific designs is necessarily limited and an assimilation of the information from a range of experiments could lead to much greater insight. It is in this spirit that the present results are reported.

The present work began with an experimental program aimed at verifying an inviscid-plus-boundary layer method for designing CD compressor blading (Sanger, 1983). The comparison of experimental with design and predicted off-design performance of a particular CD cascade (hereafter referred to

as the Sanger cascade) was reported (Sanger and Shreeve, 1986), and it was clear from the study that off-design and stalling behavior were not predicted adequately using boundary-layer codes. In order to provide detailed experimental data with which to assess existing and developing viscous codes, in particular their ability to predict stall, a complete mapping of the flow through the cascade was made using a two-component laser-Doppler velocimeter (LDV) at design and two higher incidence angles (Elazar, 1988). Preliminary assessments made by Elazar of boundary layer (McNally, 1970), interactive boundary layer (Snir, 1988), and Navier–Stokes (Shamroth et al., 1984) code predictions showed that only the Navier–Stokes code gave reasonable results. It was also clear however, that transition modeling was critical in obtaining the good agreement. The experimental results for the boundary layer devel-
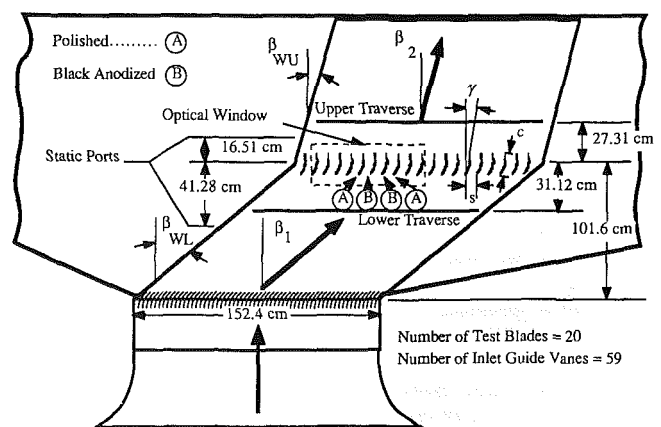
Fig. 1 Schematic of the cascade wind tunnel

SURVEY STATIONS

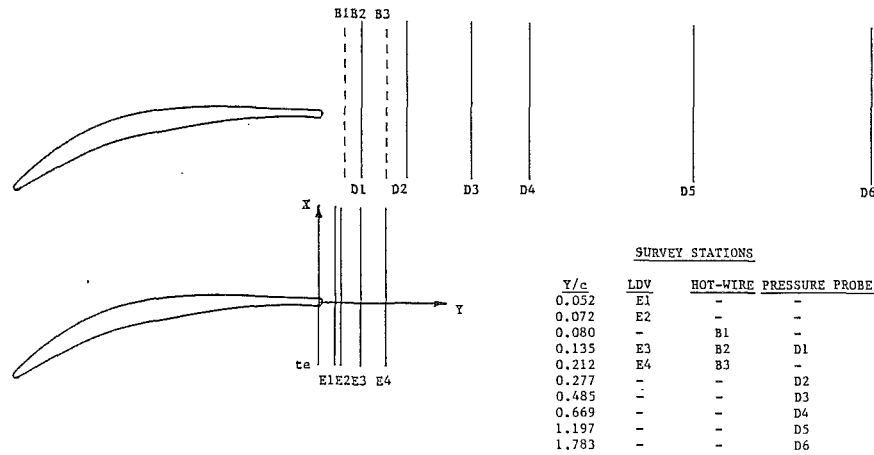| Y/c	LDV	HOT-WIRE	PRESSURE PROBE
0.052	E1	–	–
0.072	E2	–	–
0.080	–	B1	–
0.135	E3	B2	D1
0.212	E4	B3	–
0.277	–	–	D2
0.485	–	–	D3
0.669	–	–	D4
1.197	–	–	D5
1.783	–	–	D6

Fig. 2 Cascade geometry and measurement locations

opment in the Sanger cascade with sufficient information to permit its use for preliminary code assessment purposes were given in an earlier paper (Elazar and Shreeve, 1990). A report containing all test results is to be issued (Shreeve and Elazar, 1989).

For code assessment, the Sanger cascade was found to provide a unique test case. The surprising feature of the flow field was that the suction side boundary layer was found to remain completely attached at the trailing edge at incidence angles that were thought from the loss measurements to be "stalling." A leading edge separation bubble was observed to grow as the incidence was increased, but losses could reach four times the minimum loss for the cascade (Classick, 1989) without the appearance of any trailing edge separation (Murray, 1989). This contrasts significantly with the behavior of a double-circular arc (DCA) compressor cascade, on which a similarly detailed mapping was made (Deutsch and Zierke, 1987, 1988; Zierke and Deutsch, 1990), wherein an unsteady separation occurred on the suction side at positive incidence angles.

In view of the steady and attached flow found at the trailing edge of the Sanger cascade, LDV measurements made in the blade wake are again useful as a well-prescribed test case for viscous calculations. The point must be made, however, that the LDV technique gives accurate measurements only of the velocity field. As was stated earlier (Elazar and Shreeve, 1990), the loss coefficient for the cascade could not be evaluated accurately from LDV data alone, and the uncertainty introduced by an assumption as to the pressure field was comparable in magnitude to the loss itself. In order to assess completely the ability of emerging viscous codes to predict off-design behavior, and in particular the losses (Davis et al., 1988), it is

desirable to have equally accurate measurements of the velocity field and the losses.

Consequently, the present paper presents results of LDV measurements made in the wakes of the Sanger cascade at increasing incidence (Elazar, 1988), and relates them to calibrated pressure probe (Dreon, 1986) and hot-wire probe (Baydar, 1988) measurements. The values obtained for the loss coefficient and the recovery of the static pressure from the lower values measured on the blade trailing edge are analyzed and are shown to be consistent with the effect of wake mixing.

Test Facility and Instrumentation

The subsonic cascade wind tunnel and operating instrumentation were as described by Sanger and Shreeve (1986). The configuration of the wind tunnel is shown in Fig. 1. The tests involved 20 test blades across a test section width of 1.524 meters. The blade span was 25.4 cm. Inlet air angle was adjusted by rotating the lower side walls and inlet guide vanes. The test blading was mounted to a rack, which translated to a new position as the angle was changed. At each angle the outlet end walls were adjusted so that the downstream wall static pressure was atmospheric and nearly uniform in the blade-to-blade direction. The guide vane position was selected such that the wall static pressure was nearly uniform in the blade-to-blade direction. An upstream blade-to-blade survey using a calibrated five-hole pressure probe verified near uniformity of the flow over six blade passage widths. Examples of profiles showing the degree of uniformity and periodicity of the flow field are given by Sanger and Shreeve (1986) and Elazar and Shreeve (1990). It is important to note that the 59

—————— Nomenclature ——————
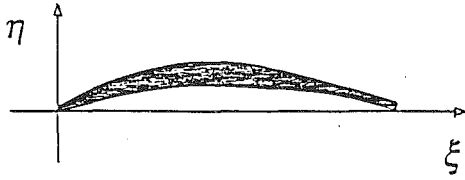
AVDR	=	axial velocity-density ratio	v	=	velocity component normal to blade surface	
c	=	blade chord = 12.73 cm				
C_p	=	pressure coefficient	V	=	velocity	
d	=	distance normal to the blade surface	X	=	transverse (horizontal) displacement	
d_{te}	=	diameter of the trailing edge	Y	=	axial (vertical) displacement	
D	=	NASA diffusion factor	β	=	air angle defined in Fig. 1	
k	=	defined in equation (6)	δ^*	=	displacement thickness	
M	=	Mach number	Δ	=	defined in equation (5)	
P	=	pressure	ξ	=	blade coordinate defined in Table 1	
q	=	dynamic pressure				
Re	=	Reynolds number	η	=	blade coordinate defined in Table 1	
s	=	blade spacing	σ	=	solidity = c/s	
u	=	velocity component parallel to blade surface	$\bar{\omega}$	=	mass-averaged loss coefficient	

Subscripts

c	=	chord
min	=	minimum
p	=	pressure side
ref	=	reference, upstream
s	=	suction side
t	=	stagnation
te	=	trailing edge station
wu	=	upper wall of cascade
wl	=	lower wall of cascade
1	=	upstream
2	=	downstream

Table 1 Blade coordinates, cascade geometry and nominal test conditions

ξ (mm)	η (pressure side) (mm)	η (suction side) (mm)
0.000	0.114	0.114
0.056	———	0.213
0.145	0.005	———
0.564	0.112	0.498
1.128	0.257	0.780
1.692	0.394	1.024
2.256	0.526	1.240
2.819	0.648	1.425
3.383	0.759	1.577
3.947	0.838	1.684
4.511	0.889	1.755
5.075	0.912	1.791
5.639	0.912	1.798
6.203	0.894	1.781
6.767	0.869	1.730
7.330	0.841	1.651
7.894	0.805	1.549
8.458	0.765	1.430
9.022	0.714	1.295
9.586	0.653	1.151
10.150	0.577	0.998
10.714	0.485	0.843
11.278	0.371	0.686
11.841	0.226	0.528
12.405	0.048	0.368
12.510	0.010	———
12.609	———	0.310
12.725	0.157	0.157

Blade Type	Controlled Diffusion
Number of Blades	20
Blade Spacing	7.62 cm
Chord	12.73 cm
Solidity	1.67
Leading Edge Radius	0.114 cm
Trailing Edge Radius	0.157 cm
Thickness	7%
Setting Angle	14.2 °±0.1°
Stagger Angle	14.4 °±0.1°
Span	25.40 cm
NOMINAL TEST CONDITIONS	
Reynolds No.(chord)	720,000
Inlet	
Total Temperature	294 K
Total Pressure	1.03 ATM
Mach Number	0.25
Exit	
Static Pressure	1.00 ATM

Fig. 3 Boundary layers measured at the blade trailing edge

inlet guide vanes, spaced only 2.54 cm apart, generated wakes that were well mixed and barely detectable just ahead of the test blades. The free-stream turbulence level was measured consistently to be 1.4 ± 0.7 percent.

The geometry of the cascade and axial locations of blade-to-blade surveys (made at midspan) are shown in Fig. 2. The geometry of the cascade is given in Table 1.

Data presented herein are from three studies. LDV measurements were made by Elazar (1988) of the flow through the passage formed by blades 7 and 8 from the left-hand end in Fig. 1. The wake flow was measured behind blade 7 at stations E1–E4 in Fig. 2.

The LDV velocity field measurements were referred to an upstream (uniform) inlet velocity derived from LDV surveys 0.3 chord lengths "axially" upstream and plenum conditions at the time of the individual measurement (Elazar and Shreeve, 1989). Details of the TSI two-component LDV system are given in the cited reference.

Calibrated five-hole pressure probe measurements were made by Dreon (1986) in the wake of blade 10. Two United Sensor Corporation cylindrical probes (Model DA-125) were used at the stations labeled "upper traverse" and "lower traverse in Fig. 1. The "upper traverse" corresponds to Station D6 in Fig. 2. A United Sensor Corporation conical probe (Model DC-125) was used for wake surveys nearer to the blade, at stations D1–D5 shown in Fig. 2. The probes were calibrated (in a free jet) and used in a yaw-balanced mode (Dreon, 1986), establishing calibration surfaces for dimensionless velocity and pitch angle in terms of two pressure difference coefficients. A special yaw angle probe was also used to provide a reference for yaw angle measurements in the blade wakes.

Single component hot-wire measurements were made by Baydar (1988) at stations B1–B3 in Fig. 2 in the near wake of blade 10. The hot wire was calibrated in situ using a Prandtl probe at the same blade-to-blade location, well outside the wake, and with the two probe tips 2.54 cm on either side of the spanwise tunnel centerline. TSI anemometer (Model IFA-100), digitizer (Model IFA-200), and software (DAP) were used with an IBM PC-AT computer. Details of the measurements are given by Baydar (1988).
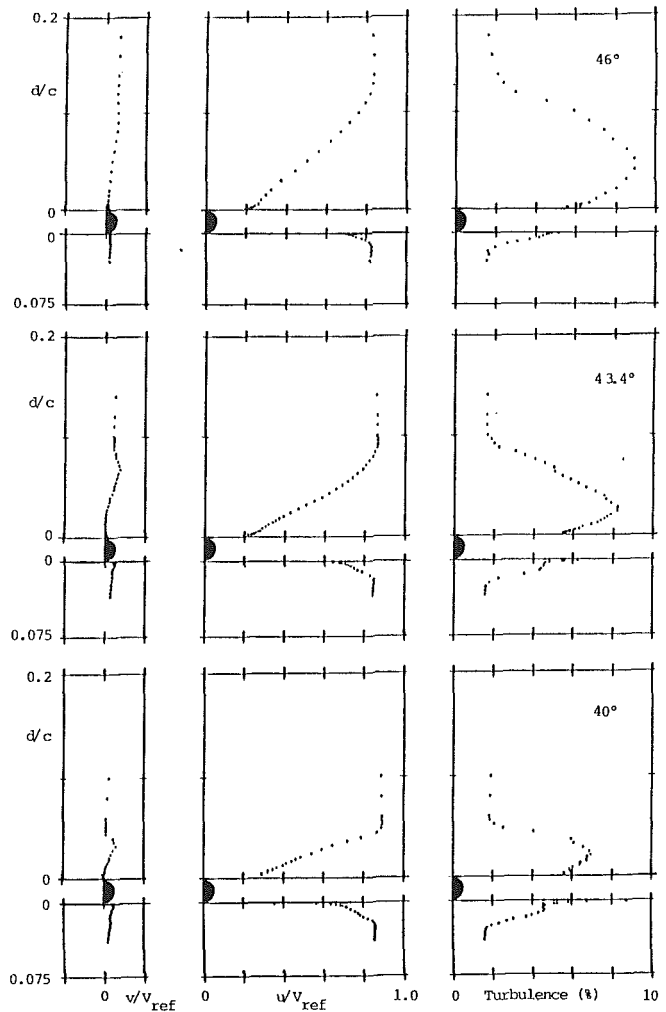
Results and Discussion

LDV Measurements. The results of two-component LDV surveys made in the blade-to-blade direction at the axial station of the center of radius at the blade trailing edge are shown in Fig. 3. The figure shows the axial (u) and transverse (v) components of the mean velocity and the turbulence level on the pressure and suction sides of the blade trailing edge, at three inlet air angles (40, 43.4, and 46 deg). The velocity components are shown as a ratio of the (uniform) inlet velocity. The turbulence level is also referred to the inlet (rather than to the local "free-stream") velocity. The displacement scale (from top to bottom) covers half a blade space, so that the extent of the viscous layer in relation to the blade passage can be easily appreciated. At an air inlet angle of 46 deg the two viscous layers and metal thickness are seen to occupy 35 percent of the area at the trailing edge.

It is interesting to note that there were significant differences in the behaviors of the boundary layers on the suction and pressure sides of the blade as incidence was increased (Elazar, 1988). On the suction side, the boundary layer increased in thickness as incidence was increased, but the turbulence profile showed that the layer retained the characteristics of a fully
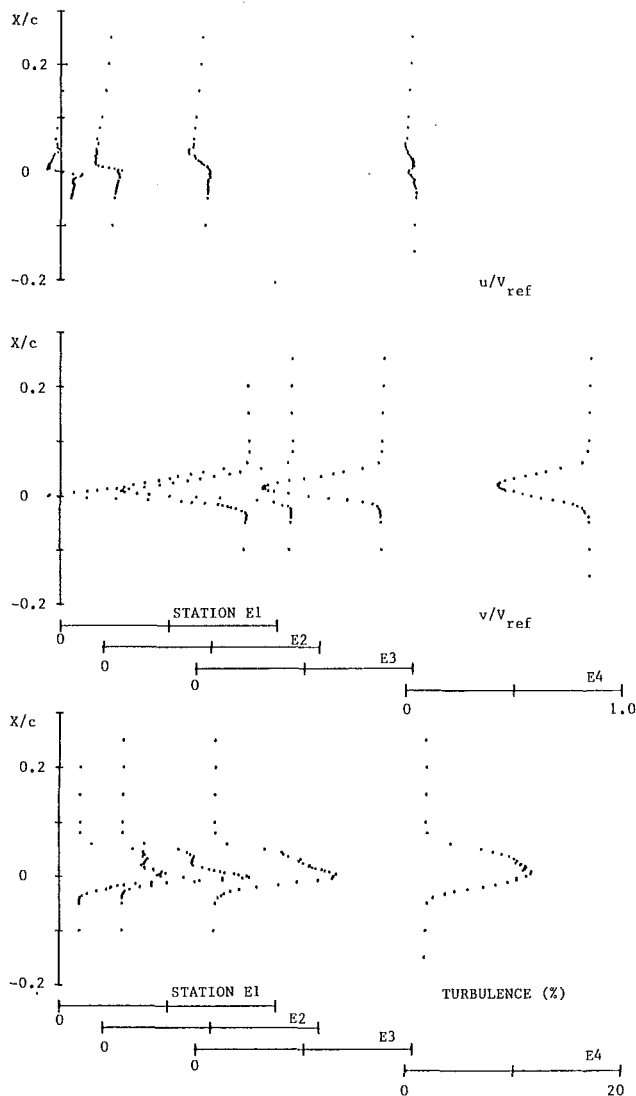
Fig. 4(a)   LDV wake surveys at $\beta_1 = 40$ deg
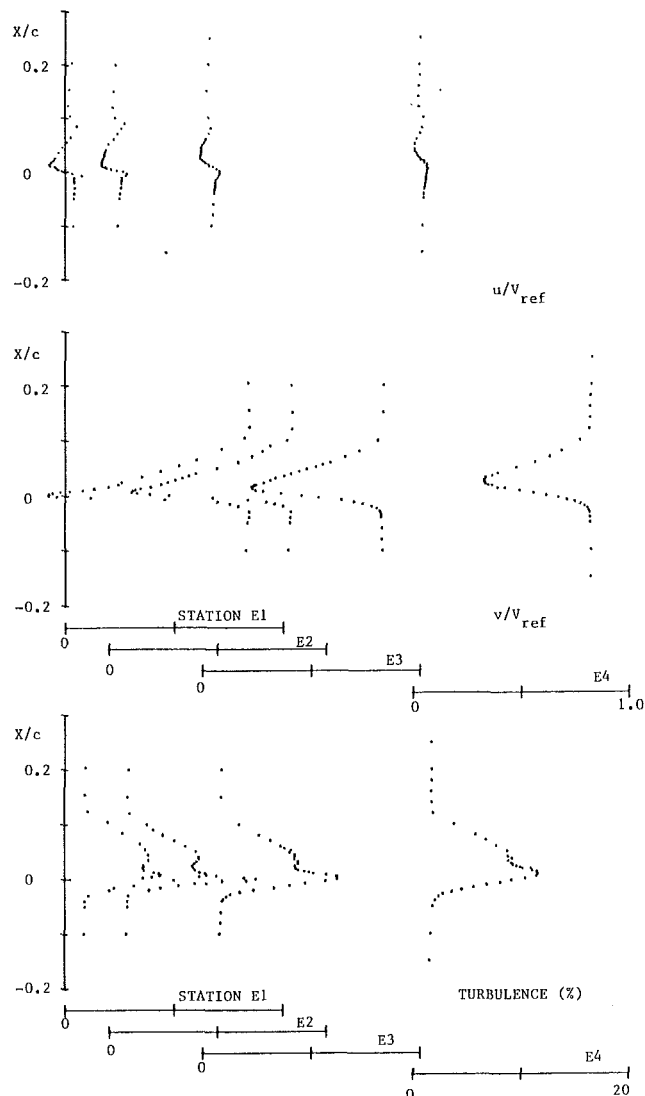
Fig. 4(b)   LDV wake surveys at $\beta_1 = 43.4$ deg

turbulent boundary layer. On the pressure side, at inlet air angles of 40 and 43.4 deg, the velocity profiles were very similar to each other in every respect. At 46 deg however, the boundary layer was discernibly thinner and the turbulence levels within the layer decreased. These differences have to do with how transition occurred on the two sides of the blade. On the suction side, transition occurred over a laminar separation bubble near the blade leading edge. While the bubble grew as incidence was increased, reattaching at 46 percent chord at an air inlet angle of 46 deg, the boundary layer downstream of reattachment appeared always to be fully turbulent. On the pressure side of the blade, transition occurred naturally within the boundary layer over a significant fraction of the chord. Toward the trailing edge, the outer flow was accelerated significantly. The differences in stagnation point location, transition location and length, and acceleration toward the trailing edge as the incidence angle was changed, resulted in a significantly reduced boundary layer thickness on the pressure side of the blade at the highest inlet air angle of 46 deg.

The results of LDV surveys of the wake of the seventh blade are shown in Fig. 4. The surveys were made at distances $0.052c$, $0.072c$, $0.135c$, and $0.212c$, or, equivalently $2.15d_{te}$, $2.96d_{te}$, $5.56d_{te}$, and $8.7d_{te}$ (where d_{te} is the diameter at the blade trailing edge), downstream of the center of curvature of the trailing edge. The mean velocity components and the turbulence levels are shown in the figure.

It is first noted that the wake was, in general, highly asymmetric. The asymmetry was most pronounced at the station closest to the trailing edge, becoming less pronounced downstream, as mixing occurred. Only at $\beta_1 = 40$ deg, at the most downstream station (8.7 d_{te}). was the wake nearly symmetric. Reversed flow was measured at $2.15d_{te}$ at $\beta_1 = 40$ deg and $\beta_1 = 43.4$ deg, but not at $\beta_1 = 46$ deg. Mixing was most rapid at $\beta_1 = 40$ deg. Figure 5 shows the variation in wake minimum velocity with distance downstream. It is interesting to note the differences that occurred at the three inlet flow angles. Since the pressure side boundary layers at the trailing edge were similar at $\beta_1 = 40$ deg and $\beta_1 = 43.4$ deg, it was possibly the thinner pressure side boundary layer at $\beta_1 = 46$ deg that led to a shorter reverse flow region at the highest angle.

The transverse velocity components approached ± 10 percent of the inlet velocity at the most upstream location ($2.15d_{te}$) and became almost constant at the most downstream station ($8.7d_{te}$). The constant value of approximately 1 percent of the inlet velocity was consistent with the presence of a small deviation angle.

The distributions of turbulence level show the wake asymmetry most clearly. The turbulence level was considerably higher (reaching 15 percent at $\beta_1 = 40$ deg), in the area of the wake containing the pressure side boundary layer. The suction
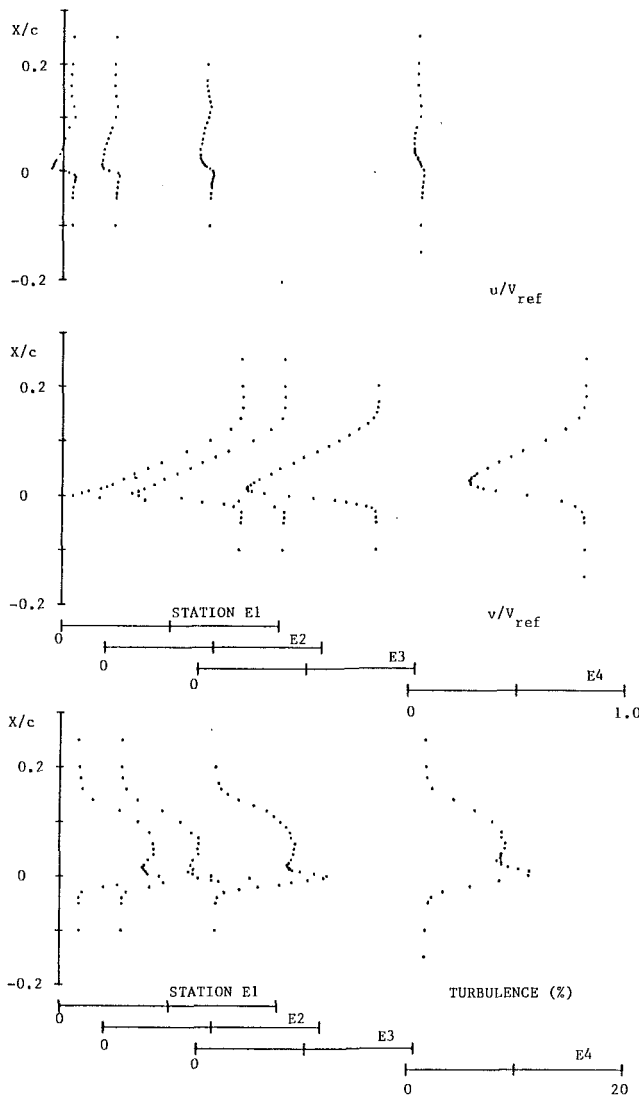
Fig. 4(c)   LDV wake surveys at $\beta_1 = 46$ deg

Fig. 5   Wake minimum velocity from LDV measurements

side boundary layer generated turbulence in the wake of 8 percent or less.

Hot-Wire Measurements. Single component hot-wire measurements obtained by Baydar (1988) in the wake of the tenth blade are compared at corresponding axial stations with LDV measurements, made by Elazar (1988) in the wake of the seventh blade, in Fig. 6. In general, good agreement was obtained. Exceptional agreement was found in the mean velocity at $\beta_1 = 40$ deg. At $\beta_1 = 46$ deg, similar values of the minimum velocity were measured, but the hot wire showed the wake to be shifted slightly toward less deviation. Peak turbulence levels were in very good agreement at both $\beta_1 = 40$ deg and $\beta_1 = 46$ deg. However, the hot wire indicated somewhat higher turbulence levels than did the LDV in the region of the wake containing the suction-side boundary layer. No satisfactory explanation has been found for this difference.   Since the hot wire could not be positioned with the equivalent accuracy that could be achieved with the LDV measurement volume, and since only the velocity magnitude could be obtained from the single wire, no further hot-wire measurements were made.

Pressure Probe Measurements. Measurements were made with a calibrated five-hole conical pressure probe behind the tenth blade at one axial station at which LDV measurements were made behind the seventh blade; namely, $0.135c$ down-

stream of the trailing edge center of radius. The measured velocity profiles are compared in Fig. 7 at $\beta_1 = 40$ deg and $\beta_1 = 43.4$ deg. Truly excellent agreement was seen at $\beta_1 = 40$ deg. At $\beta_1 = 46$ deg, some disagreement was evident, with the LDV measurements showing a somewhat wider and deeper wake. Two reasons for disagreement can be considered. First, the conical pressure probe was 0.32 cm in diameter and hence could interfere with the flow being measured in the very near wake. Unfortunately optical windows could not be installed at the tenth blade where the probe measurements were made so this could not be examined. It was noted that at $\beta_1 = 40$ deg, the wake was better mixed at the probe station, and interference might be less. Second, small differences might be present between the wakes of different blades at increased incidence angles. Since the wakes of the blades are developed from suction-side boundary layers, which develop downstream of growing separation bubbles, some differences are to be expected. Future experiments will examine this point more carefully. In general, the large number of test blades (20) circumvents the problem of achieving flow periodicity in the test section.

Wake velocity profiles measured by Dreon (1986) using the calibrated conical probe at five downstream stations and a calibrated cylindrical probe at the farthest downstream station are shown in Fig. 8 for $\beta_1 = 40$ deg and $\beta_1 = 43.4$ deg. The path of the wake minimum velocity away from the suction surface is shown in Fig. 9, where LDV data near to the trailing edge are included.

The total pressure profiles (the results of direct measurement of stagnation pressure at the tip of each probe) were qualitatively similar to the velocity profiles. From the velocity, stagnation pressure, and stagnation temperature (measured in the wind tunnel plenum) all properties of the flow were calculated at each location in the survey. By integration over one blade passage, values were obtained for the mass-averaged loss coefficient ($\bar{\omega}$, Sanger and Shreeve, 1986), the NASA diffusion factor (D), and the axial velocity-density ratio (AVDR) at each survey station. The results are shown in Fig. 10. Very consistent results are noted with the exception of the one data point indicated. The uncertainties in the quantities derived from the probe measurements can be judged from the following: The two cylindrical probes (at the most upstream and downstream traverse positions) were traversed across two blade spaces. The two probes were then interchanged and the traverses were repeated. The maximum variation in the properties derived from each blade space and each probe position (4 cases) was found to be 7.3 percent in the loss coefficient, 3.3 percent in the diffusion factor, and 0.67 percent in the AVDR.

Static Pressure Recovery. The static pressure was obtained
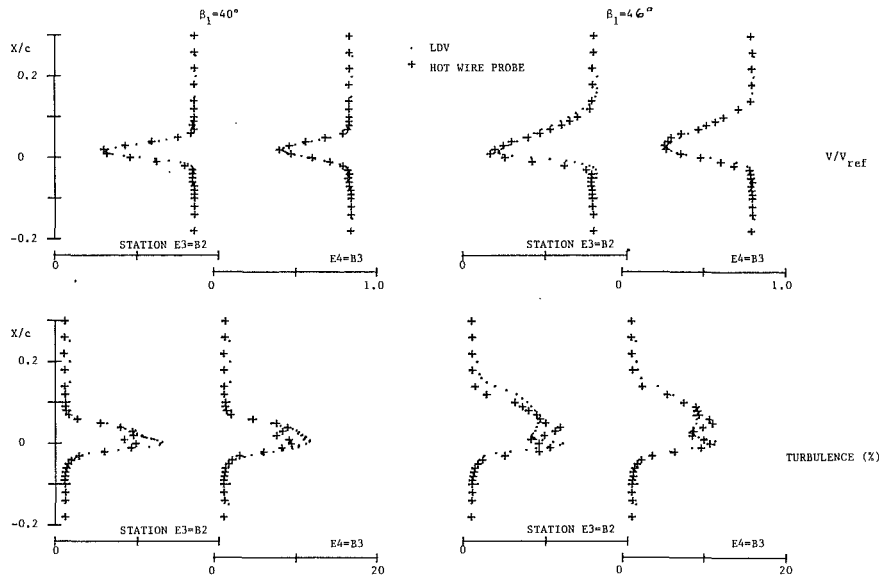
Fig. 6 Comparison of hot-wire and LDV wake measurements
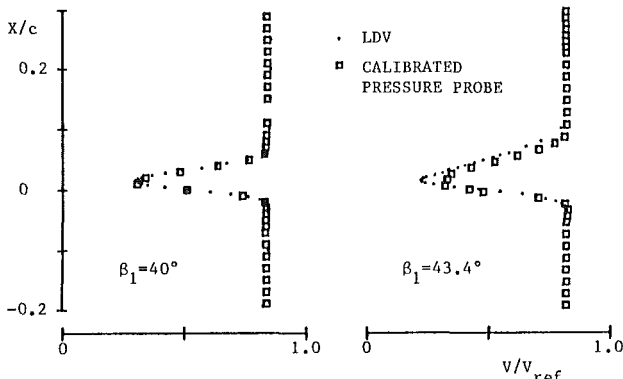
Fig. 7 Comparison of wake velocity profiles from LDV and calibrated pressure probe measurements at station E3 = D1

Fig. 8 Wake velocity distributions from calibrated pressure probe measurements

Fig. 9 Location of the wake minimum velocity from LDV and calibrated pressure probe measurements

from the calibrated pressure probe at each point in the survey. Compared with the velocity and stagnation pressure variation through the wake, the variation in the static pressure was small. An example of the indicated static pressure variation through the wake is shown for $\beta_1 = 43.4$ deg in Fig. 11.

The static pressure variation was associated with a flow angle variation, which is shown in Fig. 12. [The flow angle was derived from the nonintrusive LDV measurements. However, the qualitative behavior of the flow angle through the wake seen in Fig. 12 was confirmed by Dreon (1986) using a special flow angle probe designed for shear layers.] It is also noted that the static pressure level outside the wake increased progressively, moving downstream of the trailing edge.

The degree to which the pressure level changed downstream of the blading is illustrated in Fig. 13. On this figure are shown the pressures measured on the surfaces of the blading in relation to the static pressure measured by the probe at the upper traverse station nearly 1.8 chord lengths downstream (station D6 in Fig. 2). It is evident that the static pressure rise downstream of the trailing edge was a very significant fraction (~ 30 percent) of the overall pressure rise across the cascade. The accuracy of this somewhat surprising observation was immediately questioned. However, calculations of losses from the very detailed LDV measurements alone had not proved successful because it was found that the assumption of static pressure level determined the loss magnitude.

The relationship of the static pressure rise and loss coefficient can be appreciated most easily by assuming the flow to be
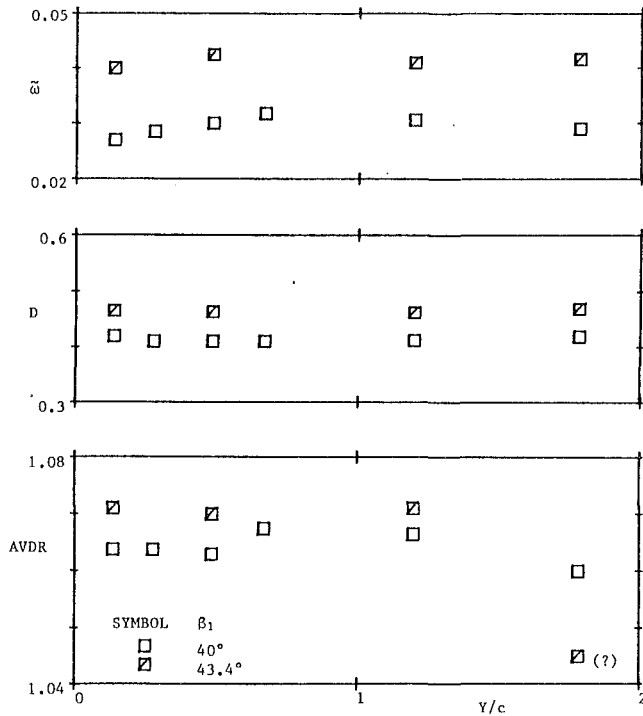
Fig. 10 Loss coefficient, diffusion factor, and AVDR from probe surveys at six downstream stations
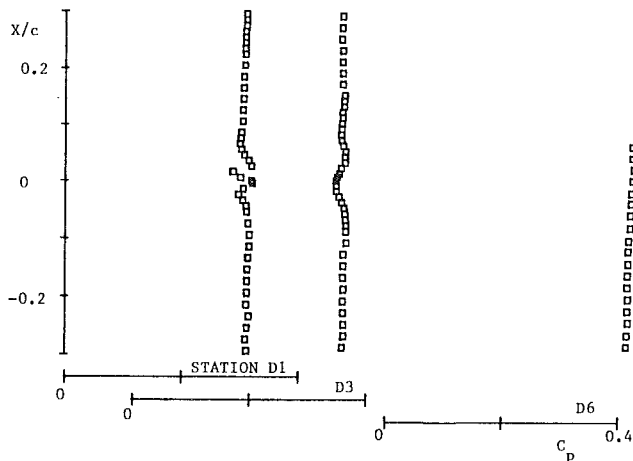
Fig. 11 Static pressure rise coefficient measured by the calibrated pressure probe in the wake at $\beta_1 = 43.4$ deg
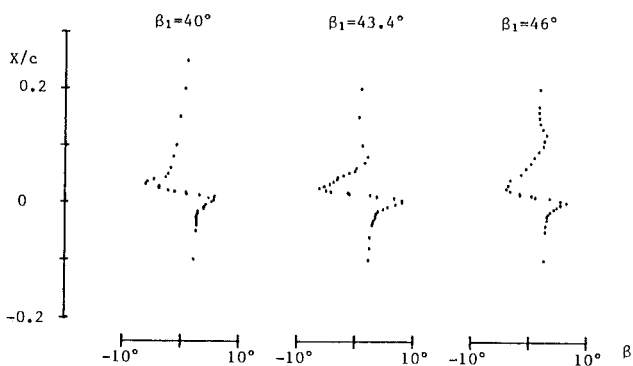
Fig. 12 LDV measurements of the flow angle in the wake at station E3

incompressible and fully mixed out at station D6. Then, the pressure rise coefficient is given by:
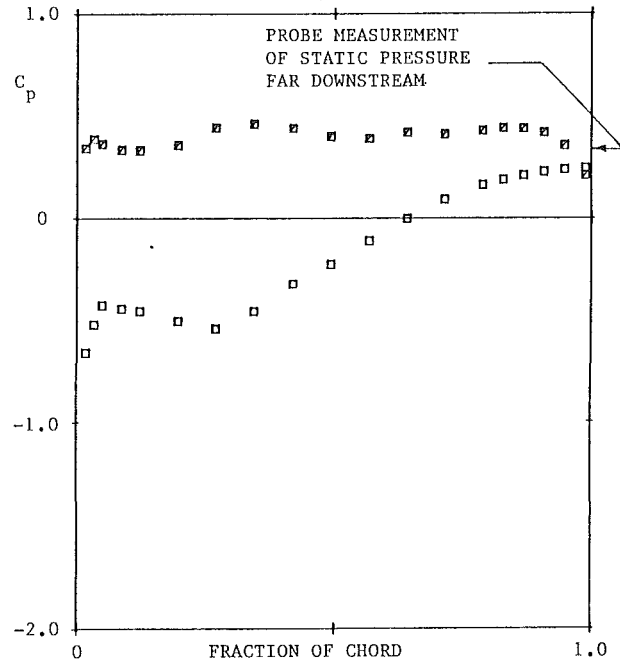
Fig. 13(a) Blade surface pressure at midspan for $\beta_1 = 40$ deg
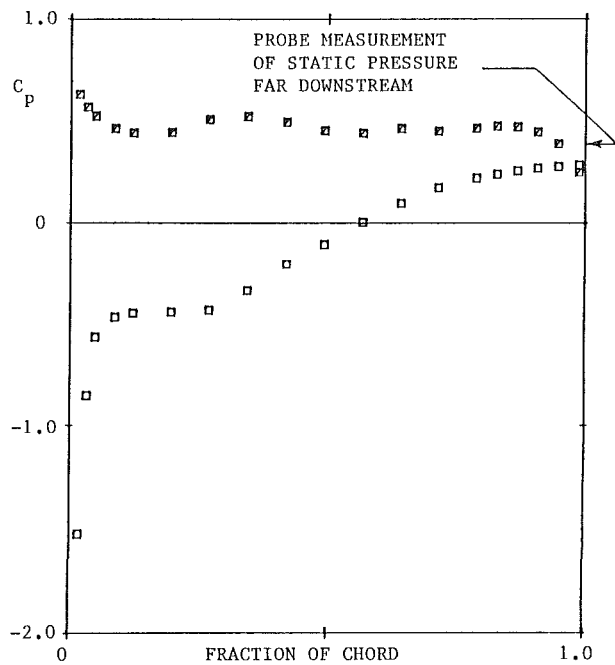
Fig. 13(b) Blade surface pressure at midspan for $\beta_1 = 43.3$ deg

$$C_{p2} = \frac{P_2 - P_1}{q_1} = \frac{P_{t2} - P_{t1}}{q_1} = \frac{\frac{1}{2}\rho(V_2^2 - V_1^2)}{q_1} = 1 - \frac{V_2^2}{V_1^2} - \tilde{\omega} \quad (1)$$

or

$$C_{p2} = 1 - (\text{AVDR})^2 \left(\frac{\cos\beta_1^2}{\cos\beta_2^2}\right) - \tilde{\omega} \quad (2)$$

The mixing-out process from the trailing edge is illustrated in Fig. 14. One blade space is shown with boundary layer displacement thicknesses of δ_s^* and δ_p^* on the suction and pressure sides, respectively. Conservation of momentum and mass for constant area axial flow gives

$$\frac{P_2 - P_{te}}{\frac{1}{2}\rho V_2^2} = 2 \left[\frac{s}{s - (d_{te} + \delta_s^* + \delta_p^*)} - 1 \right] \quad (3)$$

so that

Fig.14 Illustration of the mixing analysis

The LDV evaluates the first bracketed term (by integration in the nonuniform case) very accurately. However, the loss coefficient is a relatively small difference between the two much larger (bracketed) terms on the right-hand side. At any specific wake station, the value of Δ in the second term can be up to 30 percent of the term itself. Thus a reasonable assumption as to the magnitude of Δ (as a percentage of its value) can easily lead to an error in $\tilde{\omega}$ that is comparable in magnitude to its value. In contrast, the loss coefficient evaluated from the pressure probe measurements is the difference between weighted averages of measured stagnation pressure distributions. While the probe calibration for velocity enters into the calculation because the weighting factor is the local mass flux, the result depends to first order upon the direct measurement of stagnation pressure.

Thus it is argued that while LDV measurements are used widely to obtain velocity data for code verification purposes, viscous codes can not be validated using LDV data alone.

Since an important function of the code is to predict the losses, accurate measurements of losses must also be made in the experiment. In the absence of such measurements, numerical losses generated by the code can easily be reconciled with the velocity data through a seemingly reasonable assumption as to the pressure field.

$$C_{p2} = C_{pte} + \left[\frac{P_2 - P_{te}}{\frac{1}{2}\rho V^2{}_1}\right]\left[\frac{V_1^2}{V_2^2}\right] = C_{pte} + \Delta \qquad (4)$$

where

$$\Delta = 2\left[\frac{k\sigma}{1 - k\sigma}\right](\text{AVDR})^2\left(\frac{\cos\beta_1}{\cos\beta_2}\right)^2 \qquad (5)$$

and

$$k = \frac{d_{te}}{c} + \frac{\delta_s^*}{c} + \frac{\delta_p^*}{c} \qquad (6)$$

The following table gives the results of calculating c_{p2} using equation (4), using LDV measurements of δ_s^* and δ_p^* and probe measurements of AVDR and β_2. The result is compared with the probe measurements of C_{p2} far downstream and C_{p2} evaluated using equation 2:

β_1(deg)		40	43.4
β_2(deg)	From cylindrical	2	2
AVDR	probe, far	1.065	1.07
$\tilde{\omega}$	downstream	0.029	0.042
δ_s^*/c	From LDV	0.0189	0.0286
$\delta_p{}^*/c$	surveys	0.0035	0.0027
d_{te}/c		0.025	0.025
k	From equation (6)	0.0474	0.0563
Δ	From equation (5)	0.1146	0.1256
C_{pte}	Average of pressure and suction surface taps	0.224	0.263
C_{p2}	From equation (4)	0.339	0.389
C_{p2}	From probe	0.32–0.34	0.37–0.39
C_{p2}	From equation (2)	0.310	0.354

Clearly the static pressure rise downstream of the trailing edge is consistent with the mixing of the boundary layers in the wake of the blade.

The difficulty in evaluating the loss purely from LDV measurements of velocity can be seen by rewriting equation (1) as

$$\tilde{\omega} = 1 - \frac{V_2^2}{V_1^2} - C_{p2} = \left[1 - \frac{V_2^2}{V_1^2}\right] - [C_{pte} + \Delta] \qquad (7)$$

Conclusions

Measurements have been obtained of the flow and losses in a controlled diffusion compressor cascade that provide an unusual test case for viscous code calculations. Of significance to code validation are the following features found to be present as the inlet air angle was progressively increased:

1 a laminar leading-edge separation, turbulent reattachment bubble on the suction side of the blade, with reattachment moving progressively downstream;

2 natural transition on the pressure side of the blade;

3 no further separation ahead of the trailing edge to angles at which losses exceeded four times the minimum for the cascade;

4 a "simple" wake developing from fully attached boundary layers at the trailing edge. [It is noted that Baydar (1988) showed from a spectral analysis of the hot-wire signal that vortex-shedding was not present at $\beta_1 = 40$, 46, and 48 deg. Vortex shedding was shown to occur at specific flow velocities at flow angles corresponding to negative incidence in earlier tests (Sanger and Shreeve, 1986).]

In obtaining data to be used for the validation of viscous code predictions of losses, it is important to measure the pressure field and the velocity field with equal precision.

The following were concluded in relation to blade design:

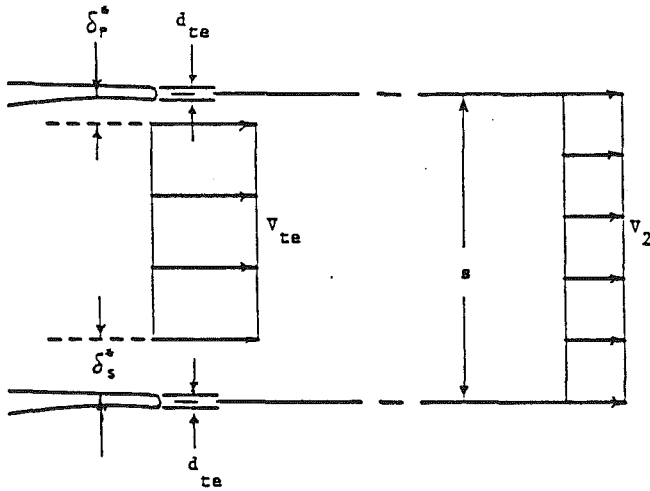1 The off-design performance of the Sanger cascade showed that trailing edge separation can be avoided by design and need not develop automatically as a result of increasing incidence. [The adverse gradient downstream of reattachment was found to decrease with increasing incidence while the suction under the separation intensified (Elazar and Shreeve, 1990).] While this is an attractive off-design characteristic, it might disappear if the separation bubble (which contributes to the losses) was eliminated or reduced by redesign.

2 If the flow can be designed to remain attached to the trailing edge, the trailing edge geometry, in principle, can be shaped to maximize pressure recovery and minimize losses due to mixing. Better understanding of the near-wake region of a highly loaded cascade and further development of viscous computational ability are required for such an optimization. However, it is clear even now that the thickness of the blade at the very trailing edge contributed a predictable increment to the losses.

Acknowledgments

References

Baydar, A., 1988, "Hot-Wire Measurements of Compressor Blade Wakes in a Cascade Wind Tunnel," M. S. Thesis, Naval Postgraduate School, Monterey, CA.

Classick, M., 1989, "Off-Design Loss Measurements in a Compressor Cascade," M. S. Thesis, Naval Postgraduate School, Monterey, CA.

Davis, R. L., Hobbs, D. E., and Weingold, H. D., 1988, "Prediction of Compressor Cascade Performance Using a Navier–Stokes Technique," ASME JOURNAL OF TURBOMACHINERY, Vol. 110, No. 4, pp. 520–531.

Deutsch, S., and Zierke, W. C., 1987, "The Measurement of Boundary Layers on a Compressor Blade in Cascade: Part 1—A Unique Experimental Facility," ASME JOURNAL OF TURBOMACHINERY, Vol. 109, pp. 520–526.

Deutsch, S., and Zierke, W. C., 1988 "The Measurement of Boundary Layers on a Compressor Blade in Cascade: Part 2—Suction Surface Boundary Layers," ASME JOURNAL OF TURBOMACHINERY, Vol. 110, pp. 138–145.

Deutsch, S., and Zierke, W. C., 1988, "The Measurement of Boundary Layers on Compressor Blade in Cascade: Part 3—Pressure Surface Boundary Layers and the Near Wake," ASME JOURNAL OF TURBOMACHINERY, Vol. 110, pp. 146–152.

Dreon, J. W., 1986, "Controlled Diffusion Compressor Blade Wake Measurements," M. S. Thesis, Naval Postgraduate School, Monterey, CA.

Elazar, Y., 1988, "A Mapping of the Viscous Flow Behavior in a Controlled Diffusion Compressor Cascade Using Laser Doppler Velocimetry and Preliminary Evaluation of Codes for the Prediction of Stall," Ph.D. Thesis, Naval Postgraduate School, Monterey, CA.

Elazar, Y., and Shreeve, R. P., 1990, "Viscous Flow in a Controlled Diffusion Compressor Cascade With Increasing Incidence," ASME JOURNAL OF TURBOMACHINERY, Vol. 112, pp. 256–266.

Hobbs, D. E., Wagner, J. H., Dannenhoffer, J. F., and Dring, R. P., 1982, "Experimental Investigation of Compressor Cascade Wakes," ASME Paper No. 82-GT-299.

Hobbs, D. E., and Weingold, H. D., 1984, "Development of Controlled Diffusion Airfoil for Multi-stage Compressor Applications," ASME *Journal of Engineering for Gas Turbines and Power*, Vol. 106, pp. 371–378.

McCormick, D. C., Patersen, R. W., and Weingold, H. D., 1988, "Experimental Investigation of Loading Effects on Simulated Compressor Airfoil Trailing Edge Flowfields," AIAA Paper No. 88-0365.

McNally, W. D., 1970, "Fortran Program for Calculating Compressible Laminar and Turbulent Boundary Layers in Arbitrary Pressure Gradients," NASA TN D-5681.

Murray, K. D., 1989, "Automation and Extension of LDV Measurements of Off-Design Flow in a Subsonic Cascade Wind Tunnel," A. E. Thesis, Naval Postgraduate School, Monterey, CA.

Patersen, R. W., and Weingold, H. D., 1985, "Experimental Investigation of a Simulated Compressor Trailing Edge Flow Field," *AIAA Journal*, Vol. 21, No. 5, pp. 768–775.

Sanger, N. L., 1983, "The Use of Optimization Techniques to Design Controlled-Diffusion Compressor Blading," ASME *Journal of Engineering for Power*, Vol. 105, pp. 256–264.

Sanger, N. L., and Shreeve, R. P., 1986, "Comparison of Calculated and Experimental Cascade Performance for Controlled Diffusion Compressor Stator Blading," ASME JOURNAL OF TURBOMACHINERY, Vol. 108, pp. 42–50.

Sanz, J. M., 1988, "Automated Design of Controlled Diffusion Blades," ASME JOURNAL OF TURBOMACHINERY, Vol. 110, pp. 540–544.

Shamroth, S. J., McDonald, H., and Briley, W. R., 1984, "Prediction of Cascade Flow Fields Using the Averaged Navier–Stokes Equations," ASME *Journal of Engineering for Gas Turbines and Power*, Vol. 106, pp. 383–390.

Shreeve, R. P., and Elazar, Y., 1989, "Laser Doppler Velocimeter Data From a Controlled Diffusion Compressor Cascade for Viscous Code Validation," Technical Report, NPS 67-89-001, Naval Postgraduate School, Monterey, CA (in preparation).

Snir, Z., 1988, "Investigation of Incompressible Cascade Flows Using a Viscous/Inviscid Interaction Code," M.S. Thesis Naval Postgraduate School, Monterey, CA.

Zierke, W. C., and Deutsch, S., 1990, "The Measurement of Boundary Layers on a Compressor Blade in Cascade: Part 4—Flow Fields for Incidence Angles of −1.5 and −8.5 Degrees," ASME JOURNAL OF TURBOMACHINERY, Vol. 112, pp. 241–255.

The Effects of Wake Mixing on Compressor Aerodynamics

R. P. Dring
United Technologies Research Center,
East Hartford, CT 06108

D. A. Spear
Pratt and Whitney Aircraft,
East Hartford, CT 06108

A methodology based on wake mixing has been developed that enables more accurate predictions of compressor airfoil pressure distributions when the airfoil is operating downstream of an airfoil row that has strong wakes. The methodology has an impact on throughflow analysis, on airfoil-to-airfoil flow analysis, and on the interpretation of experimental data. It is demonstrated that the flow in the endwall region is particularly sensitive to mixing due to the strong wakes caused by the secondary flow and corner separation that commonly occur in this region. It is also demonstrated that wake mixing can have a strong impact on both airfoil incidence and deviation as well as on loading. Differences of up to 13 deg and 30 percent in loading are demonstrated.

Introduction

Axial compressor airfoils operate in an aerodynamic environment that is three-dimensional, compressible, viscous, and unsteady. In spite of this complexity, the analytical tools that designers typically have at their disposal are remarkably accurate, especially when one considers that most of these tools are two-dimensional, or quasi-three-dimensional at best. Furthermore, except for a few recent examples (e.g., Gundy-Burlet et al., 1989), these analytical tools are based on the assumption that the flow is steady.

The unsteadiness of the flow in a compressor airfoil row is due to the airfoil moving through: (1) the potential fields of both the upstream and downstream airfoil rows, and (2) the wakes of the upstream rows. There is a wealth of data in the literature that documents the fact that these wakes can be both very deep and wide, especially at the relatively close axial spacings between airfoil rows common to modern compressor design.

An example of such wakes can be seen in the total pressure data presented in Fig. 1 for the flows downstream of the second-stage rotor and stator of a large-scale, two-stage compressor (Fig. 2). This, and many additional data for this compressor are discussed in the following references: Dring et al. (1983), Dring and Joslyn (1986, 1989), and Joslyn and Dring (1985). All the traverse and airfoil pressure distribution measurements in this compressor were made with long lengths of instrumentation tubing between the pressure port in the flow and the transducer. They are, therefore, viewed as being indicative of time-averaged results. These data are an extreme example of a highly distorted (nonaxisymmetric) flow. It is on the verge of rotating stall and is not representative of design practice. However, because of the severity of the wakes, it is a good test case for the methodology presented here.

The impact that these nonaxisymmetries have on through-

a) ROTOR EXIT (ROTARY TOTAL PRESSURE)
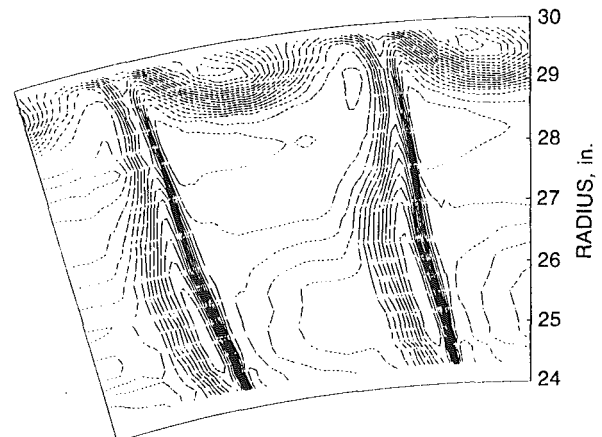
b) STATOR EXIT (TOTAL PRESSURE)
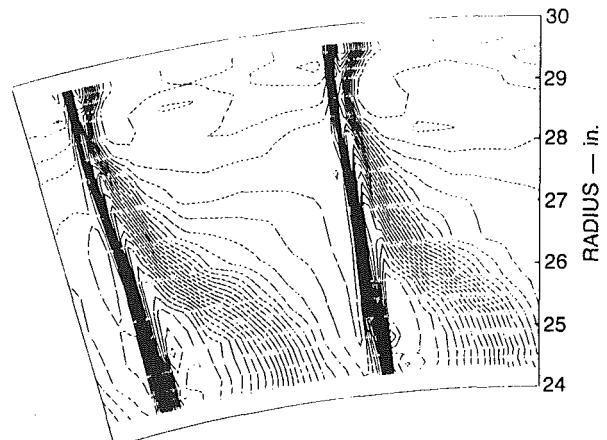
Fig. 1 Second-stage rotor and stator exit total pressures at near-stall conditions, $\phi = 0.45$
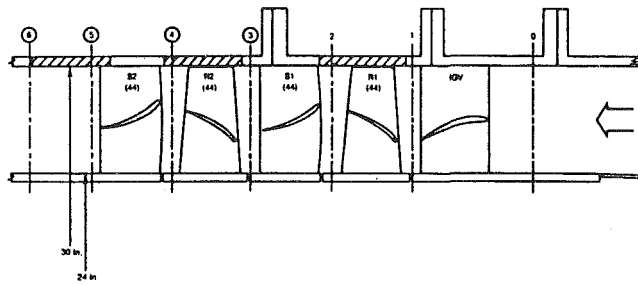
Fig. 2 Two-stage compressor geometry

Fig. 3 First-stage stator exit at 5 percent span, relative pressures and flow angle at near-stall conditions, $\phi = 0.45$ (x = mixed, m = mass average, a = area average)

flow analysis has been examined by Dring and Oates (1990a, 1990b). This work presented a mathematically rigorous methodology for specifying the input and for interpreting the output of an analysis of a highly nonaxisymmetric flow. The present work is an extension of this reasoning to the airfoil-to-airfoil flow analysis.

The question to be addressed here is whether there is a reasonably accurate methodology that can be applied to calculate an airfoil pressure distribution when the flows entering and exiting the airfoil row are both nonuniform and unsteady. The discussion will be limited to two- (or quasi-three-) dimensional, steady, airfoil-to-airfoil flow predictions (e.g., Caspar et al., 1980).

The approach to be followed in developing this methodology will be to examine the nature of a highly nonuniform flow in a compressor (Fig. 1) and the pressure distribution on an airfoil operating in this flow. It will be shown that the nonuniform flow can be related to an equivalent steady, uniform flow that results in a surprisingly accurate prediction of the airfoil pressure distribution. This equivalent condition is determined by performing a simple two-dimensional mixing calculation (Stewart, 1959) on the nonuniform inlet and exit flows. It is not assumed that the flow is actually fully mixed, only that the mixed-out flow is aerodynamically "equivalent" to the unmixed flow. It will be demonstrated that the mixing analysis can produce incidence and deviation angles that differ by as much as 13 deg from the "average" angles in the nonaxisymmetric flow. Furthermore, the mixing analysis can produce incident dynamic pressures (airfoil loadings), which differ by as much as 30 percent from the "average" dynamic pressure in the nonaxisymmetric flow.

As an example, it will be demonstrated that the poor agreement between measured and computed pressure distributions that had previously been attributed to the effects of unsteadiness and hub corner separation could be greatly improved by using mixed-out information.

As a separate issue, it will also be demonstrated that the throughflow analysis by Dring and Oates (1990a, 1990b) contains all of the information necessary to carry out the mixing calculation with a reasonable degree of accuracy.

Application of the Wake Mixing Process

There are major departures from axisymmetry in turbomachinery flow due to the airfoil wakes. Figure 1 illustrates examples of such wakes in the flow downstream of the second stage rotor and stator of a large-scale, low-speed compressor (Fig. 2) operating at near-stall conditions (Dring and Joslyn, 1986). These wakes appear as unsteadiness to the downstream rows because of the relative motion between them. They are due to the airfoil boundary layers, tip leakage, endwall secondary flow, and corner separation. A number of previous works that either discuss, or show evidence of, corner separation are included in the References.

Various flow quantities relative to the second-stage rotor at 5 percent span (from the hub) were determined from a circumferential traverse (in the absolute frame of reference) of the first-stage stator wake with the compressor operation at near-stall conditions (Fig. 3). The circumferential variations (in the stator frame of reference) of the relative inlet angle and the relative total and static pressures are shown. These spatial variations correspond to temporal variations in the flow incident on the second-stage rotor. The axial gap between the stator and the rotor was 29 percent of chord. The traverse data

Nomenclature

B_x	= airfoil axial chord	U	= wheel speed	
C	= absolute flow speed	W	= relative flow speed	
CP	= pressure coefficient = $(P - P_{t,0}/Q_{Um})$	X	= axial coordinate	
		α	= absolute flow angle from axial	
DCT	= defined in Eq. (15)			
P	= pressure	β	= relative flow angle from axial	
PTREL	= relative total pressure	θ	= circumferential distance	
PS	= static pressure	ρ	= density	
$P_{t,0}$	= compressor inlet absolute total pressure	τ	= airfoil pitch	
Q_{Um}	= dynamic pressure based on midspan wheel speed	ϕ	= flow coefficient = (C_x/U_m)	

Subscripts

m = midspan
x = axial component
t = tangential component
1 = airfoil incident quantities

Superscripts

$-a$ = pitchwise area average
$-m$ = pitchwise mass average
$\tilde{}$ = mixed-out
$\hat{}$ = defined in Eqs. (6) and (7)
$'$ = fluctuation from the density average

in Fig. 3 were acquired at a location only 14 percent chord upstream of the rotor leading edge. The relative inlet angle varied by about 40 deg. The relative total pressure varied by about 60 percent of the average relative dynamic pressure. The static pressure varied by about 20 percent of the average relative dynamic pressure.

If it is one's intent to predict the pressure distribution on a rotor operating in this highly nonuniform inflow, there is a need to develop a methodology for determining the steady inlet conditions, which are aerodynamically equivalent to the nonuniform inlet conditions shown in Fig. 3. The area and mass average (a&m) of the various quantities are shown in Fig. 3, but it is not clear that these averages have any physical significance in computing the airfoil pressure distribution.

An equivalent steady inlet condition should have the same mass flow and the same axial and tangential momentum as the spatially varying inlet conditions. These requirements are precisely those of a two-dimensional mixing process (Stewart, 1959). In the analysis it will be assumed: (1) that the stream tube height is constant during mixing (i.e., a purely two-dimensional mixing process), (2) that the mixing occurs at a fixed radius, and (3) that the radial component of velocity has a negligible role in the mixing process. It is important to realize that mixing is only being used to evaluate an equivalent uniform flow condition at the measurement plane. It is not being assumed that mixing is actually occurring in the flow. Hence assumptions (1) and (2) are valid even for a flowpath where the stream surface radius is varying strongly.

For incompressible flow such a mixing process is expressed as follows:

Conservation of mass

$$C_x^{-a} = \text{const} \tag{1}$$

Conservation of axial momentum

$$P^{-a} + (\rho \cdot C_x^{-a} \cdot C_x^{-m}) = \text{const} \tag{2}$$

Conservation of tangential momentum

$$C_x^{-a} \cdot C_t^{-m} = \text{const} \tag{3}$$

This shows that the angles based on C_x^{-a} and on C_t^{-m} or W_t^{-m} are constant during the mixing process. These are the mixed-out absolute and relative flow angles:

$$\tilde{\alpha} = \arctan(C_t^{-m}/C_x^{-a}) \tag{4}$$

$$\tilde{\beta} = \arctan(W_t^{-m}/C_x^{-a}) \tag{5}$$

It will be demonstrated that, in spite of the fact that the flow incident on compressor airfoils is very unsteady (i.e., very nonuniform) due to the passing wakes of upstream airfoils, the mixed-out flow angles produce an accurate prediction of the time-averaged airfoil pressure distribution. It is important to remember that it is not being assumed that the wakes are actually mixed out, only that the mixed condition is an "equivalent" steady condition. The mixed-out relative flow angle has been indicated by the x in Fig. 3. It is 4.7 deg greater than the mass-averaged angle, i.e., a more positive incidence.

The results of using both the mass-averaged and the mixed-out relative flow angles in the flow aft of the first stator (Fig. 3) for the prediction of the pressure distribution of the second stage rotor at 3.2 percent span are shown in Fig. 4. The mass-averaged relative inlet angle (β^{-m}) was used in Fig. 4(a) and the mixed-out angle ($\tilde{\beta}$) was used in Fig. 4(b). The 4.7 deg change toward a more positive incidence has had a powerful impact on the computed (Caspar et al., 1980) pressure distribution. At this 3.2 percent span location the rotor was operating in the unsteady inflow environment of the first-stage stator exit at a radial location close to the 5 percent span location (Fig. 3). Recall also that this nonuniform flow was at a location only 14 percent chord upstream of the rotor. Parenthetically, although the stream tube height is constant in
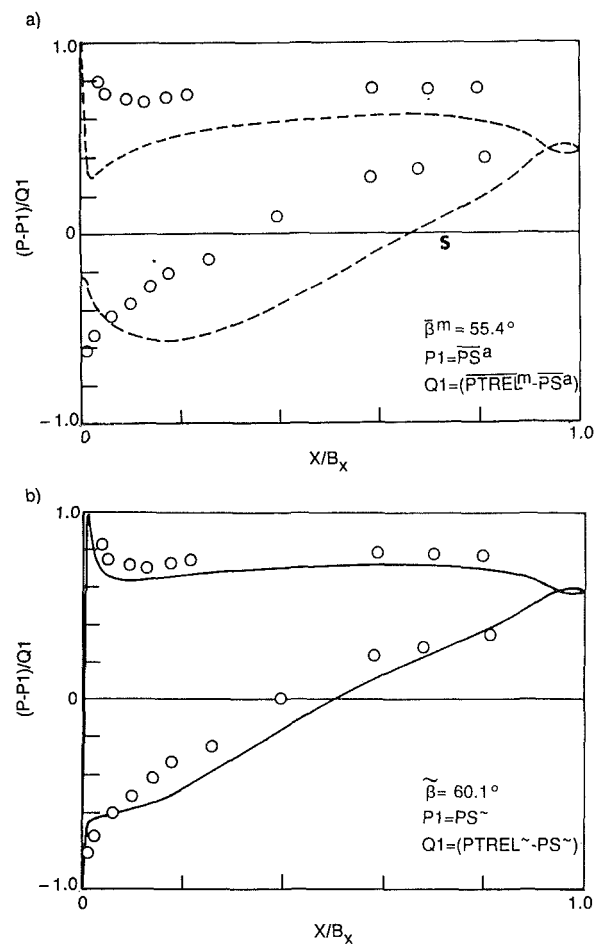
Fig. 4 Second-stage rotor pressure distribution at 3.2 percent span at near-stall conditions, $\phi = 0.45$

the mixing process, it does change across the airfoil row from inlet to exit. This height ratio was based on the change in measured area-averaged axial velocity (which is conserved in mixing) across the row.

Not only has the inlet flow angle been changed between Figs. 4(a) and 4(b), but the inlet dynamic and static pressures (Q1 and P1) have also been changed. This has resulted in a shift in the measured data (the symbols), which can be seen most clearly at the suction surface data point at 40 percent chord. The data in Fig. 4(a) were plotted based on the mass-averaged inlet relative total pressure and the area-averaged inlet static pressure (see Fig. 3). The data in Fig. 4(b) were plotted based on the mixed-out inlet relative total pressure and the mixed-out inlet static pressure (see Fig. 3). This difference in incident relative dynamic pressure amounted to an apparent 16 percent increase in the airfoil loading, i.e., a 16 percent reduction in the rotor inlet relative dynamic pressure. Thus, in addition to the 4.7 deg change in incidence, the 16 percent reduction in loading also improved the agreement between the measured and computed results.

In the absence of radial transport, basing the inlet and exit conditions on mixed-out quantities will cause the axial and tangential components of force on the airfoil to equal the changes in the axial and tangential components of momentum. Only the mixed-out quantities give this balance and in the present example (Fig. 4) this amounted to a 16 percent error in airfoil loading (tangential force).

A comparison of the measured tangential force on the rotor with the measured change in the flux of tangential momentum from inlet to exit indicated that the two values were within 9 percent of each other at the 3.2 percent span location. This
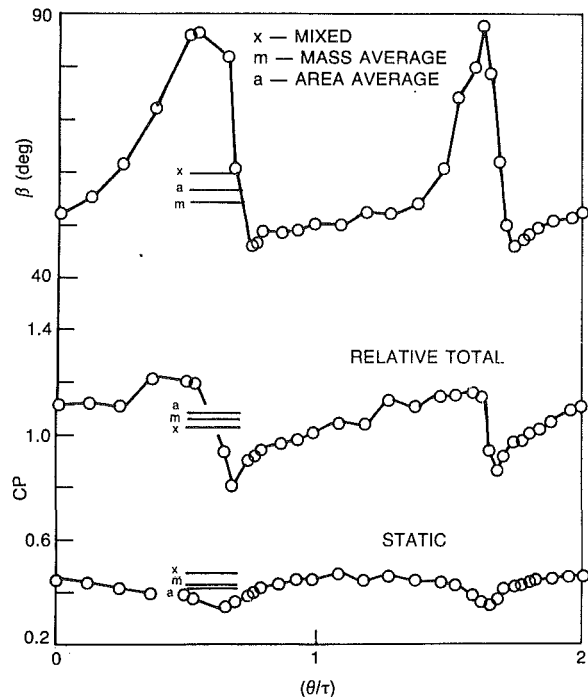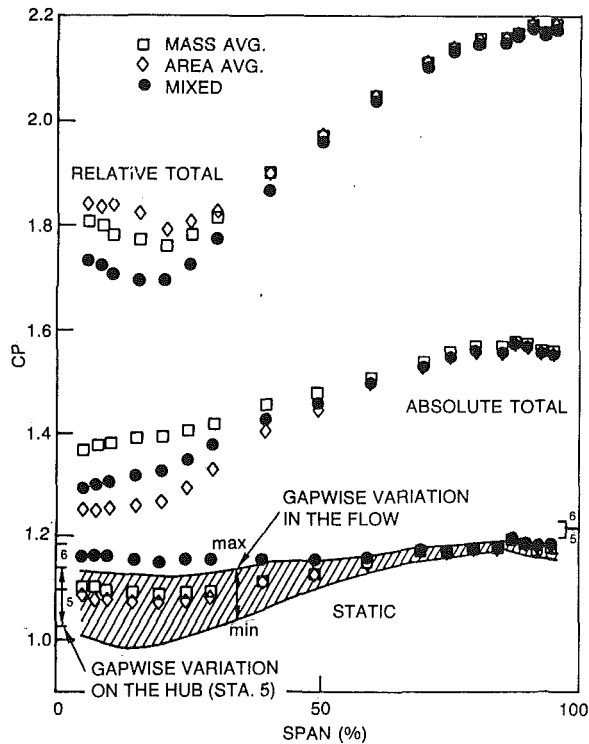
Fig. 5 Second-stage stator exit pressures at near-stall conditions, $\phi = 0.45$

Fig. 6 Second stage stator exit pressures at nominal design conditions, $\phi = 0.51$

difference is due in part to measurement error but primarily to radial transport between the inlet and exit measuring stations (Stations 3 and 4, Fig. 2). The tangential force on the airfoil is about 9 percent less than the change in the flux of tangential momentum. This difference can be seen in Fig. 4(b) in that the area within the computed curve is somewhat greater than the area within the measured data points. This issue of an imbalance between airfoil force and flow momentum due to radial transport will be mentioned again below in regard to the second stator (where the imbalance is on the order of 100 percent).

Prior to this examination of mixing, the poor agreement between the measured and computed results in Fig. 4(a) had been attributed to unsteadiness and to the presence of hub corner separation on the rotor (Dring and Joslyn, 1986). The S on the $CP = 0$ axis indicates the start of the hub corner separation (as indicated by surface flow visualization). However, as shown in Fig. 4(b), in spite of the unsteadiness and the hub corner separation, a much improved prediction was achieved using the mixed-out inlet flow data.

The mixed-out quantities produce a more accurate prediction of the pressure distribution because they relate the distorted flow (Fig. 3) to an equivalent steady undistorted flow having the same axial and tangential momentum. Since two-dimensional mixing conserves mass flow, and axial and tangential momentum, the mixing process does not affect either AVDR or the axial and tangential forces acting on the airfoil.

Differences in incidence and deviation as large as 13 deg and differences in inlet dynamic pressure as large as 30 percent due to wake mixing will be demonstrated below.

Effect of Wake Mixing on Pressure

Now that it has been demonstrated that mixing can have an important impact on airfoil flow analysis, let us examine the magnitude of this impact at other locations in the compressor and at other flow conditions. First we will examine its effect on pressure. The second-stage stator produced the most severely distorted flow in the compressor (Fig. 1b). The spanwise
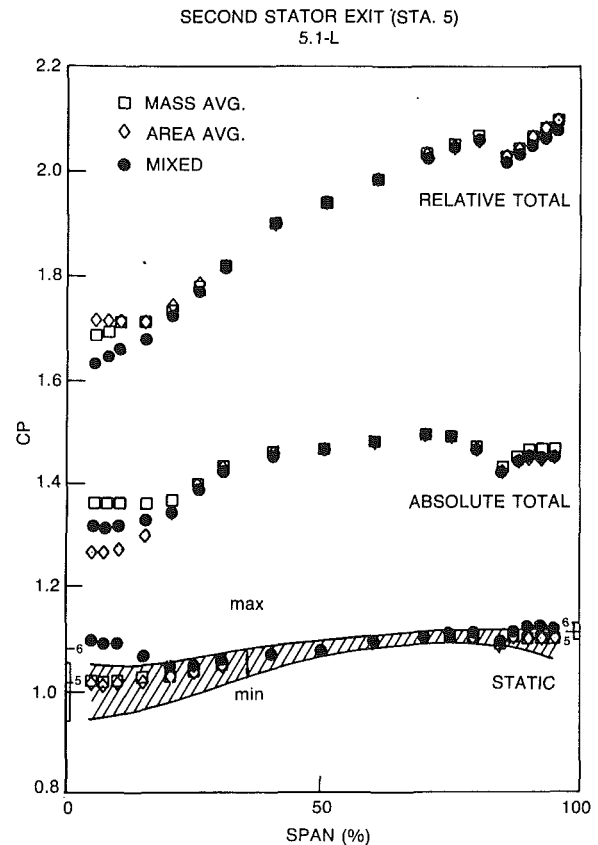
distributions of the area- and mass-averaged pressures, as well as the mixed-out pressures, are shown in Fig. 5 for the near-stall condition.

Since the traverse data were acquired relatively close to the stator (15 percent of chord aft) there was a strong pitchwise variation in the static pressure. This variation is indicated by the cross-hatched band in Fig. 5.

The pitchwise variation of the static pressure was also measured on the flowpath hub and tip at the traverse plane aft of the second stator (Station 5). These bands and their area averages are shown in Fig. 5 at 0 and 100 percent span (the hub and tip). Similar hub and tip static pressure measurements one chord further downstream (at Station 6) showed practically no pitchwise variation, but they were at a considerably higher level, especially at the hub.

It is noteworthy that both the band of static pressure at the traverse plane (Station 5) and the area average correspond very closely to those measured on the flowpath hub and tip. Furthermore, the higher level of the mixed-out static pressure corresponds very closely to the flowpath data at Station 6, especially at the hub. It is gratifying to see that such a complicated flow can be described with such a simple model.

It can also be seen that the mixing process has a powerful impact on the absolute and relative total pressures. In particular, at 15 percent span the mixed-out relative dynamic pressure is 30 percent smaller than that based on the mass-averaged relative total pressure and the area-averaged static pressure. This would have a strong influence on the interpretation of the pressure distribution (i.e., airfoil loading) measured on a third-stage rotor at this span location.

These effects are not limited to very highly loaded, near-stall conditions. It is shown in Fig. 6 that while the effects are weaker at nominal design conditions, they are still quite strong. In particular, at 5 percent span the mixed-out relative dynamic

Fig. 7 Second-stage stator exit flow angles at nominal design conditions, $\phi = 0.51$
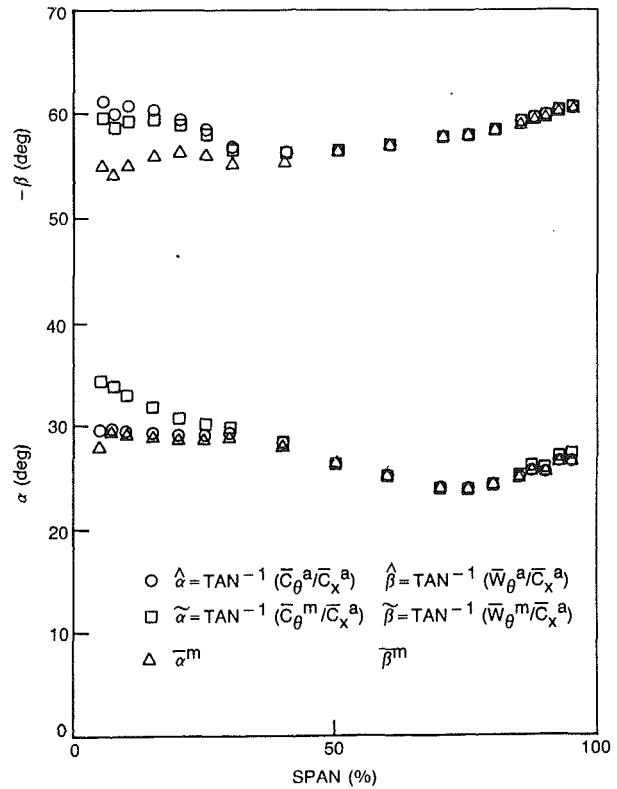
Fig. 8 First-stage stator exit flow angles at near-stall conditions, $\phi = 0.45$

pressure is 25 percent smaller than that based on the mass-averaged relative total pressure and the area-averaged static pressure. Corner separation is present on this stator even at the nominal design condition (Joslyn and Dring, 1985).

Effects of Wake Mixing on Flow Angles

The impact of mixing on the absolute and relative flow angles aft of the second stator at the nominal design condition is shown in Fig. 7. It can be seen that even at these more benign conditions mixing produces incidence and deviation angle profiles that differ from the mass-averaged profiles by as much as 8 deg near the hub.

An additional flow angle definition is included in this and in the following figures. This is the flow angle employed in throughflow analysis (Dring and Oates, 1990a, 1990b). It is based on the density- (or area-) averaged velocity components. The reason for this is that these are the averaged velocity components that naturally arise in a throughflow analysis (Hirsch and Warzee, 1979):

$$\hat{\alpha} = \arctan(C_t^{-a}/C_x^{-a}) \qquad (6)$$

$$\hat{\beta} = \arctan(W_t^{-a}/C_x^{-a}) \qquad (7)$$

The angles needed for throughflow analysis ($\hat{\alpha}$ and $\hat{\beta}$) and the mixed-out flow angles ($\tilde{\alpha}$ and $\tilde{\beta}$) are related to each other as follows:

$$\tan(\tilde{\alpha}) = \tan(\hat{\alpha}) + [(C_t' \cdot C_x')^{-a}/(C_x^{-a})^2] \qquad (8)$$

$$\tan(\tilde{\beta}) = \tan(\hat{\beta}) + [(W_t' \cdot C_x')^{-a}/(C_x^{-a})^2] \qquad (9)$$

The primed quantities are the variations from the density average. However, since the flow being considered here is nearly incompressible, the density and area average are very nearly equal. Accordingly, the primed quantities will be based on area averages:

$$C_x' = (C_x - C_x^{-a}) \qquad (10)$$

$$C_t' = (C_t - C_t^{-a}) \qquad (11)$$

$$W_t' = (W_t - W_t^{-a}) \qquad (12)$$

and since

$$W_t = C_t - U \qquad (13)$$

then,

$$W_t' = C_t' \qquad (14)$$

It is fortunate that both of these angles ($\hat{\alpha}$ and $\hat{\beta}$, as well as $\tilde{\alpha}$ and $\tilde{\beta}$) can be calculated in the throughflow analysis. Specifically, the throughflow analysis for nonaxisymmetric flow by Dring and Oates (1990a, 1990b) contains a parameter that accounts for the difference between the area and mass averages of the tangential velocity. This parameter is defined as follows (assuming that area and density averages are equal):

$$DCT = (C_t^{-a} - C_t^{-m})/U_m \qquad (15)$$

This parameter is not directly input to the throughflow analysis. Rather, it is calculated from other input data. From the throughflow calculation the following information is available (either as input data, or as a computed results): $\hat{\alpha}$, $\hat{\beta}$, DCT, and (C_x^{-a}/U_m). with this information the following relationships can be evaluated:

$$\tan(\tilde{\alpha}) = \tan(\hat{\alpha}) - [DCT/(C_x^{-a}/U_m)] \qquad (16)$$

$$\tan(\tilde{\beta}) = \tan(\hat{\beta}) - [DCT/(C_x^{-a}/U_m)] \qquad (17)$$

Thus it is possible, with no additional information, for the throughflow analysis of Dring and Oates (1990a, 1990b) to compute the angles that are needed for the airfoil flow analysis, $\tilde{\alpha}$ and $\tilde{\beta}$. In fact, there is no need for $\hat{\alpha}$ and $\hat{\beta}$. The throughflow analysis could be carried out using $\tilde{\alpha}$ and $\tilde{\beta}$ as input and then calculating the angles needed to relate the density-averaged velocity components ($\hat{\alpha}$ and $\hat{\beta}$).

It is also possible to calculate the mixed-out dynamic pressure from the throughflow analysis of Dring and Oates (1990a, 1990b). The throughflow calculation provides both C_x^{-a} and W_t^{-a}. W_t^{-m} can be calculated from Eq. (15). These then give
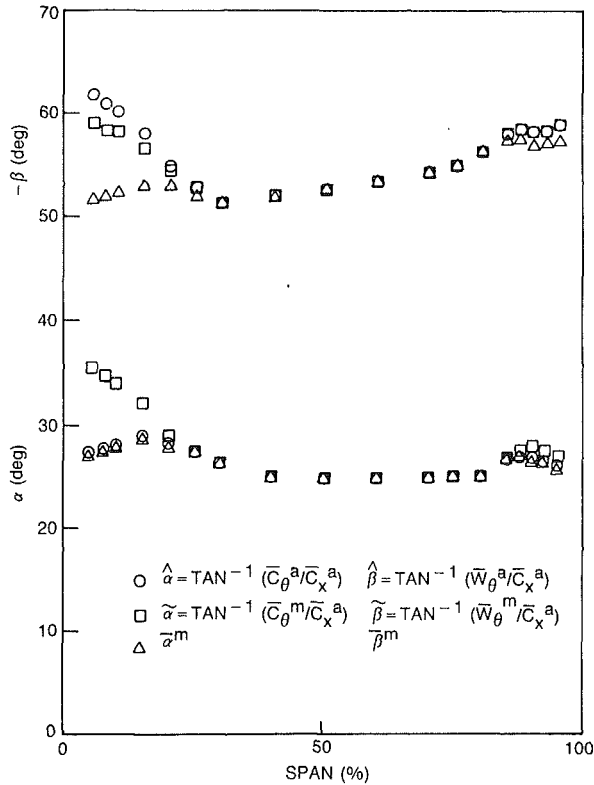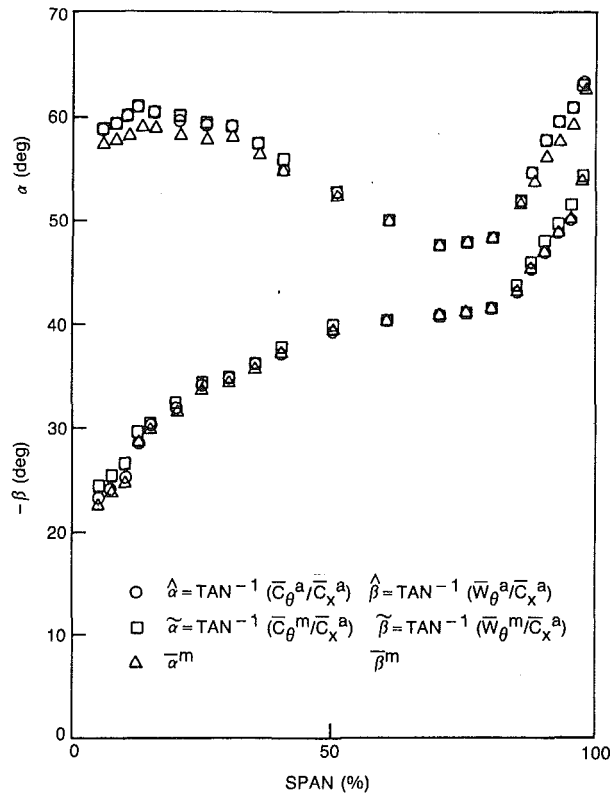
Fig. 9 Second-stage rotor exit flow angles at near-stall conditions, $\phi = 0.45$

Fig. 10 Second-stage stator exit flow angles at near-stall conditions, $\phi = 0.45$

the mixed-out dynamic pressure (the radial velocity component usually being relatively small):

$$\bar{Q}_{\text{ref}} = 1/2 \cdot \rho \cdot ([C_x^{-a}]^2 + [W_t^{-m}]^2) \tag{18}$$

The calculation of the mixed-out total and static pressures requires some approximation. This will be discussed below in connection with Fig. 10.

The spanwise distributions of the flow angles at the near-stall flow condition downstream of the first-stage stator (Station 3) and downstream of the second-stage rotor and stator (Stations 4 and 5) are shown in Figs. 8, 9, and 10. At the first stator exit, the 5 deg difference between the mixed-out and mass-averaged relative flow angles shown in Fig. 3 corresponds to the results plotted in Fig. 8 at 5 percent span. Notice that there is also a 5 deg difference in the first stator absolute exit angle. These differences decrease dramatically toward midspan as the influence of the first-stage stator hub corner separation diminishes.

The second-stage rotor and stator exit angle profiles at the near-stall condition are plotted in Figs. 9 and 10. These are the same conditions as those for the total pressure contour data shown in Fig. 1. Although the trends are the same, the magnitudes of the angle differences aft of the rotor (Fig. 9) are much smaller than those aft of the stators (Figs. 8 and 10). Hence, the effect of wake mixing at the inlet to the second stator is relatively weak ($\Delta\alpha \le 2$ deg).

The largest angle differences are those aft of the second-stage stator (Fig. 10). These second stator exit conditions correspond to those for the pressure data shown in Fig. 5. The magnitude of the difference between the various angle definitions for both the absolute flow angle (deviation) and the relative flow angle (incidence) is about 13 deg. Here again, the magnitude of the difference decreases toward midspan as the effect of the second stator hub corner separation diminishes.

Had there been a third-stage rotor on the compressor it would have been very strongly impacted by the effects of mixing. Near the 15 percent span location, both the 10 deg dif-
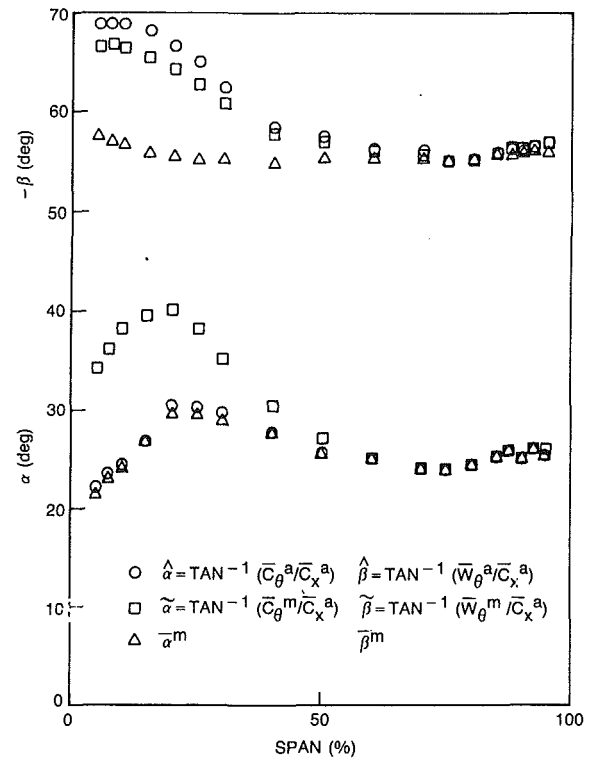
Table 1 Second stator exit at 5 percent span and near-stall conditions

Quantity	Exact	Approximate	Error
C_x^{-a}/U_m	0.300		
C_x^{-m}/U_m	0.431	0.505	17%
C_t^{-a}/U_m	0.121		
C_t^{-m}/U_m	0.204		
W_t^{-m}/U_m	−0.696		
Arctan(C_t^{-a}/C_x^{-a})	22.0°		
Arctan(C_t^{-m}/C_x^{-m})	25.3°	22.0°	3.3°
$\bar{Q}_{rel}$	0.574	0.574	0%
CPS^{-a}	1.083		
$\overline{CPS}$	1.161	1.205	8% $\bar{Q}_{rel}$
$\overline{CPTREL}$	1.735	1.779	8% $\bar{Q}_{rel}$

ference between the mass-averaged and the mixed-out relative flow angles (Fig. 10) and the 30 percent difference in the relative incident dynamic pressure (Fig. 5) would have led to an entirely different airfoil pressure distribution prediction.

While the calculation of the mixed-out flow angles and dynamic pressure (Eqs. (16), (17), and (18)) can be carried out exactly with the information available in the throughflow analysis (Dring and Oates, 1990a, 1990b), the calculation of the mixed-out total and static pressures requires some additional information. Carrying out the mixing calculation (Eqs. (1), (2), and (3)) requires the specification of the following averaged quantities: C_x^{-a}, C_x^{-m}, W_t^{-m}, and P^{-a}. Each of these quantities is already calculated as part of the throughflow analysis, with the exception of C_x^{-m}. However, even this quantity can be calculated with reasonable accuracy when the approximation is made that the area- and mass-averaged velocity
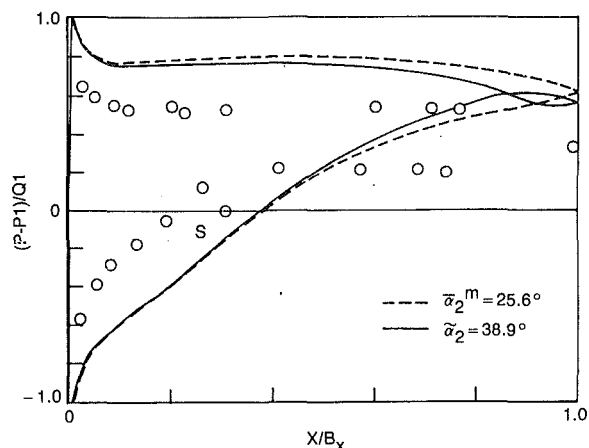
Fig. 11 Second-stage stator pressure distribution at 12.5 percent span at near-stall conditions, $\phi = 0.45$

vectors relative to the upstream airfoil are parallel. For the flow aft of a stator this approximation implies:

$$(C_t^{-m})/(C_x^{-m}) \approx (C_t^{-a})/(C_x^{-a}) = \tan(\hat{\alpha}) \qquad (19)$$

This approximation has no affect either on the dynamic pressure (Eq. (18)) or on the force on the airfoil. It only affects the pressure distribution by an additive constant, i.e., the pressure level, not the pressure distribution. As a "worst case" example, consider the second stator exit, at the near-stall condition, and at 5 percent span (Table 1).

Note that this approximation (Eq. (19)) has no effect on the relative dynamic pressure $((Q_{ref}^-)$. It only affects the pressure distribution by an additive constant on the mixed-out static and relative total pressures (CP̃S and CPT̃REL). Even for this "worst case" situation where the local blockage approaches 40 percent (Joslyn and Dring, 1985) the approximation leads to an error in pressure level of only 8 percent of the relative dynamic pressure.

Even at the near-stall condition the impact of mixing on the various second stator inlet flow angles was relatively weak ($\Delta\alpha_1 \approx 2$ deg, Fig. 9). Its effect on the stator exit angle, however, was very strong ($\Delta\alpha_2 \approx 13$ deg, Fig. 10). The effect of this range of exit flow angle on the second stator pressure distribution is shown in Fig. 11 for the 12.5 percent span location. The results at other span locations near the hub were similar. This comparison shows the insensitivity of the computed pressure distribution to the large differences (≈ 13 deg) between the mixed-out and mass-averaged exit flow angles.

The poor agreement between the measured and computed results at 12.5 percent span on this stator is due to the massive hub corner separation and the three-dimensional nature of the flow that it produces. At this span location the hub corner separation starts at 30 percent chord (as indicated by the S on the $CP = 0$ axis of Fig. 11). A comparison of the computed stator pressure distribution (based on upstream and downstream traverse data) and the measured pressure distributions shows a difference of about 100 percent in tangential force. Radial transport has caused the change in tangential momentum across the stator (at this span location) to be twice that indicated by the pressure distribution. This difference does not represent a failure of the wake mixing methodology; rather it is an indication of additional flow mechanisms that have not been accounted for. As mentioned above this difference was much smaller for the rotor (Fig. 4). A more exhaustive examination of this issue of radial transport is in progress.

Conclusions

By using a wake mixing methodology to relate a nonuniform inlet flow to an equivalent uniform inlet flow, a potential flow

analysis was demonstrated to give an accurate prediction of a rotor airfoil pressure distribution with the airfoil operating with a very distorted and unsteady inlet flow. The unsteady inlet flow was caused by the passing wakes of a closely coupled upstream stator row. In axial compressors this mixing methodology can have a powerful impact on both incidence and deviation and also on airfoil loading. Differences of up to 13 deg and 30 percent in loading were demonstrated. Much of the disagreement between the measured and computed airfoil pressure distributions that had previously been attributed to unsteadiness and to corner separation was eliminated by using mixed inlet conditions.

Specific observations and conclusions are as follows:

1 The use of inlet and exit conditions based on wake mixing (as opposed to average conditions) can result in significant improvement in the agreement between measured and computed airfoil pressure distributions.

2 Differences of up to 13 deg in both incidence and deviation were demonstrated to occur due to wake mixing.

3 Differences of up to 30 percent in incident dynamic pressure were demonstrated to occur due to wake mixing.

4 These differences were present at near-stall conditions and, to a lesser degree, even at nominal design conditions.

5 The mixing methodology does not rely on mixing actually occurring but only on the fact that mixing provides an equivalent uniform flow condition.

6 The mixing methodology was demonstrated to be successful even for a situation where there were unsteady variations in the inlet angle of 40 deg at an plane located only 14 percent of chord upstream of the airfoil leading edge.

7 While the exit flow angles calculated from the various angle definitions can be very different, the airfoil pressure distribution analysis is much less sensitive to this difference than to difference in inlet angle.

8 There is sufficient information in the throughflow analysis of Dring and Oates (1990a and 1990b) to calculate all the mixed-out quantities with a reasonable degree of accuracy.

9 The concepts that have been presented here should be of value in analyzing the growing body of LDV and hot-film data that is becoming available for compressors. This will be particularly true in relating this flow field information to measured airfoil pressure distributions and to computed results.

Acknowledgments

References

(* = References that discuss, or show evidence of, corner separation.)

Caspar, J. R., Hobbs, D. E., and Davis, R. L., 1980, "Calculation of Two-Dimensional Potential Cascade Flow Using Finite Area Methods," *AIAA Journal*, Vol. 18, No. 1, pp. 103–109.

*Cyrus, V., 1986, "Experimental Study of the Flow in an Axial Compressor Stage," ASME Paper No. 86-GT-118.

*Cyrus, V., 1988, "Effect of the Inlet Velocity Profile in the Three-Dimensional Flow in a Rear Axial Compressor Stage," ASME JOURNAL OF TURBOMACHINERY, Vol. 110, pp. 434–440.

*Dong, Y., Gallimore, S. J., and Hodson, H. P., 1987, "Three-Dimensional Flows and Loss Reduction in Axial Compressors," ASME JOURNAL OF TURBOMACHINERY, Vol. 109, No. 3, pp. 354–361.

*Dring, R. P., Joslyn, H. D., and Hardin, L. W., 1982, "An Investigation of Compressor Rotor Aerodynamics," ASME *Journal of Engineering for Power*, Vol. 104, No. 1, pp. 84–96.

*Dring, R. P., Joslyn, H. D., and Wagner, J. H., 1983, "Compressor Rotor Aerodynamics," *Viscous Flow Effects in Turbomachines*, AGARD-CP-351, Copenhagen, Denmark.

*Dring, R. P., and Joslyn, H. D., 1986, "An Assessment of Single- and Multi-

stage Compressor Flow Modeling, Part II. Near-Stall Conditions," Final Report Prepared Under Contract No. N00014-85-C-0657 for the Naval Air Systems Command.

*Dring, R. P., and Joslyn, H. D., 1989, "The Effects of Compressor Endwall Flow on Airfoil Incidence and Deviation," presented at the AGARD-PEP 74th Specialists' Meeting, B—Secondary Flows in Turbomachinery.

Dring, R. P., and Oates, G. C., 1990a, "Throughflow Theory for Nonaxisymmetric Turbomachinery Flow: Part I—Formulation," ASME JOURNAL OF TURBOMACHINERY, Vol. 112, pp. 320–327.

Dring, R. P. and Oates, G. C., 1990b, "Throughflow Theory for Nonaxisymmetric Turbomachinery Flow: Part II—Assessment," ASME JOURNAL OF TURBOMACHINERY, Vol. 112, pp. 328–337.

*Gallus, H. E., and Hoenen, H., 1986, "Experimental Investigations of Airfoil and Endwall Boundary Layers in a'Subsonic Compressor Stage," ASME Paper No. 86-GT-143.

Gundy-Burlet, K., Rai, M., and Dring, R., 1989, "Two-Dimensional Computations of Multi-stage Compressor Flow Using a Zonal Approach," AIAA Paper No. AIAA-89-2452, presented at the Joint Propulsion Conference, Monterey, CA and submitted to the AIAA *Journal of Propulsion and Power*.

Hirsch, C., and Warzee, G., 1979, "An Integrated Quasi-3D Finite Element Calculations Program for Turbomachinery Flows," ASME *Journal of Engineering for Power*, Vol. 101, No. 1, pp. 141–148.

*Horlock, J. H., 1966, "Wall Stall in Compressor Stages," ASME *Journal of Basic Engineering*, Vol. 88, No. 3, pp. 637–648.

*Joslyn, H. D., and Dring, R. P., 1985, "Axial Compressor Stator Aerodynamics," ASME *Journal of Engineering for Gas Turbines and Power*, Vol. 107, No. 2, pp. 485–493.

*Lakshminarayana, B., and Horlock, J. H., 1967, "Leakage and Secondary Flows in Compressor Cascades," ARC R&M 3483.

*McDougall, N. M., 1989, "A Comparison Between the Design Point and Near-Stall Performance of an Axial Compressor," ASME JOURNAL OF TURBOMACHINERY, Vol. 112, pp. 109–115.

*Schultz, H. D., and Gallus, H. E., 1988, "Experimental Investigation of the Three-Dimensional Flow in an Annular Compressor Cascade," ASME JOURNAL OF TURBOMACHINERY, Vol. 110, pp. 467–478.

*Schultz, H. D., Gullus, H. E., and Lakshminarayana, B., 1990a, "Three-Dimensional Separated Flow Field in the Endwall Region of an Annular Compressor Cascade in the Presence of Rotor–Stator Interaction: Part I—Quasi-Steady Flow Field and Comparison With Steady-State Data," ASME JOURNAL OF TURBOMACHINERY, Vol. 112, pp. 669–678.

*Schultz, H. D., Gallus, H. E., and Lakshminarayana, B., 1990b, "Three-Dimensional Separated Flow Field in the Endwall Region of an Annular Compressor Cascade in the Presence of Rotor–Stator Interaction: Part II—Unsteady Flow and Pressure Field," ASME JOURNAL OF TURBOMACHINERY, Vol. 112, pp. 679–690.

Stewart, W. L., 1959, "Analysis of Two-Dimensional Flow Loss Characteristic Downstream of Turbomachine Blade Rows in Terms of Basic Boundary Layer Characteristics," NACA TN-3515.

*Tao, D., and Wang, C., 1988, "Experimental Study of End-Wall Flow in a Compressor Stage," AIAA *Journal of Propulsion and Power*, Vol. 4, No. 2, March–Apr., pp. 157–163.

*Wagner, J. H., Dring, R. P, and Joslyn, H. D., 1985, "Inlet Boundary Layer Effects in an Axial Compressor Rotor: Part I—Blade-to-Blade Effects," ASME *Journal of Engineering for Gas Turbines and Power*, Vol. 107, No. 2, pp 374–380.

*Wisler, D. C., 1985, "Loss Reduction in Axial Flow Compressors Through Low-Speed Model Testing," ASME *Journal of Engineering for Gas Turbines and Power*, Vol. 107, No. 2, pp. 354–363.

stage Compressor Flow Modeling, Part II. Near-Stall Conditions,'' Final Report Prepared Under Contract No. N00014-85-C-0657 for the Naval Air Systems Command.

*Dring, R. P., and Joslyn, H. D., 1989, "The Effects of Compressor Endwall Flow on Airfoil Incidence and Deviation," presented at the AGARD-PEP 74th Specialists' Meeting, B—Secondary Flows in Turbomachinery.

Dring, R. P., and Oates, G. C., 1990a, "Throughflow Theory for Nonaxisymmetric Turbomachinery Flow: Part I—Formulation," ASME JOURNAL OF TURBOMACHINERY, Vol. 112, pp. 320-327.

Dring, R. P. and Oates, G. C., 1990b, "Throughflow Theory for Nonaxisymmetric Turbomachinery Flow: Part II—Assessment," ASME JOURNAL OF TURBOMACHINERY, Vol. 112, pp. 328-337.

*Gallus, H. E., and Hoenen, H., 1986, "Experimental Investigations of Airfoil and Endwall Boundary Layers in a Subsonic Compressor Stage," ASME Paper No. 86-GT-143.

Gundy-Burlet, K., Rai, M., and Dring, R., 1989, "Two-Dimensional Computations of Multi-stage Compressor Flow Using a Zonal Approach," AIAA Paper No. AIAA-89-2452, presented at the Joint Propulsion Conference, Monterey, CA and submitted to the AIAA *Journal of Propulsion and Power*.

Hirsch, C., and Warzee, G., 1979, "An Integrated Quasi-3D Finite Element Calculations Program for Turbomachinery Flows," ASME *Journal of Engineering for Power*, Vol. 101, No. 1, pp. 141-148.

*Horlock, J. H., 1966, "Wall Stall in Compressor Stages," ASME *Journal of Basic Engineering*, Vol. 88, No. 3, pp. 637-648.

*Joslyn, H. D., and Dring, R. P., 1985, "Axial Compressor Stator Aerodynamics," ASME *Journal of Engineering for Gas Turbines and Power*, Vol. 107, No. 2, pp. 485-493.

*Lakshminarayana, B., and Horlock, J. H., 1967, "Leakage and Secondary Flows in Compressor Cascades," ARC R&M 3483.

*McDougall, N. M., 1989, "A Comparison Between the Design Point and Near-Stall Performance of an Axial Compressor," ASME JOURNAL OF TURBOMACHINERY, Vol. 112, pp. 109-115.

*Schultz, H. D., and Gallus, H. E., 1988, "Experimental Investigation of the Three-Dimensional Flow in an Annular Compressor Cascade," ASME JOURNAL OF TURBOMACHINERY, Vol. 110, pp. 467-478.

*Schultz, H. D., Gullus, H. E., and Lakshminarayana, B., 1990a, "Three-Dimensional Separated Flow Field in the Endwall Region of an Annular Compressor Cascade in the Presence of Rotor–Stator Interaction: Part I—Quasi-Steady Flow Field and Comparison With Steady-State Data," ASME JOURNAL OF TURBOMACHINERY, Vol. 112, pp. 669-678.

*Schultz, H. D., Gallus, H. E., and Lakshminarayana, B., 1990b, "Three-Dimensional Separated Flow Field in the Endwall Region of an Annular Compressor Cascade in the Presence of Rotor–Stator Interaction: Part II—Unsteady Flow and Pressure Field," ASME JOURNAL OF TURBOMACHINERY, Vol. 112, pp. 679-690.

Stewart, W. L., 1959, "Analysis of Two-Dimensional Flow Loss Characteristic Downstream of Turbomachine Blade Rows in Terms of Basic Boundary Layer Characteristics," NACA TN-3515.

*Tao, D., and Wang, C., 1988, "Experimental Study of End-Wall Flow in a Compressor Stage," AIAA *Journal of Propulsion and Power*, Vol. 4, No. 2, March-Apr., pp. 157-163.

*Wagner, J. H., Dring, R. P, and Joslyn, H. D., 1985, "Inlet Boundary Layer Effects in an Axial Compressor Rotor: Part I—Blade-to-Blade Effects," ASME *Journal of Engineering for Gas Turbines and Power*, Vol. 107, No. 2, pp 374-380.

*Wisler, D. C., 1985, "Loss Reduction in Axial Flow Compressors Through Low-Speed Model Testing," ASME *Journal of Engineering for Gas Turbines and Power*, Vol. 107, No. 2, pp. 354-363.

—————— DISCUSSION ——————

N. A. Cumpsty[1]

The flow out of and into blades is strongly nonuniform and it is clearly of concern that an effective averaging procedure be adopted. One must therefore welcome attempts to place

[1] Whittle Laboratory, University of Cambridge, Madingley Road, Cambridge CB3 0DY United Kingdom.

this on a more secure foundation. I would, however, like to question a deduction drawn by the authors from their Fig. 4. The improvement in the comparison between the measured pressure distribution at 3.2 percent span and that predicted using a two-dimensional method is taken to be evidence that unsatisfactory comparisons are a result of incorrect averaging. This is not the only reason that two-dimensional methods can give inaccurate predictions near endwalls.

In the 1989 Gas Turbine Conference there was a paper by Wadia and Becher (1990) that showed the importance of the spanwise effects in the regions near the endwalls. Very great differences were seen between the pressure distributions calculated by two-dimensional and three-dimensional methods; the three-dimensional inviscid method was able to predict the pressure distribution remarkably well even very close to the endwalls. Very plausibly it was deduced that two-dimensional methods were unable to give the correct pressure distribution near the endwalls when the local flow is approaching the leading edge at large incidence. Would the authors care to comment on their conclusion in the light of this?

References

Wadia, A. R., and Beacher, B. F., 1990, "Three-Dimensional Relief in Turbomachinery Blading," ASME JOURNAL OF TURBOMACHINERY, Vol. 112, pp. 587-598.

Authors' Closure

We appreciate the time and though that Professor Cumpsty has given to the work we presented in this paper. He is certainly correct in pointing out that there is more than one mechanism that can cause two-dimensional methods to fail to give accurate results near endwalls. Our paper addresses the issue of the effect of strong circumferential gradients, such as the wakes of an upstream airfoil row, and how this nonuniform inflow can be related to a "kinematically equivalent" uniform inflow. Wadia and Beacher (1990) address the issue of strong radial gradients and how three dimensionality in the endwall region can produce a relief in the severe leading edge loading that would be expected from a two dimensional analysis. These two mechanisms are very different effects and in all probability both are present to some extent in most applications. It is difficult, however, to comment on their relative contributions to the work presented here and to that presented by Wadia and Beacher (1990). It has been determined (Wadia, 1990) that neither contains sufficient information to examine both mechanisms.

It is clear, however, that both strong radial gradients and strong upstream wakes can have a major impact on airfoil loading. It is also important to realize that while the mixing approach presented here has been applied to experimental results, it can also be applied to computational results. This could occur when the upstream boundary conditions for a three-dimensional prediction of the flow in an airfoil row are based on relating the three-dimensional flow exiting the upstream row to an equivalent axisymmetric condition.

References

Wadia, A. R., 1990, Private communication.

H. M. Jang
Department of Mechanical Engineering,
University of Michigan,
Ann Arbor, MI 48109

J. A. Ekaterinaris
Navy–NASA Joint Institute of Aeronautics,
Monterey, CA 93943

M. F. Platzer
Department of Aeronautics and Astronautics,
Naval Postgraduate School,
Monterey, CA 93943
Mem. ASME

T. Cebeci
Department of Aerospace Engineering,
California State University,
Long Beach, CA 90840
Mem. ASME

Essential Ingredients for the Computation of Steady and Unsteady Blade Boundary Layers

Two methods are described for calculating pressure distributions and boundary layers on blades subjected to low Reynolds numbers and ramp-type motion. The first is based on an interactive scheme in which the inviscid flow is computed by a panel method and the boundary layer flow by an inverse method that makes use of the Hilbert integral to couple the solutions of the inviscid and viscous flow equations. The second method is based on the solution of the compressible Navier–Stokes equations with an embedded grid technique that permits accurate calculation of boundary layer flows. Studies for the Eppler-387 and NACA-0012 airfoils indicate that both methods can be used to calculate the behavior of unsteady blade boundary layers at low Reynolds numbers provided that the location of transition is computed with the e^n method and the transitional region is modeled properly.

1.0 Introduction

The unsteady flows that occur in multistage axial turbomachines have a strong impact on the efficiency, aerodynamic stability of the compression system, aeroelastic stability, and noise generation [1]. The state of the art in turbomachinery has advanced to the point where further significant improvements will have to come from the understanding and control of the unsteady flows within the turbomachines. For this reason, in recent years increasing attention and effort have been devoted to experimental and computational investigations on various unsteady flow phenomena in turbomachines. A review of these efforts can be found in [2], showing that substantial progress has been achieved in the calculation of unsteady inviscid flows for single blade rows and, to some extent, for multiblade rows and for three-dimensional flows. The inclusion of unsteady viscous flow effects, on the other hand, has only recently been attempted for two-dimensional [3] and three-dimensional [4] flows. This task is further complicated by the frequent occurrence of separation bubbles on blades where, at design incidence and at Reynolds numbers between 10^5 and 10^6, transition in the separated laminar shear layer may be followed by a rapid reattachment of the transitioning or turbulent shear layer. This produces the so-called "short bubble," a somewhat misleading term because midchord bubbles on turbomachine blades can easily extend over several percent of chord. With further reduction in Reynolds number, the extent of the bubble increases to form a "long bubble" and, depending on the flow conditions, the bubble may burst. This

phenomenon is accompanied by a major increase in drag and decrease in circulation with associated changes in pressure distribution over the whole blade. At off-design conditions, the separation bubble migrates toward the leading edge on the suction or pressure surface with increasing positive or negative incidence.

While the prediction of the influence of flow unsteadiness due to blade row interactions and inlet distortion is still in its infancy, much progress has been made in computing steady airfoil flows for a range of Reynolds number and angles of attack using two approaches, one based on the solution of the full compressible Navier–Stokes equations and the other on solving a combination of inviscid and boundary layer equations. In both approaches, it is important that the conservation equations be solved accurately in full or reduced forms and that they include accurate methods for computing the location of transition and for modeling the turbulent flow including the transitional region. Recent studies, conducted at high Reynolds numbers [5], show that as long as there is no, or very little, flow separation on the airfoil, no wake calculation is required. With increasing flow separation, the importance of the wake flow increases, and in the near- and post-stall regions, its effect becomes significant. High Reynolds number studies indicate that while the calculated results are relatively insensitive to the location of the transition at low angles of attack, they become sensitive with increasing angle of incidence and play a very important role in near-stall and post-stall conditions. Similar studies conducted at low Reynolds numbers show that the wake flow and location of transition are important at all angles of attack and they must be computed interactively with the solution of the conservation equations [6, 7]. This method neglects the effect of normal pressure

---

Contributed by the International Gas Turbine Institute and presented at the 35th International Gas Turbine and Aeroengine Congress and Exposition, Brussels, Belgium, June 11–14, 1990. Manuscript received by the International Gas Turbine Institute January 5, 1990. Paper No. 90-GT-160.

gradient across the shear layer, which becomes increasingly more important as the flow separation increases. The consequences of this approximation are not known at this time.

The present paper addresses the prediction of unsteady blade boundary layer flows by two methods briefly described in the following section. The first is based on the extension of the steady interactive boundary-layer method of [5] and the second on the Navier–Stokes method of [8]. Section 3 presents the application of these methods to two test cases. Since the blade data on unsteady low Reynolds number flows are scarce, two separate types of airfoil flow are considered. The first is a steady low Reynolds number flow over an Eppler airfoil measured in the Langley low-turbulence pressure tunnel for a Reynolds number of 10^5 and the second an unsteady flow over a NACA-0012 airfoil subject to ramp-type motion at a Reynolds number of 2.7×10^6. In the first test case, calculations made use of only the interactive method, in contrast to the second case, which used both methods. The paper concludes with a summary of the more important findings.

2.0 Computational Methods

2.1 Viscous–Inviscid Interaction Method. The interactive method for steady incompressible flows is described for high and low Reynolds number flows in [5] and [6], respectively, and makes use of an inverse boundary-layer method coupled to a panel method with an interactive formula suggested by Veldman [9]. The boundary-layer equations are solved subject to the usual boundary conditions with the external velocity $U_e^o(x)$ computed from inviscid flow theory and the perturbation velocity $\delta U_e(x)$ computed from the Hilbert integral

$$\delta U_e(x) = \frac{1}{\pi} \int_{x_a}^{x_b} \frac{d}{d\sigma} (U_e \delta^*) \frac{d\sigma}{x - \sigma} \quad (1)$$

with integration region confined to (x_a, x_b).

In the extension of this method to unsteady incompressible flows, we again make use of a panel method [10], which is similar to that of Hess and Smith [11]. This method utilizes the procedure of Basu and Hancock [12] to model the wake and represents the shape of the airfoil by a large number of panels (typically 100 panels) such that each panel has constant source strength, which varies from panel to panel and a constant vorticity strength, which is the same for all panels. The wake is represented by a series of free vortices shed from the trailing edge in response to incidence changes in accordance with the Helmholtz–Kelvin law of conservation of total vorticity. The airfoil's lift response then is obtained by subdividing the incidence history into sufficiently small time steps and computing the source and vorticity distributions for each time step. Further details of this method can be found in [10, 13].

The unsteady boundary-layer equations are expressed in terms of an eddy viscosity, ϵ_m, so that continuity and momentum equations

$$\frac{\partial u}{\partial x} + \frac{\partial v}{\partial y} = 0 \quad (2)$$

$$\frac{\partial u}{\partial t} + u \frac{\partial u}{\partial x} + v \frac{\partial u}{\partial y} = \frac{\partial U_e}{\partial t} + U_e \frac{\partial U_e}{\partial x} + \frac{\partial}{\partial y} \left[(\nu + \epsilon_m) \frac{\partial u}{\partial y} \right] \quad (3)$$

are solved subject to the boundary conditions

$$y = 0, \quad u = v = 0; \quad y \to \infty, \quad u \to U_e(x, t) \quad (4)$$

on the airfoil and with $y = 0$ denoting the dividing streamline that separates the upper and lower parts of the inviscid flow in the wake, subject to the following conditions:

$$y \to \pm \infty, \quad u \to U_e(x, t); \quad y = 0, \quad v = 0 \quad (5)$$

with $U_e(x, t)$ given by $U_e = U_e^o + \delta U_e(x, t)$. The eddy viscosity formulation of Cebeci and Smith [14] is used with special emphasis on the transitional region.

$$\epsilon_m = \epsilon_{m_i} = L^2 |\frac{\partial u}{\partial y}| \gamma_{tr} \qquad 0 \le y \le y_c \quad (6a)$$

$$\epsilon_m = \epsilon_{m_o} = 0.0168 U_e \delta^* \gamma_{tr} \qquad y_c \le y \le \delta \quad (6b)$$

The crossover distance y_c is defined as the location where the eddy viscosities of the inner and outer regions coincide. The parameters L and γ_{tr} are given by

$$L = 0.4y[1 - e^{(-y/A)}], \quad A = 26\nu u_\tau - 1, \quad u_\tau = \left(\nu \frac{\partial u}{\partial y} \right)_{max}^{1/2}$$

$$\gamma_{tr} = 1 - e^{\left[-G(x - x_{tr}) \int_{x_{tr}}^x \frac{dx}{U_e} \right]} \quad (7)$$

Here γ_{tr} corresponds to the expression suggested by Chen and Thyson [15] with x_{tr} denoting the location of the beginning of transition and G a parameter defined by

$$G = \left(\frac{3}{C^2} \right) \frac{U_e^3}{\nu^2} Re_{x_{tr}}^{-1.34} \quad (8)$$

where the transition Reynolds number $Re_{x_{tr}} = (U_e x_{tr} / \nu)$ and C is a constant with a recommended value of 60. The expression for γ_{tr} was obtained from data based on attached flows and is less likely to be applicable to flows with separation. For this reason, a correlation formula was devised by Cebeci [6] to represent C of equation (8) by

$$C^2 = 213[\log Re_{x_{tr}} - 4.7323] \quad (9)$$

For the wake flow calculations following the study of Chang et al. [16], the eddy-viscosity formulation for wall boundary-layer formulas was modified and expressed in the form

$$\epsilon_m = (\epsilon)_w + [(\epsilon_m)_{te} - (\epsilon_m)_w]e^{\left[-\frac{x - x_{te}}{20\delta_{te}} \right]} \quad (10)$$

where $(\epsilon_m)_w$ denotes the eddy viscosity for the far wake given by the maximum of $(\epsilon_m)_w^l$ and $(\epsilon_m)_w^u$ defined by

$$(\epsilon_m)_w^l = 0.064 \int_{-\infty}^{y_{min}} (U_e - u)dy \quad (11a)$$

$$(\epsilon_m)_w^u = 0.064 \int_{y_{min}}^{\infty} (U_e - u)dy \quad (11b)$$

with y_{min} the location where $u = u_{min}$.

Nomenclature

α =	angle of attack, deg	ρ =	density
γ =	ratio of specific heats	ω =	frequency
γ_{tr} =	intermittency factor	a =	speed of sound
Δt =	time step	c =	chord length
ϵ =	dissipation coefficient	c_l =	lift coefficient
ϵ_m =	eddy viscosity	e =	total energy per unit volume
ξ, η =	transformed coordinates		
ξ_x, η_x =	metrics of the transformation	k =	reduced frequency = $\dot{\alpha}c/2U_\infty$

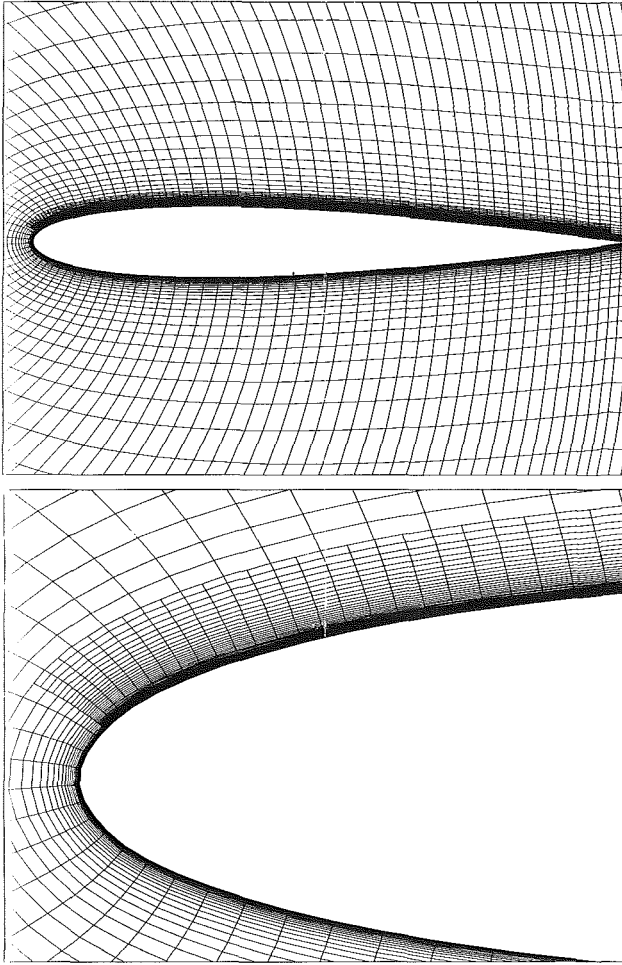|	
M =	Mach number
p =	pressure
u, v =	Cartesian velocity components
U, V =	contravariant velocities
$\delta U_e(x)$ =	perturbation velocity
$U_e^o(x)$ =	external velocity
x, y =	Cartesian coordinates

Fig. 1 General view and detail of the grid around the NACA 0012 airfoil; the global grid is indicated with dashed lines, and the embedded refined grid for the boundary layer calculation is shown with solid lines

2.2 Navier–Stokes Methods. For compressible flows the full, unsteady, two-dimensional, compressible Navier–Stokes equations were solved. In a curvilinear coordinate system (ξ, η) the governing equations are

$$\frac{\partial \hat{q}}{\partial t} + \frac{\partial \hat{F}}{\partial \xi} + \frac{\partial \hat{G}}{\partial \eta} = \frac{1}{Re}\left(\frac{\partial \hat{R}}{\partial \xi} + \frac{\partial \hat{S}}{\partial \eta}\right) \tag{12}$$

where $\hat{q}$ is the conservative variable vector $\mathbf{q} = (\rho, \rho u, \rho v, e)^T$, and $\hat{F}$, $\hat{G}$ are the nonlinear inviscid terms given by

$$\hat{F} = \frac{1}{J}\begin{pmatrix} \rho U \\ \rho u U + \xi_x p \\ \rho v U + \xi_y p \\ (e+p)U - \xi_t p \end{pmatrix}, \ \hat{G} = \frac{1}{J}\begin{pmatrix} \rho V \\ \rho u V + \eta_x p \\ \rho v V + \eta_y p \\ (e+p)V - \eta_t p \end{pmatrix} \tag{13}$$

and the viscous term $\hat{R}$ is given by

$$\hat{R} = \frac{1}{J}\begin{pmatrix} 0 \\ \tau_{xx}\xi_x + \tau_{yx}\xi_y \\ \tau_{xy}\xi_y + \tau_{yy}\xi_y \\ \xi_x\left[\tau_{xx}u + \tau_{xy}v + K\left(\frac{\partial a^2}{\partial x}\right)\right] + \xi_y\left[\tau_{xy}u + \tau_{yy}v + K\left(\frac{\partial a^2}{\partial y}\right)\right] \end{pmatrix} \tag{14}$$

and similarly for $\hat{S}$. Here ρ is the density, e is the total energy per unit volume and $p = (\gamma - 1)\,[e - \rho/2(u^2 + v^2)]$ is the pressure. The quantities U, V are the contravariant velocity components given by

$$U = \xi_t + u\xi_x + v\xi_y, \qquad V = \eta_t + u\eta_x + v\eta_y \tag{15}$$

where $\xi_t = \eta_t = 0$ for steady flow solutions, and ξ_t, η_t are determined from the body motion for the unsteady case.

$$\tau_{xx} = \frac{2\mu}{3}\left(2\frac{\partial u}{\partial x} - \frac{\partial v}{\partial y}\right), \tau_{yy} = \frac{2\mu}{3}\left(2\frac{\partial v}{\partial y} - \frac{\partial u}{\partial x}\right), \tau_{xy} = \mu\left(\frac{\partial u}{\partial y} + \frac{\partial v}{\partial x}\right) \tag{16}$$

and

$$K = \frac{\mu}{Pr(\gamma - 1)} \tag{17}$$

The curvilinear coordinate system $\xi = \xi(x, y)$, $\eta = \eta(x, y)$, referred to as the computational domain, is linked to the physical domain x, y through the metrics, ξ_x, ξ_y, η_x, η_y and the Jacobian $J = \xi_x\eta_y - \xi_y\eta_x$ of the transformation. The integration is performed with the finite difference factored Beam–Warming algorithm [17]. The approximately factorized form of the algorithm is

$$[I + (\Delta t/2)(\delta_\xi A^n_{j,k} + (D_{impl})_\xi)] \tag{18}$$
$$\times [I + (\Delta t/2)(\delta_\eta B^n_{j,k} + (D_{impl})_\eta)]\Delta q^n_{j,k} = (RHS)^n$$

where

$$(RHS)^n = \Delta t\,(-\delta_\xi F^n_{j,k} - \delta_\eta G^n_{j,k} + \delta_\xi R^n_{j,k} + \delta_\eta S^n_{j,k} - \epsilon_{expl}(D_{expl})^n_{j,k}) \tag{19}$$

The dissipation term D_{impl} is added for numerical stability, and the explicit dissipation D_{expl} is added to eliminate oscillations in the neighborhood of shocks. The explicit dissipation term is determined from the spectral radius as described in [18]. The eddy viscosity was calculated from the Baldwin–Lomax eddy viscosity model of [19].

The attached flow region is solved with the compressible boundary-layer equations with an embedded grid approach. A detail of the two-grid arrangement for Navier–Stokes and the embedded boundary layer grid is shown in Fig. 1. The boundary-layer equations for a generalized coordinate system [20] are

Continuity

$$\frac{\partial}{\partial t}\left(\frac{\rho}{J}\right) + \frac{\partial}{\partial \xi}\left(\frac{\rho U}{J}\right) + \frac{\partial}{\partial \eta}\left(\frac{\rho V}{J}\right) = 0 \tag{20}$$

ξ *momentum*

$$\rho\frac{\partial u}{\partial t} + \rho U\frac{\partial u}{\partial \xi} + \rho V\frac{\partial v}{\partial \eta} + \left(\xi_x\frac{\partial p}{\partial \xi} + \eta_x\frac{\partial p}{\partial \eta}\right)$$

$$= J\frac{\partial}{\partial \xi}\,[\tau_{xx}\xi_x + \tau_{xy}\xi_y] + J\frac{\partial}{\partial \eta}\,[\tau_{xx}\eta_x + \tau_{yx}\eta_y] \tag{21}$$

Normal momentum

$$\frac{\partial p}{\partial \eta} = 0 \tag{22}$$

Energy

$$\rho\frac{\partial H}{\partial t} - \frac{\partial p}{\partial t} + \rho u\frac{\partial H}{\partial \xi} + \rho v\frac{\partial H}{\partial \eta}$$

$$= J\frac{\partial}{\partial \xi}\left\{\xi_x\left[\tau_{xx}u+\tau_{xy}v+K\left(\frac{\partial a^2}{\partial x}\right)\right]+\xi_y\left[\tau_{xy}u+\tau_{yy}v+K\left(\frac{\partial a^2}{\partial y}\right)\right]\right\}$$

$$+ J\frac{\partial}{\partial \eta}\left\{\eta_x\left[\tau_{xx}u+\tau_{xy}v+K\left(\frac{\partial a^2}{\partial x}\right)\right]+\eta_y\left[\tau_{xy}u+\tau_{yy}v+K\left(\frac{\partial a^2}{\partial y}\right)\right]\right\}$$

$$(23)$$

Here $H = (e+p)/\rho$ is the enthalpy per unit volume, and the other quantities have the same definitions as before. Equations (20)–(23) are supplemented by the equation of state

$$\frac{\rho}{\rho_\infty} = \frac{pT_\infty}{Tp_\infty} \tag{24}$$

or

$$\frac{T}{T_\infty} = \frac{(\gamma-1)}{a_\infty^2}\left[H - \frac{u^2+v^2}{2}\right] \tag{25}$$

Viscous or inviscid solutions can be obtained for the global grid by marching in time from an initial condition. Steady solutions are obtained by marching in time from free-stream initial conditions until convergence to the steady state. Similarly, unsteady flows are computed by marching in time from a steady flow initial condition. After the global grid solution is computed, the boundary layer equations can be solved in the secondary grid using as initial condition at the inflow the velocity profile obtained by the viscous flow solution. The additional computational time needed for the boundary layer solution is negligible compared to the total time required for a complete viscous or inviscid flow solution. Typical execution time to complete the ramp pitch-up case from 0 to 15.5 deg was approximately one hour on the Cray-YMP. Boundary conditions at the edge of the boundary layer are provided by the pressure and velocity distribution of a viscous or inviscid global flow solution for the outer region. Grid refinement is applied for the boundary-layer calculation and the values of the flow parameters at the extra boundary points are obtained by simple interpolation of the flow variables obtained from the viscous solution. For unsteady calculations the boundary layer equations are solved at each time step.

3.0 Results and Discussion

Two separate flows are considered to evaluate the prediction of blade boundary layers. The first corresponds to a steady low Reynolds number flow and the second to an unsteady flow

at a relatively high Reynolds number. At low Reynolds numbers the extent of the separation bubble is significant; the transition location occurs inside the bubble and must be computed interactively with the flow field calculations. In the Navier–Stokes method transition modeling is not as yet included and therefore the calculations were performed only with the interactive method. Both methods were used to perform the unsteady flow calculations since this flow had no separation bubble due to the high Reynolds number, and the extent of the transition region was very small.

The low Reynolds number experimental data of [21] contain measurements for the Eppler-387 airfoil in the Langley Low-Turbulence Pressure Tunnel. The tests were conducted over a Mach number range from M = 0.3 to M = 0.13 and a chord Reynolds number range from 6×10^4 to 4.6×10^5. Lift and pitching moment data were obtained from wake surveys. Oil flow visualization was used to determine laminar separation and turbulent reattachment locations. Comparisons of these results with data obtained for this airfoil in two other facilities were included in [21].

The calculations reported here with the interactive procedure described in the previous section are for a chord Reynolds number of 10^5 and for a range of angles of attack from 0 to 6 deg. Additional calculations for higher angles of attack, including post-stall and higher Reynolds numbers, are in progress and will be reported separately in [22].

Before the results for this airfoil are presented, it is useful to give a brief description of the solution procedure used to perform the inviscid and boundary-layer calculations and the stability calculations for determining the location of transition with the e^n method [6]. The calculations were begun by computing the pressure distribution on the airfoil and in the wake without viscous effects. Next, the displacement thickness resulting from this pressure distribution was obtained from the solution of the boundary layer equations with the calculations starting at the forward stagnation point, proceeding in the inverse mode first with laminar flow only. Once the velocity profiles were determined, the location of transition was computed by using the e^n method based on the linear stability theory: The Orr–Sommerfeld equation was solved by initiating the stability calculations at the first x station where the Reynolds number exceeded the critical value established for similar boundary layers. Several dimensional frequencies at different x locations were then computed on the lower branch of the neutral stability curve in order to determine the amplification rates so that the location of transition could be determined from the e^n method with $n = 10$. The inverse laminar boundary layer calculations were then performed up to the transition location, after which turbulent flow calculations
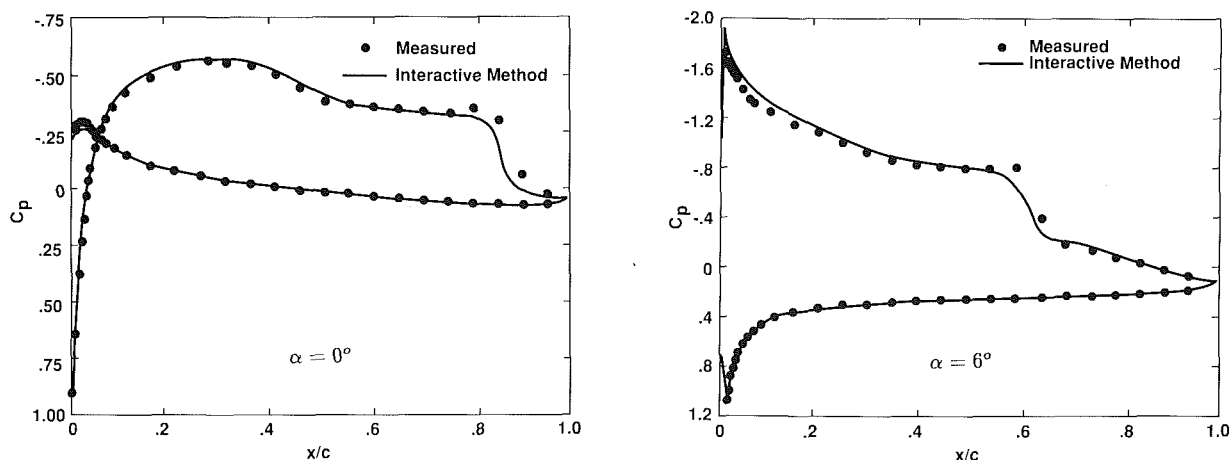
Fig. 2 Comparison of calculated (——) and measured (symbols) distributions of pressure coefficient for the Eppler airfoil at Re $= 1 \times 10^5$
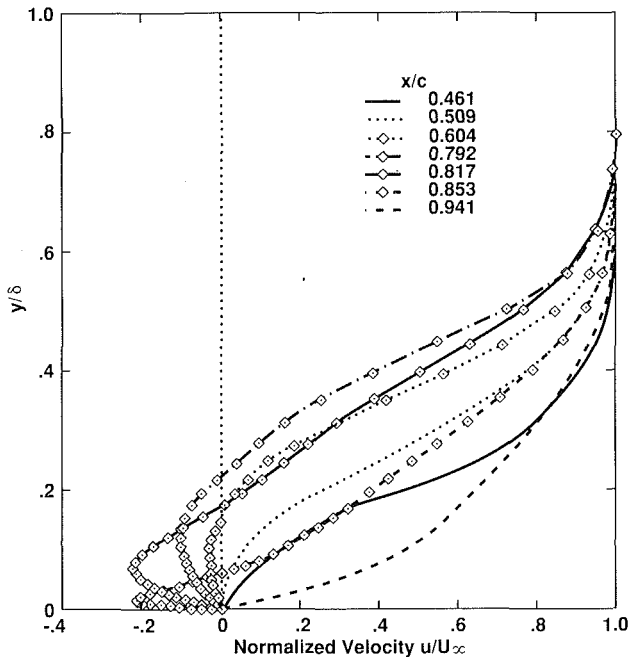
Fig. 3 Computed boundary layer profile at x/c = 0.461, 0.509, 0.604, 0.766, 0.792, 0.805, 0.817, 0.853, and 0.941 for the Eppler airfoil

x/c
— 0.461
····· 0.509
·◇· 0.604
·◇· 0.792
◇ 0.817
◇· 0.853
– – 0.941

Table 1 Experimental and calculated chordwise separation (LS) and reattachment (TR) and transition $(x/c)_{tr}$ locations on the upper surface of the Eppler airfoil

	Experiment		Calculated		
.deg	LS	TR	$(x/c)_{tr}$	LS	TR
0	0.45	0.87	0.76	0.50	0.87
2	0.41	0.79	0.68	0.45	0.79
4	0.35	0.73	0.62	0.40	0.73
5	0.34	0.67	0.585	0.38	0.69
6	0.33	0.62	0.54	0.35	0.64

Table 2 Measured and calculated values of lift (c_l) and total drag (c_d) coefficients

	Stuttgard Experiments		Delft Experiments		Langley Experiments		Interactive Method	
	c_l	c_d	c_l	c_d	c_l	c_d	c_l	c_d
0	0.320	0.0207	0.365	0.0151	0.370	0.0167	0.391	0.0154
2	0.520	0.0216	0.545	0.0190	0.587	0.0203	0.589	0.0169
4	0.700	0.0208	0.725	0.0223	0.778	0.0230	0.793	0.0197
5	0.780	0.0206	0.810	---	0.873	0.0237	0.893	0.0206
6	0.860	0.0203	0.895	0.0230	0.974	0.0224	0.994	0.0209

Fig. 4 Pressure coefficient distributions predicted by the interactive method: Re = 2.7×10^6, k = 0.0127

were performed on the airfoil and in the wake. The displacement thickness distribution resulting from these calculations was used to determine a blowing velocity distribution, which enabled the inviscid flow equations to be solved again subject to a new boundary condition. This process was repeated interactively until the solutions of both boundary-layer and inviscid flow equations converged.

Figure 2 compares measured and calculated distributions of pressure coefficients for angles of attack of 0 and 6 deg, and Fig. 3 presents the velocity profiles at α = 0 deg for a Reynolds number of 10^5. As can be seen from Fig. 2, with two small exceptions, the calculated results agree with measurements within experimental accuracy. In the immediate vicinity of the

leading edge and near the turbulent reattachment region where the gradient of the pressure coefficient changes sign rapidly, the calculations are slightly in error. Also, the calculated results do not capture perfectly the constant values of pressure coefficient associated with the separation bubbles. The results in Fig. 3 show that the region of reversed velocities is significant on the airfoil and the numerical method has no difficulties in computing the flow under these conditions.

Further details of the results shown in Figs. 2 and 3 are presented in Tables 1 and 2. The calculated values of the chordwise location of laminar separation (LS), turbulent reattachment (TR), and the onset of transition are given in Table 1. The experimental results of this table are subject to some uncertainty because of difficulties associated with the surface flow visualization technique. With this proviso, comparison between measured and calculated values must be considered outstanding. It should be noted that the transition location obtained from the e^n method occurs within the separation bubble in all cases, and in accord with experimental observation, leads to reattachment some distance downstream.

The lift and drag coefficients obtained from this method are

Fig. 5 Pressure coefficient distributions predicted by the Navier–Stokes method: Re = 2.7 × 10⁶, k = 0.0127

Fig. 6 Modified ramp angle of attack time history

cation of transition, and the ramp change in the angle of attack (shown in Fig. 6) was assumed to be given by

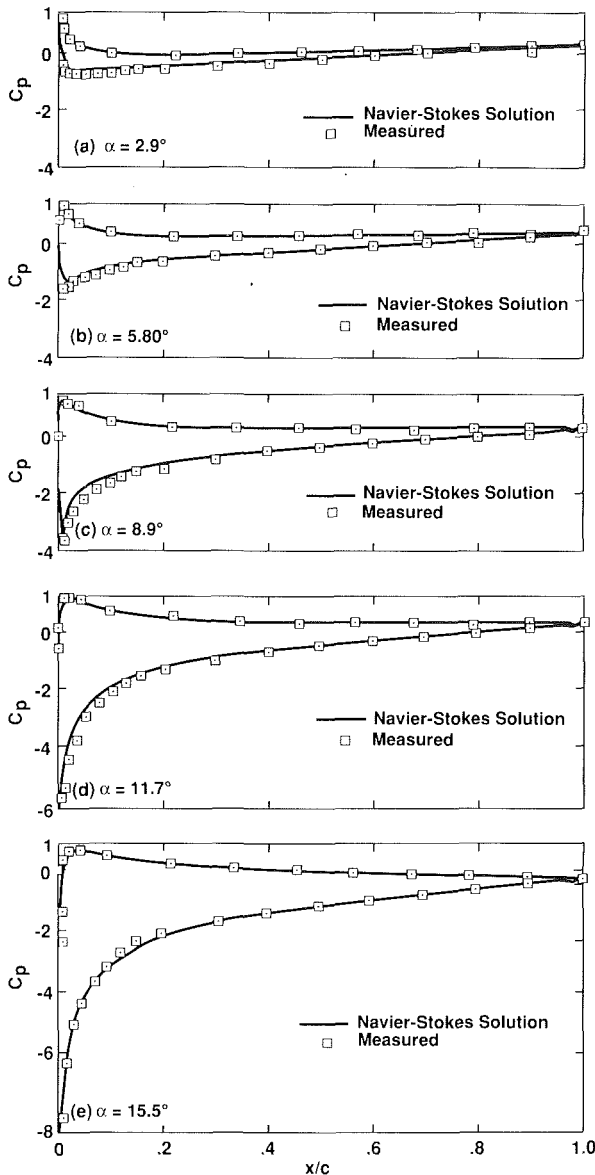$$\alpha(t) = -2\alpha_{max}T^3 + 3\alpha_{max}T^2 \qquad (26)$$

where T is the nondimensional time required to complete the ramp motion from 0 deg to α_{max}. This ramp change in angle of attack was held fixed for one nondimensional time after the end of the ramp motion. It is useful to point out that while the interactive method is based on the assumption of incompressible flow, the Navier–Stokes method is for a compressible flow. Calculations performed with the Navier–Stokes equations for a Mach number of 0.2 and 0.3, however, showed no effect of compressibility on the results.

Figures 4 and 5 show that the predictions of both methods are in good agreement with the experimental data, although the Navier–Stokes computations slightly underpredict the suction peaks at the lower incidence. Figures 7 and 8 present a comparison between the velocity profiles computed by both methods at two chordwise locations corresponding to $x/c = 0.5$ and $x/c = 0.9$ at several angles of incidence. While there is reasonably good agreement at low incidences, the two profiles begin to deviate significantly at higher incidences. These differences are to be expected because different sets of equations are solved. In the boundary layer computations, equations (2) and (3), the normal momentum equation is neglected, whereas in the Navier–Stokes calculations, equation (12), all terms are retained. Furthermore, different turbulence models were used. Nevertheless, Fig. 8(e) shows that both procedures predict the onset of flow reversal at $\alpha = 15.5$ deg for $x/c = 0.9$. Unfortunately, there are no experimental data available to verify this prediction and to assess the accuracy of the two methods.

Unsteady flow calculations performed at other reduced frequencies indicate that unsteady inviscid flows can be calculated with the present panel method for reduced frequencies up to $k = 0.015$. At higher frequencies the predictions of the panel method begin to differ from those of the Navier–Stokes method. For example, the results in Fig. 9, which correspond to a reduced frequency of $k = 0.043$ over a NACA-0012 airfoil pitching from 0 to 5 deg, show that even though both methods correctly predict the asymptotic approach to the steady-state lift value, there are significant differences during the transient phase. We believe that these differences are due to the manner in which the Kutta condition is introduced in the panel method and thus require further studies.

4.0 Summary

Two methods are described and applied to study the effects of low Reynolds number and flow unsteadiness on blade boundary layers. The first is based on an interactive boundary layer scheme in which the inviscid flow is computed by a panel

listed in Table 2 together with the experimental results obtained in the Stuttgart, Delft, and Langley wind tunnels. In general, the calculated lift coefficients are higher than the Stuttgart and Delft measurements but very close to the Langley measurements. The calculated drag coefficients, on the other hand, show overall good agreement with all sets of data.

The unsteady flow calculations for the NACA-0012 airfoil subject to ramp-type motion, as described in detail in [23], were performed by using both interactive and Navier–Stokes methods for a Reynolds number of 2.7 × 10⁶ and for a nondimensional pitch rate k defined by $k = \dot{\alpha}c/2U_\infty = 0.0127$. The airfoil chord was 10.16 cm, the pitch rate 1280 deg/s, pitching from 0 to 15.54 deg, at a free-stream Mach number of M = 0.3. The experimental data include upper and lower surface pressure distributions for incidence angles of 2.9, 5.8, 8.9, 11.7, and 15.5 deg.

Figures 4 and 5 compare measured and calculated distributions of pressure coefficients for incidence angles of 2.9, 5.8, 8.9, 11.7, and 15.5 deg, with Fig. 4 showing the predictions of the interactive method and Fig. 5 those of the Navier–Stokes method. In both methods, the flow was assumed to be fully turbulent due to the lack of experimental data about the lo-
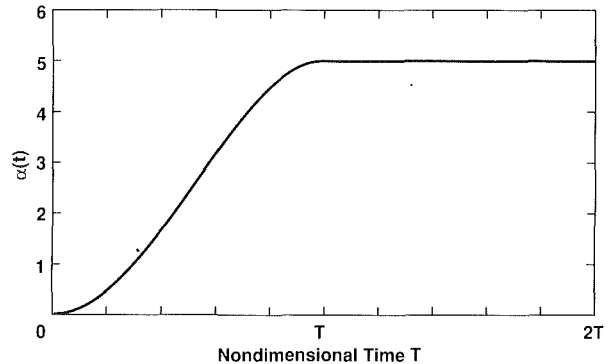
Fig. 7 Comparison of the boundary-layer profiles computed with both methods, for the 50 percent chord: Re = 2.7 × 10⁶, k = 0.0127

method and the boundary layer flow by an inverse method that uses the Hilbert integral to couple the solutions of the inviscid and viscous flow equations. The second method is based on the solution of the compressible Navier–Stokes equations, which employs an embedded grid technique for accurate boundary layer calculations with small computational cost. Calculated results obtained for the low Reynolds number flow with a combination of the interactive method and e^n method show good agreement with experimental data. The results also indicate the importance of transition at such low Reynolds numbers and show that regardless of the method used to compute the flow field, the onset of transition must be determined interactively and the transitional region must be modeled properly. Calculated results obtained with both methods for a NACA-0012 airfoil subject to a ramp-type motion at relatively high Reynolds number also indicate good agreement with experimental data. The calculations for this flow indicate computer times of about one hour on the Cray YMP for the Navier–Stokes method and about 30 seconds for the interactive method on a VAX computer. Since the calculation of the onset of

(a) $\alpha = 2.9°$

(a)

(d) $\alpha = 11.7°$

(d)

(b) $\alpha = 5.8°$

(b)

(e) $\alpha = 15.5°$

Normalized Velocity u/U_∞

(e)
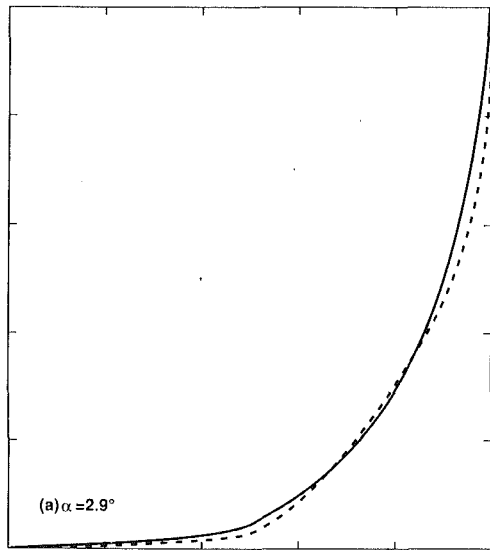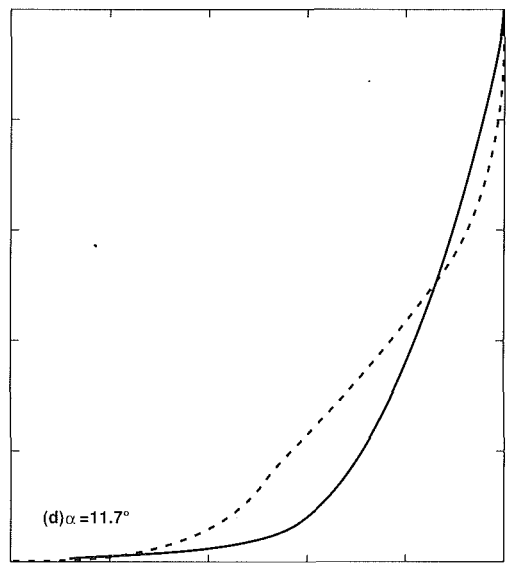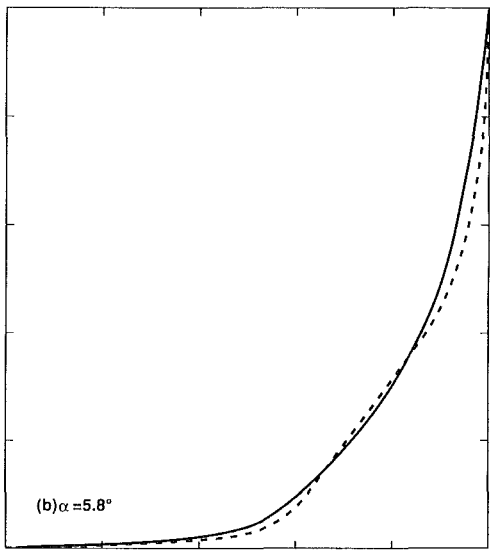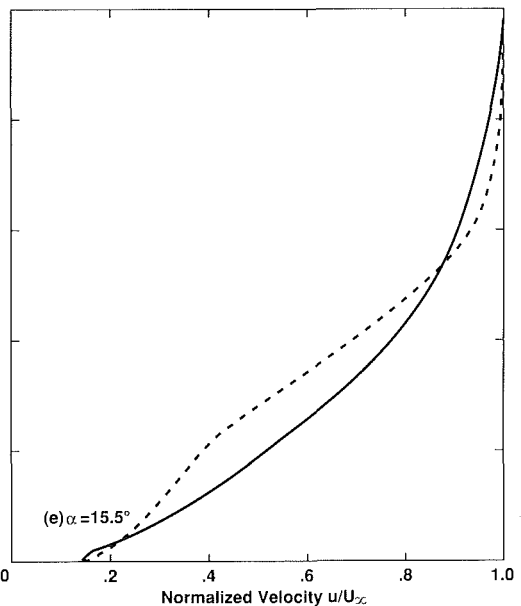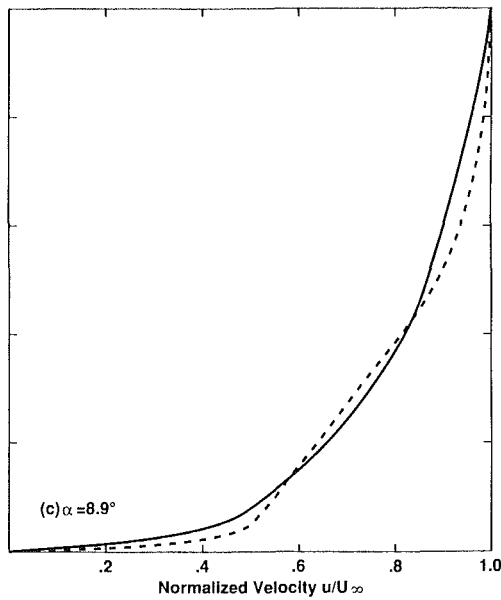
Fig. 8 Comparison of the boundary-layer profiles computed with both methods, for the 90 percent chord: Re $= 2.7 \times 10^6$, $k = 0.0127$

(c) $\alpha = 8.9°$

Normalized Velocity u/U_∞

(c)
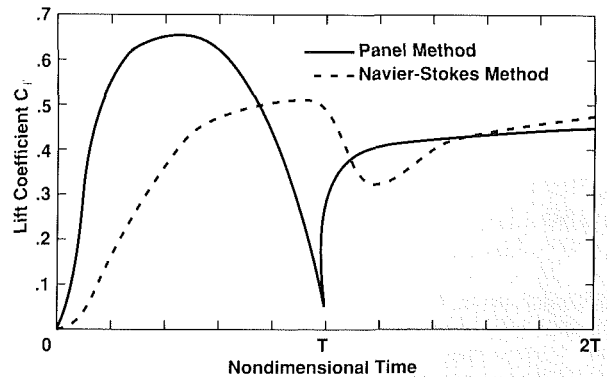
Fig. 9 Lift coefficient variation for a ramp change in angle of attack α from 0 to 5 deg, for $t = 0$ to $t = T$, and then at $\alpha = 5$ deg for $t = T$ to $t = 2T$; Re $= 1 \times 10^6$, for the Navier–Stokes solution, $k = 0.043$

transition requires that the flow field be computed several times, these results suggest that the extension of the Navier–Stokes method to low Reynolds number flows in which the flow field and transition are calculated interactively may be costly.

Acknowledgments

References

1 Mikolajczak, A. A., "The Practical Importance of Unsteady Flow," AGARD CP, No. 177, Apr. 1976, pp. 1.1–1.12.

2 Platzer, M. F., and Carta, F. O., "Unsteady Turbomachinery Aerodynamics," AGARDograph, No. 298, Vol. 1, Mar. 1987.

3 Gundy-Burlet, K. L., Rai, M. M., and Dring, R. P., "Two-Dimensional Computations of Multi-stage Compressor Flows Using a Zonal Approach," AIAA Paper No. 89-2482, 1989.

4 Rai, M. M., "Three-Dimensional Navier–Stokes Simulations of Turbine Rotor-Stator Interaction; Part 1, Methodology, Part 2, Results," *Journal of Propulsion and Power*, Vol. 5, No. 3, May 1989, pp. 307–319.

5 Cebeci, T., Clark, R. W., Chang, K. C., Halsey, N. D., and Lee, K., "Airfoils With Separation and the Resulting Wakes," *J. Fluid Mech.*, No. 163, 1986, pp. 323–347.

6 Cebeci, T., "Essential Ingredients of a Method for Low Reynolds Number Airfoils," *AIAA Journal*, Vol. 27, No. 12, 1989, pp. 1680–1688.

7 Walker, G. J., Subroto, P. H., and Platzer, M. F., "Transition Modeling Effects on Viscous/Inviscid Interaction Analysis of Low Reynolds Number Airfoil Flows Involving Laminar Separation Bubbles," ASME Paper No. 88-GT-32, 1988.

8 Ekaterinaris, J. A., "Compressible Studies on Dynamic Stall," AIAA Paper No. 89-0024, 1989.

9 Veldman, A. E. P., "New Quasi-Simultaneous Method to Calculate Interactively Boundary Layers," *AIAA Journal*, No. 19, 1981, p. 769.

10 Teng, N. H., "The Development of a Computer Code (U2DIIF) for the Numerical Solution of Unsteady, Inviscid and Incompressible Flow Over an Airfoil," M.S. Thesis, Naval Postgraduate School, Monterey, CA, 1987.

11 Hess, J. L., and Smith, A. M. O., "Calculation of Potential Flow About Arbitrary Bodies," *Progress in Aeronautical Sciences*, Pergamon Press, Oxford, Vol. 8, 1966, pp. 1–138.

12 Basu, B. C., and Hancock, G. J. "The Unsteady Motion of a Two-Dimensional Airfoil in Incompressible Inviscid Flow," *J. Fluid Mech.*, Vol. 87, 1987, pp. 157–168.

13 Jang, H. M., "A Viscous–Inviscid Interactive Method for Unsteady Flows," Ph.D. Thesis, University of Michigan, Ann Arbor, MI, 1990.

14 Cebeci, T., and Smith, A. M. O., *Analysis of Turbulent Boundary Layers*, Academic Press, New York, 1974.

15 Chen, K. K., and Thyson, N. A., "Extension of Emmons' Spot Theory to Flows on Blunt Bodies," *AIAA Journal*, Vol. 9, 1971, pp. 821–825.

16 Chang, K. C., Bui, M. N., Cebeci, T., and Whitelaw, J. H., "The Calculation of Turbulent Wakes," *AIAA Journal*, Vol. 24, 1986, p. 200.

17 Beam, R. M., and Warming, R. F., "An Implicit Factored Scheme for the Compressible Navier–Stokes Equations," *AIAA Journal*, Vol. 16, No. 4, Apr. 1978, pp. 393–402.

18 Pulliam, T. H., "Artificial Dissipation Models for the Euler Equations," *AIAA Journal*, Vol. 24, No. 12, Dec. 1986, pp. 1931–1940.

19 Baldwin, B. S., and Lomax, H., "Thin Layer Approximation and Algebraic Model for Separated Turbulent Flows," AIAA Paper No. 78-257, 1978.

20 Steger, J. L., VanDalsem, W. R., Panaras, A. G., and Rao, K. V., "A Formulation for the Boundary-Layer Equations in General Coordinates," NASA TM100079, June 1988.

21 McGhee, R. J., Jones, G. S., and Jouty, R., "Performance Characteristics From Wind-Tunnel Tests of a Low Reynolds Number Airfoil," AIAA Paper No. 88-0607, Jan. 1988.

22 Cebeci, T., McIlvaine, M., Chen, H. H., and Liebeck, R. H., "Calculation of Low Reynolds Number Flows at High Angles of Attack," AIAA Paper No. 90-0569, Jan. 1990.

23 Landon, R. H., "NACA 0012 Oscillatory and Transient Pitching," AGARD Report No. 702, 1981.

Similarity Behavior in Transitional Boundary Layers Over a Range of Adverse Pressure Gradients and Turbulence Levels

J. P. Gostelow

University of Technology, Sydney,
Sydney, Australia

G. J. Walker

University of Tasmania,
Hobart, Tasmania,
Australia

Boundary layer transition has been investigated experimentally under low, moderate, and high free-stream turbulence levels and varying adverse pressure gradients. Under high turbulence levels and adverse pressure gradients a pronounced subtransition was present. A strong degree of similarity in intermittency distributions was observed, for all conditions, when the Narasimha procedure for determination of transition inception was used. Effects of free-stream turbulence on the velocity profile are particularly strong for the laminar boundary layer upstream of the transition region. This could reflect the influence of the turbulence on the shear stress distribution throughout the layer and this matter needs further attention. The velocity profiles in wall coordinates undershoot the turbulent wall layer asymptote near the wall over most of the transition region. The rapidity with which transition occurs under adverse pressure gradients produces strong lag effects on the velocity profile; the starting turbulent boundary layer velocity profile may depart significantly from local equilibrium conditions. The practice of deriving integral properties and skin friction for transitional boundary layers by a linear combination of laminar and turbulent values for equilibrium layers is inconsistent with the observed lag effects. The velocity profile responds sufficiently slowly to the perturbation imposed by transition that much of the anticipated drop in form factor will not have occurred prior to the completion of transition. This calls into question both experimental techniques, which rely on measured form factor to characterize transition, and boundary layer calculations, which rely on local equilibrium assumptions in the vicinity of transition.

Introduction

Boundary layer transition is not yet fully understood and attempts to predict it theoretically have not been entirely successful. Designers have tended to rely on correlations of experimental data for determining the beginning and end of the transition region. These correlations have generally been derived from flows having no streamwise pressure gradient, reflecting the considerable body of experimental data available for this condition and the paucity of available data for flows with pressure gradients, especially for diffusing flows.

The scarcity of information on flows under streamwise pressure gradients is emphasized by a recent critical survey of transition data performed by Dey and Narasimha (1988). They were able to identify only six data sets for which turbulent spot formation rates for transition in accelerating flows could be evaluated. No suitable data could be identified for decelerating flow cases and a correlation of spot formation rates in this regime was not attempted.

Under adverse (positive) pressure gradients existing corre-

lations have predicted excessive transition lengths for both attached flows and separated shear layers. In the latter case the use of existing correlations has led to the prediction of a completely separated shear layer where observations indicate the existence of a laminar separation bubble.

A major problem with the interpretation of transition data is the variety of different criteria used to define the extent of the laminar–turbulent transition zone. The most consistent definition of the state of transition has proved to be the observation of turbulent intermittency. Some measurements of transition in a streamwise pressure gradient, in which observations of intermittency have been reported in addition to the other boundary layer properties, have been made by Narasimha (1957), Abu-Ghannam and Shaw (1980), Fraser et al. (1988), Ashworth et al. (1989), and Gostelow and Blunden (1988).

The work by Gostelow and Blunden combined measurements of intermittency in transitional flow situations over a wide range of adverse pressure gradients with the location of transition inception by plotting $F(\gamma) = [-\ln(1-\gamma)]^{1/2}$. This technique, originally suggested by Narasimha, was instrumental in identifying a universal distribution of intermittency in the transition zone.

Table 1 Values of pressure gradient parameter, λ_{θ_t}, for each nominal turbulence level and for designated pressure gradient settings DP0–DP9

Grid	No Grid	Grid 3	Grid 4
Tu, %	0.3	3.1	5.3
DP0	-0.005	-0.000	-0.003
DP1	-0.012	-0.012	-0.011
DP2	-0.024	-0.021	-0.019
DP3	-0.034	-0.020	-0.030
DP4	-0.043	-0.024	-0.031
DP5	-0.055	-0.028	-0.044
DP6	-0.069	-0.041	-0.047
DP7	-0.079	-0.075	-0.052
DP8		-0.083	-0.050
DP9			-0.063

This work led to the publication by Walker and Gostelow (1990) of a new correlation indicating a marked reduction of transition length in a strongly diffusing flow. The observed behavior was explained in terms of the influence of pressure gradients on the physics of turbulent breakdown and spot formation, a model originally proposed by Walker (1987).

The model predicts that, instead of the lengthy "breakdown in sets" regime experienced in the absence of a streamwise pressure gradient, transition under adverse pressure gradients is characterized by a rapid process, which involves the continuous development and breakdown of Tollmien–Schlichting waves. This was demonstrated by examining appropriate velocity traces and the corresponding spectra. Progression from the zero pressure gradient model to one appropriate to adverse pressure gradients is evolutionary in nature. This progression results in a marked reduction in transition length as even a mild adverse pressure gradient is imposed. The new model was expressed in transition length correlations, which could be readily incorporated into existing design procedures.

The measurements of Gostelow and Blunden had indicated a similar trend for transition length in a moderately turbulent free stream, as did measurements under a higher turbulence level reported by Gostelow (1989).

The previous papers had examined the effects of turbulence level and adverse pressure gradients in isolation and in this paper the combined effects of both variables are investigated. Because the introduction of significant free-stream turbulence results in changed transition behavior, the comparisons made in this paper are for low, moderate, and high free-stream turbulence levels.

The range of turbulence levels and pressure gradients tested

Fig. 1 Intermittency distributions with the corresponding $F(\gamma)$ for differing adverse pressure gradients in a highly turbulent free stream

is wide and it is therefore pertinent to consider whether the data revealed any degree of similarity over the whole range. In introducing his universal intermittency distribution for transitional boundary layers Narasimha had raised questions about its validity under strong pressure gradients. It was therefore planned to scrutinize the current data for any discrepancies in intermittency distribution; it was additionally proposed to investigate streamwise variations in velocity profiles and the associated integral properties from a similar perspective.

———— Nomenclature ————

c_f = skin-friction coefficient
$F(\gamma) = [-\ln(1-\gamma)]^{1/2}$
H = form factor = δ^*/θ
H' = normalized form factor = $(H-H_e)/(H_t-H_e)$
Tu = turbulence level, percent
U = free-stream velocity
u = local velocity
u^+ = dimensionless velocity = u/u^*
u^* = friction velocity = $\sqrt{\tau_w/\rho}$
x = streamwise distance from leading edge
y = normal distance from wall

y^+ = dimensionless distance from wall = yu^*/ν
γ = intermittency factor
δ = absolute thickness (based on $u/U = 0.99$)
δ^* = displacement thickness
η = dimensionless distance = $(x-x_s)/(x_e-x_s)$
θ = momentum thickness
λ = distance from $\gamma = 0.25$ to $\gamma = 0.75$
λ_θ = pressure gradient parameter = $(\theta^2/\nu) \cdot (dU/dx)$

ν = kinematic viscosity
ξ = dimensionless distance = $(x-x_t)/\lambda$
ρ = density
τ_w = wall shear stress

Subscripts

e = end of transition ($\gamma = 0.99$)
lam = laminar value
s = start of transition ($\gamma = 0.01$)
t = start of transition (Narasimha definition)
turb = turbulent value

Fig. 2 Intermittency distributions, for high, moderate, and low turbulence levels and a wide range of adverse pressure gradients, obtained by application of the Narasimha procedure

Fig. 3 Intermittency traverses for high and low free-stream turbulence and for nominal intermittency levels of 10, 50, and 90 percent in the wall layer

Intermittency Distributions

All measurements were made in the low-speed wind tunnel described by Gostelow and Blunden. The high-turbulence measurements were performed with a biplanar grid mounted upstream, giving nominal turbulence levels of 5.3 percent for

Grid 4 and 3.1 percent for Grid 3; with no grid present the turbulence level was 0.3 percent. Nominal turbulence levels were measured in a plane 20 mm upstream of the leading edge. The boundary layer grew on the surface of a flat plate 600 mm wide. The plate had a smooth surface finish and the nose was of a slender elliptical section. Care was taken to avoid any possibility of leading edge separation. Measurements of turbulence level in the free stream and of intermittency in the boundary layer were made using a single hot-wire probe. Boundary layer traverses used a pitot tube with a 1.2 mm × 0.72 mm flattened head. Intermittency measurements were facilitated by the use of an on-line intermittency meter designed by Alt (1987) and all data were logged by computer.

Adverse pressure gradients of varying strength were imposed by using a fairing mounted above the plate. This could be rotated incrementally about an axis located 20 mm upstream of the leading edge. Streamwise pressure gradients were measured using centerline static taps with free-stream velocity measurements for confirmation.

The high turbulence measurements undertaken with Grid 4 present covered ten different adverse pressure gradient cases, designated DP0–DP9. Moderate turbulence measurements with Grid 3 present covered nine adverse pressure gradients, designated DP0–DP8. The further series recorded without a turbulence grid consisted of eight different adverse pressure gradients designated DP0–DP7. In each case DP0 approximates a pressure gradient of zero with higher designations approaching the highest sustainable pressure gradients for attached laminar layers. Table 1 lists the values of pressure gradient parameter at transition inception, λ_{θ_t}, corresponding to the designated pressure gradients DP0–DP9.

Testing without a grid present was less comprehensive than with turbulence grids in place, fewer intermittency values being established, and this is reflected in the relatively sparse data set at low turbulence levels. In testing on Grid 4, measurement

difficulties were experienced for the higher intermittency levels of DP0 and DP1; these resulted in the highest recorded intermittency levels being a little lower than the usual 99 percent completion value. This affected the quality of results for transition completion for those two cases.

Figure 1 presents results from the 5.3 percent turbulence level Grid 4 intermittency measurements and values of $F(\gamma)$ as a function of dimensionless distance, η. Consistency of transition inception, intermittency distributions, and of the representation of the transition region as a whole, was maximized when the Narasimha procedure for determination of inception was adopted. Essentially, that portion of the $F(\gamma)$ curve between 25 and 75 percent intermittency was fitted with a straight line, the zero $F(\gamma)$ intercept of which defined η_t, the location of transition inception. The process is illustrated in Fig. 1. This procedure also provided characteristic length scales for transition, λ. As can be seen from Fig. 2, incorporation of the values of η_t and λ obtained from the $F(\gamma)$ curves into a new dimensionless distance, ξ, resulted in distributions that gave good agreement with the universal intermittency distribution of Narasimha

$$\gamma = 1 - \exp(-0.412\xi^2) \qquad (1)$$

That this applies to the high, moderate, and low turbulence levels of 5.3, 3.1, and 0.3 percent, respectively, over a wide range of pressure gradients, is demonstrated in Fig. 2.

It is quite clear that consistency is maximized by adopting the Narasimha procedure for fitting the intermittency distribution and determining the effective transition inception, t. That inception location was accordingly used to define the pressure gradient parameter at transition inception, λ_{θ_t}, which is the independent variable used to represent the strength of the adverse pressure gradient. Transition completion, e, was represented by the 99% intermittency value.

Results of testing with a turbulence level intermediate between that of Grids 3 and 4 were reported by Gostelow (1989). In that paper it was shown that adoption of λ_{θ_t} to define transition inception removed ambiguities in measurements of transition length and also extended the available range of pressure gradient parameter.

If no pressure gradient is present, the $F(\gamma)$ plot may be expected to be approximately linear in accordance with equation (1). Narasimha (1985), however, has shown that when a pressure gradient is applied the $F(\gamma)$ plot may experience a sudden change in slope from a subcritical level to a supercritical level at a "subtransition" point. Figure 1 demonstrates this behavior clearly. The subtransition has the effect of providing an ambiguous and erroneous transition inception location if the 1 percent intermittency definition is chosen (Gostelow, 1989). Fortunately these difficulties are avoided if the procedure of extrapolating the $F(\gamma)$ line back from 25 percent intermittency is adopted since this avoids the subcritical region entirely.

Subtransition behavior is significantly influenced by both free-stream turbulence and streamwise pressure gradient. Observations suggest a steady increase in the length of the subtransition region of low intermittency flow upstream of x_t as the free-stream turbulence level is increased. Increasing the adverse pressure gradient has a similar effect and, as seen from Fig. 1, this is particularly evident for high turbulence levels.

Figure 3 presents traverse results giving variations in intermittency through the boundary layer for a moderate adverse pressure gradient (DP3) at the highest and lowest turbulence levels and nominal intermittency levels of 10, 50, and 90 percent. Under low levels of free-stream turbulence the distributions exhibit a plateau, centered around $y/\delta = 0.2$, and fall off in the outer region of the boundary layer. A fall in intermittency is also observed as the wall is approached, typically for $y/\delta < 0.1$, and this is presumably due to viscous effects.
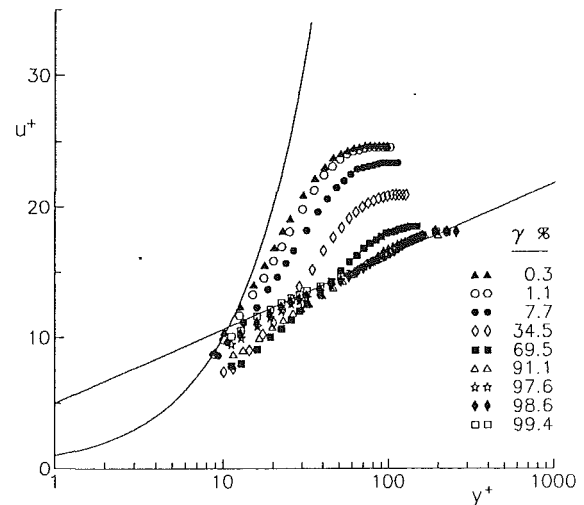
Fig. 4 Representative dimensionless velocity profiles for all measured intermittency values; moderate levels of pressure gradient and turbulence level (Grid 3, DP4)

Under highly turbulent free-stream conditions the observed intermittency in the free stream is nonzero and the intermittency either increases or remains roughly constant with y/δ in the outer region of the boundary layer. A region of nearly constant intermittency is still observed in the vicinity of $y/\delta = 0.2$. The intermittency again falls close to the wall as for the low-turbulence case, although some slight differences in behavior can be seen.

It is noted that a fixed threshold level for turbulence detection was used throughout the boundary layer. For the high turbulence case free-stream disturbances, which exceeded this threshold, gave rise to a nonzero intermittency outside the boundary layer. The high values of intermittency in the outer part of the boundary layer under high free-stream turbulence conditions are therefore partially due to the diffusion of turbulent energy from the free stream and will overestimate the true boundary layer intermittency.

An important conclusion from Fig. 3 is that, if the objective is an indication of the state of the boundary layer transition that is consistent for all free-stream turbulence levels, the appropriate measurement location, and that adopted here, is the incipient turbulent wall region around $y/\delta = 0.2$. Although diffusion effects from the turbulent free stream had little effect on the intermittency readings inboard of this location, further out the effects were strong.

Velocity Profiles

A typical set of boundary layer velocity profiles through the transition region, plotted in the dimensionless wall coordinate form of u^+ against y^+, is presented in Fig. 4. This set of profiles, corresponding to a moderate free-stream turbulence level (Grid 3) and a moderate adverse pressure gradient (DP4), is representative of profiles over the range covered in this investigation.

The skin friction at transition inception was determined by linear extrapolation of readings closest to the wall on the basis of $u^+ = y^+$. The value at transition completion was obtained using the power law formulation

$$\tau_w/\rho = 0.0464(\nu/U\delta)^{1/4}U^2/2 \qquad (2)$$

Skin friction values at intermediate intermittencies were obtained using the Emmons (1951) formulation

$$c_f = (1 - \gamma)c_{flam} + \gamma c_{fturb} \qquad (3)$$

A matrix of figures, having different values of free-stream turbulence and streamwise pressure gradient, is presented in
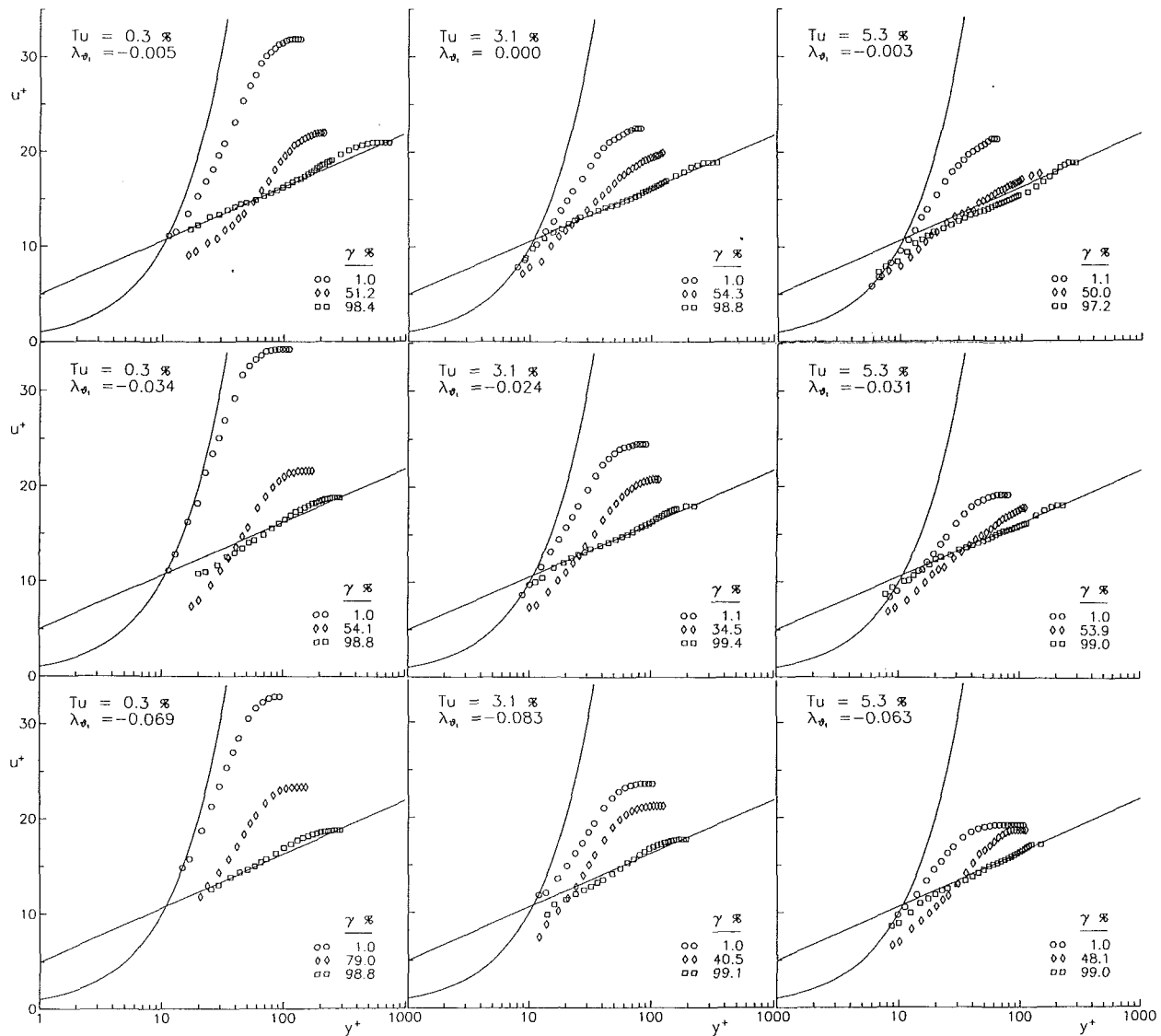
Fig. 5 Dimensionless velocity profiles for low, moderate, and high turbulence levels and zero, moderate, and strong pressure gradients

Fig. 5. Each graph gives velocity profiles for the start and end of transition (1 and 99 percent intermittency) and for an intermediate value. It was decided to limit the profiles presented in Fig. 5 to three intermittency values to clarify the trends; also whereas testing on Grids 3 and 4 encompassed a large number of intermittency values, as in Fig. 4, testing with no grid present was in general limited to the three intermittency values.

For 1 percent intermittency and low turbulence levels the profiles lie close to the laminar viscous flow asymptote, $u^+ = y^+$. For 99 percent intermittency the profiles follow the law of the wall asymptote

$$u^+ = 2.439 \ln y^+ + 5.0 \qquad (4)$$

in the turbulent wall layer region $y^+ > 30$, apart from the wake region in the outer part of the boundary layer. The profiles taken with intermediate levels of intermittency show a significant undershoot of the turbulent wall asymptote in the inner part of the layer; this is thought to be associated with a rapid increase in shear stress achieved by the low-inertia fluid at the wall and a slower change in flow velocity further out, causing reductions in the level of dimensionless velocity. Errors in evaluating the transitional skin friction values using equation (3) could have been an additional factor.

The influence of pressure gradient on the dimensionless velocity distributions for the end of transition is only slight. Strong adverse pressure gradients, which would tend to produce laminar separation at transition inception, are relatively mild for the ensuing turbulent boundary layer. The most significant effect of pressure gradient is to cause an increasing undershoot of the turbulent wall layer asymptote as the pressure gradient becomes more adverse; this possibly reflects the lower initial value of wall friction velocity, u^*, and a relatively greater rate of increase of u^* in the initial stages of transition.

Free-stream turbulence has a strong effect on the preceding laminar layer; results show a strong and consistent trend toward lower values of u^+ in the outer region of the boundary layer as Tu is increased. This may result from an increase in wall shear stress throughout the layer associated with the higher levels of free-stream turbulence. There is an associated reduction in undershoot of the turbulent wall layer asymptote for the intermediate intermittency velocity profiles and the velocity profiles at transition completion show a more extensive region of the wall similarity with increasing turbulence level. These observations are consistent with the reduced lag in adjustment of form factor, H, during transition under high free-stream turbulence conditions.

Although the $F(\gamma)$ procedure provided a consistent basis for

Fig. 6   Raw and normalized distributions of form factor variation through transition under high free-stream turbulence conditions

Fig. 7   Raw and normalized distributions of form factor variation through transition under moderate free-stream turbulence conditions

defining the physical extent of transition there remain, under high turbulence levels and at low intermittencies, significant deviations from the usual laminar layer profiles. Free-stream turbulence changes the entire velocity profile and therefore affects both the form factor and the skin friction.

Variation in Form Factor

All velocity traverses were integrated to give information on the variation of integral parameters through the transition region. Results for the high, medium, and low free-stream turbulence cases are presented in Figs. 6, 7, and 8, respectively. The curves of H as a function of ξ are widely spread due to the different values of H upstream and downstream of transition associated with variations in pressure gradient, free-stream turbulence, and Reynolds number. An additional set of curves provides the variation of normalized form factor $H' = (H - H_e)/(H_t - H_e)$, following a procedure similar to that of Abu-Ghannam and Shaw. This eliminates differences in starting conditions and in the fall in H through transition and allows the similarity of the form factor distributions between transition inception and completion to be examined.

Normalization of the form factor distribution significantly reduces the spread in the data. A universal normalized distribution cannot be expected because of the subtransition effects on the preceding laminar layer and the lag effects on the developing turbulent layer. The scatter in the normalized curves is, however, no greater than that reported by Abu-Ghannam and Shaw despite the coverage of a wider range of pressure gradients.

Various authors have assumed some form of similarity in the form factor variation as a basis for describing transitional flow behavior. Dhawan and Narasimha (1958) gave the following approximate relation:

$$H' = \exp(-0.412\xi^2) \tag{5}$$

which implies a linear relation between form factor and intermittency. This gave a fair fit to the experimental cases considered. Abu-Ghannam and Shaw (1980) examined a wider range of experimental data and fitted the approximate relation

$$H' = 1 - \sin(\pi\eta/2) \tag{6}$$

where $\eta = \xi/3.36$. Equations (5) and (6), designated DN and AGS respectively, have been plotted in Figs. 6 and 7, and 8 to permit a comparison with the variation in normalized form factor observed in the present investigation.

The measured values of H at transition inception ($\xi = 0$) are noticeably below the Falkner–Skan values for steady laminar boundary layers having the same local value of pressure gradient parameter, λ_{θ_t}. This is evidently due to the presence of slight turbulent mixing in the subtransition zone upstream of transition inception. The deficit in initial form factor values increases as the free-stream turbulence level becomes higher and the subtransition is more extensive. There is a tendency for dH/dx to be negative at transition inception although this behavior is less pronounced for higher adverse pressure gradients. Measurements, with a nominal turbulence level of 2 percent, in a mild favorable pressure gradient by Blair (1982), and under zero pressure gradient by Suder et al. (1988), also show that H has fallen well below the fully laminar level prior to the commencement of transition.

The value of H at the end of transition ($\xi = 3.36$) appears to have stabilized only for the low adverse pressure gradient cases DP0 and DP1. There is a systematic trend for dH/dx to become increasingly negative at $\xi = 3.36$ as the pressure gradient becomes more adverse. This effect becomes more pronounced as the free-stream turbulence level is reduced. It is most clearly seen for the low turbulence data of Fig. 8, where the observations were made over an extended range of stream-
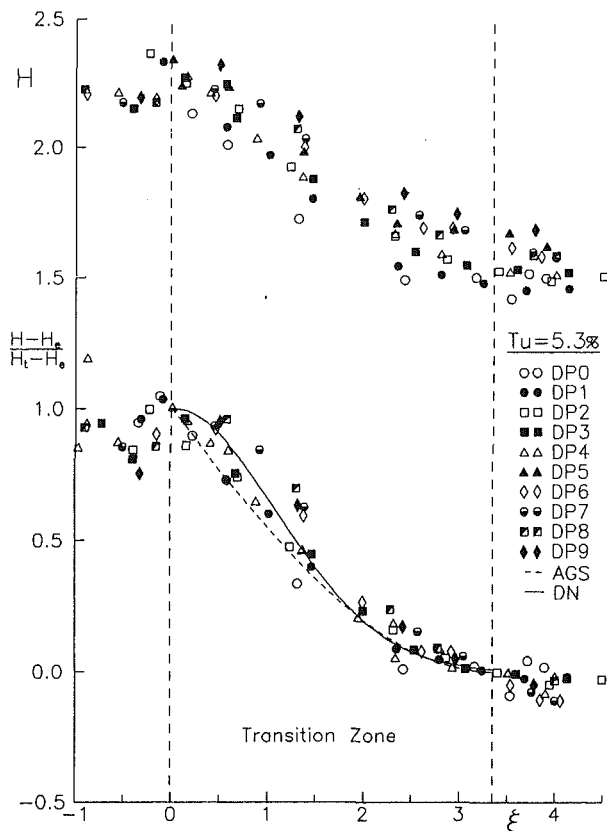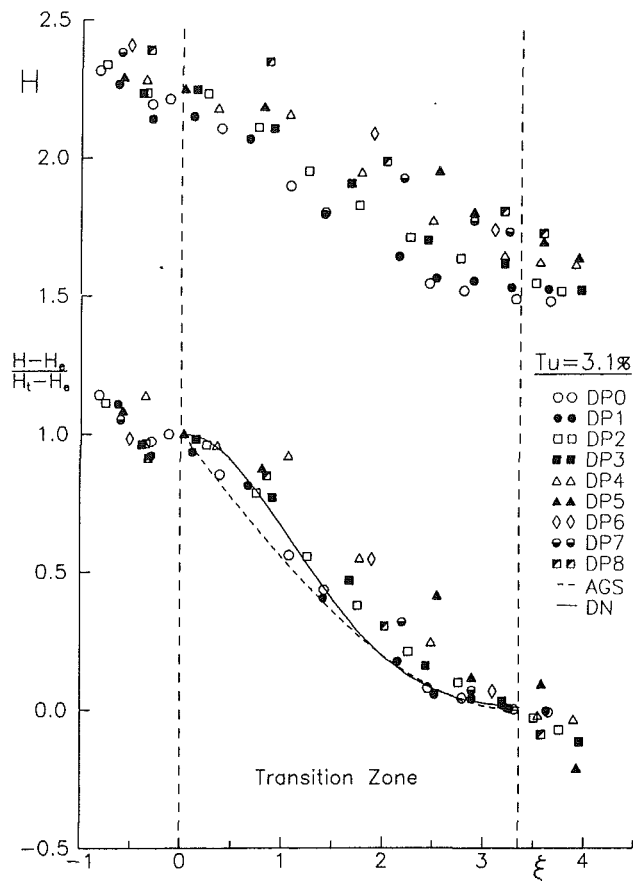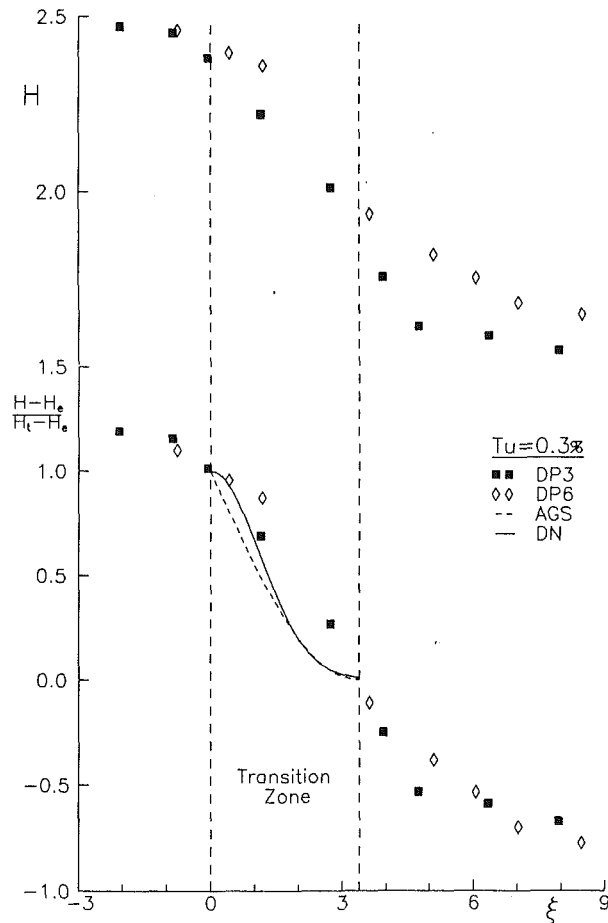
Fig. 8 Raw and normalized distributions of form factor variation through transition under low free-stream turbulence conditions

Fig. 9 Ratio of transition length to absolute thickness, as a function of pressure gradient parameter, for all three turbulent levels

wise positions upstream and downstream of the transition region.

Figure 8 shows that for the strong adverse pressure gradient case DP6, the form factor continues to fall markedly after the intermittency measurements have indicated transition completion, with about half the total drop in H occurring for $\xi > 3.36$. The streamwise distance required to achieve stability of the velocity profile in this case is more than double the transition length. This emphasizes the need in experimental studies on transition for boundary layer traverses to be taken well upstream and downstream of the transition region.

One reason for increased lag effects in strong adverse pressure gradient boundary layers is the greater change in form factor through the transition region in this case. This arises because the laminar boundary layer form factor prior to transition increases much more rapidly than that of the ensuing turbulent layer as the pressure gradient becomes stronger. The reduced lag effects for high free-stream turbulence conditions can be partly explained by the associated lower values of H prior to transition reducing the change in H to be effected over the transition region; another factor could be the possible modification of turbulent mixing in the boundary layer as a result of disturbances in the free stream.

The principal cause of increased lag effects under adverse pressure gradient conditions, however, is thought to be the time inherently required by the boundary layer velocity profile to regain local equilibrium after a disturbance. The experiments of Clauser (1956) suggested that a streamwise distance of between ten and fifty absolute thicknesses was required for a fully turbulent layer to regain equilibrium.

In Fig. 9 all readings from the three turbulence levels have
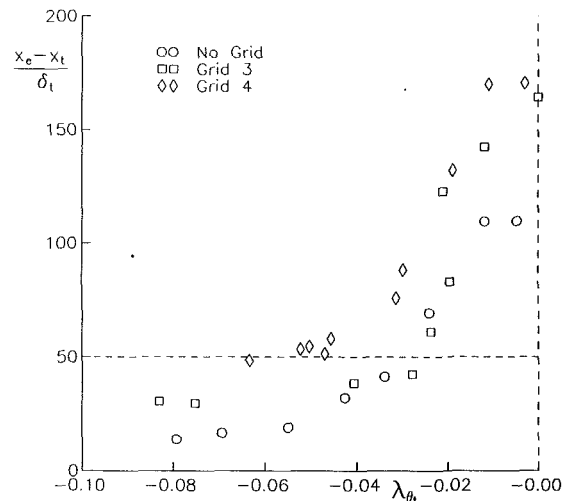
been plotted on the basis of transition length divided by absolute thickness at transition inception. The criterion of fifty absolute thicknesses is indicated for reference purposes. Whereas for zero and low adverse pressure gradients the transition length comfortably exceeds the criterion, this is not the case for strong adverse pressure gradients. Any point with a stronger adverse pressure gradient parameter at transition inception than -0.04 has a transition length of the order of fifty absolute thicknesses or lower and the potential to exhibit strong lag effects. If the points are reviewed individually it becomes clear that the designated pressure gradients, which show a spread on the $H'-\xi$ plot, are those which have a transition length shorter than fifty absolute thicknesses. Those showing the greatest lag are from the low turbulence level situation of Fig. 8 and correspond to the points on Fig. 9 giving the lowest values of the ratio of transition length to absolute thickness. Transition lengths for zero pressure gradient flows are typically an order of magnitude greater than those for strong adverse pressure gradients.

The distributions of normalized form factor, described by equations (5) and (6), diverge somewhat over the forward part of the transition zone but the difference does not exceed the scatter in the observed values of H'. Dhawan and Narasimha's approximation tends to give a better representation of the experimental data in this region, but neither of the equations permits a variable value of dH/dx at transition inception to allow for subtransition effects in the preceding laminar layer.

Over the rearward part of the transition zone the approximate distributions of $H'(\xi)$ described by equations (5) and (6) agree quite closely. Comparisons of the normalized form factor values in this region support the previous observations that lag effects tend to increase for stronger adverse pressure gradients, and to decrease with higher levels of free-stream turbulence. Again neither equation can accommodate the significant negative values of dH/dx at transition completion ($\xi = 3.36$), which are associated with large lag effects.

In general the Abu-Ghannam and Shaw relation (equation (6)) agrees most closely with the data for the zero pressure gradient cases. The Dhawan and Narasimha relation (equation (5)) represents data well for a weak adverse pressure gradient. Stronger adverse pressure gradients are not well represented, even if measured values of x_t and x_e are used, giving rise to higher form factors than predicted by the equations due to lag effects on the developing boundary layer. The deviations for strong adverse pressure gradients would be considerably greater if local equilibrium values for H_t and H_e were employed, as would be the case in a boundary layer calculation where these values were not known a priori.

The foregoing observations call into question the common experimental approach of using form factor variations to define the extent of transition. The use of boundary layer calculation methods relying on the existence of local equilibrium conditions in the transition region and the emerging turbulent boundary layer should also be questioned. In particular, the practice of linearly combining the laminar and turbulent properties in proportion to the intermittency is unlikely to provide a representative solution for transitional flow under strong adverse pressure gradient conditions.

Conclusions

Measurements of boundary layer transition covering a wide range of turbulence levels and adverse pressure gradients have been reported. Results are presented for high, moderate, and low turbulence levels. Under high levels of free-stream turbulence and adverse pressure gradient the results exhibit a pronounced subtransition. It is shown that use of the Narasimha procedure for determining transition inception gave a strong degree of similarity in the observed streamwise variation of intermittency through the transition region for all conditions.

The intermittency distributions through the boundary layer exhibited a plateau in the incipient turbulent wall layer region extending to about $y/\delta = 0.2$. Within this region the free-stream conditions had only minor effects. In the outer part of the boundary layer the intermittency distributions were more strongly influenced by turbulence level and pressure gradient. The observed distribution in the outer layer under high free-stream turbulence may have overestimated the intermittency.

Effects of free-stream turbulence on the velocity profile in the early stages of transition are particularly strong. In the subtransition regime the entire velocity profile appears to be affected; the influence of free-stream turbulence on preceding laminar boundary layers needs further attention. There is a pronounced undershoot in the dimensionless velocity profile for intermediate values of intermittency under all conditions tested.

Under the adverse pressure gradients typical of axial flow compressor operation, transition occurs much more rapidly than had previously been appreciated. Lag effects on the velocity profile are strong and the form factor responds sufficiently slowly to the perturbation imposed by transition that, in the short transition regions prevalent, much of the expected reduction in form factor may not have occurred prior to the end of transition. This raises questions about the use of form factor as an indicator of the extent of transition in experimental work. The physical effects of transition are not confined to the immediate transition region and future experimental investigations of transition should include boundary layer traverses taken an adequate distance upstream and downstream of the transition zone.

The existence of significant lag effects is not consistent with the derivation of integral properties by linear combination of laminar and turbulent values. For boundary layer calculations simple integral methods will not be appropriate under these conditions and alternative approaches should be considered. Some form of lag approach appears to be necessary; the incorporation of the Narasimha intermittency distribution is a logical starting point since it provides the most consistent similarity basis under all conditions of adverse pressure gradient and free-stream turbulence.

References

Abu-Ghannam, B. J., and Shaw, R., 1980, "Natural Transition of Boundary Layers—The Effects of Turbulence, Pressure Gradient, and Flow History," *Journal of Mech. Eng. Sci.*, Vol. 22, No. 5.

Alt, P., 1987, "An Intermittency Meter for Investigating Boundary Layer Transition," University of Technology, Sydney, Technical Report No. NSWIT/ME17.

Ashworth, D. A., LaGraff, J. E., and Schultz, D. L., 1989, "Unsteady Interaction Effects on a Transitional Turbine Blade Boundary Layer," ASME JOURNAL OF TURBOMACHINERY, Vol. 111, pp. 162–168.

Blair, M. F., 1982, "Influence of Free-Stream Turbulence on Boundary Layer Transition in Favorable Pressure Gradients," ASME *Journal of Engineering for Power*, Vol. 104, pp. 678–685.

Clauser, F. H., 1956, "The Turbulent Boundary Layer," *Advances in App. Mech.*, Vol. IV, pp. 1–51.

Dey, J., and Narasimha, R., 1988, "An Integral Method for the Calculation of 2-D Transitional Boundary Layers," Dept. of Aerospace Eng., Indian Institute of Science, Report No. 88FM7.

Dhawan, S., and Narasimha, R., 1958, "Some Properties of Boundary-Layer Flow During the Transition From Laminar to Turbulent Motion," *Journal of Fluid Mech.*, Vol. 3, pp. 418–436.

Emmons, H. W., 1951, "The Laminar-Turbulent Transition in a Boundary Layer—Part 1," *Journal of Aero. Sci.*, Vol. 8.

Fraser, C. J., Milne, J. S., and Gardiner, I. D., 1988, "The Effect of Pressure Gradient and Freestream Turbulence Intensity on the Length of Transitional Boundary Layers," *Proc. Instn. Mech. Engrs.*, Vol. 202, No. C3, pp. 195–203.

Gostelow, J. P., and Blunden, A. R., 1988, "Investigations of Boundary Layer Transition in an Adverse Pressure Gradient," ASME JOURNAL OF TURBOMACHINERY, Vol. 111, pp. 366–375.

Gostelow, J. P., 1989, "Adverse Pressure Gradient Effects on Boundary Layer Transition in a Turbulent Free Stream," presented at the 9th ISABE, Athens, Greece.

Narasimha, R., 1957, "On the Distribution of Intermittency in the Transition Region of the Boundary Layer," *J. Aero. Sci.*, Vol. 24, p. 711.

Narasimha, R., 1985, "The Laminar-Turbulent Transition Zone in the Boundary Layer," *Progress in Aerospace Science*, Vol. 22, pp. 29–80.

Suder, K. L., O'Brien, J. E., and Reshotko, Eli, 1988, "Experimental Study of Bypass Transition in a Boundary Layer," NASA TM-100913.

Walker, G. J., 1987, "Transitional Flow on Axial Turbomachine Blading," AIAA Paper No. 87-0010, and *AIAA Journal*, Vol. 27, No. 5, pp. 595–602.

Walker, G. J., and Gostelow, J. P., 1990, "Effects of Adverse Pressure Gradients on the Nature and Length of Boundary Layer Transition," ASME JOURNAL OF TURBOMACHINERY, Vol. 112, pp. 196–205.

The foregoing observations call into question the common experimental approach of using form factor variations to define the extent of transition. The use of boundary layer calculation methods relying on the existence of local equilibrium conditions in the transition region and the emerging turbulent boundary layer should also be questioned. In particular, the practice of linearly combining the laminar and turbulent properties in proportion to the intermittency is unlikely to provide a representative solution for transitional flow under strong adverse pressure gradient conditions.

Conclusions

Measurements of boundary layer transition covering a wide range of turbulence levels and adverse pressure gradients have been reported. Results are presented for high, moderate, and low turbulence levels. Under high levels of free-stream turbulence and adverse pressure gradient the results exhibit a pronounced subtransition. It is shown that use of the Narasimha procedure for determining transition inception gave a strong degree of similarity in the observed streamwise variation of intermittency through the transition region for all conditions.

The intermittency distributions through the boundary layer exhibited a plateau in the incipient turbulent wall layer region extending to about $y/\delta = 0.2$. Within this region the free-stream conditions had only minor effects. In the outer part of the boundary layer the intermittency distributions were more strongly influenced by turbulence level and pressure gradient. The observed distribution in the outer layer under high free-stream turbulence may have overestimated the intermittency.

Effects of free-stream turbulence on the velocity profile in the early stages of transition are particularly strong. In the subtransition regime the entire velocity profile appears to be affected; the influence of free-stream turbulence on preceding laminar boundary layers needs further attention. There is a pronounced undershoot in the dimensionless velocity profile for intermediate values of intermittency under all conditions tested.

Under the adverse pressure gradients typical of axial flow compressor operation, transition occurs much more rapidly than had previously been appreciated. Lag effects on the velocity profile are strong and the form factor responds sufficiently slowly to the perturbation imposed by transition that, in the short transition regions prevalent, much of the expected reduction in form factor may not have occurred prior to the end of transition. This raises questions about the use of form factor as an indicator of the extent of transition in experimental work. The physical effects of transition are not confined to the immediate transition region and future experimental investigations of transition should include boundary layer traverses taken an adequate distance upstream and downstream of the transition zone.

The existence of significant lag effects is not consistent with the derivation of integral properties by linear combination of laminar and turbulent values. For boundary layer calculations simple integral methods will not be appropriate under these conditions and alternative approaches should be considered. Some form of lag approach appears to be necessary; the incorporation of the Narasimha intermittency distribution is a logical starting point since it provides the most consistent similarity basis under all conditions of adverse pressure gradient and free-stream turbulence.

Acknowledgments

References

Abu-Ghannam, B. J., and Shaw, R., 1980, "Natural Transition of Boundary Layers—The Effects of Turbulence, Pressure Gradient, and Flow History," *Journal of Mech. Eng. Sci.*, Vol. 22, No. 5.

Alt, P., 1987, "An Intermittency Meter for Investigating Boundary Layer Transition," University of Technology, Sydney, Technical Report No. NSWIT/ME17.

Ashworth, D. A., LaGraff, J. E., and Schultz, D. L., 1989, "Unsteady Interaction Effects on a Transitional Turbine Blade Boundary Layer," ASME JOURNAL OF TURBOMACHINERY, Vol. 111, pp. 162–168.

Blair, M. F., 1982, "Influence of Free-Stream Turbulence on Boundary Layer Transition in Favorable Pressure Gradients," ASME *Journal of Engineering for Power*, Vol. 104, pp. 678–685.

Clauser, F. H., 1956, "The Turbulent Boundary Layer," *Advances in App. Mech.*, Vol. IV, pp. 1–51.

Dey, J., and Narasimha, R., 1988, "An Integral Method for the Calculation of 2-D Transitional Boundary Layers," Dept. of Aerospace Eng., Indian Institute of Science, Report No. 88FM7.

Dhawan, S., and Narasimha, R., 1958, "Some Properties of Boundary-Layer Flow During the Transition From Laminar to Turbulent Motion," *Journal of Fluid Mech.*, Vol. 3, pp. 418–436.

Emmons, H. W., 1951, "The Laminar-Turbulent Transition in a Boundary Layer—Part 1," *Journal of Aero. Sci.*, Vol. 8.

Fraser, C. J., Milne, J. S., and Gardiner, I. D., 1988, "The Effect of Pressure Gradient and Freestream Turbulence Intensity on the Length of Transitional Boundary Layers," *Proc. Instn. Mech. Engrs.*, Vol. 202, No. C3, pp. 195–203.

Gostelow, J. P., and Blunden, A. R., 1988, "Investigations of Boundary Layer Transition in an Adverse Pressure Gradient," ASME JOURNAL OF TURBOMACHINERY, Vol. 111, pp. 366–375.

Gostelow, J. P., 1989, "Adverse Pressure Gradient Effects on Boundary Layer Transition in a Turbulent Free Stream," presented at the 9th ISABE, Athens, Greece.

Narasimha, R., 1957, "On the Distribution of Intermittency in the Transition Region of the Boundary Layer," *J. Aero. Sci.*, Vol. 24, p. 711.

Narasimha, R., 1985, "The Laminar-Turbulent Transition Zone in the Boundary Layer," *Progress in Aerospace Science*, Vol. 22, pp. 29–80.

Suder, K. L., O'Brien, J. E., and Reshotko, Eli, 1988, "Experimental Study of Bypass Transition in a Boundary Layer," NASA TM-100913.

Walker, G. J., 1987, "Transitional Flow on Axial Turbomachine Blading," AIAA Paper No. 87-0010, and *AIAA Journal*, Vol. 27, No. 5, pp. 595–602.

Walker, G. J., and Gostelow, J. P., 1990, "Effects of Adverse Pressure Gradients on the Nature and Length of Boundary Layer Transition," ASME JOURNAL OF TURBOMACHINERY, Vol. 112, pp. 196–205.

—————— **DISCUSSION** ——————

W. B. Roberts[1]

1   Would the authors please clarify the physical phenomenon that is shown in Fig. 9? It appears from this figure that an increase in turbulence level leads to an increase in transition length. This is contrary to the effect that is observed for transition length on flat plates.

2   It appears from Fig. 9 that the effect of adverse pressure gradient is much more important for transition length than the turbulence level. Would the authors please comment?

I commend the authors for their work on transition. It is sorely needed and greatly appreciated.

Authors' Closure

The authors appreciate the helpful questions and comments of Dr. Roberts. He correctly observes that under zero pressure gradient conditions the trend of measurements taken by several authors is for the transition length to decrease with an increase in turbulence level. In this context the transition length is most frequently described by a difference between length or momentum thickness Reynolds numbers, Re_x or Re_θ, at transition onset and completion. A compilation of such data was presented by Gostelow and Blunden (1988). At zero pressure gradient the authors' own data are fully consistent with that trend.

The situation is complicated by the different ways in which the various authors have defined the onset and completion of transition and by the changes in parameters, such as Re_x, Re_θ,

[1]Director and Senior Associate, Flow Application Research, Fremont, CA 94539.

An Experimental Study of Local Wall Shear Stress, Surface Static Pressure, and Flow Visualization Upstream, Alongside, and Downstream of a Blade Endwall Corner

A. K. Abdulla

Turbomachinery Laboratory,
Department of Mechanical Engineering,
The City College of New York,
New York, NY 10031

R. K. Bhargava

Boyce Engineering International Inc.,
Houston, TX 77099

R. Raj

Turbomachinery Laboratory,
Department of Mechanical Engineering,
The City College of New York,
New York, NY 10031

The experimental study reported in this paper was performed to acquire information on the distribution of wall shear stress and surface static pressure in a blade endwall corner. The blade endwall corner region investigated was divided into three sections: 0.4 chord length upstream of the blade leading edge, inside the endwall corner region, and one chord length downstream of the blade trailing edge. The maximum increases in the values of wall shear stress were found to exist on the endwall, in the corner region, between the blade leading edge and the location of maximum blade thickness (≈ 140 percent maximum increase, compared to its far upstream value, at $x/D = 6$). Surface flow visualization defined the boundaries of the vortex system and provided information on the direction and magnitude of the wall shear stress. The acquired results indicated that the observed variations of wall shear stress and surface static pressure were significantly influenced by the interaction of secondary flows with pressure gradients induced by the presence of blade curvature.

Introduction

A major part of the secondary flow losses in turbomachines is due to the interaction of the wall boundary layer with the blade rows in the blade endwall region. The secondary flow in this region is a complex three-dimensional, rotational, slender shear flow. A common feature observed experimentally in this region is the occurrence of three-dimensional separation of the boundary layer, upstream of the blade leading edge, with curved separation lines present on the endwall surface ahead of the blade, as shown in Fig. 1. When a boundary layer developed on the endwall approaches the blade, it will experience an adverse pressure gradient, causing the boundary layer to be skewed (deflected) resulting in generation of streamwise vorticity just upstream of the blade leading edge. The boundary layer separates in the vicinity of the blade leading edge and the separation point is called the "saddle point" (nodal or standoff point of separation). This separated boundary layer then rolls up, forming a horseshoe shaped vortex that wraps around the blade leading edge. The flow dominated by the horseshoe vortex is known as "secondary flow of the first kind" or "skew-induced secondary flow." The size and strength of the horseshoe vortex have been reported to be strongly
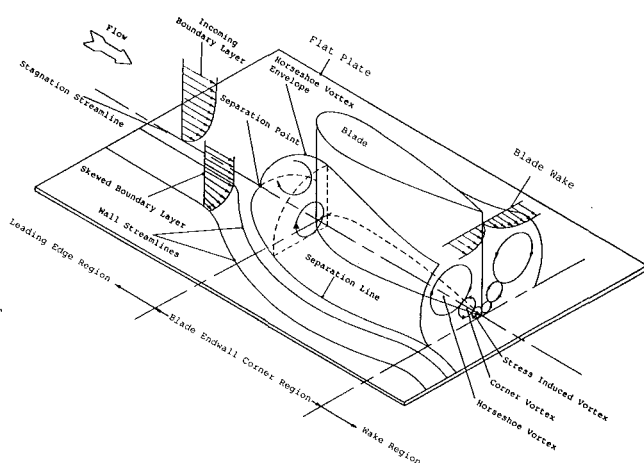

Fig. 1 Schematic showing the formation of the horseshoe vortex by the skewing and the separation of the two-dimensional boundary layer ahead of the blade leading edge; the vortex system at the trailing edge is suggested by Hazarika et al. [8]

---

dependent on the blade leading edge shape [1, 2]. A thicker incident boundary layer resulted in a larger horseshoe vortex [3].

In a turbine cascade, the evolution of different types of secondary flows has been described by many investigators [4–7]. In a simplified blade endwall corner, in addition to the horseshoe vortex, Hazarika et al. [8] suggested the existence of another vortex termed the corner vortex, in a region between the horseshoe vortex and the corner formed by two bodies, within a short distance downstream of the blade leading edge. The rotational direction of the abovementioned corner vortex was observed opposite to that of the horseshoe vortex [8]. The presence of a corner vortex was also reported by Dickinson [9] and Gorski et al. [10]. In addition to the corner vortex, Hazarika et al. [8] also observed the formation of a pair of counterrotating vortices between the corner vortex and the corner formed by the two bodies downstream of the maximum thickness section of the blade. These counterrotating vortices were noted to be produced by the action of anisotropic and inhomogeneous turbulence, i.e., Reynolds stress gradients in the plane normal to the primary (streamwise) flow direction [8]. This kind of secondary flow is known as "secondary flow of the second kind" or "stress-induced secondary flow." They proposed that one of these vortices (next to the blade surface) will merge with the corner vortex (see Fig. 1).

Surface oil flow visualization studies made by Sepri [11], Chu and Young [12], the measurements conducted by Binder and Romey [13] downstream of a turbine stator, and by Naranjit [14] and Barber [3] downstream of a wing-body junction, implied that some secondary flows existed far downstream of the trailing edge. It follows that the complex vortex structure generated ahead and downstream of the blade leading edge will shed down and influence not only the endwall corner region but also the wake region generated at the trailing edge of the blade.

The Preston tube has been extensively used in different three-dimensional flows [15–21] and has been found easy to use. It was found that accurate results, even in three-dimensional turbulent flows, can be obtained with the Preston tube if the probe is aligned with the local flow direction [20, 21].

Surface static pressure is commonly measured by wall pressure taps. However, due to the large number of measuring points needed at some stations, it was not practical to use wall pressure taps. Instead, a conventional static pressure probe was used, resting on the surface, to measure the surface static pressure. Sproston and Goksel [22] calibrated a static pressure probe resting on the surface against the conventional wall pressure taps in zero as well as nonzero pressure gradient flows. The agreement between the two methods was within 2 percent of the free stream dynamic head. More recently, Bhargava and Raj [23] investigated the surface static tube accuracy in three-dimensional turbulent flows and showed that the surface static tube can be used with a maximum error of less than 7 percent of free-stream dynamic head compared to the conventional technique.

It should be mentioned that the experimental results reported here are from two investigations carried out independently but on the same test model. In one study, two regions, namely, upstream of the blade leading edge and inside the endwall corner, were investigated. The second study included the region downstream of the blade trailing edge. Some of the results presented in this paper were reported by Bhargava et al. [15]. The main objective of combining the abovementioned two studies was to understand the influence of secondary flows and blade curvature on the distribution of wall shear stress and surface static pressure in the entire endwall corner region.

Experimental Method

A low-speed open circuit wind tunnel, having nonuniformity in the free-stream mean velocity of less than ±0.5 percent in the test section, was used for the experiments. The free-stream turbulence intensity in the test section, in the absence of the test model, was less than 0.1 percent at a flow velocity of 20 m/s and higher. The experimental data was acquired at a free-stream velocity of 27.3 ± 0.3 m/s.

The blade endwall corner test model was constructed by mounting two NACA 65-015 base profile blades fixed on either side of the flat plate along the centerline as shown in Fig. 2. The blades had a chord and a span of 25.4 cm and 21.9 cm, respectively, with a leading edge diameter of 1.27 cm and a 0.254 cm trailing edge diameter. The test model was fixed in the test section with the flat plate in a horizontal position midway between the top and bottom test-section walls. A schematic of the test model with the measuring stations is shown in Fig. 2. The locations of the axial measuring stations are given in Table 1.

A combination of two grids was used to create a free-stream turbulence level of 1.5 percent at 107 cm downstream of the grids (location of the blade leading edge). This higher than normal level of free-stream turbulence was introduced in order to prevent a separation bubble and to increase the boundary layer thickness over the blade surface.

Two surface flow visualization techniques were used, namely, oil film and dot matrix surface flow visualizations. Surface oil film flow visualization was carried out using lampblack mixed
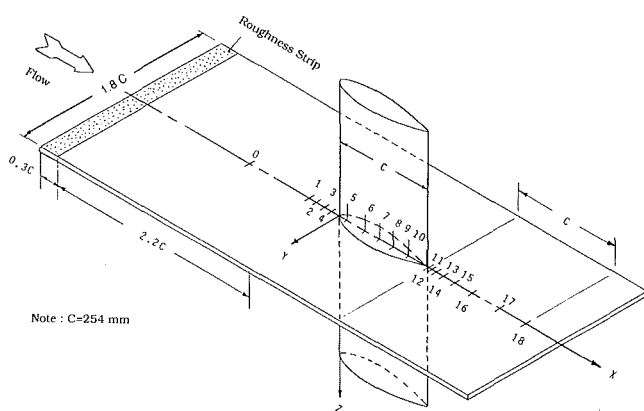
Fig. 2 Schematic of the test model and the measuring stations

Note : C=254 mm

Nomenclature

c = airfoil chord length
C_p = static pressure coefficient
p = surface static pressure
p_{ref} = reference static pressure (equal to ambient pressure)
D = blade leading edge diameter

U_∞ = local free-stream mean velocity in X direction
X, Y, Z = coordinates in the frame of reference of the test model
x, y, z = distances in X, Y, and Z directions, respectively
ρ = density of air

τ_w = local wall shear stress
$\tau_{w\infty}$ = wall shear stress one chord length upstream of the blade leading edge
τ_{wmin} = local minimum wall shear stress
τ_{wmax} = local maximum wall shear stress

Table 1 Locations of the axial measuring stations

Station #	Axial Distance x (mm)	x/c (c=254 mm)	x/D (D=12.7 mm)
0	-254.0	-1.0	-20.0
1	-101.6	-0.4	-8.0
2	-76.6	-0.3	-6.0
3	-50.8	-0.2	-4.0
4	-25.4	-0.1	-2.0
5	25.4	0.1	2.0
6	76.2	0.3	6.0
7	127.0	0.5	10.0
8	152.2	0.6	12.0
9	203.2	0.8	16.0
10	251.0	0.99	19.75
11	254.0	1.0	20.0
12	260.4	1.025	20.5
13	266.7	1.05	21.0
14	279.4	1.1	22.0
15	304.8	1.2	24.0
16	355.6	1.4	28.0
17	431.8	1.7	34.0
18	508	2.0	40.0

Table 2 Preston tube details

Probe No.	size	outer dia. (mm)	inner dia. (mm)	inner/outer dia.
1	Small Preston tube	0.8128	0.4953	0.6094
2	Medium Preston tube	1.0795	0.6858	0.6353
3	Large Preston tube	1.2700	0.8380	0.6600

All Dimensions are in mm

Probe No. 1   Probe No. 2   Probe No. 3

Fig. 3 Schematic of the Preston probes

with #2 Diesel and Oleic acid as dispersing agent. Surface streamline flow visualization was carried out using polyurethane enamel paint and mineral spirits, a technique similar to the one used by Langston and Boyle [24].

The wall static pressure was measured using a commercially available pitot-static probe of 1.59 mm outer diameter. A Kiel probe was used to measure the reference total pressure, which was maintained constant during the entire experiment.

The wall shear stress measurements were achieved with the specially constructed Preston tubes along with the calibration equations suggested by Patel [25]. Three sizes of Preston tube were constructed from stainless steel hypodermic needle tubing with the dimensions as provided in Table 2. Figure 3 shows a schematic of the Preston tubes employed in the experiment. The geometrically similar circular Preston tubes were chosen to have, as nearly as possible, a ratio of inner to outer diameters of 0.6, to be within the size range of Preston tubes used by Patel [25] in obtaining the calibration equations for measuring the local wall shear stress. Also, the available sizes of hypodermic needles have approximately this ratio. Finally, this type of tube is robust and any thinner tube will be liable to damage and difficult to construct. The tubes were bent to the shapes shown in Fig. 3 so that the tip of the probe could be rotated concentrically about its axis of rotation (stem). This is important when aligning the probe tip with the flow direction to avoid displacing the tip away from the desired measuring point, because in a flow situation where wall shear stress changes appreciably over a small distance, the Preston tube tip displacement can give an error in the measured value of the wall shear stress. Preston tube No. 1 was used to measure the wall shear stress upstream and in the corner region. Preston tube No. 2 was used to measure wall shear stress downstream of the corner. Preston tube No. 3 was used to corroborate the results of Preston tubes No. 1 and No. 2. The probes were positioned with a traversing mechanism and a rotary device.

It should be mentioned here that all measurement points were taken on the right-hand side (looking downstream) of the geometric plane of symmetry (centerplane), i.e., positive y. Attempts were made to attain flow symmetry across the centerplane by placing two pitot-static probes, one on each side, at mirror image locations, and the blade alignment was adjusted to give equal pressure readings for both probes. However, absolute flow symmetry could not be achieved. Similar observations can also be made from the total pressure profiles of Barber [3], and McMahon et al. [26].
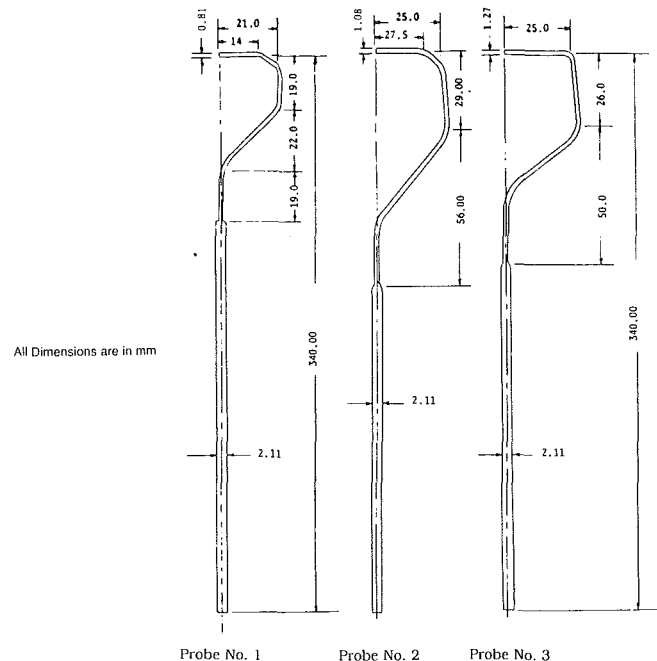
Results and Discussion

Flow Visualization. An overall photograph of the flow pattern on the flat plate surface is shown in Fig. 4. In this photograph, the dot traces are actually wall streaklines, or in other words, the curve composed of all fluid particles that have passed over the dye dot. The wall streamlines (limiting streamlines) and wall streaklines are identical for a steady flow. It was observed that the wind tunnel start-up did not measurably affect the steady-state flow visualization final pattern [24]. The resulting flow pattern on the flat plate surface shows a typical horseshoe vortex that forms ahead of the blade leading edge with a saddle point located at a distance of approximately 10 mm upstream of the blade leading edge. From this saddle point two separation streamlines originate and wrap around the blade, one on each side.

The perpendicular distance (distance in Y direction) between the separation streamline and the blade surface increases to a maximum of 13 mm at the location of maximum blade thickness, then starts decreasing to a minimum of 7 mm at the downstream axial location of 203 mm. These observations are identical to those observed by Hazarika et al. [8] on a similar test model. As the flow proceeds downstream, the perpendicular distance between the limiting separation streamline and the blade surface increases and is 12 mm at the location of the trailing edge. Proceeding downstream of the blade trailing edge, the distance between the limiting separation streamline and the centerplane continues to increase and reaches 40 mm at axial location of one chord length downstream of the blade trailing edge (see Figs. 4 and 5).

At the trailing edge location, two more limiting streamlines form, one on each side of the centerplane, which will be labeled as "wake limiting streamlines." A general flow diagram constructed from flow visualization is presented in Fig. 5. The wake limiting streamlines seem to diverge the separation limiting streamlines away from the centerplane. The curvature imposed upon the separation streamlines is at its largest at the trailing edge location and diminishes as the flow proceeds downstream. The displacement effect imposed by the blade wake limiting streamlines upon the oncoming upstream flow is caused by the induced pressure gradients in the downstream vicinity of the trailing edge (see Fig. 8). This effect diminishes as the flow proceeds farther downstream of the blade trailing
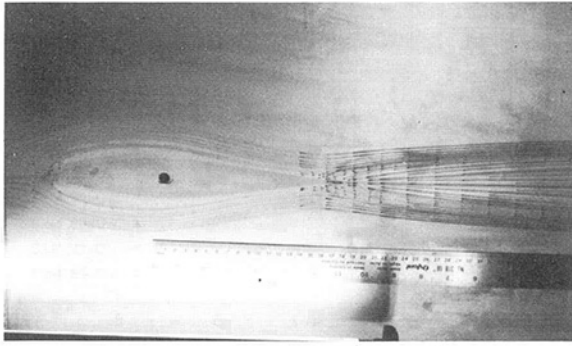
Fig. 4 Photograph of the surface streamlines on the plate surface (blade removed)
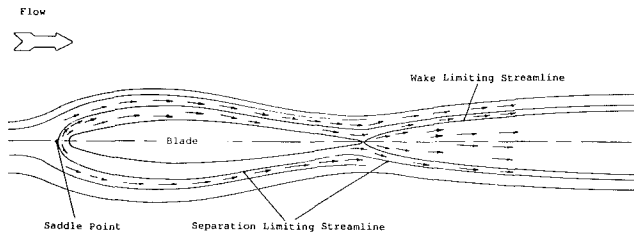
Fig. 5 Flow diagram of the surface streamlines obtained from surface flow visualization

Fig. 6 Surface static pressure distribution upstream of the blade leading edge [15]

Fig. 7 Surface static pressure distribution in the blade endwall corner region [15]

edge and the limiting separation streamlines become essentially parallel to the centerplane. The divergence of the streamlines can be attributed to the downwash contribution of the horseshoe vortex in this region. Surface oil film flow visualization results gave a continuous pattern of these streaks.

The video tape recorded, while performing the surface oil film flow visualization, showed that there were two regions in which the oil film was swept away first. In other words, these are two regions where the flat plate surface beneath the oil film has been revealed earlier than the rest of the surface. The first region, in the endwall corner region, covers the area that extends from $x/D = 2$ to $x/D = 6$ and between the blade surface and the limiting separation streamline. The second region is the area just downstream of the corner formed by the blade trailing edge and the flat plate surface and bounded by the wake limiting streamlines. The appearance of the first region can be explained in conjunction with the results of the local wall shear stress in the corner region. The high magnitude of wall shear stress in this region sweeps the oil film downstream with greater shearing action than the other regions (see Fig. 11(a)). In the second region, i.e., downstream of the trailing edge, the wall shear stress levels are of low magnitude (see Fig. 12). The appearance of the surface in this case (i.e., in the second region) can be attributed to the induced pressure gradients in this region (see Fig. 8), which displace the oncoming upstream oil film away from this region and prevent it from being covered again.

Surface Static Pressure. The static pressure coefficient is defined as

$$C_p = (p - p_{ref})/0.5 \, \rho \, U_\infty^2$$

where p = local surface static pressure; p_{ref} = reference static pressure (taken as atmospheric pressure); $0.5 \, \rho \, U_\infty^2$ = free-stream dynamic pressure measured at one chord upstream of the blade leading edge.

Surface static pressure variation upstream of the blade leading edge is shown in Fig. 6. In the upstream region of the blade leading edge, surface static pressure decreases in the Y direction. The rate of decrease is maximum at axial Station #4
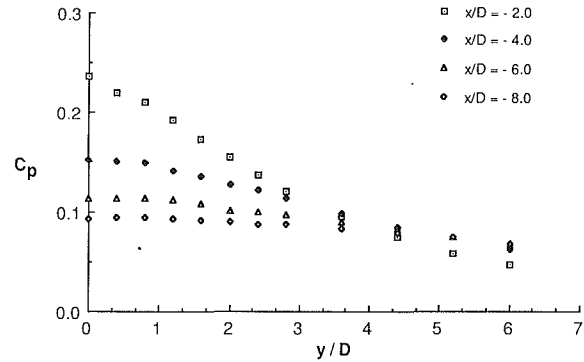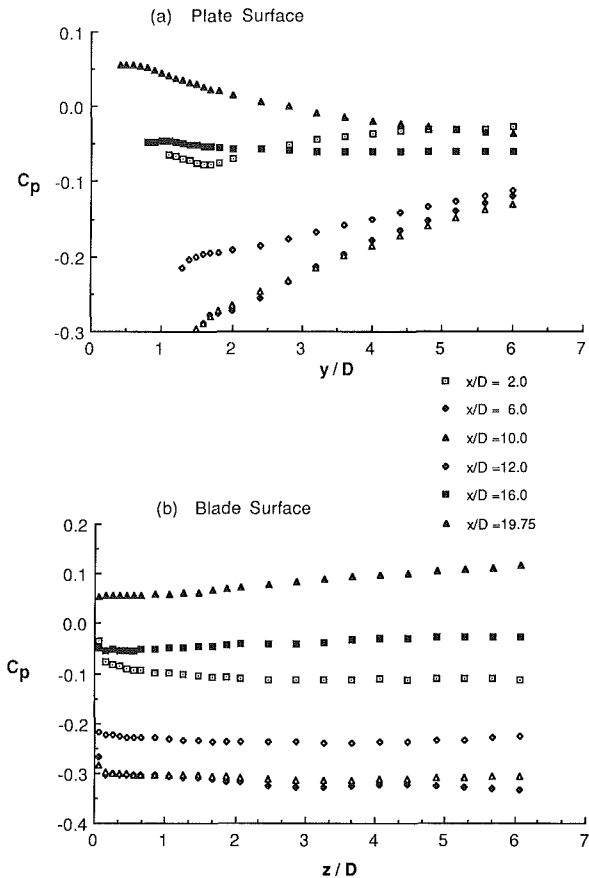
$(x/D = -2)$, in the vicinity of the blade leading edge. At a distance of $y/D \approx 6$, the value of C_p approaches approximately (within 2 percent of free-stream dynamic head) its value far upstream, at $x/D = -20$, of the blade leading edge.

In the corner region, the variation of C_p on the flat plate surface is shown in Fig. 7(a). At each axial station up to $x/D = 12$, except at $x/D = 2$, static pressure decreases as the cornerline (defined as the line of intersection of two surfaces forming the corner region) is approached, in comparison to static pressure far away from the cornerline. This observed variation occurs because the streamlines are more curved near the cornerline as compared to those far away from the blade surface. However, at $x/D = 2$, the value of C_p increases by a small amount in the close vicinity of the cornerline. The trend in C_p variation reverses downstream of $x/D = 12$. Also, the rate at which surface static pressure decreases, at any axial

Fig. 8 Surface static pressure distribution downstream of the blade trailing edge

Fig. 9 Comparison of wall shear stress values measured by the three sizes of Preston probe

station (except at $x/D = 16$ and $x/D = 19.75$), as the cornerline is approached, is larger upstream compared to that downstream of the maximum blade thickness location. In the streamwise direction, along the corner, the static pressure first decreases up to $x/D = 10$ and, thereafter, it increases as the flow approaches near the blade trailing edge. This trend can be mainly attributed to the presence of streamwise curvature. The flow is expected to accelerate in the axial direction from the blade leading edge up to its maximum thickness point ($x/D = 8$) and then decelerate as the blade trailing edge is approached.

On the blade surface, static pressure variation at different axial stations is relatively smaller in comparison to that on the flat plate surface (Fig. 7(b)). At each axial station, except at $x/D = 16$ and $x/D = 19.75$, the static pressure increases as the cornerline is approached as compared to its value far away from the cornerline. However, at two axial stations, i.e., at $x/D = 16$ and $x/D = 19.75$, the surface static pressure decreases as the cornerline is approached. In general, at any axial station, the observed increase or decrease in C_p value is within 5 percent of the free-stream dynamic head. In the streamwise direction C_p variation is as expected on the blade surface. At a given axial station on the wing surface of a simplified wing-body junction Shabaka [18] also reported very little variation in surface static pressure. Sepri [11] measured surface static pressure on the blade in a junction flow and found very small variation in Z direction at different axial stations. Therefore, the present study supports the findings of earlier investigators [11, 18].

Surface static pressure distribution on the flat plate for all axial stations downstream of the trailing edge ($x/D = 20$ to $x/D = 40$) is shown in Fig. 8. Surface static pressure is maximum at the corner region formed by the trailing edge and the flat plate, as a result of the stagnation point there. It decreases in both the downstream (X) and the transverse (Y) directions away from the trailing edge. The rate of decrease in C_p is high at axial stations in the vicinity of the trailing edge and it is reduced downstream. Flat plate surface static pressure distribution downstream of the blade is similar to the static pressure distribution of the isolated airfoil wake reported by Munukutla [27]. The presence of maximum surface static pressure, at the trailing edge corner formed by two flat plates with aligned leading edges, has also been reported by Nakayama and Rahai [28]. It is consistent with the endwall corner region flow data of Hazarika et al. [8], on the same test model, at axial stations in the upstream vicinity of the trailing edge. This region of induced pressure gradient exists downstream of the blade trailing edge up to $x/D \approx 28$ (i.e., Station #16).
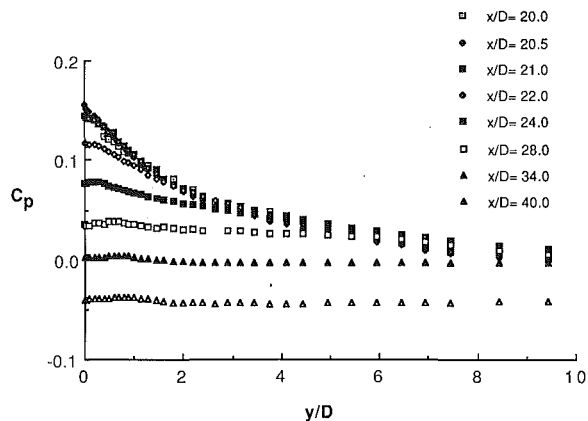
Wall Shear Stress. Local wall shear stress distribution, measured by the three sizes of Preston tube, at two axial sta-

tions, namely, Station #14 and Station #16 ($x/D = 22$ and $x/D = 28$) is shown in Fig. 9. Values of the local wall shear stress for the three sizes of Preston tubes compared well and were within an error of less than 5 percent. It is clear that Patel's calibration equations adequately account (within the experimental error) for the tube size.
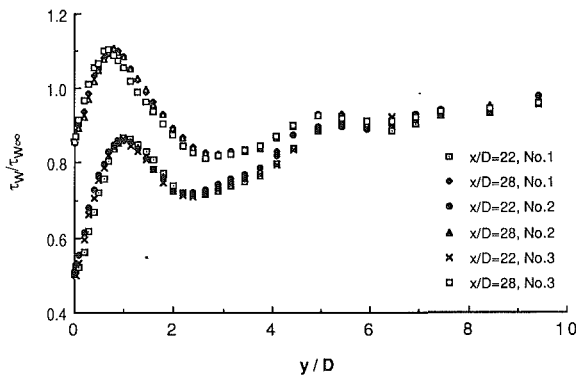
The nondimensional wall shear stress (normalized by the far upstream value of the wall shear stress at $x/D = -20$ and $y/D = 0$) upstream of the blade leading edge at four axial stations is shown in Fig. 10. This presentation of the local wall shear stress instead of the usual skin friction coefficient is selected because the local free-stream velocity varies at different axial locations. Moreover, in the corner region it is difficult to define the local free-stream velocity because of the interacting nature of shear layers. The local wall shear stress at $x/D = -20$ and $y/D = 0$ is approximately (within 3 percent) equal to the two-dimensional value at the same axial location. In Fig. 10 the distance y is normalized by the blade leading edge diameter because in the upstream region the flow is expected to be influenced more by the size and shape of the blade leading edge than the blade chord. It is clearly observed that the wall shear stress decreases as the blade leading edge is approached. The maximum decrease (≈ 40 percent) in the wall shear stress occurs near the stagnation streamline where the adverse pressure gradient is also maximum. The wall shear stress values are found to reach the two-dimensional value within a distance of $\approx 6D$ in the Y direction at different axial stations.

Wall shear stress variation on the flat plate surface, in the corner region, is shown in Fig. 11(a). At different axial stations up to $x/D = 12$, the shear stress increases as the cornerline is approached and very close to the cornerline it decreases. However, at Stations #9 and #10 ($x/D = 16$ and $x/D = 19.75$) the wall shear stress value first decreases then increases as the cornerline is approached. In the close vicinity of the cornerline, wall shear stress again decreases. It is quite evident that the maximum value of the wall shear stress and its location from the cornerline change at different axial stations (see Fig. 11(a)). The maximum value of $\tau_w/\tau_{w\infty}$ occurs at $x/D = 6$ and it is almost 2.4 times the far upstream value of the wall shear stress.

On the blade surface (Fig. 11(b)), at a given axial station, the local wall shear stress increases under the horseshoe vortex core and achieves a maximum value in the corner region and then is alleviated at far distances and reaches an asymptotic value (the wall shear stress value at $z/D \approx 6$). Also at axial stations, downstream of the maximum blade thickness location, the asymptotic values of the wall shear stress are lower than its upstream values. The maximum value of the wall shear stress and its location from the cornerline changes. However, the trend in variation of the location of maximum value at various axial stations is different in comparison to that observed on the flat plate surface in the corner region. It can be noted that at Stations #9 and #10 ($x/D = 16$ and
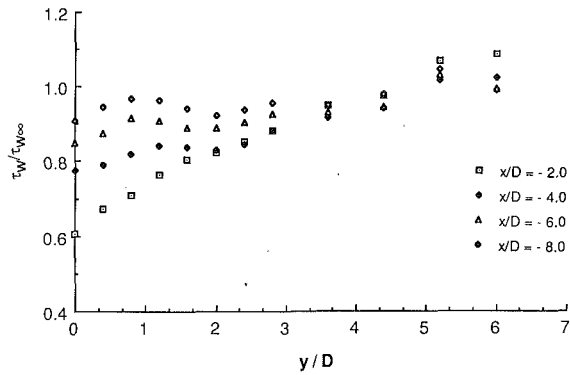
Fig. 10 Wall shear stress variation upstream of the blade leading edge [15]
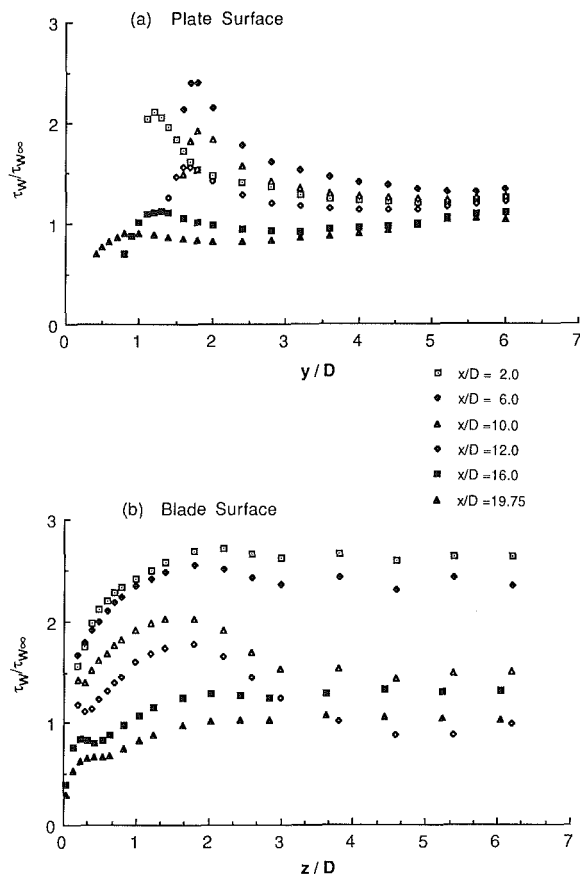
Fig. 11 Wall shear stress variation in the blade endwall corner [15]

Fig. 12 Wall shear stress variation downstream of the blade trailing edge

x/D = 19.75), Fig. 11(b), there is a relatively small increase (if any) in the values of wall shear stress as the cornerline is approached. This indicates the presence of vortical flow closer to the blade and can be due to the corner vortex suggested by Hazarika et al. [8].

In the corner region, at different axial stations, the maximum values of the wall shear stress are consistently higher on the blade surface compared to that on the flat plate surface of the test model (Fig. 11). This is caused by the thinner boundary layer on the blade surface, resulting in higher velocity gradients, compared to that on the flat plate at the same axial location. Asymptotic values (the wall shear stress value at $y/D \approx 6$) of the wall shear stress on the flat plate surface in the corner region are higher by approximately 25 percent than the far upstream value. However, on the blade surface preceding the maximum thickness of the blade, asymptotic values

are still high but are lower than the values upstream of the blade maximum thickness. This is caused by the presence of blade curvature. The flow is expected to accelerate up to the location of maximum thickness, giving rise to higher velocity gradients. In the region downstream of the blade maximum thickness, the flow is expected to decelerate, resulting in lower velocity gradients. On the flat plate surface the location of the maximum value of the wall shear stress moves from 4 mm near the blade leading edge location to 11 mm at the last station (x/D = 19.75). However, on the blade surface the location of the maximum value of wall shear stress first moves closer to the cornerline and then moves away from it to a distance of $\approx$ 45 mm at the last axial station (x/D = 19.75).

From the aforementioned observations, it can be summarized that streamwise curvature thus introduced will give rise to stretching or compressing of the horseshoe vortex, depending on the type of curvature, resulting in intensification or attenuation of vorticity. On the flat plate surface of the test model, the maximum value of wall shear stress at different axial stations first increased up to the maximum blade thickness location (see Fig. 11). This increase can possibly be associated with the horseshoe vortex stretching because of the presence of acceleration in the flow. However, downstream of the blade maximum thickness location the flow decelerates, and the horseshoe vortex gets attenuated, and as a result maximum value of the wall shear stress is observed to decrease. The variation in the location of the maximum value of the wall shear stress on both surfaces in the corner region suggests that the horseshoe vortex gets distorted in the downstream direction as it moves along the corner.

The variation of the normalized local wall shear stress on the flat plate surface downstream of the corner region is shown in Fig. 12. A common trend is obvious at all stations: Departing the centerplane (y/D = 0), with local minimum wall shear stress (labeled τ_{wmin1}), the wall shear stress rises sharply from τ_{wmin1} to a local maximum value of τ_{wmax1}. This is a region of downwashed wake. This rise is then followed by a sharp fall to another local minimum value of τ_{wmin2} (flow upwash) and finally, it rises to its local asymptotic value (wall shear stress far from the centerplane; i.e., two-dimensional value). It is

clear from these trends that three dimensionality in the flow will persist far downstream of the blade trailing edge ($>x/D$ = 40 or one chord length). The value of wall shear stress at the centerplane ($\tau_{w\min1}$) increases from a very small value of 0.14 $\tau_{w\infty}$ at Station #12 (x/D = 20.5) to the local asymptotic value at Station #18 (x/D = 40). This is an indication of the wake recovery (wake deficit is reduced). Proceeding downstream of the blade trailing edge, the rate of rise from $\tau_{w\min1}$ to $\tau_{w\max1}$ decreases while the rate of decrease from $\tau_{w\max1}$ to $\tau_{w\min2}$ essentially remains the same. The rate of increase from $\tau_{w\min2}$ to $\tau_{w\infty}$ decreases, as the flow proceeds downstream, and the increase ceases at an axial location of approximately 1.5 c (x/D = 30). The monotonic increase in the values of $\tau_{w\min1}$ and $\tau_{w\max1}$ in the downstream direction is an indication of a recovery in the flow.

Conclusions

The measurements of surface static pressure, local wall shear stress, and flow visualizations were made to cover regions from 0.4 chord length upstream of the blade leading edge to one chord length downstream of the blade trailing edge. The following conclusions can be drawn from the results of these measurements:

1 Flow visualization on the flat plate surface (endwall), in the blade endwall corner region, confirmed the presence of a single horseshoe vortex. It also confirmed the presence of high magnitude of wall shear stress on the flat plate between the blade leading edge and the point of maximum thickness.

2 Surface static pressure varies significantly on the flat plate surface of the test model. However, on the blade surface, at any axial station, static pressure variation in the transverse (Z) direction is marginal. Downstream of the corner region surface static pressure is maximum at the blade trailing edge location and it decreases in both the downstream and transverse directions.

3 On the flat plate surface, in the corner region, the local wall shear stress increases significantly in the region very close to the blade surface as compared to the far upstream value except at two axial stations (x/D = 16 and x/D = 19.75). The trend in distribution of the wall shear stress on the blade surface is not similar to that on the flat plate surface. Downstream of the blade trailing edge, local wall shear stress increased to values exceeding the values found in the undisturbed boundary layer at that axial location.

4 Results obtained from wall shear stress measurements indicated that three dimensionality in the flow exists far downstream of the trailing edge of the blade and extends more than one chord length. Also, in the region upstream of the blade leading edge and in the corner region the endwall effects dominated up to 8D and 6D, respectively.

5 Values of the local wall shear stress, measured by the three sizes of Preston tubes, compared well and were within the experimental error ($<$ 5 percent). This indicates that Patel's calibration equations adequately accounted for the tube size.

References

1 Mehta, R. D., "Effect of Wing Nose Shape on the Flow in a Wing/Body Junction," *Aeronautical Journal*, Dec. 1984, pp. 456–460.

2 Kubendran, L. R., McMahon, H. M., and Hubbart, J. E., "Turbulent Flow Around a Wing/Fuselage-Type Juncture," *AIAA Journal*, Vol. 24, No. 9, Sept. 1986, pp. 1447–1452.

3 Barber, T. J., "An Investigation of Strut-Wall Intersection Losses," *Journal of Aircraft*, Vol. 15, No. 10, Oct. 1978, pp. 676–681.

4 Sonoda, T., "Experimental Investigation on Spatial Development of Streamwise Vortices in a Turbine Inlet Guide Vane Cascade," ASME Paper No. 85-GT-20, 1985.

5 Sieverding, C. H., "Recent Progress in the Understanding of Basic Aspects of Secondary Flows in Turbine Blade Passages," ASME *Journal of Engineering for Gas Turbines and Power*, Vol. 107, Apr. 1985, pp. 248–257.

6 Langston, L. S., "Crossflows in a Turbine Cascade Passage," ASME *Journal of Engineering for Power*, Vol. 102, Oct. 1980, pp. 866–874.

7 Langston, L. S., Nice, M. L., and Hooper, R. M., "Three-Dimensional Flow Within a Turbine Cascade Passage," ASME *Journal of Engineering for Power*, Vol. 99, Jan. 1977, pp. 21–28.

8 Hazarika, B. K., Raj, R., and Boldman, D. R., "The Three-Dimensional Fluid Flow Phenomena in the Blade End-Wall Corner Region," ASME Paper No. 86-GT-179, 1986.

9 Dickinson, S. C., "Flow Visualization and Velocity Measurements in the Separated Region of an Appendage/Flat-Plate Junction," presented at Ninth Biennial Symposium on Turbulence, University of Missouri—Rolla, Oct. 1984.

10 Gorski, J. J., Govindan, T. R., and Lakshminarayana, B., "Computation of Three-Dimensional Turbulent Shear Flows in Corners," *AIAA Journal*, Vol. 23, No. 5, May 1985, pp. 685–692.

11 Sepri, P., "An Investigation of the Flow in the Region of the Junction of a Wing and a Flat Surface Normal to the Wing Span," Queen Mary College, Dept. Report, QMC ER-1002, 1973.

12 Chu, J. K., and Young, A. D., "A Further Investigation of Viscous Effects in a Wing Plate Junction," Queen Mary College Department Report, QMC ER-1003, 1975.

13 Binder, A., and Romey, R., "Secondary Flow Effects and Mixing of the Wake Behind a Turbine Stator," ASME *Journal of Engineering for Power*, Vol. 105, 1983, pp. 33–39.

14 Naranjit, S., "An Investigation of the Flow Over a Wing-Body Combination," Ph.D. Thesis, University of London, United Kingdom, 1976.

15 Bhargava, R., Raj, R., and Boldman, D. R., "Wall Shear Stress Measurement in Blade End-Wall Corner Region," ASME Paper No. 87-GT-181, 1987.

16 Bragg, G. M., "The Turbulent Boundary Layer in a Corner," *Journal of Fluid Mechanics*, Vol. 36, 1969, pp. 485–503.

17 Mojola, O. O., and Young, A. D., "An Experimental Investigation of the Turbulent Boundary Layer along a Streamwise Corner," AGARD Conference Proceeding No. 93, London, 1971, p. 12-1.

18 Shabaka, I. M. M. A., "Turbulent Flow in an Idealized Wing-Body Junction," Ph.D. Thesis, University of London, United Kingdom, 1979.

19 Scheiman, J., and Kubendran, L. R., "Juncture Flow Measurements Using Laser Velocimetry," Paper No. AIAA-85-1612.

20 Prahlad, T. S., "Wall Similarity in Three-Dimensional Turbulent Boundary Layers," *AIAA Journal*, Vol. 6, No. 9, Sept. 1968, pp. 1772–1774.

21 Bhargava, R. K., "An Experimental Study of Near Wall Flow Parameters in the Blade End-Wall Corner Region," Ph.D. Dissertation, The City University of New York, New York, 1989.

22 Sproston, J. L., and Goksel, O. T., "The Calibration of a Surface Static Tube," *Aero. Journal, Technical Notes*, Feb. 1972, pp. 101–103.

23 Bhargava, R. K., and Raj, R., "Surface Static Tube Accuracy in Three-Dimensional Turbulent Flows," *Proceeding, 31st Heat Transfer and Fluid Mechanics Institute*, June 1989, pp. 231–240.

24 Langston, L. S., and Boyle, M. T., "A New Surface-Streamline Flow Visualization Technique," *Journal of Fluid Mechanics*, Vol. 125, 1982, pp. 53–57.

25 Patel, V. C., "Calibration of the Preston Tube and Limitations on Its Use in Pressure Gradients," *Journal of Fluid Mechanics*, Vol. 23, Part 1, 1965, pp. 185–208.

26 McMahon, H. M., Metari, P., and Yoo, K. M., "Mean Velocities and Reynolds Stresses in the Juncture Flow and in the Shear Layer Downstream of an Appendage," GITAER Report, 1987, Georgia Institute of Technology, Atlanta, GA.

27 Munukutla, S. S., "Turbulent Wake Development Behind Streamlined Bodies," Ph.D. Thesis, University of Iowa, Ames, IA, 1981.

28 Nakayama, A., and Rahai, H. R., "Measurements of Turbulent Flow Behind a Flat Plate Mounted Normal to the Wall," *AIAA Journal*, Vol. 22, No. 12, Nov. 1984, pp. 1817–1819.

Advances in the Numerical Analysis of Linearized Unsteady Cascade Flows

W. J. Usab, Jr.[1]

J. M. Verdon

Theoretical and Computational
Fluid Dynamics,
United Technologies Research Center,
East Hartford, CT 06108

This paper describes two new developments in the numerical analysis of linearized unsteady cascade flows, which have been motivated by the need for an accurate analytical procedure for predicting the onset of flutter in highly loaded compressors. In previous work, results were determined using a two-step or single-pass procedure in which a solution was first determined on a rectilinear-type cascade mesh to determine the unsteady flow over an extended blade-passage solution domain and then on a polar-type local mesh to resolve the unsteady flow in high-gradient regions. In the present effort a composite procedure has been developed in which the cascade- and local-mesh equations are solved simultaneously. This allows the detailed features of the flow within the local mesh region to impact the unsteady solution over the entire domain. In addition, a new transfinite local mesh has been introduced to permit a more accurate modeling of unsteady shock phenomena. Numerical results are presented for a two dimensional compressor-type cascade operating at high subsonic inlet Mach number and high mean incidence to demonstrate the impact of the new composite- and local-mesh analyses on unsteady flow predictions.

Introduction

The development of theoretical analyses to predict unsteady flows in axial-flow turbomachines has been motivated primarily by the need to predict the aeroelastic behavior of the blading, e.g., the onset of blade flutter and the amplitudes of aerodynamically forced blade vibrations. For such purposes aerodynamic analyses must be capable of predicting the unsteady loads that act on the blades and arise from various sources of unsteady excitation, i.e., prescribed structural (blade) motions and external aerodynamic excitations. For flutter applications it is only necessary to predict the unsteady loads arising from prescribed blade motions, while for forced response applications the unsteady loads due to incident entropic, vortical, and acoustic disturbances are also required.

For the most part, the unsteady aerodynamic analyses that have been developed for turbomachinery aeroelastic applications consider the blades of an isolated, usually two-dimensional, cascade. Viscous effects are neglected and the unsteady fluctuations are regarded as sufficiently small so that a linearized treatment of the unsteady flow is justified. Linearizations that include the effects of realistic design features, such as blade geometry, mean blade loading, and operation at transonic Mach numbers, have been actively developed over the past decade (for reviews see Verdon, 1987 and Acton and Newton, 1987). Here, the unsteady flow is regarded as a small-

amplitude harmonic (in time) fluctuation about a fully nonuniform mean or steady flow. The steady flow is determined as a solution of nonlinear inviscid equations, while the unsteady flow is governed by linear equations with variable coefficients that depend on the underlying steady flow. Although analyses based on this type of linearization (see Atassi and Akai, 1980; Whitehead, 1982; Verdon and Caspar, 1984; and Hall and Crawley, 1989) have received considerable attention in recent years, significant advances in the associated numerical solution procedures are still required.

This paper described contributions to the numerical analysis of linearized unsteady flows around the vibrating blades of compressor-type cascades operating at high subsonic inlet Mach number and at high mean incidence. It builds upon the LIN-FLO (Linearized INviscid FLOw) analysis developed by Verdon and Caspar (1982, 1984) and is motivated by the need to provide an unsteady aerodynamic analysis for the prediction of subsonic/transonic positive incidence flutter in compressor blade rows. Subsonic/transonic positive incidence flutter is the most common type of flutter encountered in the fan and compressor stages of axial-flow turbomachines. It usually occurs in blading that is highly loaded and operating at high subsonic inlet Mach number. Flutter in bending, torsion, and coupled (bending-torsion) blade vibration modes have been observed over a reduced frequency (based on relative inlet flow speed and blade chord) range extending from 0.4 to 1.6 (see Fleeter, 1979).

The linearized unsteady aerodynamic analysis, LINFLO, accounts for the important effects of blade geometry, mean pressure rise (or fall) across a blade row, and shocks and their
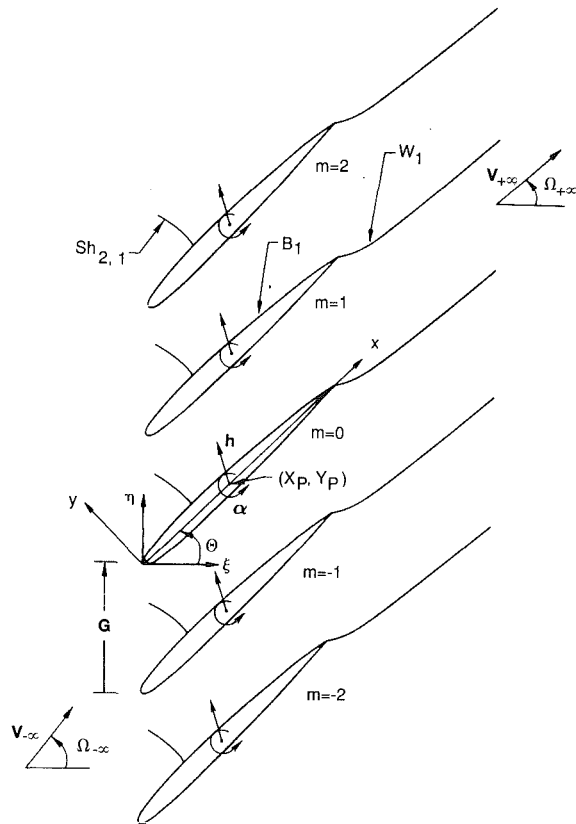
Fig. 1 Two-dimensional vibrating transonic compressor cascade;
$M_{+\infty} < M_{-\infty} < 1$

Fig. 2 Steady-state, ————, and instantaneous, ----, blade, wake, and shock positions

motions. The unsteady equations are solved numerically using an implicit least-squares finite-difference approximation that is applicable on arbitrary grids. Because of the stringent and often conflicting requirements placed on the construction of a computational mesh for cascade flows, a two-step solution procedure was adopted in previous work. The basic approach was first to capture large-scale unsteady phenomena on an H-type cascade mesh of moderate density and then to determine detailed phenomena on a polar-type local grid of high density. The cascade mesh covers an extended blade-passage solution domain; the local mesh covers and extends well beyond a region of high velocity gradient, e.g., a region surrounding a rounded blade of leading edge (Verdon and Caspar, 1982) or a region containing a shock (Verdon and Caspar, 1984). The mean shock locus was approximated as being normal to the airfoil surface in the local unsteady calculation. Information determined by the cascade-mesh solution provided the outer boundary-condition information for the local calculation, but there was no other communication between the two calculations. Thus, the local solution was essentially a correction to the cascade solution over the local-mesh region.

In the present effort improvements have been made to these numerical solution methods so that flows around realistic compressor blades operating at high subsonic inlet Mach number and high mean incidence can be considered. For such applications the local solution must provide an accurate description of the flow both in the vicinity of a rounded blade leading edge as well as in the vicinity of a shock. In addition, the global and local solutions should be coupled so that local unsteady information is allowed to impact the flow over an entire blade-passage solution domain. Finally, a local-mesh topology in which mesh lines conform closely to the true mean shock locus should be employed. These considerations are addressed in the present paper and demonstrated through several example calculations.
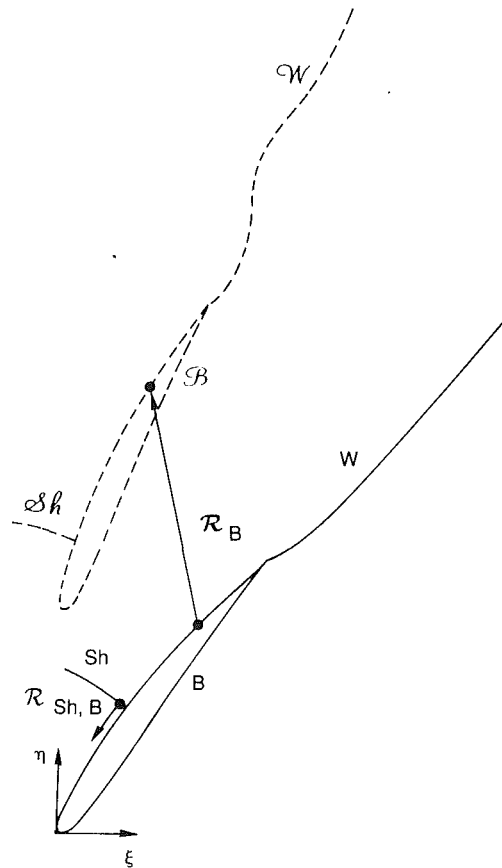
Problem Description

We consider time-dependent adiabatic flow, with negligible body forces, of an inviscid non-heat-conducting perfect gas through a two-dimensional vibrating cascade (see Fig. 1). In the following discussion all physical quantities are dimensionless. Lengths have been scaled with respect to blade chord, time with respect to the ratio of blade chord to the upstream free-stream speed, density and velocity with respect to the upstream free-stream speed, density and velocity, respectively, and pressure with respect to the product of the upstream free-stream density and the square of the upstream free-stream speed. The mean of steady-state positions of the blade chord lines coincide with the line segments $\eta = \xi \tan \Theta + mG$, $0 \le \xi \le \cos \Theta$, $m = 0, 1, 2, \ldots$, where ξ and η are Cartesian coordinates attached to the blade row and pointing in the cascade axial and "circumferential" directions, respectively, m is a blade number index, Θ is the cascade stagger angle, and G is the cascade gap vector, which is directed along the η axis with magnitude equal to the blade spacing.

We consider the special case in which prescribed blade motions are the only source of unsteady excitation. These motions are of small amplitude, periodic in time and in the η direction, i.e.,

$$\mathfrak{R}_B(\mathbf{x} + m\mathbf{G}, t) = Re\{\mathbf{r}_B(\mathbf{x})\exp[i(\omega t + m\sigma)]\}, \ \mathbf{x}\epsilon B \qquad (1)$$

The relative displacement vector, $\mathfrak{R}$, measures the displacement of a point on a moving surface (blade, wake, or shock) relative to its mean position (see Fig. 2). In equation (1) $\mathbf{x}$ is a position vector, t is time, $Re\{\ \}$ denotes the real part of $\{\ \}$, $\mathbf{r}$ is a complex displacement-amplitude vector with $|\mathbf{r}_B| \sim \mathcal{O}(\epsilon)$, ω is the frequency of the blade motion, σ is the phase angle between the motions of adjacent blades, and B refers to the mean position of the reference ($m = 0$) blade surface.

The flows far upstream ($\xi < \xi_-$) and far downstream ($\xi > \xi_+$) from the blade row are assumed to be at most small irrotational steady perturbations of a uniform free stream. In addition, blade shape and orientation relative to the inlet free-stream direction, the inlet-to-exit mean static pressure ratio, and the amplitude, frequency, and mode of the blade motion are assumed to be such that the flow remains attached to the blade surfaces. Thus thin vortex sheets or unsteady wakes emanate from the blade trailing edges and extend downstream. Finally, any shocks that might occur are assumed to be of weak to moderate strength, have small curvature, and terminate in a continuous region of the flow, i.e., at a sonic point.

As a consequence of our assumptions regarding shocks, the flow far upstream of the blade row, and the type of unsteady excitation, the time-dependent flow through the cascade can be regarded as isentropic and irrotational. In this case, the field equations that govern the flow reduce to

$$\frac{\partial \tilde{\rho}}{\partial t} + \nabla \cdot (\tilde{\rho} \nabla \tilde{\Phi}) = 0 \tag{2}$$

and

$$\tilde{\rho}^{(\gamma - 1)} = (\gamma M_{-\infty}^2 \tilde{P})^{(\gamma - 1)/\gamma} = (M_{-\infty} \tilde{A})^2$$
$$= 1 - (\gamma - 1)M_{-\infty}^2 \{ \partial \tilde{\Phi}/\partial t + [(\nabla \tilde{\Phi})^2 - 1/2] \} \tag{3}$$

where $\tilde{\Phi}$, $\tilde{\rho}$, $\tilde{P}$, and $\tilde{A}$ are the time-dependent velocity potential, density, pressure, and speed of sound propagation, respectively, M is the Mach number of the undisturbed or steady flow, γ is the specific heat ratio of the fluid, and the subscript $-\infty$ refers to the upstream free-stream condition. The admissible solutions to equations (2) and (3), for the present application, are those in which acoustic disturbances in the far field ($\xi \lesssim \xi_\mp$) either attenuate with increasing axial distance from the blade row or propagate and carry energy away from or parallel to the blade row.

The foregoing equations must be supplemented by boundary conditions at moving blade surfaces, $\mathcal{B}_m$, and jump conditions at moving wakes, $\mathcal{W}_m$, and shocks, $S\hbar_{m,n}$. Here, the subscript n refers to the nth shock associated with the mth blade. In particular, the flow must be tangential to the moving blade surfaces, the fluid pressure and normal velocity component must be continuous across blade wakes, and mass and tangential momentum must be conserved across shocks. In addition to the field equations and surface conditions, information on the uniform inlet and exit flow conditions must be specified. Both steady and unsteady departures from these uniform conditions are determined as part of the time-dependent solution.

For aeroelastic design applications the traditional approach is to examine limiting forms of the foregoing time-dependent nonlinear equations with the intention of providing unsteady aerodynamic response information efficiently and economically. One such approach, in which the unsteady flow is regarded as a small perturbation of a fully nonuniform mean flow, is described below.

Linearized Unsteady Aerodynamic Formulation

The equations governing small-amplitude time-dependent departures from a nonuniform mean flow are determined by first expanding the unsteady flow variables into asymptotic series in ϵ, where $|\mathcal{R}| \sim \mathcal{O}(\epsilon) \ll 1$. In addition, Taylor series expansions for the flow variables and relations between the unit tangent, τ, and normal $\mathbf{n}$, vectors at a point on a moving surface, S, and the corresponding vectors at the location of this point on the mean surface, S, are applied to refer information at a moving blade, wake, or shock surface to the mean position of this surface. The equations for the steady and first order unsteady flows are then obtained by substituting the foregoing expansions into the full time-dependent governing equations, equating terms of like power in ϵ and neglecting terms of higher than first-order in ϵ.

The equations that govern the steady background flow, which is assumed to be known in the present study, follow after replacing the time-dependent flow properties, $\tilde{\Phi}$, $\tilde{P}$, $\tilde{\rho}$, $\tilde{A}$, and $\tilde{\mathbf{V}}$ by their zeroth-order or steady counterparts, Φ, P, $\bar{\rho}$, A, and $\mathbf{V}$, respectively, in the nonlinear governing equations and setting temporal derivatives equal to zero. Numerical procedures for determining two-dimensional steady potential flows through cascades have been developed extensively, particularly for flows with subsonic inlet and exit Mach numbers. The usual practice is to solve the conservative form of the mass-balance equation throughout the entire fluid domain. Thus, shock-jump conditions are usually not imposed directly. Instead, shock phenomena are captured through the use of special differencing techniques.

The Linearized Unsteady Problem. It follows from the differential form of the mass conservation law, equation (2), the Bernoulli relations, equation (3), the corresponding steady equations, and the asymptotic expansions for the flow variables that the linearized unsteady flow is governed by the field equations

$$i\omega\rho + \nabla \cdot (\bar{\rho} \nabla \phi + \rho \nabla \Phi) = 0 \tag{4}$$

and

$$\rho/\bar{\rho} = \gamma^{-1} p/P = \frac{2}{\gamma - 1}(a/A) = -A^{-2}\frac{\overline{D}\phi}{Dt} \tag{5}$$

where ϕ, ρ, p, and a are the complex amplitudes of the first harmonic unsteady velocity potential, density, pressure, and speed of sound propagation, respectively, and $\overline{D}/Dt = i\omega + \mathbf{V} \cdot \nabla$ is a mean flow convective derivative operator. Equations (4) and (5) can be combined to yield a single equation for the first-order velocity potential, i.e.,

$$A^2 \nabla^2 \phi = \frac{\overline{D}^2 \phi}{Dt^2} + (\gamma - 1)\nabla^2 \Phi \frac{\overline{D}\phi}{Dt} + \nabla(\nabla \Phi)^2 \cdot \nabla \phi/2 \tag{6}$$

The following conditions on the linearized unsteady perturbation apply at blade, B_m, wake, W_m, and shock, $Sh_{m,n}$, mean positions (Verdon, 1987). Note that the unit vectors $\mathbf{n}$ and τ are directed such that $\mathbf{n} \times \tau = \mathbf{e}_z$ points out from the page. The first-order flow tangency condition applies at mean blade surfaces ($\mathbf{x} \in B_m$) and has the form

$$\nabla \phi \cdot \mathbf{n} = [i\omega \mathbf{r}_{B_m} + (\nabla \Phi \cdot \tau)(\tau \cdot \nabla)\mathbf{r}_{B_m} - (\mathbf{r}_{B_m} \cdot \nabla)\nabla \Phi] \cdot \mathbf{n} \tag{7}$$

In addition, since the steady velocity and pressure are continuous and have continuous derivatives across blade wakes, i.e., the downstream mean-flow stagnation streamlines ($\mathbf{x} \in W_m$), the first-order wake jump conditions reduce simply to

$$[\![\nabla \phi]\!] \cdot \mathbf{n} = 0 \text{ and } \left[\!\!\left[\frac{\overline{D}\phi}{Dt} \right]\!\!\right] = 0 \tag{8}$$

Finally, the conservation laws for mass and tangential momentum at shocks ($\mathbf{x} \in Sh_{m,n}$) yield the conditions

$$[\![\bar{\rho} \nabla \phi + \rho \nabla \Phi]\!] \cdot \mathbf{n} = [\![\bar{\rho}]\!](i\omega + (\nabla \Phi \cdot \tau)\tau \cdot \nabla)(\mathbf{r}_{Sh_{m,n}} \cdot \mathbf{n})$$
$$+ (\mathbf{r}_{Sh_{m,n}} \cdot \mathbf{n})\tau \cdot \nabla([\![\bar{\rho}]\!] \nabla \Phi \cdot \tau) \tag{9}$$

and

$$[\![\phi]\!] = -\mathbf{r}_{Sh_{m,n}} \cdot \mathbf{n}[\![\nabla \Phi]\!] \cdot \mathbf{n} \tag{10}$$

where it has been assumed that shocks terminate in the fluid at sonic points.

Equations (9) and (10) provide two relations for determining the jump in the unsteady potential, $[\![\phi]\!]$, at the mean position of a shock and the relative shock displacement normal to the mean shock locus, $\mathbf{r}_{Sh_{m,n}} \cdot \mathbf{n}$. These equations can be combined to provide a single relation that governs the jump in the un-

steady potential across a shock, i.e.,

$$[[(i\omega E + F)\phi]] + [[G\phi_n]] + [[H\phi_\tau]] = 0 \qquad (11)$$

where the functions E, F, G, and H depend only on the mean flow variables. Recall that blade mean positions and unsteady motions are prescribed, but wake and shock mean positions and displacements must be determined as part of the steady and unsteady solutions, respectively. Wake motions, however, have no direct impact on the solution to the linearized unsteady problem nor, therefore, on the aerodynamic response at the blade surfaces.

We have assumed that the potential mean or steady flow is at most a small (i.e., of $\mathcal{O}(\epsilon)$) perturbation from a uniform stream both far upstream ($\xi < \xi_-$) and far downstream ($\xi > \xi_+$) from the blade row. Thus, in these regions and to within the first-order approximation considered here, the unsteady field equation and wake-jump conditions can be reduced to the constant coefficient equations of classical linearized theory for which analytical solutions can be determined (Verdon, 1989). These solutions describe the unsteady potential fluctuations in the far field that are produced by acoustic and wake vortical disturbances. They can be matched to a near-field numerical solution, and thereby serve to complete the specification of the linearized unsteady boundary-value problem.

Aerodynamic Response at a Moving Blade Surface. Numerical resolutions of the nonlinear steady and linearized unsteady problems are required to determine the aerodynamic response information needed for aeroelastic applications, i.e., the unsteady pressures and global unsteady airloads acting on the blades. Because of the cascade geometry and the assumed form of the blade motion (i.e., periodic in η), such resolutions are required only over a single extended blade-passage region. In addition, since analytic far-field solutions can be determined, the numerical solution domain can be further restricted to a single extended blade-passage region of finite extent.

The pressure acting at the instantaneous position of a point on the mth blade surface is

$$\tilde{P}_{\mathcal{B}_m}(\tau, t) = P_B(\tau) + Re\{p_\mathcal{B}(\tau)e^{i(\omega t + m\sigma)}\} +$$
$$\sum_n p_{Sh_{m,n}}(\tau, t) + \dots, \qquad (12)$$

where τ is a coordinate measuring distance in the counterclockwise (or τ) direction along a blade surface, and the subscripts B and $\mathcal{B}$ refer to the mean and instantaneous positions of the reference blade. The first two terms on the right-hand side of equation (12) are the steady and first-harmonic unsteady, i.e.,

$$p_\mathcal{B} = -\bar{\rho}D\phi/Dt + (\mathbf{r}_B \cdot \nabla)P, \quad \mathbf{x} \in B \qquad (13)$$

components of the fluid pressure acting at the mth moving blade surface, $\mathcal{B}_m$. The third term represents the anharmonic contribution to the unsteady surface pressure caused by the motions of shocks along the surface of the mth blade, and is determined by analytically continuing the solutions to the steady and the linearized unsteady boundary-value problems from the mean to the instantaneous shock locations (Williams, 1979). It should be noted that although the unsteady pressure disturbance is not everywhere harmonic, its regions of anharmonicity are small. Consequently, as demonstrated by Ehlers and Weatherill (1982), the first-order global coefficients are harmonic in time.

The conditions usually considered in turbomachinery aeroelastic applications are those in which each incremental two-dimensional blade section undergoes a rigid-body motion, i.e.,

$$\mathbf{r}_B(\mathbf{x}) = \mathbf{h} + \alpha \times \mathbf{R}_P \qquad (14)$$

For such conditions the unsteady force and moment are the only global response parameters needed to analyze the aeroelastic behavior of the blading. In equation (14) $\mathbf{h}$ defines the amplitude and direction of blade translations, $\alpha = \alpha \mathbf{e}_z$ defines the amplitude and direction of the blade rotations, and $\mathbf{R}_P$ is a position vector extending from the mean position of the reference blade axis of rotation (i.e., from the point X_P, Y_P) to points on the mean position of the reference blade surface. These rigid two-dimensional motions model bending and torsional vibrations of actual rotor blades.

The linearized unsteady force and moment acting on the reference ($m = 0$) blade are given by

$$\mathbf{f} = \alpha \times \mathbf{F} - \oint_B p_\mathcal{B} \mathbf{n} d\tau + \sum_n r_{Sh_n,B}([[P_B]]\mathbf{n}_B)_{Sh_n} \qquad (15)$$

and

$$m_\mathcal{P} = \oint_B p_\mathcal{B} \mathbf{R}_P \cdot d\tau - \sum_n r_{Sh_n,B}([[P_B]]\mathbf{R}_P \cdot \tau_B)_{Sh_n} \qquad (16)$$

Here, $\mathbf{F}$ is the steady force, the moment is taken about a moving pitching axis located at $\mathbf{x}_\mathcal{P} = \mathbf{x}_P + \mathbf{h}e^{i\omega t}$, $\mathbf{f}$ and $m_\mathcal{P}$ are the complex amplitudes of the linearized unsteady force and moment, respectively, $\mathbf{r}_{Sh_n,B} = (\mathbf{r}_{Sh_n} - \mathbf{r}_B) \cdot \tau$ is the complex amplitude of the relative displacement of the shock foot in the counterclockwise or τ direction along the moving blade surface, and the terms within the summations in equations (15) and (16) account for the concentrated loads due to shock motion and are evaluated at the shock roots.

Numerical Analysis

A numerical solution of the linear, variable-coefficient, unsteady, boundary-value problem is required over a single, extended blade-passage region of finite extent. The unsteady differential equation, in this case equation (6), must be solved in continuous regions of the flow subject to boundary or jump conditions imposed at the mean positions of the blade, wake and shock surfaces. Blade mean positions are prescribed, and the mean positions of wake and shock surfaces are determined as part of the steady solution. Finally, the unsteady near-field numerical solution must be matched to far-field analytical solutions at finite distances ($\xi = \xi_\mp$) upstream and downstream from the blade row.

In this discussion we will consider, for simplicity, flows in which at most a single shock occurs in each blade passage. Because of the stringent and conflicting requirements placed on a computational mesh for cascade flows, a zonal approach will be adopted. That is, a sheared H-type cascade mesh of moderate density will be used to capture large-scale unsteady phenomena over an extended blade-passage solution domain, and a local surface-fitted mesh of high density will be used to resolve high-gradient phenomena in the vicinity of a rounded blade leading edge or near a shock. For application to compressor cascades operating at high mean incidence, the local mesh wraps around a blunt blade leading edge, and if the mean flow is transonic and discontinuous, it also contains the shock and the entire supersonic region ahead of the shock.

Two different zonal solution procedures will be considered. The first is the single-pass procedure described by Verdon and Caspar (1982, 1984). Here a solution is first determined on the cascade mesh. This solution is used to define the unsteady potential distribution on the outer boundary of the local mesh, and then, a local-mesh solution is determined. The final solution to the unsteady boundary-value problem is taken to be the local solution in the region covered by a local mesh and the cascade solution elsewhere. Thus, the local-mesh solution provides a local correction to the cascade-mesh solution, but this correction does not influence the solution outside the region covered by the local mesh. As we shall see below, this assumption is a reasonable one for subsonic flows, but leads to erroneous predictions for discontinuous transonic flows.

The second approach is a new composite solution procedure described below. Here the discrete equations are written separately for the cascade and local meshes and are coupled implicitly through special interface conditions. This results in a single composite system of finite-difference equations that describe the unsteady flow over the entire solution domain.

Both the single-pass and the composite solution procedures use the same discrete approximations within the cascade- and local- mesh domains. The difference between the two approaches lies in the discrete approximations that are applied along the boundaries of the cascade and local meshes. In the single-pass procedure a Dirichlet boundary condition based on the previously computed cascade-mesh solution is imposed in the local calculation. In the composite procedure special discrete coupling conditions are imposed along the boundaries of an overlap zone between the cascade and local meshes.

Difference Approximations. Since the finite-difference model has been described in detail by Caspar and Verdon (1981), we will provide only a brief outline here. Discrete approximations to the various linear operators, which make up the unsteady boundary-value problem, are obtained using an implicit, least-squares, interpolation procedure. This leads to a nine-point "centered" difference star at subsonic points within either the cascade or local mesh domains. At blade surface boundary points a nine-point one-sided difference star is used on the cascade and polar local meshes, while a one-sided six-point star is used on the new transfinite local mesh. Since the unsteady field equation is hyperbolic rather than elliptic in supersonic regions, the difference approximation at supersonic points is determined in the following manner. First, the field equation is expressed in local canonical coordinates that are aligned with and normal to the local steady flow direction. Discrete approximations to streamwise derivatives are retarded or upwinded along the cascade tangential and the local circumferential mesh lines using a nine-point, one-sided, difference star. Normal derivatives are approximated using the standard nine-point centered star, resulting in a twelve-point difference star at supersonic points.

Unsteady shock phenomena are captured on the cascade mesh. Shocks are fitted on the local mesh by inserting a double mesh line at the mean shock location and then imposing the jump condition, equation (11). The latter is approximated using one-sided difference expressions (first-order accurate on the upstream or supersonic side and second-order accurate on the downstream or subsonic side) to evaluate the normal derivatives of the unsteady potential at the mean shock position. At those points on the downstream shock mesh line at which the steady flow is continuous (i.e., at points lying beyond the end of the shock), the condition $[\![\phi]\!] = 0$ is imposed. It is important to note that the unsteady shock-jump condition involves jumps in the steady or mean-flow derivatives across the shock. Since a shock capturing method is used to compute the mean flow in the present work, the steady shock-jump information is determined using a first-order accurate extrapolation of the mean-flow variables from upstream and downstream of the smeared shock to the upstream and downstream sides, respectively, of the estimated mean shock position. The latter is defined as the locus of all points in the smeared shock at which $M = 1$. The errors associated with this approximation have been minimized by using a very dense steady calculation mesh in the vicinity of the shock, thereby reducing the distance over which the shock is smeared.

For each mesh the resulting system of linear algebraic equations is block-tridiagonal for subsonic flow and block-pentadiagonal for transonic flow. In the single-pass solution procedure both the cascade- and local-mesh solutions are determined using a direct block inversion scheme. Composite (cascade/local mesh) solutions are determined using a different scheme, which is described below.
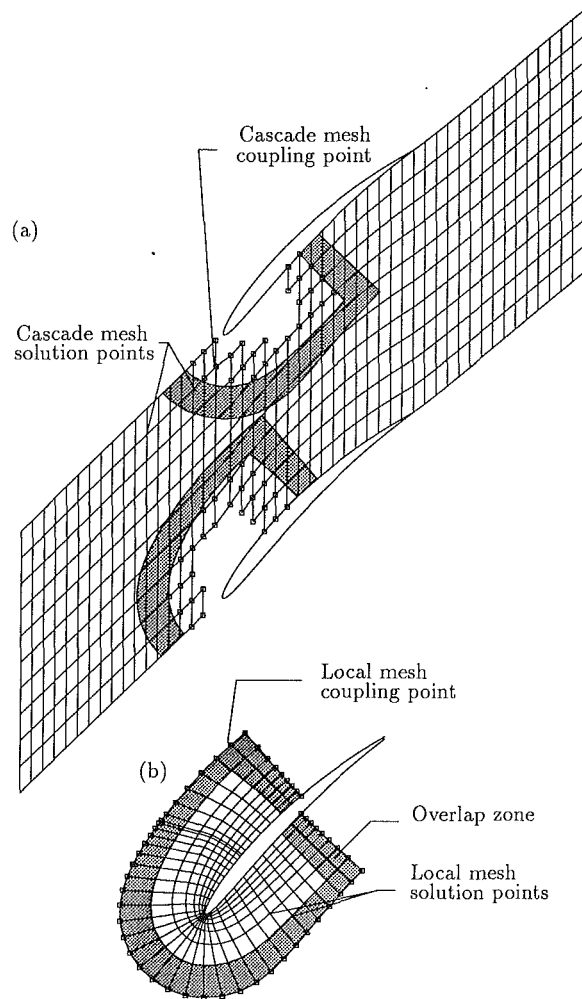
Fig. 3 Mesh point classification: (a) cascade mesh; (b) local mesh

Composite Solution Procedure. The mesh structure used in the unsteady analysis consists of a combination of a global cascade mesh and a local body-fitted mesh. Since these differ topologically, it is appropriate to adopt a zonal solution procedure for overlapping meshes (e.g., see Boppe, 1980). Thus, a composite mesh is constructed by overlapping the cascade and local meshes. In the region of intersection between the two meshes (i.e., the region covered by the local mesh), certain cascade mesh points are eliminated, depending upon their location within the local mesh domain.

To construct the composite system of discrete equations we first identify mesh points as either cascade-mesh solution points, local-mesh solution points, cascade-mesh coupling points, or local-mesh coupling points, as indicated in Fig. 3. This classification is based upon the locations of the cascade and local mesh points relative to predefined overlap zone, which is adjacent to the outer boundary of the local mesh. The overlap zone is defined conveniently in terms of local mesh indices by stepping in n cells from the outer boundary of the local mesh. As presently implemented, the width of the overlap zone can be different along different segments of this boundary. Once the overlap zone is specified, cascade mesh points are classified as being solution points if they lie exterior to the interior boundary of the overlap zone, or as coupling points if they are needed to complete the difference stars for the cascade-mesh solution points. Coupling points usually lie within two mesh points from the interior boundary of the overlap zone. This range allows for an upwind difference approximation to be applied at the cascade-mesh solution points lying within the overlap zone. The remaining points of the cascade mesh are

eliminated. Similarly, those local-mesh points lying within the outer boundary of the local mesh are classified as solution points; those points on this boundary, as coupling points. Upon combining the difference approximations at the cascade and local-mesh solution and coupling points, we obtain the composite system of discrete equations that approximate the unsteady boundary-value problem.

At cascade and local-mesh solution points the discrete approximations to the unsteady equations are determined as described above. Thus the block tri- or pentadiagonal structure is preserved at such points. The discrete equations at cascade-mesh coupling points are determined as follows. For each coupling point we locate the corresponding local-mesh cell that contains this point. This local cell is then triagulated on the shortest diagonal. Within the triangle containing the cascade-mesh coupling point a bilinear interpolation operator is constructed to define the value of the unsteady potential at the cascade-mesh coupling point in terms of its values at the three surrounding local mesh points making up the triangle. For example, if the cascade-mesh coupling point was found to be located in a triangle defined by points, (i, j), $(i+1, j)$ and $(i, j+1)$ on the local mesh, the interpolation would be expressed as

$$\phi_{I,J} = W_1 \phi_{i,j} + W_2 \phi_{i,j+1} + W_3 \phi_{i+1,j} \qquad (17)$$

where

$$W_1 = [(y_{i+1,j} - y_{i,j+1})(x_{i,j+1} - x_{I,J})$$
$$- (x_{i+1,j} - x_{i,j+1})(y_{i,j+1} - y_{I,J})]/\Delta$$

$$W_2 = 1 + [(y_{i+1,j} - y_{i,j+1})(x_{i,j+1} - x_{I,J}) \qquad (18)$$
$$- (x_{i+1,j} - x_{i,j+1})(y_{i,j+1} - y_{I,J})]/\Delta$$

$$W_3 = - [(y_{i,j} - y_{i,j+1})(x_{i,j+1} - x_{I,J})$$
$$- (x_{i,j} - x_{i,j+1})(y_{i,j+1} - y_{I,J})]/\Delta$$

and

$$\Delta = (x_{i+1,j} - x_{i,j+1})(y_{i,j} - y_{i,j+1})$$
$$- (x_{i,j} - x_{1,j+1})(y_{i+1,j} - y_{i,j+1})$$

Here, the subscripts I and J are cascade mesh indices and i and j are local mesh indices.

A similar interpolation is constructed to relate the unsteady potential at each local-mesh coupling point to its values at the points that define the cascade-mesh cell enclosing this coupling point. Since the axial lines of the cascade mesh are parallel, a four-point bilinear interpolation is used, i.e.,

$$\phi_{i,j} = W_1 \phi_{I,J} + W_2 \phi_{I,J} + W_3 \phi_{I+1,J+1} + W_4 \phi_{I+1,J}, \qquad (19)$$

where

$$W_1 = (1 - W_x)(1 - W_y), \quad W_2 = (1 - W_x)W_y$$

$$W_3 = W_x W_y, \qquad \qquad W_4 = W_x(1 - W_y)$$

$$W_x = (x_{i,j} - x_{I,J})/(x_{I+1,J} - x_{I,J}) \qquad (20)$$

$$W_y = (y_{i,j} - y_A)/(y_B - y_A)$$

$$y_A = (1 - W_x)y_{I,J} + W_x y_{I+1,J}$$

and

$$y_B = (1 - W_x)y_{I,J+1} + W_x y_{I+1,J+1}$$

The inclusion of these coupling equations into the system of discrete equations destroys the previous block diagonal structure. Although each coupling equation involves points that are spatially close to the coupling point under consideration, the former are not necessarily neighbors in the composite equation system. Therefore, the final system of discrete equations contains a sparse coefficient matrix of large band width. Conse-

quently, special storage and inversion techniques are required to achieve an efficient solution.

There has been a significant amount of research done in recent years on developing efficient storage and inversion techniques for sparse matrices. The approach usually taken for solving a linear system of equations that contains a large unstructured sparse coefficient matrix is to first recast the matrix into a compact vector description (or sparse matrix format), where only the nonzero elements of the original matrix and one or more pointer vectors are stored. This format is defined so as to minimize storage requirements while maximizing the computational efficiency of matrix manipulations, i.e., multiplication, transposition, inversion, etc. General routines for performing these manipulations are written in terms of the sparse matrix description.

For the present application we have employed the sparse matrix package developed by Eisenstat et al. (1977). This work has been assembled into a package of routines call the Yale Sparse Matrix Package (YSMP), with each routine written in the Yale Sparse Matrix Format. Since the original Yale package was written for systems of real equations, for the present application it was necessary to extend this package for application to complex systems. Once the composite system of unsteady equations is cast into the appropriate format, it can be solved using Gaussian elimination.

Calculation Meshes

As noted previously, the mesh structure used in the present analysis consists of a combination of a global cascade mesh and a local body fitted mesh. The cascade mesh is an H-type mesh composed of axial lines ($\xi = $ const) that are parallel to the blade row and tangential curves that are precentile averages of the upper and lower boundaries of the extended blade-passage solution domain. The tangential mesh lines at the upper and lower boundaries of the solution domain coincide with the meanflow stagnation streamlines downstream of the blade row. This mesh facilitates the imposition of the blade-to-blade periodicity condition, i.e., $\phi(\mathbf{x} + m\mathbf{G}) = \phi(\mathbf{x})e^{im\sigma}$, and the matching of the analytic and numerical unsteady solutions at the far upstream ($\xi = \xi_-$) and far downstream ($\xi = \xi_+$) boundaries.

For the results presented in this paper a cascade mesh with 100 axial lines and 30 tangential curves was applied. This mesh extended from one axial chord upstream to one axial chord downstream from the blade row (i.e., $-1 \le \xi/\cos \Theta \le 2$). For the most part uniform mesh spacings were used with $\Delta\xi = 0.04 \cos \Theta$ and $\Delta\eta = 4$ percent of the distance along axial lines between the upper and lower boundaries, but axial mesh lines were concentrated near blade edges and over the first 30 percent of blade chord where axial spacings of $\Delta\xi = 0.01 \cos \Theta$ were used. Tangential lines were concentrated near the upper and lower boundaries, i.e., near the blades and their wakes, of the solution domain. Small axial mesh spacings over the forward 30 percent of the blades were used in an effort to capture high gradient and shock phenomena in the H-mesh calculation. This is important for a single-pass calculation because the H-mesh solution provides outer boundary-condition information for the local-mesh calculation. For a composite-mesh calculation an H-mesh with uniform axial spacings is sufficient.

Local Meshes. Two different types of local mesh have been considered: a polar mesh and a new transfinite mesh (Fig. 4). The polar local mesh used by Verdon and Caspar (1982, 1984) is composed of radial and circumferential lines, normal and roughly parallel, respectively, to the reference blade surface. The mean shock locus is approximated as a line normal to the mean blade surface that extends out from the point at which a steady shock impinges on this surface.
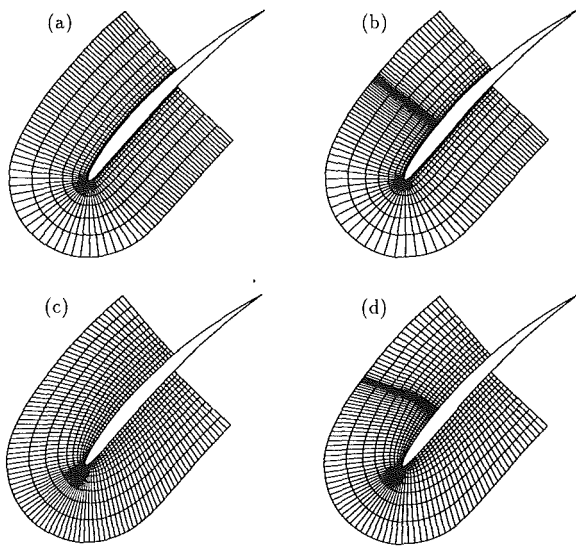
Fig. 4 Local meshes for NACA 0006 test cases: (*a*) polar local mesh—subsonic flow; (*b*) polar local mesh—transonic flow; (*c*) transfinite local mesh—subsonic flow; (*d*) transfinite local mesh—transonic flow

Fig. 5 Surface Mach number distributions for the example NACA 0006 cascade: (*a*) subsonic flow; $M_{-\infty} = 0.7$, $\Omega_{-\infty} = 55$ deg; (*b*) transonic flow; $M_{-\infty} = 0.8$, $\Omega_{-\infty} = 58$ deg

One objective of the present study was to provide a more accurate representation of unsteady shock phenomena by imposing the shock-jump conditions at the true predicted mean shock location. Since the mean shock locus can be determined from the steady calculation, we can require that a local mesh line for the unsteady calculation coincide with this locus and subsequently replace this line with upstream and downstream shock mesh lines. The shock jump relations can then be formulated and imposed along the shock mesh lines. With this approach the complexity of modeling the shock in the unsteady analysis is reduced to a mesh generation problem.

The transfinite local mesh is constructed using a direct algebraic mesh generation scheme along with a transfinite or multivariate interpolation. This allows a great deal of control in distributing mesh points and a convenient means of constraining the mesh so that it will conform to one or more internal boundaries. Further, it has been found to be very efficient in terms of both the storage requirement and the computation time required to generate the mesh. Finally, this approach can be easily extended to satisfy additional constraints. A good description of algebraic mesh generation techniques, including the method of transfinite interpolation, is given by Thompson et al. (1985). In the present effort the generalized transfinite interpolation procedure described by Eriksson (1982) has been used.

The local meshes used for the results presented in this paper consisted of 12 "circumferential" and 100 "radial" lines. The circumferential mesh lines wrapped around the leading edge of the reference blade and extended from radial lines emanating from the upper and lower surfaces of the blade at $\xi = 0.5 \cos \Theta$. The radial lines extended outward from the airfoil to one-half the minimum distance (i.e., the throat) between adjacent blades. The circumferential lines were concentrated near the blade surface, and the radial lines were concentrated near a shock, if present. The polar and transfinite local meshes used in the present study are shown in Fig. 4. The radial lines of the transfinite mesh conform to the actual shape of the mean shock locus. In addition, the transfinite mesh has a smoother distribution of mesh points in the vicinity of a blade leading edge.

Demonstration of Solution Procedures

We proceed to demonstrate the effects of implementing the transfinite or shock-conforming local mesh and the composite-

mesh solution procedure into the linearized unsteady flow analysis (LINFLO) of Verdon and Caspar (1982, 1984). We will restrict our consideration to unsteady flows, excited by prescribed small-amplitude harmonic blade motions, through a two-dimensional compressor ($M_{+\infty} \leq M_{-\infty}$) cascade operating at subsonic inlet and exit conditions. The example cascade has a stagger angle, Θ, of 45 deg and a gap/chord ratio, G, of unity. The blades are constructed by superposing the thickness distribution of a modified NACA four-digit series airfoil, i.e.,
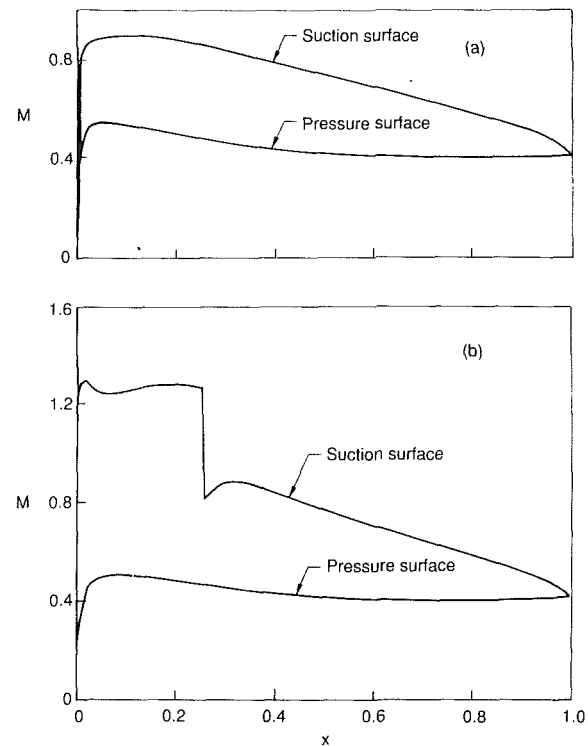
$$T(x) = H_T[2.969x^{1/2} - 1.26x - 3.516x^2$$
$$+ 2.843x^3 - 1.036x^2], \; 0 \leq x \leq 1 \quad (21)$$

on a circular-arc camber line. Here, H_T is the nominal blade thickness and the coefficient of the x^4 term in equation (21) differs from that used in the standard airfoil definition (i.e., -1.015) so that the example blades close in wedge-shaped trailing edges. The camber distribution is given by

$$C(x) = H_C - R + [R^2 - (x - 0.5)^2]^{1/2}, \; 0 \leq x \leq 1 \quad (22)$$

where $H_C \, (>0)$ is the height at midchord and $R = (2H_C)^{-1}(0.25 + H_C^2)$ is the radius of the circular-arc camber line. For the present application we set $H_T = 0.06$ and $H_C = 0.05$ to study the unsteady aerodynamic response to a vibrating cascade of cambered NACA 0006 airfoils.

We consider two different uniform inlet operating conditions. In one case the inlet Mach number, $M_{-\infty}$, and flow angle, $\Omega_{-\infty}$, are 0.7 and 55 deg, respectively; in the other, $M_{-\infty} = 0.8$ and $\Omega_{-\infty} = 58$ deg. The steady flows through the cascade are assumed to satisfy a Kutta condition at blade trailing edges and therefore, only inlet uniform-flow information must be specified. For $M_{-\infty} = 0.7$ and $\Omega_{-\infty} = 55$ deg, the mean or steady flow through the cascade is entirely subsonic; for $M_{-\infty} = 0.8$ and $\Omega_{-\infty} = 58$ deg, it is transonic with a single normal shock occurring in each blade passage. The predicted blade-surface Mach number distributions, as determined using the full-potential analysis of Caspar (1983) in which shocks are captured in transonic calculations, are shown in

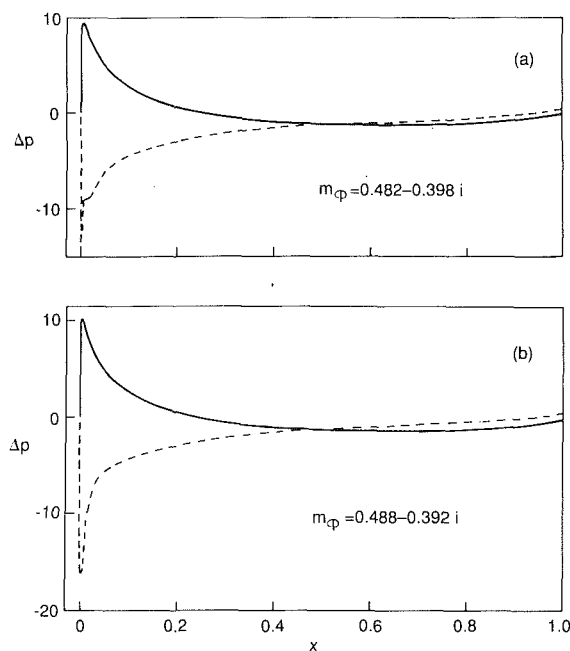Fig. 6 Unsteady aerodynamic response to torsional blade vibrations of the subsonic NACA 0006 cascade; $\alpha = (1, 0)$, $\omega = 1$, $\sigma = 180$ deg; (a) single-pass solution using polar local mesh; (b) single-pass solution using transfinite local mesh:———— in-phase component (real part) of Δp; ————out-of-phase component (imaginary part)

Fig. 5. The subsonic mean flow stagnates on the pressure surface of the blade at $x = 0.0005$, and the Mach number reaches a maximum value of 0.916 on the suction surface at $x = 0.109$. The exit Mach number and flow angle are 0.446 and 40.2 deg, respectively. The transonic flow stagnates at $x = 0.002$ on the pressure surface, and the normal shock emanates from the suction surface at $x = 0.258$. The Mach numbers at the base of the shock are 1.282 on the upstream side and 0.816 on the downstream side, and the exit Mach number and flow angle are 0.432 and 40.3 deg, respectively.

Predictions, based on single-pass and composite solutions, for the unsteady aerodynamic response at the reference ($m = 0$) blade of the NACA 0006 cascade are given below. These include first harmonic pressure differences, i.e., $\Delta p(x) = p_B(x, y_-) - p_B(x, y_+)$, aerodynamic moments, m_{φ}, and, where appropriate, shock displacements, $r_{Sh,B}$, for blades undergoing pure pitching (torsional) oscillations about their midchord points, i.e., X_P, $Y_P = 0.5$, 0. The torsional motions are assumed to occur at unit frequency, $\omega = 1$, an interblade phase angle σ of 180 deg, and a complex amplitude α of (1, 0). Predicted unsteady potential contours are also presented to illustrate unsteady solutions over extended blade-passage domains. Additional predictions, based on composite solutions on the transfinite local mesh, for the global unsteady aerodynamic response behavior of the example NACA 0006 cascade can be found in Verdon and Usab (1988).

Single-Pass Solutions. Response predictions based on the single-pass solution procedure are shown in Figs. 6 and 7. Note that if $Im\{\alpha\} = 0$, the real and imaginary parts of a reference blade complex response parameter represent the response components that are in- and out-of-phase, respectively, with the reference blade displacement. The results in Figs. 6 and 7 were obtained from two different calculations: one using the polar-type local mesh and the other, the transfinite local mesh. The response predictions for the subsonic (M$_{-\infty} = 0.7$, $\Omega_{-\infty} = 55$ deg) NACA 0006 cascade shown in Fig. 6 reveal an analytic behavior for Δp in the vicinity of the leading edge in which both the real and imaginary components of the pressure dif-
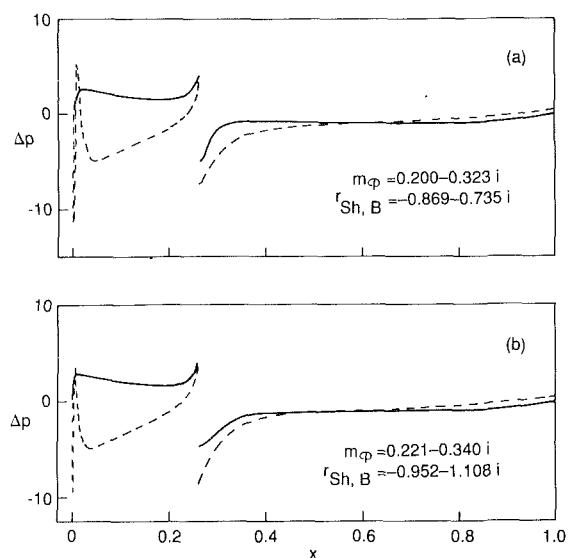

Fig. 7 Unsteady aerodynamic response to torsional blade vibrations of the transonic NACA 0006 cascade; $\alpha = (1, 0)$, $\omega = 1$, $\sigma = 180$ deg: (a), (b), ———— and ————as in Fig. 6

ference are zero at the leading edge point and reach local extrema very close (i.e., at approximately $x = 0.004$) to this point. The two local meshes yield nearly identical pressure differences and moments, but there are discrepancies between the predicted pressure-differences near the leading edge. The transfinite local-mesh calculation gives the more reasonable behavior because it provides the better mesh point distribution in the immediate vicinity of the blade leading edge.

Response predictions for the transonic (M$_{-\infty} = 0.8$, $\Omega_{-\infty} = 58$ deg) NACA 0006 cascade are shown in Fig. 7. Here, the unsteady potential and hence, the first harmonic unsteady pressure, are discontinuous at the mean shock location. The relative displacement of a shock along a blade surface and hence, the shock-induced unsteady airloads, depend upon the jump in the unsteady potential at the shock root. Recall that the shock-fitted unsteady solution yields both harmonic and anharmonic local unsteady responses, but the first-order global unsteady airloads are harmonic. The two local mesh solutions considered in Fig. 7 give slightly different unsteady pressure differences downstream of the shock and very different shock displacements along the blade surface. These differences indicate the sensitivity of an unsteady transonic solution to the numerical modeling of the shock. Since the "radial" lines of the transfinite local mesh conform to the shape of the mean shock locus, this mesh should provide the better resolution of a discontinuous transonic flow.

Contours of the in-phase component of the unsteady potential, i.e., $Re\{\phi\}$, for the example subsonic and transonic NACA 0006 cascades are shown in Fig. 8. These contours were determined from single-pass calculations using the transfinite local meshes shown in Figs. 4(c) and 4(d), respectively. In the single-pass procedure the solution on the cascade mesh fixes the values of ϕ on the outer boundary of the local mesh. Thus, the potential contours will be continuous at this boundary but, in general, their slopes will be discontinuous. Such discontinuities are indicative of errors in the single-pass solution. Slope discontinuities are apparent in the potential contours shown in Fig. 8, particularly the contours for the unsteady transonic flow.

The single-pass solutions determined on polar and transfinite local meshes yield very similar response predictions for the subsonic example, but somewhat different predictions for the discontinuous transfinite flow. The latter differences are to be expected since the transonic mesh has been constructed and implemented so that shock phenomena can be modeled more accurately in linearized unsteady flow calculations.
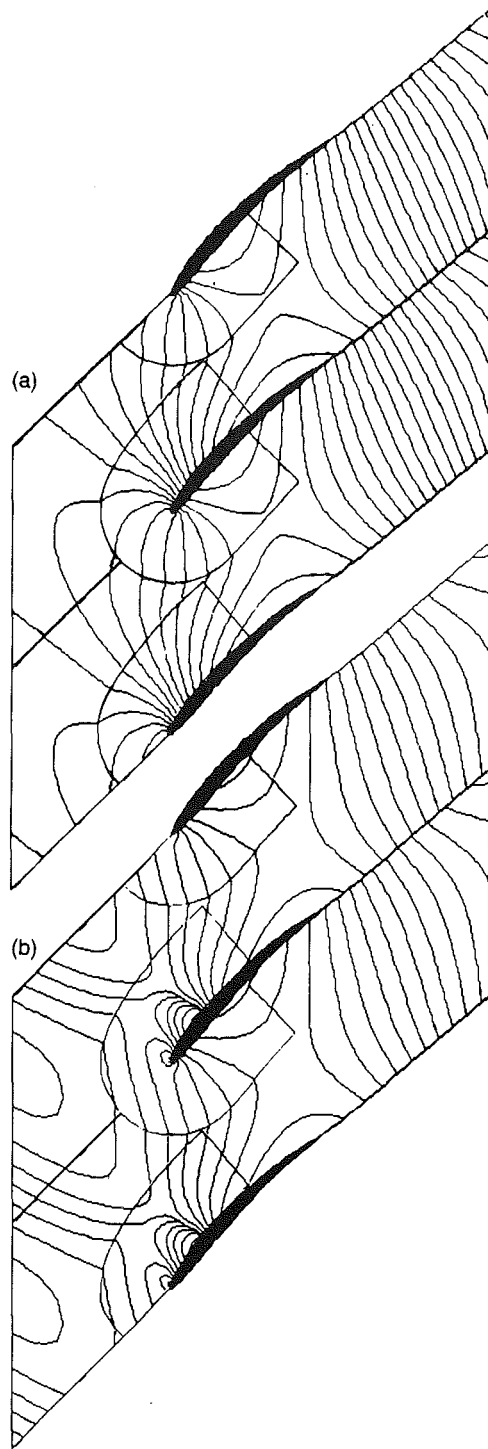
Fig. 8 Contours of the in-phase component of the unsteady potential, $Re\{\phi\}$**, as determined from single-pass solutions for the subsonic (a) and transonic (b) NACA 0006 cascades undergoing torsional blade vibrations at** $\alpha = (1, 0)$**,** $\omega = 1$**, and** $\sigma = 180$ **deg**

Fig. 9 Contours of the in-phase component of the unsteady potential as determined from composite solutions for the subsonic (a) and transonic (b) NACA 0006 cascades undergoing torsional blade vibrations at $\alpha = (1, 0)$**,** $\omega = 1$**, and** $\sigma = 180$ **deg**

Composite Solutions. With the single-pass solution procedure the detailed resolution of the flow in the local-mesh region cannot impact the solution over the remainder of the extended blade-passage solution domain. As we shall see, this places serious limitations on the accuracy of single-pass solutions, particularly for transonic flows in which shocks extend well into the blade passages. In contrast, with the composite solution procedure the cascade and local-mesh finite-difference

equations are solved simultaneously, thereby allowing the accurate resolution of the flow in the local region to impact the entire unsteady flow solution.
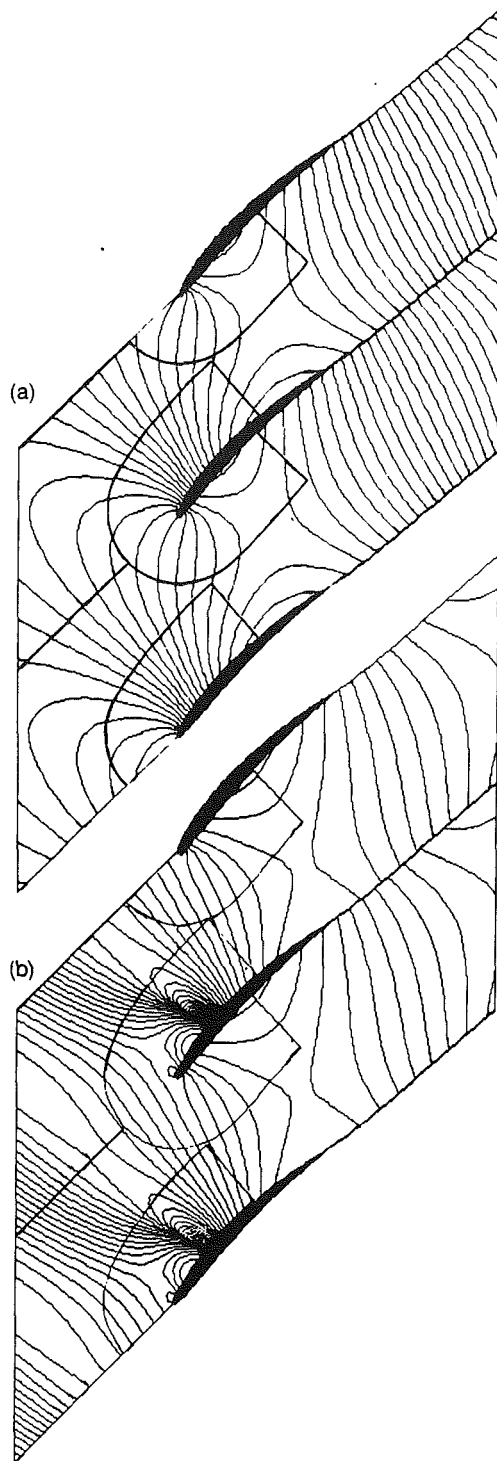
Contours of the in-phase component of the unsteady potential as determined from composite solutions for the example subsonic and transonic NACA 0006 cascades are shown in Fig. 9. The transfinite local mesh was employed for both calculations. The composite calculations yield potential contours
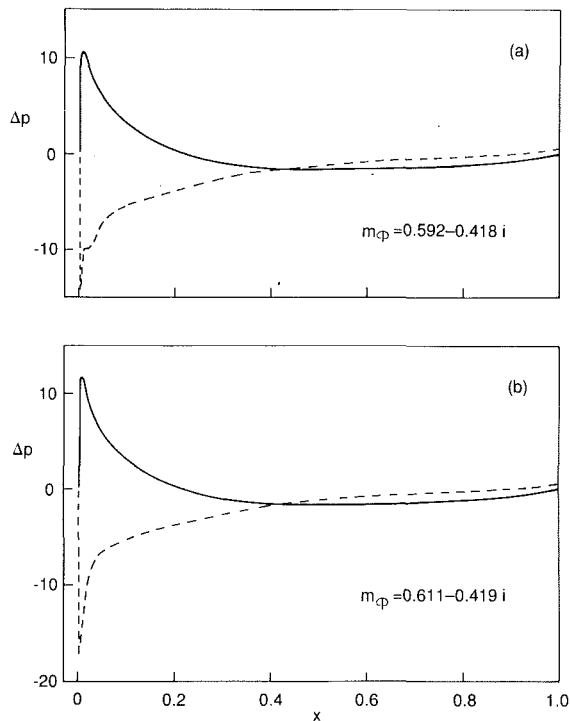
Fig. 10 Unsteady aerodynamic response to torsional blade vibrations of the subsonic NACA 0006 cascade; $\alpha = (1, 0)$, $\omega = 1$, $\sigma = 180$ deg: (a) composite solution using polar local mesh; (b) composite solution using transfinite local mesh: ---- in-phase component of Δp; ————out-of-phase component

Fig. 11 Unsteady aerodynamic response to torsional blade vibrations of the transonic NACA 0006 cascade; $\alpha = (1, 0)$, $\omega = 1$, $\sigma = 180$ deg: (a), (b), ----, and ————as in Fig. 10

that have continuous slopes at the outer boundary of the local mesh, indicating that the errors inherent to the single-pass procedure have been eliminated. A comparison of the single-pass (Fig. 8a) and composite (Fig. 9a) potential contours for the subsonic cascade indicates that the two procedures yield very similar unsteady flow fields with the composite procedure predicting a somewhat greater variation in the potential upstream of the blade row. A similar comparison of the single-pass (Fig. 8b) and composite (Fig. 9b) transonic potential contours reveals dramatic differences between the results obtained from the two procedures. In particular, the composite-mesh solution shows much greater variations in the potential in the vicinity of the shock and upstream of the blade row. The upstream variations are caused by a propagating acoustic response disturbance. The composite solution yields a much greater amplitude for this disturbance than that predicted by the single-pass solution. Thus, the results shown in Figs. 8(b) and 9(b) indicate that the detailed resolution of the unsteady flow in the vicinity of a shock can have a profound effect on the predicted linearized unsteady flow throughout the extended blade-passage solution domain.

Unsteady pressure-difference distributions for the subsonic NACA 0006 cascade as determined from composite solutions are shown in Fig. 10. These distributions are very similar to those predicted by the single-pass procedure (Fig. 6). However, differences occur near the blade leading edge and over the forward half of the blade giving rise to different predictions for the unsteady moment. Although the composite calculation provides a more accurate resolution of an unsteady subsonic flow than a single-pass calculation, it appears that the two procedures will predict very similar overall characteristics. The differences between the polar and transfinite local mesh composite predictions (Fig. 10) for the unsteady pressure differences and the unsteady moment are quite small and mirror those between the corresponding single-pass predictions. Thus, it appears that subsonic composite solutions determined on
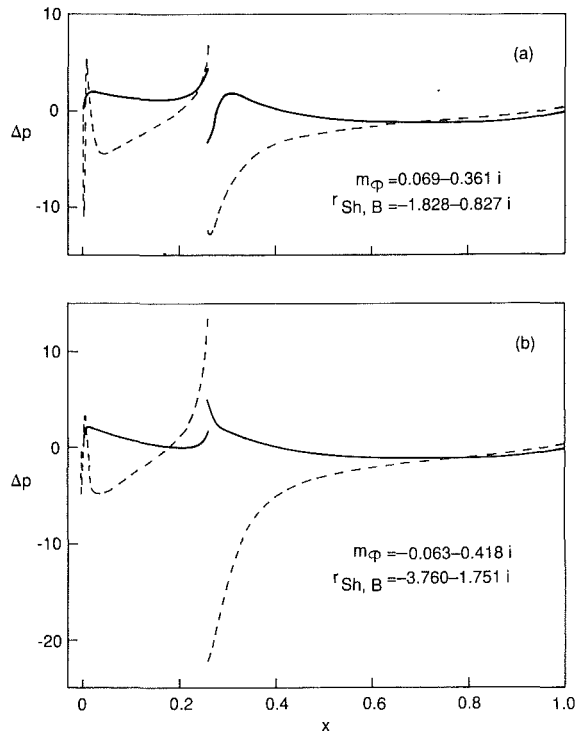
the polar and transfinite local meshes will show only small quantitative differences.

Unsteady pressure-difference distributions for the transonic NACA 0006 cascade as determined from composite solutions on the polar and transfinite local meshes are shown in Fig. 11. There are substantial differences between these results and those determined from the single-pass calculations (Fig. 7) as well as between the composite results on the polar and transfinite local meshes. These differences occur because the composite procedure allows shock phenomena to impact the predicted unsteady flow field over the entire extended blade-passage domain, and the transfinite mesh allows a more accurate implementation of the unsteady shock-jump condition.

The single-pass and composite transonic calculations on the polar local mesh provide qualitatively similar unsteady pressure-difference behaviors along the blade, but the composite calculation predicts enhanced shock effects. The single-pass and composite calculations on the transfinite local mesh yield very different behaviors for the out-of-phase component of the unsteady pressure difference upstream and downstream of the shock. There are also dramatic differences between the single-pass and composite predictions for the unsteady aerodynamic moments and shock displacments. The differences between the composite solutions on the polar and transfinite local meshes depicted in Fig. 11 indicate the sensitivity of the linearized unsteady solution to the numerical modeling of shock effects.

We have attempted to demonstrate the merits of using a composite solution procedure and a transfinite local mesh to resolve linearized unsteady subsonic and transonic cascade flows. For subsonic flow, the new (composite calculation using a transfinite local mesh) and the old (single-pass calculation using a polar local mesh) procedures predict very similar unsteady flow fields. However, the predicted pressure-difference distributions in the vicinity of a blade leading edge and over the forward half of a blade differ giving rise to quite different

predictions for the unsteady aerodynamic moment. For transonic flow, the composite procedure allows the detailed resolution of the flow near a shock to impact the predicted unsteady field throughout the entire solution domain, an important feature missing from the single-pass procedure.

Transonic composite solutions are quite sensitive to the numerical modeling of shock effects. Our results indicate that it is important to fit shocks in unsteady transonic calculations and to represent shock phenomena accurately. Unfortunately, the nonlinear full potential analysis of Caspar (1983), which has been used to provide the steady background flow information for our unsteady transonic calculations, employs a single-pass calculation on a polar local mesh and shocks are captured in the nonlinear steady calculation. In the future, an effort should be undertaken to develop a cascade full potential analysis with shock-conforming local-mesh and composite-mesh solution capabilities. In addition, shocks should be fitted in this steady calculation.

Conclusions

The analysis described in this paper accounts for the effects of real blade geometry, mean blade loading, and operation at transonic Mach numbers on the linearized unsteady aerodynamic response of an isolated two-dimensional cascade. Therefore, it offers great potential for meeting the needs of turbomachinery aeroelastic designers for an efficient unsteady aerodynamic analysis that represents the essential physics of the flows associated with turbomachinery blade vibrations.

In the present effort two needed improvements to an existing numerical treatment of linearized unsteady cascade flow have been described. One involves the construction and implementation of a new transfinite local mesh so that unsteady shock phenomena can be modeled accurately. The transfinite local mesh was also found to yield a better resolution of unsteady phenomena in the vicinity of a rounded blade leading edge. The second improvement, the development of a composite-mesh solution procedure, allows the detailed resolution of the flow in the vicinity of a rounded blade leading edge or a shock to impact the linearized unsteady solution over an entire extended blade-passage solution domain. The composite approach is particularly important for transonic flows in which shocks extend well into blade passages. An added benefit associated with the composite procedure is that cascade axial mesh lines do not have to be packed near blade leading edges or near shocks since the cascade-mesh solution is no longer used to establish a boundary condition for a local-mesh calculation.

Acknowledgments

References

Acton, E., and Newton, S. G., 1987, "Numerical Methods for Unsteady Transonic Flow," *AGARD Manual on Aeroelasticity in Axial-Flow Turbomachines*, Vol. 1, *Unsteady Turbomachinery Aerodynamics*, Chap. VI, M. F. Platzer and F. O. Carta, eds., AGARD-AG-298.

Atassi, H., and Akai, T. J., 1980, "Aerodynamic and Aeroelastic Characteristics of Oscillating Loaded Cascades at Low Mach Number, I. Pressure Distribution, Forces and Moments," ASME *Journal of Engineering for Power*, Vol. 102, No. 2, pp. 344–351.

Boppe, C. W., 1980, "Computational Transonic Flow About Realistic Aircraft Configurations," NASA CR 3243.

Caspar, J. R., 1983, "Unconditionally Stable Calculation of Transonic Potential Flow Through Cascades Using an Adaptive Mesh for Shock Capture," ASME *Journal of Engineering for Power*, Vol. 105, No. 3, pp. 504–513.

Caspar, J. R., and Verdon, J. M., 1981, "Numerical Treatment of Unsteady Subsonic Flow Past an Oscillating Cascade," *AIAA Journal*, Vol. 19, No. 12, pp. 1531–1539.

Ehlers, F. E., and Weatherill, W. H., 1982, "A Harmonic Analysis Method for Unsteady Transonic Flow and Its Application to the Flutter of Airfoils," NASA CR 3537.

Eisenstat, S. C., Gursky, M. C., Schultz, M. H., and Sherman, A. H., 1977, "The Yale Sparse Matrix Package. II. The Nonsymmetric Codes," Research Report No. 114, Yale University, Department of Computer Science, New Haven, CT.

Ericksson, L. E., 1982, "Generation of Boundary-Conforming Grids Around Wing-Body Configurations Using Transfinite Interpolation," *AIAA Journal*, Vol. 20, No. 10, pp. 1313–1320.

Fleeter, S., 1979, "Aeroelasticity Research for Turbomachine Applications," *Journal of Aircraft*, Vol. 16, No. 5, pp. 320–326.

Hall, K. C., and Crawley, E. F., 1989, "Calculation of Unsteady Flows in Turbomachinery Using the Linearized Euler Equations," *AIAA Journal*, Vol. 27, No. 6, pp. 777–787.

Thompson, J. F., Warsi, Z. U. A., and Mastin, C. W., 1985, *Numerical Grid Generation—Foundations and Applications*, North-Holland, New York.

Verdon, J. M., 1987, "Linearized Unsteady Aerodynamic Theory," AGARD *Manual on Aeroelasticity in Axial-Flow Turbomachines*, Vol. 1, *Unsteady Turbomachinery Aerodynamics*, Chap. II, M. F. Platzer and F. O. Carta, eds., AGARD-AG-298.

Verdon, J. M., 1989, "The Unsteady Flow in the Far Field of an Isolated Blade Row," *Journal of Fluids and Structures*, Vol. 3, No. 2, pp. 123–149.

Verdon, J. M., and Caspar, J. R., 1982, "Development of a Linear Unsteady Aerodynamic Analysis for Finite-Deflection Subsonic Cascades," *AIAA Journal*, Vol. 20, No. 9, pp. 1259–1267.

Verdon, J. M., and Caspar, J. R., 1984, "A Linearized Unsteady Aerodynamic Analysis for Transonic Cascades," *Journal of Fluid Mechanics*, Vol. 149, pp. 403–429.

Verdon, J. M., and Usab, W. J., Jr., 1988, "Advances in the Numerical Analysis of Linearized Unsteady Cascade Flows," Technical Report AFWAL-TR-88-2055, Department of the Air Force, Aeronautical Systems Division, Wright-Patterson AFB, OH.

Whitehead, D. S, 1982, "The Calculation of Steady and Unsteady Transonic Flow in Cascades," Report CUED/A-Turbo/TR 118, Cambridge Univ. Engineering Dept., Cambridge, United Kingdom.

Williams, M. H., 1979, "Linearization of Unsteady Transonic Flows Containing Shocks," *AIAA Journal*, Vol. 17, No. 4, pp. 394–397.

Analysis of Unsteady Compressible Viscous Layers

G. D. Power

J. M. Verdon

K. A. Kousen

Theoretical & Computational Fluid Dynamics,
United Technologies Research Center,
East Hartford, CT 06108

The development of an analysis to predict the unsteady compressible flows in blade boundary layers and wakes is presented. The equations that govern the flows in these regions are transformed using an unsteady turbulent generalization of the Levy-Lees transformation. The transformed equations are solved using a finite difference technique in which the solution proceeds by marching in time and in the streamwise direction. Both laminar and turbulent flows are studied, the latter using algebraic turbulence and transition models. Laminar solutions for a flat plate are shown to approach classical asymptotic results for both high and low-frequency unsteady motions. Turbulent flat-plate results are in qualitative agreement with previous predictions and measurements. Finally, the numerical technique is also applied to the stator and rotor of a low-speed turbine stage to determine unsteady effects on surface heating. The results compare reasonably well with measured heat transfer data and indicate that nonlinear effects have minimal impact on the mean and unsteady components of the flow.

Introduction

Because of relative motions between adjacent blade rows, the flows through turbomachinery blade passages are inherently unsteady. However, theoretical approaches to design and development are generally based on steady-state aerodynamic analyses along with the use of empirical correlations to account for unsteady effects. Important areas in which theoretical unsteady aerodynamic analyses have had an impact on design are in the prediction of the aeroelastic and aeroacoustic behavior of the blading. For such applications reliance is placed on linearized inviscid analyses along with empirical correlations to account for the effects of viscous separations. Since unsteady viscous effects can impact the time-averaged or steady-state performance, as well as the aeroelastic and aeroacoustic responses of the blading, efficient calculation methods for unsteady viscous flows are an important goal for current and future research.

For flows of practical interest, the Reynolds number is usually sufficiently high that the complete flow field can be divided conceptually into two regions: an "inner" viscous or dissipative region and an "outer" inviscid region. Sets of reduced equations derivable from the Navier-Stokes equations may be applied in both regions, e.g., the Euler equations in the outer inviscid region and Prandtl's boundary-layer equations in the inner viscous region. Flows occurring at or near design operating conditions remain essentially attached to the blade surfaces. Therefore, the inner region consists of thin (boundary) layers that lie along the surfaces of each blade and merge into thin wakes that extend downstream of the blade row. The principal interaction between the flows in the outer inviscid

and the inner viscous regions arises from the displacement thickness effect, which leads to thickened semi-infinite equivalent bodies and corresponding changes in surface pressures. If the inviscid/viscid interaction is "weak," the complete flow problem can be solved sequentially with the pressure being determined by the inviscid flow. However, flows through blade rows usually involve both a weak overall interaction and local strong displacement interactions caused by, for example, viscous layer separations, shock/boundary-layer interactions, and trailing-edge/near-wake interactions. In these cases the inviscid and viscous layer equations must be solved simultaneously, such that the pressure depends upon the flows in both the inviscid and viscous layer regions.

As a step toward the goal of providing a strong inviscid/viscid interaction analysis for unsteady flows through turbomachinery blade rows, an unsteady viscous layer analysis that is applicable to both blade boundary layers and wakes is described in this paper. Here the viscous layer equations are first transformed using an extension, for unsteady turbulent flows, of the Levy-Lees transformation. In terms of the new variables, the growth of the boundary layer is minimized and density is eliminated from the governing equations. The transformed equations are discretized using first-order backward differences in the streamwise direction and in time and second-order central differences in the normal direction. The resulting algebraic equations are quasi-linearized about a previous iterative solution and marched implicitly, first in time and then in the streamwise direction, such that a block tridiagonal system of algebraic equations must be inverted at each step. The solution is marched in time over several periods of unsteady excitation from an initial steady solution, and in the streamwise direction from an approximate time-dependent, upstream flow solution.

In this paper the foregoing analysis is applied to several standard flows to test its accuracy. One case, which has been

---

studied previously by numerous authors, involves an oscillating free stream over a flat-plate airfoil. For this example predictions agree with previous laminar solutions and, when compared with previous turbulent solutions, fall within the level of uncertainty inherent to unsteady turbulence and transition models. The analysis is also applied to the stator vanes and rotor blades of the turbine stage investigated experimentally by Dring et al. (1982, 1986). Analytical predictions for this configuration are found to be in reasonable agreement with measured heat transfer rates along the stator and rotor blade surfaces and give some indication of the relative importance of nonlinear effects on the unsteady flows caused by stator/ rotor interactions.

Viscous Layer Equations

We consider high Reynolds number (Re) unsteady flow, with negligible body forces, of a perfect gas with constant specific heats and Prandtl number (Pr). In the present discussion all variables are dimensionless. Lengths have been scaled with respect to a reference length (typically the blade chord), time with respect to the reference length divided by the upstream free-stream flow speed, density and viscosity with respect to their upstream free-stream values, velocity with respect to the upstream free-stream speed, pressure with respect to twice the upstream free-stream dynamic pressure, and temperature with respect to the square of the upstream free-stream speed divided by the specific heat at constant pressure.

The equations that govern the flow in the viscous layer are derived from the conservation laws for mass, momentum, and energy and can be expressed in the form

$$\frac{\partial \rho}{\partial t} + \frac{\partial (\rho u)}{\partial s} + \frac{\partial (\rho v)}{\partial n} = 0 \tag{1}$$

$$\rho \frac{Du}{Dt} = -\frac{\partial p}{\partial s} + \frac{1}{Re}\frac{\partial}{\partial n}\left(\mu\frac{\partial u}{\partial n} - \rho\overline{u'v'}\right) \tag{2}$$

and

$$\rho \frac{DH}{Dt} = \frac{\partial p}{\partial t} + \frac{1}{Re}\frac{\partial}{\partial n}\left[\mu\left(1 - \frac{1}{Pr}\right)u\frac{\partial u}{\partial n} + \frac{\mu}{Pr}\frac{\partial H}{\partial n} - \rho\overline{H'v'}\right] \tag{3}$$

Here, t is time, and the coordinates s and n measure distances along and normal to, respectively, a blade surface and its associated reference wake streakline. The latter emanates from the blade trailing edge and is entirely contained within the viscous wake. In addition, ρ, p, H, and μ are ensemble (or Reynolds) averaged values of the fluid density, pressure, total enthalpy, and molecular viscosity, respectively, u and v are the averaged values of the velocity components in the streamwise (s) and normal (n) directions, u' and v' are the component velocities associated with turbulent fluctuations, and the overbar denotes a turbulent correlation, which is to be determined empirically. As a consequence of the high Re, thin-layer approximation, the pressure in the viscous layer is a function only of s and t and $H = T + u^2/2$. We assume that the interaction between the flows in the viscous layer and the external inviscid stream is weak and, therefore, that the pressure is determined by the outer inviscid flow.

In addition to the foregoing equations, the equation of state for a perfect gas, i.e.,

$$p = \frac{\gamma - 1}{\gamma}\rho T \tag{4}$$

where γ is the specific heat ratio (constant pressure to constant volume) of the fluid, a law relating the molecular viscosity to the temperature, e.g.,

$$\frac{\mu}{\mu_R} = \left(\frac{T}{T_R}\right)^{3/2}\frac{T_R + T_S}{T + T_S} \tag{5}$$

and equations relating the turbulent correlations $\overline{u'v'}$ and $\overline{H'v'}$ to ensemble average flow quantities, e.g.,

$$-\rho\overline{u'v'} = \epsilon\frac{\partial u}{\partial n} \text{ and } -\rho\overline{H'v'} = \epsilon_H\frac{\partial H}{\partial n} = \frac{\epsilon}{Pr_T}\frac{\partial H}{\partial n} \tag{6}$$

are also required. Equation (5) is known as Sutherland's Law. The temperatures T_R and T_S are prescribed, and μ_R is the molecular viscosity at the temperature T_R. The turbulent correlations $\overline{u'v'}$ and $\overline{H'v'}$ have been related to mean flow gradients, using Prandtl's mixing length hypothesis. Here ϵ and ϵ_H are the eddy viscosity and eddy diffusivity, respectively, and play roles similar to their molecular counterparts. The eddy diffusivity is eliminated in a similar manner to the molecular diffusivity through the introduction of the turbulent Prandtl number, Pr_T.

Initial and Boundary Conditions

The foregoing system of field equations is parabolic in time and in the streamwise direction. Therefore, the streamwise component of the velocity and the total enthalpy must be known for all time at some upstream streamwise location, and these variables, along with the normal velocity, must be known throughout the solution domain at some initial time. Also, conditions on the fluid properties at the edge of the viscous layer, i.e.,

$$u \rightarrow u_e(s, t) \text{ and } H \rightarrow H_e(s, t) \text{ for } n \rightarrow \infty; \tag{7}$$

a no-slip condition and either a prescribed temperature or heat flux condition at a solid blade surface, i.e.,

$$u = v = 0 \text{ and } H = H_w(s, t) \text{ or } \frac{\partial H}{\partial n} = q_w(s, t) \tag{8}$$
$$\text{for } n = 0, \, s \leq s_{te};$$

and a condition on the velocity normal to a reference wake streakline, i.e.,

$$v = 0 \text{ for } n = 0, \, s > s_{te} \tag{9}$$

must be enforced. Here the subscripts w and e denote the values of the fluid properties at a solid wall and at the edge of the viscous layer, respectively, and the subscript te refers to the airfoil trailing edge point. Since the interaction between the flows in the inviscid and viscous layer regions is assumed to be weak, the edge values of the fluid properties are determined by the outer inviscid flow.

Turbulence and Transition Models

The models used here to simulate the effects of turbulence and transition on the flow in the viscous layer are the algebraic eddy viscosity model proposed by Cebeci and Smith (1974), the transition model proposed by Dhawan and Narasimha (1958), and the wake turbulence model proposed by Chang et al. (1986). Also, since flows in turbomachines are known to be characterized by high free-stream turbulence levels, a simple modification developed by Yuhas (1981) has been incorporated into the turbulence model to account for the effects of free-stream turbulence on the viscous layer. These models are easy to implement and are known to be reasonably accurate for steady flows with mild pressure gradients. Their ability to represent turbulence and transition accurately in unsteady flows is not known, and, therefore, results must be interpreted with caution.

The Cebeci–Smith algebraic model divides a boundary layer into inner, where $\epsilon = \epsilon_i$, and outer, where $\epsilon = \epsilon_o$, regions. the inner model is applied from the wall out to the point at which $\epsilon_i = \epsilon_o$; the outer model, from this point to the edge of the boundary layer. The eddy viscosity in the inner region is given by

$$\epsilon_i = \gamma_{tr}\rho\mathrm{Re}\{0.41n[1-\exp(-n/A)]\}^2\left|\frac{\partial u}{\partial n}\right| \qquad (10)$$

where

$$A = \frac{26\mu}{\rho\sqrt{\mathrm{Re}}}\left\{\left(\rho^{-1}\mu\frac{\partial u}{\partial n}\right)_w\left[1-11.8p^+\left(\frac{\mu_w}{\mu_e}\right)\left(\frac{\rho_e}{\rho_w}\right)^2\right]\right\}^{-\frac{1}{2}}$$

$$p^+ = \sqrt{\mathrm{Re}}\,\frac{\mu_e}{\rho_e}\left(\frac{\partial u_e}{\partial t}+u_e\frac{\partial u_e}{\partial s}\right)\left(\rho^{-1}\mu\frac{\partial u}{\partial n}\right)_w^{-\frac{3}{2}} \qquad (11)$$

γ_{tr} is an intermittency factor, which models transitional flow, and the term $\sqrt{\mathrm{Re}}\mu_e\rho_e^{-1}\partial u_e/\partial t$ has been included in the definition of p^+ to account for unsteady effects (see Cebeci and Keller, 1970).

The eddy viscosity in the outer region is given by

$$\epsilon_o = \gamma_{tr}\mathrm{Re}\rho u_e\chi\int_0^\infty (1-u/u_e)dn \qquad (12)$$

where

$$\chi = 1.55\chi_0(1+\pi)^{-1}, \quad \pi = 0.55[1-\exp(-0.243z_1^{1/2}-0.298z_1)]$$

$$z_1 = \begin{cases} \mathrm{Re}_\theta/425-1 & \text{for } \mathrm{Re}_\theta > 425 \\ 0 & \text{for } \mathrm{Re}_\theta \le 425 \end{cases} \qquad (13)$$

$$\mathrm{Re}_\theta = \frac{\rho_w u_e\mathrm{Re}}{\mu_w}\int_0^\infty \frac{u}{u_e}\left(1-\frac{u}{U_e}\right)dn$$

and the parameter π has been defined to account for low momentum thickness Reynolds number. The Clauser constant, χ_0, is usually set equal to 0.0168, but following Yuhas (1981) we set

$$\chi_0 = 0.01591+0.292727\sigma+1.585\sigma^2 \qquad (14)$$

where σ is the free-stream turbulence intensity, to account for the effects of free-stream turbulence on the development of the turbulent boundary layer.

Blade boundary layers can contain transitional regions of significant extent. Therefore, a transition model is needed to predict boundary-layer effects properly. Several models have been developed for steady transitional flows through correlations with experimental data. One of these is the Dhawan-Narasimha forced transition model, in which the intermittency factor is given by

$$\gamma_{tr} = 1-\exp\left[-4.6513\left(\frac{s-s_1}{s_2-s_1}\right)^2\right] \qquad (15)$$

Here s_1 and s_2 are the streamwise locations at the beginning and end of the transition region, respectively. These locations can be specified as functions of time to model unsteady transitional flows.

A wake is formed from the boundary layers off the upper and lower surfaces of a blade, and there are different eddy viscosities associated with each of these layers. At each streamwise station in the wake, equation (12) is evaluated twice: once between the lower edge of the wake and the location at which the streamwise velocity reaches a minimum value, and once between the latter position and the upper edge of the wake. This gives two eddy viscosity values, ϵ_o^- and ϵ_o^+. The maximum of these two values is designated ϵ_f. Similarly, $(\epsilon_o)_{te}$ is defined to be the maximum of the eddy viscosity values calculated on the upper and lower surfaces of the blade at the trailing edge. Then, following Chang et al. (1986), the eddy viscosity at each streamwise position in the wake is assumed to be a weighted average of ϵ_f and $(\epsilon_o)_{te}$, i.e.,

$$\epsilon_{\mathrm{wake}} = \epsilon_f + [(\epsilon_o)_{te}-\epsilon_f]\exp\left(\frac{s_{te}-s}{20\delta_{te}}\right) \qquad (16)$$

In this equation, s_{te} is the nondimensional streamwise position of the trailing edge (measured from the leading edge), and δ_{te} is the sum of the upper and lower surface boundary-layer thicknesses at the trailing edge, where the boundary-layer thickness is defined to be the distance from $\eta=0$ to the point at which $u=0.995u_e$.

Transformed Equations

For laminar flows, the Levy-Lees transformation (see Blottner, 1970) provides independent variables that effectively capture the growth of the boundary layer with increasing streamwise distance from the leading edge of a blade. In addition, the transformed equations reduce to similarity equations at the leading edge. These features facilitate the determination of a numerical solution. An extension of the Levy-Lees transformation, in which the laminar edge viscosity is replaced by an effective turbulent viscosity, was suggested by Werle and Verdon (1980) to accommodate turbulent flows. In this paper, this extension, along with an additional modification for unsteady flows, is applied.

Thus, we define new independent variables ξ, η, and τ according to

$$\xi = \int_0^s \bar{q}ds, \quad \eta = \frac{u_e\sqrt{\mathrm{Re}}}{\sqrt{2\xi}}\int_0^n \rho dn, \quad \text{and } \tau=t \qquad (17)$$

where $\bar{q} = \bar{\rho}_e\bar{u}_e\bar{\mu}_e g$, the overbar indicates the temporal mean value of an edge quantity, and $g = 1+e_o = 1+\epsilon_o/\mu$. The coordinate ξ is a function of s alone. The coordinate η, by contrast, is a function of s, n, and t. We also introduce the new dependent variables

$$F = \frac{u}{u_e}, \quad V = \frac{2\xi}{q}\left(\frac{1}{u_e}\frac{\partial\eta}{\partial t}+F\frac{\partial\eta}{\partial s}+\sqrt{\mathrm{Re}}\,\frac{\rho v}{\sqrt{2\xi}}\right), \quad \text{and } G=\frac{H}{H_e} \qquad (18)$$

After substituting equations (17) and (18) into the viscous layer equations, we find that

$$2\xi\frac{\bar{q}}{q}\frac{\partial F}{\partial\xi}+\frac{\partial V}{\partial\eta}+\frac{\bar{q}}{q}F-\hat{\alpha}\beta_\tau=0, \qquad (19)$$

$$\frac{2\xi}{qu_e}\frac{\partial F}{\partial\tau}+2\xi\frac{\bar{q}}{q}F\frac{\partial F}{\partial\xi}+V\frac{\partial F}{\partial\eta}+\beta_\tau(\hat{\alpha}F+\frac{\alpha}{2}F^2-G)$$
$$+\beta_\xi(F^2-G)-\frac{\partial}{\partial\eta}\left(l\frac{\partial F}{\partial\eta}\right)=0 \qquad (20)$$

and

$$\frac{2\xi}{qu_e}\frac{\partial G}{\partial\tau}+2\xi\frac{\bar{q}}{q}F\frac{\partial G}{\partial\xi}+V\frac{\partial G}{\partial\eta}+\Gamma_\tau(F^2-G)+\Gamma_\xi\left(\hat{\alpha}FG\right.$$
$$\left.+\frac{\alpha}{2}F^2-G\right)+\alpha\frac{\partial}{\partial\eta}\left[(\hat{l}-l)F\frac{\partial F}{\partial\eta}\right]-\frac{\partial}{\partial\eta}\left(\hat{l}\frac{\partial G}{\partial\eta}\right)=0 \qquad (21)$$

where $q=\rho_e u_e\mu_e g$, and the following parameters have been introduced:

$$l = \frac{\rho\mu(1+e)}{\rho_e\mu_e g}, \qquad \hat{l} = \frac{\rho\mu}{\rho_e\mu_e g\mathrm{Pr}}(1+e\mathrm{Pr}/\mathrm{Pr}_T),$$

$$\alpha = u_e^2 T_e^{-1}\left(1+\frac{u_e^2}{2T_e}\right)^{-1}, \qquad \hat{\alpha} = \left(1+\frac{u_e^2}{2T_e}\right)^{-1},$$

$$\qquad (22)$$

$$\beta_\tau = 2\xi(q\hat{\alpha}u_e^2)^{-1}\frac{\partial u_e}{\partial\tau}, \qquad \beta_\xi = 2\xi\bar{q}(q\hat{\alpha}u_e)^{-1}\frac{\partial u_e}{\partial\xi},$$

$$\Gamma_\tau = 2\xi(qu_eH_e)^{-1}\frac{\partial H_e}{\partial\tau}\left(\frac{u_e^2}{2T_e}\right) \text{ and } \Gamma_\xi = 2\xi\bar{q}(q\hat{\alpha}H_e)^{-1}\frac{\partial H_e}{\partial\xi},$$

where $e=\epsilon/\mu$.

Conditions on F, V, and G

In addition to the foregoing equations, the dependent variables F, V, and G must be known functions of ξ, η at an "initial" time, and F and G must be known functions of η and τ at an initial streamwise location. Also, in terms of the transformed variables, the conditions at the edge(s) of the viscous layer, on the blade surface and on the reference wake streakline, cf. equations (7), (8), and (9), have the forms

$$F \to 1 \text{ and } G \to 1 \text{ for } \eta \to \infty, \tag{23}$$

$$F = 0, \ V = 0, \text{ and } G = G_w(\xi, \tau) \text{ or}$$

$$(\partial G/\partial \eta)_w = \frac{-\sqrt{2\xi/\mathrm{Re}}\, q_w(\xi, \tau)}{\rho_e u_e H_e} \text{ for } \eta = 0, \ \xi \le \xi_{te} \tag{24}$$

and

$$V = 0 \text{ for } \eta = 0, \ \xi > \xi_{te}, \tag{25}$$

respectively.

Note that since the boundary layers on the upper and lower surfaces of a blade will generally differ, the upper and lower surface Levy–Lees variables will differ at a blade trailing edge. In the present analysis the upper surface variables are used to continue the calculation into the wake. Thus, the streamwise velocity and enthalpy in the wake must still satisfy equation (23) as $\eta \to \infty$, but $F \to u_e^-/u_e^+$ and $G \to H_e^-/H_e^+$ as $\eta \to -\infty$, where the subscripts $-$ and $+$ refer to the lower and upper sides of the wake, respectively.

For the calculations reported herein the conditions at the initial time are found from the solution of the steady boundary-layer equations subjected to mean or steady inviscid edge conditions and driven by the mean pressure distribution. The transients associated with this approximation are found to die out as the number of temporal periods increases. In addition, it can be shown that the transformed equations reduce to the Falkner–Skan similarity equations at a blade leading edge, if the flow is laminar and steady. Therefore, by setting the streamwise derivatives of the dependent variables equal to zero and starting the unsteady solution near a leading-edge stagnation point, an approximation to the true time-dependent solution can be determined at the inflow boundary. This provides approximate upstream boundary condition information for the solution of the unsteady viscous layer equations.

Numerical Solution Procedure

The partial derivatives in the transformed governing equations are approximated by finite difference expressions. First-order backward differences are applied to approximate streamwise and temporal derivatives; second-order central differences, to approximate normal derivatives. At each streamwise station the streamwise momentum and energy equations are differenced about the nodes of the computational mesh; the continuity equation, about midpoints between adjacent nodes. The streamwise momentum and energy equations contain nonlinear terms, so some method of linearizing the equations must be introduced. At each point in space and time, the equations are linearized about the previous spatial or temporal step and calculations are repeated, continually updating the linearization so that it is about the previous local iteration. This process is continued until the solutions for the flow variables converge to within a specified tolerance level. The finite-difference approximation results in a block tridiagonal system of linear algebraic equations at each step, which is solved using the Thomas block inversion algorithm.

The difference approximation is implemented on a grid that has nonuniform spacings in both the streamwise and normal directions. Uniform time steps are used. The spacings in the streamwise direction are chosen so as to cluster points near

the leading and trailing edges of a blade, with each mesh interval being set equal to a constant times the previous one, according to

$$\Delta s_{l+1} = k_s \Delta s_l \tag{26}$$

where l is the streamwise mesh point index. For the range from the leading edge of the blade to midchord, k_s is set to be greater than one. The grid is then reflected about midchord, so that the streamwise intervals from midchord to the trailing edge are each a constant factor smaller than the preceding ones. The grid is then reflected again (i.e., it becomes the original expanding grid) into the wake, where it is extended approximately five chord lengths downstream.

A stretched grid is employed in the normal direction to capture the large velocity gradients that occur near the wall and to ensure that, for turbulent flow, there are enough points near the wall to adequately resolve the laminar sublayer. Since these requirements are a function of the solution, the grid in the normal direction is calculated by trial and error. The values of η_n and Y^+ are calculated as a part of the solution. Here, n is a normal mesh point index and Y^+ is a Reynolds number based on the friction velocity, $(\tau_\omega/\rho_\omega)^{1/2}$, and the normal distance from the blade. The grid parameters, i.e., the initial spacing $\Delta\eta_1$, the number of points $N_{\max}$, and the multiplier k_n, satisfy

$$\Delta\eta_n = k_n^{(n-1)}\Delta\eta_1, \qquad n = 1, \ldots, N_{\max} \tag{27}$$

These parameters are then adjusted so that the value of η at the edge of the boundary layer is at least 8.0 for laminar flow and at least 12.0 for turbulent flow. For a turbulent flow the value of Y^+ at the first mesh point off the wall is set to be less than 1.0 so that the laminar sublayer can be resolved. Finally, a sufficient number of points are used in the normal direction so that the flow over the entire viscous layer can be resolved accurately. At present, generally, between 50 and 100 points are considered sufficient for this purpose.

The constant time step used for the time integration is based on the frequency of the imposed unsteady excitation and the number of time steps prescribed for each period of oscillation, usually around 50.

Results and Discussion

The foregoing analysis has been developed to predict the unsteady viscous layer flows that arise because of aerodynamic interactions between adjacent blade rows. However, to evaluate this analysis, solutions have first been determined for several simple flow configurations. Thus, we have considered steady laminar flow past a flat-plate airfoil having a prescribed surface heat flux, and unsteady laminar and turbulent flows past flat plates placed in oscillating free streams. After assessing the accuracy of the unsteady viscous analysis, it is applied to the turbine stage, i.e., stator and rotor, investigated experimentally by Dring et al. (1982, 1986). For the calculations described below the Prandtl number, Pr, the turbulent Prandtl number, Pr_T, and the specific heat ratio, γ, have been set equal to 0.72, 0.95, and 1.4, respectively.

Flows Over Flat-Plate Airfoils. A steady flow past a semi-infinite flat plate has been analyzed to assess the ability of the present analysis to predict the wall temperature resulting from a prescribed wall heat flux distribution. The flow conditions and the wall heat flux (q_w) are shown in Fig. 1(a). Here, $q_w = q_w^*/q_{w,\mathrm{Ref}}^*$, the superscript * refers to a dimensionless quantity, and the subscript $-\infty$ refers to the upstream free-stream condition. Note that there is an unheated length aft of the plate leading edge. The flow is laminar and has been calculated using a finite difference grid consisting of 101 uniformly spaced streamwise points with $\Delta s \approx 0.0025$ and 101 variably spaced normal points with $\Delta\eta_1 = 0.025$ and $k_n = 1.02$.
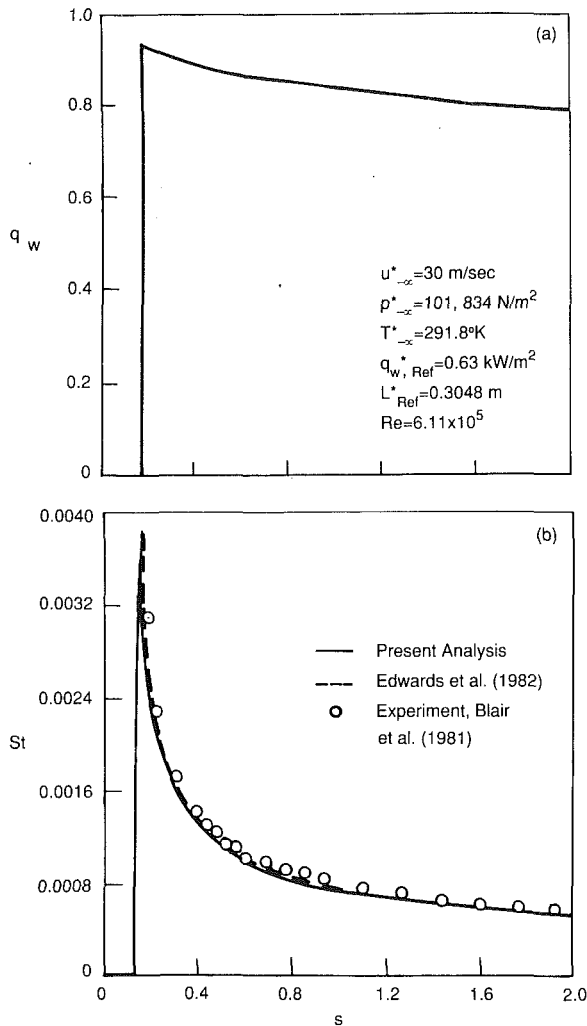
Fig. 1 Steady laminar flow over a heated flat plate: (a) prescribed wall heat transfer rate, (b) predicted Stanton number distribution
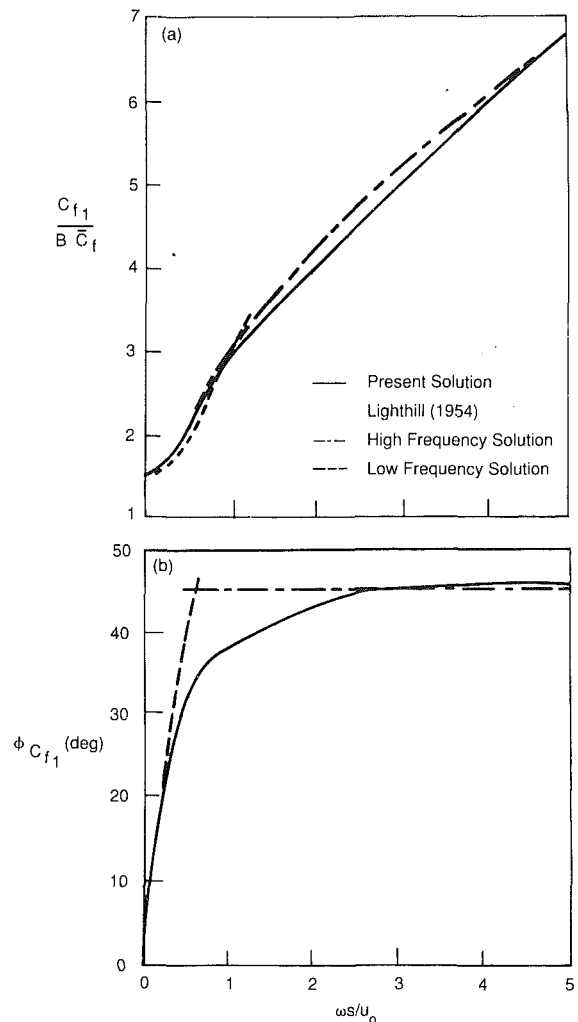

Fig. 2 Laminar flow over a flat plate in an oscillatory stream: (a) amplitude of skin friction fluctuation, (b) phase angle of skin friction fluctuation

The Stanton number (St) is defined as

$$St = \frac{q_w^*}{\rho_{-\infty}^* u_{-\infty}^* C_p^* (T_w^* - T_{0,-\infty}^*)} \qquad (28)$$

where C_p^* is the specific heat of the fluid at constant pressure and $T_{0,-\infty}^*$ is the upstream free-stream total temperature. The computed results for the Stanton number are shown in Fig. 1(b) along with the experimental measurements of Blair et al. (1981) and the finite-difference boundary-layer solution of Edwards et al. (1982). The agreement between the two calculations and the experiment is quite good, and indicates that the present analysis gives accurate predictions of heat transfer effects for steady laminar flow.

A second test case has been analyzed to assess the ability of the present analysis to predict unsteady effects. We consider the unsteady viscous flow over a flat plate that lies fixed in an oscillating free stream. Here,

$$u_e = u_0[1 + B \cos (\omega t)] \qquad (29)$$

where u_0 is the time-averaged streamwise velocity at the edge of the boundary layer, and $u_0 B$ and ω are the amplitude and frequency, respectively, of the fluctuating streamwise velocity. The laminar problem was first considered by Lighthill (1954) who developed analytic solutions for low and high reduced frequencies, i.e., $\omega s/u_0 = \omega^* s^*/u_0^*$, where the distance along the plate, s, is measured from the leading edge. Lighthill's solution indicate that the oscillatory wall shear stress leads the prescribed edge velocity by a phase angle that increases nearly

linearly with reduced frequency at low reduced frequency and by a phase angle that approaches 45 deg at high reduced frequency. Since Lighthill's original paper, these results have been verified numerically by many investigators including Ackerberg and Phillips (1972), McCroskey and Philippe (1975), and Cebeci (1977).

For the specific case considered here, we set $B = 0.15$, $u_0^* = 17.1$ m/s, and $\omega^* = 234.55$ rad/s. The computational mesh consisted of 33 points in the streamwise direction, where the mesh spacing was expanded from an initial Δs of 0.005 using a stretching factor of 1.1, and 41 points in the normal direction, expanded from an initial $\Delta \eta_1$ of 0.05 using a stretching factor of 1.07. Calculations were performed over two temporal periods of the oscillation using forty (40) uniform time steps per period. The steady flow corresponding to $B = 0$ was used as an initial condition, and it was found that transient unsteady behavior disappeared after approximately 40 time steps (one period of the oscillation).

The skin friction can be written as

$$C_f = \frac{\tau_w^*}{\frac{1}{2}\rho_{-\infty}^* u_{-\infty}^{*2}} = \overline{C}_f + C_{f_1}\cos(\omega t + \phi_{C_{f_1}}) + \dots \qquad (30)$$

where τ_w^* is the surface shear stress, the upstream free-stream density $(\rho_{-\infty}^*)$ and velocity $(u_{-\infty}^*)$ are equal to the mean density and velocity at the edge of the viscous layer, and the dots refer
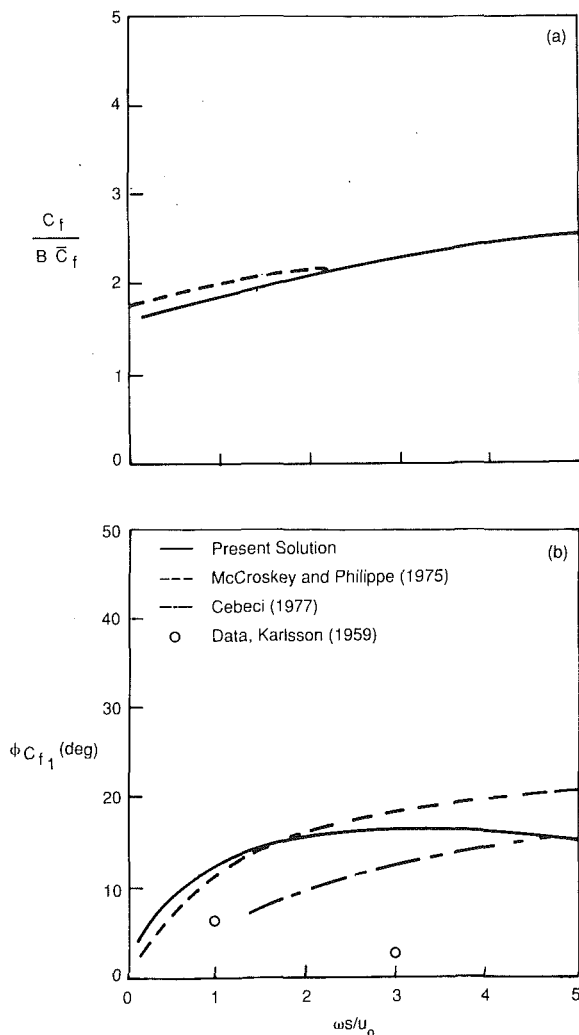
Fig. 3 Turbulent flow over a flat plate in an oscillating stream: (a) amplitude of skin friction fluctuation, (b) phase angle of skin friction fluctuation

to terms of higher order in frequency, which are assumed to be negligible in Lighthill's analysis. Numerical predictions for the amplitude C_{f_1} and phase angle $\phi_{C_{f_1}}$ of the skin friction fluctuation are shown in Fig. 2 along with predictions based on Lighthill's asymptotic solutions. The present results are in very good agreement with the asymptotic results at the extremes of the reduced frequency range considered. Furthermore, the present results are in very close agreement with those determined by Cebeci (1977) for incompressible unsteady boundary layers.

The turbulent version of the foregoing problem has been studied numerically by McCroskey and Philippe (1975) and Cebeci (1977), and experimentally by Karlsson (1959). We consider the specific case in which $u_0^* = 5.33$ m/s, $B = 0.352$, and $\omega^* = 25.13$ rad/s. Predictions for the amplitude and phase of the fluctuating skin friction are shown in Fig. 3, along with the numerical results of McCroskey and Philippe (1975) and Cebeci (1977) and Karlsson's data. The Cebeci–Smith turbulence model with an unsteady correction to the pressure gradient term was used in each of the analyses. The results indicate that the phase shift, $\phi_{C_{f_1}}$, is much smaller for turbulent flow than it is for laminar flow. However, the numerical solutions are only in qualitative agreement over the range of the reduced frequencies considered. Moreover, they do not match the two data points. The lack of agreement between the numerical predictions and the experimental measurements for this simple

flow is somewhat surprising. It is most likely due to the use of a turbulence model that is not adequate for unsteady flows and, perhaps, to experimental uncertainties. The reasons for the discrepancies between the various numerical predictions are not clear at the present time.

Turbine Stator and Rotor. We proceed to analyze the flows along the stator vanes and rotor blades of the turbine stage investigated experimentally by Dring et al. (1982, 1986). The test configuration consisted of a row of 22 stator vanes followed by a row of 28 rotor blades. Two different axial gap distances between the adjacent rows, i.e., 15 and 65 percent of blade chord, were investigated. The suction and pressure surfaces of the stator and rotor blades were instrumented to measure blade-surface pressures and temperatures. Electrically heated metal foil strips attached to the blade surfaces provided uniform heat flux distributions.

Some of the pressure taps were designed to measure the time-averaged (mean) pressure while other high response pressure transducers were designed to measured the fluctuating pressure. The latter measurements were represented and tabulated as a series of Fourier coefficients. There was an insufficient number of transducers to determine the pressure gradient fully along the entire stator and rotor surfaces for use in the boundary-layer calculation. However, numerical results that were determined using the steady potential flow analysis of Caspar et al. (1980) were found to compare quite well with the available mean pressure data. Therefore, the pressure distributions determined from this inviscid analysis were used to provide the mean surface pressure distributions required for the boundary-layer calculations. The experimental Fourier coefficients of the fluctuating pressures were spline fit to provide estimates of the unsteady surface pressure distributions. These estimates were then superimposed on the mean pressure distributions to provide the unsteady pressure distributions used in the unsteady viscous calculations.

The viscous layer equations require that the edge velocity and enthalpy as well as the pressure be known functions of the streamwise distance, s, and time, t, but the surface pressure at discrete points is the only quantity available from the data. Therefore, the Euler equations have been solved along a blade surface to determine the edge velocity and enthalpy that correspond to the measured time-varying pressure distribution along the surface.

Results for the suction and pressure surfaces of the stator and rotor blades are presented below for the 15 percent gap case. The following free-stream and reference conditions were specified for the stator and rotor:

	Stator			Rotor	
$M_{-\infty}$	=	0.0704	$M_{-\infty}$	=	0.1065
$p_{-\infty}^*$	=	100,979 N/m	$p_{-\infty}^*$	=	100,500 N/m
$T_{-\infty}^*$	=	288.1 K	$T_{-\infty}^*$	=	288.2 K
L_{ref}^*	=	0.15066 m	L_{ref}^*	=	0.16105 m
Re	=	247,156	Re	=	397,667

where M is the Mach number, L_{ref}^* is the axial blade chord, and the subscript $(-\infty)$ refers to the upstream free-stream state. The wall heat flux, q_w^*, was 0.00503 kW/m² for both the stator and rotor. The rotor blade passing frequency was 1202.6 rad/s, which corresponds to a rotation at 410 rpm with 28 rotor blades passing each stator vane during one revolution. Since there are only 22 stators, the stator passing frequency as seen from the rotor is 943.7 rad/s. Thus, the reduced frequencies (based on blade chord) of the unsteady flows in the stator and rotor are 5.94 and 5.35, respectively.

Calculations were performed for the boundary layers on both the suction and pressure surfaces of the stator and rotor blades. Numerical grids for these surfaces were constructed as detailed above. The normal grid for both the stator and the

$$p = \bar{p} + \sum_{n=1}^{\infty} p_n \cos(n\omega t + \phi_{p_n}) \qquad (31)$$

where $\bar{p}$ is the time-averaged pressure and p_n is the amplitude of the nth Fourier component of the pressure. For comparisons with experimental data we also introduce the time-averaged pressure coefficient, i.e., $\bar{C}_p = (\bar{p} - \bar{p}_{te})/\left(\dfrac{1}{2}\,\bar{\rho}_{te}\bar{V}_{te}^2\right)$, where

$V = (u^2 + v^2)^{\frac{1}{2}}$ is the local flow speed. Similarly, the Stanton number can be expressed in the form

$$\text{St} = \overline{\text{St}} + \sum_{n=1}^{\infty} \text{St}_n \cos(n\omega t + \phi_{\text{St}_n}) \qquad (32)$$

The experimental values of $\bar{C}_p$ and p_n serve as input to the boundary-layer calculations described below, and these calculations are used to predict the Stanton numbers $\overline{\text{St}}$ and St_n.

Numerical results compare reasonably well with the measurements in regions where the flow could be identified as either laminar or fully turbulent, but not as well in transition regions. In each case, the amplitudes of the Fourier terms for pressure and Stanton number decreases rapidly with increasing n. Determination of the locations of the beginning and end of the transition region was made from hot-film measurements and the measured Stanton numbers. Although the actual locations varied with time, they were assumed to be stationary for the calculations. The locations specified were $s_1 = 0.85$ and $s_2 = 1.05$ for the stator suction surface, $s_1 = 0.85$ and $s_2 = 2.5$ for the stator pressure surface, $s_1 = 0.01$ and $s_2 = 1.00$ for the rotor suction surface, and $s_1 = s_2 = 0$ (the leading edge) for the rotor pressure surface. Uncertainties concerning these locations, as well as the fact that the transition and turbulence models were not constructed for unsteady flow with heat transfer, account, perhaps, for some of the discrepancies between the calculations and the experimental data.

Stator. Results for the stator suction surface, including mean and fluctuating surface pressure and Stanton number distributions, are shown in Fig. 4. The unsteadiness on the stator is caused by the static pressure or potential flow variations associated with the downstream rotor. Since these attenuate rapidly with axial distance upstream of the rotor, unsteady effects on the stator blade are most pronounced near the trailing edge. The mean surface pressure coefficient and the amplitudes of the first three Fourier pressure terms are shown in Figs. 4(a) and 4(b), respectively. The results from the steady and unsteady boundary-layer calculations are shown in Figs. 4(c) and 4(d). Figure 4(c) contains a plot of the mean Stanton number and the corresponding unsteady envelope, along with the measured mean data. The envelope was constructed by adding to and subtracting from the mean Stanton number the sum of the amplitudes of the Fourier coefficients. As such, it is only an approximation to the envelope that would be constructed from the maximum and minimum Stanton numbers at each streamwise station. The magnitudes of the Fourier coefficients normalized by the mean Stanton number (Fig. 4d) indicate that the unsteady heat transfer effects are concentrated near the trailing edge of the stator vane, and that the second and third-harmonic responses are small compared to the first-harmonic response at the rotor blade passing frequency.

An experimental investigation by Lokay and Trushin (1970) and a theoretical investigation by Telionis (1981) indicate that unsteady pressure effects could increase the mean heat transfer rate along airfoil surfaces over the rate that would occur for the same airfoil operating in a steady flow. In order to test this hypothesis for the present configuration, a steady calculation was performed using the mean pressure distributions as input. It was found that the Stanton number distributions
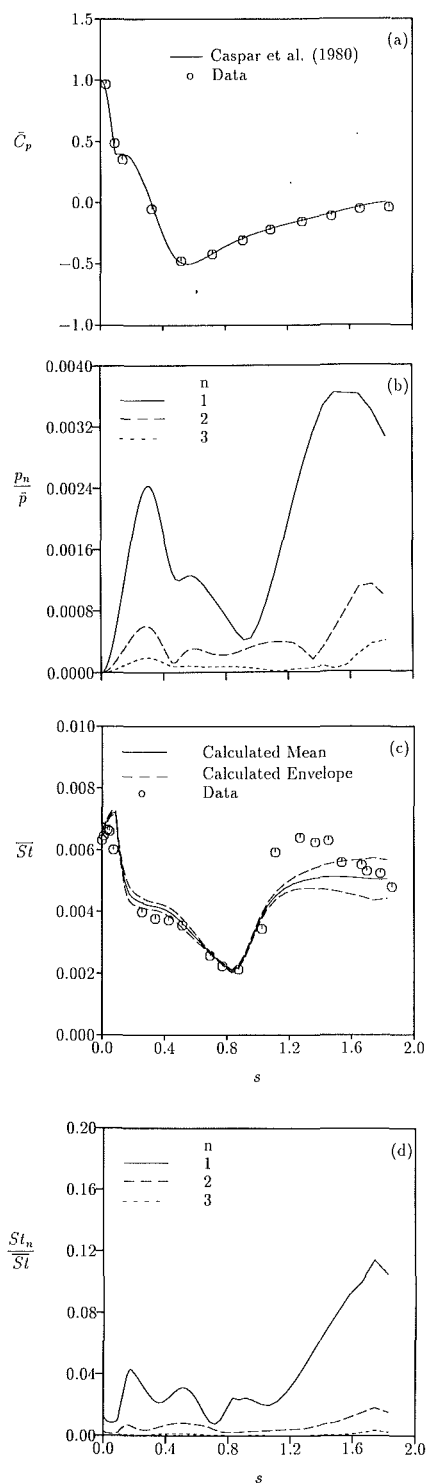
Fig. 4 Flow over suction surface: (a) mean pressure distribution, (b) first three Fourier components of pressure, (c) mean Stanton number and unsteady envelope, (d) first three Fourier components of Stanton number

rotor surfaces consisted of 41 points across the boundary layer, starting from an initial spacing of $\Delta\eta_1 = 0.002$ and expanding into the flow with a stretching factor of 1.2. Nonuniform streamwise grid spacings were used. In all cases, 100 points were used on a blade surface. The initial streamwise spacing was approximately 0.0006, and the streamwise stretching factor was 1.05. All unsteady calculations were performed over three temporal periods using 50 uniform time-steps per period.

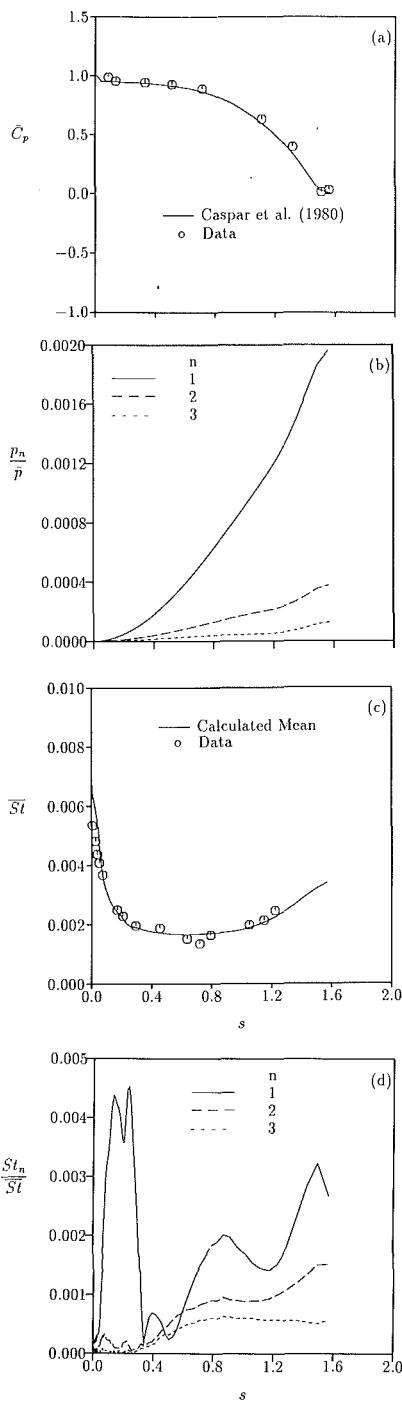The pressure can be expressed as a Fourier series, i.e.,

Fig. 5 Flow over stator blade pressure surface: (a) mean pressure distribution, (b) first three Fourier pressure components, (c) mean Stanton number, (d) first three Fourier components of Stanton number

Fig. 6 Flow over rotor blade suction surface: (a) mean pressure distribution, (b) first three Fourier pressure components, (c) mean Stanton number, (d) first three Fourier components of Stanton number

determined from this steady calculation differed only slightly from the mean Stanton number distributions determined from the unsteady calculation. This indicates that the unsteady pressure did not cause a noticeable increase in the mean heat transfer rate along the stator suction surface. The experimental measurements also bear this out because the mean Stanton number was found to be insensitive to the axial spacing between the stator and rotor.

Similar results for the stator pressure surface are shown in Fig. 5. Note that the scales uses in Figs. 4 and 5 for $p_n/\bar{p}$ and $St_n/\overline{St}$ are different. As mentioned above, the data indicated the presence of a large transition region along the stator pressure surface. The calculated mean Stanton number distribution

is shown along with the measured data in Fig. 5(c). The unsteady pressure fluctuations had an insignificant effect on the heat flux along the pressure surface; therefore, no envelope for the Stanton number is shown in Fig. 5(c). The calculated results compare very well with the measured data over the entire pressure surface, indicating that the transition and turbulence models used in the calculation are adequate if unsteady disturbances are small. Note that the maximum value of the first Fourier coefficient of the Stanton number (Fig. 5d) is less than 0.5 percent of the mean value, indicating that there is very little effect of the pressure field associated with the moving downstream rotor on the viscous layer along the pressure surface of the stator. As was the case for the stator suction surface,
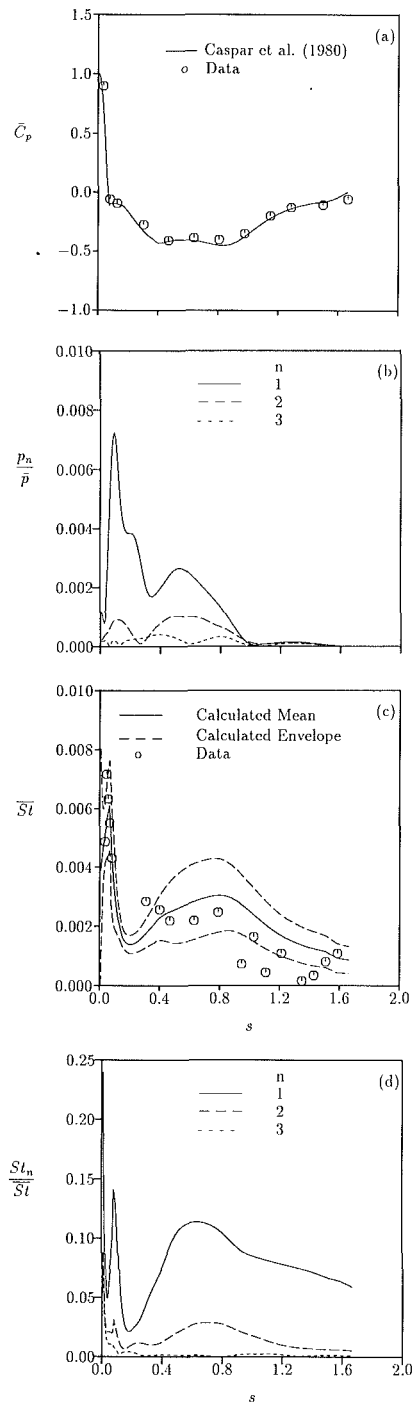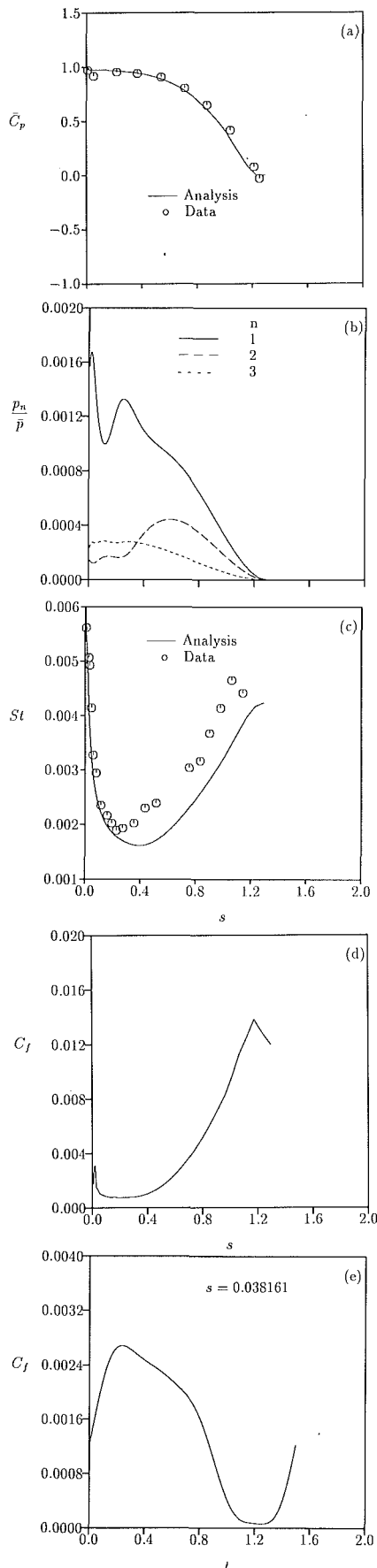
Fig. 7 Flow over rotor pressure surface: (a) mean pressure distribution, (b) first three Fourier pressure components, (c) Stanton number based on steady calculation, (d) skin friction results from steady calculation, (e) skin friction at station upstream of reverse flow region

the Stanton number distribution calculated with the steady boundary-layer analysis using the mean pressure distribution as input is identical to the mean Stanton number distribution calculated with the unsteady boundary-layer analysis.

Rotor. The rotor blades encounter a much more complicated unsteady flow field than the stator vanes because the rotor is affected by the viscous wakes coming off the stator as well as the potential flow disturbances associated with the stator. Thus each rotor blade·sees time-dependent total pressure and total temperature variations, including pockets of high free-stream turbulence, in addition to time-dependent static pressure variations.

The present unsteady calculations were performed by assuming that the effect of the upstream stator on the rotor blades was confined to the measured static pressure fluctuations. Thus, because of a lack of experimental information, we assumed that there was no increase in free-stream turbulence or change in total pressure or total temperature resulting from the stator/rotor interaction. Comparisons between steady flow predictions and the time-averaged data indicate that the latter effects do not have a very significant influence on the mean surface pressures.

The mean pressure distribution on the suction surface and the first three Fourier pressure coefficients are shown in Figs. 6(a) and 6(b). Note that unsteady pressure effects are most severe near the leading edge, the second and third Fourier components are small compared to the first, and the amplitudes of the pressure fluctuations associated with the rotor are greater than those for the stator. The results of the viscous layer calculation are shown on Figs. 6(c) and 6(d). The experiment indicates a large transition region along the suction surface, but it is difficult to determine the precise location of this region from the data. The unsteady pressure fluctuations die out as the trailing edge is approached, but the Stanton number fluctuations (Fig. 6d) persist.

The mean pressure and the spline-fit Fourier pressure coefficients for the pressure surface of a rotor blade are shown in Figs. 7(a) and 7(b), respectively. As on the rotor suction surface, unsteady pressure effects are most severe over the forward part of the blade. The data indicate that the flow is fully turbulent over most of the blade pressure surface, so instantaneous transition at the leading edge was specified for the boundary-layer calculations.

The unsteady boundary-layer calculation indicated flow reversal $(C_f < 0)$ at a point just downstream of the leading edge, and hence, could not be continued beyond this point. Instead, we applied a steady boundary-layer calculation using the experimental mean pressure distribution to provide the Stanton number and skin friction distributions shown in Figs. 7(c) and 7(d), respectively. The predicted steady Stanton number is in reasonable agreement with the measured data. The steady flow does not separate, but the skin friction does dip toward zero at a point just downstream of the leading edge, as indicated in Fig. 7(d).

If the unsteady skin friction is negative, instantaneous flow reversal could occur. This is the case for the unsteady boundary layer on the rotor pressure surface. Figure 7(e) shows a plot of the skin friction versus time at the streamwise station just upstream of the one at which C_f becomes less than zero for part of the cycle. It can be seen that, although the mean skin friction is much greater than zero, the instantaneous value dips almost to zero at $t \approx 1.2$. At the next station the instantaneous skin friction dipped below zero, indicating reverse flow, and forcing termination of the unsteady calculation. This result implies that the actual flow may contain small regions of reverse flow over part of a cycle. Upstream of the point at which flow reversal was predicted, the steady and unsteady boundary-layer calculations indicated no difference between the steady and the temporal mean value of the unsteady Stanton numbers.

Conclusions

An unsteady, compressible boundary-layer analysis has been described in which the governing equations are solved in terms of similarity-type variables to effectively capture the growth of the viscous layer. Results from this analysis were shown to compare quite well to previous numerical results for laminar steady and unsteady flows over flat-plate airfoils. For unsteady turbulent flow over a flat plate, the present numerical results and those obtained by previous investigators show similar trends, but are not in good quantitative agreement. In addition, the numerical results differ considerably from available data. This situation points, perhaps, to the need for better turbulence and transition models for unsteady flows and should be investigated in more detail in the future.

Finally, the analysis was applied to low-speed flows over stator and rotor blades, and predictions were compared with experimental measurements. The unsteady excitation (pressure) and response (Stanton number) at the fundamental or blade passing frequency were much more severe than the excitation and response at integer multiples of the blade passing frequency. Moreover, it was found that the mean heat transfer rates calculated using the unsteady boundary-layer analysis and the heat transfer rates calculated using a steady analysis were in close agreement. Thus, the unsteady pressure effects, studied herein, did not lead to enhanced mean heat transfer rates along the stator and rotor blade surfaces.

Acknowledgments

References

Ackerberg, R. C., and Phillips, J. H., 1972, "The Unsteady Laminar Boundary Layer on a Semi-infinite Flat Plate Due to Small Fluctuations in the Magnitude of the Free-Stream Velocity," *Journal of Fluid Mechanics*, Vol. 51, pp. 137–157.

Blair, M. F., Bailey, D. A., and Schlinker, R. H., 1981, "Development of a Large-Scale Wind Tunnel for the Simulation of Turbomachinery Airfoil Boundary Layers," ASME *Journal of Engineering for Power*, Vol. 103, pp. 678–687.

Blottner, F. G., 1970, "Finite Difference Method of Solution of the Boundary-Layer Equations," *AIAA Journal*, Vol. 18, pp. 193–205.

Caspar, J. R., Hobbs, D. E., and Davis, R. L., 1980, "Calculation of Two-Dimensional Potential Cascade Flow Using Finite Area Methods," *AIAA Journal*, Vol. 18, pp. 103–109.

Cebeci, T., 1977, "Calculation of Laminar and Turbulent Boundary Layers for Two-Dimensional Time-Dependent Flows," NASA CR-2820.

Cebeci, T., and Keller, H. B., 1970, "On the Computation of Unsteady Turbulent Boundary Layers," in: *Recent Research on Unsteady Boundary Layers*, E. A. Eichelbrenner, ed., Academic Press, New York.

Cebeci, T., and Smith, A. M. O., 1974, *Analysis of Turbulent Boundary Layers*, Academic Press, New York.

Chang, K. C., Bui, M. N., Cebeci, T., and Whitelaw, J. H., 1986, "The Calculation of Turbulent Wakes," *AIAA Journal*, Vol. 243, pp. 200–201.

Dhawan, S., and Narashima, R., 1958, "Some Properties of Boundary-Layer Flow During the Transition From Laminar to Turbulent Motion," *Journal of Fluid Mechanics*, Vol. 3, pp. 418–436.

Dring, R. P., Joslyn, H. D., Hardin, L. W., and Wagner, J. H., 1982, "Turbine Rotor–Stator Interaction," ASME *Journal of Engineering for Power*, Vol. 104, pp. 729–742.

Dring, R. P., Blair, M. F., Joslyn, H. D., Power, G. D., and Verdon, J. M., 1986, "The Effects of Inlet Turbulence and Rotor/Stator Interactions on the Aerodynamics and Heat Transfer of a Large-Scale Rotating Turbine Model," NASA CR-4079.

Edwards, D. E., Carter, J. E., and Werle, M. J., 1982, "Analysis of the Boundary Layer Equations Including a New Composite Coordinate Transformation—The ABLE Code," Report 81-30, United Technologies Research Center, East Hartford, CT.

Karlsson, S. K. F., 1959, "An Unsteady Turbulent Boundary Layer," *Journal of Fluid Mechanics*, Vol. 5, pp. 622–636.

Lighthill, M. J., 1954, "The Response of Laminar Skin Friction and Heat Transfer to Fluctuations in the Stream Velocity," *Proceedings of the Royal Society*, Vol. 224A, pp. 1–23.

Lokay, V. I., and Trushin, V. A., 1970, "Heat Transfer From the Gas and Flow-Passage Elements of a Rotating Gas Turbine," *Heat Transfer—Soviet Research*, Vol. 2, No. 4, pp. 108–115.

McCroskey, W. J., and Philippe, J. J., 1975, "Unsteady Viscous Flow on Oscillating Airfoils," *AIAA Journal*, Vol. 13, pp. 71–79.

Telionis, D. P., 1981, *Unsteady Viscous Flows*, Springer Series in Computational Physics, Springer-Verlag, New York.

Werle, M. J., and Verdon, J. M., 1980, "Viscid/Inviscid Interaction Analysis for Symmetric Trailing Edges," Report R79-914493-5, United Technologies Research Center, East Hartford, CT.

Yuhas, L. J., 1981, "An Optimization Technique for the Development of a Two-Dimensional Turbulent Boundary Layer Model," MS Thesis, Lehigh University, Bethlehem, PA.

K.-H. Rohne
Head of Turbocharger Development.

M. Banzhaf
Compressor Development.

ABB Turbo Systems Ltd.,
Baden, Switzerland

Investigation of the Flow at the Exit of an Unshrouded Centrifugal Impeller and Comparison With the "Classical" Jet-Wake Theory

L2F measurements of the flow at the exit of modern unshrouded centrifugal impellers with backswept blades yield a much more uniform velocity profile compared to former measurements on impellers with radial blading. Further evaluations show that the "classical" jet-wake theory assuming an isentropic jet and a wake flow congruent with the shape of the blade at the impeller exit needs correction in order to obtain meaningful results when interpreting thermodynamic measurements on centrifugal compressor stages.

Introduction

For the assessment of a centrifugal compressor stage and its further optimization, it is fundamentally essential to know where in the stage the losses occur and what the nature of the mechanisms is that leads to these drops in efficiency. When information about this has been obtained, the next step in development is to perform purposeful work on improving the components concerned.

In this connection, special significance is attached to the distinction between impeller and diffuser losses. The flow leaving the impeller of a centrifugal compressor is far from uniform. The mixing of this disturbed flow mainly takes place in the vaneless space between the impeller trailing edge and the diffuser vane leading edge and it generates further losses.

It is certainly appropriate to attribute the flow losses occurring in this region to the diffuser, whereas the mixing losses must be attributed to the impeller since they are produced there. The problem is to split these two locally inseparable phenomena within a theoretical model in an admissible manner.

One possibility for handling this problem is to apply the jet-wake calculation model according to Japikse (1985). However, there are clear differences between the results of the jet-wake calculation and the results of L2F measurements of the flow field at impeller exit of modern unshrouded impellers with backswept blading.

Such L2F measurements have been performed within the scope of the present work. Consequently correcting factors were derived from the measurements and implemented in the calculation model to obtain a more realistic picture of the flow phenomena at impeller exit.

Calculating the Impeller Losses

The division between impeller and diffuser losses can be

performed at the moment when a clear definition for the thermodynamic state at the impeller exit is found. Certainly one basis for this is the measurement of the static pressure p_2 from which the other thermodynamic values can be derived. This method is incorrect in that the mixing losses mentioned in the introduction cannot be allowed for because they occur in the vaneless space after the impeller and therefore are not included in the measurement and calculation. With this method they would wrongly be attributed to the diffuser.

Thus a theoretical model is needed by which the thermodynamic values at impeller exit can be corrected in the right manner.

One possibility is to use a calculation method called here the "classical" jet-wake model. This calculation method is based on the considerations of Dean and Senoo (1960) and the comprehensive investigations of Eckardt (1977). Japikse put it in simple equations and presented it in detail (1985, 1986).

The basic idea of the model is that the impeller exit flow can be divided into a jet and a wake zone; see Fig. 1. This idea is supported by the results of measurements presented by Eckardt and others in their works.

An example of the velocity distribution measured by Eckardt is shown in Fig. 2. In the measured profile two zones with quite different velocity levels can clearly be distinguished. This significant distribution suggests the theory that the jet zone is an isentropic core flow with high velocities and that all the losses occurring in the impeller can be attributed to the wake zone. The additional mixing loss after the impeller can then be calculated by balancing these two zones of flow.

The "Classical" Jet-Wake Theory

The assumptions of this theory are as follows:
  (a) The jet is isentropic.
  (b) The wake contains all impeller losses; it leaves the impeller congruent with the blading ($\beta_{2F} = \beta_{2B}$).
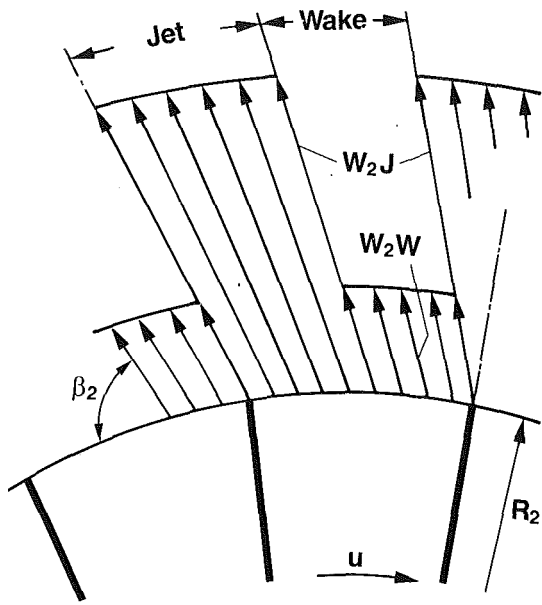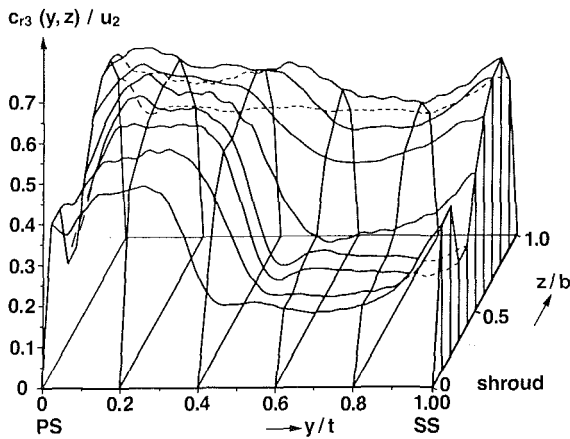 (c) The mass flow fraction of the wake is about 15–25 percent.

Fig. 1   Jet and wake zones at impeller exit

Plotter evaluation of the absolute velocity distribution
c_{r3} (y, z)/u_2 after a blade channel of an impeller,
$R/R_2 = 1.017$

Fig. 2   Impeller exit flow according to Eckardt (1977)

$$\delta = \frac{4 \cdot V_{OT}}{D_2^2 \cdot u_2}$$

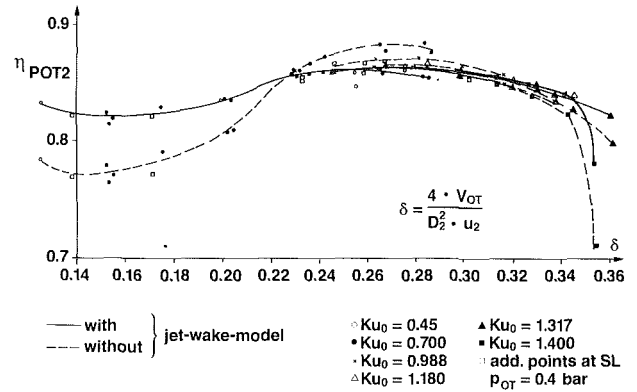| —— with	} jet-wake-model	○ $Ku_0 = 0.45$	▲ $Ku_0 = 1.317$
--- without		● $Ku_0 = 0.700$	■ $Ku_0 = 1.400$
		· $Ku_0 = 0.988$	⌐ add. points at SL
		△ $Ku_0 = 1.180$	$p_{OT} = 0.4$ bar

Fig. 3   Impeller efficiencies with and without jet-wake model (calculation model already modified as illustrated later in this paper)

In order to use this theory, the static pressure p_2 at the impeller exit must be measured; in addition the total states at stage inlet and exit must be known. The following equations apply to the jet:

$$T_{2J} = T_{0T} * (p_2/p_{0T})^{\frac{\kappa-1}{\kappa}} \tag{1}$$

$$\rho_{2J} = p_2/(R * T_{2J}) \tag{2}$$

$$w_{2J} = \sqrt{u_2^2 - 2c_p(T_{2J} - T_{0T})} \tag{3}$$

Thus the relative velocity in the jet can easily be calculated. Equation (3) implies that there is no prewhirl at the impeller inlet.

The following equations apply to the wake:

$$p_{2w} = p_{2J} = p_2$$
$$\beta_{2F} = \beta_{2B}$$

The mixing of the two zones takes place directly at the impeller exit observing the conservation of momentum in circumferential and radial direction, continuity, and the conservation of energy.

The complete system of equations is very extensive, and is presented and discussed in detail by Japikse (1985). As a result of the calculations, the jet, the wake, and the mixed-out state are completely defined. Especially the corrected static values p_{2*} and T_{2*} (* = mixed out) are known, giving the possibility for an improved calculation of the impeller efficiency.

The effect of applying that calculation method is illustrated in Fig. 3. It is obvious that the model, apart from correcting

---

Nomenclature

A = area
a = speed of sound
c = absolute velocity
c_p = specific heat
D = diameter
F_{uw} = circumferential velocity factor wake = c_{u2w}/c_{u2J}
Ku_o = circumferential Mach number = u_2/a_{0T}
$\dot{m}$ = mass flow
p = pressure
PS = blade pressure side
R = radius, gas constant
SS = blade suction side
T = temperature
t = pitch
Tu = degree of turbulence

u = circumferential velocity
$\dot{V}$ = volume flow
$\dot{V}_{rel}$ = relative volume flow = $(\dot{V} - \dot{V}_{SL})/(\dot{V}_{CH} - \dot{V}_{SL})$
w = relative velocity
z/b = relative width
α = absolute flow angle measured from tangential direction
β = relative flow angle, blade angle measured from tangential direction
δ = flow coefficient $\delta = 4V_{OT}/(D_2^2 * u_2)$
η = efficiency
κ = ratio of specific heats
ρ = density

Subscripts

$0T$ = compressor inlet total
2 = impeller exit static
$2*$ = impeller exit mixed-out static
$2T$ = impeller exit total
3 = diffuser inlet
B = blade
CH = choke
F = flow
is = isentropic
J = jet
m = in meridional direction
p, pol = polytropic
r = in radial direction
SL = surge line
u = in circumferential direction
w = wake

Table 1   Description of impeller A

Geometry:
- Impeller exit diameter   350 mm
- Blade angle at impeller exit   70 °
- Number of main blades   10
- Number of splitter blades   10

Operating conditions at K_{uo}=1.255 and $\dot{V}_{rel}$=0.1:
- Stage pressure ratio total-
  to-total   3.3
- Rotational speed   400 s-1
- Relative Mach number at
  impeller inlet   0.96
- Absolute Mach number at
  impeller exit   0.95

Table 2   Performance data of the test rig

- Max. power   1.5 MW
- Max. speed   32000 min^{-1}
- Max. volume flow   7 m^3/s
- Intake pressure   0.4-1.5 bar
- Max. pressure ratio   6

Fig. 4   Impeller A

Fig. 5   Layout of the installation: upper floor from left to right: stabilizing chamber, compressor, torque-measuring shaft and planetary gearing, asynchronous motor

the impeller efficiency, balances the characteristics quite well. By using this model, different corrected speed lines (full lines) fit very closely together for the whole volume range, just as expected as long as Reynolds and Mach number influences are negligible.

New Measurements on Impellers With Backswept Blading

Applying the "classical" jet-wake theory described in the preceding chapter to measurements on modern impellers, doubts arose, as time went by, on the reliability of the calculation method; in some cases diffuser and impeller characteristics were obtained that did not appear to be fully credible. For that reason it was decided that the impeller exit flow of modern compressors should be investigated by using up-to-date measuring methods (L2F) in order to check the fundamentals of the theory. These measurements were performed on two similar impellers referred to hereafter as impeller A and impeller B. As an example impeller A is shown in Fig. 4 and described in Table 1.

With both impellers, L2F measurements of the flow field at the impeller exit were performed at different circumferential Mach numbers and different throttling conditions. The test bed and some of the tests have briefly been described by Wittwer and Küpfer (1986). Figure 5 shows the layout of the installation, and Table 2 gives some performance data of the test rig.

In Fig. 6 the measuring position can be seen; Figs. 7–9 show velocity distributions of impeller B for $Ku_o = 1.255$ and medium throttling condition of the compressor.

It is conspicuous that the velocity profiles are much more equalized than those of Eckardt's measurements (Fig. 2). Especially the wake zone is not so sharply defined and the circumferential components seem to be almost equalized in the jet and the wake. In any case $c_{u2w} < c_{u2J}$ is valid.

The profiles obtained were evaluated numerically, a mean flow value being determined in each case for the jet and the wake zone. Jet and wake were distinguished by the following criterion: Wake exists where the local value of the meridional component is less or equal to 90 percent of the global mean value. These points are marked by black dots in Figs. 10 and 11. It can be seen that this choice is well correlated to the
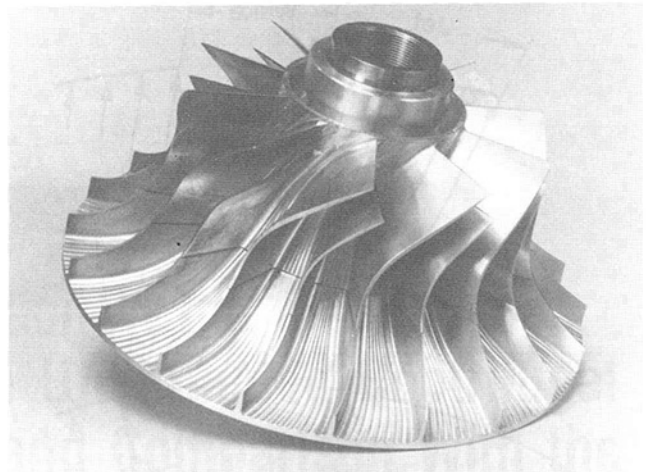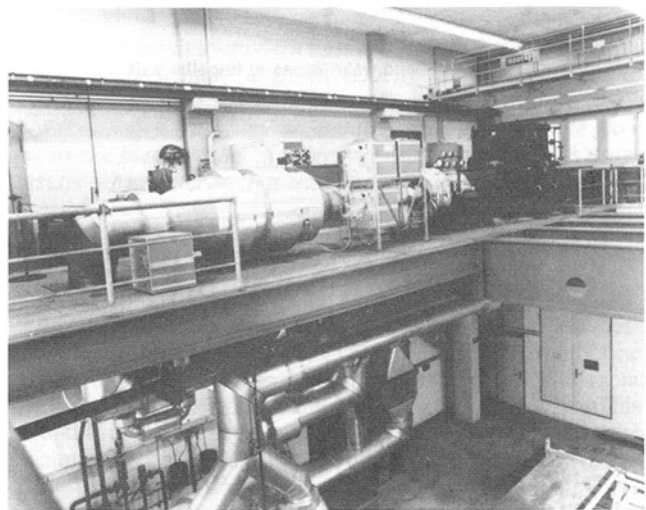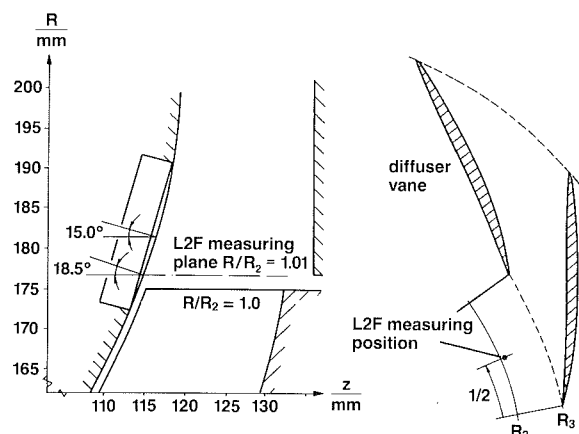
Fig. 6   Measuring position at impeller exit

distribution of the degree of turbulence, i.e., zones of low c_{m2} velocities coincide very well with zones of high degrees of turbulence.

The rear wake zone (hub wake) was excluded from the integration, for it is caused by a contour step from the impeller hub to the casing and therefore bears little relation to the real flow at the impeller exit (see also Fig. 6).

W/U2

Distribution of the relative velocity w/u_2
Ku_0	1.255	Volume flow $\dot{V}_{OT}$ 4.4
R/R_2	1.01	Diffuser position $t/2$

Fig. 7 Relative velocity at impeller exit referred to the circumferential velocity (impeller B)

Cm/U2

Distribution of the meridional component c_m/u_2
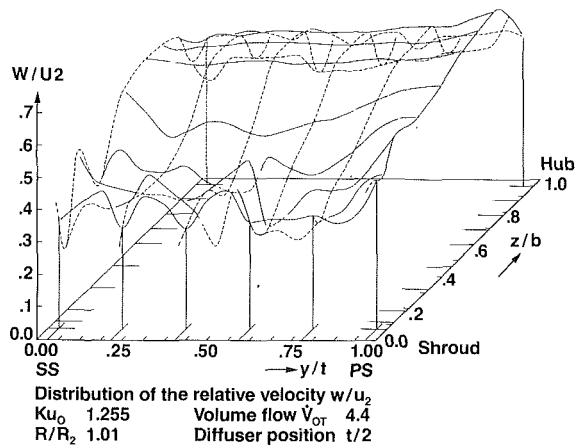|		
Ku_0	1.255	Volume flow $\dot{V}_{OT}$ 4.4
R/R_2	1.01	Diffuser position $t/2$
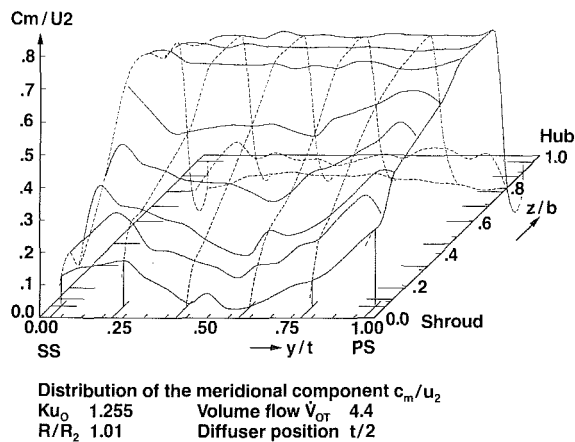
Fig. 8 Meridional velocity at impeller exit (impeller B)

Cu/U2

Distribution of the circumferential component c_u/u_2
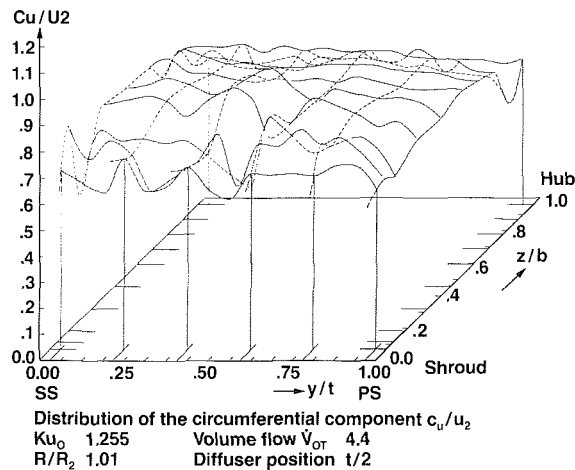|		
Ku_0	1.255	Volume flow $\dot{V}_{OT}$ 4.4
R/R_2	1.01	Diffuser position $t/2$

Fig. 9 Circumferential velocity at impeller exit (impeller B)

Figure 12 shows the numerical evaluation of the jet and wake zones together with global averaging. The results are area averaged values.

If the results of the L2F measurements are compared (after a slight corrective calculation because of detected measuring errors) to the velocity vectors of the jet-wake model, it is found that this model coincides quite well with the mixed-out state, but does not reflect the jet and wake components exactly (Fig. 13).

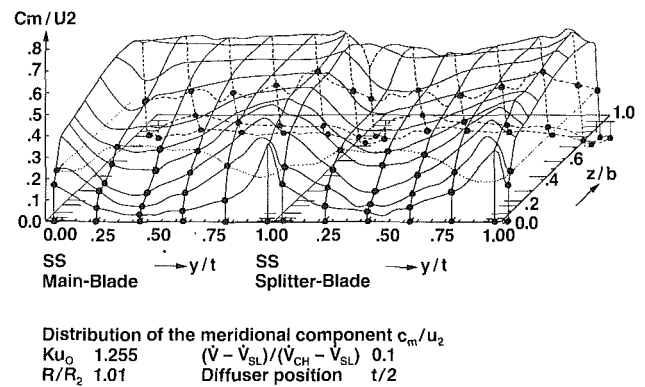This permits one to suspect that the "classical" model may

Cm/U2

Distribution of the meridional component c_m/u_2
Ku_0	1.255	$(\dot{V} - \dot{V}_{SL})/(\dot{V}_{CH} - \dot{V}_{SL})$ 0.1
R/R_2	1.01	Diffuser position $t/2$

Fig. 10 Wake zones in the c_m distribution (impeller A)

Tu

Distribution of the degree of turbulence T_u
Ku_0	1.255	$(\dot{V} - \dot{V}_{SL})/(\dot{V}_{CH} - \dot{V}_{SL})$ 0.1
R/R_2	1.01	Diffuser position $t/2$
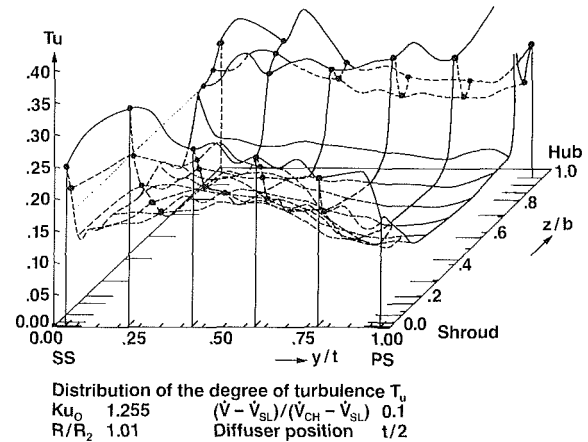
Fig. 11 Wake zones and degree of turbulence (impeller A)

L2F Velocity Measurement

Results of Integration
Ku_0	1.255	$(\dot{V} - \dot{V}_{SL})/(\dot{V}_{CH} - \dot{V}_{SL})$ 0.1
R/R_2	1.01	Diffuser position $t/2$

Jet-Wake-Zones

Extrapolationfactors for CM, CU : 0.01 0.01
Definitionfactor for wake : 0.90
Circumferential velocity U2 in m/s : 438.944

Area Mean Value		Global	Jet	Wake
C2	in m/s:	377.197	387.266	355.888
ALFA 2	in deg:	25.070	29.768	15.127
W2	in m/s:	198.820	220.112	153.757
BETA 2	in deg:	56.460	60.941	46.975
CM 2	in m/s:	160.712	191.309	95.953
CU 2	in m/s:	337.534	335.680	341.457
CR 2	in m/s:	156.347	186.338	92.868
Area	m**2:	0.02041	0.67913	0.32087
Mass Flow in kg/s:		2.300	1.861	0.438

Fig. 12 Evaluation of the jet-wake measurements (impeller A)

lead to an overly high mixing loss because of higher velocity differences.

In particular it can be seen that (a) the velocity in the jet w_{2J} is less than $w_{2j,\ is}$, and that (b) the wake flow is by no means congruent with the blading.
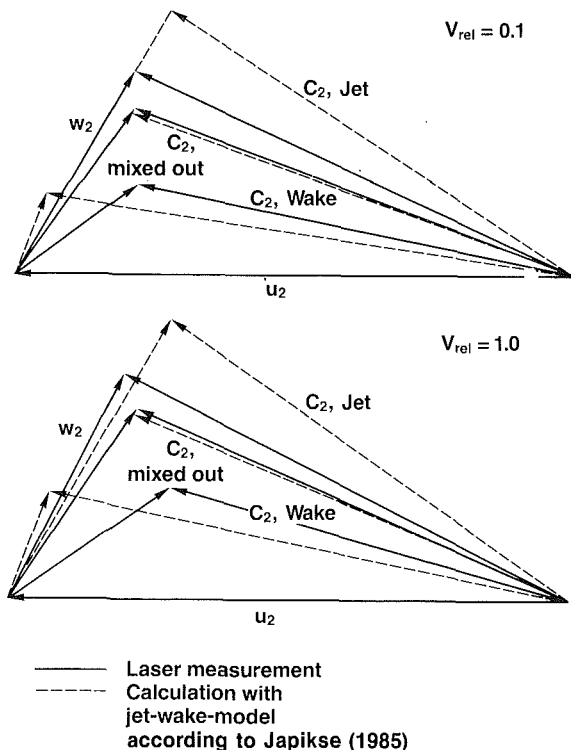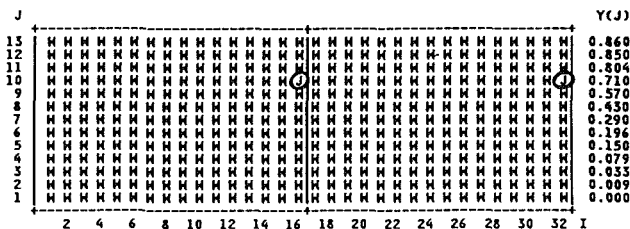
Fig. 13 Velocity vectors in jet and wake at two different operating points (impeller A)

Fig. 15 Velocity vectors in jet and wake at two different operating points, calculated with the modified model (impeller A)

L2F Velocity Measurement

Results of Integration

Ku_0	1.255	$(\dot{V} - \dot{V}_{SL})/(\dot{V}_{CH} - \dot{V}_{SL})$	0.1
R/R_2	1.01	Diffuser position	$t/2$

Jet-Wake-Zones

Extrapolationfactors for CM, CU	:	0.01 0.01
Definitionfactor for wake	:	1.42
Circumferential velocity U2 in m/s :		438.944

Area Mean Value		Global	Jet	Wake
C2	in m/s:	377.197	372.334	377.239
ALFA 2	in deg:	25.070	38.898	24.959
W2	in m/s:	198.820	**274.554***	198.171
BETA 2	in deg:	56.460	56.885	56.457
CM 2	in m/s:	160.712	229.787	160.119
CU 2	in m/s:	337.534	292.995	337.916
CR 2	in m/s:	156.347	225.121	155.757
Area	m**2,-:	0.02041	0.00850	0.99150
Mass Flow	in kg/s:	2.300	0.028	2.271

Jet: from c_{m2}, $c_{u2} \to c_2 = 372.355$ m/s, $\alpha_2 = 38.106°$

* Global correction: $\delta_\alpha = -4.355°$
$\to \alpha_2 = 33.751°$
$c_{u2} = 309.6$ m/s

$\to w_2 = 243.98$ m/s

From (3) it follows that $w_{2is} = 243.7$ m/s

The condition for isentropic flow $W_2 \approx w_{2is}$ is just satisfied at the "jet-points."
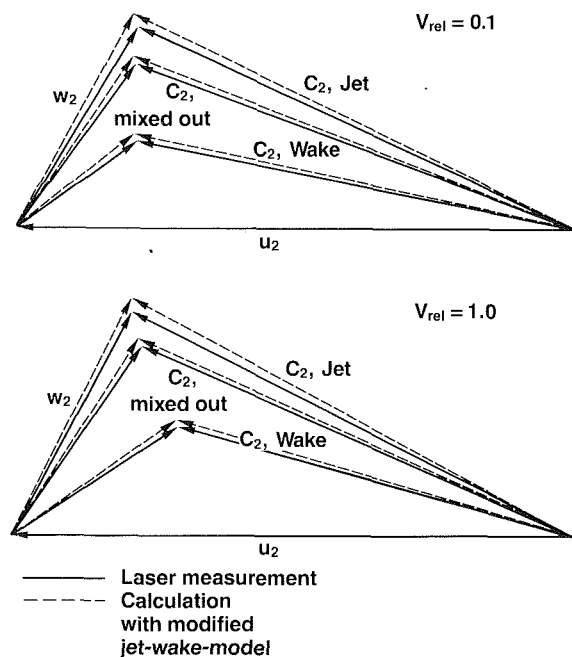
Fig. 14 Approximately isentropic stream lines (impeller A)

It was especially examined whether an isentropic core could be found at any point in the flow field. For this purpose the definition factor for the wake has been increased until only one point was left as jet point showing the maximum velocity in the flow area. The velocity of this core can be calculated from Eqs. (1) and (3). In the present case it is $w_{2,is} \approx 244$ m/s. From Fig. 14 it can be seen that the condition for "isentropic jet" is approximately satisfied only at one point in the channel.

Consequences Derived From the Investigations

The investigations performed show that the "classical" jet-wake model needs improvement. It is converted into an advanced two-zone model with a polytropic jet zone and a less "poor" wake zone where the flow must not be congruent with the blading. The new assumptions are:

(a) The jet, although it contains lower losses than the wake, is not isentropic; Eq. (1) becomes

$$T_{2J} = T_{0T} * (p_2/p_{0T})^{\frac{\kappa-1}{\kappa}/\eta_{\text{pol},J}} \qquad (4)$$

Eqs. (2) and (3) remain unchanged.

(b) To the wake zone

$$c_{u2w} = F_{uw} * c_{u2J} \qquad (5)$$

must be applied instead of $\beta_{2F} = \beta_{2B}$.

These modified conditions can easily be implemented in the calculation model used up to now. The parameters $\eta_{\text{pol},J}$ and F_{uw} as well as the wake mass flow fraction m_w/m were determined from measurements at the impeller exit.

To determine $\eta_{\text{pol},J}$ Eqs. (3) and (4) have only to be reversed:

$$T_{2J} = (u_2^2 - w_{2J}^2)/2c_p + T_{0T} \qquad (3a)$$

$$\eta_{\text{pol},J} = (\kappa - 1)/\kappa * \ln(p_2/p_{0T})/\ln(T_{2J}/T_{0T}) \qquad (4a)$$

($\eta_{\text{pol},w}$ can be determined in the same way.)

The following ranges were thus obtained for the various parameters:

$\eta_{\text{pol},J}$	$= 0.79-0.96$	but mainly $0.92-0.95$
$\eta_{\text{pol},w}$	$= 0.73-0.84$	but mainly $0.80-0.82$
F_{uw}	$= 0.81-0.99$	but mainly $0.92-0.94$
m_w/m	$= 0.11-0.21$	but mainly $0.13-0.14$
A_w/A	$= 0.29-0.425$	but mainly $0.35-0.4$
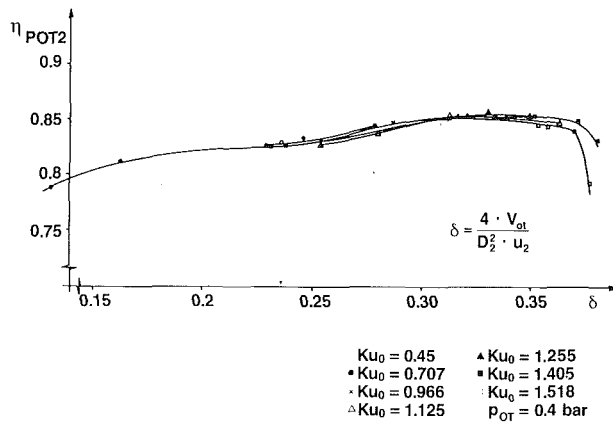
Fig. 16 Polytropic impeller efficiency (impeller A)

$$\delta = \frac{4 \cdot V_{\text{ot}}}{D_2^2 \cdot u_2}$$

$Ku_0 = 0.45$	$\blacktriangle Ku_0 = 1.255$
$\bullet Ku_0 = 0.707$	$\blacksquare Ku_0 = 1.405$
$\cdot Ku_0 = 0.966$	$Ku_0 = 1.518$
$\triangle Ku_0 = 1.125$	$P_{OT} = 0.4$ bar
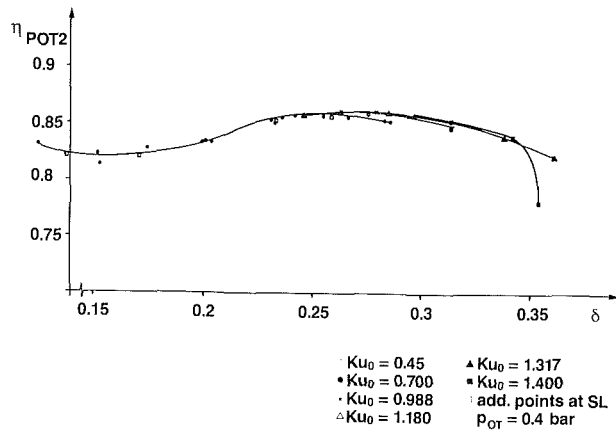
Fig. 17 Polytropic impeller efficiency (impeller B)

$\cdot Ku_0 = 0.45$	$\blacktriangle Ku_0 = 1.317$
$\bullet Ku_0 = 0.700$	$\blacksquare Ku_0 = 1.400$
$\cdot Ku_0 = 0.988$	add. points at SL
$\triangle Ku_0 = 1.180$	$P_{OT} = 0.4$ bar

These rather qualitative statements of the parameter values have deliberately been chosen in order to give an idea of the order of magnitude. It is obvious that the jet efficiency $\eta_{\text{pol},J}$ of a low-loss impeller will be higher than that of a less optimized impeller. Furthermore, the parameters depend on the throttling condition of the machine and the circumferential Mach number (i.e., speed). A precise presentation of these relationships, however, shall be reserved for later publications.

Application to an Example

The jet-wake calculation procedure was modified according to the preceding chapter and the same application case as illustrated in Fig. 13 was calculated. In particular the following values were used for the input parameters:

V_{rel}	0.1	1.0
$\eta_{\text{pol},J}$	0.875	0.875
F_{uw}	1.0	0.9
m_w/m	0.18	0.18

From Fig. 15 it can be seen that good conformity of the velocity vectors can be attained in this way.

Because of the similarity principle all operating points (apart from surge and choke) should form one single characteristic $\eta_{p0T2} = f(\delta)$ as long as the influences of Reynolds and Mach number are negligible. Differences from this expectation would have to be attributed to incorrect modeling.

Figures 16 and 17 show impeller characteristics evaluated according to the modified procedure (with constant parameters). The coincidence of the characteristics actually shows only a small influence of Reynolds and Mach number and may be taken as an indication that the calculation model works very well.

Conclusions

Flow measurements with L2F at the exit of modern centrifugal impellers have shown that the "classical" jet-wake calculation method with an isentropic jet needs correction in order to obtain meaningful results when interpreting measurements on compressors. The proposed modification to the method uses constant parameters for the time being, but even in this way a clear improvement of the calculation is achieved.

For future work it shall be reserved to demonstrate the dependence of these parameters on the throttling conditions and the speed of the machine, and to contribute to a further improvement.

References

Dean, R. C., Jr., and Senoo, Y., 1960, "Rotating Wakes in Vaneless Diffusers," ASME *Journal of Basic Engineering*, Vol. 82, p. 563–574.

Eckardt, D., 1977, "Untersuchung der Strahl/Totwasser-Strömung hinter einem hochbelasteten Radialverdichterlaufrad," DLR-FB 77-32.

Japikse, D., 1985, "Assessment of Single- and Two-Zone Modeling of Centrifugal Compressors. Studies in Component Performance: Part 3," ASME Paper No. 85-GT-73.

Japikse, D., 1986, "Centrifugal Compressor Design and Performance," Course Notes, Concepts ETI Inc., 8th ed.

Wittwer, D., and Küpfer, H., 1986, "The New Radial Compressor Test Rig Super-Martin," *Brown Boveri Review*, Vol. 73, No. 4, pp. 177–184.

H. D. Joslyn
United Technologies Research Center,
East Hartford, CT 06108

J. J. Brasz
Carrier Corporation,
Syracuse, NY 13221

R. P. Dring
United Technologies Research Center,
East Hartford, CT 06108

Centrifugal Compressor Impeller Aerodynamics: An Experimental Investigation

The ability to acquire blade loadings (surface pressure distributions) and surface flow visualization on an unshrouded centrifugal compressor impeller is demonstrated. Circumferential and streamwise static pressure distributions acquired on the stationary shroud are also presented. Data were acquired in a new facility designed for centrifugal compressor aerodynamic research. Blade loadings calculated with a blade-to-blade potential flow analysis are compared with the measured results. Surface flow visualization reveals some complex aspects of the flow on the surface of the impeller blading and hub.

Introduction

Centrifugal impellers are used in a wide variety of products ranging from conventional water pumps to space shuttle main engine fuel and oxidizer pumps, from squirrel cage fans to high pressure ratio gas turbine compressors, from tiny cryocooler compressors to large industrial petrochemical compressor stations. Although centrifugal pumps and compressors have been in use for over a century, much empiricism is still present in the compressor design process.

The individual flow channels of a centrifugal impeller are twisted three-dimensional passages making a 90 deg turn in the meridional plane and opposite blade angle turns in the first and second halves of the impeller passage. In the axial inlet section of the impeller (the inducer), the blade angle with respect to the tangent direction increases, thus allowing pressure rise through internal flow diffusion. In the radial discharge portion of the impeller (the exducer) where blade loading is dominated by Coriolis forces, the blade angle is reduced in order to prevent excessive loading. This reversal of blade angle development between impeller inlet and discharge results in the typical "S" shape of a centrifugal impeller blade contour.

Design and analysis methods for centrifugal impellers vary from simple scaling of existing designs based on similarity considerations to time-dependent viscous fully three-dimensional Navier–Stokes codes. Current centrifugal compressor design practice typically involves a process where programs of increasing complexity are successively run (Holbrook and Brasz, 1984; Platt, 1981; Krain, 1984).

Sizing is the first step in the compressor design process. After a speed selection has been made and the major design parameters have been fixed, a more detailed performance analysis is

carried out to determine off-design behavior using some kind of overall compressor performance prediction program (e.g., Jansen, 1967; Frigne and Van den Braembussche, 1979; Musgrave, 1980; Herbert, 1980; Casey and Marty, 1985). These sizing and overall performance prediction programs are very empirical in nature.

Neither the sizing nor the overall performance analysis program needs or calculates the three-dimensional geometry of the impeller. These programs always assume "well-designed" pellers. Since most performance analysis programs are in-house industrial programs, "well-designed" means similar to the previous impeller designs, which were used to calibrate the performance prediction program.

The final three-dimensional geometry of the impeller is always a compromise between manufacturability and aerodynamics. The geometry is obtained after a number of iterations between geometry generation and an aerodynamic internal flow calculation. The aerodynamic requirement is that the edge velocities along the impeller channel passage surfaces (hub, shroud, pressure and suction sides) vary smoothly through the impeller, i.e., without strong sudden decelerations, which would cause flow separation. Also, blade loading, which can be seen as the difference between suction and pressure side velocities (or pressures) should be limited. Purely inviscid blade-to-blade calculations indicate that too much blade loading reduces the relative velocities on the pressure side of the blade to unacceptably low values. In extreme cases inviscid flow reversal can occur on the pressure side of the blade. Moreover, a strong normal blade-to-blade pressure gradient forces large amounts of low-momentum fluid to accumulate at the lower pressure shroud/suction side of the passage, thus causing a larger wake to leave the impeller.

Recommended values for the major impeller design parameters, viz., blade loading and internal diffusion, have been determined over time by various industrial design groups based on test results of different impellers. Due to a lack of systematic

experiments no preferable loading choice can be made, e.g., front loading versus center loading versus uniform loading. Similarly, the question of where to reduce the relative velocity, in the initial part of the impeller (where the boundary layer is still thin) or uniformly over the blade length, has not been settled either (Dallenbach, 1961; Jansen and Kirschner, 1967). It is also important to keep in mind that the actual results of blade-loading calculations obtained from inviscid quasi-three-dimensional programs depend on the specific assumptions made with regard to impeller slip (the deviation between the discharge blade metal angle and the mass-averaged flow angle), incidence, and blockage due to boundary layer build-up. For example, the assumption of a larger slip factor will reduce the loading in the rear of the impeller predicted by a blade-to-blade analysis program.

With the advent of more powerful computers and the application of recent developments in computational fluid dynamics of viscous-inviscid interaction models as well as fully three-dimensional Navier-Stokes solvers toward centrifugal impellers (Colwill, 1980; Rhie et al., 1984; Moore and Moore, 1980), tools have become available that, in principle at least, seem to be able to predict losses and efficiencies at a more fundamental level than the existing performance prediction programs.

So far, assessment of the various impeller flow models has been lacking. How well do the current design programs predict impeller aerodynamics? How much better do the more advanced CFD programs predict impeller aerodynamics? How can the new information with more physics of the flow within the impeller, as generated by the viscous-inviscid interaction models and the fully viscous Navier-Stokes solvers, be used to come up with better designs?

In order to help answer these questions and to reduce the amount of empiricism that still exists in today's impeller design methods, a dedicated centrifugal compressor test facility has been built to allow investigation of the dominant physics of centrifugal impeller flow. The initial test vehicle has been a large, unshrouded three-dimensional industrial impeller operating with a vaneless diffuser.

It was decided to start the centrifugal compressor research program with detailed measurements of the static pressure fields on the four surfaces of the passage channel of the centrifugal impeller (blade pressure surface, blade suction surface, impeller hub, and stationary shroud) since these pressures can be compared to predictions from quasi-three-dimensional analysis programs as well as the viscous internal flow codes.

The objective of this paper is to describe the experimental setup, discuss some typical results, and compare the results with a prediction from a quasi-three-dimensional impeller internal flow program. The description of the impeller and the operating conditions is complete, thus allowing the validation
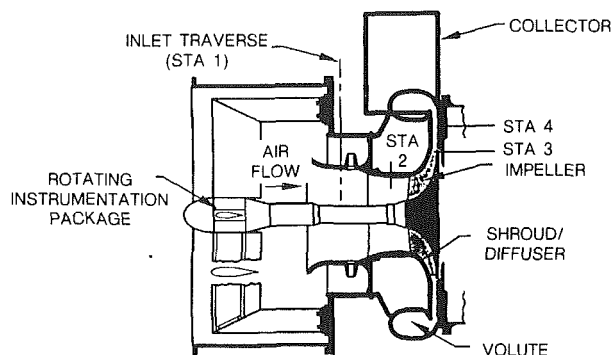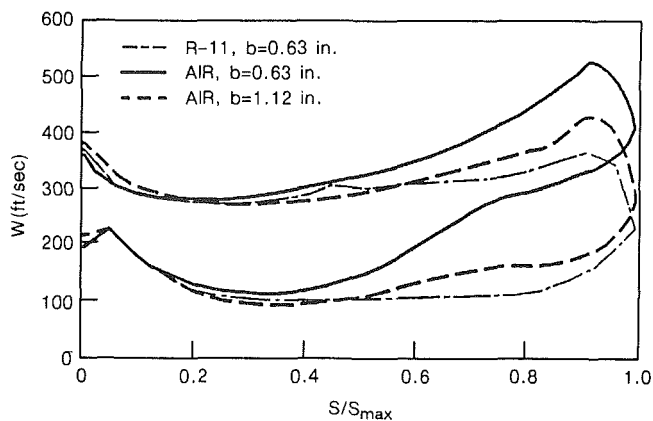

Fig. 1 Cross section of test model

Fig. 2 Effect of impeller tip width variation on blade loading

of other more detailed CFD programs (Dorney and Davis, 1990).

Test Facility

Centrifugal Compressor. The Centrifugal Compressor Aerodynamics Research Facility (CCARF) is shown in cross section in Fig. 1. It is built around a standard "off-the-shelf" Carrier Model 17DK(365) industrial chiller centrifugal compressor designed for closed cycle operation with R-11 refrigerant as the working medium. The CCARF is operated as an open cycle facility with air drawn in at atmospheric conditions as the working medium. Test impellers can be spun to 7700 rpm through a geared drive train by a 450 hp electric motor. The size of the 17DK impeller permits a reasonably high resolution array of blade static taps to be installed so that blade loading and passage diffusion can be measured directly and

---

————— Nomenclature —————

ALE = annulus area at the impeller airfoil leading edge plane
CP = pressure coefficient = $(P - PTA1)/QU_{tip}$
C_p = specific heat at constant pressure
C_v = specific heat at constant volume
Cx = average inlet axial velocity = (V/ALE)
Cx/U_{tip} = flow coefficient
f = defined in Eq. (2)
PS = static pressure

PTA = absolute total pressure
$PTA1$ = inlet absolute total pressure
$PTA5$ = discharge absolute total pressure
PTR = relative total pressure
$PTRi$ = isentropic relative total pressure
QU_{tip} = dynamic pressure based on tip speed and inlet total density
R = radius
R_{tip} = impeller tip radius
S = meridional distance
$TTA1$ = inlet absolute total temperature

U_{tip} = impeller tip speed = $(\Omega \cdot R_{tip})$
$\dot{V}$ = inlet volumetric flow rate
W = relative velocity
Wi = isentropic relative velocity
X = axial distance
β = blade angle from meridional
γ = specific heat ratio = (C_p/C_v)
θ = circumferential position
Ω = rotational speed

Fig. 3 Wide tip impeller

Fig. 4 Meridional view of impeller instrumentation sites
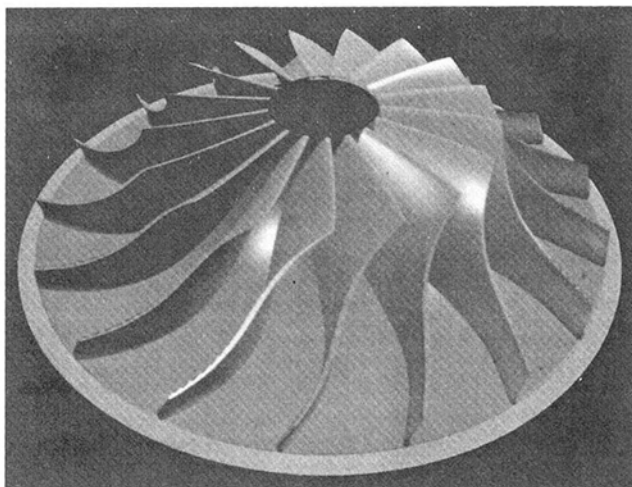
not inferred. Air is used as the working fluid to eliminate potential handling and recovery problems associated with the use of a fluorocarbon.

The original 17DK compressor was designed for a pressure ratio of 4.0 when run at 7700 rpm with R-11 refrigerant as the working fluid. With air as the working fluid, it was necessary to modify the standard impeller design by nearly doubling its tip width to reproduce the passage diffusion achieved in the standard impeller with R-11 refrigerant as the working fluid. The stationary shroud contour was not changed. This modified impeller will be referred to as the "wide tip impeller" and the rationale for the modification is illustrated in Fig. 2. In this figure, blade-to-blade calculations illustrate the effects of working medium density (air versus R-11) and tip width on impeller blade loading. Three calculated results are presented for the same impeller inlet volumetric flow rate (6750 cfm). The dash-dot-dash line represents the blade loading along the mean flow streamline (rms) for the standard impeller operating with R-11. Changing the working medium from R-11 to air results in the thick solid line. For this case, the strong acceleration region from $S/S_{max} = 0.4$ toward the impeller exit on both the suction and pressure surfaces is not typical of centrifugal compressor design practice.

Clearly, the standard 17DK impeller operating in air does not simulate the design blade loading and in all probability would not produce a similar three-dimensional flow field. By increasing the impeller tip width from 0.63 to 1.12 in., the blade loading distribution shown by the dashed line was obtained for air. These results show that the wide tip impeller operating in air closely simulates the predicted design loading for the standard impeller operating with R-11. Similar impeller modifications were made by Inoue and Cumpsty (1984) for testing at low speed an impeller designed for high-speed operation.

The wide tip impeller is shown in Fig. 3, and Fig. 4 depicts the wide tip impeller meridional section. The impeller is designed with 17 equally spaced blades with 30 deg of backsweep and a meridional passage length of 8.4 in. at the rms stream surface. The inlet shroud radius and the tip radius are 6.083 and 10.35 in., respectively. The impeller geometry is summarized in Table 1 in terms of its hub and shroud surface coordinates and wrap angle. The leading edge semicircle diameter varies from hub to shroud and is equal to the local blade thickness. At the nominal flow coefficient of 0.22, the wide tip impeller static-to-total pressure ratio is 1.22 and the channel Reynolds number based on the rms passage length is 2.78×10^5. The average static clearance along the shroud was measured to be 0.023 in.

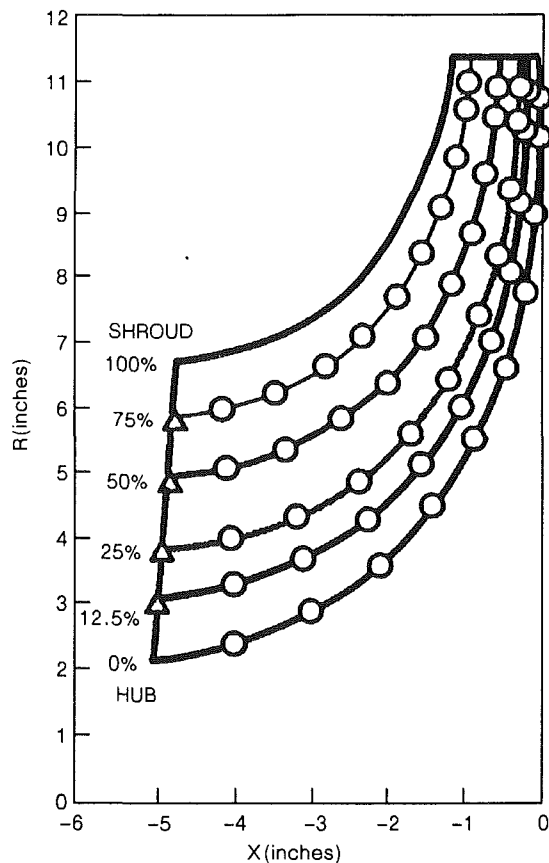The impeller discharges into a vaneless diffuser followed by a volute. The standard 17DK(365) volute (Fig. 1) is sized for volumetric flow rates based on the use of R-11 as the working medium. Because of this and the requirement to double the impeller tip width, the standard volute is undersized for use with air as the working medium. Therefore, the volute is not matched to the impeller at the impeller design inlet air flow. As a result, a circumferential pressure distortion is produced by the volute when the impeller is operated over the same range of volumetric flow rate with air in place of R-11. This is a convenient circumstance since one of the objectives for building the facility was to examine the influence of nonaxisymmetric effects on impeller blade loading.

A single 10-in. diameter discharge nozzle connects the volute to the facility exhaust ducting. The flow rate is set with a remotely controlled exhaust valve. With the wide tip impeller and the standard 17DK volute, flow coefficients from 0.31 to 0.04 can be achieved before the onset of surge.

Total pressure and temperature rise were measured in the CCARF on a "flange-to-flange" basis. Given the large mismatch between the impeller and the volute, there is no point on the speed line where the entire compressor could be considered to be operating at nominal design conditions. However, over the range of flow coefficient from "design" to "matched flow" the adiabatic efficiency of the compressor was in the range from 70 to 80 percent.

Instrumentation. Total pressure and temperature were measured with United Sensors combination probes (Model KT-8-C/A-12-C) in the inlet (Sta. 1) and in the volute discharge duct (Sta. 5, not shown). These measurements were used to determine the "flange-to-flange" total pressure ratio and adiabatic efficiency of the compressor. Shroud static pressure distributions were measured with four primary static tap arrays spaced 90 deg apart and extending from 6.2 in. upstream of the impeller leading edge to the impeller trailing edge. Eight

Table 1   17DK impeller geometry

Hub Pressure Side 3D Blade Coordinates of 17DK Impeller						
X	R	Y	Z	θ	β	Thickness
−5.060	1.897	0.088	1.895	2.644	34.000	0.3111
−4.567	2.003	0.420	1.959	12.111	31.113	0.3406
−4.099	2.143	0.715	2.021	19.475	26.115	0.3420
−3.656	2.316	0.967	2.105	24.674	19.999	0.3382
−3.238	2.522	1.184	2.227	27.993	13.504	0.3342
−2.846	2.762	1.373	2.397	29.812	7.183	0.3295
−2.479	3.035	1.540	2.615	30.494	1.451	0.3243
−2.138	3.341	1.689	2.883	30.356	−3.367	0.3209
−1.822	3.681	1.822	3.198	29.669	−7.007	0.3184
−1.531	4.053	1.944	3.556	28.668	−9.252	0.3167
−1.265	4.459	2.064	3.953	27.565	−9.932	0.3160
−1.025	4.899	2.189	4.382	26.546	−8.934	0.3160
−0.810	5.371	2.336	4.837	25.775	−6.230	0.3160
−0.620	5.877	2.519	5.310	25.383	−1.914	0.3160
−0.455	6.416	2.759	5.793	25.468	3.763	0.3160
−0.316	6.989	3.074	6.276	26.091	10.357	0.3160
−0.202	7.594	3.481	6.750	27.280	17.219	0.3160
−0.114	8.233	3.993	7.200	29.015	23.535	0.3160
−0.051	8.906	4.615	7.616	31.215	28.437	0.3160
−0.013	9.611	5.336	7.994	33.725	31.261	0.3160
0.000	10.350	6.133	8.337	36.337	32.000	0.3160

Leading edge contour is a half circle with diameter equal to the normal blade thickness.
Trailing edge contour is sharp due to impeller tip diameter machining.
Fillet radii at pressure and suction side surfaces are 0.1 and 0.2 inches, respectively.
rms surface roughness is 200 microinches.
Impeller clearance is 0.040 inches.

Shroud Pressure Side 3D Blade Coordinates of 17DK Impeller						
X	R	Y	Z	θ	β	Thickness
−4.774	6.094	0.000	6.094	0.000	57.900	0.0472
−4.456	6.105	0.456	6.088	4.285	52.394	0.0678
−4.153	6.137	0.817	6.082	7.654	47.038	0.0884
−3.864	6.190	1.111	6.089	10.339	41.936	0.1165
−3.589	6.264	1.356	6.116	12.505	37.194	0.1307
−3.328	6.360	1.568	6.164	14.274	32.902	0.1446
−3.082	6.477	1.757	6.234	15.739	29.130	0.1568
−2.849	6.615	1.931	6.327	16.973	25.932	0.1630
−2.631	6.775	2.097	6.442	18.035	23.354	0.1632
−2.427	6.956	2.261	6.578	18.972	21.432	0.1579
−2.237	7.158	2.428	6.734	19.829	20.195	0.1483
−2.061	7.381	2.602	6.908	20.641	19.661	0.1385
−1.899	7.626	2.788	7.098	21.445	19.826	0.1301
−1.752	7.892	2.991	7.303	22.273	20.650	0.1232
−1.619	8.179	3.216	7.521	23.155	22.043	0.1180
−1.500	8.488	3.468	7.747	24.118	23.845	0.1143
−1.395	8.818	3.751	7.980	25.178	25.823	0.1121
−1.304	9.169	4.069	8.217	26.343	27.681	0.1104
−1.228	9.541	4.421	8.455	27.601	29.101	0.1095
−1.165	9.935	4.806	8.696	28.927	29.854	0.1092
−1.117	10.350	5.220	8.937	30.285	30.000	0.1090

Symbols
X   – axial coordinate
R   – radial coordinate, inches.
Z,Y – impeller front view rectangular coordinates.
θ   – wrap angle (degrees, decreasing in direction of rotation)
β   – blade angle (degrees from meridional, − = direction of rotation)
thickness is normal blade thickness, inches.

additional static tap arrays spaced 45 deg apart were installed on the shroud side of the vaneless diffuser at radius ratios (R/R_{tip}) of 1.15, 1.3, and 1.45. Four static taps were installed 90 deg apart in the volute discharge duct in the same plane as the total pressure and total temperature probes (Sta. 5, not shown).

A United Sensors Model PAC-12-KL pitot-static probe was traversed radially in the inlet (Sta. 1) at a number of discharge duct valve settings (flow rates). These radial traverse data were used to calibrate the inlet flow rate relative to a reference static pressure tap located on the shroud 4.62 in. axially upstream of the impeller (Sta. 2). The correlation of volumetric flow rate (V) based on the inlet traverse with that calculated from the average shroud static pressure measured at Sta. 2 is linear. For subsequent tests, a reference flow rate was calculated based on the shroud static pressure measured at Sta. 2 and the actual flow rate was calculated by multiplying the reference flow rate by 1.037. The inlet traverse results were also used to calculate inlet mass flow and an average axial velocity (Cx) at the impeller leading edge.

To measure static pressure on the blade suction and pressure surfaces and on the hub, 114 static taps were installed on the impeller. The installation sites on the blade are shown in a meridional view (Fig. 4) of the impeller. Five spanwise arrays, each consisting of ten taps, were installed on both the pressure and suction surfaces. The "spanwise" or blade height locations correspond to annular inviscid stream surfaces that would contain 0, 12.5, 25, 50, and 75 percent of the impeller inlet flow. Ten static pressure taps were also installed halfway between the pressure and suction surfaces of one passage on the hub. The pressure taps were used for both pressure measurements and surface flow visualization.

The pressure tubes installed in the impeller were routed out of the front of the impeller hub and connected, through a hollow drive shaft, to a 60 port pneumatically actuated Scanivalve (Model 60-TR-TC) unit. A stationary transducer (Druck Model PDCR23D) was connected through a rotating seal to the pneumatic multiplexer output side of the Scanivalve. Computer controlled switching, internal to the Scanivalve, permits the transducer to be calibrated with the impeller rotating. The Scanivalve with the transducer removed was also used to distribute gaseous ammonia to the impeller pressure tap sites for surface flow visualization using an ammonia–Ozalid paper technique (Joslyn and Dring, 1986).

Stationary frame pressures (shroud and exhaust duct static pressures and the inlet traverse probe total and static pressures) were measured with two 48 port Scanivalves (Model J48). All data were acquired by using a Hewlett-Packard HP3852 via an IEEE-488 Instrumentation Bus to an HP Vectra PC (IBM PC/AT compatible) computer. Pressure measurements were taken with Scanivalve Differential Pressure Transducers PDCR23D-5PSID (0.06 percent) transducers. These transducers were calibrated using a Pneumatic Dead Weight Tester system (Ametek Model RK-50-SS) with a 0.025 percent accuracy. A five-point calibration was done for each transducer and stored in a calibration table in memory. Type K (Chromel-Alumel) thermocouples were used with software compensation with a reference junction compensation accuracy of 0.1°C.

Data Analysis

The dependent and independent variables that were used to characterize the flow through the impeller have all been non-dimensionalized. The independent variable, flow rate, was treated as a flow coefficient (Cx/U_{tip}) based on the inlet vol-
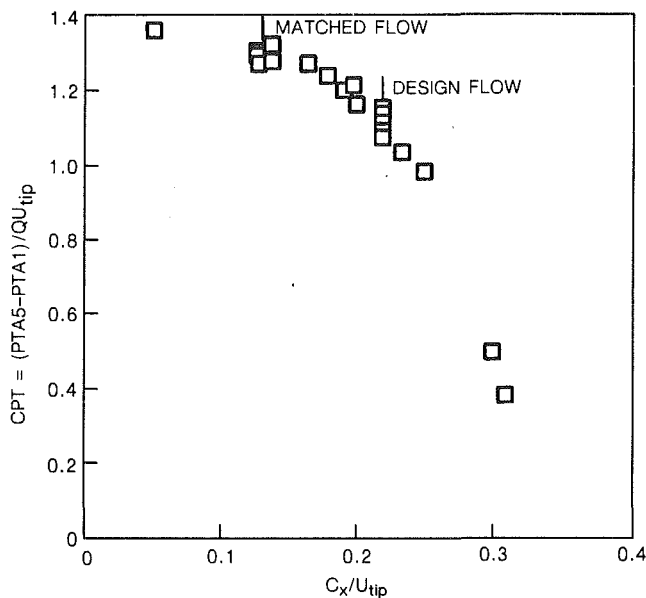
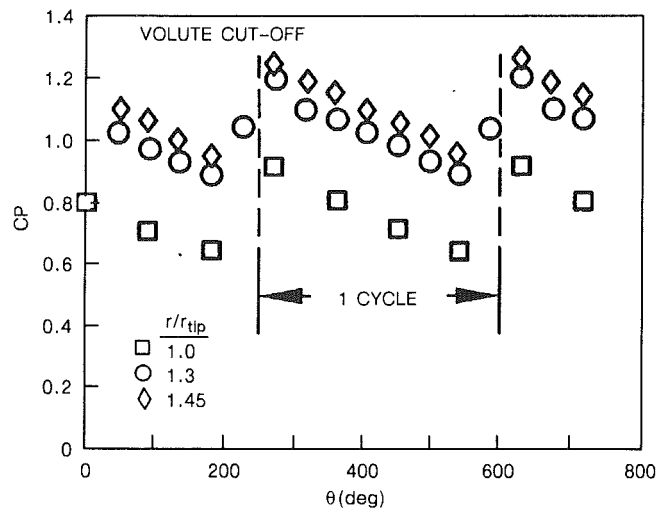Fig. 5 Flange-to-flange total pressure rise characteristic

Fig. 6 Vaneless diffuser static pressure distribution at design flow coefficient

Fig. 7 Shroud static pressure distributions at design flow coefficient

umetric flow rate, the impeller inlet annulus area, and the impeller tip speed.

The primary dependent variable was surface static pressure. This was measured both on the stationary shroud, and on the rotating impeller. The pressure data were presented in several ways. In their most primitive form they were reduced to a pressure coefficient (CP) based on the inlet absolute total pressure (PTA1) and a dynamic pressure based on inlet total density and the impeller tip speed (QU_{tip}). All of the uncertainty in the pressure coefficient is due to the measured pressure, since PTA1 was the reference pressure in all the measurements, and since QU_{tip} is known to very high accuracy ($QU_{tip} = 4.15$ psi).

Care was taken to account for the fact that the pressure sensed by the transducer at the impeller centerline was not the same as the pressure at the static pressure tap location on the impeller. This difference was due to the centrifugal force on the fluid in the rotating tube connecting the pressure tap to the transducer at the centerline. This was accounted for as follows. Since the flow entering the impeller was homenthalpic and axial, its rothalpy was uniform. The radial variation of the relative total temperature was calculated from the rothalpy and the local impeller temperature was assumed to be equal to the local relative total temperature. The fluid in the rotating instrumentation tubing was assumed to have this same radial temperature distribution. The pressure gradient was integrated from the centerline to the radius of the pressure tap location to produce the following relationship:

$$PS(R) = PS(O) \cdot \{ 1 + [R/R_{tip}]^2 f^{-1} \}^{(\gamma/\gamma - 1)} \qquad (1)$$

where

$$f = (2 \cdot C_p \cdot TTA1)/(R_{tip}^2 \Omega^2) \qquad (2)$$

The impact of this centrifugal pressure correction was relatively insensitive to the method of estimating the temperature in the instrumentation tubing owing to the relatively small change in the relative total temperature through the impeller ($\approx 45°$F). The uncertainty in this correction would cause an uncertainty in the pressure coefficient of no more than $\Delta CP \approx 2$ percent. It is planned to measure the impeller temperature at various locations in future studies so that the instrumentation tubing radial temperature distribution will be known.

The static pressure rise in the impeller is due both to centrifugal effects and to diffusion. In order to isolate these effects an isentropic relative total pressure was determined based on the fact that the flow entering the impeller was axial and had
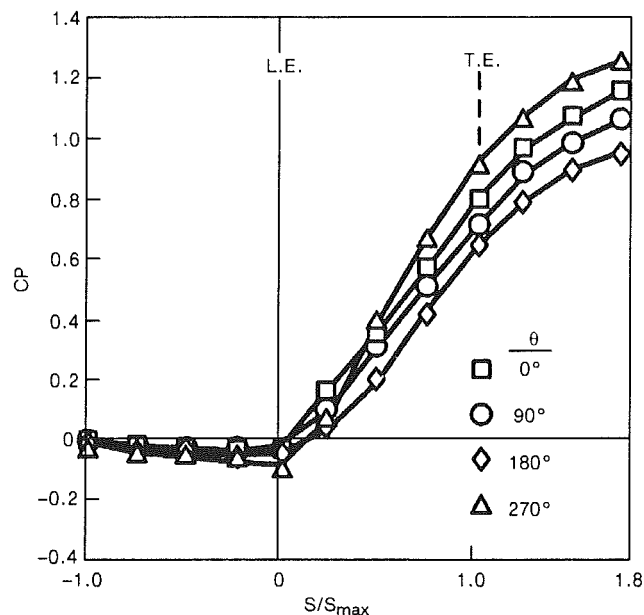
uniform absolute total pressure and total temperature. This was expressed in the form of a pressure coefficient as follows:

$$CPTRi = (\gamma - 1/\gamma) \cdot f \cdot \{ [1 + (R/R_{tip})^2 f^{-1}]^{(\gamma/\gamma - 1)} - 1 \} \qquad (3)$$

This isentropic relative total pressure, when combined with the measured surface static pressure, permits one to calculate an isentropic relative speed as follows:

$$(Wi/U_{tip})^2 = \{ 1 - (PS/PTRi)^{(\gamma - 1/\gamma)} \} \cdot \{ f + (R/R_{tip})^2 \} \qquad (4)$$

where

$$(PS/PTRi) = [CPS + f \cdot (\gamma - 1/\gamma)]/[CPTRi + f \cdot (\gamma - 1/\gamma)] \qquad (5)$$

The results presented in the following section will be based on these dimensionless parameters.

Results

The "flange-to-flange" total pressure rise characteristic of the test facility with the 17DK wide tip impeller installed is presented in Fig. 5 in terms of total pressure coefficient variation with flow coefficient. Since the 17DK compressor operates at a fixed impeller rotational speed (7700 rpm), the single
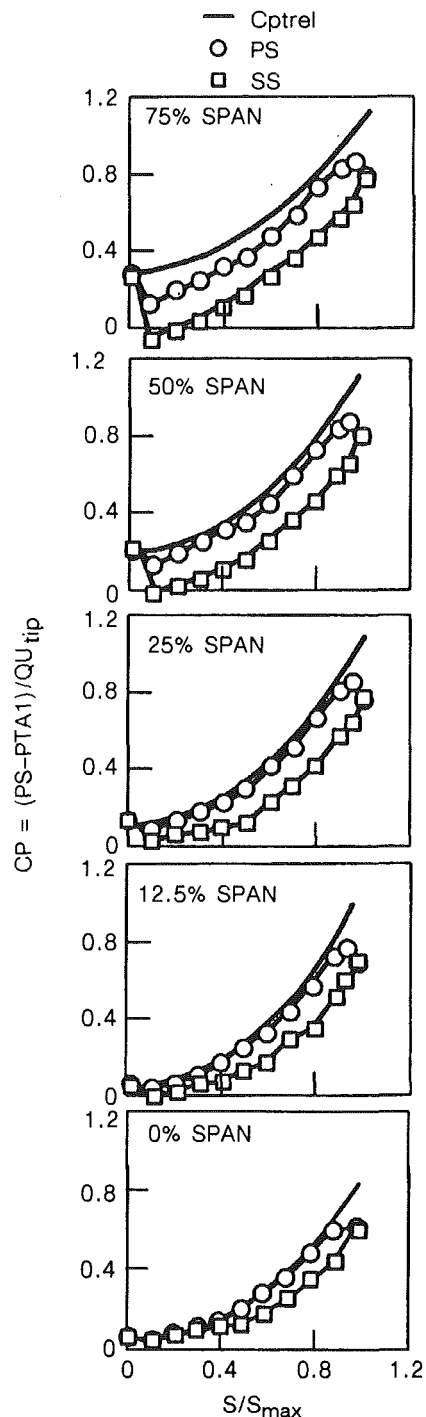
Fig. 8 Impeller pressure distributions at design flow coefficient

As mentioned earlier, the impeller was modified by increasing its tip width. When this wide tip impeller is operated at its design inlet flow, the impeller exit volumetric flow rate is over twice (2.4 times) the volute design flow rate. As a consequence, the excess flow collected by the volute is accelerated around the volute from the cutoff to the discharge. The accelerated flow results in a circumferential static pressure distortion. This static pressure distortion is evident in the circumferential static pressure distributions obtained on the shroud side of the vaneless diffuser (Fig. 6) and in the streamwise static pressure distributions (Fig. 7) obtained from four pressure tap arrays spaced 90 deg apart on the shroud.

The circumferential static pressure distributions presented at radius ratios (R/R_{tip}) of 1.0, 1.13, and 1.45 in Fig. 6 show that the distortion extends from the vaneless diffuser inlet (impeller exit, $r/r_{tip} = 1.0$) to $r/r_{tip} = 1.45$. To show the wave form of the distortion more clearly, the results are duplicated and shown over two cycles (0–720 deg). As seen in Fig. 6, the pressure initially increases near the volute cutoff, then decreases as the flow accelerates toward the volute discharge. These trends are similar to those observed by Sideris and Van den Braembussche (1987) in their study of a centrifugal water pump. The circumferentially averaged pressure coefficients at the three radius ratios (1.0, 1.3, and 1.45) are 0.753, 1.016, and 1.086, respectively. The corresponding CP variations from the average are ± 0.138, ± 0.151, and ± 0.151. These variations represent pressure distortions, relative to the circumferential averages, of ± 18.3, ± 14.9, and ± 13.9 percent, respectively. The pressure distortion imposes a strong periodic outlet boundary condition for the rotating impeller and has strong consequences relative to impeller loss, surge limit, side load, and noise generation (Stiefel, 1972; Bowerman and Acosta, 1957; Yuasa and Hinata, 1979).

Pressure measurements obtained at the four arrays on the shroud (Fig. 7) show that the distortion extends from the vaneless diffuser exit, forward through the impeller to a location $(S/S_{max} = -0.5)$ upstream of the impeller leading edge. The pressures shown at the impeller trailing edge $(S/S_{max} = 1)$ correspond to the circumferential pressure variation at $R/R_{tip} = 1.0$ previously shown (Fig. 6). This pressure distortion extends over the entire impeller and results in a circumferential variation in impeller blade loading and a net radial force acting on the impeller shaft (Stepanoff, 1948; Agostinelli et al., 1960). It also results in unsteady flow in the impeller passages.

Blade static pressure measurements were made on the impeller at five spanwise arrays (Fig. 4) and the results are presented in Fig. 8 along with the isentropic relative total pressure variation through the impeller. The measured blade static pressures are shown as the symbols and the isentropic total pressure is shown as the solid lines. The blade pressure measurements are essentially time-averaged measurements since the impeller is rotating through the distorted flow field generated by the volute. A centrifugal pressure correction (Eq. (1)) was made prior to calculating the pressure coefficients shown. The isentropic total pressure coefficient was calculated (Eq. (3)) for each spanwise array and was based on the measured inlet total pressure and total temperature. Also shown for each array are the relative total pressure coefficients obtained from Kiel probe measurements at the impeller leading edge $(S/S_{max} = 0)$. These measured relative total pressures, with the centrifugal correction applied, are in excellent agreement with the isentropic values calculated in Eq. (3). This result provides confidence in the centrifugal correction applied to the data acquired on the rotating impeller. The pressure coefficient plotted at the impeller trailing edge $(S/S_{max} = 1.0)$ is the circumferential average of the shroud static pressures measured at $R/R_{tip} = 1.0$ (Fig. 6).

Figure 8 shows that the blade loading gradually increases from hub (0 percent span) toward the tip. At all spanwise
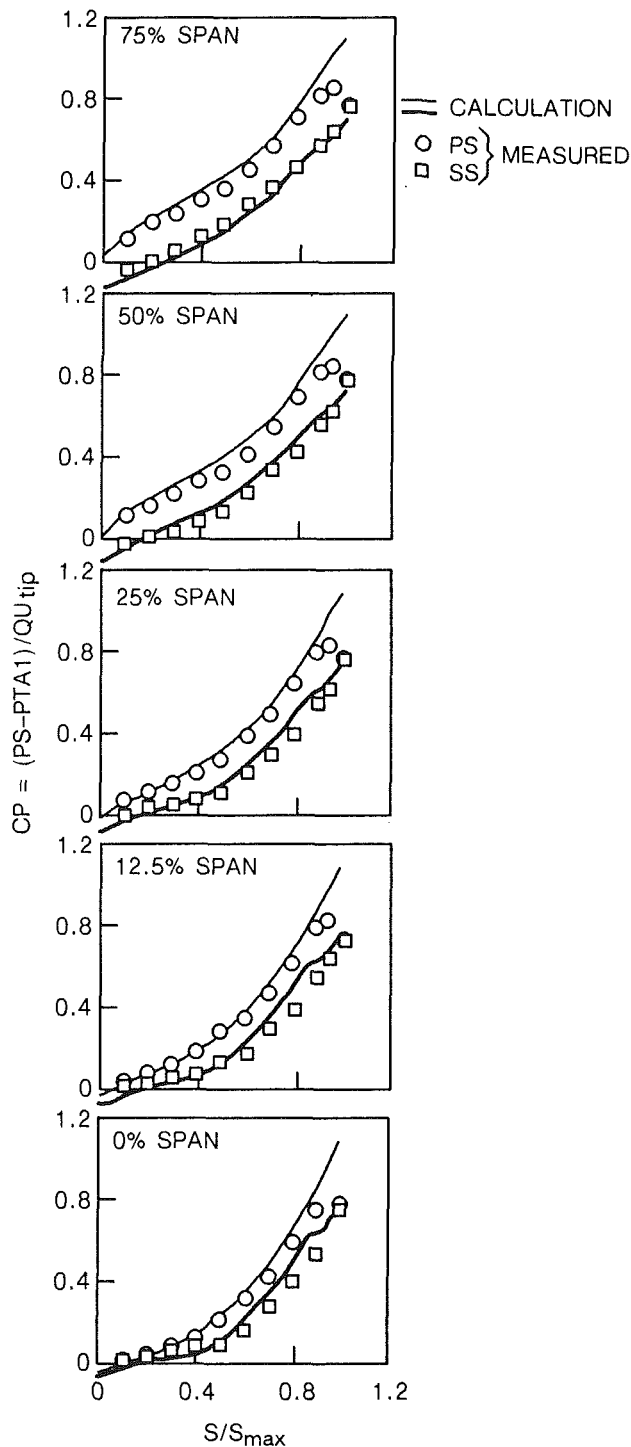
characteristic is presented. Future modifications to the facility include a variable impeller rotational speed capability. With the facility exhaust duct throttle valve full open, a CPT of 0.38 is obtained at a flow coefficient of 0.31. The highest value of the total pressure coefficient, 1.46, was obtained at a flow coefficient of 0.05, which is close to the onset of surge, which occurs just below a flow coefficient of 0.04. Two points are noted on the characteristic, "design" $(Cx/U_{tip} = 0.22)$ and "matched flow" $(Cx/U_{tip} = 0.13)$. The results to be presented below were obtained at these two flow coefficients. Design flow refers to the impeller design flow coefficient, whereas matched flow refers to the flow coefficient at which the impeller exit volumetric flow rate matches the volute design volumetric flow rate.

Fig. 9 Comparison of predicted and measured impeller pressure distributions at design flow

Fig. 10 Impeller isentropic relative velocity at design flow coefficient

locations, the loading is nearly uniform over the aft $(0.6 < S/S_{max} < 1.0)$ region of the impeller. At the 50 and 75 percent span locations, the entire blade is nearly uniformly loaded. These results are consistent with the design intent for this impeller.

Blade loadings (static pressure distributions) calculated for the design flow coefficient with a blade-to-blade potential flow analysis are compared with the measured results in Fig. 9. Although the calculated results for both the pressure and suction surfaces are slightly different from the measured results, the blade loading trend is similar. In general, the calculation

either over or underpredicted the pressure coefficient distributions on both the pressure and suction surfaces of the impeller by 5 percent. The greatest difference between predicted and measured results occurred at the hub (0 percent span). Over the aft $(0.6 < S/S_{max} < 1.0)$ portion of the impeller, the calculation overpredicted the pressure surface distribution by 10 percent and overpredicted the suction surface distribution by 7.5 percent. It should be pointed out that the analysis was not refined by changing the slip factor to obtain a better match with the measured results. The analytical result is a true prediction; it yields what a designer would predict without prior access to the experimental data.

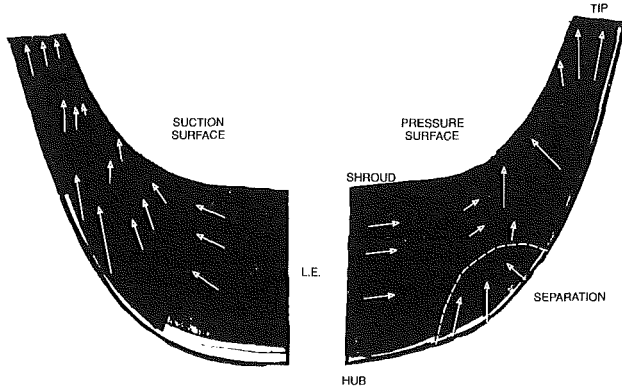Using the isentropic relative total pressure and the blade

Fig. 11 Impeller surface flow visualization at design flow

Fig. 12 Hub endwall flow visualization at design flow coefficient

static pressure, the isentropic relative speed distributions on the pressure and suction surfaces of the impeller blade were calculated (Eq. (4)) and the resulting distributions are shown in Fig. 10. The leading edge values ($S/S_{max} = 0.0$) were calculated from the inlet area averaged axial velocity and local impeller tangential velocity. At 0, 12.5, and 25 percent span, the general trend is accelerating flow from inlet to exit on both the pressure and suction surfaces. The relative speed is more nearly constant on both sides of the blade at the 50 and 75 percent span locations.

Surface flow visualizations on the pressure and suction surface sides of the impeller blade are shown in Fig. 11. Very small amounts of ammonia were discharged from the impeller surface pressure taps at 0, 25, 50, and 75 percent span locations on the impeller pressure and suction surfaces. This produced a permanent streak to appear on Ozalid paper that had been attached to the blade surfaces. Figure 11 was produced by removing the Ozalid paper from the impeller and laying it out flat. This technique is discussed by Joslyn and Dring (1986).

Near the pressure surface leading edge the streaks that start at the 25, 50, and 75 percent span taps show a smooth flow back to about a third of the way along the blade. At that point there is the beginning of a separated region ($0.2 < S/S_{max} < 0.45$) that begins near the hub (with reversed flow) and reaches the shroud about halfway along the blade. The entire center region of the pressure surface has a strong surface flow from the hub toward the shroud. Toward the trailing edge the flow returns again to a generally streamwise direction. Ammonia discharged at 0 percent span and aft of $S/S_{max} = 0.5$, remains in the junction formed by the blade and hub endwall.

The flow pattern on the suction surface is similar in that it both starts and finishes with flow predominantly in a generally streamwise direction. Also, as on the pressure surface, the flow near the middle of the blade has a noticeable component from the hub toward the shroud. However, over the entire length of the blade there is flow from the hub (0 percent span) toward the shroud and no evidence of separation.

The surface flow on the hub is shown in Fig. 12 and at midchannel it is generally in the streamwise direction, i.e., parallel to the blade. However, near the front of the blade-to-blade channel, there is a significant crossflow toward the suction surface. This crossflow occurs adjacent to the region ($0.2 < S/S_{max} < 0.45$) where the pressure surface separation (Fig. 11) occurs and the crossflow may be due to the blockage created by the separation. There is no significant evidence of the pressure surface separation in the hub flow visualization. Aft ($S/S_{max} > 0.5$) of the pressure side separation, the flow along the blade–hub endwall corner remains within the corner region. Over nearly the entire length ($S/S_{max} > 0.2$) of the suction side, however, there is a significant flow component from the blade–hub endwall corner toward the shroud.

The three dimensionality of the flow in the impeller passage is in all probability a result of both viscous and inviscid mech-
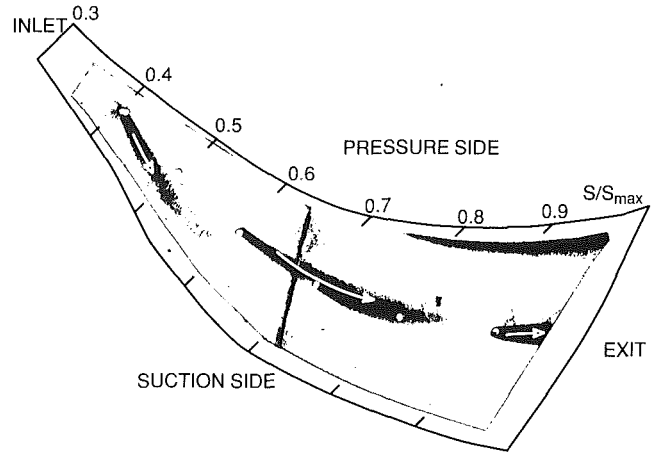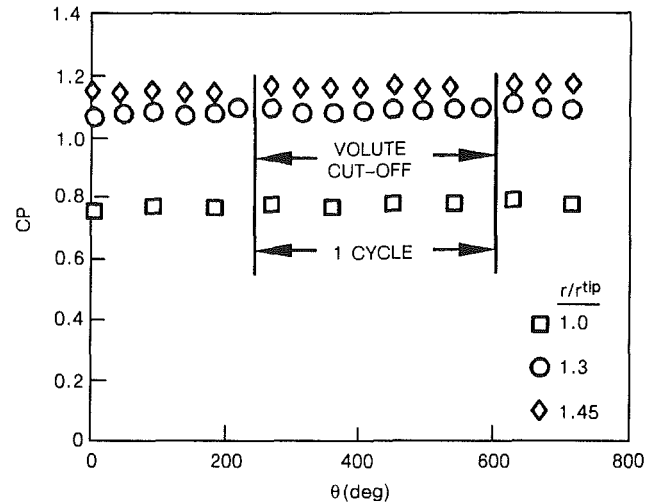

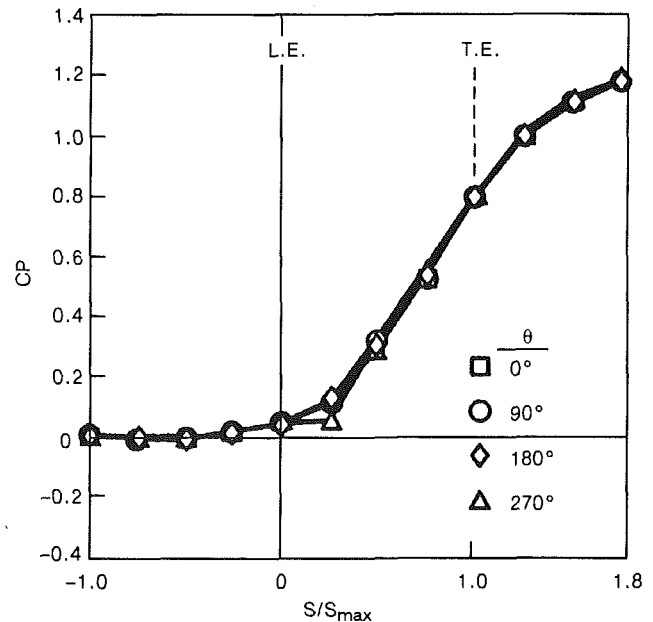Fig. 13 Vaneless diffuser static pressure distribution at matched flow coefficient

Fig. 14 Shroud static pressure distributions at matched flow coefficient

anisms. Centrifugal forces in the boundary layers on both the suction and pressure surfaces tend to drive fluid from the hub toward the shroud. Flow reversal on the pressure surface can
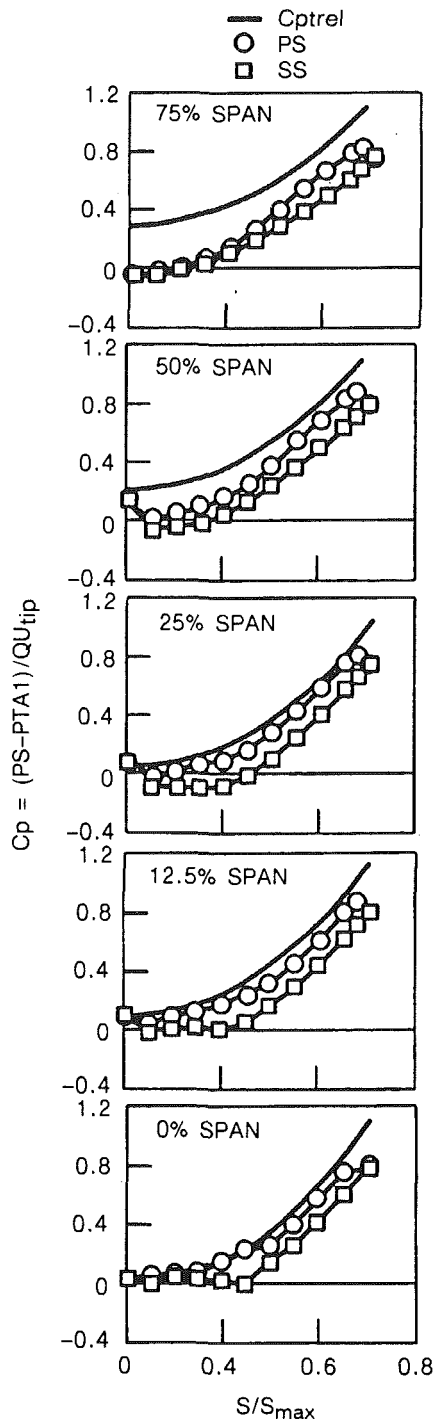
Fig. 15   Impeller pressure distributions at matched flow coefficient

closely to the location of the pressure surface flow separation (Fig. 11). This observation may simply be a coincidence, or scatter in the data, or it may be a useful indicator of flow separation.

At the matched flow coefficient ($Cx/U_{tip} = 0.13$), the impeller exit volumetric flow rate equals the volute design volumetric flow rate and the tangential or circumferential flow speed from volute cutoff to the discharge is nearly constant. Under these circumstances, there is very little, if any, circumferential static pressure distortion in either the vaneless diffuser or in the region occupied by the impeller. The circumferential static pressure distributions obtained on the shroud side of the vaneless diffuser (Fig. 13) and the streamwise static pressure distributions obtained at the four pressure tap arrays on the shroud (Fig. 14) confirm this point. The circumferential pressure distributions presented in Fig. 13 at radius ratios of 1.0, 1.3, and 1.45 are relatively uniform. The corresponding circumferentially averaged pressure coefficients are 0.771, 1.083, and 1.155, respectively. In Fig. 14, the four streamwise static pressure distributions on the shroud are essentially identical; there is minimal circumferential nonuniformity. At this flow coefficient, the impeller is operating within an axisymmetric flow field and with uniform exit conditions. In general, current centrifugal compressor design systems are based on the assumption that the impeller is operating in an axisymmetric flow field such as this.

The measured blade static pressure results, with the centrifugal pressure correction applied, and the isentropic relative total pressure (Eq. (3)) are shown in Fig. 15 for the matched flow coefficient. Compared to the results obtained at the impeller design flow coefficient (Fig. 8), there are two major differences in the matched flow results (Fig. 15). At the matched flow, the blade loading at 75 percent span is nearly zero over the first 30 percent of the blade. Also, the measured relative total pressure and the calculated isentropic relative total pressure at the leading edge ($S/S_{max} = 0$) do not agree with the measured values at the 50 and 75 percent span locations. These two results are due to the existence of a full annular recirculating flow separation region located on the shroud. This zone extends upstream and downstream of the impeller leading edge. The recirculation zone extends in the streamwise direction 3.4 in. upstream of the impeller leading edge and radially from the shroud to nearly 45 percent span. The upstream extent of the separation zone was determined from flow visualization studies using an ammonia–Ozalid paper technique (Joslyn and Dring, 1986). The streamwise extent of the separation downstream of the impeller leading edge could not be conclusively identified from the impeller surface flow visualization. The flow visualization indicated that most of the impeller suction surface was separated and had regions of very low or reversed flow. The pressure surface was primarily separated from 75 percent span toward the shroud. The existence of a recirculating flow separation at the inlet of centrifugal compressors operating at reduced flow has been demonstrated by Ribaud (1987).

occur due to either or both, separation caused by a negative pressure gradient, or inviscid flow reversal caused by the axial component of vorticity (the relative eddy) and a region of low velocity.

It is disturbing that the three-dimensional nature of the surface flow did not have a major impact on the blade pressure distributions (Fig. 8). Thus, even if one could predict the pressure distributions by some approximate method, it is no guarantee that there is no flow reversal in the blade passage. It is interesting to note in Fig. 8 that at 0 percent span and 30 percent chord and at 12.5 percent span and 50 percent chord the static pressure on the pressure surface is very close to the isentropic relative total pressure. This suggests a very low surface velocity at these locations and these locations correspond

Conclusions

The capability to acquire blade loadings (static pressure distributions) and surface flow visualization on an unshrouded centrifugal compressor impeller rotating at 7700 rpm has been demonstrated.

A data set has been acquired with which to assess fully three-dimensional Navier–Stokes codes. Blade pressure distributions and shroud static pressure distributions were acquired at the impeller design flow coefficient in the presence of a circumferential static pressure distortion (time-dependent boundary condition) generated by the volute. These data will be compared in future studies with data acquired without the presence of the circumferential distortion.

The centrifugal correction applied to the measured impeller pressures gives reliable results.

The measured blade static pressure distributions indicate that the blade-to-blade prediction gave reasonably good results at the impeller design flow and that increasing the impeller tip width resulted in blade loadings similar to what would be obtained operating an unmodified impeller in R-11.

At reduced flow, with the impeller/volute combination tested, there is no circumferential static pressure distortion. However, a relatively large region of recirculating flow exists on the shroud at the inlet of the impeller. This recirculating flow may be a controlling factor affecting the surge limit.

At both the design flow and the matched flow, the ammonia–Ozalid paper flow visualization technique showed strong flow deviations from axisymmetric stream surfaces on the impeller blade.

Acknowledgments

References

Agostinelli, A., Nobles, D., and Mocridge, C. R., 1960, "An Experimental Investigation of Radial Thrust in Centrifugal Pumps," ASME *Journal of Engineering for Power*, Vol. 82, No. 2, pp. 120–126.

Bowerman, R., and Acosta, A., 1957, "Effect of the Volute on Performance of a Centrifugal Pump Impeller," *Trans. ASME*, Vol. 79, No. 5, pp. 1057–1069.

Casey, M. V., and Marty, F., 1985, "Centrifugal Compressors—Performance at Design and Off-Design," *Proceedings of the Institute of Refrigeration*, Vol. 82, pp. 71–80.

Colwill, W. H., 1980, "Impeller Performance Prediction Using Three-Dimensional Flow Analysis," in: *Performance Prediction of Centrifugal Pumps and Compressors*, presented at the 25th Annual International Gas Turbine Conference, New Orleans, LA, pp. 125–133.

Dallenbach, F., 1961, "The Aerodynamic Design and Performance of Centrifugal and Mixed-Flow Compressors," *Centrifugal Compressors*, SAE Technical Progress Series, Vol. 3, pp. 2–30.

Dorney, D. J., and Davis, R. L., 1990, "Numerical Investigation of Flow Through a Centrifugal Compressor Impeller," ASME Paper No. 90-GT-213.

Dring, R. P., Joslyn, H. D., and Hardin, L. W., 1982, "An Investigation of

Axial Compressor Rotor Aerodynamics," ASME *Journal of Engineering for Power*, Vol. 104, pp. 84–96.

Frigne, P., and Van den Braembussche, R., 1979, "One-Dimensional Design of Centrifugal Compressors Taking into Account Flow Separation in the Impeller," Von Karman Institute Technical Note 129, Von Karman Institute, Rhode Saint Genese, Belgium.

Herbert, M. W., 1980, "A Method of Centrifugal Compressor Performance Prediction," in: *Performance Prediction of Centrifugal Pumps and Compressors*, presented at the 25th Annual International Gas Turbine Conference, New Orleans, LA, pp. 171–184.

Holbrook, G. J., and Brasz, J. J., 1984, "Experience With an Integrated Centrifugal Compressor Design Procedure," ASME Paper No. 84-GT-249.

Inoue, M., and Cumpsty, N. A., 1984, "Experimental Study of Centrifugal Impeller Discharge Flow in Vaneless and Vaned Diffusers," ASME *Journal of Engineering for Gas Turbines and Power*, Vol. 106, pp. 455–467.

Jansen, W., 1967, "A Method for Calculating the Flow in a Centrifugal Impeller When Entropy Gradients are Present," *Proceedings of the Royal Soc. Conference of the Institution of Mechanical Engineers on "Internal Aerodynamics,"* Cambridge, England, Paper 12, pp. 133–149.

Jansen, W., and Kirschner, A. M., 1967, "Impeller Blade Design Method for Centrifugal Compressors," *Proceedings of Symposium on Fluid Mechanics, Acoustics and Design of Turbomachinery*, Penn State University, NASA-SP-304, Vol. 2, pp. 537–563.

Joslyn, H. D., and Dring, R. P., 1986, "Surface Indicator and Smoke Flow Visualization Techniques in Rotating Machinery," *Heat Transfer and Fluid Flow in Rotating Machinery*, Hemisphere Publishing Corp., Washington, DC, pp. 156–169.

Krain, H., 1984, "A CAD Method for Centrifugal Compressor Impellers," ASME *Journal of Engineering for Gas Turbines and Power*, Vol. 106, pp. 482–488.

Moore, J., and Moore, J. G., 1980, "Calculations of Three-Dimensional, Viscous Flow and Wake Development in a Centrifugal Impeller," in: *Performance Prediction of Centrifugal Pumps and Compressors*, presented at the 25th Annual International Gas Turbine Conference, New Orleans, LA, pp. 61–68.

Musgrave, D. S., 1980, "The Prediction of Design and Off-Design Efficiency for Centrifugal Compressor Impellers," in: *Performance Prediction of Centrifugal Pumps and Compressors*, presented at the 25th Annual International Gas Turbine Conference, New Orleans, LA, pp. 185–189.

Platt, M., 1981, "Computerized Compressor Design," *Turbomachinery International*, May/June, pp. 22–29.

Rhie, C. M., Delaney, R. A., and McKain, T. F., 1984, "Three-Dimensional Viscous Flow Analysis for Centrifugal Impellers," Paper No. AIAA-84-1296.

Ribaud, Y., 1987, "Experimental Aerodynamic Analysis Relative to Three High Pressure Ratio Centrifugal Compressors," ASME Paper No. 87-GT-153.

Sideris, M., and Van den Braembussche, R., 1987, "Influence of a Circumferential Exit Pressure Distortion on the Flow in an Impeller and Vaneless Diffuser," ASME JOURNAL OF TURBOMACHINERY, Vol. 109, No. 1, pp. 48–54.

Stepanoff, A. J., 1948, *Centrifugal and Axial Flow Pumps*, Wiley, New York, pp. 122–136.

Stiefel, W., 1972, "Experiences in the Development of Radial Compressors," in: *Advanced Radial Compressors*, von Karman Institute LS 50, May.

Yuasa, T., and Hinata, T., 1979, "Fluctuating Flow Behind the Impeller of Centrifugal Pump," *Bull. JSME*, Vol. 22, No. 174, pp. 1746–1753.

Impeller Flow Field Measurement and Analysis

J. R. Fagan

S. Fleeter

School of Mechanical Engineering,
Purdue University,
West Lafayette, IN 47907

A series of experiments are performed to investigate and quantify the three-dimensional mean flow field in centrifugal compressor flow passages and to evaluate contemporary internal flow models. The experiments include the acquisition and analysis of LDV data in the impeller passages of a low-speed moderate-scale research mixed-flow centrifugal compressor operating at its design point. Predictions from a viscous internal flow model are then correlated with these data. The LDV data show the traditional jet-wake structure observed in many centrifugal compressors, with the wake observed along the shroud 70 percent of the length from the pressure to suction surface. The viscous model predicts the major flow phenomena. However, the correlations of the viscous predictions with the LDV data were poor.

Introduction

The design process for centrifugal compressors optimizes performance and efficiency while emphasizing safety and reliability over the operating range. Thus, these design systems are dependent upon a complete understanding of the internal fluid mechanics. However, due to the complex three-dimensional flows associated with centrifugal machinery and the lack of detailed experimental data within centrifugal compressors, analytical and computational tools are inadequate for complete modeling of the relevant flow physics. As fractional percentage increases in compressor efficiency convert to significant performance gains and fuel cost savings, the ability to characterize and subsequently predict flow phenomena such as flow separation and the strong secondary flows in turbomachinery blade rows is an essential part of the design process. This requires the development of advanced design systems for centrifugal compressors based on experimentally verified first principle models.

For axial flow turbomachines, the development of advanced design systems, i.e., the development of computational flow codes and experiments to provide benchmark data for verification and direction, are in progress. For centrifugal compressors, this advanced design system development is just beginning. It is being accomplished, at least in part, by adapting flow models developed for axial turbomachines to centrifugal compressor geometries. However, detailed and extensive three-dimensional flow field data obtained in centrifugal compressor impeller flow passages, not axial compressors, are required. It should be noted that these flow field data are of fundamental interest because the ability of the impeller to do work on the fluid is directly related to the stage pressure ratio and efficiency.

To begin to provide these needed flow field data, optical measurements of both the impeller passage mean flow field and the impeller exit periodic unsteady flow field have been made. The flow in both regions is highly three dimensional,

viscous dominated, and affected by blade surface flow separation.

A number of excellent summary articles have been presented as part of the von Karman Institute lecture series on flow in centrifugal compressors. Krain (1984) emphasized the flow field mapping done with a laser two-focus velocimeter (L2F). The research performed by Eckardt and Krain has helped to quantify the differences in the flow field due to variations in impeller geometry by making measurements in a radial blade impeller, a backswept blade impeller, and an impeller with splitter blades. All three were high-speed impellers with similar performance. The investigation by Eckardt (1976) provided the first flow field data inside the impeller passages of a high-speed compressor. However, the L2F data only provide two components of the three-dimensional velocity vector. Elder and Forster (1987) give an historical perspective, describing a series of investigations in a variety of facilities including low-speed and high-speed impellers. Of the investigations described by Elder and Forster, only Johnson and Moore (1983) measured the three-dimensional flow field in the impeller passages. However, the velocities were measured with pressure probes that were traversed in the rotating passages. In addition to the limitations associated with introducing a physical probe into the passage, the measurements were made in a high-speed impeller operating at very low speed, i.e., far from the design point.

Adler and Levy (1979) used a single component LDV to study the flow through an impeller with ten straight backswept blades. They found the impeller flow to be stable and attached, in contrast to the flow in many radial exit impellers. Durao, et al. (1979) used a single component LDV to measure the circumferential and radial velocity components in a 16-bladed centrifugal compressor impeller. Their investigation, aimed at determining the nature of the secondary flow in the blade passages, revealed the existence of two vortices of unequal strength with opposite directions of rotation. The smaller of the two vortices and the associated wake region is located immediately behind the suction surface of the blades.
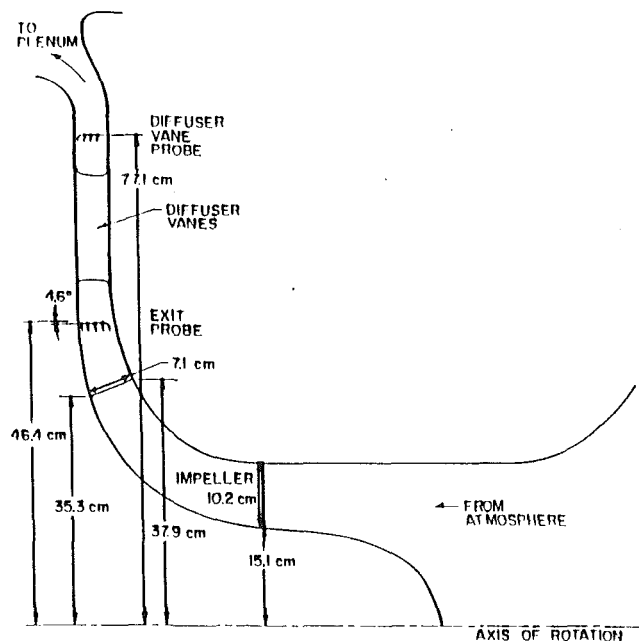
Fig. 1 Compressor flow path

Fig. 2 Impeller geometry

The overall objective of the research described herein is to provide fundamental internal three-dimensional mixed-flow centrifugal compressor flow field data appropriate for defining and studying the fluid mechanic phenomena characteristic of design point compressor operation, verifying existing mathematical models, and directing both model refinements and new model development. Specific research objectives include: (1) the quantification of the design point three-dimensional mean flow through rotating impeller blade passages, and (2) the subsequent evaluation of a viscous flow model for application to these complex flow fields.

These objectives are accomplished through a series of experiments performed in the Purdue Research Centrifugal Compressor. In particular, the technical approach quantifies the design point internal three-dimensional flow field in the impeller passages with a one-dimensional LDV. These data are then correlated with predictions obtained from a viscous turbomachinery flow model.

Research Centrifugal Compressor

The Purdue Research Centrifugal Compressor is a low-speed, moderate-scale turbomachine, which features a mixed-flow impeller with 23 backswept blades and a vaned radial diffuser. The shrouded impeller has an axial inlet, with the air exiting the impeller at an angle of approximately 70 deg from the axial direction. The compressor is driven by a 29.8 kW (40 hp) electric motor at a constant speed of 1790 rpm, with the mass flow rate controlled by a butterfly valve in the discharge piping. The compressor flow path is depicted in Fig. 1, with the impeller geometry shown in Fig. 2. Bryan and Fleeter (1987) give a complete description of the facility.
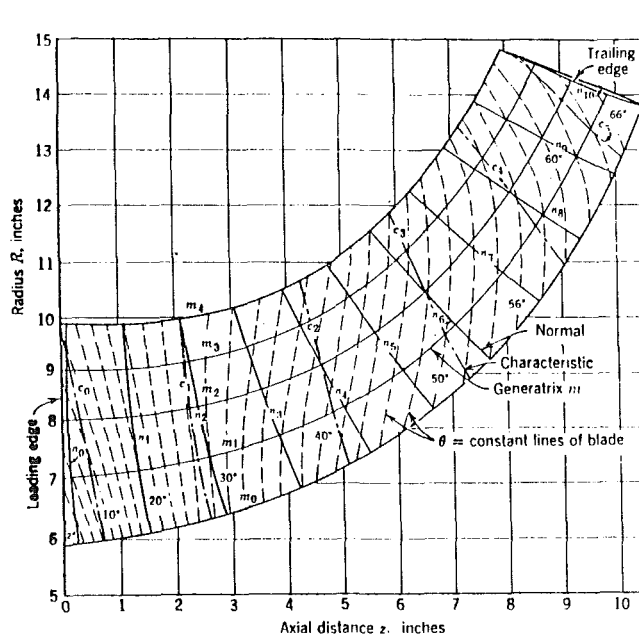
Optical access to the impeller flow passages is accomplished with a plexiglass shroud, which is fixed to the impeller. A window provides optical access to the vaneless space and the vaned radial diffuser. It is approximately 30.5 cm (12 in.) long, covers three diffuser vane passages, and extends to within 2.5 cm (1 in.) of the impeller outlet to allow measurement near the outlet. The primary facility parameters are given in Table 1.

LDV Data Analysis

LDV System. A dual-beam LDV system operated in the backscatter mode is utilized. The ellipsoidal probe volume lengths are d_m = 126.6 μm (0.005 in.), h_m = 127.2 μm (0.005 in.), and l_m = 1266 μm (0.050 in.), resulting in an enclosed probe volume of 0.0106 mm^3 (6.47 $\times$ 10^{-7} in.^{3}). The flow seeding material consists of a mixture of propylene glycol and ethanol, with a density ratio of 900:1 and a particle diameter between 0.5 and 1.5 μm. Maxwell and Seasholtz (1974) show that the amplitude ratio of these particles at the nominal absolute velocity of interest of these experiments, 80 m/s, is above 98 percent.

There is limited physical space for optical access to the impeller flow passages. Thus, a custom optics assembly was designed and fabricated in which a fiber-optic link connects the laser and preliminary optics to the final optics assembly. This enables the laser and the preliminary optics to be mounted on a fixed optical bench, with the positioning and orientation of the probe volume accomplished by traversing only the physically much smaller final optics assembly.

The preliminary optics is depicted in Fig. 3. The beam from a 4-W argon-ion laser operating at 514.5 ηm is turned 180 deg

---

Nomenclature

d_m, h_m, l_m = probe volume dimensions	w = weighting function	
De^{-2} = illumination beam diameter	α = measurement direction angle	2 = impeller exit
h = enthalpy	λ = wavelength	$1, 2, 3$ = coordinate direction
n = number of samples	ν = frequency	a, b, c = measurement direction
U = velocity	**Subscripts**	D = Doppler
	1 = impeller inlet	s = shift
		t = tangential
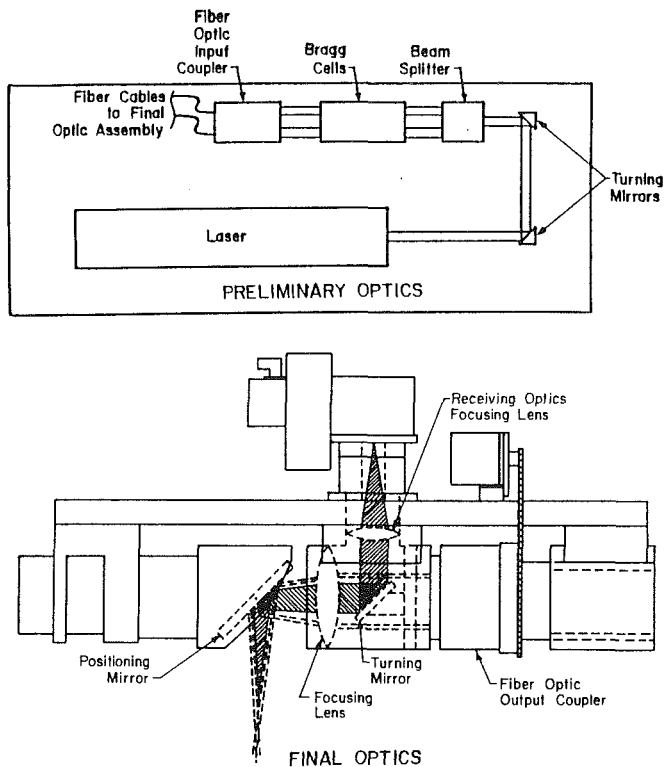
Fig. 3 Preliminary and final LDV optics

COMPRESSOR

Mean Radius (cm)

Inlet	20.8
Exit	36.8

Number of Blades	23
Backswept Blades	
Mixed-Flow	
Mass Flow (kg/s)	3.33
Flow Coefficient	0.253
Rotational Speed (rpm)	1789
Power (kW)	9.6

LDV TRAVERSING SYSTEM

Axial	Travel	Precision
x (vertical)	66.04 cm (26 in.)	0.025 mm (0.001 in.)
y (horizontal)	45.72 cm (18 in.)	0.025 mm (0.001 in.)
z (axial)	45.72 cm (18 in.)	0.025 mm (0.001 in.)
θ (mirror axis)	360°	0.018°
ϕ (mirror axis)	30°	0.450°
γ (beam rotation)	360°	360°

LDV MEASUREMENTS

Number of Samples:	3000
Number of Cycles:	16
Number of Position Bins:	20
Number of Histogram Bins:	20
Comparison:	3%
Lens Focal Length:	250 mm
Lens Half Angle:	5.711 deg

by two first surface mirrors and directed into the beam splitter. The resulting two equal power beams are individually frequency shifted: one by 40 MHz and the other by 30 MHz, for an effective frequency shift of 10 MHz. These beams are directed into a translator module, which provides the proper beam positioning for the input fiber-optic coupler. The beams are then transmitted to the final optics assembly through two polarization preserving fibers.

The final optics assembly, Fig. 3, includes the focusing lens, the probe volume positioning mirror, and the receiving optics systems. The fibers are connected to the fiber-optic output coupler, which is mounted on a bearing assembly. The output coupler can be rotated through 360 deg around the transmission beam axis and is remotely driven by a stepping motor. The beams then pass through a thin optical window, which supports the turning mirror for the backscattered signal. Finally, the beams are focused by the focusing lens. The probe volume is positioned in space by the mirror assembly, which rotates in two planes about the transmission beam axis and is driven by independent stepping motors for each of the two planes. Since the LDV system operates in the backscatter mode, the mirror and the lens are also used to collect the scattered light and image it on the photodetector surface. After the scattered light is collected by the lens, it is turned by a mirror and oriented toward the receiving optics focusing lens, which images the scattered light on the photodetector surface.

Data Acquisition. The three-dimensional velocity data are obtained by making measurements synchronized to the impeller rotation in a stationary meridional plane. An HP-1000 Data Acquisition Computer is used to control the extensive instrumentation system. This includes the setting of the compressor operating point, the positioning and orientation of the probe volume, the strobing of the illumination beams, the encoding of the rotational position, and the collection and recording of the LDV data.

Positioning and orientation of the probe volume are achieved with a six-axis traversing system. The final optics assembly can be linearly traversed as a unit along three mutually orthogonal

axes. The other three axes are incorporated in the final optics assembly, as previously described. The three linear axes have a position encoder for feedback control during translation. The positions of the rotational axes are tracked by logging the number of motor steps. Table 1 gives the limits and precision of motion of each axis.

For the LDV impeller blade passage measurements, the beams are strobed to keep the beam reflections from the passing blades from saturating the photodetectors. The frequency shift Bragg cells are also used for this strobing, with a square wave generator used to modulate the power. The wave generator has an adjustable delay and pulse length triggered by a pulse for each blade pass generated by frequency multiplying the once per revolution pulse by the number of impeller blades. The signal is validated by checking that the rotational period does not vary by more than a prescribed error.

The impeller angular position is determined with a timing circuit, which includes a 1 MHz clock circuit, which latches a timing word at the data ready pulse from the LDV system and is reset with each revolution. The timing circuit is interfaced to the computer as a second counter, with the timing word passed with the LDV word to the computer and processed with the data analysis software. Note that the large impeller mass results in negligible rotational speed fluctuations.

The LDV system is controlled by the processor, which is interfaced for data transmission and position encoder information to the HP-1000 Computer. The data are binned according to the circumferential position in the passage, with data ensembled over all the blade passages. The computer continues to collect data until a sufficient number of samples are collected in each bin. The LDV operating parameters for these experiments are given in Table 1.

Prior to making a measurement, the axis settings for the required measurement direction and probe volume half angle

must be determined. The complicated geometry of the impeller shroud prevents solution of a simple algebraic relation to find this information. An inverse ray trace algorithm, which performs an exact ray trace from the probe volume to the focusing lens, is used. Fagan (1989) gives details of the ray trace algorithm.

LDV Data Analysis. The LDV gives an instantaneous measure of the velocity at a point in the flow field. However, the value of the mean velocity and the turbulence intensity is of more interest than the instantaneous velocity. Statistical analysis is required to derive these quantities. Additionally, three independent measurements in different directions are required to resolve the three components of the mean velocity vector.

The evaluation of the statistical mean and standard deviation of the velocity is defined by Eq. (1) and (2). The velocity and the probability of measurement are correlated for laser-Doppler velocimetry measurements. Since the data are effectively equation time sampled for measurements in rotating blade passages, the weighting function is unity.

$$\overline{U} = \frac{\sum\limits_{n} U_i \, w_i}{\sum\limits_{n} w_i} \qquad (1)$$

$$[\overline{u'^2}]^{1/2} = \left[\frac{\sum\limits_{n} (U_i - \overline{U}) w_i}{\sum\limits_{n} w_i} \right]^{1/2} \qquad (2)$$

The minimum sample size for each measurement is determined by choosing an acceptable uncertainty ϵ_u for a given confidence level and using Student's t distribution. It has been demonstrated that the histogram of velocity measurements of "steady" flows taken with a laser-Doppler velocimeter has approximately a Gaussian distribution. As a consequence, measurements deviating by more than four standard deviations from the mean are rejected as noise.

Determination of the three-dimensional mean flow field using a one-dimensional velocimeter requires independent measurements in three unique directions for each location with constant flow conditions during each of the measurements. The three required measurements cannot be made in mutually orthogonal directions due to limited optical access in the impeller blade passage. The direction of each measurement is described by a normalized vector referenced to a fixed coordinate system. The axes orientation of the orthogonal coordinate system is given in Fig. 2. The mean velocity components along the three axes are then found by solving the three algebraic equations, Eqs. (3) and (4).

$$\begin{bmatrix} \overline{U}_1 \\ \overline{U}_2 \\ \overline{U}_3 \end{bmatrix} = [M]^{-1} \begin{bmatrix} \overline{U}_a \\ \overline{U}_b \\ \overline{U}_c \end{bmatrix} \qquad (3a)$$

$$[M] = \begin{bmatrix} \cos \alpha_{a1} & \cos \alpha_{a2} & \cos \alpha_{a3} \\ \cos \alpha_{b1} & \cos \alpha_{b2} & \cos \alpha_{b3} \\ \cos \alpha_{c1} & \cos \alpha_{c2} & \cos \alpha_{c3} \end{bmatrix} \qquad (3b)$$

$$\overline{U}_a = \frac{\lambda}{2 \sin \kappa_a} \overline{\nu}_{Da} \qquad (4)$$

where ν_{Da} is the measured Doppler frequency, α_{ai} denotes the angle between the measurement direction and the ith axis, U_a

is the velocity component in the measurement direction, and U_i is the velocity component along a coordinate axis.

After the data for each of the three measurements at a single location in the meridional plane are analyzed, the mean velocity vector described by three mutually orthogonal components is determined from Eqs. (3) and (4). Since these results include information about the velocity field across the circumferential extent of the passage, a small number of measurements distributed along the measurement plane from hub to shroud are sufficient to describe the three-dimensional flow field.

Velocity Measurement Accuracy. The following analysis gives an estimation of the uncertainty involved in determining the mean flow velocity vector from a typical set of measurements made with the LDV in the Purdue Research Centrifugal Compressor. The analysis of the measurement accuracy is done in two steps. First the uncertainty for each of the directional measurements is estimated. Subsequently, the uncertainty is calculated for the orthogonal velocity components. A location in the first data plane (15 percent passage) is used for this analysis, and the important parameters and experimental results are given in Table 2.

The mean velocity for each measurement is calculated from Eq. (4), with the uncertainty given in Eq. (5) and the values for each term of Eq. (5) for the three measurement directions given in Table 2. The total uncertainty for the measurement is due to three sources. The first term on the right-hand side of the equation is the contribution due to the finite bandwidth of the laser. The laser has a specified bandwidth of 20 GHz, which corresponds to an uncertainty in wavelength of 2.206 $\times$ 10^{-12}m. For this measurement the wavelength term is negligible compared to the other terms of Eq. (5). The wavelength term is nearly constant for all data and will be subsequently neglected. The second term on the right-hand side of Eq. (5) is due to uncertainty in the half-angle at the probe volume. The conventions used for this analysis estimate the half-angle uncertainty at 10 percent of the deviation caused by refraction at the shroud surfaces compared to the undeviated beam if the shroud was not there. The third term on the right-hand side of Eq. (5) is due to the uncertainty in estimating the mean from the experimental data based upon a normal distribution. The uncertainty for each of the measurements is less than 0.15 percent.

$$d\overline{U}_A = \left(\frac{\partial \overline{U}_A}{\partial \lambda}\right) d\lambda + \left(\frac{\partial \overline{U}_A}{\partial k_A}\right) dk_A + \left(\frac{\partial \overline{U}_A}{\partial \overline{\nu}_{DA}}\right) d\overline{\nu}_{DA} \qquad (5)$$

The orthogonal velocity components are determined from the velocity measurements made in nonorthogonal directions, Eq. (3). As a consequence, the uncertainty for each of the velocity components depends upon the angular separation of the measurement directions and the measurement uncertainties. The analysis is further complicated due to uncertainties in the actual measurement directions. This part of the analysis is done in two steps. The mean velocity components and uncertainties along each of the orthogonal axes are calculated with the measurement directions calculated from the ray trace model. In a subsequent step, the calculations are repeated using the measurement directions for the axis settings based upon no refraction of the beams by the shroud surfaces. The mean velocities for the two cases are compared to set an upper limit for the velocity uncertainties due to an error in determining the measurement direction. All the results are presented in Table 2. Only for the velocity along the x axis (radial direction) is the additive error above 1 percent. It is not surprising that the error is largest in this direction because optical access to the passage severely limits the angle between the measurements for resolution of the hub-to-tip components which is nearly radial for this position. Additionally, the error due to uncertainty in the measurement direction is much higher (one order of magnitude) than other sources of error. The analysis of that

Table 2 Experimental parameters, results, and uncertainty

Parameters & Results

Mass Flow Rate:	3.34 kg/s (7.35 lbm/s)
Axial Position:	3.871 cm (1.524 in)
Radial Position:	22.611 cm (8.902 in)
Time Window:	20

		A	B	C
Direction		(-.2203, -.4905, .8431)	(-.0003, .4898, .8718)	(.2185, -.0007, .9758)
Frequency (mHz)	Mean	11.316	12.888	14.394
	Error	.01295	.01061	.01461
	Standard Deviation	.3623	.2934	.4025
Half Angle (radians)		.099465	.099441	.099461

Uncertainty Due to Individual Sources

		A	B	C
$\frac{\partial U_A}{\partial \lambda} d\lambda$	(m/s)	1.257×10^{-4}	neglect	neglect
$\frac{\partial U_A}{\partial k_A} dk_A$	(m/s)	5.876×10^{-3}	6.694×10^{-3}	7.474×10^{-3}
$\frac{\partial U_A}{\partial v_{DA}} dv_{DA}$	(m/s)	3.355×10^{-2}	2.749×10^{-2}	3.785×10^{-2}
Total	(m/s)	3.955×10^{-2}	3.418×10^{-2}	4.532×10^{-2}
Error		.13%	.10%	.12%

Measurement Direction Uncertainty

	Calculated Direction			No Distortion	
	Velocity	Uncertainty		A Velocity	
	m/s	m/s	%	m/s	%
X	4.674	±.014	0.3	.166	3.6
Y	2.029	±.007	0.3	-.013	-0.6
Z	37.172	±0.74	0.2	-.036	-0.1

error is very conservative and could likely be reduced by a factor of 3 to 5.

This analysis is not an attempt to calculate the uncertainty rigorously for the results. It is an attempt to find the magnitude of the error for a typical measurement. The results demonstrate that the uncertainty in determining the mean velocity is not larger than the uncertainty in setting and controlling the mass flow rate through the machine, which is estimated at 2–3 percent.

Impeller Flow Field Modeling

The flow through the passages of a centrifugal compressor is highly complex and three dimensional. There are rapidly growing end wall and blade surface boundary layers, secondary flows driven by large blade-to-blade pressure gradients, and possible separated flow regions. As a consequence, adequate prediction of the flow field requires three-dimensional modeling techniques.

Viscous Model.

The viscous results are from a modified version of the Impact (Implicit Parabolic Computational Technique) code developed by C. M. Rhie (1983). This method uses the parabolic approximation for solving the finite volume form of the Reynolds averaged Navier–Stoke's equations. After applying the isotropic turbulent viscosity hypothesis, the system is modeled by Eqs. (6) and (7). The system of equations is thus completed

by assuming constant rothalpy and applying the perfect gas relationship.

$$\frac{\partial}{\partial x_i}(\rho u_i) = 0 \tag{6}$$

$$\frac{\partial}{\partial x_i}(\rho u_i u_j) = -\frac{\partial P}{\partial x_j} + \frac{\partial}{\partial x_i}\left[(\mu + \mu_t)\left(\frac{\partial u_i}{\partial x_j} + \frac{\partial u_j}{\partial x_i}\right)\right] - \frac{2}{3}\rho \kappa \delta_{ij} \tag{7}$$

A two equation k–ϵ eddy viscosity turbulence model modified to account for streamline curvature and Coriolis acceleration is used to close the system. The eddy viscosity μ_t is given by Eq. 8, with the scalar transport mechanisms for k and ϵ given by Eqs. 9(a) and 9(b), respectively.

$$\mu_t = C_u \rho \frac{\kappa^2}{\epsilon} \tag{8}$$

where C_u is an empirical constant; κ is the turbulent kinetic energy; and ϵ is the turbulence energy dissipation.

$$\frac{\partial}{\partial x_i}(\rho u_i \kappa) = \frac{\partial}{\partial x_i}\left[\left(\frac{\mu_t}{\sigma_k}\right)\left(\frac{\partial \kappa}{\partial x_i}\right)\right] + P - \rho\epsilon + G_c \tag{9a}$$

$$\frac{\partial}{\partial x_i}(\rho u_i \epsilon) = \frac{\partial}{\partial x_i}\left[\left(\frac{\mu_t}{\sigma_\epsilon}\right)\left(\frac{\partial \epsilon}{\partial x_i}\right)\right] + \left(\frac{\epsilon}{\kappa}\right)(C_1 P - C_2 \rho\epsilon) + G_c \frac{\epsilon}{\kappa} \tag{9b}$$

where C_1, C_2, σ_k, and σ_e are empirical constants and G_c is the streamline curvature correction proposed by Wilcox and Chambers (1977).

The governing equations are written in the form of a single general relation for an arbitrary scalar dependent variable ϕ, Eq. (10).

$$\frac{\partial}{\partial x_j}(\rho u_j \phi) = \frac{\partial}{\partial x_j}\left(\Gamma \frac{\partial \phi}{\partial x_j}\right) + S \tag{10}$$

where Γ is an effective diffusion and S is the source term.

To compute the solution, the conservative form of the general transport equation expressed in arbitrary curvilinear coordinates is integrated over a control volume, with subsequent approximations made to yield a finite-difference expression. The diffusion term in the streamwise direction is neglected to parabolize the governing equation. Linear interpolation of quantities between adjacent grid nodes results in a fully implicit expression with second-order accurate, centered differencing in the cross-stream direction and first-order accurate, upstream differencing in the streamwise direction. The difference relation is solved simultaneously at each point in the cross-stream plane and, after obtaining satisfactory convergence, the procedure is repeated at the next cross-stream plane. To treat reverse flow regions, the flare approximation is employed, which neglects convection in the throughflow direction for the region.

After the momentum equations are marched through the computational domain, the pressure is corrected in a three-step process to satisfy local and global continuity. As part of the solution process at each cross-stream plane, a one-dimensional global pressure correction is applied. Subsequently, a two-dimensional elliptic pressure correction is performed to satisfy local continuity. Finally, a three-dimensional elliptic pressure correction is executed after each complete forward marching pass. The entire solution procedure is iterated until adequate convergence of the flow field is obtained.

Initial and boundary conditions must be specified to apply this code to centrifugal geometries. The computational grid is generated in an independent program, with the impeller geometry entered through blade profiles at the hub and the shroud. The information required to start the flow code includes the three velocity components, the static pressure, the enthalpy, the turbulent kinetic energy, and the turbulence dis-

sipation at all locations in the inlet plane. The code does not require any information at the exit of the impeller and, since the input velocity specifies the mass flow, iteration of the input parameters is not required to match the mass flow.

The grid used to model the flow in the impeller of the Purdue Research Centrifugal Compressor is $15 \times 19 \times 50$, with the blade leading edge at the 8th streamwise grid and the trailing edge at the 42nd grid. The major difficulty in running the impact code is the determination of a suitable value of the inlet turbulent dissipation, which affects the turbulent viscosity as determined by the k-ϵ model.

Results

LDV flow field and unsteady pressure measurements were made to study the three-dimensional flow field in the compressor at the design operating point. Predictions from three-dimensional inviscid and viscous flow models are also presented for correlation with these flow field data.

The design operating point for the constant speed operating line (1,790 rpm) has a mass flow rate of 3.33 kg/s (7.35 lbm/s). The variation of the inlet stagnation temperature and pressure for the experiment from the nominal values of 298 K (537 R) and 101.3 kPa (14.69 psia) are less than the uncertainty in determining the compressor mass flow rate. Consequently, the corrected mass flow rate of each operating point is also constant.

LDV data were taken at five planes in the impeller passage of the Purdue Research Centrifugal Compressor. The planes are located at 16, 42, 62, 76, and 88 percent passage (Fig. 4). The three-dimensional flow field data are interpolated onto a 11×15 regularly spaced grid, with the results presented in terms of the throughflow velocity (velocity component normal to the measurement plane) and the secondary velocity vector (velocity components in the measurement plane) for each plane.

Mean Flow Field. The throughflow velocity data obtained at the design operating point are presented in Figs. 5-8. The plane 1 throughflow velocity data show a nearly linear velocity gradient from the suction to pressure surface along the passage. The throughflow velocity also increases from hub to shroud. At plane 2, the throughflow velocity data indicate a thickening of the boundary layer on the hub surface. Additionally, the velocity gradient from the suction to pressure surface is reduced. At plane 3, a low-velocity region forms on the shroud near the suction surface similar to the jet-wake pattern observed by Eckardt (1976). In planes 4 and 5, similar profiles are observed, with the extent of the deficit region from the shroud surface growing along the passage. Note that the apparent spike in the plane 3 velocity nearer the low-velocity region is an interpolation error due to the extremely steep gradient in velocity.

The design operating point secondary velocity vector and streamwise vorticity, i.e., the vorticity component normal to the measurement plane, contour data, for planes 1-5 are presented in Figs. 9 and 10, respectively. The secondary velocity vector data are somewhat difficult to interpret due to the large backsweep angle of the impeller blades. Since the data are taken at planes normal to the meridional plane, flow at the blade angle has a tangential component of velocity which is much larger than the imposed secondary flow. Consequently, the contour plots of the streamwise vorticity are also presented to define the secondary flow field. Since the positive streamwise direction is oriented into the figure, a positive vorticity corresponds to a clockwise rotation.

At plane 1, the vorticity data indicate regions of negative vorticity in several locations. However, the secondary velocity data show no discernible rotation of the flow in these regions. The plane 3 data show that rotation of the flow is discernible when the magnitude of the normalized vorticity exceeds 1.2.
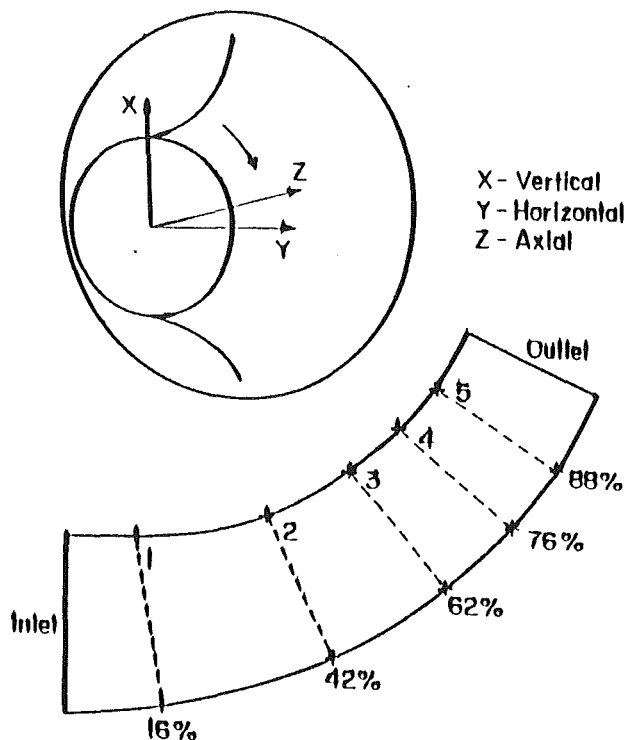

Fig. 4 Orthogonal coordinate system orientation and LDV measurement plane locations

Consequently, this value will be used as a minimum when discussing the presence of vorticity in the flow.

The first significant secondary flow is observed at plane 3. A region of positive vorticity exists along the shroud corresponding to the deficit region observed in the throughflow velocity results. The magnitude of the streamwise vorticity is highest at approximately 70 percent of the distance from the pressure to the suction surface near the shroud. A region of weak negative vorticity is found along the suction surface, with the highest magnitude occurring at approximately 50 percent of the distance from hub to shroud. The secondary velocity vector results show the turning of the flow in both these locations, with the turning on the suction surface limited to the first grid near the blade surface. At plane 4, the extreme turning of the flow and high vorticity along the shroud has dissipated. Regions of weak positive vorticity are observed in the shroud pressure and shroud suction corners. A similar pattern is observed at plane 5, with a large magnitude increase of the vorticity in the region of the shroud suction corner.

Turbulence Intensity and Enthalpy. The standard deviation of the velocity fluctuations and the enthalpy at each grid point is also determined. Unfortunately, it would require six independent measurements at each location to determine the standard deviation of the velocity fluctuations along each of the mutually orthogonal axes from which the turbulence intensity could be determined. Thus, for the results presented herein the turbulence intensity is estimated by the standard deviation of the velocity fluctuations in the measurement directions and normalized with the square of the impeller exit rotational speed, Eq. (11). The enthalpy is calculated by finding the product of the blade rotational speed and the tangential component of the absolute velocity at each location assuming a reference enthalpy of zero at the inlet to the impeller. The enthalpy is also normalized with the square of the impeller exit rotational speed.

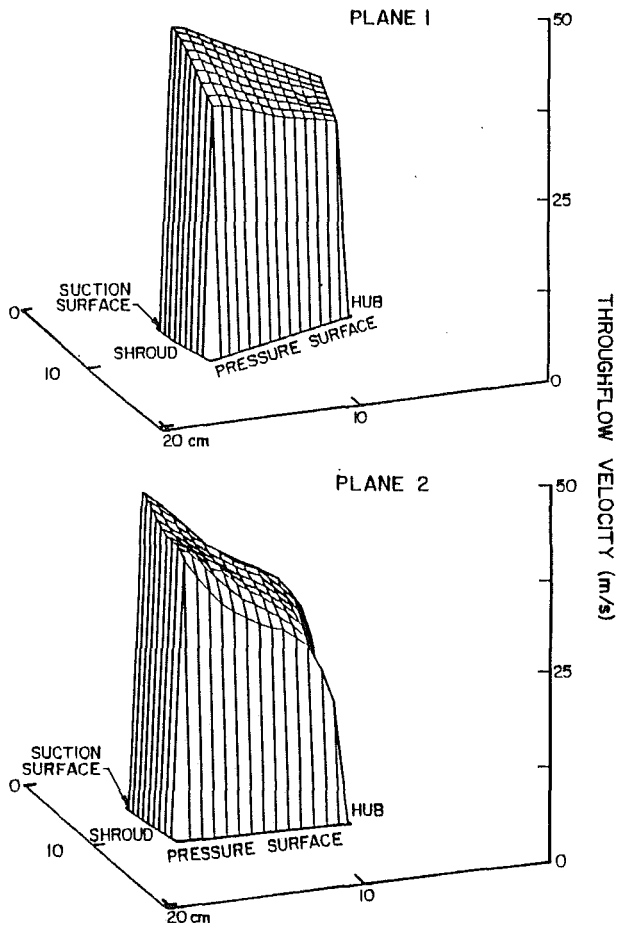$$T = \sqrt{\frac{\frac{1}{3}(U_A^2 + U_B^2 + U_c^2)}{U_T^2}} \qquad (11)$$

PLANE I

PLANE 2

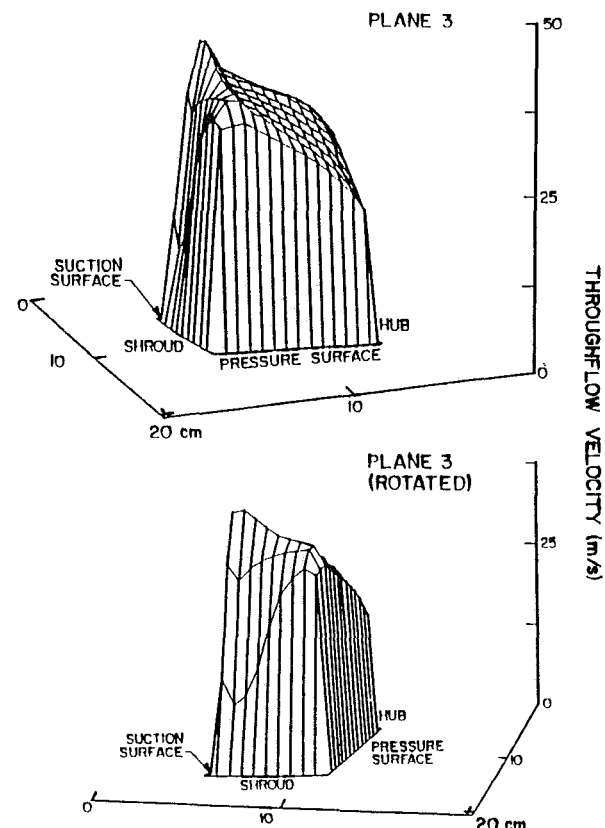Fig. 5   LDV throughflow velocity data for planes 1 and 2

PLANE 3

PLANE 3
(ROTATED)

Fig. 6   LDV throughflow velocity data for plane 3

PLANE 4
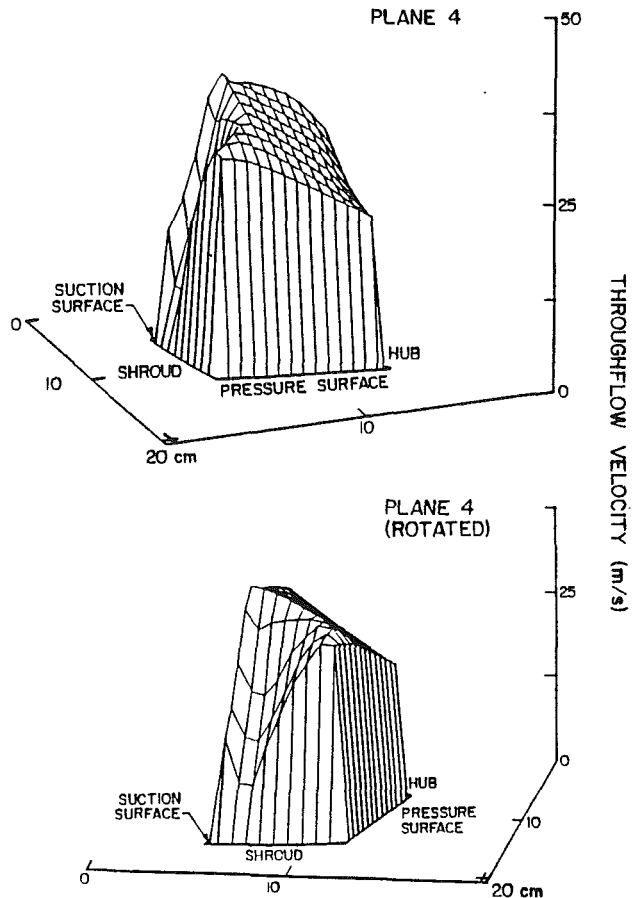
PLANE 4
(ROTATED)

Fig. 7   LDV throughflow velocity data for plane 4

PLANE 5
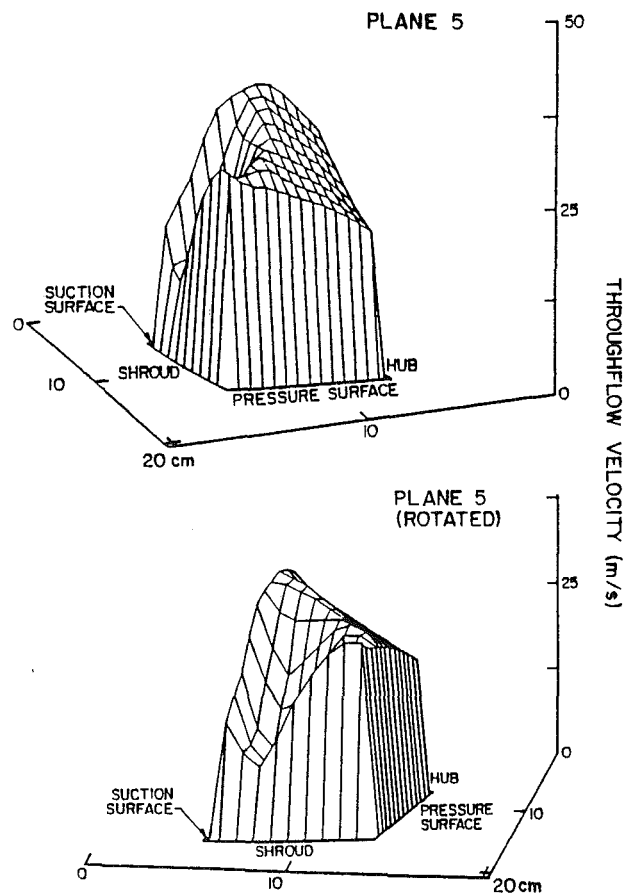
PLANE 5
(ROTATED)

Fig. 8   LDV throughflow velocity for plane 5
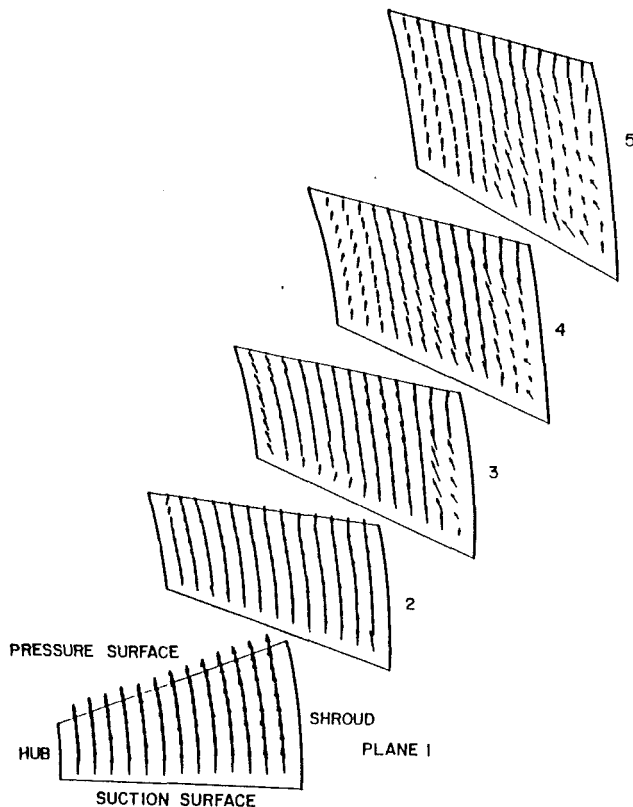
Fig. 9 LDV secondary velocity vector data for planes 1-5

Contour	Normalized Vorticity
1	-2.80
2	-2.00
3	-1.20
4	-0.40
5	0.40
6	1.20
7	2.00
8	2.80

Fig. 10 LDV vorticity contour data for planes 1-5

The design operating point turbulence intensity contour results are given in Fig. 11. At plane 1, the turbulence intensity is low across the entire plane. Regions of higher turbulence are located in the hub pressure corner and along the suction surface at the second plane. At plane 3, regions of high turbulence are still found in these locations and additionally, the high turbulence intensity associated with the velocity deficit region is observed on the shroud near the suction surface. At planes 4 and 5, the turbulence associated with the growing deficit region is observed, with the turbulence at the hub pressure corner and along the suction surface reduced.

The design operating point enthalpy data contours are presented in Fig. 12. The enthalpy is negative over 55 percent of plane 1, with the net power input to the flow over the first 16 percent of the passage zero. The enthalpy rise over the plane is fairly constant between planes 1 and 2. At plane 3, an interesting feature of backswept blades is first observed. Namely, work is done on the air as the relative velocity is reduced because the tangential component of the absolute velocity and subsequently the enthalpy of the air is increased. However, the power input to the air in the low-throughflow velocity regions is small because the mass flow is small. As a consequence, the regions of highest enthalpy are in the boundary layers. A similar trend is observed in planes 4 and 5.

The LDV results indicate a slight disturbance to the flow near the hub in the first 40 percent of the passage. This is observed in the throughflow velocity and turbulence intensity results at plane 2. These results indicate a boundary layer in the hub pressure corner, which becomes smaller at plane 3. Another indication of a flow disturbance is the region with negative enthalpy observed near the hub in plane 1. However, all indications of a disturbance disappear as the flow is turned radially. At plane 3, a deficit region with large positive vorticity similar to the jet-wake flow found in most centrifugal compressors is observed. The deficit or wake region is located on the shroud but not in the suction corner. Through the re-
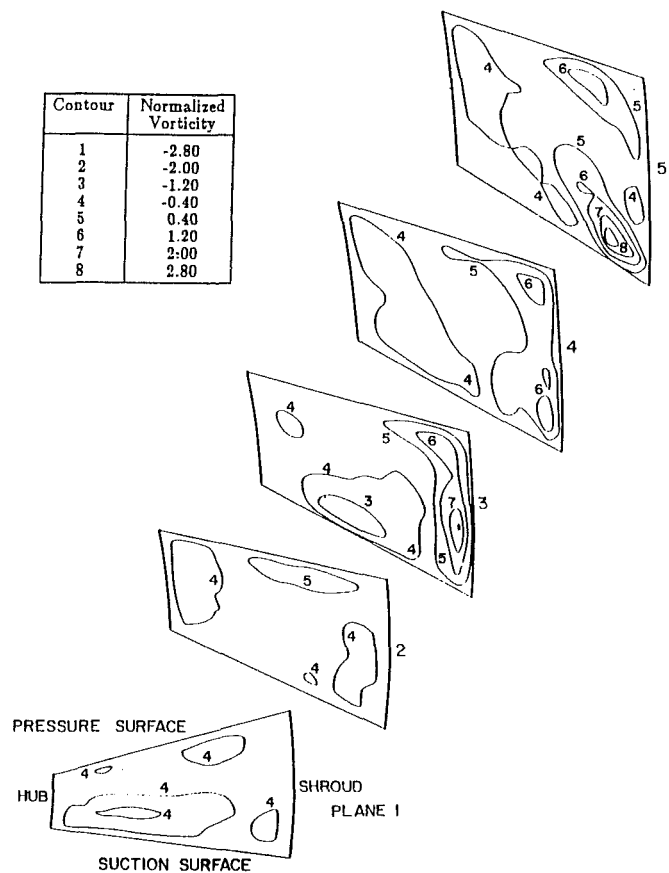
mainder of the passage, the extent of the deficit region continues to grow. At the final data plane, regions of positive vorticity are located on either side of the wake.

Viscous Flow Field Predictions. Rhie's impact code (1983) is used to predict the design operating point flow field in the Purdue Research Centrifugal Compressor. These predictions are presented in terms of the throughflow and secondary velocities, corresponding to the presentation of the experimental results. At the design point, the mass flow rate is 3.40 kg/s (7.50 lbm/s), which is 2.0 percent higher than the nominal flow rate at which the experimental flow field measurements were made. The predictions are presented at planes 1-5 (15, 41, 62, 76, and 88 percent passage), near the location of the LDV measurement planes. Throughflow velocity results are given in Figs. 13 and 14, with the secondary velocity vector results from the inlet to the exit of the impeller presented in Fig. 15.

The throughflow velocity at plane 1 indicates a smooth gradient from hub to shroud. The predicted velocity near the hub is slightly less than the velocity in the shroud region. At plane 2, similar trends are indicated, with the addition of a predicted high velocity region near the shroud along the suction surface. The throughflow velocity prediction at plane 3 indicates that the high-velocity region extends over most of the passage height from hub to shroud. At plane 4, a region of very low throughflow velocity is predicted at the shroud wall near the suction surface. The results at plane 5 show reverse flow at the shroud suction corner.

Analysis of the secondary velocity results indicates some interesting characteristics. However, there appears to be no strong vortical structure. At plane 1, the secondary flow is minimal. At planes 2, 3, and 4, a significant velocity component in the hub-to-shroud direction oriented outwardly is predicted

Contour	Normalized Turbulence Intensity
1	0.05
2	0.10
3	0.15
4	0.20
5	0.25
6	0.30
7	0.35
8	0.40
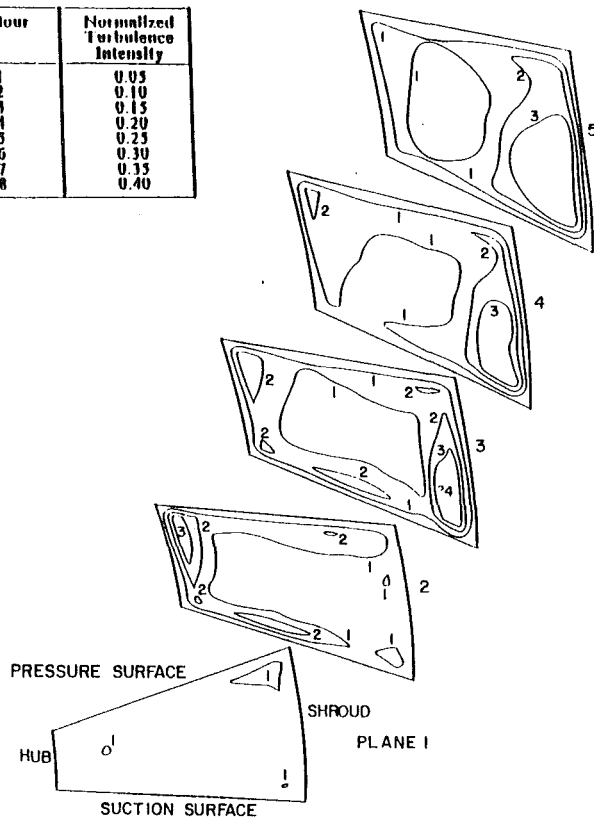
Fig. 11 LDV turbulence intensity data for planes 1-5

Contour	Normalized Enthalpy
1	0.00
2	0.10
3	0.20
4	0.30
5	0.40
6	0.50
7	0.60
8	0.70
9	0.80
10	0.90
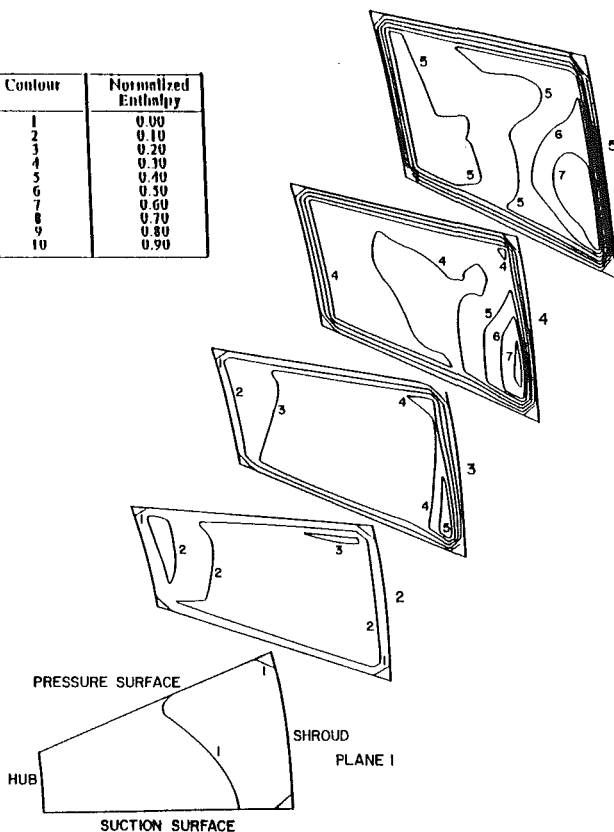
Fig. 12 LDV enthalpy contour data for planes 1-5

along the pressure surface at the shroud suction surface. The region of predicted reverse flow is also evident in the secondary velocity vector results at plane 5.
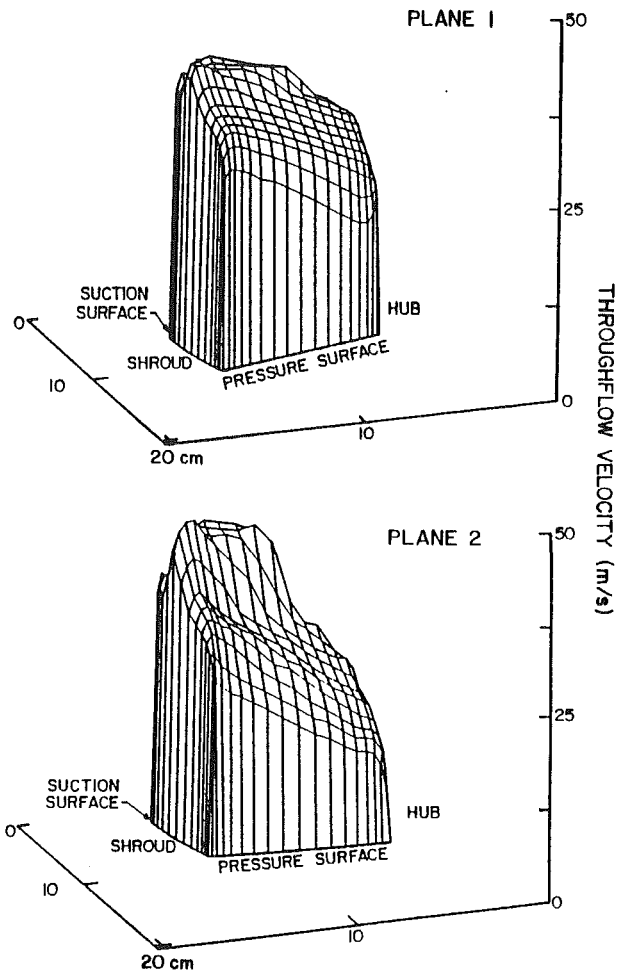
Fig. 13 Viscous throughflow velocity predictions for planes 1 and 2

Correlations. The predictions from the viscous code capture the flow phenomena but show poor correlation with the data. The code predicts the jet-wake region observed in the experimental data. However, the code does not accurately predict the streamwise position where the wake region starts nor the position of the maximum velocity deficit in the measurement plans. Although the start of the wake region is clearly observed at plane 3 in the LDV results, this phenomenon is first seen in the predictions at plane 4. The model also predicts that the wake region is located in the shroud suction corner, which is inconsistent with the LDV results. Finally, the model predicts a high-velocity region in the passage, which is not observed in the experimental results.

Summary and Conclusions

A series of experiments were performed to investigate and quantify the three-dimensional mean flow field in centrifugal compressor flow passages and to evaluate contemporary internal flow models. The experiments include the acquisition and analysis of LDV data in the impeller passages of a low-speed moderate-scale research mixed-flow compressor operating at its design point. Predictions from appropriate inviscid and viscous internal flow models were then correlated with these data.

The LDV data show the traditional jet-wake structure observed in many centrifugal compressors. This structure, characterized by a local velocity deficit region near the blade suction surface along the shroud, is observed along the shroud 70 percent of the length from the pressure to the suction surface.
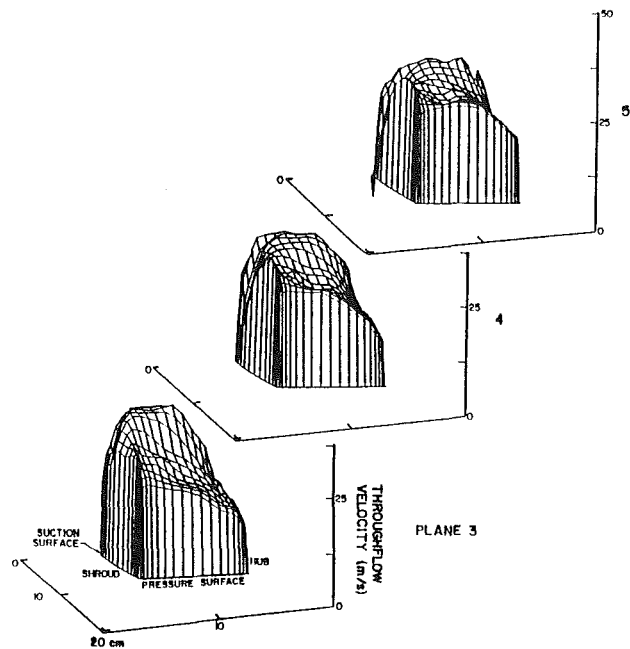
Fig. 14 Viscous throughflow velocity predictions for planes 3, 4, and 5

Fig. 15 Viscous planes 1–5 secondary velocity vector predictions

Application of the viscous flow model to predict the compressor flow field was moderately successful. The viscous code predicted the major phenomena in the flow field, specifically the wake structure near the end of the passage. However, the viscous model showed poor correlation with the data. It predicted that the wake was located in the shroud suction corner different from the LDV results at the design operating point. It also predicted a high-velocity region in the core flow, which was not observed in the experimental data. These results suggest that although current models can now predict phenomena associated with viscous regions in the impeller passage as well as the structure in the potential region of the flow, further development is required before modeling can be used to predict the internal flow field accurately.

Acknowledgments

References

Adler, D., and Levy, Y., 1979, "A Laser-Doppler Investigation of the Flow Inside a Backswept, Closed, Centrifugal Impeller," *Journal of Mechanical Engineering Science*, Vol. 21, pp. 1–6.

Bryan, W. B., and Fleeter, S., 1987, "The Effect of Prewhirl on the Internal Aerodynamics and Performance of a Mixed Flow Centrifugal Compressor," USAAVSCOM Technical Report TR-87-C-35, Dec.

Denton, J. D., 1983, "An Improved Time-Marching Method for Turbomachinery Flow Calculation," ASME *Journal of Engineering for Power*, Vol. 105, pp. 514–524.

Durao, F. G., Goulas, A., and Whitelaw, J. H., 1979, "Measured Velocity Characteristics of the Flow in the Impeller of a Centrifugal Compressor," ASME Paper No. 79-HT-32.

Eckardt, D., 1976, "Detailed Flow Investigations Within a High-Speed Centrifugal Compressor Impeller," ASME *Journal of Fluids Engineering*, Vol. 98, pp. 390–402.

Elder, R., and Forster, C., 1987, "Measurements in Centrifugal Compressors," von Karman Institute for Fluid Dynamics Lecture Series.

Fagan, J. R., 1989, "An Investigation of the Three-Dimensional Flow Field in a Centrifugal Compressor," Ph.D. Thesis, Purdue University, Aug.

Johnson, M. W., and Moore, J., 1983, "The Influence of Flow Rate on the Wake in a Centrifugal Impeller," ASME *Journal of Engineering for Power*, Vol. 105, pp. 33–39.

Krain, H., 1984, "Experimental Observations of the Flow in Impellers and Diffusers," von Karman Institute for Fluid Dynamics Lecture Series, 1984-07, May.

Maxwell, B. R., and Seasholtz, R. G., 1974, "Velocity Lag of Solid Particles in Oscillating Gases and in Gases Passing Through Normal Shock Waves," NASA TN-D7490.

Rhie, C. M., 1983, "Basic Calibration of a Partially-Parabolic Procedure Aimed at Centrifugal Impeller Analysis," AIAA Paper No. 83-0260.

Wilcox, D. C., and Chamber, T. L., 1977, "Streamline Curvature Effects on Turbulent Boundary Layers," *AIAA Journal*, Vol. 16.

Mechanics on the Tip Clearance Loss of Impeller Blades

Y. Senoo

Miura Company Ltd.,
Matsuyama, Ehime, 799-26, Japan
Fellow ASME

For predicting the tip clearance loss of turbomachines, different equations are published in the literature based on different principles. In 1986 the present author postulated a new theory where the pressure loss consisted of two parts: the pressure loss induced by the drag force of the leaked flow, and the pressure loss to support the axial pressure difference without blades in the tip clearance zone. It has been suggested that the two losses were the same loss looked from two different viewpoints, or at least a part of the former was included in the latter or vice versa. In this paper the pressure loss due to the tip clearance is examined based on a macroscopic balance of forces, and the two kinds of loss are derived. Furthermore, it is shown that the former comes from the induced drag, which is parallel to the blade, while the latter comes from the missing blade force normal to the blade in the clearance zone. Because these two forces are mutally perpendicular, the two losses are entirely different in nature and they do not even partially overlap. It is also made clear quantitatively how the loss of the kinetic energy of leaked flow is related to the induced drag of the clearance flow.

Introduction

In many turbomachines there are clearances between edges of impeller blades and the casing. As a result, a certain amount of reduction in the performance is inavoidable due to the tip clearance. It is essential for turbomachine designers to predict the influence of the tip clearance correctly. A lot of research on the subject has been reported in the literature. It is divided into three groups:

1 The performance change of turbomachines due to the tip clearance is measured experimentally, and empirical equations are proposed based on the assumed loss mechanism.

2 Details of flow near the blade tip are measured with an advanced technique for better understanding of the phenomena.

3 By means of CFD, the flow pattern and the entropy change are predicted and compared with experimental data.

In 1987, the present author reviewed the literature on tip clearance and he was quite embarrassed on the inconsistent presentations of tip clearance loss by different authors. In Vavra's textbook (1960) it is written that the tip clearance loss is proportional to the square of the lift coefficient, while in papers written by Lakshminarayana (1970) and by Roberts et al. (1986) the loss is proportional to the 1.5th power of the lift coefficient. On the other hand, according to Senoo and Ishida (1986, 1987) the loss is the sum of the two terms, one proportional to the lift coefficient and the other proportional to the 1.5th power of the lift coefficient. These different relations have been derived based on different hypotheses on the mechanics of pressure loss due to the tip clearance.

Obviously all of these equations cannot be correct, but all of these empirical equations are widely used by adopting em-

pirical correction coefficients and by limiting the range of application to near the design condition. By means of CFD, it may be possible to predict the flow pattern and the pressure loss for individual cases of blade tip clearance, but it is too much to clarify the relationship between the pressure loss and many parameters such as the tip clearance ratio, the blade and impeller geometries, and operating conditions, such as the flow coefficient and the lift coefficient.

The purpose of this paper is to examine thoroughly the pressure loss due to the tip clearance by means of the principle of mechanics, and to make clear whether the various hypotheses on the tip clearance loss in the literature correctly represent the mechanics of pressure loss, and finally to determine which equation is rational and applicable in a wide range of operation.

Simplification of Problems

The flow near the blade tip is complicated by at least three factors: the rotation of the impeller or motion of blades relative to the casing, the secondary flow in the boundary layer along the casing induced by the pressure gradient between blades, and the leakage through the tip clearance of blades. Of course, the influences of these three factors on the flow and on the pressure loss are interrelated, and the total loss is not a simple sum of the three independent losses. However, it is important to understand the three factors separately before we can attack the combined phenomena. There are many papers regarding secondary flows induced by motion of rotor blades relative to the casing and also by the pressure gradient between blades, and the physics of secondary flow is well understood. However, regarding the flow phenomena near the clearance between the blade tip and the casing, even the physics or mechanics of pressure loss is not clear as mentioned before, although everybody agrees that there is leakage.
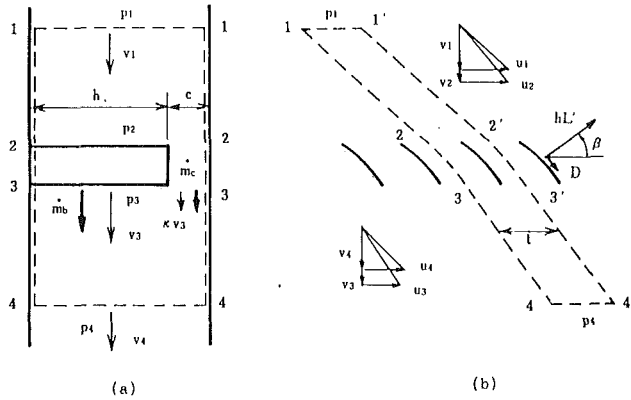
Fig. 1 Blade zone, clearance zone and control volume

In order to make the problems simple, in this paper a linear cascade is adopted instead of an impeller. The blade span in the cascade is $2h$, and at both ends there is a clearance c between the blade tip and the endwall of the wind tunnel, and only one half of the span is considered. Furthermore, it is assumed that the flow is inviscid and there is no boundary layer on the endwall of the wind tunnel.

In the present analysis the two-dimensional flow without tip clearance is called the standard flow, where the half-span of the blade is $h + c$. The tip of the standard blade is cut off to make a clearance c at the edge of the blade. The cascade is inserted into the wind tunnel, then it leaks through the clearance from the pressure side to the suction side of blades.

The height of the wind tunnel is divided into two zones, the clearance zone of thickness c and the cascade zone of thickness h. They are parallel to each other. For the time being, it is assumed that the condition of flow in the cascade zone is identical to the standard flow. If the mean axial velocity in the clearance zone were less than that of the standard flow, the total flow rate through the wind tunnel would be a little less than that of the standard cascade.

Inoue et al. (1986) have observed that the leaked jet flow through the clearance rolled up and detached from the endwall downstream. The pressure distribution on the blades may be influenced by the leakage. However, for the time being, it is assumed that the standard pressure distribution on the blades prevails over the entire span $h + c$, including the imaginary blade surface in the clearance zone of height c. This assumption is generally accepted, providing that the clearance c is small compared to the chord length and the blade span, although it will be slightly adjusted later when necessary.

The leak through the tip clearance is induced by the local pressure difference $p_p - p_s$ between the pressure surface and the suction surface of a blade, and the velocity component w_n normal to the blade camber line is expressed as $w_n = \sqrt{2(p_p - p_s)/\rho}$.

If the flow coefficient or the contraction coefficient is α, the leakage rate per unit length of chord is $q = \alpha \rho c w_n$. In principle, if the contraction coefficient α is larger than 0.5, the pressure on the pressure side of the blade is reduced toward the blade tip, and the integrated deficit of the pressure force is $(2\alpha - 1)c(p_p - p_s)$, or effectively a length of $(2\alpha - 1)c$ of the blade near the tip does not carry any blade-loading. That is, the effective span of blades is reduced and the effective tip clearance is $2\alpha c$ instead of c.

In the present analysis, it is assumed that $\alpha = 0.5$ and the lift force per unit span L' works uniformly along the span. In cases of $\alpha > 0.5$, if the effective clearance $c_e = 2\alpha c$ and the effective span $h_e = h - (2\alpha - 1)c$ are substituted for c and h, all the equations in the following chapters are applicable without any further modification.

Balance of Forces on a Large Control Volume and Pressure Losses

In cases of axial flow fans, the axial pressure difference created by the impeller must be supported even in the annular clearance zone between the casing and the disk covering the impeller outer diameter. Therefore, the axial velocity in the annular zone is probably less than the axial velocity in the impeller zone, but we can assume that the flow becomes uniform further downstream.

Figure 1(a) is the side view of a cascade, which corresponds to the axial sectional view of an impeller. Sections 1 and 4 of the control volume indicated by the dotted lines are far from the cascade, so that the velocity is uniform, while sections 2 and 3 are just upstream and downstream of the cascade. Figure 1(b) corresponds to the developed surface of revolution of an impeller outer diameter, where the two parallel surfaces 1–4 and 1′–4′ of the control volume are separated by just one pitch t of the blades, so that the velocity and pressure distributions are identical on the two surfaces. Therefore, they have no effect on the balance of forces on the control volume.

The balance of forces in the axial direction on the control volume is expressed as

$$p_c t(h+c) = hL' \sin \beta - D \cos \beta \qquad (1)$$

where $p_c = p_4 - p_1$ and β is the vector mean flow angle at the cascade measured from the axial direction, while hL' and D are the lift and the drag forces on a blade as indicated. Since no drag force is assumed for blades in an inviscid flow, D is the drag force induced by the tip clearance if there is any. If the pressure difference at the standard condition $c = 0$ is expressed as $p_4 - p_1 = p_0$, Eq. (1) is reduced to

$$p_0 = (L'/t) \sin \beta$$
$$p_0 - p_c = p_c(c/h) + (D/ht) \cos \beta \qquad (2)$$

It should be noted that the first term on the right-hand side of Eq. (2) is related neither to the flow rate $\dot{m}_c$ passing through
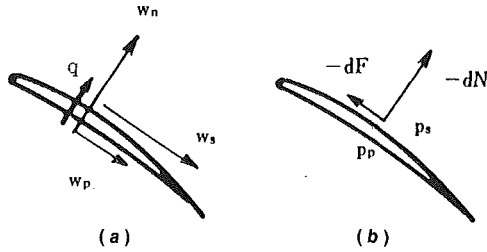
Fig. 2 Effects of leakage through tip clearance

Fig. 3 Flow in clearance zone and control volume

the clearance zone nor to the leakage flow rate q through the tip clearance.

Regarding the balance of forces in the tangential direction,

$$\dot{m}_b(u_2 - u_3) = hL'\cos\beta + D\sin\beta \qquad (3)$$

In section 4, where the flows through the cascade zone and the clearance zone mix together, the tangential velocity component is

$$u_4 = (u_3\dot{m}_b + u_2\dot{m}_c)/(\dot{m}_b + \dot{m}_c) \cong u_3 + (u_2 - u_3)\kappa c/h \qquad (4)$$

where $\kappa c/h = \dot{m}_c/\dot{m}_b$, or the axial velocity at the clearance zone is κ times the axial velocity at the blade zone. Since $u_4 \cong u_3$, Eq. (4) becomes

$$\rho(u_4^2 - u_3^2) = 2\rho u_3(u_2 - u_3)\kappa c/h$$

$$= (\kappa c/h)4p_0 u_3/(u_2 + u_3) \cong (\kappa c/h)4p_c u_3/(u_2 + u_3) \qquad (5)$$

The total pressure loss p_l is defined as

$$p_l = p_0 - p_c - (\rho/2)(u_4^2 - u_{3i}^2) \qquad (6)$$

where u_{3i} is the value of u_3 for $c = D = 0$, and according to Eq. (3)

$$u_{3i} - u_3 = D\sin\beta/\dot{m}_b \qquad (7)$$

Using Eqs. (2), (5), and (7), Eq. (6) becomes

$$p_l \cong p_c(c/h)[1 - 2\kappa u_3/(u_2 + u_3)] + (D/ht)/\cos\beta \qquad (8)$$

From this equation it is clear that the total pressure loss is less as κ is larger, but even when $\kappa = 1.0$ and $D = 0$, the loss is not zero because $u_3 < u_2$ for decelerating cascades. For reference, κ can be estimated using Eq. (11) in the following chapter.

According to Eq. (8) the total-pressure loss consists of two parts. That is, in addition to the pressure loss p_{ll} due to the induced drag of the leakage through the tip clearance, tentatively expressed as the last term, there is a pressure loss p_{lp} proportional to the product of the tip clearance ratio c/h and the pressure rise p_c across the cascade. According to Eq. (1), p_c is approximately proportional to the lift coefficient of blade; therefore, a part of the tip clearance loss is almost proportional to the lift coefficient. Nobody had noticed this important fact until 1986.

Leakage and Drag

The pressure difference across the blade tip accelerates the fluid on the pressure side of the blade toward the suction side, and the leak velocity or the velocity component normal to the blade w_n is

$$w_n = \sqrt{2(p_p - p_s)/\rho}$$

Since the velocity component parallel to the blade is not changed by the pressure difference, it keeps the magnitude on the pressure side w_p even after it comes to the suction side of the blade where the standard velocity w_s parallel to the blade prevails, and obviously w_p is smaller than w_s. They are indicated in Fig. 2(a).

If it is desired to compensate for the disturbance due to leakage and to re-establish the original condition of flow, a normal force to the blade
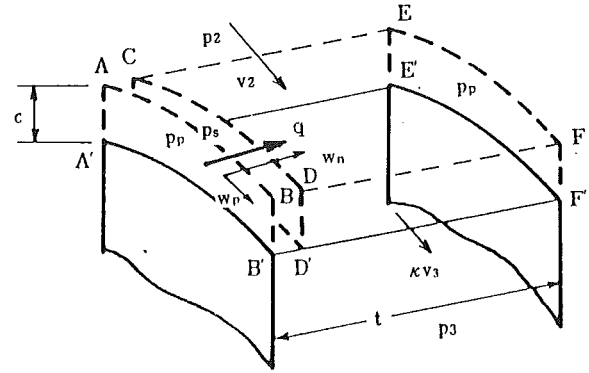
$$dN = w_n q = (c/2)\rho w_n^2 = c(p_p - p_s) \qquad (9)$$

and a parallel force to the blade

$$dF = (w_s - w_p)q \qquad (10)$$

are required per unit chord length of the blade. That is, the tip clearance has added to the standard flow two force vectors indicated in Fig. 2(b).

The normal force dN is nothing but the blade force, which is borne by the blade element in the clearance zone in the case of the standard flow. Since the blade element is missing in the case of cascade with a tip clearance, it is quite natural that this much force is required to re-establish the standard flow.

On the other hand, it seems strange that a drag force $-dF$ parallel to the blades is induced by the leakage, because in an inviscid flow pressure is the only force and it is always normal to the blade. In cases of cambered blades, however, if the pressure distribution is shifted downstream by the leakage, the direction of the integrated blade force or the lift force is slightly turned downstream, and from the viewpoint of the standard flow, the small component of the lift force generated perpendicular to the standard lift force is a drag force. The reason such conditions of flow and the force are induced by the leakage through the tip clearance will be explained in the following chapters.

Flow Near the Blade Tip

In the clearance at the blade tip, there is no blade to support the pressure difference $p_p - p_s$ across the blade and as a result it leaks. In Fig. 3, the difference of the pressure forces acting on the surfaces AA'B'BA and CC'D'DC is balanced with the momentum of the leakage integrated along the chord $\int q w_n dl$. Regarding the control volume in the tip clearance zone between two blades, CC'D'DC and EE'F'FE, the pressure forces on the two curved surfaces are obviously just enough to stop the momentum of leakage.

In the case of standard condition, there is no leakage and the pressure forces on the two curved surfaces of the control volume contribute to support the axial pressure force $ct(p_3 - p_2)$ and also to change the tangential momentum of the throughflow by $\rho ctv(u_2 - u_3)$. If there is a tip clearance, the pressure difference is used to stop the leakage velocity through the blade tip as mentioned before, and it cannot afford to support the axial pressure force and to change the tangential momentum of the throughflow similarly to the standard flow.

Lack of the tangential force component is acceptable if there is no throughflow in the tip clearance zone, or if the tangential velocity component of the throughflow remains unchanged.

On the other hand, the axial pressure force $ct(p_3 - p_2)$ must be supported somehow by means of change of the axial momentum of flow and the shear force on the border surface of the control volume. If the axial velocity component at the inlet section AA'E'EA of the control volume is v_2, and the velocity component at the exit section DD'F'FD is κv_2, being retarded

by the axial pressure gradient, the balance of the flow rate is squeezed from the control volume of the clearance zone into the blade zone, with the local axial velocity component, which varies from v_2 to κv_2 depending upon the axial location. Consequently, the balance of forces of the control volume in the axial direction is expressed as

$$\rho c \kappa v_2^2 (1 - \kappa) + \rho c (1 - \kappa) v_2^2 [1 - (1 + \kappa)/2] \cong c(p_3 - p_2) - S$$

It is reduced to

$$\rho v_2^2 (1 - \kappa^2)/2 = p_3 - p_2 - S/c \qquad (11)$$

where tS is the axial component of the shear force acting on the plane $C'D'F'E'C'$, one blade pitch of the border plane between the clearance zone and the blade zone.

It is clear from Eq. (11) that κ becomes smaller as $p_3 - p_2 \cong p_c$ is larger and eventually becomes zero and imaginary. In cases where κ is imaginary in Eq. (11), it flows into the control volume from both the upstream section $AEE'A'A$ and the downstream section $DFF'D'D$ and it flows out from the bottom surface of the control volume into the blade zone with positive or negative axial velocity component v. If p_c is very large, it is possible that a reverse flow prevails even in the upstream section $AEE'A'A$. It should be noted that the shear force tS becomes larger as κ is smaller or as the reverse flow becomes stronger, and the large shear force contributes to prevent κ from decreasing too much or to reduce the reverse flow.

As mentioned above, in order to balance the axial component of forces in the clearance zone, the help of the blade force in the blade zone is necessary, i.e., the unbalanced force is transmitted from the clearance zone to the blade zone through the shear force tS and the momentum change of flow through the border plane $C'D'F'E'C'$. The force between the two zones is an internal force for the large control volume, which covers the two zones. The force tS does not appear in Eqs. (2) and (8), but the entropy changes due to the shear force and the momentum exchange or mixing are automatically included.

Regarding the leakage through the tip clearance of blades, the fluid comes from everywhere on the pressure side of blade without being limited to the clearance zone. That is, on the pressure side of the blade the influence of leakage spreads to the blade zone.

In the clearance zone, a secondary flow is induced in a blade pitch because the axial velocity in the clearance zone is less than the axial velocity v in the blade zone. That is, the tangential pressure gradient between blades is too large for the momentum of flow in the clearance zone to flow along the blades, and a secondary flow toward the suction side of blade is created. The direction of the secondary flow is opposite to the leak through the tip clearance of blades. The two opposite flows meet and form a spanwise flow, which finally rolls up to form a vortex, as measured by Inoue et al. (1986).

That is, both upstream and downstream of the leak through the blade tip clearance, the influence of leakage is not limited to the clearance zone; consequently the pressure distribution and the blade loading near the blade tip are clearly influenced by the leakage or the clearance. This fact qualitatively supports the postulation in the last chapter that the pressure distribution along the blade near the tip is modified by the leakage and the direction of the integrated pressure force is not identical to that of the standard flow.

Pressure Loss Due to Induced Drag

It is well known that the drag force on a wing or a blade of finite span flying in a sky is larger than the drag force on the same blade with the identical lift force in a two-dimensional flow, and the difference is attributed to the induced drag. When a blade flies at a velocity U with a lift force L, a vortex that is proportional to the velocity U and the lift coefficient C_L is induced along the blade, and if the span is finite a pair of tubes
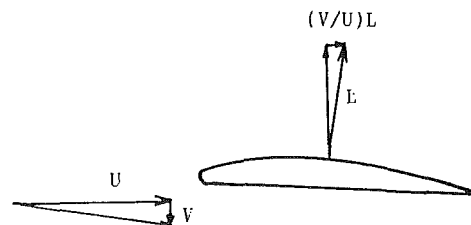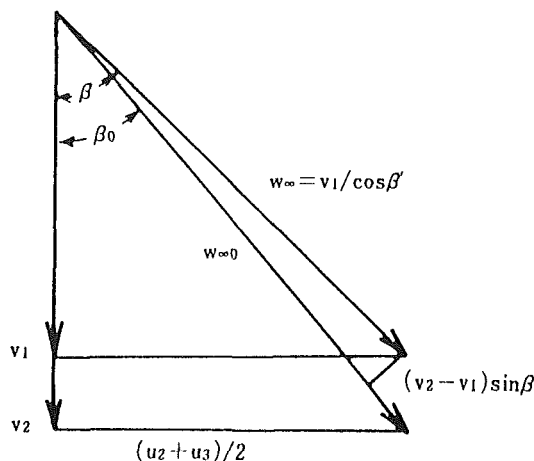

Fig. 4 Induced drag of wing

Fig. 5 Vector mean velocities near and far from cascade

of the vortex are shed downstream from the both ends of the span. By the shed vortices a velocity V, which is opposite to the direction of lift and proportional to $C_L U$, is induced near the blade. Therefore, as shown in Fig. 4, the direction of flow near the blade is inclined by arctan V/U relative to the direction of flight. Since the lift force is perpendicular to the direction of flow, the lift force L has a force component $(V/U)L$ against the direction of flight. That is, a drag force is induced.

In other words, the pressure distribution around a wing does not create a drag force to the local flow, but the downwash makes the blade loading near the leading edge lighter compared with the original two-dimensional flow. Due to the camber of blade the integrated blade force is oriented somewhat downstream in comparison with the lift force of the original two-dimensional flow. As a result the lift force has a component of drag force, from the viewpoint of the original two-dimensional flow.

If there is leakage through the tip clearance of blades in a cascade, the direction of leak flow is different from that of the two-dimensional flow in the blade zone, and the difference forms a shear layer or a vortex sheet, which is shed downstream from the edge of blades. It is not easy to evaluate the influence quantitatively, but similarly to the case of a flying wing, the direction of the lift force is modified a little and it has a drag component proportional to the lift force.

In the former chapter it was proved that the momentum component in the direction of blade chord of the leakage is less than that of the standard flow of the same flow rate and the difference is quantitatively expressed as $-\int dF$. In this chapter, from where and how the defect of momentum has come is qualitatively clarified.

Pseudo-Induced Drag

The drag force D in Eqs. (1), (2), and (8) corresponds to the drag mentioned above, or $D = -\int dF$. However, the loss of total pressure is not zero even when $D = 0$. Comparing the vector mean velocity $w_{\infty 0}$ of sections 2 and 3 near the cascade with the vector mean velocity w_∞ of sections 1 and 4 far from the cascade in Fig. 1, it is clear that the directions of the two velocity vectors are different as shown in Fig. 5.

If it is assumed that there is no flow through the tip clearance zone, observing Fig. 5, the angular difference of the vectors is expressed as follows:

$$\tan (\beta - \beta_0) = (v_2 - v_1) \sin \beta / (v_1 / \cos \beta)$$

$$\cong (c/h) \sin \beta \cos \beta \quad (12)$$

It is clear that the ideal life force $L'h$ of the cascade relative to the local flow with the vector mean flow angle β_0 has a virtual drag force component $L'h(c/h) \sin \beta \cos \beta$ relative to the flow with the vector mean flow angle β. The pressure loss based on the virtual drag force is clearly proportional to L' or the lift coefficient of the blades, and the way the loss is related to the lift coefficient is somewhat similar to that of the induced drag of a wing, although the angular difference is independent of the lift coefficient. That is, even the pressure loss expressed as the first term of Eq. (8) can be considered as a pseudo-induced drag.

The real induced drag $-\int dF$ due to the leakage through the blade tip clearance is proportional to $C_L^{1.5}$ as will be demonstrated in the following chapter. Therefore, it may be allowed to say that the tip clearance loss consists of a pseudo-induced drag, which is proportional to C_L, and a real induced drag, which is proportional to $C_L^{1.5}$. However, in the literature it is simply assumed that the tip clearance loss is nothing but the induced drag, and following the case of flying wing, it is proportional to $(c/h)C_L^2$ without demonstrating any reason.

The concept of induced drag was originally developed for a flying wing. In that case, it is clearly demonstrated that the direction of the lift force has changed by $\arctan V/U$, which is proportioned to C_L; consequently the induced drag is proportional to C_L^2. It does not mean that the induced drag due to the leakage through the tip clearance of the blade is also proportional to C_L^2. When $c/h = \infty$, the induced drag D is certainly proportional to C_L^2, but obviously the relation that D is proportional to $(c/h)C_L^2$ in the literature is not correct.

Drag and Loss of Mechanical Energy Due to Leakage

In the preceding chapters, the increment of drag force D due to the tip clearance leakage and the resulting pressure loss p_{ll}, the last term of Eq. (8), is not quantitatively related to the kinetic energy of leaked flow. When a strut is inserted in a uniform flow, the loss of mechanical energy per unit time is the product of the drag force acting on the strut and the velocity before it is disturbed by the strut, and the loss is also equal to the product of the pressure loss and the flow rate. This relation is applicable to any flow.

As mentioned before, if there is leakage through the tip clearance of blade, there is a distribution of drag force $-dF$ along the chord. The loss of mechanical energy due to the leakage can be estimated in the way mentioned above. At a certain point along the chord of a blade, the pitch mean velocity between blades is about $(w_p + w_s)/2$, while it is proved that the drag force due to the leakage across the blade tip is $-dF = q(w_p - w_s)$. Therefore, the loss of mechanical energy per unit time and unit length along the chord is

$$dE = [(w_s + w_p)/2]q(w_s - w_p)$$
$$= (\rho c/2)(w_s^2 - w_p^2)^{1.5}/2 \quad (13)$$

Equation (13) shows that the loss is just equal to the product of the leakage rate q and the kinetic energy of the velocity component normal to the blade of the leaked flow. The pressure loss is expressed as the ratio $\int dE/Q$ where $Q \cong [(w_s + w_p)/2]ht \cos \beta$ is the flow rate through one pitch of the blades. We can easily prove that the pressure loss agrees with p_{ll}, or the last term of Eq. (8) where $D = -\int dF = \int (w_s - w_p)qdl$.

If the camber of the blades is not very large, the lift force acting on a blade per unit span is expressed as the integration along the chord of the pressure difference across the blade, or

$$C_L l w_\infty^2 / 2 \cong \int (w_s^2 - w_p^2)dl/2 \quad (14)$$

Combining Eqs. (13)' and (14), the loss E due to the leakage across the blade tip can be expressed

$$E = \int dE = k\rho cl \, C_L^{1.5} w_\infty^3$$

and the pressure loss is

$$p_{ll} = E/(thw_\infty \cos \beta_\infty) = k \rho (c/h)(1/t)C_L^{1.5} w_\infty^2 / \cos \beta_\infty \quad (15)$$

where the proportionality constant k varies depending upon the load distribution along the chord. This equation agrees with the Rain's equation in Vavra's textbook (1960) except for the proportionality constant.

Summary

In a decelerating cascade with a blade tip clearance, if it is desired to re-establish the standard flow without the tip clearance, in addition to the missing blade force at the tip clearance, a force parallel to the blade is required. Because these two components of forces are missing compared with the standard flow and they are perpendicular to each other, two different kinds of pressure loss are induced.

In the literature two schools on the tip clearance loss of cascade are popular. According to one school, it is based on the induced drag of blade due to the tip clearance and it is proportional to C_L^2. In the other school, it is the loss of the kinetic energy of leakage and it is proportional to $C_L^{1.5}$. In this paper it is shown that the force component parallel to the blade is induced by the momentum defect of the leakage and the pressure loss is proved to be identical to the loss of the kinetic energy of the leakage through the tip clearance. Since the drag force due to the leakage can occur in an inviscid flow, it can be considered as an induced drag. That is, these two theories in the literature are two different views of one phenomenon. The most important fact is that those theories do not include the other half of the tip clearance loss. It comes from the missing lift force of blade in the clearance zone.

The author feels that in the present paper the mutual relationship between the leakage flow loss, induced drag loss, and clearance loss due to the axial pressure gradient is made clear for the first time. It should be noted that the leakage loss is only a part of the pressure loss due to the tip clearance, and the former should not be used as a synonym of the latter.

Postscript

1 The pressure distribution near the blade tip is modified by the leakage and an induced drag force is generated, but in this paper, it is assumed that the total lift force of the blade hL' is not changed. If the lift force is decreased by the tip clearance of impeller, the driving force of the impeller is reduced and the axial pressure rise p_c is also reduced, but the pressure loss expressed in Eq. (8) is hardly influenced.

2 In 1986 the present author had postulated that the pressure loss due to the tip clearance of cascade consists of three parts: the loss due to leakage, the loss for supporting the annular clearance zone along the shroud against the meridional pressure gradient, and the loss to take care of the spanwise distortion of the velocity distribution in the blade zone. In this paper, the last part is omitted partly because it is a common problem for a boundary layer in a decelerating flow, and partly because it can be included in the second cause of loss by increasing the effective tip clearance, because the two losses are the same kind of loss due to an adverse pressure gradient.

3 In cases of mixed flow compressors, the gas density, the blade height, and the meridional component of velocity vary from the inlet to the exit of impeller. Therefore, the equations derived in this paper should be applied to a short distance along the shroud and the equations should be integrated from

the inlet to the exit of the impeller. Furthermore, the Coriolis acceleration influences the blade loading, which is the cause of leak. In the author's previous papers (Senoo and Ishida, 1986; Senoo, 1987), these factors are incorporated without using a lift coefficient, which is not a pertinent parameter for blades of mixed-flow impellers.

4 In 1977, the performance changes due to the tip clearance were experimentally examined very thoroughly for three types of centrifugal compressor with the rated pressure ratio of 6 by Klassen et al. (1977a, 1977b) and Beard et al. (1978). Regarding these experimental data Senoo and Ishida (1987) predicted the tip clearance effects at different shaft speeds and pressure ratios as well as the effects at different flow rates at the design speed, and good agreement with experimental data were demonstrated. There is no other paper in the literature that compares the predicted effect of the tip clearance with experimental data over a wide operating range of an impeller. Since the blade loading varies with the condition of operation, good agreement in a wide operating range means that the relationship between the losses and the blade loading or the lift coefficient used in the prediction well represents the mechanics of tip clearance loss.

Acknowledgments

References

Beard, M. G., Pratt, C. M., and Timmis, P. H., 1978, "Recent Experience on Centrifugal Compressors for Small Gas Turbines," ASME Paper No. 78-GT-193.

Inoue, M., Kuroumaru, M., and Fukuhara, M., 1986, "Behavior of Tip Leakage Flow Behind an Axial Compressor Rotor," ASME JOURNAL OF TURBOMACHINERY, Vol. 108, pp. 7–14.

Klassen, H. A., Wood, J. R., and Schumann, L. F., 1977, "Experimental Performance of a 13.65-centimeter-Tip-Diameter Tandem-Bladed Sweptback Centrifugal Compressor Designed for a Pressure Ratio of 6," NASA Technical Paper 1091.

Klassen H. A., Wood, J. R., and Schumann, L. F., 1977, "Experimental Performance of a 16.10-centimeter-Tip-Diameter Sweptback Centrifugal Compressor Designed for a 6:1 Pressure Ratio," NASA Technical Memorandum X-3552.

Lakshminarayana, B., 1970, "Methods of Predicting the Tip Clearance Effects in Axial Flow Turbomachinery," ASME *Journal of Basic Engineering*, Vol. 92, pp. 467–482.

Roberts, W. B., Serovy, G. K., and Sandercock, D. M., 1986, "Modeling the 3-D Flow Effects on Deviation Angles for Axial Compressor Middle Stages," ASME *Journal of Engineering for Gas Turbines and Power*, Vol. 108, pp. 131–137.

Senoo, Y., and Ishida, M., 1986, "Pressure Loss Due to the Tip Clearance of Impeller Blades in Centrifugal and Axial Blowers," ASME *Journal of Engineering for Gas Turbines and Power*, Vol. 108, pp. 32–37.

Senoo, Y., 1987, "Review: Pressure Losses and Flow Field Distortion Induced by Tip Clearance of Centrifugal and Axial Compressors," *JSME International Journal*, Vol. 30, pp. 375–385.

Senoo, Y., and Ishida, M., 1987, "Deterioration of Compressor Performance Due to Tip Clearance of Centrifugal Impellers," ASME JOURNAL OF TURBOMACHINERY, Vol. 109, pp. 55–61.

Vavra, M. H., 1960, *Aero Thermodynamics and Fluid Flow in Turbomachines*, Wiley, New York, p. 381.

Secondary Flow and Loss Distribution in a Radial Compressor With Untwisted Backswept Vanes

G. Sipos

Institute of Thermal Turbomachines
and Power Plants,
Technical University of Vienna,
Vienna, Austria

The unshrouded impeller and the vaneless diffuser of a single-stage radial compressor have been investigated at three flow rates. Three-dimensional velocities and pressures were measured at a tip speed of 84 m/s by an L2F-velocimeter, a slanted single hot-wire probe, and piezoresistive pressure transducers. The measurements show that upstream of the blading the averaged meridional inlet flow angle is about 54 deg and a periodic variation of the meridional flow angle of about 25 deg occurs near the casing wall. Further, an inlet vortex in the clockwise direction appears and an initial whirl is induced. The specific work of the initial whirl corresponds to approximately 12 percent of the enthalpy losses between inlet pipe and diffuser outlet. In the beginning of the passage, the inlet vortex is suppressed and a solid body vortex in the counterclockwise direction can be observed. At the outlet, a heavy flow deceleration at the blade suction side with subsequent separation can be seen. Increasing the flow rate decreases the wake and causes a more uniform loss distribution in this area. The measured secondary vortex flow and rotary stagnation pressure gradients are compared with test results from impellers with inducer. The incidence of the investigated impeller is greater than that of the impellers with inducer, but the wake-jet outlet flows are very similar. Inlet losses could be reduced by improving incidence angles by matching the blade angles to the inlet flow angles. Smaller blade angles at the shroud would reduce or eliminate separation at the leading edge, and the resulting reduction in low-momentum fluid along the suction surface would help to avoid separation on that surface near the outlet.

Introduction

Many experiments and theoretical investigations have shown that the impeller flow of radial compressors is significantly influenced by secondary effects (Eckardt, 1975; Kano et al., 1982; Lindner, 1984; Sipos, 1984; Müller and Sipos, 1985; Rohne and Baumann, 1988). Centrifugal and Coriolis forces cause the deviation of the streamlines from the wall contour, and, in the rotating system, gradients of the reduced static pressure occur in the channel cross-sectional areas. Flow migration in the opposite direction at the casing wall and hub results in a channel vortex (Bosman, 1980). Additionally, the reduced static pressure gradients induce transport of boundary layer material along the impeller channel walls. As a result of both these effects, high-energy fluid will be replaced by low-energy fluid and a wake will be generated close to the impeller outlet.

This process can be observed particularly clearly in radial impellers without inducer (Adler and Levy, 1979; Hamkins

and Flack, 1987). In this type of impeller, the flow will be directed into the radial direction in many cases with very strong curvature, before entering the blading. High curvature frequently causes flow separation at the casing wall with distorted absolute inlet velocity profile and pressure gradients even at optimum operating conditions. So, the effects mentioned above will be intensified. Furthermore, large variations of incidence angle from hub to shroud may cause leading edge separation and the resulting flow distortion in the tangential direction. Because of the usually wide and short channels, the vortex development may be influenced by the flow gradients in axial and tangential direction, probably in the whole impeller channel. Thus, loss distribution and channel flow of this type of impeller are more difficult to predict than those of high-performance radial impellers where, because of the inducer, the inlet flow distribution is usually uniform.

Motivation

As the literature shows (Bosman, 1980; Moore et al., 1984; Renyong et al., 1985; Lapworth and Elder, 1988; Moore and Moore, 1988), most of the mathematical methods dealing with
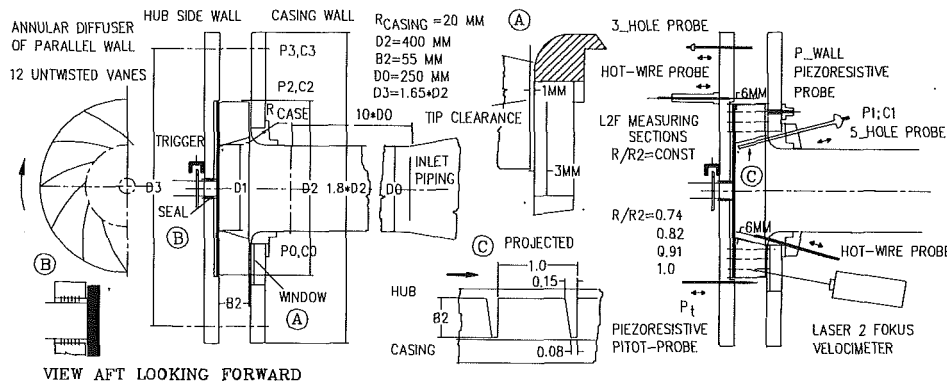
Fig. 1 Experimental setup and instrumentation

the calculation and prediction of the secondary flow in radial compressor impellers are very complex, so that an application in industrial practice would be difficult. Further, most of these papers consider high-performance impellers with axial flow inlet and inducer [I-impeller].

Supposing that some characteristic features of the flow could be recognized and modeled, they could be the basis of a less sophisticated calculation method. Especially for radial impellers with blades in the radial plane and without inducer [C-impeller], simpler design tools would be desirable. This paper, therefore, attempts:

(*a*) to show the influence of the distorted inlet flow on the secondary flow in C-impellers and to find characteristic flow patterns suitable for mathematical flow modeling;

(*b*) to supply experimental data for C-impellers for comparison with later flow calculations; and

(*c*) to show some significant differences between the secondary flow and loss distribution of I- and C-impellers.

Experimental Setup

Figure 1 shows the experimental setup and test object. The unshrouded test impeller of 400 mm diameter has 12 untwisted backswept blades and is followed by a bladeless annular diffuser of parallel walls. Inlet and outlet blade angles measured in the mean radial plane are 30 and 40 deg, respectively. Diameter ratios D_1/D_2 at the hub and at the casing are 0.61 and 0.68, respectively; the impeller width ratio B/D_2 is 0.1375. The inlet cross-sectional area is reduced by the finite blade thickness at the hub by 15 percent, and at the casing by 8 percent. The casing wall radius R_{CASE} to outlet diameter D_2 ratio of 0.05 is typically small. The inlet piping diameter ratio D_0/D_2 is

<hr>

Nomenclature

a, b = linearized hot-wire calibration constants

B = impeller width, mm

C = time-averaged absolute velocity, m/s

C_{pt} = stagnation pressure loss coefficient between inlet piping and blade leading edge

D = diameter, mm

$\bar{\bar{e}}$ = unit vector

E = linearized hot-wire voltage, V

F_{cf} = centrifugal force, N

F_{Cor} = Coriolis force, N

h = specific enthalpy, J/kg

N = impeller speed, rpm

P_s = time-averaged static pressure, Pa

P_t = time-averaged stagnation pressure, Pa

P_{sr} = time-averaged reduced static pressure in rotating coordinate system, Pa; $P_{sr} = P_s - \rho/2 * U^2$

P_{tr} = time-averaged reduced stagnation pressure in rotating system, Pa; $P_{tr} = P_s + \rho/2 * (W^2 - U^2)$

Q = mass flow, kg/s

r, u, z = coordinates in radial, circumferential and axial direction (Fig. 10)

R = radius, mm

Ro = Rossby number = F_{cf}/F_{Cor}

t = time between two subsequently passing blades

T = absolute temperature, K

Tu_w = turbulence coefficient of the relative flow

U = circumferential velocity, m/s; $U = R * \Omega$

W = time-averaged relative velocity, m/s

x = vector product

X = normalized coordinate of length in circumferential direction = $u/(D * \Pi/Z)$

Y = distance from hub to measuring point along measuring plane normalized by the distance from hub to casing along measuring plane

Z = blade number

α = absolute flow angle, measured counterclockwise from the tangential direction, projected on the r-u plane, deg (Fig. 7)

β = relative flow angle, measured clockwise from the tangential direction, projected on the r-u plane, deg

ϵ = meridional inlet flow angle measured from the z direction, deg (Fig. 7)

η = impeller efficiency

ρ = fluid density, kg/m³

Ω = impeller angular velocity, 1/s

Subscripts

BL = blade

I = incidence

IS = isentropic

m = average over the display section

opt = operating point of optimum impeller efficiency

p = projected

r, u, z = radial, circumferential, and axial components of velocity

R = at radius R

t = stagnation value

0 = impeller inlet piping

1 = blade inlet

2 = impeller outlet

3 = diffuser outlet

$1 - 0$ = difference between positions 1 and 0

$2 - 1$ = difference between positions 2 and 1

$3 - 0$ = difference between positions 3 and 0

$R - 0$ = difference between positions R and 0

Superscripts

$'$ = fluctuation component

$\bar{}$ = vector

$\bar{}$ = time-averaged mean value

0.625, and a straight inlet pipe length of $10*D_0$ is provided to avoid inlet flow distortion. Tip clearance between casing wall and blade front edge is approximately 1 mm; diffuser outlet diameter is $1.8*D_2$. Furthermore, a 3-mm-thick rectangular glass window of 40×120 mm size was provided in the casing wall so that laser velocity measurements could be made in the rotating impeller passages up to diameter ratio $D/D_2 = 0.7$.

Mass flow rate was measured by an orifice plate and controlled by a throttle in the inlet piping. The L2F measurements were carried out in four measuring stations of constant diameter ratio at $D/D_2 = R/R_2 = 0.74$, 0.82, 0.91, and 1.0, and averaged over the 12 impeller channels. Additional linearized hot-wire measurements were made in a distance of approximately 6 mm from the impeller blade leading and trailing edge applying a single hot-wire slanted probe. The hot-wire probe could be traversed along the blade edge and rotated around its axis. The instantaneous wall pressure was measured by a piezoresistive pressure transducer in the four L2F measuring stations. The same type of pressure transducer was applied in a specially designed Pitot probe of low directional sensitivity. The Pitot probe was placed at the same diameter as the hot-wire probe and traversed along its axis to measure the blade-to-blade variations in the instantaneous stagnation pressure at different spanwise stations of the impeller outlet. For time-averaged flow measurements at the impeller inlet, a standard pneumatic five-hole probe was used, and in the diffuser at $D/D_2 = 1.65$, a pneumatic three-hole probe was used.

Test and Evaluation Methods

The hot-wire probe, together with a three-dimensional probe calibration method (Sipos, 1986), made it possible to determine the components of the time-averaged velocity vectors directly out of the calibration maps in every measuring point. The mean velocity vector was calculated at every channel point from four ensemble-averaged hot-wire voltages determined in four different characteristic angular positions of the probe. From the measured velocity distribution, a difference vector field representing the secondary flow was calculated at the diffuser outlet, and the circumferential variation of the blade inlet flow was determined. In the calculation of loss distributions from the L2F velocity and the ensemble-averaged wall pressure values, a constant static pressure was assumed across the impeller width. Because of the straight and parallel walls, only a little curvature of the streamline, hence only small pressure gradients, can be expected in a great part of the impeller channel. The instantaneous signals were stored on magnetic tape and evaluated by an analogue pulse-amplitude-modulation circuit later on to determine the ensemble-averaged hot-wire and pressure signal values.

Choice of Test Operating Points

The flow experiments were carried out without inlet control vanes at a constant speed of 4000 rpm corresponding to a circumferential velocity of 83.7 m/s. The impeller performance curves at this constant speed are displayed in Fig. 2. Stagnation pressure rise between station 0 in the inlet pipe and station 3 in the diffuser was measured by a three-hole probe and plotted against the mass flow rate. Isentropic impeller efficiency was calculated from the stagnation values of h and defined as

$$\eta_{IS,t} = (h_{3,IS,t} - h_{0,t})/(h_{3,t} - h_{0,t}) \qquad (1)$$

The L2F, wall-pressure and hot-wire measurements were made at $Q = 1.7$ kg/s, corresponding to maximum impeller efficiency. In order to show the effect of the increased flow rate on the secondary flow and loss distribution, the hot-wire and instantaneous stagnation pressure measurements were repeated, additionally, at $Q = 1.9$ kg/s, corresponding to the relative flow rate of $Q/Q_{opt} = 1.12$. Time-averaged flow ex-
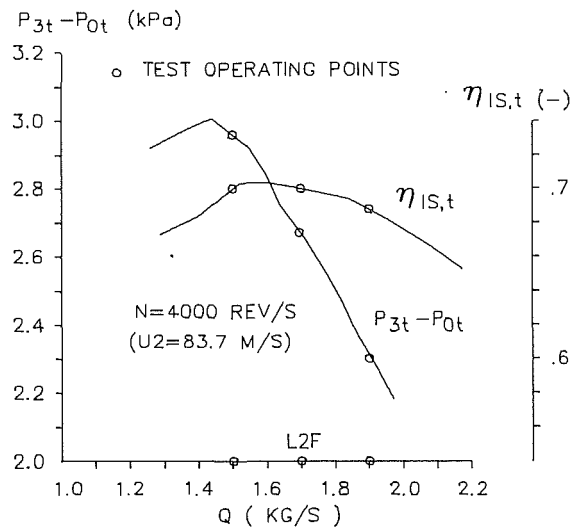

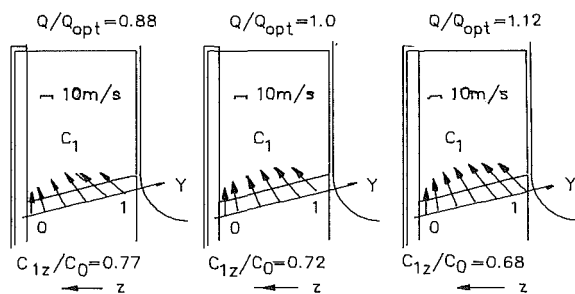Fig. 2 Performance curves of test impeller

Fig. 3 Meridional velocity vectors close to the blade leading edge, measured by a five-hole pneumatic probe at three flow rates
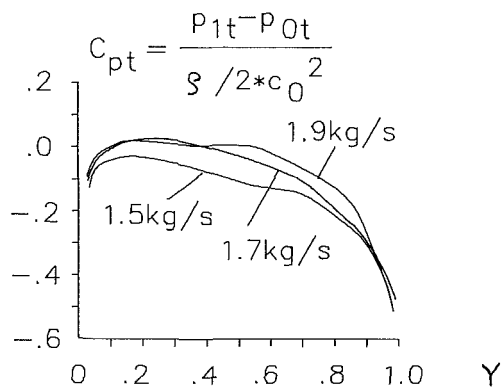

Fig. 4 Axisymmetric approximation of the total pressure losses along the blade leading edge

periments were made at relative flow rates of $Q/Q_{opt} = 0.88$, 1.0, and 1.12.

Tolerances and Accuracy

The accuracy of the flow rate and pneumatic pressure measurements was about ± 0.03 kg/s and ± 10 Pa, respectively. The tolerance of the hot-wire and pneumatic five-hole probe measurements can be estimated at ± 2 m/s for the velocity and ± 2 deg for the flow direction. The relative error of velocity components measured by the L2F velocimeter is about 1.5 percent for the mean velocity and 5 percent for the turbulence values. Because of the stable ambient temperature, the instantaneous pressure measurement showed a zero drift of only about ± 20 Pa.
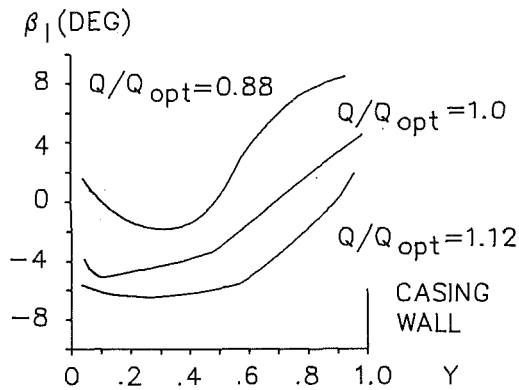
Fig. 5 Axisymmetric approximation of the incidence angles projected onto the u-r plane along the blade leading edge
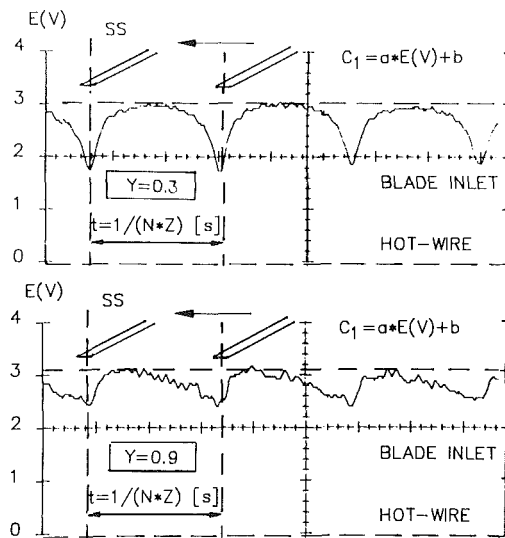

Fig. 6 Instantaneous hot-wire signal pattern close to the blade leading edge, averaged over 64 cycles

Fig. 7 Ensemble-averaged absolute velocity C_1/U_2, and inlet flow angles α and ϵ close to the blade leading edge at optimum flow rate

Blade Inlet Flow

Time-Averaged Flow Measurements. Figures 3 and 4 show the flow variables close to the blade inlet measured by a pneumatic five-hole probe. Because the probe effectively integrates the blade-to-blade flow variations, the curves can be considered as the axially symmetric approximation of the actual inlet flow distribution. The figures show the following characteristics:

(a) As shown in Fig. 3, velocity distribution follows the strong meridional curvature of the casing wall, but velocity vectors of nearly constant length close to the casing indicate a thick boundary layer. The fluid enters the blading in the measuring section with considerable axial velocity components. The normalized mean value of the axial velocity is $C_{1z}/C_0 = 0.72$ at $Q/Q_{opt} = 1.0$. The mean meridional flow angle ϵ is 54 deg.

(b) According to Fig. 3, the meridional flow angle ϵ close to the casing wall differs considerably from the meridional angle of the wall contour. Further, in Fig. 4, large total pressure losses between the inlet station and the impeller leading edge near the casing can be seen. The flow parameters displayed in Figs. 3 and 4 indicate flow separation on the casing wall upstream of the measuring station at each of the three flow rates.

(c) In the r-u plane, the flow separation on the casing wall causes positive incidence angles near the casing wall and negative incidence angles close to the hub at optimum flow rate; see Fig. 5. Thus, additional flow separation can be expected close to the casing at the blade suction side and close to the hub at the blade pressure side.
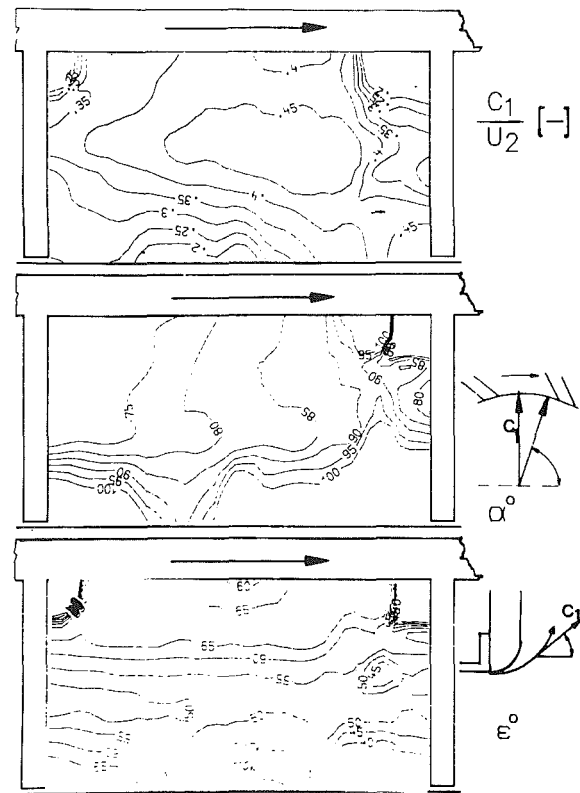
(d) Varying the flow rate has little influence on the meridional flow angle ϵ and on the axial gradient of the stagnation pressure; Figs. 3 and 4. Much greater differences can be found in the incidence angles along the blade leading edge in Fig. 5. At flow rates greater than optimum, at $Q = 1.9$ kg/s, negative incidence occurs almost along the entire leading edge. At flow rates less than optimum, the incidence angle is practically zero in the hub region and becomes positive near the casing wall. Thus, in addition to the losses generated between stations 0 and 1, incidence losses occur at increased flow rate in the hub region and at reduced flow rate in the casing region. Therefore, the reduced stagnation pressure gradient in the axial direction will be decreased downstream of the measuring station by increasing the flow rate.

Instantaneous Flow Measurements. In addition to the results of the time-averaged measurements, further information about the inlet flow characteristic can be obtained by the three-dimensional hot-wire measurements at optimum flow rate close to the blade leading edge.

Figure 6 shows the linearized signal pattern of a single hot-wire slanted probe near the hub and the casing wall. The curve near the hub shows a practically uniform velocity distribution, which is only influenced by the blockage of the blades. The curve close to the casing demonstrates additional circumferential flow distortion, indicating the effects of flow separation on the casing wall.

The isotachs of the normalized absolute inlet velocity C_1/U_2 and the isoclines of the meridional and circumferential inlet flow angles ϵ and α indicate the periodic fluctuation of the absolute flow on the inlet surface; see Fig. 7. Close to the casing wall, low velocities resulting from the flow separation upstream of the measuring station can be seen. The wake will be accelerated by the passing of the blades. Low velocities can be observed in the hub-suction side corner as well. The fluid enters the blading in this region with negative incidence (see
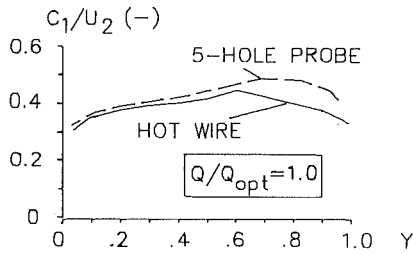
Fig. 8 Circumferentially averaged absolute velocity C_1/U_2 measured by hot-wire and five-hole probe, at $\dot{Q}/Q_{opt} = 1.0$

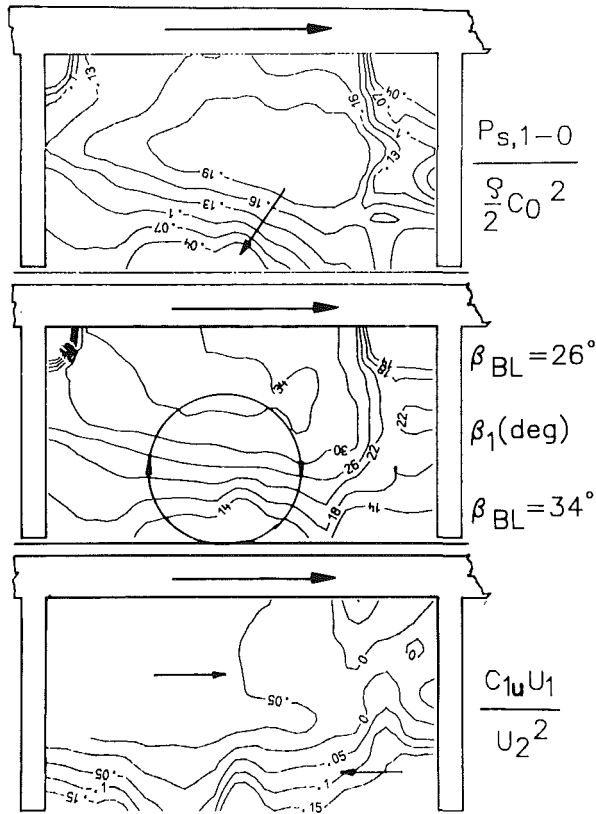Fig. 10 Inviscid passage vortex and circulation in a rotating axial to radial bend

Fig. 9 Ensemble-averaged static pressure difference $P_{s,1-0}/(\rho/2 * C_0^2)$, relative flow angle β_1, and normalized moment of momentum $C_{1u} * U_1/U_2^2$ close to the blade leading edge at optimum flow rate

flow, the pneumatically averaged velocities are higher than numerically averaged instantaneous values.

The relative flow angle β_1, the normalized moment of momentum $C_{1u} * U_1/U_2^2$, and the static pressure difference P_{s1-0} distribution can be seen in Fig. 9. The static pressures were calculated assuming an axially symmetric stagnation pressure distribution measured by a five-hole probe. The relative flow angles were determined by projection on the $r-u$ plane.

Considering that the blade inlet angles at the hub and casing wall are 26 deg and 34 deg, the isocline map indicates, similar to Fig. 5, projected mean incidence angles of about -5 deg and $+12$ deg, respectively. The parallel isoclines in the middle of the passage show an inlet vortex in the clockwise direction of rotation (Binder and Romey, 1983). The inlet vortex corresponds well to the inviscid passage vortex (Bosman, 1980). In a rotating curved passage, as shown in Fig. 10, the relative passage vortex acts in a sense such that its circulation cancels the circulation due to the blade rotation. As the impeller angular velocity is constant and it only contributes an axial component of circulation, the streamwise component of the passage vortex generates a clockwise circulation in the orthogonal cross section. The intensity of the streamwise vorticity decreases when the direction of the meridional streamlines becomes increasingly radial. Interacting with the meridional flow deflection, this component of the passage vortex may induce deloading of the region casing/blade suction side in the axial to radial bend. The small relative angles at the hub near the blade suction side may be explained by the flow about the blade leading edge; see Fig. 1. Because of the blade thickness and negative incidence, the fluid is forced to bypass the blade along the suction side with a strong change of relative flow direction locally resulting in positive incidence angles in the measuring section near the blade suction side.

The influence of the incidence and of the flow about the blade leading edge on the energy addition can be observed in the moment of momentum distribution as well. In a great part of the passage positive momentum occurs. Close to the casing, much greater negative momentum can be observed in a small region while, near the suction side, the moment of momentum is approximately zero. The averaged moment of momentum amounts to about 1.5 percent of U_2^2, representing an initial whirl in the measuring plane in the direction of rotation. According to Eq. (2), the enthalpy rise of the impeller will be reduced by this whirl.

$$P_{2-0,m}/\rho = C_{2u,m} * U_2 - C_{1u,m} * U_{1,m} \qquad (2)$$

In the case of an ideal inlet vortex, the averaged moment of momentum would be near zero at chosen operating conditions. In the present case the spanwise distribution of the incidence is not symmetric; see Fig. 5. This and the flow about the relatively thick blade leading edge close to the hub add velocity components of direction of rotation to the relative flow. Flow distortion along the impeller width and the thick and unrounded leading edge act as a vane control device. Assuming 70 percent impeller efficiency (Fig. 2), the resulting

Fig. 5); this low-momentum fluid indicates the stagnation of flow at the blade suction surface. Every time a blade crosses the absolute streamlines, the meridional flow changes its direction from 65 deg to about 40 deg. The two subsequent peaks and dents in the isoclines show that the meridional flow angle alternates approximately at two times blade frequency. The circumferential inlet flow angles differ considerably from 90 deg, indicating tangential velocity components in the inlet cross section, except in the hub-suction side corner region. At the casing wall, they are about 100 deg, at the hub, close to the pressure side, 75 deg.

The normalized absolute velocity C_1/U_2 in Fig. 7 seems to have a distribution opposite to that of Fig. 3 measured by the five-hole probe. Figure 8 shows the circumferentially averaged velocities measured by hot-wire probe and the velocities directly measured by the five-hole probe compared along the blade leading edge. The average values measured by the five-hole probe are actually higher than the hot-wire values near the case. The difference is probably caused by the fluctuation of C_1 and ϵ. The pneumatic probe tends to store the peak pressures. Because of its integrating character, in a fluctuating
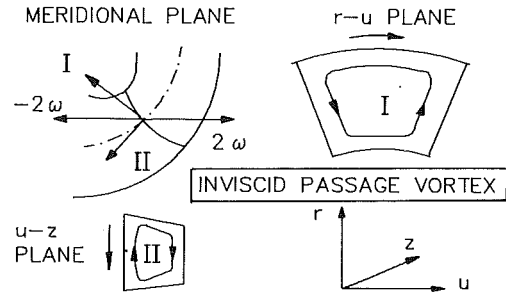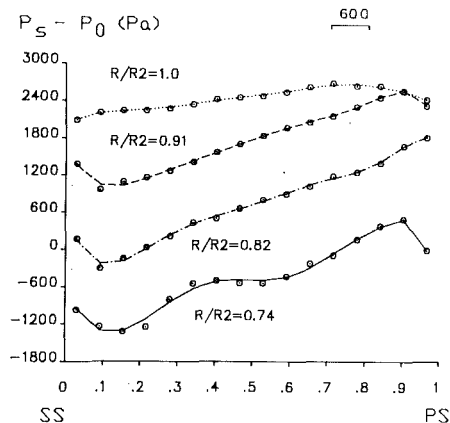
Fig. 11 Instantaneous wall pressure rise $P_s - P_0$ along the casing wall at optimum flow rate

Fig. 12 Measuring and display sections in the rotating impeller channel

amount of $C_{1u,m} * U_{1,m}$ corresponds to approximately 12 percent of the enthalpy losses between stations 0 and 3. Improving the shape of the blade leading edge and matching the blade angles to the inlet flow, the initial whirl might be reduced.

In the isobar plot, regions of high pressure correspond to the regions of low-momentum fluid in Fig. 7. They show that the fluid in the boundary layer on the casing wall flows up to the blade inlet against a time-variable pressure gradient. The amplitude of the static pressure is approximately 50 percent of the mean pressure difference between inlet pipe and blade inlet (stations 0 and 1). The high-pressure phase is much longer than would correspond to the blade thickness. This may have an influence on the flow separation primarily caused by the meridional curvature of the wall. Increasing back pressure promotes separation while decreasing back pressure accelerates the boundary layer. Therefore, separation may occur at a greater distance from the blade leading edge in the phase of high back pressure, than in the phase of low back pressure. So, an unstable separation point on the casing wall can be expected.

The tangential gradient of static pressure opposite to the direction of rotation over part of the passage at the casing wall has the same sense as the pressure gradient, which will be developed by impeller rotation. This pressure gradient is caused by the separation on the casing wall, the incidence and the unfavorable shape of the blade edge, that is from viscous effects. It will increase blade loading near the casing downstream of the measuring section, and thus reduced deloading of the casing/blade suction side region through the inviscid passage vortex can be expected in the first part of the impeller channel.

Flow in the Impeller Channel

Measurements at Optimum Flow Rate. The flow distribution in the rotating impeller channel can be described, first, by the isoclines of the relative flow measured by the L2F velocimeter and the isobars of the normalized reduced stagnation pressure. The isobars were calculated from the instantaneous wall pressure rise distribution in Fig. 11 measured by a piezoresistive wall-pressure transducer along the casing wall. The isoclines were interpreted with respect to the vortex structure as described by Binder and Romey (1983). The four measuring stations at $R/R_2 = $ const are shown in Fig. 12. Further flow value distributions can be interpolated in the cross sections at $Y = $ const and in the blade congruent sections at $X = $ const. The coordinates of the channel points are normalized in each of the three cross sections. The reference values are $D * \Pi/Z$ in the tangential, B in the axial, and $R_2 - R_1$ in the radial direction.
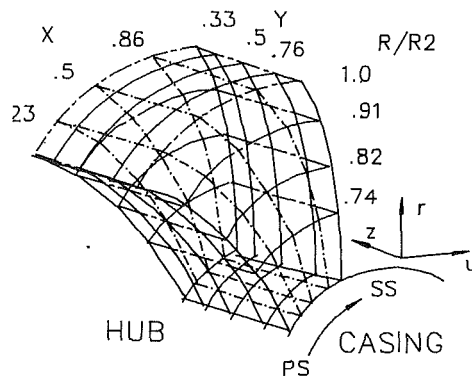
The approximately parallel isoclines in Fig. 13 at $R/R_2 = 0.74$ indicate a counterclockwise solid body vortex close to the pressure side. This means that the passage vortex has decayed up to this station, and circulation in the opposite sense has been developed by the increased blade loading near the case. At $R/R_2 = 0.82$, this solid body vortex is moved from the blade pressure surface toward the center of the channel. Near the impeller outlet, the character of the secondary flow will be altered. At $R/R_2 = 0.91$, the closed isoclines show a typical potential vortex with a second vortex of opposite sense at the hub/suction side region. At $R/R_2 = 1$, the center of the potential vortex is moved back toward the blade pressure side. The noticeably low relative flow angles in the casing wall/suction side corner might indicate the leakage flow and a possible separation in the blade tip region, which might cause the backward movement of the vortex at the casing wall.

The isobars clearly show the loss regions near the casing wall at $R/R_2 = 0.74$. These correspond well to the separation at the casing wall and along the blade leading edge. At $R/R_2 = 0.82$, a continuous wake zone can be observed along the casing wall, which is located nearer the blade pressure side than at $R/R_2 = 0.91$. At the outlet, this wake can be found, again, in the midregion of the casing wall. At $R/R_2 = 0.91$, a second wake appears at the location of the second vortex in the suction side/hub corner and remains present up to the outlet. The relatively big negative values of the normalized reduced total pressures indicate considerable losses in the wake zones.

The isotachs and the turbulence coefficient maps in the radial planes at $Y = $ const show some additional features of the relative flow; see Fig. 14. At $Y = 0.33$, the expected deceleration of the relative flow can be seen on the blade pressure side. The inlet separation at the blade leading edge, caused by the negative incidence in Fig. 5, is clearly indicated by the increased turbulence coefficients. At $Y = 0.76$, a second significant flow deceleration occurs at the blade suction side, near the outlet, as demonstrated by the low W/U_2 and high Tu_w values of less than 0.5 and higher than 20 percent, respectively. The cross section is abruptly blocked by the wake in a large region. The volume of the stagnant fluid, which is considerably larger than can be supposed by measurements in the impeller outlet, will be gradually reduced downstream by the secondary vortex flow.

The position of the wake in the impeller passage can be seen in Fig. 15. The isotachs of the radial velocity components in three display sections ($X = $ const in Fig. 12) are circumferentially projected in the meridional plane. Using Figs. 7 and 13, the position of low-momentum fluid can be qualitatively extrapolated from the locations of the deceleration zones at the casing wall in the whole impeller channel. Driven by the passage vortex, the deceleration zone at the casing wall first extends in the meridional bend from the suction side toward the pressure side. In the middle of the passage it proceeds toward the
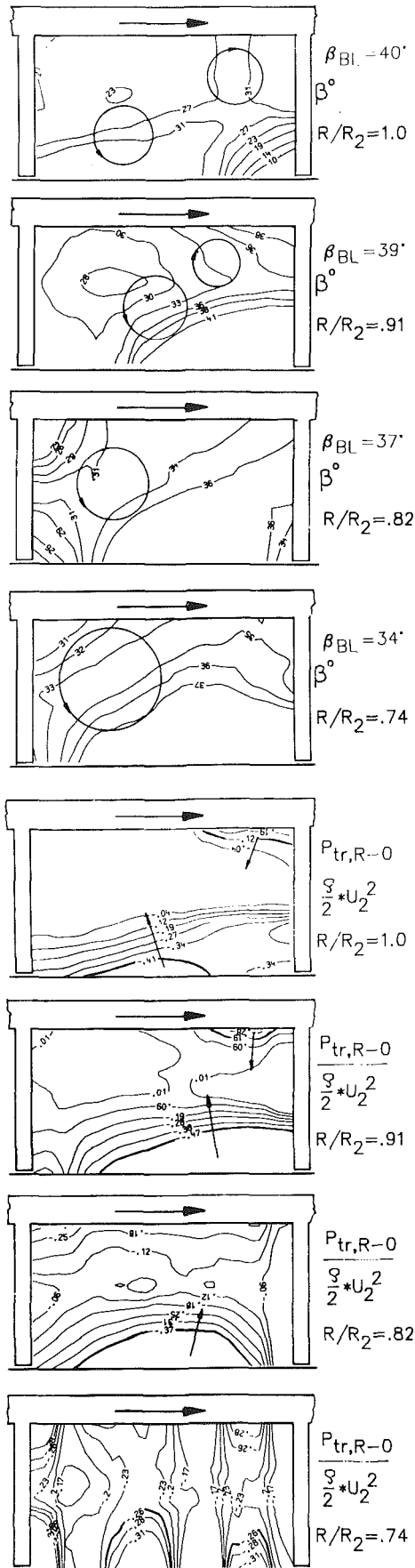
Fig. 13 Relative flow angle β and reduced stagnation pressure loss coefficient $P_{t,r,R-0}/(\rho/2 * U_2^2)$ in the four L2F measuring stations of $R = $ const (Fig. 12), at optimum flow rate, calculated with the instantaneous wall pressure in Fig. 11
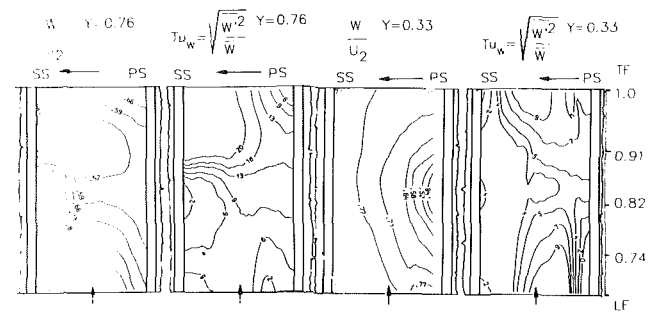

Fig. 14 Relative velocity W/U_2, turbulence coefficient of the relative flow Tu_w (percent) at two constant spanwise locations in the u–r plane
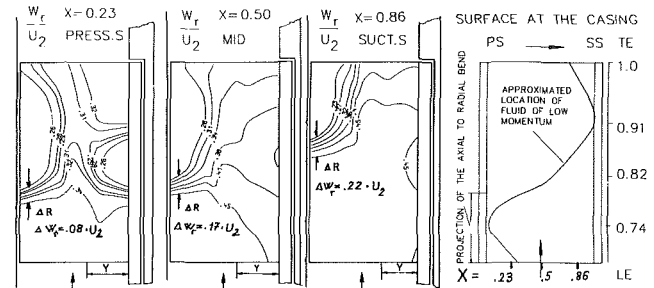

Fig. 15 Radial velocity (W_r/U_2) in the blade congruent sections projected circumferentially into the meridional plane, for three different values of $X = $ const (Fig. 12)
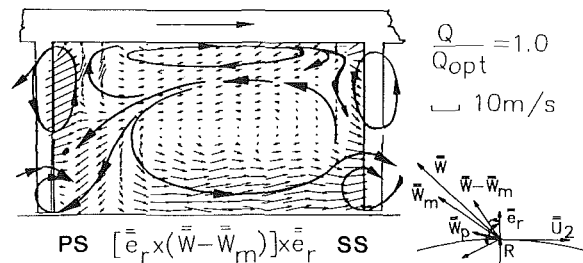

Fig. 16 Difference vector plot at the impeller outlet, at optimum flow rate, measured by a single hot-wire slanted probe

suction side, reaching the blade suction surface at about $R/R_2 = 0.9$. The streamwise velocity gradient will be increased in the downstream direction as well. This might be caused by the stagnation effect of the secondary flow on the blade suction side.

Figures 13–15 qualitatively show the development of the secondary flow in the impeller channel. Quantification of the secondary flow can be accomplished at the impeller outlet by three-dimensional hot-wire measurements; see Fig. 16. In the present investigation, the secondary velocity vector is viewed by the projection of the vector difference $\overline{\overline{W}} - \overline{\overline{W}}_m$ into the u–z plane. As the vector $\overline{\overline{e}}_r x(\overline{\overline{W}} - \overline{\overline{W}}_m)$ is normal to the plane of $\overline{\overline{e}}_r$ and $\overline{\overline{W}} - \overline{\overline{W}}_m$, it must be in the u–z plane. The vector product of $\overline{\overline{e}}_r x(\overline{\overline{W}} - \overline{\overline{W}}_m)$ with the unit vector normal to the u–z plane $\overline{\overline{e}}_r$, $\overline{\overline{W}}_p$, is hence again in the plane of $\overline{\overline{e}}_r$, and $\overline{\overline{W}} - \overline{\overline{W}}_m$; see Fig. 16. Thus, the normal projection of the difference vector $\overline{\overline{W}}_p$ onto the u–z plane can be expressed as

$$\overline{\overline{W}}_p = [\overline{\overline{e}}_r x(\overline{\overline{W}} - \overline{\overline{W}}_m)]x\overline{\overline{e}}_r. \qquad (3)$$

Although the secondary flow is not exactly expressed by this viewing technique, the slip factor will not be included, and the vortex structure of the fluid can be nearly recognized.

The vector plot indicates the similar main secondary flow pattern, which can be deduced from the isoclines in Fig. 13 at

Fig. 18 Difference vector plot at the impeller outlet, at increased flow rate, measured by a single hot-wire slanted probe
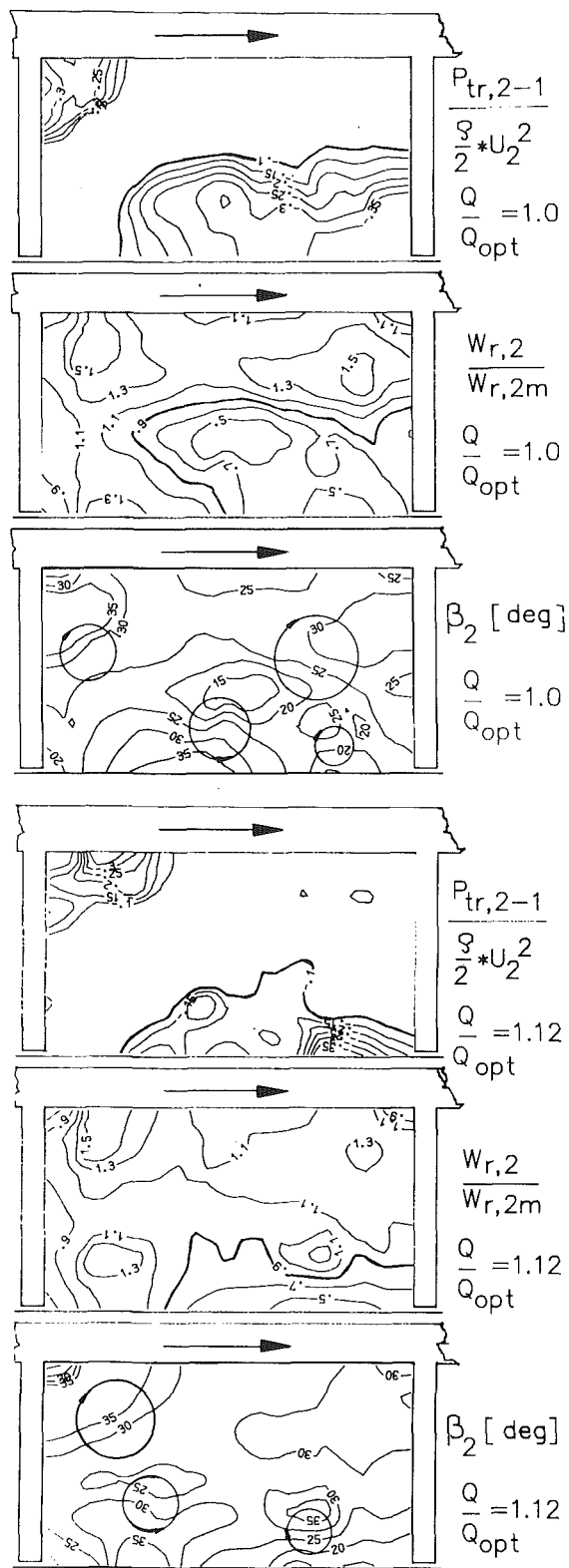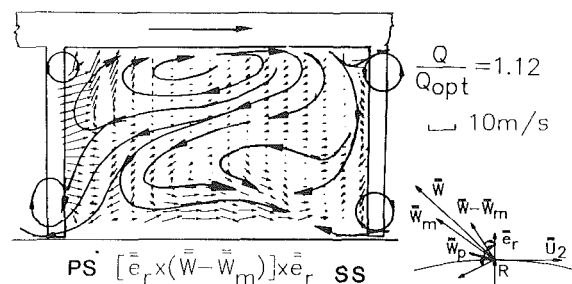

Fig. 17 Reduced stagnation pressure loss coefficient $P_{tr,2-1}/(\rho/2 * U_2^2)$, measured by an instantaneous Pitot probe, radial velocity referred to the average value of the cross section $W_{r2}/W_{r2,m}$ and relative flow angle β_2, measured by a single hot-wire slanted probe, at optimum and increased flow rates close to the blade trailing edge

$R/R_2 = 1.0$, and corresponds well to the secondary flow in a backswept rotating bend found by Johnson (1978). Further, a rather suppressed boundary layer flow to the casing wall can be recognized at the blade suction side. The interpretation of

the difference vectors near the blade surface is rather difficult because the hot-wire measurement could only be carried out approximately 6 mm behind the impeller outlet area and, thus, the separating wake vortices downstream of the trailing edge are superimposed on the boundary layer secondary flow. So, the vectors downstream of the blade trailing edge might include the time-averaged projection of the Kármán vortex street on the u–z plane as well. Because of the pressure gradients in the z direction, the Kármán vortices represent a spirally developing flow. Their projection on the r–u plane would result in the well-known vortex street for two-dimensional flows behind a flush body. In this case, the two vortices behind the trailing edge in Fig. 16 should be considered as flow separations alternatingly following each other.

Secondary Flow and Loss Distribution at Increased Flow Rate. Based on the results of time-averaged measurements at varied flow rates at the blade inlet, a decreasing wake and a less distinct secondary flow can be expected at increased flow rates. The comparison of the isoclines, isotachs, and isobars of the reduced total pressure measured by a single slanted hot-wire and instantaneous Pitot probe behind the outlet cross section in the operating points of $Q/Q_{opt} = 1$ and $Q/Q_{opt} = 1.12$ support the same assumption; see Fig. 17. The isoclines show smaller flow angle differences at the higher flow rate than at the optimum flow rate. This indicates a more intensive mixing at the channel outlet. Considering the isotachs $W_{r2}/W_{r2,m} = 0.9$ as the edge of the wake, the wake takes up 30 percent at the optimum flow rate, and at the higher flow rate only about 15 percent of the outlet cross section. In the isobar map, the region of losses more than 10 percent is smaller as well. Further, the isobars show that the losses are more uniformly distributed in the cross section. They cannot be considered to be concentrated in the wake while this assumption still seems to be allowable at the optimum flow rate.

The changes in the secondary flow can be followed by the vector plots in Fig. 18. The boundary layer flow toward the casing wall can be clearly identified at the blade suction side, and the displacement of the vortex in the direction of rotation at the pressure side close to the hub can be seen as well. The potential vortex in the counterclockwise direction close to the casing wall is partly suppressed, and the vortex at the hub is intensified. The colliding vectors indicate this process in the casing wall/suction side corner.

Flow in the Diffuser

Figure 19 shows the distribution of the circumferentially averaged absolute velocity and flow angle in the spanwise direction at the diffuser inlet and outlet.

At the diffuser inlet, close to the casing wall, small flow angles and high velocities can be seen, whereas large angles and moderate velocities are found at the hub side wall. Close to the diffuser outlet, the small flow angles can be found at the hub side wall, while the large flow angles are located at the casing wall. While the static pressure is approximately
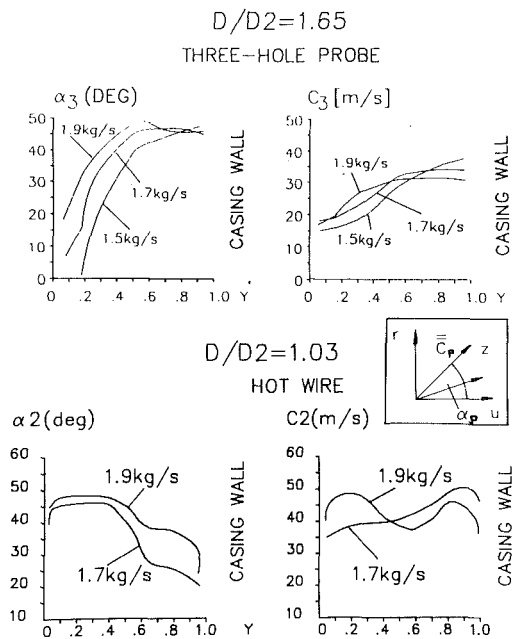
D/D2=1.65
THREE-HOLE PROBE

D/D2=1.03
HOT WIRE

Fig. 19 Velocities C_2 and C_3 and flow angles α_2 and α_3 projected on the r-u plane, along the diffuser width at constant flow rates, at the diffuser inlet and outlet

equalized in the measuring plane at $D/D_2 = 1.65$, the axial gradient of the stagnation pressure is directed to the casing wall. Compared with the diffuser inlet, it has the opposite sense. Similar results were published by Inoue and Cumpsty (1984), investigating a high-performance impeller (I-impeller) with an annular diffuser of parallel walls.

Varying the flow rate, there are no significant changes in the tendency of velocity and stagnation pressure development in the diffuser. The curves in Fig. 19 show that, corresponding to the measurements of Inoue and Cumpsty (1984), reverse flow at the hub side wall can occur at decreased flow rates, while increasing the flow rate results in a slightly more uniform velocity distribution.

Discussion of Results of Impeller Measurements: Comparison With Results of I-Impellers

Optimum Flow Rate. Comparing the inlet velocity distribution of the test impeller with experimental results of I-impellers, some significant differences can be seen. As shown in Fig. 5, the investigated impeller has strongly varying incidence angles, while in I-impellers like the impeller of the Ghost-Jet-Engine investigated by Johnson and Moore (1983a) or the high-performance compressor impeller investigated by Hayami et al. (1985), the relative inlet flow angle matches the blade inlet angles. Inlet velocity measurements in other C-impellers like the NACA-48-inch impeller (Moore and Moore, 1988) or an industrial blower impeller of simple construction (Cau et al., 1987) demonstrated a characteristic very similar to the test impeller. In both impellers, large incidence angles of alternating sense were found along the blade leading edge, resulting from the considerable inlet flow distortion, which might also influence the clockwise inlet vortex.

Considering the velocity distributions in the channels of the Ghost and in those of the test impellers, further significant differences can be observed. The Ghost impeller, having a nondistorted inlet flow, shows a secondary flow corresponding to the rotation and meridional curvature of the channel in the whole passage. At the beginning of the passage, the wake is located at the corner casing wall/suction side. In the axial-to-radial bend, centrifugal forces are increased in the orthogonal

direction with respect to the Coriolis force in the tangential direction, and the Ro number is increased. Therefore, a secondary flow from the hub to the casing wall is developed along the blade surface and the wake extends in this region along the casing wall. In the radial part of the channel, meridional streamline curvature and thus the Ro number are decreased. The secondary flow becomes less intensive, and the wake is, again, placed at the suction side.

In the investigated C-impeller, a solid body vortex dominates the flow close to the pressure side in the first half of the channel. Secondary flow resulting from the meridional curvature of the streamlines cannot be recognized. The wake is found at the middle of the casing wall; see Fig. 13. At about half of the passage length, at approximately $R/R_2 = 0.8$, this solid body vortex will be suppressed by the high centrifugal force caused by the beginning slip and the consequent rapid change of the flow angle. In the outlet part of the channel, beginning at about $R/R_2 = 0.85$, the potential character of the passage vortex indicates that the secondary flow might be determined rather by the impeller rotation and the tangential curvature of the passage than by the inlet vortices. In this region, because of the slip, the streamline curvature is practically zero, and the Ro number is very low. So, the wake is placed closer to the blade suction side. Caused by the increasing slip and blockage effect of the flow separation at the blade suction side at the outlet, velocity and Ro number will be increased, and the wake extends again at the casing wall when leaving the flow channel. Thus the location of the wake in the impeller passage is opposite to that of the Ghost impeller.

Considering the flow angles in the wake at the outlet in I-impellers with radial ending blades, the flow direction in the wake is about that of the blade in the whole passage (Eckardt, 1975; Johnson and Moore, 1983a). In the test impeller, blade-congruent relative flow could only be found up to $R/R_2 = 0.91$. In the outlet region, wake flow angles become rapidly smaller. Similarly, very small relative flow angles were found in an I-impeller of a turbocharger with backward swept blades in the outlet region (Rohne and Baumann, 1988) and in a C-impeller with backswept logarithmic blades (Hamkins and Flack, 1987). The different outlet flow angles might be explained by the acceleration of the fluid and the increased Ro number in impellers of backswept vanes close to the outlet.

Consequently, smaller blade angles close to the casing wall would result in higher velocities, hence in further increase of the Ro number in the test impeller. Similar to the effect of increased flow rates, the wake would be located closer to the pressure side and a more uniform velocity distribution may be expected.

Increased Flow Rate. At I-Impellers, the wake extends closer to the casing wall than at optimum flow rate (Johnson and Moore, 1983b; Inoue and Cumpsty, 1984). When the relative velocity is increased, the centrifugal force will rise more rapidly than the Coriolis force. Consequently, the Ro number becomes greater, and wake displacement to the casing wall will be supported. At the test impeller, for the same reason, the wake is pressed to the casing wall and the vortices along the casing wall are located closer to the pressure side than at optimum flow rate; see Fig. 17. Further, a more developed secondary flow to the casing wall along the suction side can be seen in Fig. 18, which will be practically suppressed at optimum flow rate; see Fig. 16.

Summary

Based on instantaneous flow measurements, the following flow characteristics were observed in the present compressor with untwisted, backswept vanes:

(a) Because of the great curvature in the axial-to-radial bend, flow separation occurred at the casing wall, causing

nonuniform incidence along the blade leading edge. This induced a tangential static pressure gradient, which reduced blade deloading by the inviscid passage vortex near the casing wall. Furthermore, asymmetric distribution of the incidence angles along the blade leading edge generated an initial whirl.

(b) In the impeller channel, the wake extended from the casing wall toward the suction side. Therefore, it bypassed the radial pressure gradient, and separation was avoided until the blade surface was reached. The flow separation was clearly indicated by the rapidly increasing turbulence at the blade suction side.

(c) In the annular diffuser, the wake was found at the casing wall at the inlet and close to the hub side wall at the outlet.

(d) With the inlet vortex, nonuniform incidence angles and the twofold curvature of the flow channels in the meridional and tangential direction, there are four factors to be considered when modeling the passage flow. The inlet vortex and, subsequently, the solid body passage vortex dominate the flow in the first half of the channel. In the outlet region of the impeller channel, the passage curvature seems to determine the secondary flow.

Recommendations

The time-averaged and instantaneous flow measurements qualitatively describe the impeller flow characteristics. To quantify the effects summarized above, further experiments should be made.

The impeller losses induced by the uniform incidence angles and the relatively thick blade leading edge might be diminished by improving the shape of the blade leading edge and by twisting the blades. Smaller blade angles at the casing would reduce or eliminate separation at the leading edge, and the resulting reduction in low-momentum fluid along the suction surface would help to avoid separation on that surface near the outlet.

Acknowledgments

References

Adler, D., and Levy, Y., 1973, "A Laser-Doppler Investigation of the Flow Inside a Backswept, Closed, Centrifugal Impeller," *J. Mech. Eng. Sci.*, Vol. 21, No. 1.

Binder, A., and Romey, R., 1983, "Secondary Flow Effects and Mixing of the Wake Behind a Turbine Stator," ASME *Journal of Engineering for Power*, Vol. 105, pp. 40–46.

Bosman, C., 1980, "An Analysis of Three-Dimensional Flow in a Centrifugal Compressor Impeller," ASME *Journal of Engineering for Power*, Vol. 102, pp. 619–625.

Cau, G., Mandas, N., Manfrida, G., and Nurzia, F., 1987, "Measurements of Primary and Secondary Flows in an Industrial Forward-Curved Centrifugal Fan," ASME *Journal of Fluids Engineering*, Vol. 109, pp. 353–358.

Eckardt, D., 1975, "Untersuchung der Laufradströmung in hochbelasteten Radialverdichterstufen," *Forschungsbericht Verbrennungskraftmaschinen*, No. 183.

Hamkins, C. P., and Flack, R. D., 1987, "Laser Velocimeter Measurements in Shrouded and Unshrouded Radial Flow Pump Impellers," ASME JOURNAL OF TURBOMACHINERY, Vol. 109, pp. 70–76.

Hayami, H., Senoo, Y., and Ueki, H., 1985, "Flow in the Inducer of a Centrifugal Compressor Measured With a Laser Velocimeter," ASME *Journal of Engineering for Gas Turbines and Power*, Vol. 107, pp. 534–540.

Inoue, M., and Cumpsty, N. A., 1984, "Experimental Study of Centrifugal Impeller Discharge Flow in Vaneless and Vaned Diffusers," ASME *Journal of Engineering for Gas Turbines and Power*, Vol. 106, pp. 455–467.

Johnson, M. W., 1978, "Secondary Flow in Rotating Bends," ASME *Journal of Engineering for Power*, Vol. 100, pp. 553–560.

Johnson, M. W., and Moore, J., 1983a, "Secondary Flow Mixing Losses in a Centrifugal Impeller," ASME *Journal of Engineering for Power*, Vol. 105, pp. 24–32.

Johnson, M. W., and Moore, J., 1983b, "The Influence of Flow Rate on the Wake in a Centrifugal Impeller," ASME *Journal of Engineering for Power*, Vol. 105, pp. 33–39.

Kano, F., Tazawa, N., and Fukao, Y., 1982, "Aerodynamic Performance of Large Centrifugal Compressors," ASME *Journal of Engineering for Power*, Vol. 104, pp. 796–804.

Lapworth, B. L., and Elder, R. L., 1988, "Computation of the Jet-Wake Flow Structure in a Low-Speed Centrifugal Impeller," ASME Paper No. 88-GT-217.

Lindner, E., 1984, "Untersuchungsergebnisse zur Radialradströmung," *Wissenschaftliche Zeitschrift der TU-Dresden*, No. 33, Heft 4.

Moore, J., Moore, J. G., and Timmis, P. H., 1984, "Performance Evaluation of Centrifugal Compressor Impellers Using Three-Dimensional Viscous Flow Calculations," ASME *Journal of Engineering for Gas Turbines and Power*, Vol. 106, pp. 475–481.

Moore, J., and Moore, J. G., 1988, "Secondary Flow, Separation and Losses in the NACA 48-Inch Centrifugal Impeller at Design and Off-Design Conditions," ASME Paper No. 88-GT-101.

Müller, K. J., and Sipos, G., 1985, "Untersuchungen der Strömung in einem radialen Ventilatorlaufrad," *VDI-Berichte*, No. 572, pp. 373–386.

Renyong Tu, He Lu, and Wang Yanling, 1985, "Theoretical Analysis and Experimental Research of Three-Dimensional Flow of Centrifugal Impeller," ASME Paper No. 85-IGT-79.

Rohne, K. H., and Baumann, K., 1988, "Untersuchungen der Strömung am Austritt offener Radialverdichterlaufräder und Vergleich mit der klassischen Jet-Wake-Theorie," *VDI-Berichte*, No. 706, pp. 263–282.

Sipos, G., 1984, "Kombiniertes Meß- und Rechenverfahren für die Bestimmung der instationären Strömung an Ventilatorlaufrädern," *Forsch. Ing.-Wesen*, Vol. 50, No. 4, pp. 123–130.

Sipos, G., 1986, "Anwendung und Weiterentwicklung eines Hitzdraht-Messverfahrens zur Erfassung der drei-dimensionalen Austrittsströmung von Radialgebläsen," *Mitteilungen des Institutes für Dampf- und Gasturbinen der TU-Wien*, No. 14.

Centrifugal Compressor Inlet Guide Vanes for Increased Surge Margin

C. Rodgers
Chief Conceptual Design,
Sundstrand Power Systems,
San Diego, CA 92123

This paper describes the results of compressor rig testing with a moderately high specific speed, high inducer Mach number, single-stage centrifugal compressor, with a vaned diffuser, and adjustable inlet guide vanes (IGVs). The results showed that the high-speed surge margin was considerably extended by the regulation of the IGVs, even though the vaned diffuser was apparently operating stalled. Simplified one-dimensional analysis of the impeller and diffuser performances indicated that at inducer tip Mach numbers approaching and exceeding unity, the high-speed surge line was triggered by inducer stall. Also, IGV regulation increased impeller stability. This permitted the diffuser to operate stalled, providing the net compression system stability remained on a negative slope.

Introduction

Flow ranges for a single-stage centrifugal compressor are dictated by the stalling characteristics of the impeller and the diffuser. These are intrinsically controlled by the diffusion capability or attainable static pressure rise of the blade and vane rows. Both vaned and vaneless diffuser systems are used for centrifugal compressors. However, the requirement for maximum efficiency at high Mach numbers makes the use of vaned diffuser systems almost mandatory. The impeller and diffuser must be matched adjacent to their peak efficiency flow conditions.

The stationary vaned diffuser tends to be the flow-controlling component. Its overall Mach number level and inlet blockage are higher than those of the inducer, which operates with a large radial variation of Mach numbers from hub to shroud. The diffuser must also accept an already diffused flow from the impeller. This results in nonuniform entrance conditions, which further aggravate its stalling sensitivity. These conditions curtail the compressor operating range. As a result, stationary diffusers for centrifugal compressors have received considerable attention. Attainment of a large flow range requires that the impeller and the diffuser be capable of extended operation into their stalled or positive incidence regions to a flow where static pressure rise plateaus and compressor surge are eventually triggered. Stage surge is believed to stem from operation on the unstable (positive slope) portion of the overall compressor characteristic. This occurs when static pressure ratio increases with increasing flow. One effective method of increasing compressor operating range is to provide sufficient impeller stability. This allows the downstream diffuser to operate slightly into its positive incidence zone, even though the diffuser static pressure recovery versus flow characteristic exhibits a positive slope.

Previous studies by the author on centrifugal impeller dif-

fusion limitations were presented in [1]. These pertained to analysis of a single, experimental, high Mach number centrifugal, backswept impeller of near-optimum configuration. Test results on this particular impeller indicated·stall whenever the velocity diffusion ratio W_{1rms}/W_2 (based on mixed impeller exit condition) exceeded 1.6. It was, therefore, suggested that such a simple limiting velocity ratio could be used as an initial design guideline to indicate impeller stalling proximity.

A similar condition of the stalling conditions of centrifugal compressor channel-type diffusers was correlated for several stages, covering a wide specific speed range. For any given stage, it was determined that stage surge (when triggered by diffuser stall) occurred near a constant mean stream velocity diffusion ratio between the impeller tip and diffuser throat. This diffusion ratio attained a maximum value of 1.8 for impeller tip Mach numbers less than unity. It was not unique for all stages, being more intimately coupled with throat blockage accumulation. This was a function of diffusion rate. This was identified by testing some vaned diffusers beyond the stall limit. In these instances, rapid blockage accumulation precipitated an immediate decrease in channel diffuser and system static pressure recovery.

Since the publication of [1, 2], the author has conducted additional centrifugal compressor research and development. These studies relate to the stalling characteristics of high specific speed, high Mach number, single-stage centrifugal compressors. The incentive for this subsequent research has been the requirement to increase the power density of small gas turbine auxiliary power units (APUs) and turbojets. This was achieved by increasing the airflow/frontal area.

As a consequence of these incentives, advanced high specific high Mach number compressor inducer components are working at inducer tip relative Mach numbers above 1.4. These inducers exhibit airflow swallowing capabilities similar to advanced turbofan axial compressor stages. In achieving these goals, it is highly desirable to maintain the major attributes of the centrifugal compressor. These include low cost, workable operating ranges, and if possible, fixed geometry. This

Fig. 1 Efficiency versus specific speed

Fig. 2 Test impeller and diffuser
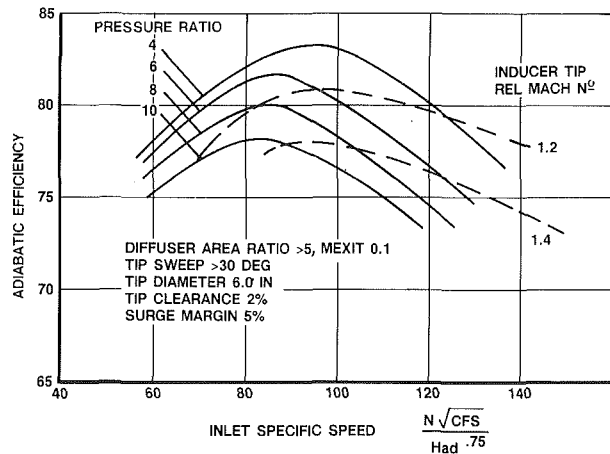
does result in some acceptable compromise in peak efficiency inherent with higher specific speed geometries, as indicated in Fig. 1.

The objective of this paper is to present test results for a high specific speed, high Mach number, single-stage backswept centrifugal compressor with an impeller tip diameter of 165 mm (6.5 in.). Operating parameters include stage pressure ratios up to 5.5, with maximum airflow capacity Q/Q_{crit} equal to 0.87, of the choked inducer annulus flow. Testing of this impeller was conducted with and without axial inlet adjustable inlet guide vanes (IGVs). Testing results demonstrated that operating range increased with the use of IGV regulation.

Compressor Design Features

The test compressor was one of several recently designed and tested for application in small high-speed gas turbine APUs. The major geometric details are listed in Table 1. Figure 2 shows the test impeller with eight long and eight alternate splitter blades. These blades have a tip backsweep angle of 40 deg. The compressor was originally designed for the following performance on air, at sea level, standard 288 K (59 R) conditions:

Compressor design point

Rotational speed, rpm	64,643
Pressure ratio	4.85
Airflow, pps	3.15
Specific speed	116
Adiabatic efficiency (total-static), percent	77.0
Inlet prewhirl, deg	0

Table 1 Test compressor geometric features

Inducer Tip Diameter	mm (in)	108.5 (4.27)
Impeller Tip Diameter	mm (in)	165 (6.50)
No. of Impeller Blades		16
Impeller Tip Width	mm (in)	9.4 (0.37)
Impeller Tip Backsweep	deg	40
Vaneless Space Diameter Ratio	%	12
No. of Diffuser Vanes		17
Diffuser Exit Diameter	mm (in)	262 (10.3)

Initial tests were conducted with this compressor and an axial inlet. These tests showed that with a cold shroud clearance of 0.23 mm (0.009 in.), it was possible to achieve the design performance level with an inducer tip thickness of 0.043 mm (0.017 in.). Subsequent to initial mapping, it was decided to investigate the influence of IGV regulation on the compressor performance. A set of 13 uncambered axial IGVs were manufactured for installation into the flowpath as illustrated in Fig. 3.

Apparatus and Procedures

The test turbodrive rig is shown in Fig. 4. It was essentially

---

Nomenclature

A = area
C.F.S. = volume flow
D = diameter
H_{ad} = adiabatic head
IGV = inlet guide vane
P = total pressure
M = Mach number
Mu = $U2/(g\gamma R T_1)^{0.5}$ = DeLaval number
Ns = $N(\text{C.F.S.})^{0.5} (H_{ad})^{-0.75}$ = specific speed
Q = flow function = $W\sqrt{T}/AP$
q = impeller work factor = $\Delta H/U_2^2$
R = gas constant
rms = root mean square
T = total temperature
U = impeller tip speed

W = flow, relative velocity
α = air angle (relative to axial)
γ = specific heat ratio
Δ = difference
θ = prewhirl angle (relative to axial)

Subscripts

1 = impeller
2 = impeller tip
3 = diffuser throat
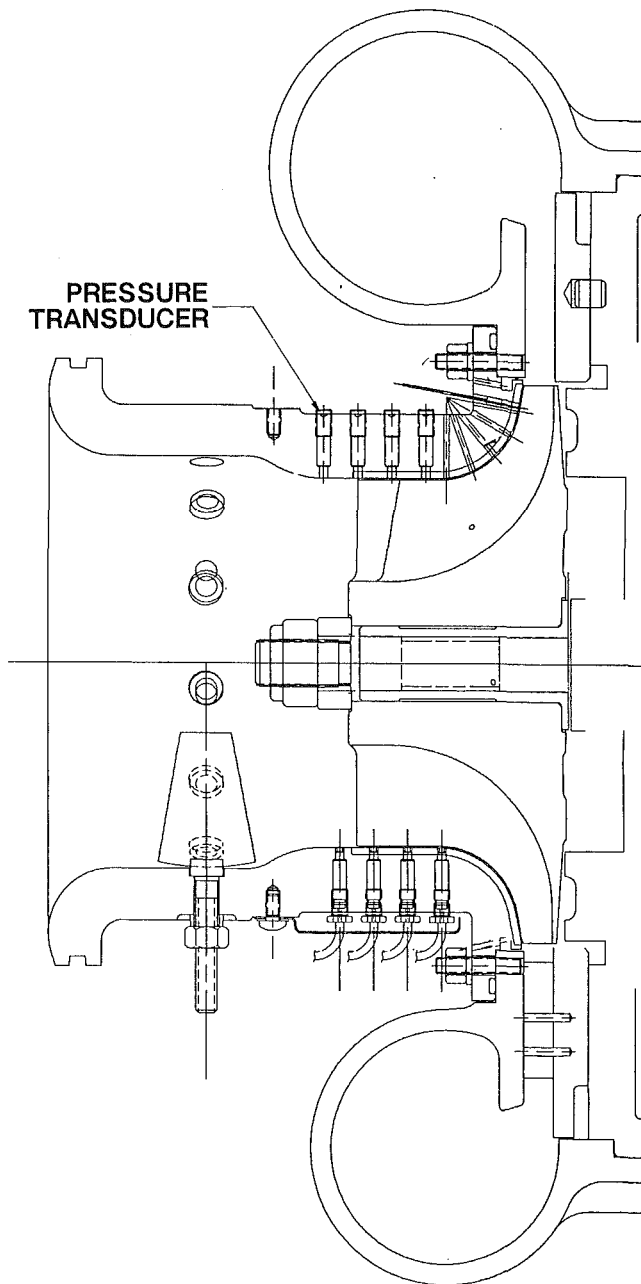c = compressor, critical
E = diffuser exit
t = tip
w = relative

Journal of Turbomachinery

PRESSURE
TRANSDUCER

Fig. 3 Test compressor flowpath

power requirements. At the maximum test speed, the inlet was throttled to approximately 0.75 bar.

The compressor performance was mapped by setting a predetermined corrected speed and gradually increasing the back pressure to determine the stable operating range. Several data points evenly spaced between choke and audible surge were obtained for each speed line. Discharge ducting volume from the impeller tip to the back pressure throttling valve was approximately 40 times the enclosed volume of the impeller.

Instrumentation and Data Reduction

The compressor instrumentation shown in Table 2 was used to define the impeller performance. Thirteen static pressure taps were equally spaced along the outer stationary shroud of the impeller. These extended from the inducer inlet to the impeller exit. Due to the small impeller tip width, tip instrumentation was confined to five static pressures. These were equally spaced around a circumferential cavity at the impeller tip. Copper-constantan thermocouples were used for measurement for the compressor inlet and discharge temperatures. At 100 percent design speed, the typical scatter in inlet and exit discharge temperatures was on the order of $\pm 1.0°F$.

Test measurements used in the calculation of one-dimensional impeller performance were inlet total pressure and temperature, average tip static pressure, scroll exit total temperature, and airflow. Flow continuity, impeller geometry (with 10 percent flow blockage allowance at the impeller tip), and temperature rise were used together with a Wiesner slip factor of 0.875, and a specific heat ratio of 1.395 to calculate vector conditions at the impeller inlet and exit.

The diffuser static pressure recovery and diffusion ratio between the impeller tip and diffuser throat were calculated on a one-dimensional basis. These calculations used the prescribed impeller tip conditions and the measured diffuser throat static pressure.

Compressor speed was indirectly measured from a casing-mounted vibration pickup. This pickup used a frequency analyzer to track the first-order resonance. Speed variation when mapping along a constant speed line was on the order of ± 0.1 percent. This was essentially a consequence of a very stable air supply system, and fine control of the compressor back-pressure.

Compressor Test Performances

The overall performance of the test compressor without the IGVs installed is presented in Fig. 5. Total-to-static pressure ratio (referenced to engine conditions), and corresponding adiabatic efficiency, are shown. These are presented versus flow function ratio Q/Q_{crit}, with the DeLaval number as a parameter. At the design pressure ratio of 4.85 and corrected flow of 3.15 pps, the overall efficiency was 77 percent with a surge margin of 12 percent. At the maximum test DeLaval number of 1.73, peak pressure ratio was 5.6, with a corresponding efficiency of 76 percent. Maximum flow function ratio at this tip speed was 0.87, as limited by inducer choking. Compressor peak efficiency, with the particular diffuser match, was 79.6 percent at a pressure ratio of 4.05.
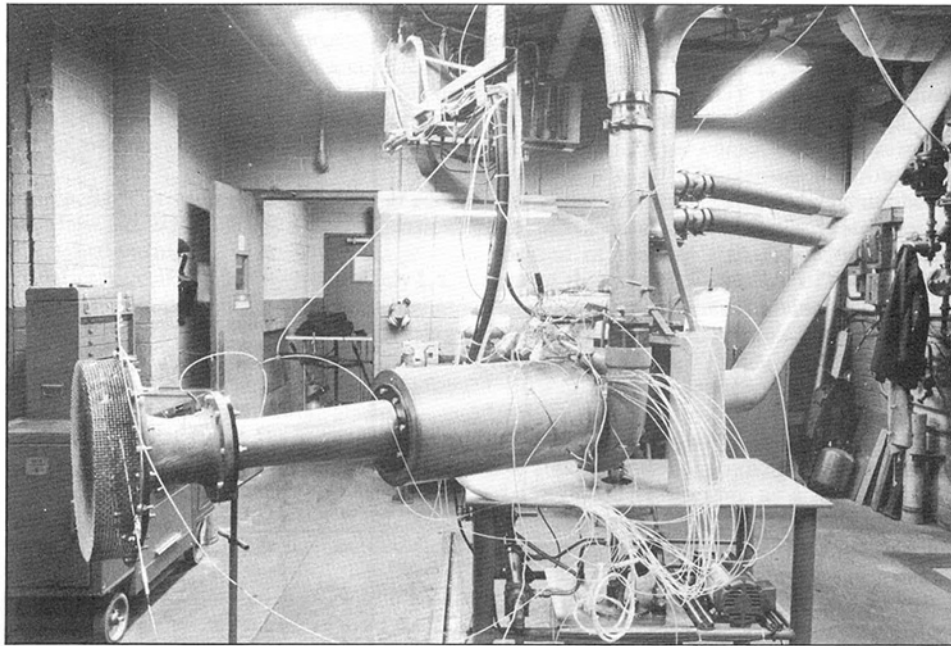
a commercially available turbocharger, modified to accept the test impeller together with its axial inlet and diffuser. For test expediency, the turbocharger type discharge volute was installed. This was used instead of the typical 90-deg bend and annular deswirl cascade of the actual engine application. Comparative calibration of both discharge systems had been previously conducted. They permitted translation of the test rig data to engine compressor exit (static) pressure reference conditions. The inlet shroud was coated with an abradable aluminum epoxy material to permit nondestructive testing at the close operational clearances.

Warm air for the turbine drive was provided by plant compressed air. The compressor inlet-air system comprised a 115 mm (4.5 in.) ASME venturi dumping into a 25.4-cm (10-in.) duct. This was subsequently attached to the vaned IGV inlet.

A restrictor place was installed at the dump section for subatmospheric throttling of the compressor inlet. This was a means of matching turbine drive output power to compressor

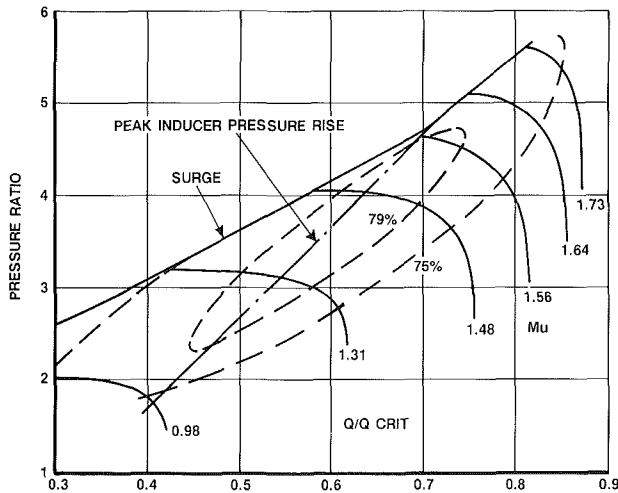Fig. 4   Compressor test rig

Fig. 5   Compressor test performance map; θ_1 = 0 deg
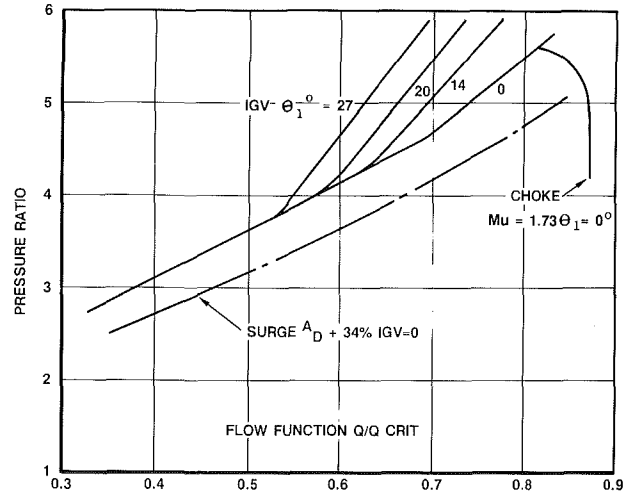

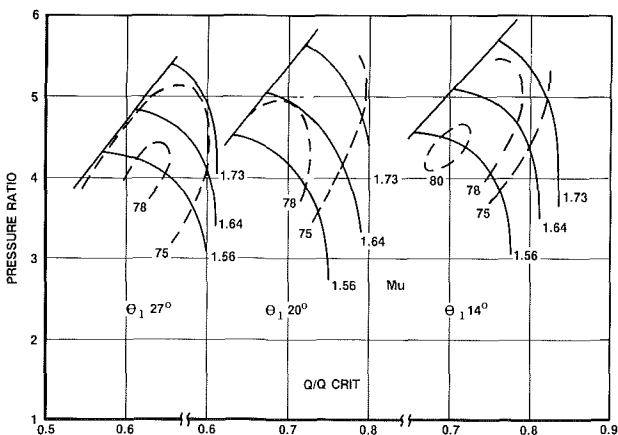
Fig. 7   Effect of prewhirl on surge lines

Fig. 6   Compressor test performance map; θ_1 = 27, 20, 14 deg

The small working flow range at the highest test tip speed was thought to be controlled by both inducer choke and stall. Since it was desirable to maintain the maximum flow through-

put, the use of the IGVs was recommended as a possible solution to increasing the flow range.

The IGVs were subsequently installed, and three test maps (Figs. 6, 7, and 8), were obtained at the following conditions:

DeLaval number Mu	1.56	1.64	1.73
θ_1 prewhirl angle, deg	14	20	27

Examination of the effect of increasing prewhirl shows considerable displacement of the surge line toward lower flows with increasing tip speeds. Although not shown, spot tests at lower DeLaval numbers of 1.31 and 0.98 showed no significant change relative to the zero degree prewhirl surge line. The overall effect of prewhirl on the compressor surge line is indicated by Fig. 7. There the working range at a pressure ratio of 5.5 is 27 percent from surge at θ_1 = 27 deg, to near choke at θ_1 = 0 deg.

Note: Some additional testing was conducted with a negative prewhirl setting of −14.0 deg, which showed a reduction in efficiency of 5 percent points at all speeds.

Previous testing used IGVs on a lower specific speed 5.5:1 pressure ratio [1] compressor. This showed a significant displacement of the surge line with IGV regulation using a vaneless
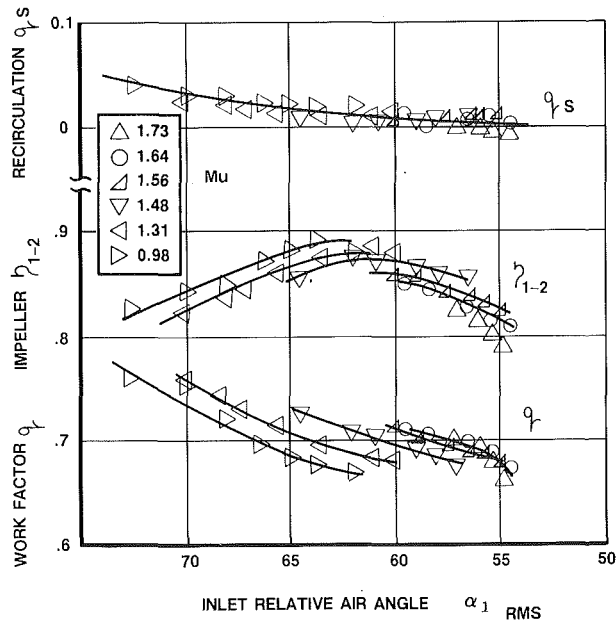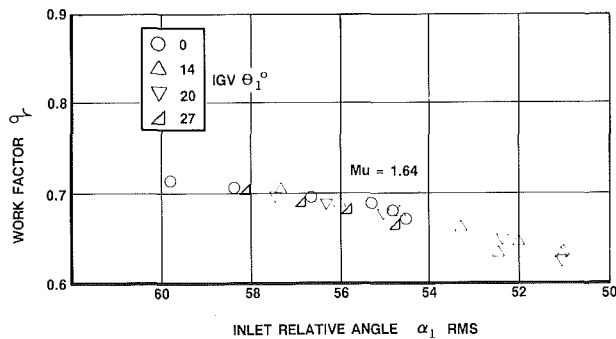
Fig. 8 Stage performance characteristics

Fig. 9 Work factor versus inlet air angle

Fig. 10 Stall parameters at surge

Fig. 11 Inducer tip incidences at surge

diffuser. However, there was essentially no surge line displacement when a vaned diffuser was installed. These results are generally supported by the open literature. They classically follow the trends of diffuse dominant surge characteristics for centrifugal compressors with subsonic inlet conditions.

The large increase in flow range with this particular high specific speed test compressor, which had a vaned diffuser, conflicted with past (lower inlet Mach number) compressor performance trends. This prompted an examination of the individual component matching to corroborate the supposition that the inducer could be the critical flow controlling component.

Component Matching Analysis

Prior to conducting a matching analysis of the impeller and diffuser characteristics, a normalized stage performance characteristic was prepared for the impeller. This is shown in Fig. 8, where work factor q, impeller efficiency, and disk function plus recirculation losses are plotted, versus inlet relative air angle ($\alpha_1$rms) for the zero prewhirl condition. As mentioned previously, the impeller tip vector conditions were computed using the Wiesner slip factor of 0.875 for 16 blades with 40 deg backsweep. Excess enthalpy was contributed to disk friction and recirculation losses. These losses are shown to increase from zero at choke conditions to 4 percent at the lowest test tip speed and flow coefficient.

Since an exit traverse of the IGVs was not conducted, it was necessary to calculate the prewhirl angle based upon the IGV
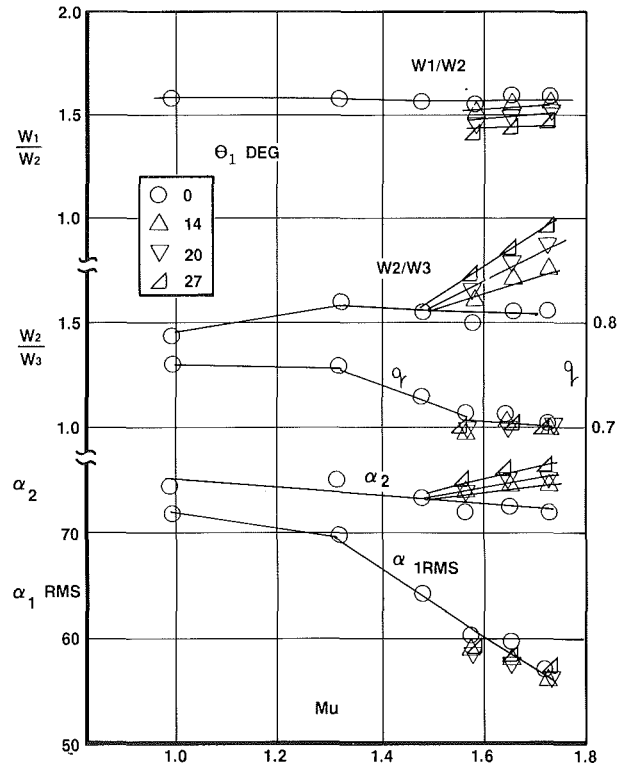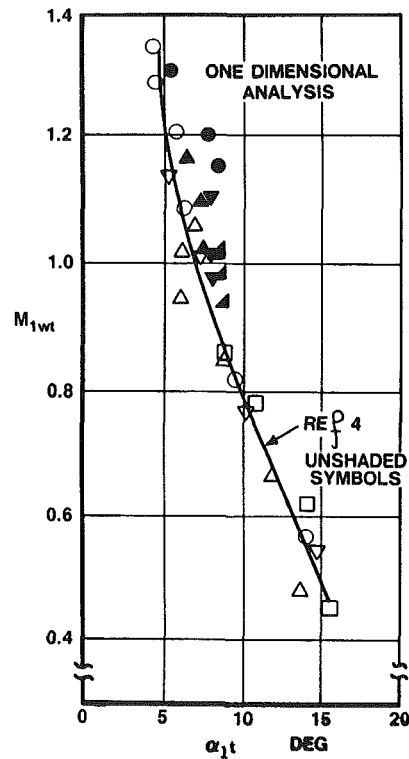
metal angle setting and conservation of angular momentum. The calculated prewhirl angles were 14, 20, and 27 deg, respectively. They were used to compute the comparative work coefficient q versus inlet flow angle shown in Fig. 9. This figure exhibits satisfactory data consistency at Mu = 1.56 for all inlet conditions.

A prognosis of which element may be precipitating surge can be obtained by examination of the variation of impeller

and diffuser incidences and/or loading parameters along the surge line, as a function of tip speed. Accordingly, impeller inlet (relative) and exit (absolute) air angles, work coefficient and diffusion ratio, together with diffuser diffusion ratio for all surge points are plotted versus DeLaval number in Fig. 10. These data reveal the following:

• A near-constant impeller diffusion ration W_1/W_2, at zero prewhirl of approximately 1.6, with slightly lower diffusion ratios at increasing prewhril settings.
• A near-unique diffuser ratio W_2/W_3 of approximately 1.6, and diffuser inlet angle at zero prewhirl, with much higher diffusion ratios and higher inlet air angles with increasing prewhirl settings.
• A near-constant relationship of work factor $q(=0.7)$ for all IGV settings at the higher DeLaval numbers.

It was deduced from these trends and [1, 2] that, at zero prewhirl conditions, compressor surge was probably triggered by the diffuser. This was indeed confirmed by a subsequent test, with the diffuser throat area increased 34 percent. This resulted in lateral displacement of the surge line as indicated in Fig. 7.

The large displacement of the high-speed surface line with IGV position appeared due to either reduction in inducer incidence with IGV regulation, and/or reduction in impeller loading (work factor q or diffusion ratio W_1/W_2).

Detailed examination of the impeller shroud static pressure distribution for the zero prewhirl test indicated a peak inducer static pressure just downstream of throat, followed by a slight reduction and eventual large increase after the bend. The flow corresponding to this weak inducer static pressure is plotted in Fig. 5. The figure shows flow correspondence with the high-speed surge line slope, and kink or break, when the diffuser takes over surge control. Of equal significance is that the locus of maximum inducer static pressure also corresponds to a line of constant work factor $q = 0.7$. Subsequent examination of the IGV test cases indicated that surge was coincident with maximum inducer static pressure rise. These observations are corroborated by the excellent work of Senoo [3–5]. He studied the surge characteristics of a supersonic centrifugal compressor with a vaned IGV and a vaneless diffuser. Senoo showed that at inducer tip relative Mach numbers approaching greater than unity, inducer stall precipitated compressor surge. He disproved impeller inlet to exit diffusion ratio as the precipitating factor. This was postulated to occur as a consequence of shock wave separation of the inducer suction surface boundary with consequent increase of the impeller tip blockage.

Inducer tip incidences at surge are shown versus inducer tip relative Mach number in Fig. 11. These findings compare favorably with the one-dimensional results of Senoo.

The surging characteristics of compressors are governed not only by individual component stalling characteristics, but also by the combined manner in which these components influence the net compression system stability. Yoshinaka [6] concluded that surge of a typical centrifugal compressor occurred only when both components (inducer and diffuser) are operating at or beyond stall. Surge is typically synonymous with the inflection of overall system static pressure rise with flow. A highly stable, negative slope, rotor characteristic, just coming off choke, can stabilize a downstream diffuser to operate on its stalled (positive slope) characteristic. This is clearly supported by these results.

Conclusions

Compressor rig testing was conducted on a moderately high specific speed, high inducer Mach number, single-stage centrifugal compressor with a vaned diffuser and adjustable inlet guide vanes. Testing showed that the high-speed surge margin was considerably extended by the regulation of the IGVs. This

occurred even though the vaned diffuser was apparently operating stalled. These results conflict with some other lower Mach number compressors where the vaned diffuser would dominate surge and IGV regulation was similar to the effect of changing speed, without a significant shift in surge line.

One-dimensional component performances with the test compressor at all IGV settings were observed. They indicated that at inducer tip relative Mach numbers greater than approximately unity, the surge line corresponded to the expected position of inducer stall. These performances also demonstrated that the high stability of the impeller at flows greater than inducer stall (i.e., moving toward inducer choke) permitted the diffuser to operate further into stall as IGV closure was increased.

It was observed that the high-speed surge line, as triggered by inducer stall, also corresponds to a nearly unique constant value of the impeller work coefficient "q." It is postulated that this corresponds to the maximum static pressure recovery of the impeller, working as a diffuser. It also suggests that further increases in work factor (as exhibited at lower speed) are associated with flow recirculation and disk windage effects with increased tip blockage.

It is difficult to achieve practical working flow ranges for high specific speed and/or high pressure ratio single-stage centrifugal compressors. To do this efficiently requires some form of variable geometry and/or bleed takeoff in the flow path. The most palatable options for the system designer, in order of preference, are:

• (First)   Bleed
• (Second)   Inlet guide vanes
• (Third)   Variable diffuser vanes

Increasing displacements of surge line require increasing large amounts of bleed, and/or vane modulation. Therefore, a tradeoff is necessary to assess net system weight and cost for each option.

The work reported herein stems from the generic technology advancement of a series of small, high specific speed, high Mach number, centrifugal compressors. This was coupled with competitive demands to apply the technology immediately to small high power density gas turbines. Development time and effort are of utmost importance in imposing limitations upon test scoping and instrumentation. In retrospect, the use of inducer shroud-mounted, high-frequency transducers and/or LDV optical surveys could have more precisely pinpointed the outset of inducer stalling. The further possibility of utilizing sensitive thermocouples close to the inducer tip might serve as a method for detecting stall and flow recirculation. Notwithstanding, the simplified one-dimensional component performance analysis adopted was successful. It provided a high degree of confidence that inducer incidence (or diffusion) control through the use of vaned IGVs can provide significant performance improvements for this type of centrifugal compressor stage.

Note

The following units were used in evaluation of the compressor performance. Equivalent metric conversions are noted.

Item	English	Metric conversion
Ns	rpm $(cfs)^{0.5}H_{ad}^{-0.75}$	1 rpm $(M^2/S)^{0.5-0.75}$ $= 0.412 \times Ns$
C; U; W	fps	1 m/s = 3.281 fps
D;	in.	1 cm = 0.3937 in.
$\alpha 1$; γ^2 deg γ^1 γ^2	deg	deg
P; p	psia	1 kg/m^2 = 1.422 $\times$ 10^3 psia
T	deg R	deg K = deg R/1.8

Acknowledgments

The author wishes to acknowledge Sundstrand Power Systems for permission to publish this paper and the efforts of his colleagues, in particular, A. C. Jones, R. Thompson, and V. Mason, involved in compression systems.

References

1 Rodgers, C., "Impeller Stalling as Influenced by Diffusion Limitations," ASME *Journal of Fluids Engineering*, Vol. 99, 1977, pp. 84–97.

2 Rodgers, C., "The Performance of Centrifugal Compressor Channel Diffusers," ASME Paper No. 82-GT-10, 1982.

3 Senoo, Y., et al., "Pressure at Shroud and Flow in a Supersonic Centrifugal Impeller," GTSJ Paper No. 42, 1977.

4 Senoo, Y., et al., "Experimental Study on Flow in a Supersonic Centrifugal Impeller," ASME Paper No. 78-GT-2, 1978.

5 Hayami, H., Senoo, Y., and Ueki, H., "Flow in the Inducer of a Centrifugal Compressor Measured With a Laser Velocimeter," ASME *Journal of Engineering for Gas Turbines and Power*, Vol. 107, 1985, pp. 534–540.

6 Yoshinaka, T., "Surge Responsibility and Range Characteristics of Centrifugal Compressors," presented at the Second International Gas Turbine Conference, Tokyo, Japan, 1977.

K. Kaneko

T. Setoguchi

Department of Mechanical Engineering,
Saga University,
Saga, Japan

M. Inoue

Department of Mechanical Engineering,
Power Division,
Kyushu University,
Fukuoka, Japan

Passive Control of Unstable Characteristics of a High Specific Speed Diagonal-Flow Fan by an Annular Wing

Passive Control of the unstable characteristics of a high specific speed diagonal-flow fan has been proposed. It is possible to eliminate the unstable characteristics of the pressure-flow rate curve in a low-flow region without deterioration of performance at design point. The control action is done naturally (passively) without any energy input. The inlet nozzle of an ordinary diagonal-flow fan was replaced by an annular wing with a Göttingen 625 airfoil section. The mechanism of the passive control and the optimum geometric parameter are discussed on the basis of performance tests and internal flow measurements.

Introduction

A diagonal-flow airfoil fan has the merits of both an axial fan and a radial fan, that is, relatively high efficiency, low noise level, and wide operating range. Recently, with the advent of reliable aerodynamic design methods on the basis of the quasi-three-dimensional flow analysis and various numerical techniques, a diagonal-flow fan becomes applicable for wider ranges of specific speed than ever. However, as the specific speed increases, the pressure-flow rate curve of a diagonal-flow fan tends to indicate an unstable characteristic, i.e., a positive gradient, in a low-flow region similar to an axial flow fan. It is desirable to eliminate or moderate the unstable characteristics especially in the case of a high-capacity fan.

Some of the authors formerly clarified the relationship between the unstable characteristics and blading parameters, such as aspect ratio, solidity (Kaneko et al., 1986), and design angle of attack (Kaneko et al., 1988). According to these investigations, it was possible to moderate the unstable characteristics in the low-flow region by suitable choice of blade element. However, the positive gradient could not be eliminated in the case of a high specific speed diagonal-flow fan.

In the case of an axial flow fan, some devices such as blade separator, air separator, and various kinds of casing treatments were proposed and tested in order to improve the unstable characteristics in a low flow region (Aziminan et al., 1987; Bard, 1987; Miyake et al., 1987; Tanaka and Tsukuda, 1977). Among these techniques, the air-separator equipment led to the noticeable effects of preventing rotating stall and stabilizing the unstable characteristics.

In the case of a centrifugal pump, a backflow recirculator (Sloteman et al., 1984) and a guide vane system (Breugelmans and Sen, 1982) were proposed to stabilize the pump operation at partial flow rates.

Recently, the authors tried to apply an air separator to the high specific speed diagonal-flow fan to investigate its effectiveness. Figure 1 (*a*) shows the performance characteristics of the fan with the air separator in comparison with the cases of normal casing and an axial fan with the same specific speed as the diagonal-flow fan. The pressure-flow characteristics of the axial fan indicates a steep positive gradient in a low-flow range, where operation becomes unstable. In the case of the diagonal-flow fan, the positive gradient becomes more moderate. On the other hand, it changes from positive to negative by equipping the air separator.

The main action of the air separator is to separate and remove the circulating reverse flow at the tip region that causes unstable characteristics at a low flow rate. The low-momentum air flow at the tip region is exhausted through the gap into the air-separator passage that leads to the inlet duct of the fan as shown in Fig. 1 (*b*).

Although the air separator operates very effectively at low flow rate, the pressure rise and efficiency decrease noticeably at a high flow region. This resulted from the fact that the air drawn into the rotor through the air-separator gap disturbs the main flow seriously when flow rate is high. In such a device improving the unstable characteristics in the low flow region, it is important that there be no negative effect at the design point.

In this paper, proposed is a passive control of the unstable characteristics of a high specific speed diagonal-flow fan by the use of an annular wing. The annular wing overcomes the weak point of the air separator described above and leads to no deterioration of fan performance at the design point. The effectiveness and mechanism of the passive control as well as the optimum geometry of the annular wing are discussed on the basis of the detailed internal flow measurements.
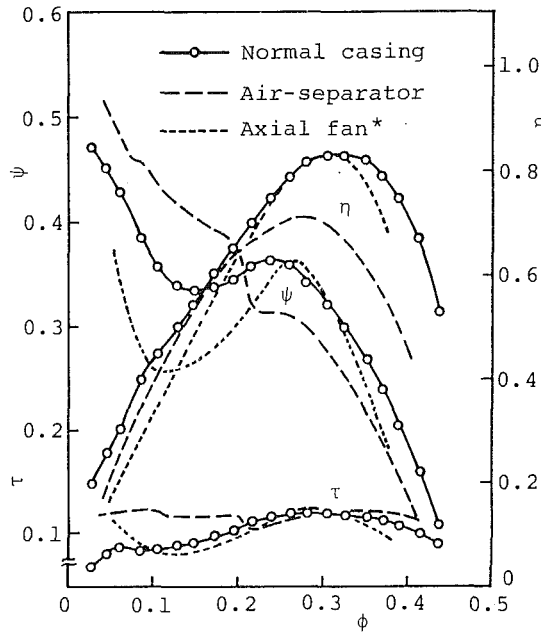
(a) Fan performance characteristics
(* Kaneko et al.,1985)
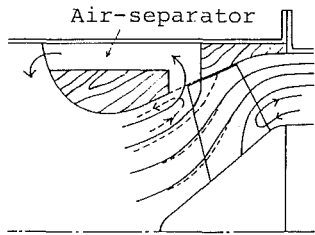
(b) Schematic flow pattern at low flow rate

Fig. 1 Improvement of unstable characteristics of diagonal-flow fan by air separator

Fig. 2 Diagonal-flow fan with annular wing
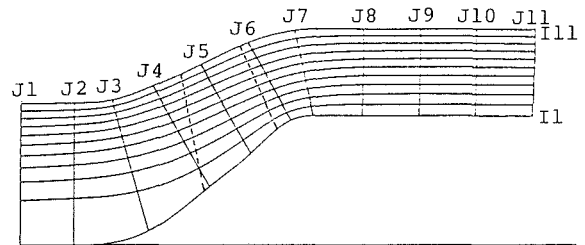
Fig. 3 Design meridional streamlines

Table 1 Specification of diagonal-flow fan

Total pressure coefficient	$\psi_D = 0.25$
Flow coefficient	$\phi_D = 0.345$
Specific speed	$n_s = 1620$ (rpm, m³/min, m)
Angle of casing	25 deg
Angle of hub	40 deg
Hub ratio (at stator)	0.6

Experimental Apparatus and Procedure

Outline of Blade Element Design.   The schematic view of the tested fans is shown in Fig. 2, and its specifications are listed in Table 1. The specific speed is 1620 (rpm, m³/min, m), which is a common value for an axial-flow fan. The reason for giving such a high specific speed is to compare the performance characteristics with those of an axial flow fan.

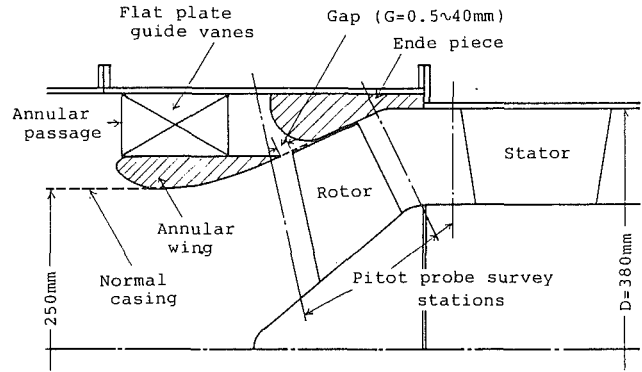The rotor was designed by the use of a quasi-three-dimen- sional design method with the cascade data. In particular, the method of streamline curvature is used to calculate the me- ridional streamlines for the specified conditions at the inlet and outlet of the rotor and outlet of the stator. The design meridional streamlines are shown in Fig. 3.

The stream surface, which is obtained by rotating the mer- idional streamline about axis, is transformed into a two-di- mensional plane. The blade elements are selected on this plane on the basis of two-dimensional cascade data (Ikui et al., 1974) of NACA 65-series compressor blade. Then, the blade camber is corrected theoretically, taking account of stream surface inclination and axial velocity change (Inoue et al., 1980). The

———— Nomenclature ————

C_L = camber of NACA 65-series air- foil (corrected value)

C_{L0} = camber of NACA 65-series air- foil (reference value)

D = inner diameter of duct at stator, m

G = gap between trailing edge of annular wing and leading edge of rotor, mm

n = rotational speed, rpm

n_s = specific speed

p_t = total pressure, Pa

Q = flow rate, m³/min

ΔQ = flow rate exhausted through annular passage, m³/min

r = radius, m

T = torque, N·m

u^* = reference circumferential veloc- ity of rotor defined by $u^* = \omega D/2$, m/s

V_m = meridional velocity, m/s

V_θ = swirl velocity, m/s

β = relative flow angle, deg

γ = stagger angle, deg

η = fan efficiency (total to total) defined by $\eta = \psi \cdot \phi / \tau$

θ = inclination of meridional streamline, deg

λ = hub ratio at stator

ρ = density of air, kg/m³

σ = solidity

τ = torque coefficient defined by $\tau = 4nT / \{15\rho D^2(1-\lambda^2)u^{*3}\}$

ϕ = flow coefficient defined by $\phi = Q / \{15\pi D^2(1-\lambda^2)u^*\}$

ψ = total pressure coefficient de- fined by $\psi = p_t / (0.5 \rho u^{*2})$

ω = angular velocity

Subscripts

1 = inlet

2 = outlet

h = hub

t = tip

Table 2 Specifications of rotor and stator

	Rotor	Stator
Blade section	NACA 65	Circular-arc
Number of blades	6	11
Mean solidity	0.80	1.30
Mean aspect ratio	0.84	0.67
Mean chord length	111 mm	113 mm
Vortex pattern	Free vortex	Free vortex

Table 3 Rotor blading parameters

I	β_1 deg	β_2 deg	γ deg	σ	C_{L0}	C_L	θ deg
1	47.3	15.2	27.7	1.10	1.76	0.23	40.0
3	55.8	38.1	44.3	0.91	1.28	0.46	29.0
5	60.4	49.0	52.5	0.83	0.94	0.35	24.6
7	63.4	55.5	57.1	0.78	0.74	0.21	23.6
9	66.4	60.3	61.0	0.74	0.59	0.10	23.9
11	68.5	63.8	64.0	0.71	0.49	0.02	25.0

iteration procedure was done to adjust solidity and aspect ratio to the specified values shown in Table 2. The selection of the stator blade element was carried out using the two-dimensional cascade data of circular-arc blade (Ikui et al., 1974). No correction was done for the stator blade, since it operates under axial flow conditions.

The selected rotor blading parameters are listed in Table 3, where β_1, β_2, γ, σ, and c_{L0} denote the reference values for the two-dimensional plane, and C_L is the corrected value. The outlines of the rotor and stator are shown in Fig. 4.

Design of Annular Wing. The inlet nozzle of a normal diagonal-flow fan was replaced by an annular wing with Göttingen 625 section as shown in Fig. 2. The geometry of the annular wing is simpler than the air separator shown in Fig. 1.

The chord length of the annular wing is 130 mm and the thickness ratio is 0.2. These values were selected so that the suction surface of the Göttingen profile almost fitted the inner surface of the inlet nozzle.

It is important to give an optimum gap between the trailing edge of the annular wing and the leading edge of the rotor tip. In this experiment, the effect of G on the performance was examined, varying G from 0.5 mm to 40 mm. In the cases of small gaps, the annular wing was shifted in the axial direction. In the cases of large gaps ($G > 20$), the trailing edge of the annular wing was cut off so as to get the specified gaps.

Besides the value of the gap, the dimension of the rotor tip opening and the shape of the end piece are important, because they control the flow in the tip region. One third of the meridional chord length of the rotor tip is open to the annular passage, as shown in Fig. 2. This is determined with reference to the case of the air-separator for an axial fan (Miyake et al., 1987). The inner surface of the casing end piece was finished to a round shape with radius of 35 mm.

Eight flat plate guide fins are installed axially in the annular passage between the annular wing and the outer casing to remove the swirl velocity component of the exhausted flow from the rotor.

Fan Performance Test and Internal Flow Measurement. Performance tests were conducted according to the test code JIS (Japanese Industrial Standard) B 8330. The stage performances including the rotor and the stator are obtained by correcting the overall performance taking the pressure loss of the duct and the friction torque of rotor shaft bearings into consideration.

The internal flow measurements were made using a five-hole pitot probe. The pitot probe was composed of five nickel tubes of 0.7 mm o.d. Yaw angle was determined by the zero method and pitch angle was determined by the fixed method. At three stations (21 mm ahead of the leading edge, 19 mm
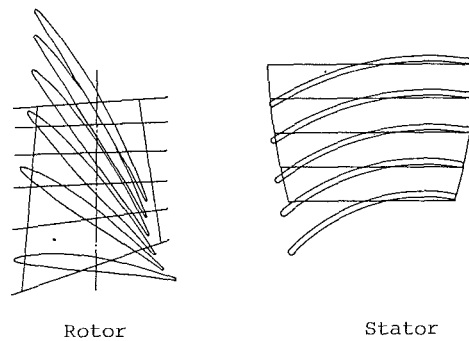
Fig. 4 Outline of rotor and stator
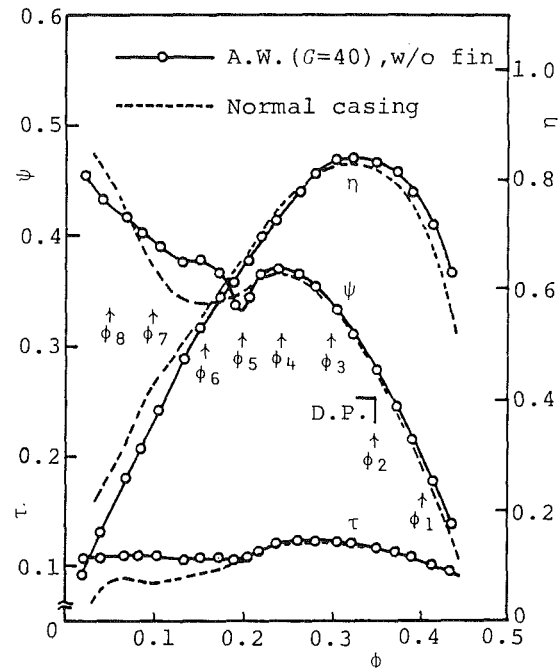
Fig. 5 Effect of annular wing on performance characteristics [annular wing ($G = 40$), w/o fin]

behind the trailing edge of the rotor, 17 mm ahead of the leading edge of the stator) indicated in Fig. 2, the pitot probe survey and data sampling were carried out automatically by the use of a microcomputer. Velocity vector, total pressure, and static pressure are calculated by means of the calibration curves of the probe.

A supplementary hot-wire measurement was carried out at the rotor inlet to examine the existence of rotating stall in the low flow range. The measuring position is the same as the pitot survey. A single hot-wire element was arranged normal to the axial direction. The output signal from a single hot wire was analyzed through FFT analyzer.

The test Reynolds number was 2.3×10^5 based on the relative inlet velocity and chord length of the rotor blade at mean radius.

Results and Discussion

Characteristics of the Fan With Annular Wing. The performance characteristics curves of the fan with annular wing of $G = 40$ are shown in Fig. 5 in comparison with those of the normal diagonal-flow fan. The mark of arrow with ϕ_2 corresponds to the design flow coefficient.

The dashed lines in the figure indicate the case of the normal casing. Stall occurs near a flow coefficient of ϕ_4, and then total pressure coefficient ψ drops with decreasing flow coef-
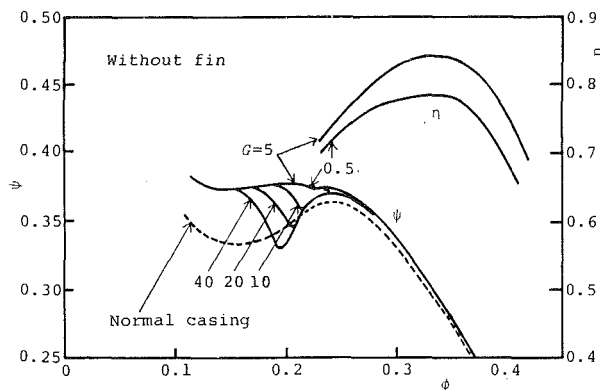
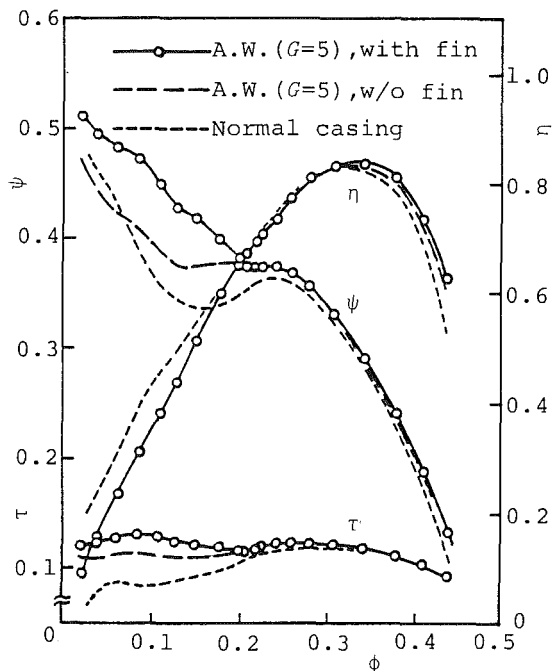Fig. 6 Effect of gap on fan performance characteristics

Fig. 7 Effect of annular wing and fin on performance characteristics [annular wing ($G = 5$)]

ficient. Again ψ rises from a flow coefficient of ϕ_6 to the shut-off condition. The stall point is defined here as the flow coefficient corresponding to the peak of the pressure curve, because this diagonal-flow fan indicates a gradual stall and an apparent behavior of stall such as an axial fan is not observed.

The maximum efficiency of 85 percent is attained at a slightly lower flow coefficient than the design point. The torque characteristics show a character of limit-load at high flow coefficient. The unstable characteristics are also noticeably improved in comparison with the axial fan with the same specific speed; see Fig. 1(a).

The solid lines in Fig. 5 indicate the characteristics for an annular wing with $G = 40$. Total pressure drops noticeably between the flow coefficients ϕ_4 and ϕ_5 due to strong stall, but it recovers at slightly lower flow coefficient. Therefore the pressure dip appears near ϕ_5. The torque coefficient becomes higher than the case of the normal casing in the lower flow region.

Although a certain decrease in efficiency is observed in the low-flow range due to a recirculating flow through the annular passage as will be shown later, this annular wing gives a higher efficiency at high flow range. This is due to a decrease in flow drag accompanying with the annular wing as well as an in-
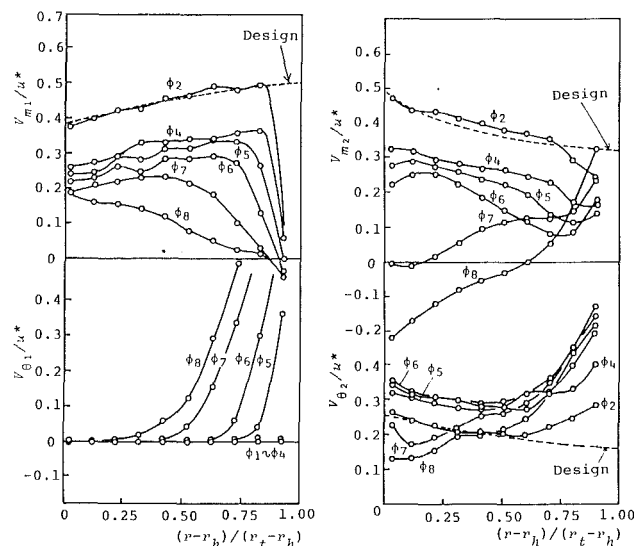

(a) Rotor inlet (b) Rotor outlet

Fig. 8 Velocity distribution (normal casing)

crease in inlet area of the flow passage. There is no such deterioration of efficiency at high-flow range as in the case of the air separator shown in Fig. 1.

The effect of the gap G on the pressure characteristics is shown in Fig. 6 for $G = 0.5$–40. The depth of the dip on the characteristic curve becomes shallower with decreasing G, and the position of the dip moves to the right. The dip becomes negligibly small in the case of $G = 5$, and there exists no dip on the pressure curve for $G = 0.5$. It is observed from this result that the value of the gap has no influence on the position of stall point. However, it has substantial effect on the position and the depth of the dip.

It is desirable to give a smaller gap from the viewpoint of elimination of the positive part on the pressure curve. But, in the case of the smallest gap of $G = 0.5$, the maximum efficiency drops by 5 percent as shown in the figure. The reason for this negative effect in the high-flow region appears that the inlet condition of the air from the annular passage to rotor tip is not proper because the air is forced to flow in through the tip section of the rotor.

Figure 7 shows the effects of the annular wing and the guide fins in the case of $G = 5$. The addition of guide fins causes increases in torque coefficient and total pressure coefficient in the low-flow region. Also in this case, the fan performance suffers no negative effect at a high-flow coefficient.

Thus the annular wing with a gap of $G = 5$ and with guide fins is very effective in improving the unstable characteristics in a low-flow region, and at the same time it operates well at the design point. It is concluded that the optimum value of the gap is $G = 5$ mm in the present diagonal-flow fan.

Internal Flow Distribution. In this section, the mechanism of the passive control by the annular wing is discussed on the basis of the internal flow measurements.

Figures 8(a) and 8(b) show the meridional and swirl velocity distributions at rotor inlet and outlet for the normal casing. The symbols ϕ_n shown in the figures correspond to the flow coefficients indicated in Fig. 5. The meridional and swirl velocity distributions at a flow coefficient of ϕ_2 almost coincide with the design values except at the tip region, where the effects of an inlet boundary layer, tip leakage, and secondary flow are pronounced. When the flow coefficient decreases, the inlet meridional velocity V_{m_1} in the tip side tends to decrease more quickly than in the hub side, and there exists a reverse flow at the tip section at a low flow coefficient. The same tendency
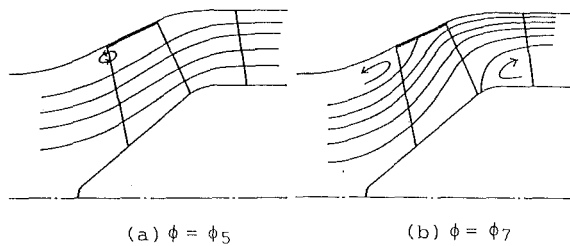
(a) $\phi = \phi_5$ (b) $\phi = \phi_7$

Fig. 9 Schematic meridional flow pattern (normal casing)

.(a) $\phi = \phi_5$ (b) $\phi = \phi_6$
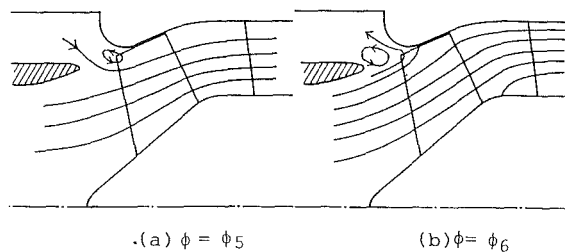
Fig. 11 Schematic meridional flow pattern ($G = 40$, w/o fin)
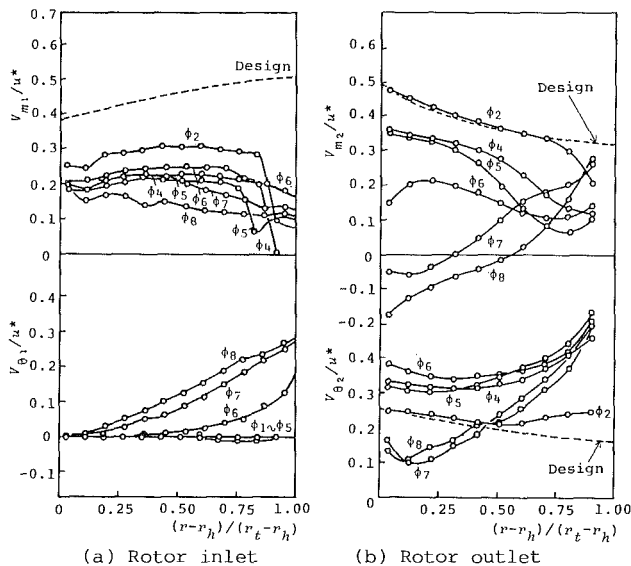

(a) Rotor inlet   (b) Rotor outlet

Fig. 10 Velocity distribution [annular wing ($G = 40$), w/o fin]

appears in the variation of V_{m_2} up to a flow coefficient of ϕ_6. However, distribution of V_{m_2} reverses suddenly between ϕ_6 and ϕ_7 due to a large stall region at the hub side.

A strong swirl velocity component V_{θ_1} is observed in the inlet flow at flow coefficients of ϕ_5 to ϕ_8. The radial extent of the swirling flow is considerably wider in comparison with that of the reverse flow. According to the hot-wire measurement at the rotor inlet, a rotating stall was detected at the rotor tip region in the low-flow coefficients $\phi \le \phi_4$. It appears that the wide swirl region is induced by the rotating stall as well as the recirculating reverse flow at rotor tip.

From these results, it is found that when flow coefficient is reduced, stall occurs at inlet tip region first and pressure characteristic curve drops from ϕ_4 as shown in Fig. 5. Then the pressure rises from ϕ_6 to ϕ_8 because of the change in meridional flow pattern.

Figures 9(a) and 9(b) show schematic meridional flow patterns for ϕ_5 and ϕ_7, which are estimated from the meridional velocity distributions at three pitot probe survey stations shown in Fig. 2. When flow coefficient is reduced to ϕ_5, outlet meridional streamlines shift downward due to the appearance of the reverse flow at rotor tip. This flow condition corresponds to the stall or unstable region on the pressure characteristics in Fig. 5.

Two large reverse flow regions appear at a flow coefficient of ϕ_7, and main streamlines bend radially in the rotor as shown in Fig. 9(b). Accordingly the pressure-flow rate curve has a negative gradient there, i.e., a stable characteristic. This relation between the characteristic curve and the meridional flow patterns is similar to that of an axial fan.

The meridional and swirl velocity distributions of the fan with the annular wing ($G = 40$) are shown in Figs. 10(a) and 10(b). In this case, inlet meridional velocity V_{m_1} is considerably

lower at the high-flow rate in contrast to the case of the normal casing. This drastic decrease in V_{m_1} is caused by the fact that a part of inlet flow comes from the annular passage. As a result, the main flow apparently decreases.

It is noted that V_{m_1} for flow coefficients of ϕ_4 and ϕ_5 are very low at the tip region. This is probably due to the blockage effect of the low-energy fluid accumulated there. These flow coefficients correspond to the stall region in Fig. 5. At a slightly lower flow coefficient of ϕ_6, the meridional velocity distribution at the tip region recovers. The recovery of inlet velocity is caused by an inception of exhaust of the low-energy air at that portion through the annular passage, as will be shown later.

Although the inlet swirl velocity decreases considerably in comparison with the normal casing, it still remains as shown in Fig. 10(a), since the swirling flow of the exhausted air comes by way of the annular passage around the leading edge of the annular wing at low flow coefficients. In this case of $G = 40$, a rotating stall was first detected at ϕ_7.

Outlet meridional and swirl velocity distributions at the design flow coefficient almost coincide with the design values, as shown in Fig. 10(b). When flow coefficient is reduced to ϕ_5, V_{m_2} indicates a peculiar distribution. V_{m_2} decreases noticeably at the tip region; however, it remains high at the hub side. This meridional velocity distribution is pronounced from the stall at the tip region. The high value of V_{m_2} at the hub region causes a decrease in V_{θ_2} there. This effect and a stall at tip section are the main reasons for the dip on the pressure characteristic curve shown in Fig. 5. On the other hand distribution of V_{m_2} becomes flatter when the flow coefficient decreases to ϕ_6, where the exhaust of air has already begun through the annular passage.

The schematic meridional flow patterns estimated from the internal flow measurement are illustrated in Figs. 11(a) and (b). It is easy to understand that the drastic changes in V_{m_1}, V_{m_2} and the fan performance between ϕ_5 and ϕ_6 are caused by the inception of the exhaust of low energy air through the annular passage.

The internal flow distributions for annular wing with a gap of $G = 5$ are shown in Figs. 12(a) and 12(b). The guide fins are installed in the annular passage to remove the swirl component in this case.

In a high-flow range, the value of V_{m_1} is generally higher in comparison with Fig. 10(a). This means that a smaller quantity of air flows in through the annular passage than in the case of $G = 40$ due to narrower gap. Velocity distributions are almost flat, and V_{m_1} at the tip region does not drop in all the flow coefficients in contrast to the cases of the normal casing and $G = 40$. In this case, an inception of exhaust comes earlier than in the case of $G = 40$. The inception is observed to occur between ϕ_4 and ϕ_5 as shown in the next section. It appears that a better flow condition is expected at low flow coefficients. The inlet swirl velocity component is almost eliminated by the guide fins. There is an appreciable negative swirl velocity component at the tip region when the flow rate is extremely reduced.

As to the rotor outlet, the distribution of V_{m_2} at a flow coefficient of ϕ_5 is improved as shown in Fig. 12(b). As a
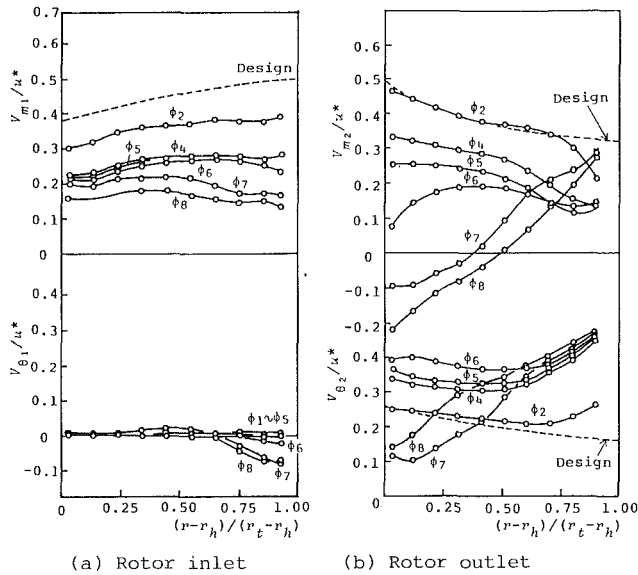
Fig. 12 Velocity distribution [annular wing (G = 5), with fin]

(a) $\phi = \phi_5$ (b) $\phi = \phi_7$

Fig. 13 Schematic meridional flow pattern (G = 5, with fin)

Fig. 14 Effect of gap on flow rate in annular passage

result, V_{θ_2} rises higher at the hub side in comparison with Fig. 10(b).

Figures 13(a) and 13(b) show the schematic meridional flow patterns for G = 5 at flow coefficients of ϕ_5 and ϕ_7, respectively. It is clear from Fig. 13(a) that the flow pattern is significantly improved in comparison with Fig. 11(a) especially at the tip region, since the low-energy fluid is exhausted into the annular passage.

At a flow coefficient of ϕ_7, the circulating reverse flow at tip region indicated in Fig. 9(b) is completely displaced into the annular passage as shown in Fig. 13(b). On the other hand, a reverse flow region at rotor outlet extends radially and the inclination of streamlines become steeper.

Thus the annular wing with G = 5 is very effective to improve the flow condition at the unstable operation region or the positive gradient region. The desirable effects mentioned above contribute to rises in torque coefficient and total pressure coefficient in that region, as shown in Fig. 7. As a result, it leads to a stable operation of the diagonal-flow fan in the otherwise unstable region.

Flow Rate of Exhausted Air Through the Annular Passage. The ratio of the flow rate of exhausted air through the annular passage ΔQ to discharge Q of the fan is shown in Fig. 14 in the cases of G = 40 and 5. ΔQ is calculated from $\Delta Q = Q_1 - Q$, where Q_1 is obtained by integrating V_{m_1} at the main inlet passage. A part of the air is induced from the annular passage when flow coefficient is high. On the other hand, a part of the air is exhausted through the annular passage when the flow coefficient is low.

According to Fig. 14, a nearly constant rate of air is induced in the high flow range, namely, $\Delta Q/Q$ = 0.35 for G = 40 and 0.1 for G = 5. Inception of exhaust occurs when flow coefficient is reduced to about 0.2, and the rate of exhausted air becomes extremely high in the low-flow range. The flow coefficient corresponding to the inception of exhaust has a significant effect on the performance of the fan as discussed above. It becomes higher with decreasing G, which results in the fact that the dip on the pressure curve moves to the right as shown in Fig. 6.

Conclusions

In order to improve the unstable characteristics of a high specific speed diagonal-flow fan, a passive control is proposed by the use of an annular wing. It operates well in a low-flow
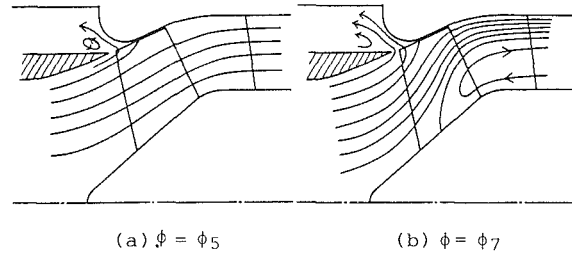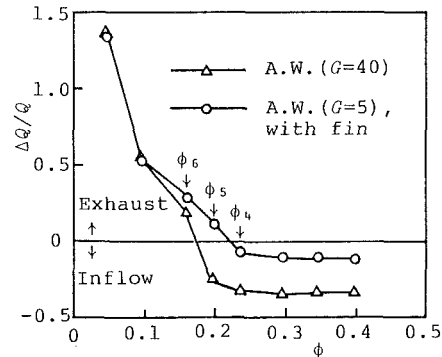
region as well as at the design point. The main conclusions are as follows:

1 It is possible to improve an unstable characteristic of a high specific speed diagonal-flow fan by introducing an annular wing at the inlet of the rotor. It leads to no performance deterioration at the design point.

2 In the case of a wide gap between the trailing edge of the annular wing and the leading edge of the rotor tip, a concave-shaped dip appears on the pressure-flow rate characteristic curve. However, the dip disappears with decreasing gap. An extremely small gap leads to the deterioration of fan performance.

3 The optimum gap is G = 5 mm in the present diagonal-flow fan.

4 The flat plate guide fins installed in the annular passage remove the inlet swirl, and give pressure rise in a low flow region.

Uncertainty

The uncertainties relative to each maximum value are as follows: ψ: ± 0.8 percent, ϕ: ± 0.6 percent, τ: ± 0.5 percent, V_m/u^*, and V_θ/u^*: ± 3 percent, $\Delta Q/Q$: ± 3 percent.

References

Aziminan, A. R., McKenzie, A. B., and Elder, R. L., 1987, "A Tip Treatment for Axial Flow Fans and Compressors," *Industrial Fans—Aerodynamic Design*, Mechanical Engineering Publications Limited for The Institution of Mechanical Engineers, London, pp. 35–41.

Bard, H., 1987, "The Stabilisation of Axial Fan Performance," *Industrial Fans—Aerodynamic Design*, Mechanical Engineering Publications Limited for The Institution of Mechanical Engineers, London, pp. 101–106.

Breugelmans, F A. E., and Sen, M., 1982, "Prerotation and Fluid Recirculation in the Suction Pipe of Centrifugal Pumps," *Proceedings of the Eleventh Turbomachinery Symposium*, Texas A&M University, pp. 165-180.

Ikui, T., Inoue, M., and Kaneko, K., 1974, "Design Method of Circular-Arc Cascade," *Journal of Turbomachinery Society of Japan* [in Japanese], Vol. 2, No. 2, pp. 17-22.

Ikui, T., Inoue, M., Kamada, Y., and Tashiro, M., 1974, "Improvement and Extension of Carpet Diagram for NACA65 Series Compressor Cascade," *Journal of Turbomachinery Society of Japan* [in Japanese], Vol. 2, No. 5, pp. 444-457.

Inoue, M., Ikui, T., Inoue, M., Kamada, Y., and Tashiro, M., 1980, "Quasi Three-Dimensional Design of Diagonal Flow Impellers by Use of Cascade Data," *Proceedings of the 10th Symposium of IAHR*, pp. 403-414.

Kaneko, K., Setoguchi, T., Nakano, T., and Inoue, M., 1985, "Effect of Blade Surface Roughness on Performance of Axial Flow Fans With Different Blade Camber," *Bulletin of JSME*, Vol. 28, No. 241, pp. 1411-1446.

Kaneko, K., Setoguchi, T., Hayashi, S., and Inoue, M., 1986, "Studies on a Diagonal-Flow Airfoil Fan With Low Loading," *Bulletin of JSME*, Vol. 29, No. 255, pp. 2932-2937.

Kaneko, K., Setoguchi, T., Tanaka, T., and Inoue, M., 1988, "Improvement of Aerodynamic Performance of a Diagonal-Flow Fan in Low Flow Range," *Transactions of the Japan Society of Mechanical Engineers* [in Japanese], Vol. 54, No. 505, pp. 2458-2464.

Miyake, Y., Inaba, T., and Kato, T., 1987, "Improvement of Unstable Characteristics of an Axial Flow Fan by Air-Separator Equipment," ASME *Journal of Fluids Engineering*, Vol. 109, pp. 36-41.

Sloteman, D. P., Cooper, P., and Dussourd, J. L., 1984, "Control of Backflow at the Inlets of Centrifugal Pumps and Inducers," *Proceedings of the First International Pump Symposium*, Texas A&M University, pp. 9-22.

Tanaka, T., and Tsukuda, Y., 1977, "Stall Margin Improvement by Casing Treatment—Its Mechanism and Effectiveness," ASME *Journal of Engineering for Power*, Vol. 99, pp. 121-133.

Dynamic Control of Centrifugal Compressor Surge Using Tailored Structures

D. L. Gysling

J. Dugundji

E. M. Greitzer

A. H. Epstein

Gas Turbine Laboratory,
Department of Aeronautics and Astronautics,
Massachusetts Institute of Technology,
Cambridge, MA 02139

A new method for dynamic control of centrifugal compressor surge is presented. The approach taken is to suppress surge by modifying the compression system dynamic behavior using structural feedback. More specifically, one wall of a downstream volume, or plenum, is constructed so as to move in response to small perturbations in pressure. This structural motion provides a means for absorbing the unsteady energy perturbations produced by the compressor, thus extending the stable operating range of the compression system. In the paper, a lumped parameter analysis is carried out to define the coupled aerodynamic and structural system behavior and the potential for stabilization. First-of-a-kind experiments are then conducted to examine the conclusions of the analysis. As predicted by the model and demonstrated by experiment, a movable plenum wall lowered the mass flow at which surge occurred in a centrifugal compression system by roughly 25 percent for a range of operating conditions. In addition, because the tailored dynamics of the structure acts to suppress instabilities in their initial stages, this control was achievable with relatively little power being dissipated by the movable wall system, and with no noticeable decrease in steady-state performance. Although designed on the basis of linear system considerations, the structural control is shown to be capable of suppressing existing large-amplitude limit cycle surge oscillations.

Introduction

The operating range of turbomachinery compression systems is very often limited by the onset of fluid dynamic instabilities. Surge is a self-excited, essentially one-dimensional instability, which is characterized by oscillations in area-averaged mass flow and pressure rise, and is generally the most important instability in centrifugal compression systems. Surge can cause reduced performance and efficiency of the turbomachine, and, in some cases, failure due to the large unsteady aerodynamic forces on the blades (Stenning, 1980).

To avoid surge, the compression system is generally operated away from the "surge line," the boundary between stable and unstable operation on the pressure rise versus mass flow performance map. Operating the compressor at some distance from this line, on the negatively sloped part of the compressor speedlines, can ensure stable operation. Doing this, however, may result in a performance penalty since peak performance and efficiency often occur near the surge line (Dean and Young, 1977).

The goal of the research described here is to develop methods to extend the stable operating range by modifying the dynamic behavior of the compression system to suppress surge. This would allow compressor operation in previously unusable, or even previously unstable, regions of the compressor map. The experimental phase of the current research is focused on centrifugal compression systems, although the analysis applies to axial compression systems as well.

Dynamic Surge Suppression

Surge is the manifestation of a dynamic instability, which occurs when the compressor feeds more mechanical energy into disturbances than the rest of the system can dissipate. The result is an oscillatory disturbance that grows exponentially, until limited by nonlinearity, into a limit cycle (surge cycle). The key to dynamic surge suppression, therefore, lies in increasing the system's ability to dissipate or damp this disturbance energy (Epstein et al., 1989).

There have been several investigations of surge suppression, all in recent years, using closed-loop active control to increase system damping. Ffowcs Williams and Huang (1989) used a movable plenum wall, driven by a signal proportional to the unsteady plenum pressure, to suppress surge in a centrifugal turbocharger. Pinsley et al. (1991) describe active stabilization using a variable area throttle valve, also driven by a signal proportional to the unsteady plenum pressure. Both of these studies demonstrated that surge can be suppressed in the linear regime, before the disturbances grow to large amplitude, by modification of system dynamics through closed-loop control.

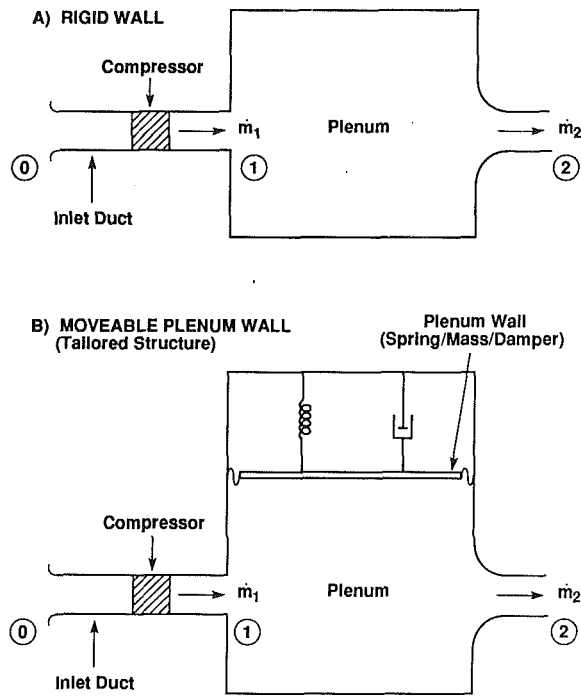There has been little previous work on stabilization using

Fig. 1 Schematic of rigid (fixed) wall (a) and movable plenum wall (b) compression systems

structural feedback. In this approach, the dynamic properties of the system are modified so that the compression system becomes inherently stable, without external input. A limited analytical investigation of such a control scheme has been carried out by Chen (1987). He found that a variable area throttle valve, modeled as a mass-spring-damper driven by plenum pressure perturbations, would have a stabilizing effect, but that a flexible plenum wall with no damping would be destabilizing.

Scope of the Present Work

The work reported here is directed at surge suppression in centrifugal compression systems using tailored structural dy-

namics as a feedback mechanism. A movable plenum wall is used as the tailored structure. The movable wall acts as a mass-spring-damper system driven by unsteady pressure perturbations in the plenum, and its motion is thus coupled to the compression system dynamics. A schematic of a generic rigid compression system and a modified compression system having a tailored structure is shown in Figs. 1(a) and 1(b).

It will be demonstrated that an appropriately tailored moving plenum wall can significantly extend the stable operating range of a compression system. The aeroelastic coupling between the wall and the basic compression system allows the damper on the moving wall to dissipate mechanical energy associated with flow disturbances, thereby suppressing surge. The degree of suppression depends on matching the structural dynamics to the system fluid dynamics. A set of nondimensional parameters, which govern the interaction between the compression system and the wall, are thus presented and their influence is developed. Experiments are carried out to evaluate the actual performance of the flexible plenum wall system and the analytical model.

System Modeling

The basic lumped parameter model of the compression system has been used by other authors to investigate surge for a rigid plenum configuration (e.g., Emmons et al., 1955; Greitzer, 1981). In this description, system inertia is represented by the fluid in the inlet ducting, system compliance is due to the compressibility of the fluid in the plenum, and system damping (positive or negative) is due to the compressor and the throttle.

The differential equations describing the compression system with flexible plenum wall are given below.

Inlet duct momentum

$$(P_0 + \Delta P_c - P_p)A_{in} = \frac{d(\rho_0 A_{in} L_c C_x)}{dt} \tag{1}$$

The quantity ΔP_c is the compressor pressure rise, which is a known function of mass flow, $\dot{m}$.

Mass conservation in the plenum

$$\dot{m}_1 - \dot{m}_2 = \frac{d(\rho_p V_p)}{dt} \tag{2}$$

Nomenclature

a	=	speed of sound
A_{in}	=	compressor inlet area
A_p	=	plenum movable wall area
B	=	stability parameter $= (U/2a)\sqrt{(V_{\text{plenum}}/A_{in}L_c)}$ $= (U/2\omega_H L_c)$
C_x	=	axial velocity
f	=	Coulomb friction force
F	=	nondimensional Coulomb friction force $= f/(\rho_0 U^2 A_p)$
I	=	rotational inertia of turbospool
L	=	effective length
m	=	mass of plenum wall
$\dot{m}$	=	mass flow
P	=	pressure
ΔP	=	pressure difference
ΔP_c	=	compressor pressure rise
ΔP_t	=	throttle pressure drop
q	=	wall displacement
Q	=	wall frequency parameter

U	=	impeller exit tip speed
v	=	nondimensional wall velocity
V	=	volume
W	=	nondimensional wall aeroelastic coupling parameter
ζ	=	nondimensional wall damping ratio parameter
η	=	nondimensional wall displacement
ρ	=	density
τ	=	nondimensional time $= \omega_H t$
ϕ	=	mass flow coefficient $= \dot{m}/(\rho_0 U A_{in})$
ψ	=	plenum pressure coefficient $= (P_p - P_0)/0.5\rho_0 U^2$
ψ_c	=	compressor pressure rise coefficient $= \Delta P_c/0.5\rho_0 U^2$
ψ_t	=	throttle pressure drop coefficient $= \Delta P_t/0.5\rho_0 U^2$

ω_H	=	Helmholtz frequency $= a\sqrt{A_{in}/V_p L_c}$
ω_p	=	frequency of wall mass-spring-damper system
$d\psi_c/d\phi$	=	slope of compressor characteristic

Subscripts

c	=	compressor
in	=	compressor inlet
p	=	plenum
t	=	throttle; tip of impeller exit
0	=	ambient conditions
1	=	compressor exit
2	=	plenum exit

Operators

$\delta(\ )$	=	perturbation quantity in analysis
$\overline{(\ )}$	=	time averaged
$(\ )'$	=	fluctuation in experimentally measured quantity

Throttle pressure drop characteristic

$$P_p - \Delta P_t = P_0 \qquad (3)$$

The throttle pressure drop ΔP_t is also a known function of mass flow.

Wall dynamics

$$m\ddot{q} + c\dot{q} + kq = (P_p - P_{\text{auxiliary plenum}})A_p \qquad (4)$$

Linearizing and nondimensionalizing the equations of motion as shown in the appendix yields the following nondimensional equations describing the linear stability of the system:

Inlet duct momentum

$$\frac{d\delta\dot{\phi}_1}{d\tau} = B\left[\left(\frac{d\psi_c}{d\phi}\right)\delta\phi_1 - \delta\psi\right] \qquad (5)$$

Mass conservation in the plenum

$$\frac{d\delta\dot{\psi}}{d\tau} = \frac{1}{B}[\delta\phi_1 - \delta\phi_2] - \frac{\bar{\rho}_p}{\rho_0}\frac{2}{M_t^2}\delta v \qquad (6)$$

Throttle pressure drop characteristic

$$\delta\psi = \frac{\rho_0}{2\bar{\rho}_t}\frac{\bar{\phi}^2}{\bar{\psi}}\delta\phi_2 \qquad (7)$$

Wall dynamics

$$\frac{d\delta v}{d\tau} = (2WB^2)\delta\psi - \left(2\sqrt{\frac{P_0\bar{\rho}_p}{\bar{P}_p\rho_0}}\,\zeta Q\right)\delta v - \left(\frac{\bar{\rho}_p}{\rho_0}Q^2\right)\delta\eta \qquad (8)$$

$$\frac{d\delta\eta}{d\tau} = \delta v \qquad (9)$$

In Eqs. (5)–(9), nondimensional pressure rise and mass flow coefficients, ψ and ϕ, are defined as

$$\psi = \frac{\Delta P}{\frac{1}{2}\rho_0 U^2}, \quad \phi = \frac{\dot{m}}{\rho_0 A_{in}U}$$

The nondimensional wall displacement, η, is given as

$$\eta = \frac{A_p q}{V_p}$$

In Eqs. (6)–(9), perturbation variables are denoted by $\delta(\ )$, and steady-state variables are represented by $(\bar{\ })$. Nondimensional time is defined in terms of the Helmholtz frequency, $\tau = \omega_H t$, where the Helmholtz frequency is defined as:

$$\omega_H = \bar{a}_p\sqrt{\frac{A_{in}}{V_p L_c}}$$

Other definitions can be found in the appendix.

The parameter $d\psi_c/d\phi$ is the slope of the nondimensional compressor pressure rise characteristic and is linked directly to the onset of the surge instability. In the regions of the compressor map where this slope is negative, both the throttle and compressor act to damp out flow disturbances. In the positively sloped regions, the compressor adds energy to disturbances while the throttle continues to dissipate unsteady energy. For a rigid wall system, therefore, the flow through the system becomes unstable when the compressor feeds more energy into disturbances than the throttle can extract.

Nondimensional Parameters. The behavior of the system described by Eqs. (5)–(9) has a complex parametric dependence involving the following nondimensional parameters.

The *B-parameter* has a major influence on the surge dynamics of the compression system (Greitzer, 1981). It is defined as:

$$B = \frac{U}{2\omega_H L_c} = \frac{U}{2\bar{a}_p}\sqrt{\frac{V_p}{A_{in}L_c}}$$

For the fixed wall compression system at a given operating point, the magnitude of the (positive) compressor characteristic slope required for disturbances to grow is set by the B-parameter, which can be viewed as providing a measure of the coupling between mass flow oscillations through the compressor and through the throttle. The larger the B-parameter, the more isolated the throttle is (from the compressor), and the less able to remove energy from flow disturbances. As the B-parameter increases, therefore, surge occurs at a smaller positive compressor slope.

The *tip Mach number* (based on plenum conditions) is defined as:

$$M = \frac{U}{a_p}$$

The tip Mach number enters the system equations as a measure of the effect of wall motion on the mass balance in the plenum. It thus does not appear explicitly for a fixed wall configuration. The tip Mach number affects the coupling of wall motion to compression system dynamics by determining the degree to which plenum pressure responds to wall motion. The pressure and mass flow fluctuations are functions of tip Mach number (they scale as M^2 at low speed), but the wall motion is not. The Mach number is thus a measure of this aerodynamic-structural coupling, rather than a representation of the importance of compressibility in the system dynamic model. The larger the Mach number, the smaller the effect a given non-
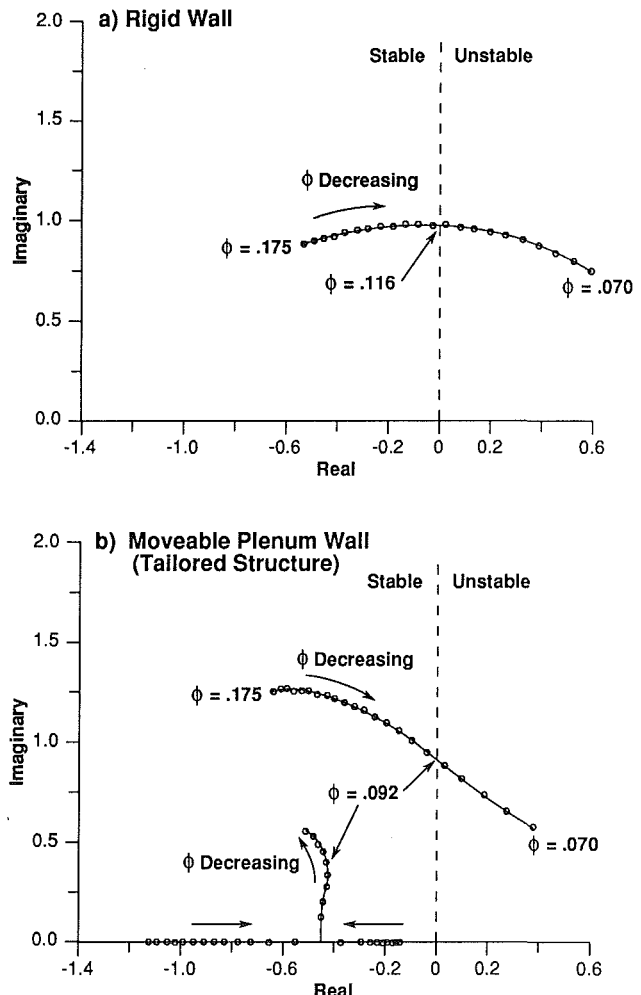

Fig. 2 Root locus plots for rigid wall (*a*) and movable plenum wall (*b*) compression systems: $B = 0.5$, $M = 0.4$, $W = 0.11$, $\zeta = 1.5$, $Q = 0.51$ for movable wall system

dimensional wall motion has on nondimensional mass flow and pressure perturbations in the system.

The parameters W, ζ, and Q determine the wall dynamic characteristics relative to the unsteady behavior of the basic (rigid wall) compression system. W *is an aeroelastic coupling parameter* defined as

$$W = \frac{\rho_0 A_p^2 L_c^2}{m \overline{V}_p}$$

This parameter determines the degree to which the wall responds to the pressure fluctuations in the plenum. Increasing the W-parameter implies a greater wall response to perturbations in plenum pressure.

ζ *is the critical damping ratio* of the plenum wall mass-spring-damper system, corrected to remain independent of compressor operating conditions. Correction is necessary since the aerodynamic spring constant, and hence, the wall natural frequency, varied with plenum pressure. ζ is defined as

$$\zeta = \frac{c}{2m\omega_p} \sqrt{\frac{\overline{P}_p}{P_0}}$$

Q *defines the ratio of natural frequencies* for the wall mass-spring-damper system and for the fixed wall compression system (the Helmholtz frequency), also corrected so that it is independent of compressor operating point.

$$Q = \frac{\omega_p}{\omega_H} \sqrt{\frac{\rho_0}{\overline{\rho}_p}}$$

Linear Stability Analysis

Linear analysis of the system stability for a given set of operating conditions leads to the set of equations shown below:

$$
\begin{bmatrix}
B\left(\dfrac{d\overline{\psi}_c}{d\overline{\phi}}\right) - s & -2B\dfrac{\overline{\psi}}{\overline{\phi}} & 0 & 0 \\[2ex]
\dfrac{\overline{\phi}}{2B\overline{\psi}} & -\dfrac{1\overline{\phi}}{2B\overline{\psi}} - s & 0 & -\dfrac{\overline{\rho}_p}{\rho_0}\dfrac{1}{M^2}\dfrac{\overline{\phi}}{\overline{\psi}} \\[2ex]
0 & 0 & -s & 1 \\[2ex]
0 & 2WB^2\dfrac{\overline{\psi}}{\overline{\phi}} & -\dfrac{\overline{\rho}_p}{\rho_0}Q^2 & -2\zeta Q\sqrt{\dfrac{P_0\overline{\rho}_p}{\overline{P}_p\rho_0}} - s
\end{bmatrix}
$$

$$
\times
\begin{bmatrix}
\delta\phi_1 \\
\delta\phi_2 \\
\delta\eta \\
\delta v
\end{bmatrix}
=
\begin{bmatrix}
0 \\
0 \\
0 \\
0
\end{bmatrix}
\qquad (10)
$$

Equation (10) constitutes an eigenvalue problem for the (complex) growth rate, s, involving two coupled dynamic systems: the compression system, with variables $\delta\phi_1$ and $\delta\phi_2$, and the moving wall, with variable $\delta\eta$ and δv. The terms associated with the uncoupled fixed wall compression system and the moving plenum wall dynamics are located on the tridiagonal of the stability matrix. The two nonzero terms located off the tridiagonal are the aeroelastic coupling terms.

Solving the eigenvalue problem as a function of B, M, ϕ, W, ζ, and Q and using the experimentally determined compressor characteristics of Pinsley (1988) enables prediction of the instability onset condition for various system and control parameters. The fixed wall behavior is obtained in the limit of either $W = 0$ or $Q = \infty$. Either has the effect of making the wall appear massive and the spring constant stiff, or essentially rigid.

To illustrate the trends obtained from the stability computations, a root locus plot for a fixed wall system with $B =$

0.5 is shown in Fig. 2(a). The compressor pressure rise characteristic used is based on a third-degree polynomial curve fit of Pinsley's (1988) measured 70K speedline as shown in Fig. 3, the measurements being conducted using a close coupled throttle to avoid surge. The abscissa and ordinate of the root locus plots are nondimensionalized by the system Helmholtz resonator frequency. The roots are plotted as a function of nondimensional flow coefficient for flow coefficients ranging from 0.175 to 0.070 in increments of 0.005. As the mass flow decreases and the compressor slope increases, the poles are driven from the left half-plane (stable) to the right half-plane (unstable), with the imaginary axis defining the neutral stability point. The behavior is that of a (positively or negatively) damped second-order system. The neutral stability point for this fixed wall system (at $\phi = 0.116$), as indicated on the compressor characteristic in Fig. 3, occurs near the peak of the characteristic, which is located at $\phi = 0.120$.

The introduction of a movable plenum wall introduces a second mode of oscillation to the compression system. A root locus plot for the two modes is shown in Fig. 2(b), again using the compressor characteristic shown in Fig. 3. One characteristic frequency is somewhat close to the Helmholtz frequency, but there is now another frequency that is associated primarily with the wall motion. More importantly, however, the neutral stability point occurs well past the peak of the characteristic in the positively sloped region at $\phi = 0.92$; this is also indicated in Fig. 3. Away from instability (high mass flow), the moving wall system has one (damped) oscillatory mode and one nonoscillatory (overdamped) mode. Near instability, the two modes exhibit increased fluid-structure coupling and both become oscillatory.

To optimize the moving wall compression system performance, a parametric study was performed. Since the B-parameter and Mach number are not independent quantities (both scale with wheel speed), the relation between these two parameters in this study is based on selecting values for the dimensions of the compression system that were typical of modern compression machines as well as convenient from an experimental view point. The parameter search showed that movable wall performance is optimized, over the range of B-parameters and Mach numbers used, with the following control parameters: $W = 0.11$, $\zeta = 1.5$, and $Q = 0.51$. (These parameters were used in Fig. 2b.)

The steady state mass flow coefficient by itself (i.e., explicitly rather than through the effect on compressor characteristic slope) is not a very useful indication of stability for the optimized moving wall system. Determining the maximum com-
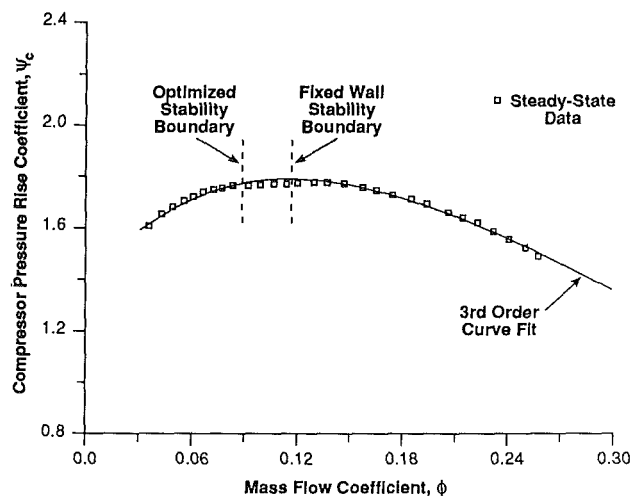

Fig. 3 Compressor pressure rise characteristic used in analysis; data of Pinsley (1988)
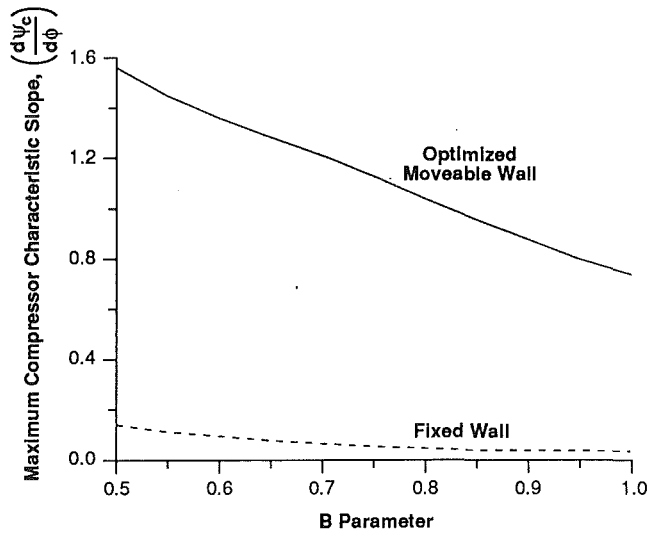
Fig. 4 Maximum achievable compressor characteristic slope for stable compressor operation versus B-parameter
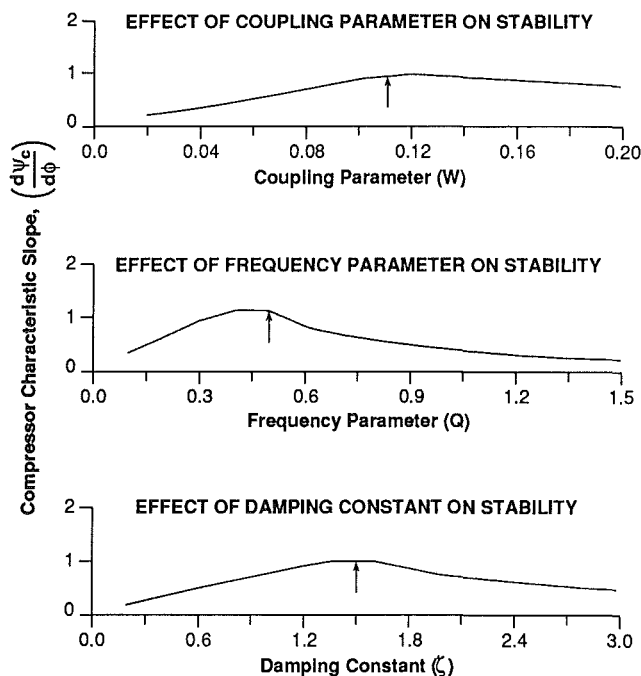

Fig. 5 Effect of tailored structure control parameters on maximum achievable compressor characteristic slope for stable operation. ↑ indicates optimum value from parameter search.
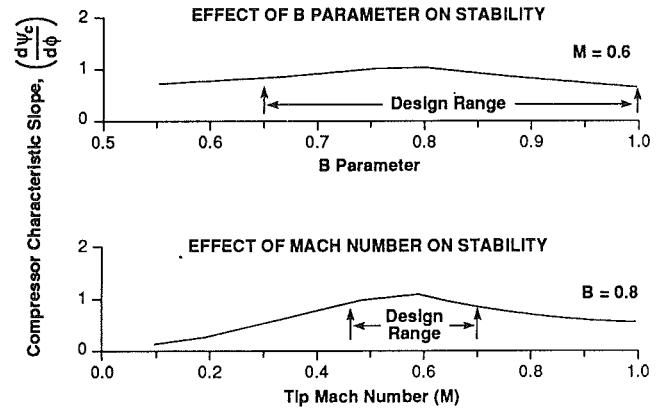

Fig. 6 Independent effects of B-parameter and tip Mach number on maximum achievable compressor characteristic slope for stable operation

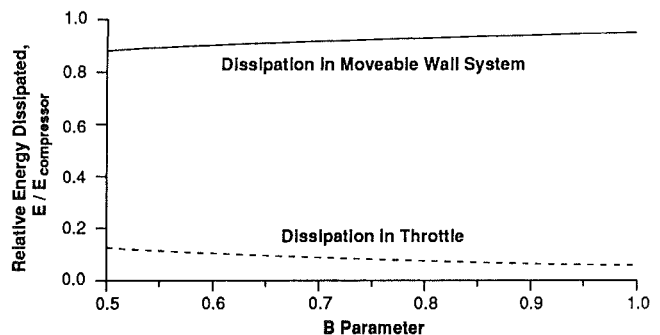Fig. 7 Comparison of perturbation energy dissipation in throttle and in movable wall system; relative units

pressor characteristic slope at which the system was stable versus the B-parameter was found to be a much more useful discriminant for the effectiveness of the control strategy. The maximum stable slope versus B-parameter for the fixed wall system and for the (optimized) moving wall system is shown in Fig. 4; as indicated, the movable wall system is capable of stable operation at a positive compressor slope that can be an order of magnitude larger than that for the fixed wall system.

We can also plot maximum stable slope versus each of the control parameters about the optimized values to see how rapidly one departs from optimum conditions. Figure 5 shows the variations in maximum stable slope versus W, ζ, and Q, respectively. The optimized values are indicated by arrows. Although substantial changes in the structural control parameters away from the optimized configuration will degrade performance, the stabilization is insensitive to small (± 25 percent, say) variations. This implies that the system need not be "re-

tuned" for each compressor operating condition. The independent effects of B-parameter and tip Mach number, for a system with a fixed set of control parameters, are shown in Fig. 6 where one parameter is held constant and the other varied. As discussed, although the tip Mach number does not directly affect the stability of a system with a fixed wall, it is an important parameter for the stability of the moving wall system.

Energy Analysis

To examine the physical mechanism associated with stabilization, it is useful to look at the perturbation energy. From this viewpoint, the system is unstable when more energy is fed into any mode of oscillation over a cycle than is removed; neutral stability corresponds to zero net energy input. Because the modes are orthogonal, it is only necessary to consider one mode at a time. If any mode is unstable, the system is unstable. The analysis is given by Gysling (1989) and we present here only the central result.

Figure 7 shows the relative perturbation energy input and dissipation over a cycle at the neutral stability point, as a function of the B-parameter for the mode that becomes unstable first. Energy dissipation due to the wall motion is dominant, being more than ten times that for the throttle over a large range of B-parameters. The stabilization due to the wall is thus direct dissipation through plenum wall motion, rather than modification of the system dynamics to promote increased dissipation in the throttle, as was the case in the throttle control experiments reported by Pinsley et al. (1990).

Time-Domain Analysis and Nonlinear Aspects

The linear analysis yielded a set of optimized, nondimensional control parameters, which gave large increases in the
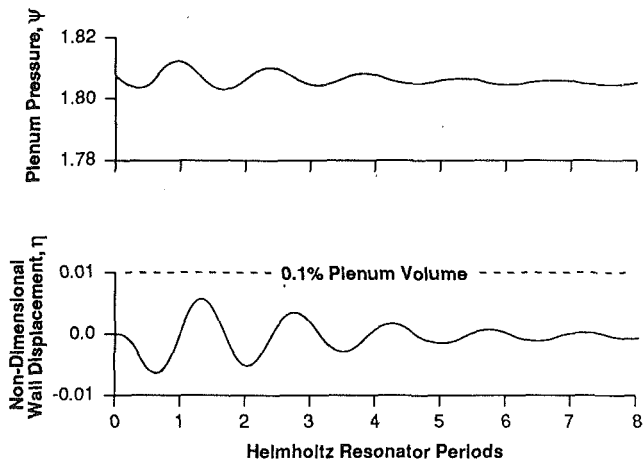
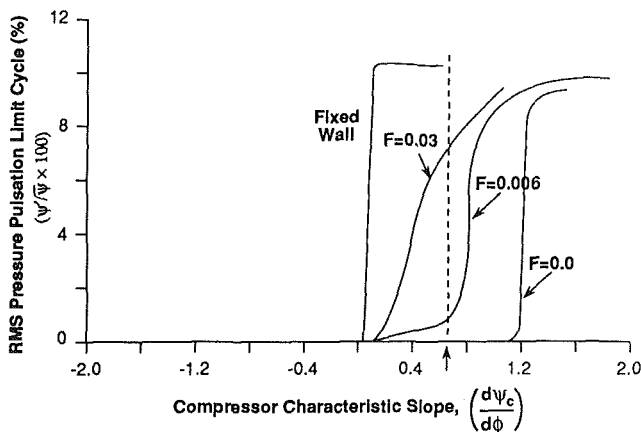Fig. 8 Wall motion and plenum response to impulse of 0.01 $\bar{\psi}\tau$; optimized system parameters

Fig. 9 Effect of Coulomb friction on limit cycle amplitude; optimized system parameters

Fig. 10 Effect of Coulomb friction on transient system response; compressor characteristic slope $(d\psi_c/d\phi) = 0.66$ (dashed line on Fig. 9)

stable flow regime. The response beyond the initial instability, i.e., the nonlinear system behavior, is also of interest. Nonlinear computations were thus performed to assess the effects of finite amplitude disturbances and of nonlinearities in the wall dynamics. The equations of motion were integrated using the Newmark time-averaged acceleration method (Bathe and Wilson, 1976). As in the linear analysis, the compressor characteristic shown in Fig. 3 was used.

As an example of the results, Fig. 8 shows the time response of the optimized system to a small impulsive disturbance at the inlet operating near the linearly predicted stability line ($\phi = 0.096$). Wall motion and pressure perturbations exhibit essentially damped harmonic motion. A more interesting point, to be discussed further in connection with the experiments, is that the nonlinear computations showed that introducing wall motion into a fixed wall system undergoing deep surge cycles could suppress the surge. In other words, even though the control scheme was designed based on linear analysis, it was useful for oscillations that were strongly nonlinear.

An important use of the nonlinear analysis was to examine the effect of Coulomb friction in the wall dynamics. The presence of Coulomb friction, in a strict sense, invalidates the linearity assumption. However, the degree to which the accuracy of the linear model is affected is a function of the ratio of the Coulomb friction forces compared to the other, essentially linear, forces in the system (Halfman, 1962). To assess this, computations were carried out with a constant magnitude friction force imposed on the wall in the direction opposite to
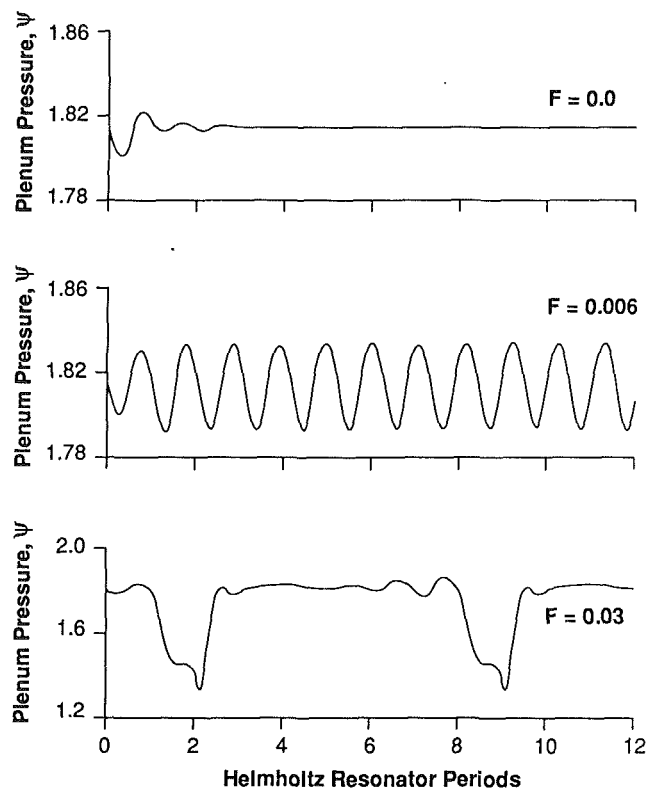
its motion, to model the sliding friction present in an actual design.

One important result of the Coulomb friction is that it prevents the wall from responding to disturbances below a threshold level, i.e., disturbances must grow to a critical amplitude before the wall can respond. Therefore, in a strict sense, operating points to the left of the natural surge line remain linearly unstable for the actual (nonideal) tailored structure system. The linear instability that results from the presence of Coulomb friction grows into a limit cycle, whose amplitude (for a given compression system and set of control parameters) is a function of the nondimensional friction force, F, defined as

$$F = \frac{f}{\rho_0 U^2 A_p}$$

and the slope of the compressor characteristic.

The effect of Coulomb friction on surge suppression is demonstrated in Fig. 9 where the root mean square of the calculated limit cycle pressure fluctuations, divided by the steady-state pressure rise, is plotted versus the local compressor characteristic slope, for various nondimensional friction levels. The vertical dashed line denotes the value of slope corresponding to the results in Fig. 10, discussed below. The maximum value of the slope prior to deep surge (large amplitude oscillation) decreases with increasing friction levels. The deep surge boundary for the nonlinear system with Coulomb friction agrees well with the linear stability boundary in the limit of zero friction. With increasing Coulomb friction levels, however, the performance of the movable plenum wall system approaches that of the fixed wall system. Analysis showed that the movable plenum wall became unable to suppress surge significantly past the rigid wall surge line for nondimensional friction levels greater than $F = 0.02$.

As examples of predicted limit cycles with different levels of Coulomb friction, the time response of systems with various levels of Coulomb friction to a small impulse (0.01 in units of
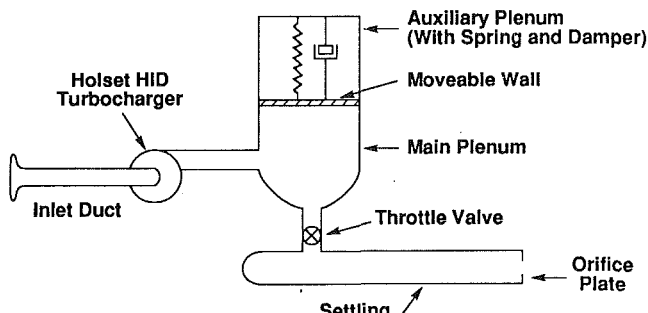
Fig. 11 Schematic of experimental facility

Fig. 12 Effect of leakage on maximum achievable compressor characteristic slope for stable operation with optimized system

$\overline{\psi}\tau$) is shown in Fig. 10. Parameters are given in the figure caption. The amplitude of each limit cycle is indicated in Fig. 9.

The disturbance decays in the system without Coulomb friction, but grows into a limit cycle in the systems with Coulomb friction. For the system with a small amount of Coulomb friction ($F = 0.006$) the limit cycle is small and approximately sinusoidal (mild surge) with frequency near the predicted Helmholtz frequency. However, for the system with larger Coulomb friction ($F = 0.030$), the limit cycle is no longer sinusoidal and contains regions of reversed flow (deep surge).

Experiment Design

The basic prediction is that a properly designed moving plenum wall can substantially increase the stable flow range of a centrifugal compression system. To investigate this experimentally, a design study was undertaken to match the nondimensional control parameters, while minimizing the effects of nonlinearities, in a physically realistic device.

The conceptual design was based on use of an existing centrifugal compressor facility, constructed to investigate active throttle control of surge. The facility is described in detail by Pinsley (1988); however, the major components will be outlined here. The centrifugal compressor was a Holset model H1D turbocharger. The impeller has an inlet area of 0.00125 m² with hub-to-tip radius ratio of 0.37 and exit tip diameter of 0.055 m. The compressor has no inlet guide vanes, six blades, six splitter blades, and a vaneless diffuser. A schematic of the compression system facility is shown in Fig. 11.

Design of Movable Plenum Wall

Several different ways to implement the control scheme mechanically were reviewed. A major constraint was that the wall had to be capable of withstanding large steady-state and transient pressure loading, yet still respond to small amplitude perturbations in plenum pressure. A rigid piston serving as the plenum wall, and an aerodynamic spring, were determined to be practical solutions to these constraints. In particular, a design utilizing a separate, explicit spring, mass, and damper was attractive since it facilitated parametric experimentation. No attempt was made to engineer a "flight weight" system.

To serve as the movable wall, the rigid piston was mounted on a shaft, guided by linear bearings, and allowed to float between the main plenum and an auxiliary plenum. The seal between the two plenums was made with a low-friction, convoluted diaphragm. A small-diameter tube connected the two plenums so they were isolated for high-frequency pressure disturbances (i.e., surge oscillations), but steady-state pressures were equalized so that no steady-state load existed on the piston. A mechanical spring was used to maintain a constant equilibrium position for the piston over various operating conditions since at steady state, the plenum wall had no preferred
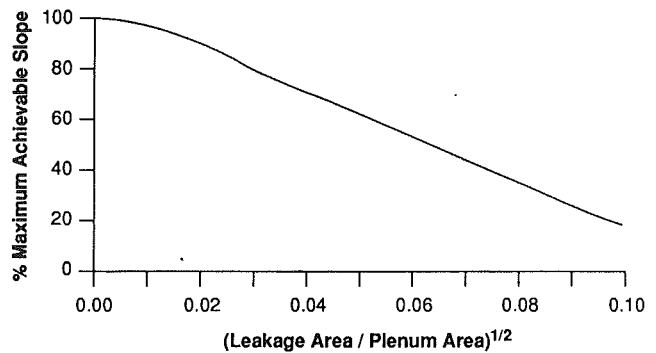
Table 1 Design specifications for the flexible plenum wall experimental facility

B Parameter	0.65 to 1.0
Helmholtz Frequency	18.5 Hz to 19.9 Hz
W Parameter	0.11
Q Parameter	0.51
ζ Parameter	1.5 to 3.0
Area of Wall	0.0669 m²
Mass of Wall	6.2 kg
Volume of Plenum	0.0108 m³
Inlet Duct Length	1.16 m
Inlet Area	0.00125 m²
Auxiliary Plenum Volume	0.0388 m³
Aerodynamic Spring Constant	24,000 n/m to 35000 n/m
Mechanical Spring Constant	2100 n/m
Damping Coefficient	1000 n s/m to 2000 n s/m
Maximum Wall Motion	+/-1.25 cm
Coulomb Friction	10 n

position. The mechanical spring also allowed the steady-state position of the wall to be adjustable.

Because the presence of the steady-state equalization tube could affect the behavior of the aerodynamic spring, computations were carried out to quantify the effect of leakage between the two plenums. The leakage was modeled as flow through an orifice plate. The results are shown in Fig. 12, where the decrease in maximum slope prior to surge is plotted versus nondimensional orifice area for the optimized system at typical operating conditions. Leakage caused small amplitude limit cycles similar to those predicted to occur as a result of Coulomb friction, so it is important that leakage be kept to a minimum.

A viscous dashpot was used for the damping. To minimize Coulomb friction, a low-friction, pneumatic, double acting actuator was modified to serve as a damper. The actuator was filled with 5W-30 oil and the ports on either end were connected through a variable area valve. Testing of various dashpots developed from the same basic design showed that the force-velocity relation for the dashpot was closely linear over the expected range of wall velocities, as well as easily adjustable.

The final rig specifications are given below in Table 1 and a detailed drawing of the movable plenum wall apparatus is shown in Fig. 13.

Experimental Data and Analysis

The compression system was investigated with fixed and flexible wall for three different sets of structural control parameters, at B-parameters ranging from 0.65 to 1.0. Steady-state measurements were used to map the compression system performance and to define the surge line for both fixed and flexible wall systems. Time-resolved measurements were used to evaluate the model assumptions and to determine the per-
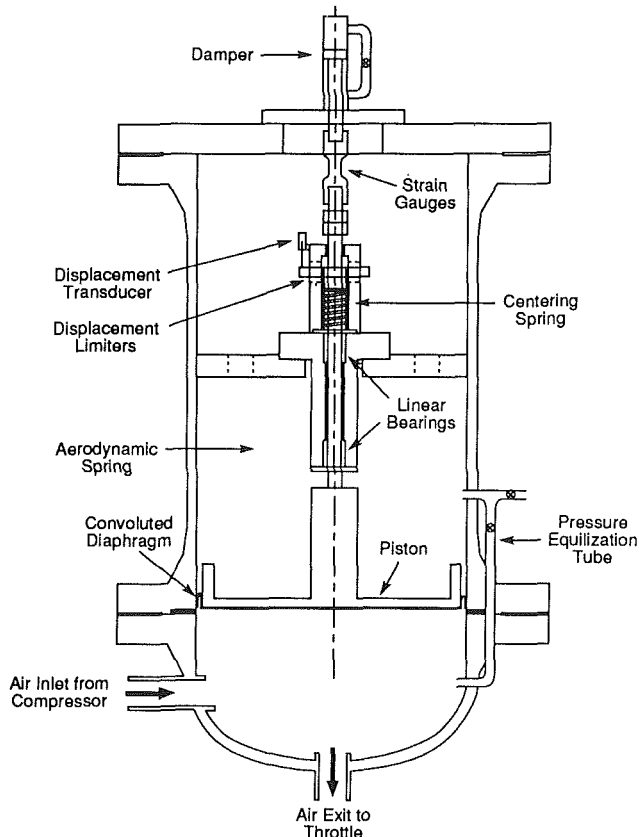
Fig. 13 Movable plenum wall (tailored structure) showing mass-spring-damper system

Fig. 14 Compressor map showing increase in stable flow region due to tailored structure for three values of damping; damping values ζ = 1.5, 2.25, 3.0, other parameters at optimized values

Fig. 15 Limit cycle pressure pulsation amplitude versus mass flow coefficient; 90K speedline, optimized movable wall system

formance characteristics of components in the compression system and in the flexible wall.

Steady-State Behavior. The experimental compression system could be operated in a fixed wall configuration by shutting the steady-state pressure equalization line and bleeding the auxiliary plenum to atmospheric pressure. Pressure in the main plenum then forced the wall against its upper stops, yielding a fixed wall configuration. Forcing the plenum wall against the upper stop resulted in increasing the plenum volume approximately 5 percent, and, hence, the B-parameter 2.5 percent, which had a slightly destabilizing effect on the fixed wall compression system. Any movement of the surge line to the left due to wall motion will thus slightly overestimate the actual increase in stable flow range, although this difference is small compared to the difference seen between the fixed and flexible wall systems. (We have not tried to correct for this in the data presentation, but it should be noted that our estimates of the shift in surge flow coefficient due to this change in B-parameter are roughly one-half percent of the surge mass flow as a worst case (at low speed), and one or two tenths of a percent at higher speeds. Thus, these changes are, in general, two orders of magnitude less than the difference between the fixed wall and the movable wall surge points.)

The compressor was operated at corrected speeds (referenced to 288 K) ranging from 60,000 rpm to 100,000 rpm, corresponding to a range of B-parameters of 0.65 to 1.0. The steady-state performance is reported in terms of (inlet total to plenum static) pressure ratio and mass flow, given in standard cubic feet per minute (SCFM). Mass flow is also given in some of the figures in terms of nondimensional flow coefficient, annulus-averaged inlet axial velocity divided by tip speed.

Because it was of interest to operate with the movable plenum wall in the optimized as well as in the nonoptimized configurations, speedlines for the movable wall system were recorded
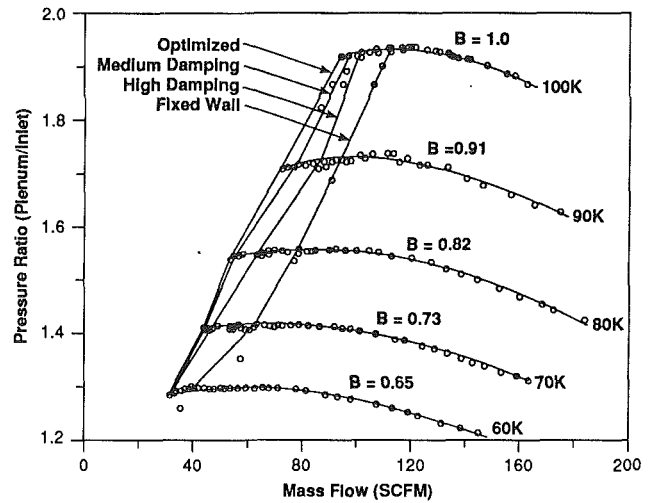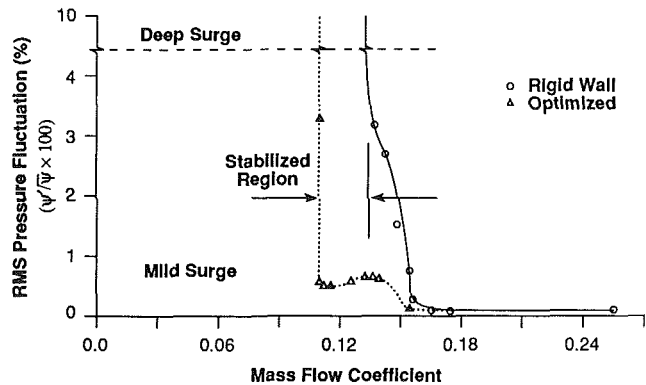
with various levels of wall damping. The wall was operated at the theoretically optimized configuration (W = 0.11, Q = 0.51, ζ = 1.5) as well as at values of ζ = 2.25 and 3.0.

The steady-state compressor performance map for the three movable wall configurations and the fixed wall system is shown in Fig. 14. The steady-state pressure ratio is unaffected by the presence of the moving wall in the stable flow range of the fixed wall system, but the surge line is moved to the left substantially. Also, the degree of surge suppression achieved is dependent on the movable wall control parameters, as predicted. The optimized configuration performed the best, with the performance of the other two configurations decreasing as one moved farther from optimum. A surge line recorded for the movable plenum wall system with a lower than optimum damping ratio (ζ = 0.75) confirmed that movement in either direction in parameter space away from the optimal damping ratio was destabilizing.

Figure 15 shows the root-mean-square value of the fluctuations in plenum pressure versus mass flow coefficient for the fixed wall system and the optimized movable plenum wall system at B = 0.91 (90K speedline). On the negative sloped region of the speedline (above ϕ = 0.155), the rms pressure fluctuations for fixed and movable wall systems are the same. However, small-amplitude limit cycles exist in the stabilized region. Based on the results of numerical calculations, these limit cycles can be attributed to Coulomb friction in the wall motion and pressure equalization leakage. Small amplitude
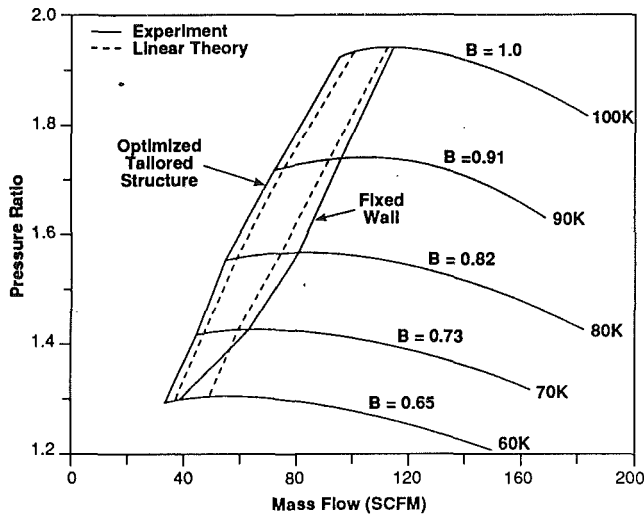
Fig. 16 Predicted and measured stability limits; compressor characteristics approximated by third-order fit

Fig. 17 Amplitude of pressure fluctuations versus mass flow; optimized system (90K speed, $B = 0.91$)

Fig. 18 Compressor characteristic with points at which time-resolved data are shown

limit cycles also occur over a limited range of mass flow in the fixed wall system prior to deep surge; these, however, appear to be a result of nonlinearities in the compressor and throttle characteristics.

Figure 16 shows predicted and experimentally determined surge lines for the rigid wall and for the optimized system. The predicted surge line is based on the linear instability point as determined by the eigenvalue stability analysis described previously. The experimental surge line is defined as the onset of deep surge (i.e., reverse flow); this also marked the points at which the time-mean pressure ratio dropped sharply. The compressor characteristics used are from a third-degree polynomial curve fit of the speedlines measured by Pinsley (1988).

The experimental results can be compared to the nonlinear calculations by examining the amplitudes of pressure fluctuations in the plenum as a function of mass flow. As inputs to the calculation, the friction force present during wall motion was measured to be approximately 10 N and the leakage was estimated to be equivalent to a 0.003 m diameter orifice plate. The results of the calculation and experiment for the optimized system operating at $B = 0.91$ are shown in Fig. 17, where the amplitude of the small plenum pressure limit cycles before the onset of deep surge are shown versus mass flow coefficient. The linear stability boundary is also shown in the figure for comparison. The linear analysis does not predict the small-amplitude limit cycles in the stabilized region, but it is able to portray accurately the onset point for deep surge. The reason is that the oscillations are the result of nonlinear effects, described above. If the nonlinear effects are small, which is inherent in the experimental design, the linearly predicted stability limit corresponds to the onset of deep surge. The nonlinear analysis shows limit cycles in the stabilized region, although the detailed relationship between mass flow and limit cycle amplitude is not captured.

Transient System Behavior

Time-resolved measurements were recorded for the fixed wall compression system and for the moving wall system at three control parameter configurations. The measurements were made on the 70K and 90K speedlines, corresponding to B-parameters of 0.73 and 0.91. The data shown are from the former, at the points marked on Fig. 18.

As noted previously, the flow through the compression system becomes progressively more unsteady as the system approaches the surge line. To demonstrate this, the time resolved nondimensional mass flow coefficient and the nondimensional
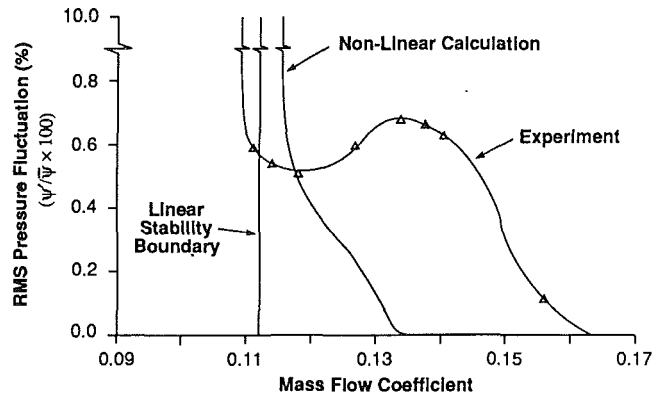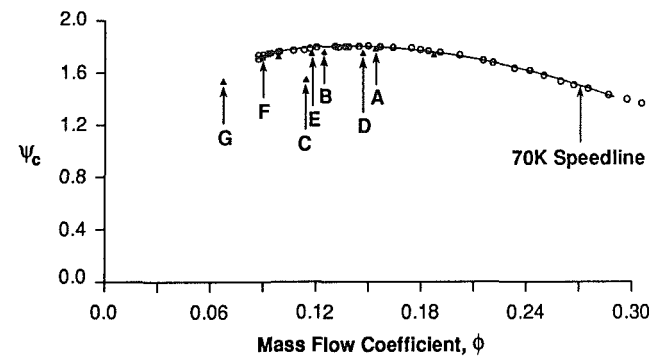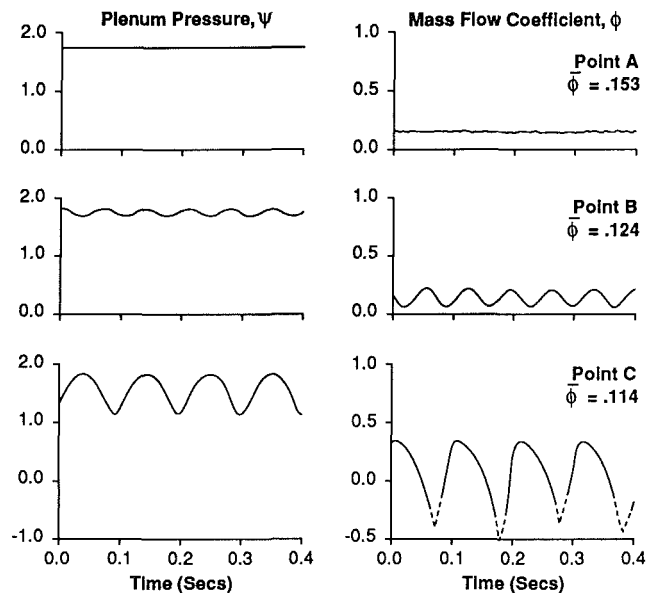

Fig. 19 Measurements of time-resolved plenum pressure and mass flow in fixed wall system (70K speed, $B = 0.73$)

pressure rise for the fixed wall system are shown in Fig. 19 for three operating points (marked A–C in Fig. 18). The transient mass flow measurements (taken in the inlet duct) are based on a linearized hot-wire calibration and the large oscillations in mass flow are presented for qualitative information only. The data shown correspond to points in both stable and unstable operating regions.

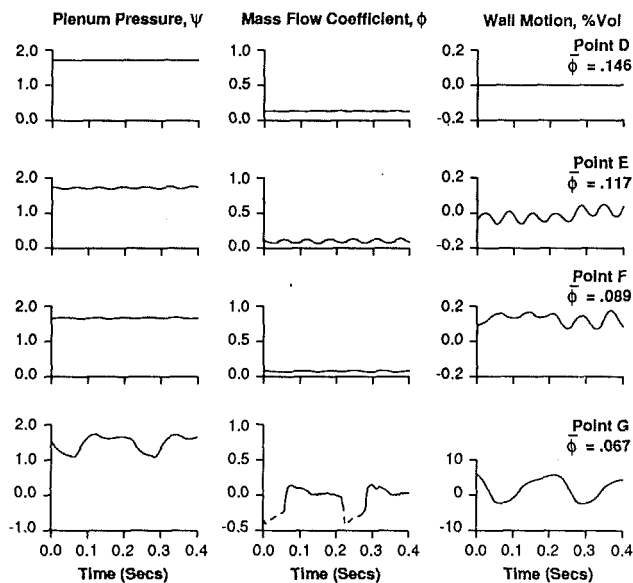For flows near point A, on the negative slope region of the

Fig. 20 Measurements of time-resolved plenum pressure, mass flow, and wall motion in optimized movable wall system (70K speed, B = 0.73)

Fig. 21 Experimental time history showing suppression of fixed wall system deep surge when wall is released (optimized system, B = 0.91)

compressor characteristic, stable operation with only slight unsteadiness is exhibited.

Point B is slightly to the left of the peak of the compressor characteristic. Small-amplitude limit cycles (mild surge) are seen. The frequency of the mild surge cycle is approximately 14.5 Hz, compared to the predicted Helmholtz frequency of 17.5 Hz.

At mass flows corresponding to points C and below, on the positive slope region of the speedline, the compressor is in deep surge. The time-averaged pressure rise and mass flow are decreased and the frequency of the oscillations has changed to approximately 10 Hz. The hot wire does not distinguish reversed flow, and the reversed flow regions are shown with a dashed line. The decrease in frequency is associated with the time needed for plenum blow-down and repressurization, as described by Fink (1988).

With the moving wall system, small-amplitude limit cycles existed over the stabilized region. Figure 20 shows the non-dimensional mass flow, pressure rise, and corresponding non-dimensional wall motion for the medium damping configuration operating at the 70K speedline for four operating points, D, E, F, and G, shown on the compressor characteristic in Fig. 18.

Point D is in smooth operation on the negatively sloped region of the map. The steady-state and unsteady behavior is similar to point A for the fixed wall configuration. The position of the wall is shown to be stationary, indicating that the disturbances in the stable system are not large enough to overcome the wall friction.

Points E and F are located on the positively sloped, stabilized region of the characteristic and exhibit small amplitude limit cycles. The maximum wall motion required to stabilize the system is approximately 0.1 percent of the plenum volume and the power dissipated is approximately 0.05 percent of the steady power needed to drive the compressor.

At point G, in deep surge, the pressure and mass flow traces are similar in amplitude to those with the fixed wall, although the fluctuations have a much lower natural frequency (4–5 Hz). Also, in deep surge, the wall is shown to be hitting the displacement limiters, as indicated by the flat spots on the time trace of the wall motion.

Introduction of a movable plenum wall can also eliminate deep surge when wall motion is initiated during an existing fixed wall surge cycle. This is demonstrated by the time history
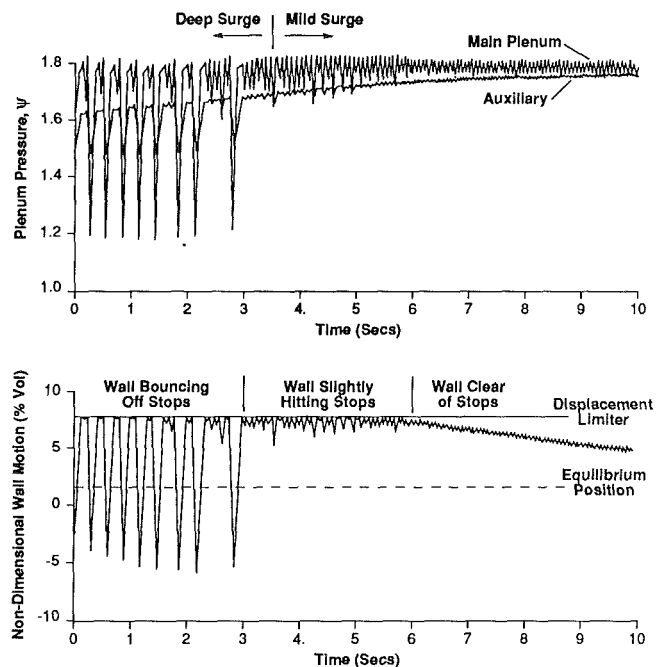
shown in Fig. 21, where fixed wall surge is suppressed by equalizing the auxiliary and main plenum pressures, thus freeing the wall from the displacement limiters. The time traces in Fig. 21 show the wall bouncing on the stops as the auxiliary plenum pressure equalizes. When the wall clears the stops, the deep surge cycle is suppressed. Although not shown, the wall continues to move toward its steady-state equilibrium position as the pressures in the auxiliary and main plenums equalize.

Two other points should be made about the time history shown in Fig. 21. First, the time scale over which the surge suppression occurs is considerably longer than any time scale associated with the system oscillations because it is set by the filling time (through the small equalization tube) of the auxiliary plenum. Second, as seen in previous figures, the deep surge regime is one in which the oscillations are strongly nonlinear, with mass flow oscillations greater than the time averaged mass flow. This indicates that the use of tailored structure can suppress surge even when the oscillations have large amplitude. In this connection it should be noted that similar behavior has been found by Pinsley et al. (1991) and Ffowcs Williams and Huang (1989) using different active control schemes. Such behavior emphasizes that successful use of dynamic control is not restricted to the small amplitude regime.

Dynamic Response of System Components

Compressor Behavior. One of the major assumptions used in modeling the compression system is that the compressor remains on its steady-state characteristic during transient operation, at least for frequencies on the order of the Helmholtz frequency. To check this, the unsteady pressure rise versus mass flow relation (i.e., the compressor transfer function) can be calculated directly from the unsteady data and compared to the quasi-steady slopes. The unsteady data were taken from operating points exhibiting small amplitude limit cycles. The instantaneous pressure rise versus mass flow slope was determined from measurements of inlet mass flow and plenum pressure, due corrections being made for the inertia of the fluid in the inlet duct. Only self-excited oscillations were examined, so that measurements were obtained only at or near the system resonant frequency where there was an acceptable signal-to-noise ratio.
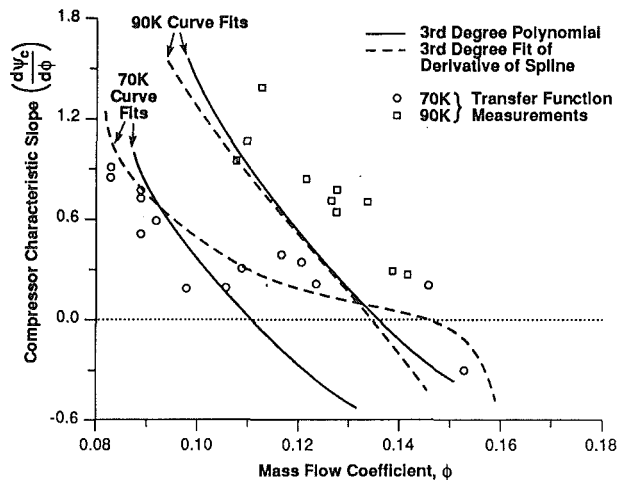
Fig. 22 Measured compressor transfer function and compressor characteristic slope values obtained from curve fits to steady-state data

The compressor slope, as measured, yielded a real and imaginary part. The real part represents the instantaneous slope of the compressor characteristic. The imaginary part can be viewed as a lag term, similar to that discussed by Fink (1988), which accounts in a rudimentary fashion for the unsteady aerodynamics within the compressor. The real part of the transfer function is plotted versus steady state mass flow coefficient for the 70K and 90K speedlines in Fig. 22. The data are from both fixed and movable wall systems, indicating that, as would be expected, the presence of the wall has no noticeable effect on the instantaneous characteristic slope. Also plotted in the figure are the slopes resulting from two methods of fitting the steady-state data; the derivative of a third-order polynomial curve fit, and a third-order polynomial fit of the derivative of a cubic spline fit of the steady-state compressor data. (It is important to note that, as can be inferred from Fig. 22, accurate determination of the slope is difficult to do.) As shown, the compressor characteristic slopes determined from the steady-state data and those determined from unsteady data are in reasonable agreement. In particular, the unsteady data fall within the variance between the two steady-state slopes calculated by curve fits. The assumption of quasi-steady behavior thus appears to be an adequate representation of the instantaneous compressor slope over the range of flow coefficients investigated.

The time lag for both the 70K and 90K speedlines was approximately 5–10 ms, corresponding to 0.065–0.13 Helmholtz resonator periods. The compressor throughflow time can be estimated at approximately 3.0 ms. The lag term is thus on the order of the throughflow time of the compressor and it seems plausible to attribute the lag to unsteady aerodynamic effects *within* the compressor passages. This is in agreement with the conclusions of Fink (1988), who determined that a lag term on the order of compressor throughflow time was needed for agreement between the predicted and experimental behavior of a compression system in deep surge. Fink also found that a lag term of this order should have a negligible effect on system stability over the range of B-parameter investigated, so it appears that the quasi-steady compressor slope is adequate for predicting the onset of surge.

Another assumption used in the present treatment is that the wheel speed remains constant for perturbations in mass flow and pressure rise. This is not strictly correct because pressure and mass flow perturbations vary the power requirements of the compressor, and hence cause the wheel speed to vary. Fink (1988) assessed this assumption and showed that variable wheel speed had a stabilizing effect on the compression system. The degree of stabilization was shown to be a function of a nondimensional parameter, defined as

$$\text{Wheel inertia parameter} = \frac{2\rho_0 L_c A_{in} R_T^2}{I}$$

where I is the moment of inertia of the wheel and R_T is the tip radius. Using Fink's results, variations in wheel speed were found to have negligible effect on the stability of the compression system used in the present experiments.

An alternative way to address this point is to note that if the wheel speed and pressure fluctuations were strongly coupled, the nondimensional pressure rise and wheel speed variations during mild surge would be roughly the same order. However, for a typical (say 2.5 percent rms) pressure fluctuation, the measured wheel speed fluctuations are only 0.2 percent, an order of magnitude less. The assumption of constant wheel speed is thus adequate for modeling the small perturbation response, and hence linear stability, of the compression system.

Conclusions

Dynamic control using tailored structure has been shown to be effective in suppressing centrifugal compressor surge. The use of a movable plenum wall shifted the surge line to the left roughly 25 percent in flow over a significant portion of the corrected speed range examined. The effectiveness of surge suppression is a function of a set of nondimensional parameters, which govern the aeroelastic coupling of the wall to the compression system dynamics.

The present scheme was found to be robust, suppressing surge over a wide range of operating conditions with no adjustments to the parameters. Use of a movable wall was also demonstrated to lead to suppression of existing (highly nonlinear) surge cycles. In the stabilized region of the compressor map, surge was suppressed with no time average change in the compressor operating point.

The amount of control action (wall motion) required is a function of the nonlinearities in the wall dynamics, such as Coulomb friction and leakage. For the optimized configuration investigated in this research, the nominal limit cycle wall motion in the stabilized region was roughly 0.1 percent of plenum volume, with frequencies near the Helmholtz frequency. Pressure fluctuations in the stabilized region were on the order of 0.5 percent of the mean pressure rise of the compressor.

Time-resolved data were used to verify some of the major assumptions in the modeling of the compression system. Compressor transfer function measurements showed that a quasi-steady compressor characteristic gave a reasonable representation of the instantaneous compressor characteristic slope. These measurement also indicated that the improvement in surge margin is due to modification of the system dynamics, rather than a result of modifying the compressor characteristics by altering the local flow in the compressor. The smallness of the measured wheel speed variations supported the predictions that wheel speed variation would not significantly affect system stability.

In general, all aspects of the experimental investigations confirmed that the lumped parameter model of the compression system provided a useful description of the system dynamics, both with and without the movable plenum wall.

The physical mechanism responsible for the surge suppression with the flexible wall is unsteady energy dissipation due to the wall motion.

The maximum stable compressor characteristic slope is better measure of the effectiveness of this control scheme rather than the minimum stable mass flow coefficient. The steady-state mass flow coefficient has little effect, in an explicit way, on the stability of the compression system with the movable wall, and the dominant influence of mass flow is through the relation between mass flow and compressor slope implied by the compressor characteristic.

Nonlinear solution of the system equations showed the existence of small-amplitude limit cycles in the stabilized region in agreement with measurement. These limit cycles were found to result primarily from Coulomb friction and leakage.

Acknowledgments

References

Bathe, K.-J., and Wilson, E. L., 1976, *Numerical Methods in Finite Element Analysis*, Prentice-Hall, Inc., Englewood Cliffs, NJ, p. 322.

Chen, G. T., 1987, "Active Control of Turbomachinery Instabilities—Initial Calculations and Results," M.S. Thesis, Department of Aeronautics and Astronautics, MIT, Cambridge, MA.

Dean, R. C., Jr., and Young, L. R., 1977, "The Time Domain of Centrifugal Compressor and Pump Stability and Surge," ASME *Journal of Fluids Engineering*, Vol. 99, pp. 53–63.

Emmons, H. W., Pearson, C. E., and Grant, H. P., 1955, "Compressor Surge and Stall Propagation," *ASME Transactions*, Vol. 77, pp. 455–469.

Epstein, A. H., Ffowcs Williams, J. E., and Greitzer, E. M., 1989, "Active Suppression of Compressor Instabilities," *J. Propulsion and Power*, Vol. 5, pp. 204–211.

Ffowcs Williams, F. E., and Huang, X., 1989, "Active Stabilization of Compressor Surge," *J. Fluid Mech.*, Vol. 204, pp. 245–262.

Fink, D. A., 1988, "Surge Dynamics and Unsteady Flow Phenomena in Centrifugal Compressors," Ph.D. Thesis, Department of Aeronautics and Astronautics, MIT, Cambridge, MA.

Gysling, D. L., 1989, "Dynamic Control of Centrifugal Compressor Surge Using Tailored Structure," M.S. Thesis, Department of Aeronautics and Astronautics, MIT, Cambridge, MA.

Greitzer, E. M., 1981, "The Stability of Pumping Systems—The 1980 Freeman Scholar Lecture," ASME *Journal of Fluids Engineering*, Vol. 103, pp. 193–242.

Halfman, R. L., 1962, *Dynamics*, Addison-Wesley Publishing Company, Inc., Reading, MA, p. 335.

Pinsley, J. E., 1988, "Active Control of Centrifugal Compressor Surge," M.S Thesis, Department of Aeronautics and Astronautics, MIT, Cambridge, MA.

Pinsley, J. E., Guenette, G. R., Epstein, A. H., and Greitzer, E. M., 1991, "Active Stabilization of Centrifugal Compressor Surge," ASME JOURNAL OF TURBOMACHINERY, Vol. 113, this issue.

Stenning, A. H., 1980, "Rotating Stall and Surge," ASME *Journal of Fluids Engineering*, Vol. 102, pp. 14–20.

APPENDIX

Derivation of the Equations of Motion for the Movable Plenum Wall System

Consider the compression system shown in Fig. 1(b). The following assumptions are used: The flow in the inlet ducting is one-dimensional, incompressible, inviscid, and unsteady; the plenum pressure is spatially uniform and plenum processes are isentropic; the fluid inertia in the throttle is negligible; the compressor follows a quasi-steady characteristic; and the throttle pressure drop mass flow relation is parabolic.

The momentum equation applied to the compressor duct yields

$$P_0 + \Delta P_c - P_p = \frac{L_c}{A_{in}} \frac{d\dot{m}_1}{dt} \qquad (A1)$$

where L_c is the equivalent length of the compressor duct. Mass conservation in the plenum yields

$$\dot{m}_1 - \dot{m}_2 = \frac{d(\rho_p V_p)}{dt} \qquad (A2)$$

The pressure drop across the throttle can be written in terms of the throttle mass flow as

$$\Delta P_t = \frac{1}{2} \frac{\dot{m}_2^2}{\rho_t A_t^2} \qquad (A3)$$

Finally, the motion of the wall is given by

$$m\ddot{q} + c\dot{q} + kq = (P_0 - P_{\text{aux plenum}})A_p \qquad (A4)$$

where q is defined as the position of the wall away from the equilibrium position of the wall.

Writing the fluid dynamic variables as mean $((\overline{\ }))$ plus small perturbations $(\delta(\ ))$ and linearizing the compressor and throttle characteristics about a time-mean operating point yields equations for the perturbation quantities:

$$\left(\frac{\overline{d\Delta P_c}}{d\dot{m}}\right)\delta\dot{m}_1 - \delta P_p = \frac{L_c}{A_{in}} \frac{d(\delta\dot{m}_1)}{dt} \qquad (A5)$$

$$\delta\dot{m}_1 - \delta\dot{m}_2 = \frac{\overline{V}_p}{\overline{a}_p^2} \frac{d\delta P_p}{dt} + \overline{\rho}_p A_p \frac{d\delta q}{dt} \qquad (A6)$$

In Eq. (A6), the isentropic assumption has been used, and volume change has been expressed as the product of plenum area A_p and perturbation displacement δq.

We introduce the following nondimensional quantities:

$$\phi = \frac{\dot{m}}{\rho_0 A_{in} U} \qquad\qquad \tau = \omega_H t$$

$$\psi_c = \frac{\Delta P_c}{\frac{1}{2}\rho_0 U^2} \qquad\qquad B = \frac{U}{2\omega_H L_c}$$

$$\psi_t = \frac{\Delta P_t}{\frac{1}{2}\rho_0 U^2} \qquad\qquad \delta\eta = \frac{A_p \delta q}{\overline{V}_p}$$

$$\psi = \frac{P_p - P_0}{\frac{1}{2}\rho_0 U^2} \qquad\qquad M = \frac{U}{\overline{a}_p}$$

Using these equations, Eqs. (A5) and (A6) can be written as

$$\left(\frac{\overline{d\psi_c}}{d\phi}\right)\delta\phi_1 - \delta\psi = \frac{1}{B} \frac{d\delta\phi_1}{d\tau} \qquad (A7)$$

and

$$\delta\phi_1 - \delta\phi_1 = B\frac{\delta\psi}{d\tau} + \frac{\overline{\rho}_p}{\rho_0} \frac{B}{M^2} \frac{\delta\eta}{d\tau} \qquad (A8)$$

The throttle pressure drop equation can be written as

$$\delta\psi = \frac{\rho_0}{\overline{\rho}_t}\left(\frac{\overline{d\psi_t}}{d\phi}\right)\delta\phi_2$$

or $\qquad\qquad\qquad\qquad\qquad\qquad\qquad (A9)$

$$\delta\psi = \frac{\rho_0}{\overline{\rho}_t}\left(\frac{\overline{\phi}^2}{2\overline{\psi}}\right)\delta\phi_2$$

For the wall motion, we define the following nondimensional control parameters:

$$W = \frac{\rho_0 A_p^2 L_c^2}{m V_p}$$

$$\zeta^* = \frac{c}{2m\omega_p}$$

$$Q^* = \frac{\omega_p}{\omega_H}$$

The wall dynamics can then be written in nondimensional form as:

$$\frac{d^2\delta\eta}{d\tau^2} + 2\zeta^* Q^* \frac{d\delta\eta}{d\tau} + Q^{*2}\delta\eta = WB^2\delta\psi \qquad (A10)$$

Using the algebraic relation between $\delta\psi$ and $\delta\phi_2$, the throttle characteristic can be used to eliminate $\delta\psi$ from the set of nondimensional equations. In addition, we can define

$$\delta v = \frac{d\delta\eta}{d\tau}$$

as a nondimensional wall velocity to convert Eq. (A10) into two first-order equations. Rearranging these equations, and making use of Eq. (A9), yields the following stability matrix:

$$
\begin{bmatrix}
B\left(\dfrac{d\overline{\psi}_c}{d\phi}\right) - s & \dfrac{2B\overline{\psi}}{\overline{\phi}} & 0 & 0 \\[2mm]
\dfrac{1}{B}\dfrac{\overline{\phi}}{2\overline{\psi}} & -\dfrac{1\overline{\phi}}{B2\overline{\psi}} - s & 0 & -\dfrac{\overline{\rho}_p}{\overline{\rho}}\dfrac{1}{M^2}\dfrac{\overline{\phi}}{2\overline{\psi}} \\[2mm]
0 & 0 & -s & 1 \\[2mm]
0 & WB^2\dfrac{2\overline{\psi}}{\overline{\phi}} & -Q^2 & -2\zeta Q - s
\end{bmatrix}
\begin{bmatrix}
\delta\phi_1 \\ \delta\phi_2 \\ \delta\eta \\ \delta v
\end{bmatrix}
=
\begin{bmatrix}
0 \\ 0 \\ 0 \\ 0
\end{bmatrix}
$$

The control parameters Q^* and ζ^* are referenced to the Helmholtz frequency of the compression system, which varies slightly with operating conditions. They can be modified so that they remain independent of operating conditions. Thus, substitution of the following corrected control parameters yields the stability matrix given as Eq. (10):

$$Q = Q^*\sqrt{\frac{\rho_0}{\overline{\rho}_p}} \text{ and } \zeta = \zeta^*\sqrt{\frac{\overline{P}_p}{P_0}}$$

For reference, we also note that expanding the determinant for the 2×2 stability matrix describing the fixed wall compression system leads to the characteristic equation shown below:

$$s^2 + \left[\frac{1}{\dfrac{2\overline{\psi}}{\overline{\phi}}B} - B\left(\frac{d\overline{\psi}_c}{d\phi}\right)\right]s + \left[1 - \left(\frac{d\overline{\psi}_c}{d\phi}\right)\frac{\overline{\phi}}{2\overline{\psi}}\right] = 0$$

(A11)

Dynamic instability occurs when the first term in brackets becomes negative. The condition for this is

$$\left(\frac{d\overline{\psi}_c}{d\phi}\right) > \frac{1}{B^2\dfrac{2\overline{\psi}}{\overline{\phi}}}$$

which is the fixed wall stability limit.

Active Stabilization of Centrifugal Compressor Surge

J. E. Pinsley[1]

G. R. Guenette

A. H. Epstein

E. M. Greitzer

Gas Turbine Laboratory,
Department of Aeronautics and Astronautics,
Massachusetts Institute of Technology,
Cambridge, MA 02139

Active suppression of centrifugal compressor surge has been demonstrated on a centrifugal compressor equipped with a servo-actuated plenum exit throttle controller. The control scheme is fundamentally different from conventional surge control techniques in that it addresses directly the dynamic behavior of the compression system to displace the surge line to lower mass flows. The method used is to feed back perturbations in plenum pressure rise, in real time, to a fast-acting control valve. The increased aerodynamic damping of incipient oscillations due to the resulting valve motion allows stable operation past the normal surge line. For the compressor used, a 25 percent reduction in the surge point mass flow was achieved over a range of speeds and pressure ratios. Time-resolved measurements during controlled operation revealed that the throttle required relatively little power to suppress the surge oscillations, because the disturbances are attacked in their initial stages. Although designed for operation with small disturbances, the controller was also able to eliminate existing, large-amplitude, surge oscillations. Comparison of experimental results with theoretical predictions showed that a lumped parameter model appeared adequate to represent the behavior of the compression system with the throttle controller and, perhaps more importantly, to be used in the design of more sophisticated control strategies.

Introduction

Compression system surge is a self-excited instability, evidenced by large amplitude oscillations of annulus-averaged mass flow and plenum pressure rise. Operation in surge often results in severely degraded performance, as well as unacceptable levels of system vibration.

To avoid surge, one commonly adopts a margin of safety between the surge line, the limit of stable operation, and the closest allowable operating point. However, this can prohibit operation in regions of highest efficiency or pressure rise. In this paper, experiments are described that demonstrate a new method for allowing operation in regimes that have been previously inaccessible, not only close to but beyond the "natural" surge line. The procedure used is the closed-loop feedback control of the dynamic behavior of the compression system. As will be shown, such active control techniques, which suppress the instabilities that lead to surge, can extend the range of stable operation beyond the natural surge line and enlarge the usable compressor operating region. This, in turn, can allow greater freedom not only in compressor operation, but also in design.

Active Control of Surge. There has been much work carried out on what is termed surge control, and discussions of different available techniques have been given by Boyce et al. (1983), Ludwig and Nenni (1980), and Staroselsky and Ladin (1979). The approach taken here is fundamentally different from these types of surge suppression schemes because it is

based on effecting changes in the unsteady system response, i.e., the system dynamics, rather than the steady-state behavior. More specifically, existing surge control schemes act by effectively lowering the operating line once some steady-state, near-surge operating condition is reached or detected. These strategies do not enhance stability; rather they reduce the safety margins otherwise necessary. In contrast, the approach described herein uses active control to enhance the stability of the compression system, effectively moving the surge line.

The conceptual basis for the active control scheme presented here is that the nonlinear limit cycle oscillations characterizing surge will start as small amplitude disturbances, which then grow to finite limit. Attacking this growth in the early stages thus requires only low-power, small-amplitude control actions. The basic idea is to sense the small disturbances associated with incipient surge and feed back a signal derived from them (appropriately modified as to gain and phase) into an actuator or actuators. The combination of compressor, sensors, processors, and actuators (i.e., of compressor plus controller) constitutes a new machine, having different stability properties from the compressor alone. This can be exploited to enhance the stable flow range.

The analytical framework for this approach to active control has been developed by Epstein et al. (1989), referred to henceforth as EFG. They used a lumped parameter representation of a compression system to examine two basic control strategies in which either (or both) an exit throttle or a collector (plenum) wall would be driven in response to sensed perturbations in the compressor discharge pressure. Calculations carried out using simple proportional feedback control predicted that significant shifts in the surge point could be achieved. Although
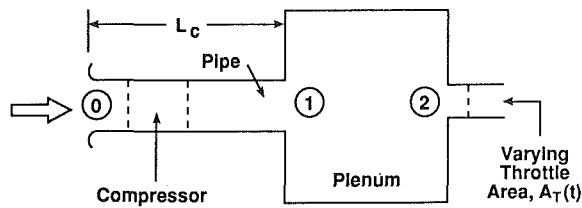
Fig. 1 Schematic of generic pumping system with active exit throttle

the compressor, the destabilizing element in the system, continues to feed energy into small-amplitude perturbations, it was shown that the controller increases the capability of other parts of the system to dissipate these unsteady perturbations. In addition, the controller power requirements were shown to scale with the square of the disturbance amplitude and were thus much less than steady-state machine power.

The present paper presents the experimental demonstration of these ideas for one of these schemes, that employing a varying exit throttle area. A schematic of the system of interest with the throttle controller at the plenum exit is shown in Fig. 1. As described in EFG, this is of some interest because, for an ideal controller at least, there need be no net average power expended to drive the throttle. Controller power requirements are thus independent of compression system power, and the increased dissipation associated with the perturbations can be regarded as due to increased leverage of the existing dissipative element in the system. It is stressed that it is the dissipation in the unsteady system behavior that is modified, so that the steady-state operating point is essentially unaffected by the control.

The present work by no means attempts to define an optimum controller configuration, but is rather a proof-of-concept examination of the ideas expressed in EFG. In this connection we note two other complementary approaches to modifying the dynamic system behavior, which have close links to the present study. One is by Ffowcs Williams and Huang (1989), who used a loudspeaker to drive a moving plenum wall, and the other by Gysling (1989), who used a tailored structural element (a moving plenum wall with a spring and dashpot) to provide increased damping of system perturbations through coupling of the aerodynamic and structural behavior. In both of these investigations, a significant increase in stable flow range was achieved.

Scope of the Present Investigation. The aim of the experiments was to demonstrate active stability enhancement (surge suppression) using throttle control of a centrifugal compressor. To design the experiments, parametric studies were initially carried out using a lumped-parameter system model; these modeling studies also served to help interpret the experimental results. Both steady-state and time-resolved data were taken to characterize the system performance with and without control. The control scheme was tested over a range of system parameters, not only to assess control effectiveness over the

range, but also to examine, in a diagnostic fashion, the effects of compressibility on the system dynamics.

Specifically, the investigation addressed the following questions:

1 Does this type of active control suppress system oscillations?

2 What will the system performance be in a controlled region of operation?

3 Will the controller adversely affect operation in normally stable regions?

4 Does the linear model accurately represent the system and the controller?

5 What parameters have the dominant influence on system controllability?

6 Can the results obtained in this experiment be generalized for other similar systems?

One can thus view the experiments as focused on two general goals. The first is demonstration of active control of a compression system over a range of parameters. The second is to verify that the basic modeling captures the system and controller dynamic behavior well enough so that this type of analysis can be used in future studies on (and designs of) more complex control schemes.

System Modeling

Lumped parameter system models have been used by many authors to examine instability inception in both axial and centrifugal compression systems, e.g., Emmons et al. (1955), Greitzer (1981), and Ffowcs Williams and Huang (1989), and there is no need to enter into a detailed description here. For reference, the derivation is sketched out in the appendix where it is shown that the nondimensional form of the linearized equations for the behavior of the nondimensional mass flow and pressure rise perturbations, $\delta\phi$ and $\delta\psi$, take the form:

$$\frac{d\delta\phi_1}{d\tau} = B\left(\overline{\frac{d\psi_c}{d\phi}}\right)\delta\phi_1 - B\delta\psi \tag{1}$$

$$\frac{d\delta\psi}{d\tau} = \frac{\delta\phi_1}{B} - \frac{1}{B\left(\overline{\frac{\partial\psi_T}{\partial\phi}}\right)_{A_T}}\delta\psi + \frac{\left(\overline{\frac{\partial\psi_T}{\partial\hat{A}_T}}\right)_\phi}{B\left(\overline{\frac{\partial\psi_T}{\partial\phi}}\right)_{A_T}}\delta\hat{A}_T \tag{2}$$

In Eqs. (1) and (2), $\delta(\ )$ denotes a perturbation quantity, τ is nondimensional time, $\hat{A}_T$ is the nondimensional control valve area, A_T/A_{in}, and B is the system stability parameter ($B = U/2\omega_H L_c$). $\overline{d\psi_c/d\phi}$ and $(\overline{d\psi_T/\partial\phi})_{A_T}$ are nondimensionalized derivatives of the compressor and throttle characteristics with respect to mass flow, $(\overline{\partial\psi_T/\partial A_T})_\phi$ is the derivative of the valve pressure rise versus valve area characteristic, and ϕ_1 is the compressor mass flow.

Equations (1) and (2) do not completely define the system dynamic behavior because the relation between the throttle

---

Nomenclature

a = speed of sound
A_{in} = impeller annulus inlet area
A_T = control valve (throttle) area
B = stability parameter defined in Eq. (A9) = $U/2\omega_H L_c$
$C_{throttle}$ = velocity at throttle exit
C_x = axial velocity
L_c = effective compressor duct length
$\dot{m}$ = mass flow
P_0 = ambient pressure
P_p = plenum pressure

ΔP = plenum to ambient pressure difference = $P_p - P_o$
ΔP_c = compressor pressure rise; ambient to plenum
ΔP_T = throttle (valve) pressure drop; plenum to ambient
t = time
U = impeller exit tip speed
V_p = plenum volume
Z = complex proportionality constant for controller
$\delta(\ )$ = perturbation quantity

ρ_o = ambient density
τ = nondimensional time = $\omega_H t$
ϕ = nondimensional flow coefficient = C_x/U
ψ = nondimensional pressure rise = $\Delta P/1/2\rho_o U^2$
ω_H = system Helmholtz resonator frequency = $a\sqrt{A_{in}/V_p L_c}$
$(\hat{\ })$ = nondimensional quantity
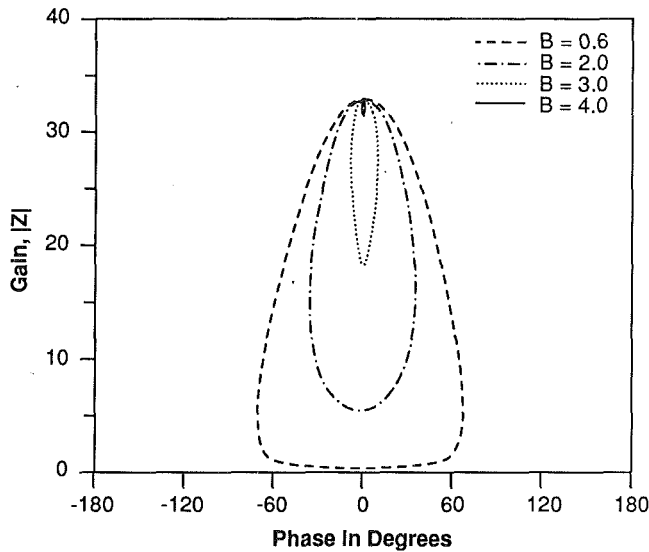$(\ )'$ = fluctuation
$(\overline{\ })$ = mean quantity

Fig. 2 Increasing B decreases variations in controller gain and phase over which the pumping system is stable (the regions within the curves); fixed operating point ($\bar{\psi} = 1.9$, $\phi = 0.12$, $\overline{d\psi/d\phi} = 1.0$)

Fig. 3 Maximum system gain is reached when instantaneous throttle line (a–a') slope becomes less steep than the compressor characteristic, inducing static instability

area perturbation is not linked to the pressure rise or mass flow perturbations. Specifying this relation defines the throttle control law and, in what follows, we take the relation to be the simple proportionality, expressed in Eq. (3):

$$\frac{\delta \hat{A}_T}{\hat{A}_T} = Z \delta \psi \qquad (3)$$

Z is a complex constant describing the gain and phase relations between sensed pressure perturbations and instantaneous valve area. Inserting Eq. (3) into the system Eqs. (1) and (2) produces two coupled equations for $\delta\phi_1$ and $\delta\psi$. These have solutions of the form $e^{s\tau}$, where the characteristic equation for S is given by:

$$S^2 + S\left[\frac{1}{B}\left(\frac{1 - \left(\overline{\frac{\partial\psi_T}{\partial\hat{A}_T}}\right)_\phi \overline{A}_T Z}{\left(\overline{\frac{\partial\psi_T}{\partial\phi}}\right)_{A_T}}\right) - B\left(\overline{\frac{d\psi_c}{d\phi}}\right)\right]$$

$$+ \left[1 - \frac{\left(\overline{\frac{d\psi_c}{d\phi}}\right)}{\left(\overline{\frac{\partial\psi_T}{\partial\phi}}\right)_{A_T}}\left(1 - \left(\overline{\frac{\partial\psi_T}{\partial\hat{A}_T}}\right)_\phi \overline{A}_T Z\right)\right] = 0 \qquad (4)$$

Equation (4) is the characteristic equation of a damped harmonic oscillator, with the damping either positive or negative depending on compressor operating point. In this context, the primary role of the the active control is to modify the damping term in the equation, increasing the stability of the oscillatory system.

Overall Results of System Modeling Studies. Several clear trends emerged from the parametric studies of the compression system, which were performed to select the control parameters. First, as pointed out by EFG, the perturbation in area should be in phase with the plenum pressure perturbation for maximum effectiveness. (Note that this statement pertains only to the particular control strategy used here; other schemes will have different optimum phases, e.g., Ffowcs Williams and Huang (1989).) In addition, the control effectiveness decreases as either or both the B-parameter and the slope of the compressor characteristic increase. Finally, for a given operating point, there is a finite range of gains and phases over which
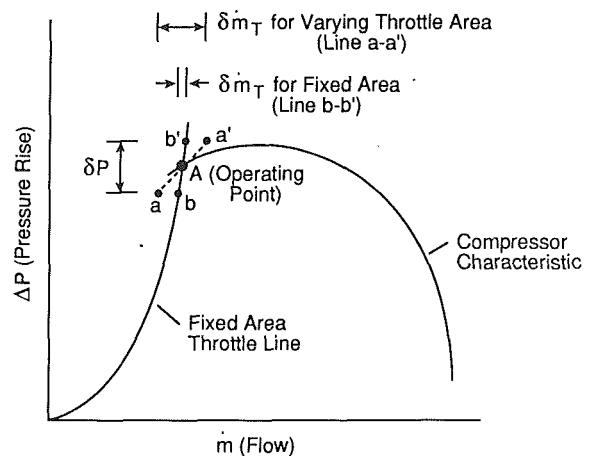
the growth of the perturbations can be suppressed. These trends imply that, for a specific operating point (specified compressor slope), the region of stability in the gain-phase plane will appear as in Fig. 2, which shows typical closed regions of stable operation for four values of the B-parameter.

The physical reason for the decreased effectiveness with increase in B-parameter is connected to the overall decrease in stability that occurs as B increases. This is well known, and has been amply discussed in the literature (e.g., Greitzer, 1981). Larger B implies a more compliant system, which means that the (unsteady) flow through the throttle is less coupled to the unsteady flow through the compressor. Control strategies using a downstream throttle would therefore be expected to lose effectiveness. We will return to this point when we discuss possible future directions for this research.

The system dynamics underlying the most effective operation occurring at zero phase have also been presented in EFG, but it is useful to summarize these arguments, since they are crucial to understanding the role of the control. The instabilities of interest occur as the result of mechanical energy being fed into the perturbations by the unsteady flow through the compressor. This energy can be offset, and the system stabilized, by dissipation in the throttle. The net (compared to the value for steady-state operation) dissipation in the throttle is proportional to the product [δ(plenum pressure)·δ(throttle mass flow)]. The throttle mass flow, $\dot{m}_T$, is

$$\dot{m}_T = \rho C_{\text{throttle}} A_T \qquad (5)$$

For values of system pressure rise small compared to ambient, the velocity at the throttle exit is given by

$$C_{\text{throttle}} = \sqrt{2\Delta P_p/\rho}.$$

Using this expression for C_{throttle}, and splitting quantities into time mean (denoted by ( )) and perturbation (denoted by δ( )), the mass flow perturbation can be written as

$$\frac{\delta \dot{m}_T}{\bar{\dot{m}}_T} = \frac{1}{2}\frac{\delta \Delta P_p}{\Delta P} + \frac{\delta A_T}{A_T} \qquad (6)$$

For a given controller gain, the product of mass flow perturbation and pressure perturbation (i.e., the dissipation) is thus maximized when δA_T and $\delta \Delta P_p$ are in phase.

The existence of a minimum level of gain needed for system stabilization should be evident. The reason for the existence of a maximum gain can be seen by invoking the above considerations and referring to Fig. 3, which shows compressor and throttle pressure differences versus flow. Consider small perturbations in pressure about a given operating point A, as indicated. The throttle mass flow fluctuations will basically track along the throttle curve and, for a fixed throttle, the
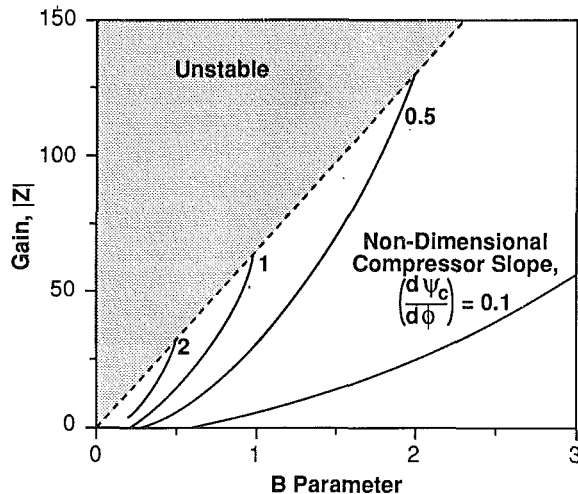
Fig. 4 Gain required to stabilize the compression system increases with increasing B and compressor slope $(\overline{d\psi_c}/d\phi)$; $\phi = 0.12$
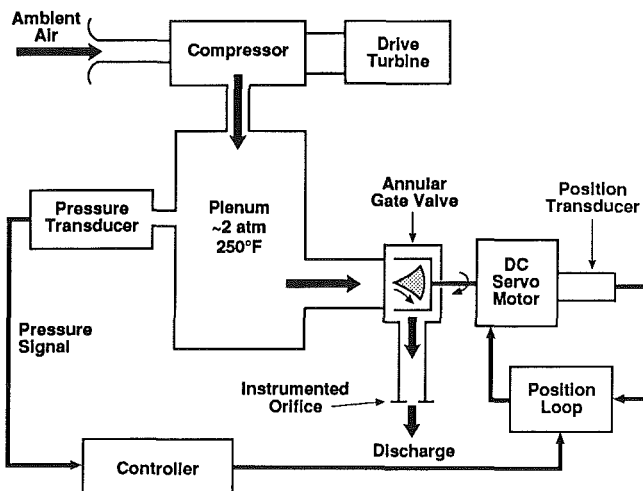

Fig. 5 Experimental setup of actively stabilized centrifugal compressor

Table 1 Compressor/Compression System Parameters

	Case I	Case II	Case III
V_p in m^3	0.0079	0.027	0.012
L_c in m	1.96	0.88	1.96
Compressor speed, RPMx1000	60-110	60-110	70
B parameter	.45-.72	1.26-1.93	.61
Helmholtz frequency, Hz	15.5	12.5	12.8

$$\frac{\overline{d\psi_c}}{d\phi} = \frac{\overline{\phi}}{2B^2\overline{\overline{\psi}}} .$$

Figure 4 portrays these trends. The figure shows the value of gain (Z) needed to stabilize a compressor operating with a given compressor characteristic slope, as a function of B.

The analytical results indicate that surge suppression can be achieved with proportional feedback on the throttle motion. However, they are based on an idealized controller and a linearized model of the system. In a real system, there can be nonlinearity and, more importantly, unmodeled dynamics of the control system, which can limit effectiveness. Thus, one must examine experimentally the degree to which the model adequately captures the essential features of the problem.

Experimental Facility and Overall Test Parameters

The turbocharger used was a Holset H1D model, which has radial blades at outlet and a vaneless diffuser. Impeller tip diameter at outlet was 5.5 cm. The test stand was built to run the turbocharger at speeds near its peak efficiency region, with $110K$ rpm selected as the maximum compressor speed at which the controller must operate. Delivery temperature and pressure associated with this speed were roughly $150°C$ and 2 atm. The stand was instrumented for both transient and steady-state measurements, with data acquistion through a microcomputer analog-to-digital interface. A schematic of the facility is shown in Fig. 5; more detail is given by Pinsley (1988).

The exit throttle was a rotary gate valve mounted at the plenum exit. Valve opening was set by rotating a ported inner sleeve relative to outer stationary ports. Valve angular position was measured with a rotary variable differential transformer angular displacement transducer. The pressure drop through the rotary gate valve was taken across diametrically opposed ports, so that the pressure loading on the valve was equalized around the circumference. Actuation force was applied normal to the flow and thus had only to overcome valve inertia and friction. The control valve was actuated by a low inertia d-c servomotor with a rated torque of 1.07 $m^2 \cdot kg/s^2$ and a torque constant of 0.064 $m^2 \cdot kg/s^2 \cdot amp$. The inertias of the motor and valve rotors were kept as small as possible $(7.1 \times 10^{-6}$ $kg \cdot m^2$ and 7.1×10^{-7} $kg \cdot m^2$, respectively) to maximize frequency response. The valve response, as tested, was flat to 80 Hz.

The compressor inlet duct length (L_c) and the plenum volume (V_p) could both be adjusted to vary the stability parameter B over a range of compressor speeds, while maintaining the system Helmholtz frequency within a relatively narrow range. This was done to minimize the possibility of encountering unmodeled controller dynamics at other frequencies. By changing geometries, it was possible to obtain varying B-parameters at a given compressor speed, or conversely the same B-parameter at varying compressor speeds. Table 1 summarizes the parameters corresponding to the conditions under which the controller was tested. Unless otherwise specified, all results below are with the Case I configuration.

The area perturbation–pressure perturbation transfer function of the valve was evaluated separately by subjecting the transducer to a known pressure signal and measuring the valve response, as described by Pinsley (1988).

mass flow will fluctuate as shown by points b and b' on the solid curve. If the throttle area is varied to be in phase with $\delta\Delta P_p$, however, the mass flow fluctuations can be considerably increased, as indicated by points a and a' on the dashed line, which represents the instantaneous throttle line seen by the system. Increasing the gain thus decreases the slope of the throttle line, relative to the fixed geometry throttle, and increases the mass flow perturbations (and hence the overall dissipation) to suppress the system dynamic instability. If the slope of the throttle line is decreased too far, however, it will become less steep than the compressor characteristic slope, so that the system becomes statically unstable. The flattest permissible slope occurs when the second bracketed term in Eq. (4) becomes equal to 0; this sets the maximum gain.

Using the above result, the requirement for the first bracketed term in Eq. (4) to be positive implies that the slope of the compressor characteristic is equal to $1/B$ at maximum gain. For given B, the limit of stabilization using the controller will thus occur at the point on the nondimensional compressor characteristic where the slope $(\overline{d\psi_c}/d\phi)$ is $1/B$. This slope can be compared with that for the natural surge point, which occurs at a value of $(\overline{d\psi_c}/d\phi)$, given by

$$\left(\frac{\overline{d\psi_c}}{d\phi}\right) = \frac{1}{B^2\left(\dfrac{\partial\psi_T}{\partial\phi}\right)_{A_T}}$$
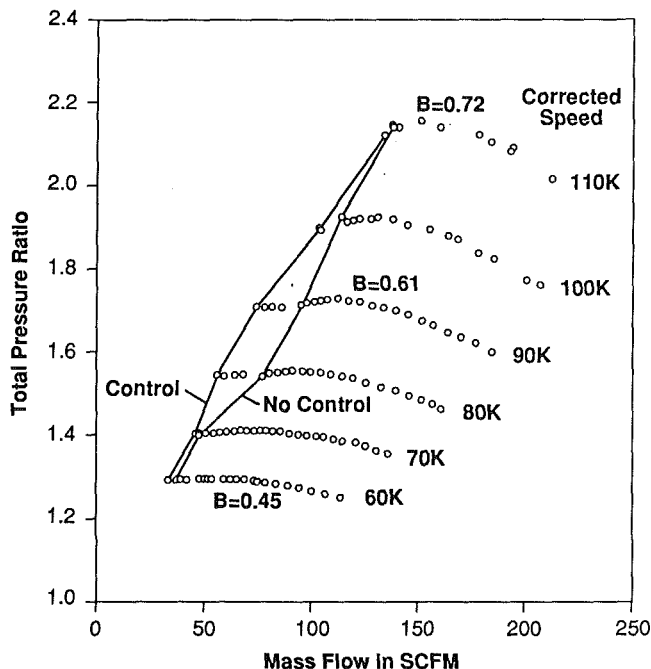
or, for a parabolic throttle curve,

Fig. 6 Compressor map showing experimentally determined effectiveness of the active control on displacing the surge line (Case I); surge line shown as solid line

Experimental Results

The effect of the controller on the compression system was evaluated from both time-averaged and time-resolved measurements. Time-resolved measurements were taken at steady-state (this includes periodically varying) operating conditions, as well as during transients, in order to illustrate the unsteady system behavior.

The most basic task of the controller is to shift the surge line to lower mass flows. Time-averaged measurements of the surge line were thus made with and without the control applied. These data are also used to examine the predicted trends with variations in B-parameter.

Time-resolved measurements were taken to examine the dynamics of the controlled compression system. The unsteady behavior of the compression system without the controller was first measured as baseline. The measurements were then repeated using the controller, with the compressor operating in both stable and unstable modes. Time-resolved measurements were also used to examine the dependence of surge characteristics on the B-parameter.

Time-Averaged Measurements. Compressor performance will be represented two ways: (1) in a conventional turbocharger map format: inlet total to plenum static pressure ratio versus standard corrected flow (in ft^3/min), and (2) as a nondimensional pressure rise

$$\psi = \frac{P_p - P_o}{\frac{1}{2}\rho_o U^2} \qquad (7)$$

versus nondimensional flow coefficient

$$\phi = \frac{C_x}{U} = \frac{\dot{m}}{\rho_o U A_{in}} \qquad (8)$$

where C_x is the axial velocity at the impeller inlet annulus and U is the rotor tip speed. This is more relevant for discussion of the fluid mechanic behavior, since the compressor curves for different speeds are roughly similar.

Figure 6 shows the compressor map for Case I, in the form

of pressure ratio versus mass flow for various corrected speeds. The values of the B-parameter are also indicated. Pressure ratio at surge ranges from approximately 1.3 at 60K rpm to 2.15 at 110K rpm. At the high speeds with the fixed throttle, surge occurs slightly to the left of the peak of the constant speedlines, at locations where the characteristic is slightly positively sloped. At the lowest speeds (60–70K rpm), the slope to the left of the peak is quite shallow and surge occurs at a mass flow much lower than the peak value. A *"knee"* in the speedline is thus observed between the 70K and 80K rpm speedlines.

Figure 6 also shows the region stabilized by the introduction of the controller. To obtain the controlled surge line, the compressor was brought close to surge on each speedline and the controller turned on at fixed gain. The control valve was closed down until the lowest attainable flow rate before deep surge (oscillations with flow reversal) was measured. The throttle was then opened, the gain increased, and the process repeated to reach another controlled operating point at the lowest stable mass flow. In these experiments the phase of the controller (i.e., the phase between pressure and throttle area perturbations) was fixed at 0 deg since, as the theoretical results predicted, attempts made with the controller at other values of phases were not as effective in decreasing the surge mass flow.

With the control operational at 80K and 90K rpm, there was a 20–25 percent decrease in surge mass flow compared to the no-control surge point. At 100K rpm, there was only slight extension of the stable region, while at 60–70K and 110K rpm the extension was negligible. There are thus two regimes in which the controller was ineffective: speeds below the "knee" of the surge line and high speeds. To examine the reason for this, tests were carried out at different speeds while holding B constant, as well as at different values of B holding speed constant. The tests were done to isolate effects of system dynamics from effects that had to do primarily with tip Mach number (or pressure ratio), for example, through variation of the speedline shapes. Stated another way, the goal of the parametric variations was to ensure that effects associated with tip Mach number alone did not limit the control scheme.

Several experiments were carried out. First, a compressor map was obtained for a system geometry with B-parameter larger by a factor of 2.7 at the same compressor speed, the "Case II" configuration. The results are shown as the solid lines in Fig. 7. The knee in the surge line has shifted down in speed due to the increased B-parameter with, again, no surge improvement achieved below the knee. The highest speed at which control is effective has also shifted to lower speed. Further, at speeds where the control was effective, the experiments that were done at the smaller B had greater increase in stable mass flow range. As was indicated by the analysis, therefore, the B-parameter plays an important role not only in determining the system stability, but also in determining the degree of control effectiveness that can be achieved.

Measurements were also made at the same value of B at two different speeds, 70K and 90K (for Case III and Case I, respectively). The results are shown in Fig. 8. Although the speedlines are not quite identical and the surge point does not occur at precisely the same value of ϕ, the shifts in the surge lines due to control are similar. We infer from this that, over the range of parameters examined, it is the increase in B-parameter (which represents a change in the system dynamic behavior) rather than the increase in tip Mach number that limits the effectiveness of the control.

The overall conclusions from the time-averaged measurements can be summarized as follows: The active control stabilizes the system at flows below the natural surge point; the compressor pressure rise in controlled operation remains near the pre-surge level; the control effectiveness decreases as B increases; and the position of the surge line knee is a function of B.
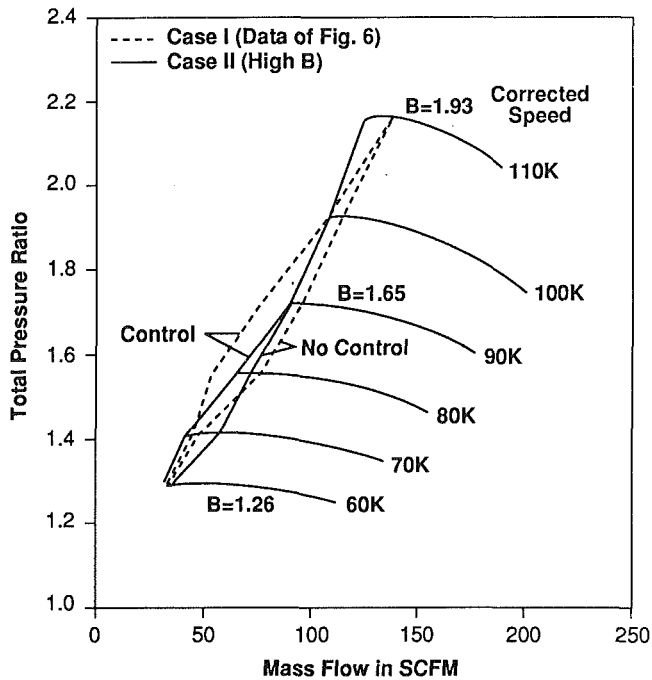
Fig. 7 Compressor map showing experimentally determined effectiveness of the active control on displacing the surge line for higher B (Case II)
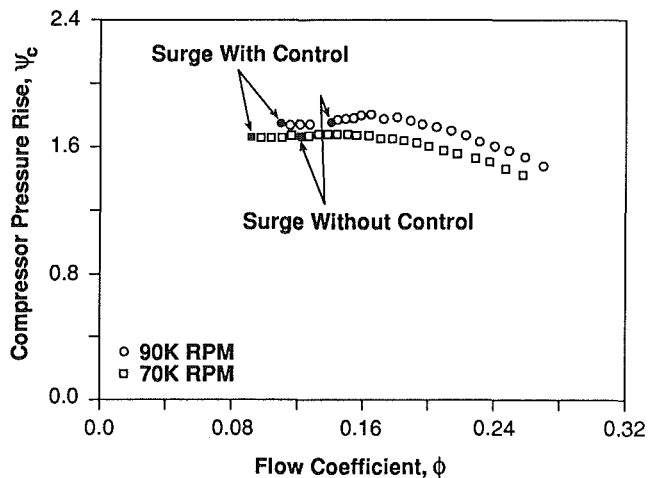

Fig. 8 70K and 90K rpm compressor characteristics at the same value of B

Time-Resolved Measurements. Although the time-averaged measurements confirmed that simple proportional control can provide significant stabilization of the system under a variety of operating conditions, the dynamic behavior of the system was also examined to explore the detailed operation of the controller. Time-resolved measurements were taken of the system pressure rise (inlet to plenum), and control valve area. From these, the time-resolved mass flow could be inferred from a mass flow balance, assuming an isentropic process in the plenum. The results of the measurements are presented in the time domain and in the nondimensional pressure rise–mass flow plane. Uncertainty in the unsteady plenum pressure is less than 1 percent of the maximum fluctuation amplitude; uncertainty in the unsteady component of the mass flow is approximately ±6 percent for deep surge and ±4 percent for mild surge for the 90K rpm conditions shown below.

With the system in the nominal (Case I) configuration, the fluctuations in pressure rise and mass flow coefficients (ψ' and ϕ') were measured at different flow coefficients along a 90K speedline. The time-mean performance is plotted in Fig.
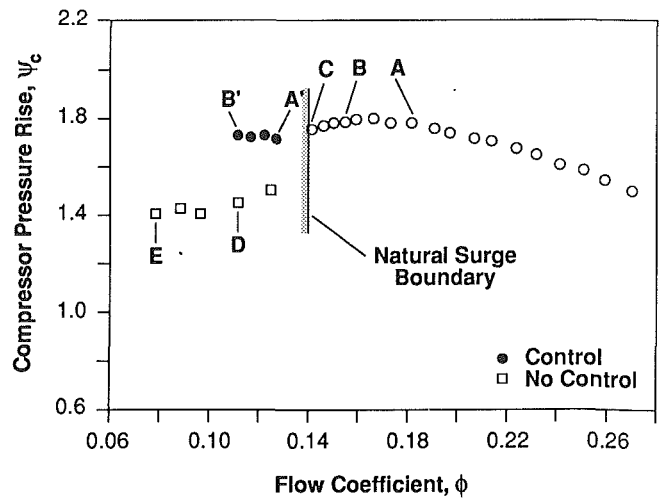

Fig. 9 Speedline indicating time-mean operating points for transient measurements
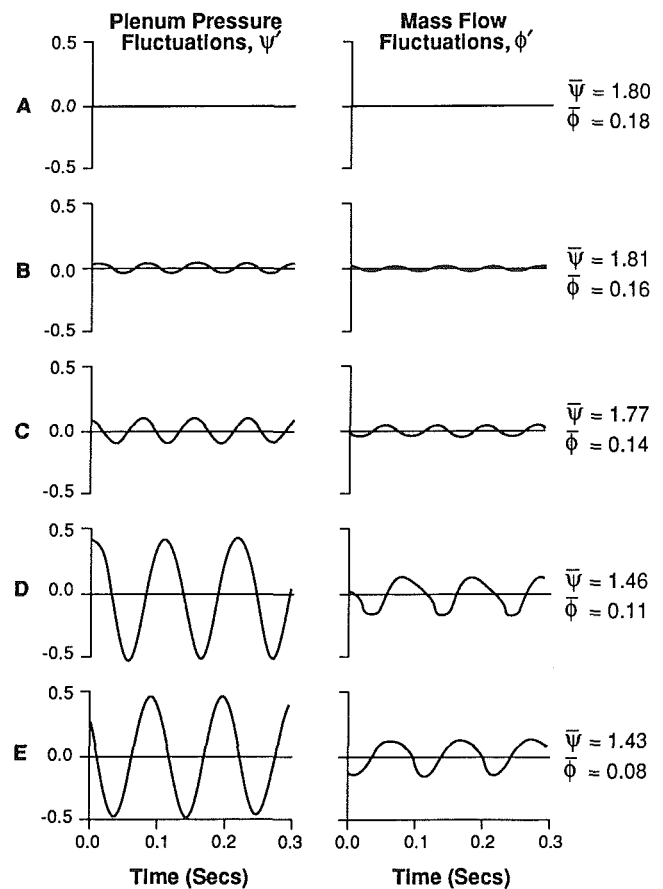

Fig. 10 Time-resolved compressor performance without control at points A-E, as indicated on Fig. 9

9 to show the conditions at which the data were taken, both with and without the control. The natural surge boundary is also indicated.

Figure 10 shows the fluctuations at points A–E, with no control applied. At point A, which lies to the right of the peak in the compressor characteristic, the compressor is operating stably. The fluctuations in pressure rise and mass flow are on the order of the noise in the system. Oscillations appear at point B, just to the left of the peak, at a frequency of 13.5 Hz, compared to the predicted Helmholtz frequency of 15.5 Hz. At this point, the slope of the compressor characteristic is very shallow and the compressor is operating in mild surge.
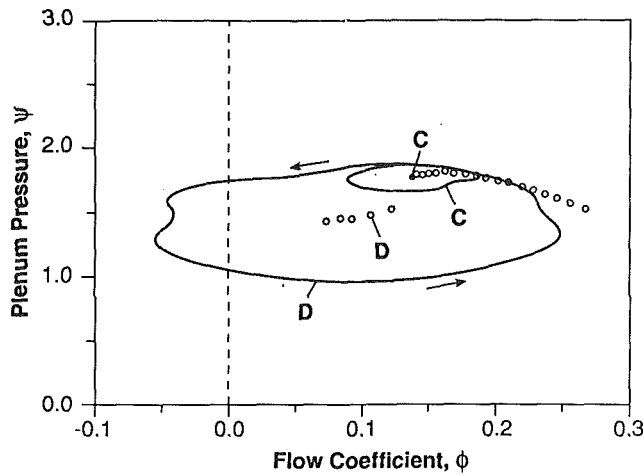
Fig. 11 Dynamic trajectory of instantaneous compressor operating points; time-mean operating points corresponding to points C and D in Fig. 9
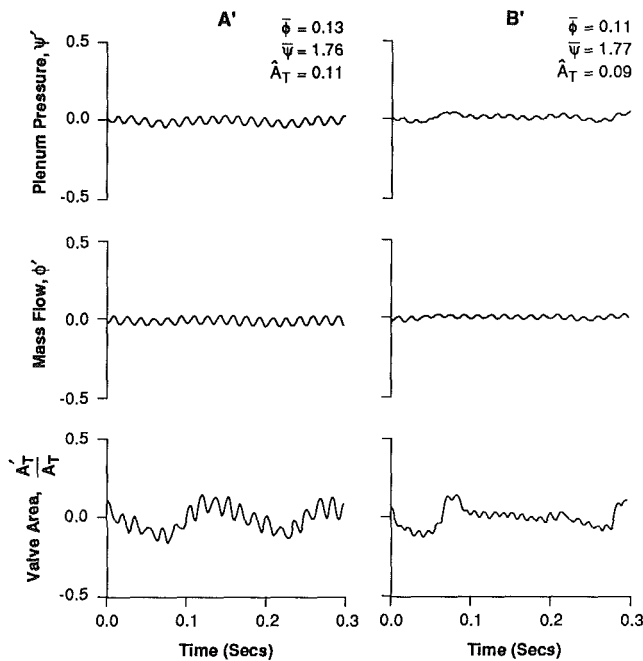

Fig. 13 Reduction in amplitude of peak pressure fluctuations with feedback control; mild surge and deep surge

Fig. 12 Time-resolved compressor performance with controller, time-mean operating points A′ and B′, as indicated on Fig. 9

Fig. 14 Transient behavior of system initially in deep surge during controller turn-on

Point C is the last stable operating point before deep surge. The compressor is still in mild surge, but the amplitude of the fluctuations has increased and the frequency has decreased slightly to 13 Hz. Points D and E show the system behavior in deep surge. The oscillations in plenum pressure and mass flow are much larger with variations in mass flow of more than ±100 percent of the steady-state value. The lowering of the frequency to roughly 9 Hz is due to the time associated with plenum blowdown and repressurization (Fink, 1988).

Figure 11 portrays the dynamic behavior in the pressure-flow plane. The figure shows a mild surge oscillation, which is associated with operation at time-averaged point C, as well as a deep surge oscillation associated with operation at point D. These time-mean points are indicated for reference. The direction in which the cycles are traced out is counterclockwise. The mass flow reversal during a portion of each deep surge cycle is evident.

The points labeled A′ and B′ in Fig. 9 show the performance with the controller. The flow coefficient at the surge point has been shifted from 0.142 to 0.112 (at point B′), a change of
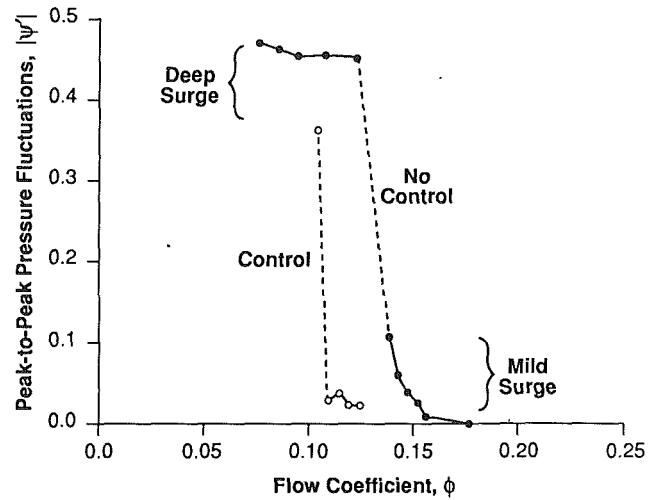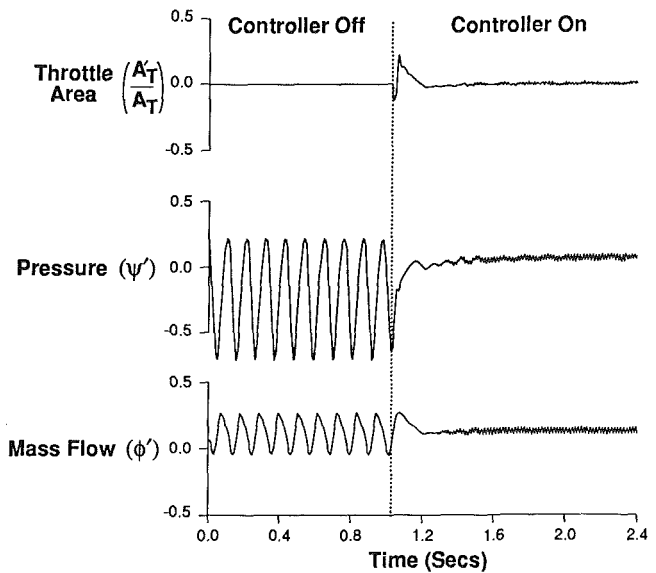
21 percent, and the compressor pressure rise is stabilized near the same level as prior to surge. The fluctuations in nondimensional mass flow, pressure rise, and valve area are plotted in Fig. 12 for each indicated controlled point. The suppression of the oscillations shown in Fig. 10 is evident; it can also be seen that there is a higher frequency now present, with a strong component at 60 Hz. This frequency is well above any that the authors associate with system aerodynamics alone, and it is suspected that it is associated with the controller dynamics.

An alternative way to examine the effect of control on the pressure fluctuations in the system is to examine the peak amplitudes as a function of flow. This is shown in Fig. 13 for the 90K speedline. With the control, the amplitude is suppressed at flow coefficients below the natural surge value to a level below that of mild surge. Even when surge can no longer be avoided, the peak amplitude of the fluctuations remains lower than those without control.

The transient behavior of the system when the control is turned on or off is also of interest as a measure of control effectiveness. Figure 14 shows the nondimensional fluctuations in the valve area and plenum pressure, as well as the variations in mass flow in the system during a transient from deep surge with the controller off, to stable operation with the controller on. (This figure can be compared with Fig. 15 of Ffowcs
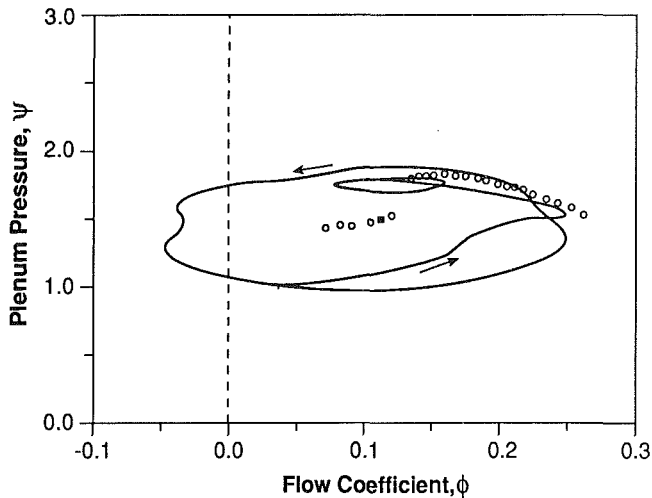
Fig. 15 Dynamic trajectory of instantaneous compressor operating point during controller turn-on transient; system initially in deep surge
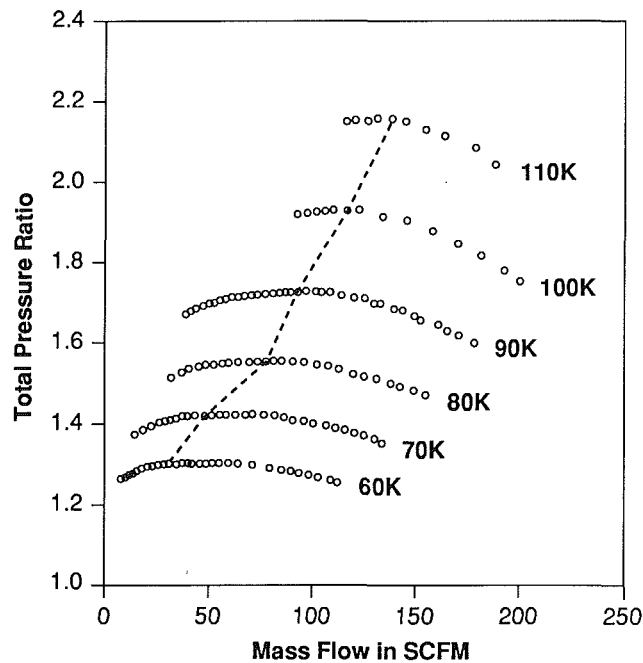

Fig. 16 Compressor map with close-coupled throttle to increase stable flow range

Williams and Huang (1989).) In the figure, time is given in dimensional form to show the actual temporal characteristics of the valve action. At $t = 1.03$ seconds, the controller is switched on at a previously set controller gain and phase. The controller captures the surge fluctuations within one to two surge cycle periods, even though the system is operating in a highly nonlinear regime. Figure 15 shows this behavior in the pressure rise–mass flow plane; the nonlinear character of the behavior prior to controller application is evident. The time mean point at the start is indicated by the solid square. Note that, although implementation of the controller shifted the time-averaged operating point along a constant throttle line from $\phi = 0.11$ to 0.12, the stabilized operating point remains within the region in which surge was encountered with no control.

Evaluation of Lumped Parameter Model

In this section, we examine the extent to which the simple, lumped parameter description is useful for active control investigations. Before describing the conclusions reached with respect to model applicability, some comments are in order
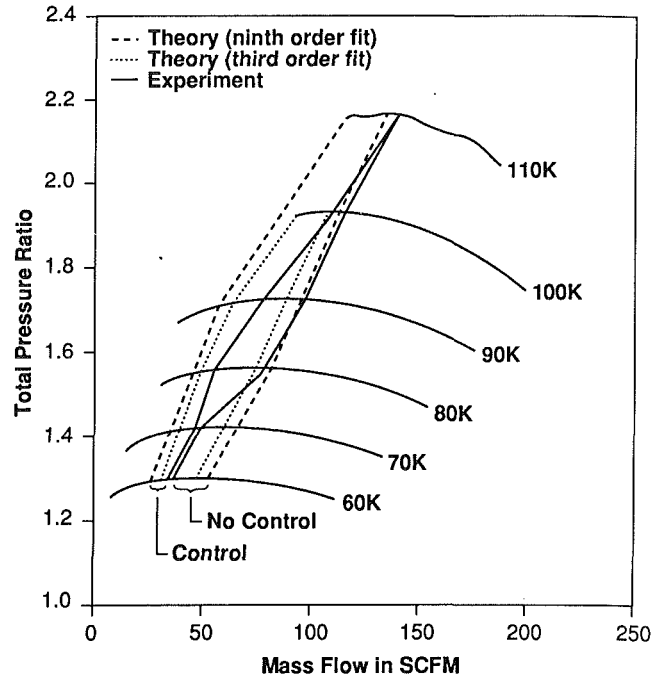

Fig. 17 Comparison of measured and theoretical compressor stability boundaries, with and without control

respect to model applicability, some comments are in order about the spirit in which the analysis is put forth. We have taken a very simple look at a complex dynamic system, whose parametric dependence was largely unexplored. The reasoning is that active control is a new area, and a high priority is to extract information about the central trends of the overall behavior rather than the detailed structure of the internal flow. Lumped parameter models have long been used in this regard and the comparison here is really focused on just one aspect of their application, the use for assessing the effect of the control action. The aim is to verify this for the present system, so as to have a reliable tool for exploring more sophisticated schemes.

In applying a lumped (or even distributed) parameter analysis, one must develop a model for the energy addition due to the compressor, which is the active element in the system. In keeping with the above intent, we have taken the compressor performance as quasi-steady so that the steady-state measured characteristic is used to represent the dynamic behavior. The steady-state characteristic can be obtained down to flows beyond the surge points shown in Figs. 6 and 7 by running the compressor with a close-coupled throttle valve. This greatly decreases the system volume (and hence the B-parameter) and increases the system stability (Dussourd et al., 1977). In the present series of experiments, the throttle valve was placed at the exit of a short pipe downstream of compressor discharge, so that the volume was reduced by a factor of 20 (B-parameter reduction of roughly 4.5). The results of doing this are shown in Fig. 16, which is a compressor map for the close coupled configuration. The instability onset points for the close-coupled geometry are the left-most data points on each speedline. Also indicated on the figure, by the dashed line, is the surge line for the previous Case I configuration (Fig. 6). The large difference in stable flow range will be discussed subsequently; here we merely note that the compressor characteristic is defined over a sufficient range that there need be no extrapolation for any of the stability computations that are discussed.

The most global considerations are those of system stability. Figure 17 thus shows the experimentally measured surge inception (solid line) for Case I, both with and without control, superimposed on compressor characteristics that are a ninth-order fit to the actual data. Two sets of theoretical calculations
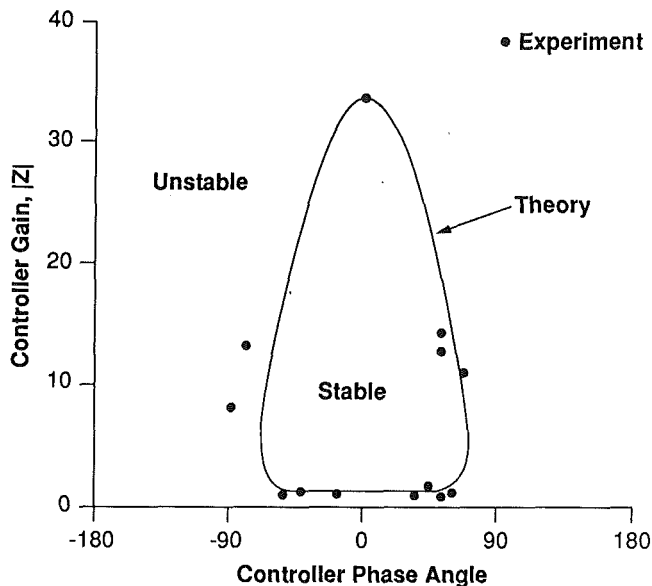
Fig. 18 Comparison of experimental and theoretical stability boundary in gain-phase space

of the instability onset are also shown: one based on the ninth-order fit shown, and one based on a third-order fit. We show both because we have examined the effects of various other fitting schemes, and these are a good representation of the spectrum of those used.

Two points can be made concerning the results shown. One is that the trends of the theory and data are in agreement at the speedlines where the control is effective, although precise quantitative predictions of the surge point are not achieved. The diminishment of control effectiveness at high and low speeds, however, is not well predicted. The second point is that, for the types of fit we examined, small changes in the fitting procedure (and thus the local slope of the curve) significantly change the predicted instability point. Thus, one can capture the *trends* in stability quite well with lumped parameter models, but uncertainties in the local slopes make precise predictions of absolute values difficult. Further comments on the ability of the basic model to illustrate system transients are given by Gysling (1989) and Fink (1988). They also conclude that the lumped parameter model is extremely useful for understanding the system behavior, but that precise numerical values for mass flow at instability onset are too much to ask for these flat compressor characteristics.

Beyond the stability prediction, one can examine other aspects of the system behavior. For example, one prediction discussed previously is that there is a closed region in the controller gain-phase plane where stable operation may be achieved. The stable gain range decreases as the phase is shifted either positively or negatively from zero, so that at a large enough magnitude of controller phase, no amount of gain will stabilize the system. Comparison between the measured stability boundary and the theoretical prediction is made at $90K$ rpm for the nominal configuration (Fig. 18). In carrying out the calculations, the compressor characteristic slope was set to match the maximum gain at zero degrees phase and the steady-state values of ϕ and ψ were taken from measurements.

Discussion and Comments on Future Research

The experiments reported on here basically represent a proof of concept demonstration that active control can be an effective means of suppression of centrifugal compressor surge. The present strategy is by no means optimal and, in fact, one reason for choosing it was that the different system components were felt to be (relatively!) easily understood and integrated. Studies have been carried out since the throttle control experiments

were completed, and these indicate that one can avoid the strong fall-off in effectiveness with B by using alternative methods (Simon, 1989). In particular, one approach that has been explored analytically is to position the valve downstream of the compressor, between compressor and plenum.

As mentioned, the stabilizing effect of a close coupled throttle has been demonstrated previously (Dussourd et al., 1976) using a *steady-state* device. The effect in the present system was illustrated in Fig. 16, which showed substantial range increase with reference to the nominal Case I surge line. To obtain this range, however, it was necessary to take a large pressure drop across the close coupled throttle, and this can be unacceptable in practice. This is not true, however, if one uses a time-varying throttle. While there is a trade between the time-averaged pressure drop that one takes across a close-coupled throttle and the increase in stable flow range, the pressure drops appear, from calculations we have carried out so far (Simon, 1989), to be considerably less than with fixed area devices. Implementation of such close coupled controls in compression systems appears to offer considerable potential and is a topic that is being aggressively pursued.

Summary and Conclusions

A theoretical and experimental study has been carried out on active control of centrifugal compressor surge. The experiments, which utilized a fast-acting downstream throttle valve, demonstrate that it is possible to suppress the growth of small-amplitude perturbations, thereby stabilizing the system, and allowing operation in previously inaccessible, because unstable, regimes. Specifically, with the controller, the minimum mass flow for stable operation was reduced by 20–25 percent from the natural surge point, with no degradation in system performance. Further, even in surge, the controlled system exhibited smaller pressure oscillations than the system without control. Because the control strategy is based on suppression of small disturbances before they grow into surge, the power needed and the amount of actuation can be extremely small.

Lumped parameter models appear to be adequate to capture the primary characteristics of the system behavior. Such models predict that effectiveness of control is strongly dependent on the system B-parameter and the slope of the compressor characteristic; these trends were confirmed experimentally.

The control achieved with the simple proportional control scheme used suggests that significant improvements are likely with more complex controllers or with different mechanisms/ locations for the actuation. Active control thus appears as a promising tool for increasing the range of stable operation and relaxing constraints on compressor operation.

References

Boyce, M. P., et al., 1983, "Tutorial Session on Practical Approach to Surge

and Surge Control Systems," in: *Proceedings of the Twelfth Turbomachinery Symposium*, Texas A&M University Turbomachinery Laboratories.

Dussourd, J. L., Pfannebecker, C. W., and Singhania, S. K., 1977, "An Experimental Investigation of the Control of Surge in Radial Compressors Using Close Coupled Resistances," ASME *Journal of Fluids Engineering*, Vol. 99, pp. 64–76.

Emmons, H. W., Pearson, C. E., and Grant, H. P., 1955, "Surge and Stall Propagation," *Trans. ASME*, Vol. 77, pp. 455–469.

Epstein, A. H., Ffowcs Williams, J. E., and Greitzer, E. M., 1989, "Active Suppression of Aerodynamic Instabilities in Turbomachines," *J. Propulsion and Power*, Vol. 5, Mar.–Apr., pp. 204–211.

Ffowcs Williams, J. E., and Huang, X., 1989, "Active Stabilization of Compressor Surge," *J. Fluid Mechanics*, Vol. 204, pp. 245–262.

Fink, D. A., 1988, "Surge Dynamics and Unsteady Flow Phenomena in Centrifugal Compressors," MIT Gas Turbine Laboratory Report No. 193.

Greitzer, E. M., 1981, "The Stability of Pumping Systems—The 1980 Freeman Scholar Lecture," ASME *Journal of Fluids Engineering*, Vol. 103, pp. 193–242.

Gysling, D. L., 1989, "Dynamic Control of Centrifugal Compressor Surge Using Tailored Structure," M. S. Thesis, Department of Aeronautics and Astronautics, Massachusetts Institute of Technology.

Ludwig, G. R., and Nenni, J. P., 1980, "Tests of an Improved Rotating Stall Control System on a J-85 Turbojet Engine," ASME Paper No. 80-GT-17.

Pinsley, J. E., 1988, "Active Control of Centrifugal Compressor Surge," M.S. Thesis, Department of Aeronautics and Astronautics, Massachusetts Institute of Technology.

Simon, J., 1989, Private Communication.

Staroselsky, N., and Ladin, L., 1979, "Improved Surge Control for Centrifugal Compressors," *Chemical Engineering*, pp. 175–184.

APPENDIX

Derivation of the System Equations

Consider the compression system shown in Fig. 1. The following assumptions are made: quasi-steady compressor and throttle behavior; uniform pressure throughout the plenum; isentropic behavior in the plenum; incompressible one-dimensional flow in the ducts; and negligible throttle inertance.

The integral form of the one-dimensional momentum equation for the compressor duct is

$$P_0 - P_1 = \rho \frac{dC_x}{dt} L_c - \Delta P_c \qquad (A1)$$

where L_c is an equivalent compressor duct length chosen to give the same dynamic response as the actual system. In terms of compressor mass flow, this can be written as:

$$P_0 - P_1 = \frac{L_c}{A_{in}} \frac{d\dot{m}_1}{dt} - \Delta P_c \qquad (A2)$$

The equation for the throttle duct pressure drop is:

$$P_1 - P_0 = \Delta P_T \qquad (A3)$$

where ΔP_T is the pressure drop across the throttle.

The throttle and compressor mass flows are linked by mass conservation in the plenum:

$$\dot{m}_1 = \dot{m}_2 + V_p \frac{d\rho_p}{dt} \qquad (A4)$$

where V_p is the plenum volume. Using the isentropic relation, this becomes

$$\dot{m}_1 = \dot{m}_2 + \frac{V_p}{a_1^2} \frac{dP_p}{dt} \qquad (A5)$$

Equations (A2), (A3), and (A5) describe the unsteady behavior of the compression system. To examine the system stability the equations are linearized about a mean operating point, with flow variables written as:

$$( ) = (\bar{\ }) + \delta( ). \qquad (A6)$$

The compressor pressure rise is

$$\Delta P_c = \overline{\Delta P_c} + \frac{\overline{d\Delta P_c}}{d\dot{m}} \delta \dot{m}_1 \qquad (A7)$$

Equation (A7) is based on the assumption that the instantaneous compressor pressure rise/flow characteristic is quasi-steady. It is shown by Fink (1988) and Gysling (1989) that this is not precisely true but that the effect on stability, which is the point investigated here, is small.

The throttle pressure drop is given by

$$\Delta P_T = \overline{\Delta P_T} + \left(\frac{\partial \overline{\Delta P_T}}{\partial \dot{m}} \right)_{A_T} \delta \dot{m}_2 + \left(\frac{\partial \overline{\Delta P_T}}{\partial A_T} \right)_{\dot{m}} \delta A_T \qquad (A8)$$

In Eqs. (A7) and (A8), overbars designate mean flow properties and A_T is the throttle valve area.

We nondimensionalize the pressures by $1/2 \rho_0 U^2$, the flow by $\rho_0 U A_{in}$, the time by $1/\omega_H$ (where ω_H is the Helmholtz resonator frequency of the system, defined in the nomenclature), and the areas by A_{in}. The nondimensional pressure and flow are denoted by ψ and ϕ. In addition, we define the nondimensional stability parameter, B, as:

$$B = \frac{U}{2\omega_H L_c} = \frac{U}{2a_1} \sqrt{\frac{V_p}{L_c A_{in}}} \qquad (A9)$$

We utilize the nondimensional derivatives of the compressor and throttle in the expression for compressor pressure rise and throttle pressure drop perturbations as follows:

$$\delta\psi_c = \left(\frac{d\psi_c}{d\phi} \right) \delta\phi_1 \quad \text{(nondimensional compressor pressure rise)}$$

$$\delta\psi_T = \left(\frac{\partial \psi_T}{\partial \phi} \right)_{A_T} \delta\phi_2 + \left(\frac{\partial \psi_T}{\partial \hat{A}_T} \right) \delta\hat{A}_T \quad \text{(throttle pressure drop)}$$

where $\hat{A}_T$ is the nondimensional area A_T/A_{in}.

Using Eqs. (A7) and (A8) in Eqs. (A2), (A3), and (A5), and nondimensionalizing, the resulting three equations can be combined into two, first-order, linearized equations involving $\delta\phi$, the nondimensional compressor mass flow perturbation, and $\delta\psi$, the nondimensional plenum pressure perturbation. These are Eqs. (1) and (2) in the main text.